

2000

Flow visualization and pressure drop for refrigerant phase change and air-water flow in small hydraulic diameter geometries

John Wesley Coleman
Iowa State University

Follow this and additional works at: <https://lib.dr.iastate.edu/rtd>

 Part of the [Chemical Engineering Commons](#), [Mechanical Engineering Commons](#), and the [Nuclear Engineering Commons](#)

Recommended Citation

Coleman, John Wesley, "Flow visualization and pressure drop for refrigerant phase change and air-water flow in small hydraulic diameter geometries " (2000). *Retrospective Theses and Dissertations*. 12317.
<https://lib.dr.iastate.edu/rtd/12317>

This Dissertation is brought to you for free and open access by the Iowa State University Capstones, Theses and Dissertations at Iowa State University Digital Repository. It has been accepted for inclusion in Retrospective Theses and Dissertations by an authorized administrator of Iowa State University Digital Repository. For more information, please contact digirep@iastate.edu.

INFORMATION TO USERS

This manuscript has been reproduced from the microfilm master. UMI films the text directly from the original or copy submitted. Thus, some thesis and dissertation copies are in typewriter face, while others may be from any type of computer printer.

The quality of this reproduction is dependent upon the quality of the copy submitted. Broken or indistinct print, colored or poor quality illustrations and photographs, print bleedthrough, substandard margins, and improper alignment can adversely affect reproduction.

In the unlikely event that the author did not send UMI a complete manuscript and there are missing pages, these will be noted. Also, if unauthorized copyright material had to be removed, a note will indicate the deletion.

Oversize materials (e.g., maps, drawings, charts) are reproduced by sectioning the original, beginning at the upper left-hand corner and continuing from left to right in equal sections with small overlaps.

Photographs included in the original manuscript have been reproduced xerographically in this copy. Higher quality 6" x 9" black and white photographic prints are available for any photographs or illustrations appearing in this copy for an additional charge. Contact UMI directly to order.

Bell & Howell Information and Learning
300 North Zeeb Road, Ann Arbor, MI 48106-1346 USA
800-521-0600

UMI[®]

**Flow visualization and pressure drop for refrigerant phase change and air-water
flow in small hydraulic diameter geometries**

by

John Wesley Coleman

**A dissertation submitted to the graduate faculty
in partial fulfillment of the requirements for the degree of
DOCTOR OF PHILOSOPHY**

Major: Mechanical Engineering

Major Professor: Srinivas Garimella

Iowa State University

Ames, Iowa

2000

Copyright © John Wesley Coleman, 2000. All rights reserved.

UMI Number: 9990441

**Copyright 2000 by
Coleman, John Wesley**

All rights reserved.

UMI[®]

UMI Microform 9990441

Copyright 2001 by Bell & Howell Information and Learning Company.

**All rights reserved. This microform edition is protected against
unauthorized copying under Title 17, United States Code.**

**Bell & Howell Information and Learning Company
300 North Zeeb Road
P.O. Box 1346
Ann Arbor, MI 48106-1346**

**Graduate College
Iowa State University**

**This is to certify that the Doctoral dissertation of
John Wesley Coleman
has met the dissertation requirements of Iowa State University**

Signature was redacted for privacy.

Major Professor

Signature was redacted for privacy.

For the Major Program

Signature was redacted for privacy.

For the Graduate College

To my parents - John and Terry Coleman, for their support, without which I could never have accomplished so much. They are indeed my true heroes. — Kim Chaewchansilp, whose moral support helped me through many tough times. — Irwan Salim — whose kindness and generosity keeps me ever focused on my work.

TABLE OF CONTENTS

LIST OF FIGURES	viii
LIST OF TABLES	xv
NOMENCLATURE	xvi
ACKNOWLEDGEMENTS	xix
ABSTRACT	xx
CHAPTER ONE. INTRODUCTION	1
CHAPTER TWO. LITERATURE REVIEW	6
Flow Regime Mapping	6
Previous Research on Large Diameter Circular Tubes	6
Previous Research on Small Diameter Circular Tubes	14
Previous Research on Rectangular Tubes	16
Need for Further Research on Flow Regime Mapping	19
Two-Phase Pressure Drop	20
Previous Research on Large Hydraulic Diameter Tubes	21
Previous Research on Small Hydraulic Diameter Tubes	25
Need for Further Research on Pressure Drop	26
CHAPTER THREE. EXPERIMENTAL SETUP	28
Adiabatic Air-Water Flow Visualization	28
Refrigerant Two-Phase R-134a Flow Visualization	31
Test Facility	32
Post-Condensers, Pump, Evaporator and the Pre-Condensers	32
The Test Section	36
Instrumentation and Data Acquisition	37
Experimental Procedures	38
System Charging	38
System Start-up	39
Test Condition Establishment and Energy Balances	40
Refrigerant R-134a Two-Phase Pressure Drop Experiments	45
Geometry of the Pressure Drop Test Section	46
Pressure Drop Test Section	49
Uncertainty Analysis	49
CHAPTER FOUR. DATA ANALYSIS AND RESULTS	51
Adiabatic Air-Water Flow Visualization Experiments	51
Adiabatic Flow Regime Descriptions	51
Stratified Flow Regime	51

Intermittent Flow Regime	52
Annular Flow Regime	52
Dispersed Flow Regime	55
Circular Tube Results	55
Rectangular Tube Results	57
R-134a Flow Visualization Experiments	59
Condensing Flow Regime Definitions	59
Annular Flow Regime	61
Wavy Flow Regime	61
Intermittent Flow Regime	63
R-134a Flow Regime Maps	64
Choice of Flow Regime Map Coordinates	64
Circular 4.91 mm Tube	65
Square 4x4 mm Tube	66
Square 3x3 mm Tube	67
Square 2x2 mm Tube	68
Square 1x1 mm Tube	68
Rectangular 4 mm (Height) x 2 mm (Width) Tube	70
Rectangular 2 mm (Height) x 4 mm (Width) Tube	71
Rectangular 6 mm (Height) x 4 mm (Width) Tube	72
Rectangular 4 mm (Height) x 6 mm (Width) Tube	72
R-134a Pressure Drop Experiments	73
Single Phase Pressure Drop Validation Results	73
Two-Phase Pressure Drop	82
Circular Tube C193	82
Circular Tube C120	82
Circular Tube C60	85
Circular Tube C30	85
Circular Tube C20	85
Square Tube S30	89
Barrel Shaped Tube B32	89
Triangular Tube T33	90
“N” Shaped Tube N21	90
Rectangular Tube RK15	92
Triangular Insert Tube W29 (I and II)	92
“Zero Length” Tubes ZLI and ZLII	94
Expansion, Contraction, and Decelerational Losses	96
The Decelerational Component	96
Expansion and Contraction Pressure Drop	97
 CHAPTER FIVE. DISCUSSION OF RESULTS	 110
Adiabatic Air-Water Flow Regimes	110
Comparison With Taitel and Dukler (1976) Results	110
Comparison with Damianides and Westwater (1988) and Fukano et al. (1989)	113

Comparison with Weisman et al. (1979)	113
R-134a Flow Regimes	116
Baseline Case Comparisons	116
Comparison with the Baker (1959) and Taitel and Dukler (1976) Maps	116
Comparison with Weismann et al. (1979)	119
Comparison with the Data of Wang et al. (1997)	121
Comparison with Troniewski and Ulbrich (1984) and Wambsganss et al. (1991)	122
Effects of Tube Shape, Hydraulic Diameter, and Aspect Ratio on Transition Lines	128
Effect of Tube Shape on Transition Lines	128
Effect of Hydraulic Diameter on Transition Lines	132
Effect of Aspect Ratio on Transition Lines	137
Flow Regime Transition Correlations in Microchannel Geometries	139
The Transition From Intermittent Flow	146
Wavy Flow Regime Boundaries	150
Transition to Annular Film and Mist Flow	157
R-134a Pressure Drop Experiments	157
Baseline Case Comparisons	160
The Lockhart-Martinelli (1949) Correlation	161
The Chisholm (1973) Correlation	162
The Friedel (1979) Correlation	166
De Souza and de Mattos-Pimenta (1995)	168
Yang and Webb (1996)	169
Wang et al. (1997)	169
Yan and Lin (1998)	170
Flow Regime Models	172
Intermittent and Discrete Wave Flow Model	172
Circular Tubes	172
Non-Circular Geometries	177
Annular Film and Disperse Wave Flow Model	179
Circular Tubes	179
Non-Circular Geometries	185
Annular Film and Mist Flow Model	187
Circular Tubes	187
Non-Circular Geometries	188
Mist Flow Model	191
Circular Tubes	191
Non-Circular Geometries	191
Overall Model Predictions	195
Effect of Hydraulic Diameter and Tube Shape on Pressure Drop	209

CHAPTER SIX. CONCLUSIONS AND RECOMMENDATIONS FOR FUTURE WORK	216
APPENDIX A – RESULTS OF INSTRUMENTATION CALIBRATION	221
APPENDIX B – UNCERTAINTY ANALYSIS	224
APPENDIX C – ALBUM OF FLUID VISUALIZATION	231
APPENDIX D – SINGLE PHASE TESTS AND TUBE VALIDATION	277
APPENDIX E – ADIABATIC AND CONDENSING PRESSURE DROPS	284
APPENDIX F – EXPERIMENTAL TRANSITION CORRELATIONS	290
APPENDIX G – ROUND TUBE ΔP COMPARISON WITH LITERATURE	295
REFERENCES CITED	304
BIOGRAPHICAL SKETCH	311

LIST OF FIGURES

Figure 1. Example of a Multilouvered Flat-Tube Heat Exchanger	2
Figure 2. Test Matrix for the Air-Water Flow Visualization Study	28
Figure 3. Air-Water Flow Visualization Test Facility	29
Figure 4. Test Matrix for Condensation Flow Visualization	32
Figure 5. Schematic of the Condensation Test Facility	33
Figure 6. Photograph of the Condensation Test Facility	34
Figure 7. Test Section Schematic for Phase II	36
Figure 8. Schematic of the Pressure Drop Test Sections	45
Figure 9. Schematic of the R-134a Pressure Drop Test Section	47
Figure 10. Air-Water Flow Regime Descriptions	53
Figure 11. Time Lapse Photographs for $t = 0.000, 0.033$ and 0.066 Seconds	54
Figure 12. Flow Regime Maps for the Four Circular Tubes Tested in Phase I of this Study	56
Figure 13. Effect of Diameter on the Air-Water Transition Lines	57
Figure 14. Example of a Condenser Tube	58
Figure 15. Air-Water Flow Map for the Rectangular Tube ($D_h = 5.36$ mm, $\alpha = 0.725$)	58
Figure 16. Comparison of the Air-Water Round and Rectangular Flow Regime Maps	59
Figure 17. Flow Regime Map for the 4.91 mm I.D. Tube	65
Figure 18. Flow Regime Map for the 4 x 4 mm Tube	66
Figure 19. Flow Regime Map for the 3 x 3 mm Tube	67
Figure 20. Flow Regime Map for the 2 x 2 mm Tube	69
Figure 21. Flow Regime Map for the 1 x 1 mm Tube	69
Figure 22. Flow Regime Map for the 4 (Height) x 2 (Width) mm Tube	70
Figure 23. Flow Regime Map for the 2 (Height) x 4 (Width) mm Tube	71
Figure 24. Flow Regime Map for the 6 (Height) x 4 (Width) mm Tube	72
Figure 25. Flow Regime Map for the 4 (Height) x 6 (Width) mm Tube	73
Figure 26. Expansion and Contraction Losses as a Function of the Area Ratio	76
Figure 27. Experimental and Theoretical Single-Phase Friction Factors for Tube C120	79
Figure 28. Relative Roughness Estimates of the Tubes Tested in Phase II of This Study	80
Figure 29. Experimental and Theoretical Friction Factors for Tube C30	80
Figure 30. Total Measured Pressure Drop for Tube C193 ($D_h = 4.91$ mm)	83
Figure 31. Differential Pressure Transducer Measurements (Tube C193, $G = 300$ kg/m ² -s)	83
Figure 32. Differential Pressure Transducer Measurements (Tube C193, $G = 600$ kg/m ² -s)	84
Figure 33. Total Measured Pressure Drop for Tube C120 ($D_h = 3.048$ mm)	84

Figure 34. Differential Pressure Transducer Measurements (Tube C120, $G = 450 \text{ kg/m}^2\text{-s}$)	86
Figure 35. Total Measured Pressure Drop for Tube C60 ($D_h = 1.524 \text{ mm}$)	86
Figure 36. Differential Pressure Transducer Measurements (Tube C60, $G = 450 \text{ kg/m}^2\text{-s}$)	87
Figure 37. Total Adiabatic Measured Pressure Drop for Tube C30 ($D_h = 0.761 \text{ mm}$)	87
Figure 38. Total Condensing Measured Pressure Drop for Tube C30 ($D_h = 0.761 \text{ mm}$)	88
Figure 39. Total Condensing Measured Pressure Drop for Tube C20 ($D_h = 0.506 \text{ mm}$)	88
Figure 40. Total Adiabatic Measured Pressure Drop for Tube S30 ($D_h = 0.762 \text{ mm}$)	89
Figure 41. Total Condensing Measured Pressure Drop for Tube S30 ($D_h = 0.762 \text{ mm}$)	90
Figure 42. Total Condensing Measured Pressure Drop for Tube B32 ($D_h = 0.799 \text{ mm}$)	91
Figure 43. Total Condensing Measured Pressure Drop for Tube T33 ($D_h = 0.839 \text{ mm}$)	91
Figure 44. Total Condensing Measured Pressure Drop for Tube N21 ($D_h = 0.536 \text{ mm}$)	92
Figure 45. Total Condensing Measured Pressure Drop for Tube RK15 ($D_h = 0.424 \text{ mm}$)	93
Figure 46. Total Condensing Measured Pressure Drop for Tube W29I ($D_h = 0.732 \text{ mm}$)	93
Figure 47. Total Condensing Measured Pressure Drop for Tube W29II ($D_h = 0.732 \text{ mm}$)	94
Figure 48. Total Adiabatic Measured Pressure Drop for Tube ZLI ($D_h = 0.761 \text{ mm}$)	95
Figure 49. Total Adiabatic Measured Pressure Drop for Tube ZLII ($D_h = 0.761 \text{ mm}$)	95
Figure 50. Decelerational Pressure Drop (Tube C30, $G = 450 \text{ kg/m}^2\text{-s}$)	98
Figure 51. Decelerational Pressure Drop (Tube C30, $G = 300 \text{ kg/m}^2\text{-s}$)	99
Figure 52. Decelerational Pressure Drop (Tube C30, $G = 600 \text{ kg/m}^2\text{-s}$)	99
Figure 53. Decelerational Pressure Drop (Tube C30, $G = 7500 \text{ kg/m}^2\text{-s}$)	100
Figure 54. Comparison of the ZLII and C30 Data Using the Expansion/Contraction Models	101
Figure 55. Adiabatic Frictional Pressure Drop for Tube C193 ($D_h = 4.91 \text{ mm}$)	102
Figure 56. Adiabatic Frictional Pressure Drop for Tube C120 ($D_h = 3.048 \text{ mm}$)	103
Figure 57. Condensing Frictional Pressure Drop for Tube C60 ($D_h = 1.524 \text{ mm}$)	103
Figure 58. Adiabatic Frictional Pressure Drop for Tube C30 ($D_h = 0.761 \text{ mm}$)	104
Figure 59. Condensing Frictional Pressure Drop for Tube C30 ($D_h = 0.761 \text{ mm}$)	104
Figure 60. Condensing Frictional Pressure Drop for Tube C20 ($D_h = 0.506 \text{ mm}$)	105
Figure 61. Condensing Frictional Pressure Drop for Tube B32 ($D_h = 0.799 \text{ mm}$)	105
Figure 62. Condensing Frictional Pressure Drop for Tube N21 ($D_h = 0.536 \text{ mm}$)	106
Figure 63. Condensing Frictional Pressure Drop for Tube RK15 ($D_h = 0.424 \text{ mm}$)	106
Figure 64. Adiabatic Frictional Pressure Drop for Tube S30 ($D_h = 0.762 \text{ mm}$)	107
Figure 65. Condensing Frictional Pressure Drop for Tube S30 ($D_h = 0.762 \text{ mm}$)	107
Figure 66. Condensing Frictional Pressure Drop for Tube T33 ($D_h = 0.839 \text{ mm}$)	108
Figure 67. Condensing Frictional Pressure Drop for Tube W29I ($D_h = 0.732 \text{ mm}$)	108

Figure 68. Condensing Frictional Pressure Drop for Tube W29II ($D_h = 0.732$ mm)	109
Figure 69. Comparison of Baseline Circular Tube ($D_h = 5.5$ mm) Air-Water Mixture Results with the Literature	112
Figure 70. Comparison of Air-Water Mixture Results with Weisman et al. (1979): Hydraulic Diameter Effects	115
Figure 71. Comparison of the Air-Water Data ($D_h = 5.50$ mm) With the Baker (1959) Map	117
Figure 72. Comparison of the R-134a Data ($D_h = 4.91$ mm) With the Baker (1959) Map	117
Figure 73. Comparison of R-134a Data ($D_h = 4.91$ mm) and Taitel and Dukler (1976) Map	120
Figure 74. Comparison of R-134a Data ($D_h = 4.91$ mm) With Transition Correlations of Weisman et al. (1979)	120
Figure 75. Comparison of R-134a Data ($D_h = 4.91$ mm) With the Results of Wang et al. (1997)	122
Figure 76. Comparison of 4 x 4 mm R-134a Data With the Flow Regime Map of Troniewski and Ulbrich (1984)	123
Figure 77. Comparison of 3 x 3 mm R-134a Data With the Flow Regime Map of Troniewski and Ulbrich (1984)	123
Figure 78. Comparison of the 4 x 6 mm and 6 x 4 mm R-134a Data With the Flow Regime Map of Troniewski and Ulbrich (1984)	125
Figure 79. Comparison of the 2 x 4 mm and 4 x 2 mm R-134a Data With the Flow Regime Map of Troniewski and Ulbrich (1984)	125
Figure 80. Comparison of the 4 x 4 mm R-134a Data With the Flow Regime Map of Wambsganss et al. (1991)	126
Figure 81. Comparison of the 3 x 3 mm R-134a Data With the Flow Regime Map of Wambsganss et al. (1991)	126
Figure 82. Comparison of the 4 x 6 mm and 6 x 4 mm R-134a Data With the Flow Regime Map of Wambsganss et al. (1991)	127
Figure 83. Comparison of the 2 x 4 mm and 4 x 2 mm R-134a Data With the Flow Regime Map of Wambsganss et al. (1991)	128
Figure 84. Intermittent Flow Regime Transitions (4.91 mm Circular and 4 x 4 mm Square Tubes)	129
Figure 85. Wavy Flow Regime Transitions (4.91 mm Circular and 4 x 4 mm Square Tubes)	129
Figure 86. Progression from Discrete (0) Waves to Disperse (3) Waves: 4.91 mm Circular Tube	130
Figure 87. Progression from Discrete (0) Waves to Disperse (3) Waves: 4 x 4 mm Square Tube	131
Figure 88. Annular Flow Regime Transitions (4.91 mm Circular and 4 x 4 mm Square Tube)	131

Figure 89. Intermittent Flow Regime Transition for the 4 x 4, 3 x 3, 2 x 2 and 1 x 1 mm Tubes	133
Figure 90. Effect of Hydraulic Diameter on the Annular Film Flow Pattern	133
Figure 91. Effect of Hydraulic Diameter on the Wavy Flow Regime	134
Figure 92. Progression From Discrete (0) to Disperse (3) Waves: 3 x 3 mm Square Tube	135
Figure 93. Progression From Discrete (0) to Disperse (3) Waves: 2 x 2 mm Square Tube	135
Figure 94. Effect of Hydraulic Diameter on the Mist Flow Pattern	136
Figure 95. Effect of Aspect Ratio on the Intermittent Regime	138
Figure 96. Effect of Aspect Ratio on the Annular Film Flow Pattern	138
Figure 97. Effect of Aspect Ratio on the Wavy Flow Regime	139
Figure 98. Progression from Discrete (0) to Disperse (3) Waves: 2(H) x 4(W) mm Rectangular Tube	140
Figure 99. Progression from Discrete (0) to Disperse (3) Waves: 4(H) x 2(W) mm Rectangular Tube	140
Figure 100. Progression From Discrete (0) to Disperse (3) Waves: 4(H) x 6(W) mm Rectangular Tube	141
Figure 101. Progression From Discrete (0) to Disperse (3) Waves: 6(H) x 4(W) mm Rectangular Tube	141
Figure 102. Effect of Aspect Ratio on the Mist Flow Pattern	142
Figure 103. Superposition of the Air-Water Data on the R-134a Map	143
Figure 104. Comparison of Superficial Velocities for R-134a Data With Air-Water Transition Lines	145
Figure 105. Transition From Intermittent Flow, Comparison with Traviss and Rohsenow (1973)	149
Figure 106. Transition From Intermittent Flow for Air-Water ($D_h = 5.5$ mm) and R-134a ($D_h = 4.91$ mm) Data Using $Fr=7$ (Soliman 1982 Criterion)	151
Figure 107. Transition from Intermittent Flow for Air-Water ($D_h = 5.50$ mm) and R-134a ($D_h = 4.91$ mm)	151
Figure 108. Transition from Intermittent Flow for Air-Water ($D_h = 2.60$ mm) and R-134a ($D_h = 3.0$ mm)	152
Figure 109. Transition from Intermittent Flow for Air-Water ($D_h = 1.75$ mm) and R-134a ($D_h = 2.0$ mm)	152
Figure 110. Transition from Intermittent Flow for Air-Water ($D_h = 1.30$ mm) and R-134a ($D_h = 1.0$ mm)	153
Figure 111. Wavy Flow Regime Boundaries for Air-Water ($D_h = 5.50$ mm) and R-134a ($D_h = 4.91$ mm)	155
Figure 112. Wavy Flow Regime Boundaries for Air-Water ($D_h = 2.6$ mm) and R-134a ($D_h = 3.0$ mm)	155
Figure 113. Wavy Flow Regime Boundaries for Air-Water ($D_h = 1.75$ mm) and R-134a ($D_h = 2.0$ mm)	156

Figure 114. Transition to Annular Flow in Air-Water ($D_h = 1.3$ mm) and R-134a ($D_h = 1.0$ mm)	156
Figure 115. Transition to Annular Flow (R-134a, $D_h = 4.91$ mm)	158
Figure 116. Transition to Annular Flow (R-134a, $D_h = 3.0$ mm)	159
Figure 117. Transition to Annular flow (R-134a, $D_h = 2.0$ mm)	159
Figure 118. Transition to Annular Flow (R-134a, $D_h = 1.0$ mm)	160
Figure 119. Comparison of the C193 Tube Data with the Literature ($G = 150$ kg/m ² -s)	163
Figure 120. Comparison of the C193 Tube Data with the Literature ($G = 300$ kg/m ² -s)	164
Figure 121. Comparison of the C193 Tube Data with the Literature ($G = 450$ kg/m ² -s)	164
Figure 122. Comparison of the C193 Tube Data with the Literature ($G = 600$ kg/m ² -s)	165
Figure 123. Comparison of the C193 Tube Data with the Literature ($G = 750$ kg/m ² -s)	165
Figure 124. Percent Errors in the Correlations ($G = 450$ kg/m ² -s)	172
Figure 125. Model Schematic for Slug and Discrete Wave Flow	173
Figure 126. Details of the Slug Flow and Discrete Wave Flow Model	174
Figure 127. Normalized Slug Length versus Ψ and λ , Circular Tubes	178
Figure 128. Predicted Versus Measured Pressure Drops, Intermittent Model, Circular Tubes	178
Figure 129. Intermittent Model Data for Non-Circular Geometries	179
Figure 130. Measured versus Predicted Pressure Drop Non-Circular Geometries	180
Figure 131. Model Schematic for Annular Film and Disperse Wave Flow	181
Figure 132. Normalized Interfacial Friction Factor Versus Martinelli Parameter, Circular Tubes	183
Figure 133. Constant C_1 as a Function of the Bond Number, Circular Tubes	184
Figure 134. Predicted versus Measured Pressure Drops, Annular Film Model, Circular Tubes	184
Figure 135. Laminar Normalized Interfacial Friction Factor Versus Martinelli Parameter, Non-Circular Tubes	185
Figure 136. Turbulent Normalized Interfacial Friction Factor Versus Martinelli Parameter, Non-Circular Tubes	186
Figure 137. Predicted Versus Measured Pressure Drops, Annular Film Model, Non-Circular Tubes	186
Figure 138. Schematic of Combined Mist and Annular Film Flow	187
Figure 139. Normalized Interfacial Friction Factor Versus Martinelli Parameter, Annular Film and Mist Flow, Circular Tubes	188
Figure 140. Constants C_0 and C_1 as a Function of the Bond Number, Annular Film and Mist Flow, Circular Tubes	189
Figure 141. Normalized Predicted Versus Measured Pressure Drop, Annular Film and Mist Flow, Circular Tubes	189

Figure 142. Normalized Interfacial Friction Factor Versus Martinelli Parameter, Annular Film and Mist Flow, Non-circular Geometries	190
Figure 143. Actual versus Measured Pressure Drop, Annular Film and Mist Flow Model, Non-Circular Geometries	190
Figure 144. Normalized Interfacial Friction Factor Versus Martinelli Parameter, Mist Flow, Circular Tubes	192
Figure 145. Constant C_1 Versus the Bond Number, Mist Flow Model, Circular Tubes	192
Figure 146. Measured Versus Predicted Pressure Drop, Mist Flow Model, Circular Tubes	193
Figure 147. Normalized Interfacial Friction Factor versus Martinelli Parameter, Mist Flow Model, Non-circular Geometries	194
Figure 148. Measured versus Predicted Pressure Drop, Mist Flow Model, Non-circular Geometries	194
Figure 149. Overall Model Predictions, Circular Tubes	196
Figure 150. Overall Model Predictions, Non-Circular Geometries	196
Figure 151. Measured versus Predicted Pressure Drop for All Models (C193 Tube, $D_h = 4.91$ mm)	197
Figure 152. Measured versus Predicted Pressure Drop for All Models (C120 Tube, $D_h = 3.05$ mm)	197
Figure 153. Measured versus Predicted Pressure Drop for All Models (C60 Tube, $D_h = 1.52$ mm)	198
Figure 154. Measured versus Predicted Pressure Drop for All Models (C30 Tube, $D_h = 0.761$ mm)	198
Figure 155. Measured versus Predicted Pressure Drop for All Models (C20 Tube, $D_h = 0.508$ mm)	199
Figure 156. Measured versus Predicted Pressure Drop for All Models (T33 Tube, Triangle, $D_h = 0.839$ mm)	199
Figure 157. Measured versus Predicted Pressure Drop for All Models (S30 Tube, Square, $D_h = 0.762$ mm - Adiabatic)	200
Figure 158. Measured versus Predicted Pressure Drop for All Models (S30 Tube, Square, $D_h = 0.762$ mm - Diabatic)	200
Figure 159. Measured versus Predicted Pressure Drop for All Models (B32 Tube, Barrel, $D_h = 0.799$ mm)	201
Figure 160. Measured versus Predicted Pressure Drop for All Models (N21 Tube, "N"-Shape, $D_h = 0.536$ mm)	201
Figure 161. Measured versus Predicted Pressure Drop for All Models (RK15 Tube, Rectangle, $D_h = 0.424$ mm)	202
Figure 162. Measured versus Predicted Pressure Drop for All Models (W29I Tube, Triangle Insert, $D_h = 0.732$ mm)	202
Figure 163. Measured versus Predicted Pressure Drop for All Models (W29II Tube, Triangle Insert, $D_h = 0.732$ mm)	203

Figure 164. Predicted Pressure Drop for All Models Using Theoretical and Experimental Transition Lines (C193 Tube, $D_h = 4.91$ mm)	203
Figure 165. Predicted Pressure Drop for All Models Using Theoretical and Experimental Transition Lines (C120 Tube, $D_h = 3.05$ mm)	204
Figure 166. Predicted Pressure Drop for All Models Using Theoretical and Experimental Transition Lines (C60 Tube, $D_h = 1.52$ mm)	204
Figure 167. Predicted Pressure Drop for All Models Using Theoretical and Experimental Transition Lines (C30 Tube, $D_h = 0.761$ mm)	205
Figure 168. Predicted Pressure Drop for All Models Using Theoretical and Experimental Transition Lines (C20 Tube, $D_h = 0.508$ mm)	205
Figure 169. Predicted Pressure Drop for All Models Using Theoretical and Experimental Transition Lines (T33 Tube, Triangle, $D_h = 0.839$ mm)	206
Figure 170. Predicted Pressure Drop for All Models Using Theoretical and Experimental Transition Lines (S30 Tube, Square, $D_h = 0.762$ mm)	206
Figure 171. Predicted Pressure Drop for All Models Using Theoretical and Experimental Transition Lines (B32 Tube, Barrel, $D_h = 0.799$ mm)	207
Figure 172. Predicted Pressure Drop for All Models Using Theoretical and Experimental Transition Lines (N21 Tube, "N" Shape, $D_h = 0.536$ mm)	207
Figure 173. Predicted Pressure Drop for All Models Using Theoretical and Experimental Transition Lines (RK15 Tube, Rectangle, $D_h = 0.424$ mm)	208
Figure 174. Predicted Pressure Drop for All Models Using Theoretical and Experimental Transition Lines (W29I Tube, Triangle Insert, $D_h = 0.732$ mm)	208
Figure 175. Comparison of Circular Tube Pressure Drops, $L/D = 500$, $G = 750$ kg/m ² -s	210
Figure 176. Comparison of Circular Tube Pressure Drops, $L/D = 500$, $G = 600$ kg/m ² -s	211
Figure 177. Comparison of Circular Tube Pressure Drops, $L/D = 500$, $G = 450$ kg/m ² -s	211
Figure 178. Comparison of Circular Tube Pressure Drops, $L/D = 500$, $G = 300$ kg/m ² -s	212
Figure 179. Comparison of Circular Tube Pressure Drops, $L/D = 500$, $G = 150$ kg/m ² -s	212
Figure 180. Comparison of Non-Circular Tube Pressure Drops, $L/D = 500$, $G = 450$ kg/m ² -s	213
Figure 181. Comparison of Non-Circular Tube Pressure Drops, $L/D = 500$, $G = 750$ kg/m ² -s	213
Figure 182. Comparison of Non-Circular Tube Pressure Drops, $L/D = 500$, $G = 600$ kg/m ² -s	214
Figure 183. Comparison of Non-Circular Tube Pressure Drops, $L/D = 500$, $G = 300$ kg/m ² -s	214
Figure 184. Comparison of Non-Circular Tube Pressure Drops, $L/D = 500$, $G = 150$ kg/m ² -s (with Corresponding Reynolds Numbers and Friction Factors)	215

LIST OF TABLES

Table 1.	Flow Meter Ranges Used in Phase I	30
Table 2.	L/D Values for the Tubes Tested in Phase I	30
Table 3.	Instrumentation Specifications	38
Table 4.	Measured Values from the EES Program	41
Table 5.	Differential Pressure Transducer Specifications	46
Table 6.	Test Matrix for the Pressure Drop Experiments	48
Table 7.	Mass Flux Cases Tested in Phase II of This Study	50
Table 8.	Uncertainty in the Quality for the C193, C30, and RK15 Tubes	50
Table 9.	Air-Water Flow Regime Classifications	52
Table 10.	Refrigerant Flow Regime Classifications	62
Table 11.	Loss Coefficients for the Fluid Expansion and Contraction	77
Table 12.	Laminar Flow Friction Factor Constants, $f \cdot Re = C$	81
Table 13.	Experimentally Derived Relative Roughness Estimates and Percent Errors in Single Phase Friction Factors	81
Table 14.	Constants for the Void Fraction Models	98
Table 15.	Liquid/Gas Properties and Non-Dimensional Numbers	118
Table 16.	Summary of the Non-Dimensional Transition Criteria for Intermittent Flow Developed in This Study	154
Table 17.	Summary of the Theoretical Transition Lines for Wavy Flow	154
Table 18.	Summary of the Theoretical Transition Lines for Annular Flow	158
Table 19.	C193 Tube Data Used in the Baseline Case Comparison Calculations	160
Table 20.	C120 Tube Data Used in the Baseline Case Comparison Calculations	173
Table 21.	Intermittent/Discrete Wave Model Constants	180
Table 22.	C120 Tube Data Used in the Baseline Case Comparison Calculations	180
Table 23.	Constants for the Annular Film and Disperse Wave Flow	187
Table 24.	Constants for the Annular Film and Mist Flow Model	191
Table 25.	Constants for the Mist Flow Model	193

NOMENCLATURE

A	Area (m ²)
Bo	Bond Number = $g(\rho_l - \rho_g)D/\sigma$
C _c	Equation Parameter
D	Diameter (m)
E	Equation Parameter
F	Modified Froude Number
f	Friction Factor
Fr	Froude Number = $G^2/(gD\rho^2)$
G	Mass Flux (kg/m ² -s)
Ga	Galileo Number = $g\rho^2D^3/\mu^2$
g	Acceleration Due to Gravity (m/s ²)
h	Height (m), Enthalpy (kJ/kg)
H	Equation Parameter
K	Dimensionless Parameter for Wavy Flow
l	Length (m)
m	Mass (kg)
N	Number
P	Pressure (Pa), Perimeter (m)
Q	Heat Duty (W)
Re	Reynolds Number = GD/μ
S	Perimeter Over Which Shear Stress Acts (m)
s	Jeffrey's Sheltering Coefficient, Slug
T	Dimensionless Parameter for Dispersed Flow, Temperature (°C)
u	Velocity in the x-direction (m/s)
V	Velocity (m/s), Volumetric Flow Rate (m ³ /s)
w	Width (m)
We	Weber Number = $G^2D/(\rho\sigma)$
x	Quality
X	Martinelli Parameter (liquid-vapor) = $[(dpdz)_l/(dpdz)_g]^{0.5}$
Y	Martinelli Parameter (liquid only-vapor only) = $[(dpdz)_{go}/(dpdz)_{lo}]^{0.5}$
z	Length (m)
Greek Symbols	
α	Tube Aspect Ratio = Height/Width, Void Fraction

β	Area Ratio
γ	Area Ratio
Γ	Property Correction Factor
δ	Thickness (m)
Δ	Change in a Variable
ε	Relative Roughness
ϕ	Multiplier
λ	Property Correction Factor
μ	Dynamic Viscosity (kg/m-s)
ρ	Density (kg/m ³)
Ψ	Two-Phase Multiplier, Property Correction Factor
σ	Surface Tension (N/m)
θ	Angle of Inclination (degree)
τ	Shear Stress (Pa)
ω	Aspect Ratio Correction Factor

Subscripts and Superscripts

\sim	Dimensionless Variable
.	Rate (Variable/Time)
+	Dimensionless Variable
ave	Average
con	Contraction
eq	Equivalent
exp	Expansion
exptl	Experimental
f	Free Flow, Frictional, Friction Factor, Film
g	Gas
go	Gas Only
h	Hydraulic
H	Homogeneous
i	Interface, In
in	Inlet
l	Liquid
lam	Laminar
lo	Liquid Only
out	Outlet

Post	After Test Section
Pre	Before Test Section
p	Ports
refg	Refrigerant
s	Superficial, for Single Fluid Flow, Separated
sat	Saturation
sub	Subcooled
sup	Superheated
t	Total, Turbulent
test	Test Section
tot	Total
turb	Turbulent
test	Test Section
TP	Two Phase
v	Vapor

ACKNOWLEDGEMENTS

There are many people who I should acknowledge and thank for their contributions to this study. Above all of those who I should thank and acknowledge is my advisor, Dr. Srinivas Garimella. I thank him for his tireless efforts, unyielding sense of duty, and guidance over the past several years. His efforts were the cornerstone of this work. — I would also like to thank my committee members for their contributions to this study, Drs. Robert Brown, Mike Pate, Ron Nelson, and Steve Hoff. Their input and direction were invaluable. — Special thanks to Modine Manufacturing Company and the American Society of Heating, Refrigeration and Air-Conditioning Engineers for their support, specifically Drs. Stephen B. Memory, Anthony C. DeVuono, and Jonathan P. Wattlelet for their stimulating technical input and guidance in the two-phase flow work. — William Dowling, for his assistance in constructing the two-phase flow test facility and in editing the two-phase flow video.

ABSTRACT

A comprehensive study of two-phase flow mechanisms and pressure drop in horizontal small hydraulic diameter tubes was conducted. Co-current flow of air-water mixtures in four round tubes and one rectangular tube with hydraulic diameters ranging from 5.5 mm to 1.3 mm were investigated. Bubble, dispersed, elongated bubble, slug, stratified, wavy, annular-wavy, and annular flow patterns were observed. The results of this work show that diameter and surface tension effects play an important role in determining the flow patterns and transitions between them.

Flow mechanisms during condensation of refrigerant R134a in small diameter round, square and rectangular tubes ($0.506 \text{ mm} < D_h < 4.91 \text{ mm}$) were also investigated. Flow mechanisms were recorded and categorized into intermittent, wavy, annular, and dispersed flow over the entire range of qualities, and for five different refrigerant mass fluxes. As the hydraulic diameter is decreased, the influence of gravity diminishes and surface tension becomes more significant, thus promoting annular and slug/plug flow, and virtually eliminating the wavy flow regime. Transition lines between the flow patterns and regimes were established based on the experimental data. Many of the significant transition lines can be represented or approximated by constant Froude number lines, both for air-water mixtures, and refrigerant R134a. This common non-dimensional basis for transitions in fluids of widely different phase properties could be useful for extending the transition criteria to other fluids, geometries and operating conditions.

Two-phase pressure drop measurements were taken on a set of 5 circular tubes and on 7 non-circular tubes (triangular, square, rectangular, barrel, and "N" shaped extruded tubes). Frictional components of the total measured two-phase pressure drops were determined by accounting for the small contributions due to expansion/contraction at the headers, and the deceleration component due to momentum change. Reasonable agreement was found between the pressure drops measured in this study for the larger tubes and correlations in the literature. Flow regime-based pressure drop correlations were developed for the following regimes: intermittent and discrete wave flows, annular and disperse wave flows, annular/mist flow, and mist flow. For each of these regimes, one correlation accounted for the circular geometries, while equations of the same functional form were developed for the non-circular geometries. It was found that the circular tube correlations were able to predict 90 percent of the data within 20 percent, while 92 percent of the non-circular tube data were predicted within 20 percent.

CHAPTER ONE. INTRODUCTION

Conventional air-conditioning systems use round-tube, plate-fin heat exchangers as evaporators and condensers to transfer heat between the refrigerant and the indoor and outdoor air. The size of these heat exchangers required to deliver a desired heat load, and conversely, the heat load delivered by a heat exchanger of a specified size, depends primarily on the heat transfer coefficients of the refrigerant and the air. The refrigerant undergoes a liquid-vapor phase change in the condenser and the evaporator, and consequently the tube-side heat transfer coefficients are significantly higher than the air-side heat transfer coefficients, often by a factor of 20-30. The introduction of fins on the air-side, and the resulting additional surface area of up to a factor of 10-15 over bare tubes, counteracts this to a large extent. Thus, even though the air-side often continues to have the governing thermal resistance, the tube-side resistance is not negligible. With the heat exchanger cost representing 10 to 25 percent of the cost of air-conditioning systems, any potential improvements in the overall heat transfer conductances, without commensurate increases in pressure drop, are of immense value in decreasing capital and/or operating costs. Manufacturers have achieved cost reductions in conventional heat exchangers through modification and optimization of the geometric parameters such as the number of tubes, tube dimensions, air-side fin depth, height, thickness, shape and pitch. However, further attempts in this direction will at best result in incremental improvements.

Automotive heat exchanger manufacturers have developed very compact flat-tube, multilouver fin heat exchangers to replace round-tube/flat-plate fin geometries used in engine cooling and air-conditioning systems. An example of a flat-tube, multilouver-fin heat exchanger is shown in Figure 1. These novel heat exchangers offer the following advantages over conventional geometries:

- Flat tubes offer a smaller frontal obstruction to air flow compared to round tubes, reducing drag and fan power
- Rectangular tube-side passages with typically smaller hydraulic diameters offer higher tube-side heat transfer coefficients
- Interrupted multilouver fins reduce boundary-layer resistances and thus result in larger air-side heat transfer coefficients
- The above two factors result in a higher overall heat transfer conductance
- By using optimized header configurations, the tube-side flow may be directed in several passes and rows, with the number of tubes per pass chosen to suit the heat transfer and pressure drop requirements and constraints

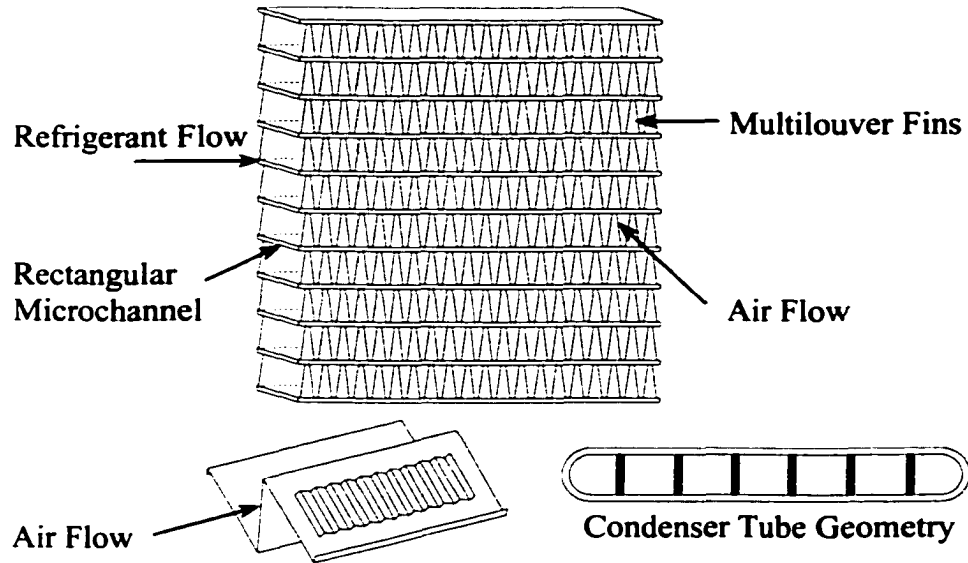


Figure 1. Example of a Multilouver Fin Flat-Tube Heat Exchanger

- Larger surface areas can be packaged into a given space or conversely, a given heat load can be transferred in a smaller volume and with less material
- Refrigerant charge reductions could result due to the much smaller cross-section/surface area ratios in the flat-tube heat exchangers

These advantages of the flat-tube, multilouver fin heat exchangers can also benefit commercial and residential air-conditioners and heat pumps. Recently conducted analyses have shown the potential for significant size reductions over conventional heat exchangers through the use of flat tube, multilouver fin heat exchangers in liquid-to-air heat exchange (Garimella et al. 1996 and 1997) and in air-cooled condensers (Garimella and Wicht 1995, Garimella and Coleman 1998). However, in spite of their use in automotive heat exchangers and the potential benefits to the residential and commercial space-conditioning industry, two-phase flow, heat transfer, and pressure drop in these tubes are not well understood, and predictive correlations are not available in the literature. Limited research has been conducted on addressing the effect of tube hydraulic diameter and shape on pressure drop during phase-change.

The pressure drop in a phase-change process such as condensation is a strong function of the local vapor quality. Accurate designs require not only estimates of average tube-side pressure drop in condensers, but an approach that accounts for the variation in flow patterns as the refrigerant undergoes a transition from 100 percent vapor to 0 percent vapor

along the length of the condenser. Using a pressure drop calculated at an average quality of 50 percent to represent the pressure drop throughout the condenser would lead to significant over- and under- predictions of the pressure drop near the outlet and inlet, depending on the tube geometry and operating conditions. Thus, for optimal design purposes, it is desirable to be able to predict the flow regime at a given quality and mass flux, and use an appropriate flow-regime based pressure drop correlation.

The particular flow regime established by a given combination of liquid and gas-phase velocities depends upon the interaction of gravity, shear (inertia) and surface tension forces. It is believed that flow mechanisms in small diameter round and rectangular tubes are different from those in larger diameter tubes primarily due to the different relative magnitudes of these forces. Most previous attempts at understanding two-phase flow in small hydraulic diameter channels have primarily used isothermal air-water mixtures. As early as 1957, Govier et al. and Govier and Short (1958) recognized the importance of the mass flow rate and tube diameter in determining flow regime transitions and pressure drops for upward flow of air-water mixtures, even though their work was limited to a relatively larger diameter range (16.0 mm to 63.5 mm) than that of the present study.

It is postulated that both the heat transfer and pressure drop characteristics of any two-phase flow are highly dependent upon the corresponding flow mechanisms. In addition, the flow mechanisms could be dependent upon the tube shape, hydraulic diameter and tube aspect ratio. The focus of this research is to identify the specific effects that the tube geometry, hydraulic diameter and tube aspect ratio have on the two-phase flow mechanisms. This information is then combined with experimentally measured two-phase pressure drops; thus allowing for *flow regime-based* pressure drop correlations. The results from this work will be valuable to the designers of components with two-phase flow such as those found in automotive condensers, commercial/residential refrigeration units, and residential air-conditioners, etc.

To accomplish this task, the present study is divided into three main phases. The objectives of the first phase of this study are to investigate the effects of tube diameter and tube shape on air-water flow regimes and transitions. The second phase of this study investigates the effect of tube shape, hydraulic diameter and aspect ratio on the flow mechanisms in two-phase flow *during condensation*. Finally, the third phase of this study utilizes the results from the previous two sets of experiments and investigates the effect of the two-phase flow mechanisms on the pressure drop in microchannel geometries.

For Phase I, a series of isothermal air-water experiments is conducted to establish the effects of tube diameter and tube shape on two-phase flow regime maps. A total of five tubes

are investigated including four round tubes and one rectangular tube. The tube diameters range from 5.5 mm to 1.3 mm. The objectives of this Phase are to:

- Document the flow regimes and transitions found in air-water systems
- Identify the effect of hydraulic diameter on the flow regime transition lines
- Investigate the effect of tube geometry on the flow regime maps
- Compare these experimentally obtained flow regime maps in the small hydraulic diameter tubes with the theoretical and experimental results found in the literature

In Phase II, this work is extended to documenting the effects of tube geometry, hydraulic diameter, and aspect ratio on the two-phase flow regime maps *during condensation* of refrigerants. A total of nine tubes are investigated including one round tube, four square tubes, and four rectangular tubes. The objectives of this Phase of the study are to:

- Investigate the effects of tube geometry on the flow regime maps by comparing the results of the round tube with the 4 x 4 mm square tube (both are of similar hydraulic diameter)
- Investigate the effects of hydraulic diameter (tube miniaturization) on the flow regime maps using the results for the 4 x 4 mm, 3 x 3 mm, 2 x 2 mm and 1 x 1 mm tubes
- Document the effects of aspect ratio on the flow regime maps using the results from the 2 x 4 mm, 4 x 2 mm, 4 x 6 mm and 6 x 4 mm tubes
- Identify the similarities and differences in the adiabatic air-water flow regime maps (Phase I) and the refrigerant flow regime maps obtained during condensation (Phase II)
- Identify and develop flow regime transition correlations based upon a consideration of the basic governing influences

In Phase III, the results from Phase I and Phase II are used to develop flow-regime based pressure drop correlations for condensation of refrigerants in microchannel geometries. The variation of the two-phase pressure drop as a function of the tube shape, refrigerant mass flux and quality in each of these microchannel tubes is investigated. A total of fourteen tubes are used in the pressure drop experiments including circular, square, triangular, rectangular, barrel, and “N” shaped flow passages. The objectives of this study are to:

- Determine the pressure drop in each of the tubes as a function of quality and mass flux
- Determine the contribution of entrance and exit effects on the two-phase pressure drop
- Investigate the effect of hydraulic diameter on the two-phase pressure drop
- Investigate the effect of tube shape on the two-phase pressure drop

- Relate the pressure drop in each tube to the respective flow mechanisms determined in Phase I and Phase II
- Develop flow-regime based pressure drop correlations that can be used in the design of condensers

This dissertation is organized as follows: Chapter two provides a review of the literature on flow regime mapping, flow regime transitions, and two-phase pressure drop. In Chapter three, detailed descriptions of the test facilities and experimental procedures are given as well as sample calculations used in the analysis of the data. Chapter four presents the results of the air-water flow visualization study (Phase I), R-134a flow visualization study (Phase II), and two-phase pressure drop study (Phase III). This includes the presentation of air-water and R-134a flow regime maps, and pressure drop measurements on the different microchannel geometries. An analysis and discussion of the data is presented in Chapter five. This chapter investigates the effects of tube geometry, diameter, and aspect ratio on the flow regime transitions in both the air-water (Phase I) and R-134a systems (Phase II) and models the flow regime transition criteria based on relevant non-dimensional parameters. Chapter five also develops flow regime-based pressure drop correlations and provides flow-mechanism based explanations for the trends found in Phase III of this study. Chapter six provides conclusions and recommendations for future work.

CHAPTER TWO. LITERATURE REVIEW

The literature pertinent to this work can broadly be categorized as follows:

- Studies on two-phase flow-regime maps
- Studies on two-phase pressure drop

Although considerable research has been conducted on the general topic of two-phase flow, the literature review presented here will identify several aspects that have not received adequate attention. Prior investigations have often simulated two-phase flow using air-water or air-oil mixtures. Much of this research has focused on relatively large diameter round tubes. Flow visualization studies using photography and X-ray techniques have been used in an attempt to understand the various mechanisms of two-phase flow, along with the transitions between these mechanisms. Some investigators have developed theory based models that explain these flow mechanisms on the basis of the governing forces. Pressure drop measurements have also been made to understand the effect of flow-related parameters such as mass flux, vapor-liquid fraction, etc., and the effects of tube geometry and orientation. There have also been some successful attempts at interpreting pressure drop data in terms of the observed flow mechanisms.

To facilitate a discussion of the literature, this chapter is divided into two main sections: flow regime mapping, and two-phase pressure drop. Each of these sections is further subdivided based on tube geometry: large round tubes, small diameter round tubes, and non-circular tubes. A distinction is also made on the basis of whether the two-phase flow phenomena were investigated using air-water mixtures or during phase change of a fluid. This comprehensive review is used to understand the experimental techniques, supporting theoretical analyses, and important results and conclusions arrived at by previous investigators. The review therefore provides some guidance for the present work. It also helps identify the deficiencies in the available literature, some of which are addressed by the present study.

Flow Regime Mapping

This section of the literature review is divided into three topics. First, flow regime mapping in large diameter circular tubes is discussed. This is followed by a section discussing flow regime mapping in small diameter circular tubes, and the third sub-section discusses flow regime mapping in non-circular tubes.

Large Diameter Circular Tubes

Bergelin and Gazley (1949) conducted two-phase pressure drop measurements using air and water in 25.4 mm and 52.45 mm circular tubes. Visual observations of the flow were made through a glass test section, and the authors classified the flow patterns as bubbling, stratified, wave, slugging, and annular flow. They reported that the pressure drop in annular flow is

predicted reasonably well by the Lockhart-Martinelli (1949) correlation. However, for stratified flows, which occur at low gas and liquid flow rates, the Lockhart-Martinelli correlation predicted a pressure drop of nearly twice the experimentally measured value.

Alves (1954) investigated air-water and air-oil two-phase flow patterns, pressure drop and holdup in a 25.4 mm circular tube and a return bend. He classified the flow into bubble, slug, plug, annular, stratified, wavy, and spray flow patterns. When both the liquid and gas were turbulent, he reported that the experimental values of the two-phase multiplier were within +20% and -30% of the values predicted by the Lockhart and Martinelli (1949) correlation. When the liquid was laminar and the gas was turbulent, the data for the oil-air mixture were within +43% and -36% of the Lockhart-Martinelli correlation for annular flows, and about 60% less than the values from the Lockhart-Martinelli correlation when the flow pattern was wavy. When both phases were laminar, he reported that the experimentally measured pressure drops were up to 17% greater than the Lockhart-Martinelli correlation for the bubble flow pattern, and up to 32% below the Lockhart-Martinelli correlation for the plug flow pattern. From the experiments on the return bend, he reported that the two-phase air-water pressure drops could be expressed as an equivalent length of straight pipe. For annular flow, the equivalent length was equal to 50 pipe diameters. He cautioned, however, that the air-oil data were not as consistent as the air-water data, but an equivalent length of 50 pipe diameters could be used as a guide in the design of return bends.

Baker (1954) developed a flow regime map with flow pattern transitions based upon functions of the mass flux of the gas phase and the liquid-to-gas ratio. This flow regime map was developed from the data of Jenkins (1947), Alves (1954) and others. The flow pattern definitions of Alves (1954), such as bubble, plug, stratified, wavy, slug, annular, and spray, were used to develop this flow regime map. Experimental pressure drops were measured in a total of 27 experiments using oil and gas with tube diameters ranging from 102 mm to 257.5 mm with data from other investigators extending this range down to a diameter of 22 mm. For each flow pattern, two-phase multipliers were calculated using a modified Fanning equation for the individual phases, and it was found that the pressure drops for the large pipes (200 mm and larger) were 40 to 60 percent less than those predicted by the Lockhart-Martinelli (1949) correlation. The sudden change in the slope of the gas two-phase multiplier, ϕ_g , and the Martinelli parameter, X , graph was attributed to a transition from annular to slug flow. An analysis of the data showed that, in the larger pipes, the onset of slug flow occurred at lower values of the Martinelli parameter and also that pipe diameter affects the two-phase flow multiplier. Baker (1954) therefore concluded that the flow pattern cannot be disregarded in creating a two-phase pressure drop correlation.

These conclusions were investigated further by a number of researchers. White and Huntington (1955) investigated the flow patterns and pressure drop in two-phase flow with three different liquids and two different gases in pipes ranging from 25.4 mm to 50.8 mm at atmospheric conditions. The flow patterns were classified as stratified, ripple, slug, wave, cresting, and semi-annular flows. Based upon the visual observations, a flow regime map was developed. No explicit dependence of the flow transitions or pressure drop on hydraulic diameter was reported. They proposed an empirical pressure drop correlation to fit their data in the wave, annular, semi-annular and cresting flow regimes. They noted that the transition from wave flow to cresting and semi-annular flow was gradual, which permitted the use of a single correlation for these regimes. This correlation was shown to agree well with the data of Jenkins (1947). The authors stated that this correlation should not be applied to stratified and slug flow patterns, and also that the correlation had not been checked against high pressure data.

Govier and Omer (1962) investigated two-phase flow patterns, liquid holdup and pressure drop using air and water in a horizontal, 26.1 mm diameter tube. The authors classified the flow patterns as bubble, plug, slug, stratified, wave (or ripple), and semi-annular (or annular) flow. They discussed the various measures for two-phase friction factors developed by prior investigators, and tried to understand the superficial friction factor in terms of the applicable flow pattern transitions. The air-water pressure drop data were in good agreement with the correlation developed by Lockhart and Martinelli (1949) when the liquid phase was turbulent. When the liquid phase was laminar, the Lockhart-Martinelli correlation tended to over-predict the two-phase pressure drop. They compared the two-phase pressure drop data with other available data and speculated that the differences may due to the effects of hydraulic diameter. Govier et al. (1957) investigated the effects of mass flow rate on the flow patterns, holdup, and pressure drop in vertical upward flows of air-water mixtures in a 26.0 mm diameter tube. They characterized the flow into four distinct flow regimes (bubble, slug, froth, ripple and film) based upon the two-phase pressure gradient. They plotted the pressure gradient versus the gas-liquid volume ratio and showed that the changes in slope of the data corresponded to a change in the flow regime. The pressure gradient, when plotted against the gas-liquid volume ratio, showed a pattern of decreasing, increasing, decreasing and then increasing slopes – thus creating four regimes. The authors found that the first regime included the transition from the bubble flow pattern to the slug flow pattern, and the slug flow pattern continued into the second regime. The second regime included the transition from slug flow to froth flow, which occurred about midway in the regime. The third regime included the transition from froth flow to ripple flow, but contained primarily the froth flow pattern. The last regime included the transition from ripple flow to film flow as well as a possible transition from film flow to mist flow. Holdup was

also investigated, and these data were plotted against the gas-liquid volume ratio. Similar results were found in the holdup curves: an inflexion was seen in the middle of regime I, and an abrupt change in slope near the end of regime II. A negative slope was exhibited in regime III and the slope became more positive as it moves into regime IV.

Govier and Short (1958) studied the effect of tube diameter on the flow pattern, holdup, and pressure drop in vertical, upward, air-water two-phase flows. The tubes ranged in diameter from 16.0 mm to 63.5 mm. Using the same regime definitions as Govier et al. (1957), the authors found that the tube diameter had little or no effect on the transition lines in regimes I and II, (bubble flow to slug flow), but had a substantial effect on the transition lines in regimes III and IV (slug flow to froth flow and froth flow to ripple flow). They also reported that the tube diameter had an effect on the holdup. The authors presented correlations for the liquid holdup in the four different regimes. Holdup and superficial friction factor were both found to be strongly affected by tube diameter. They found that the data could be correlated well by plotting superficial friction factor versus DV_L (to represent the liquid-phase Reynolds number), using a product of the superficial gas-phase Reynolds number and $D^{2.5}$ as a parameter. This correlating parameter demonstrates the strong influence of diameter on pressure drop.

Al-Sheikh et al. (1970) conducted a review of 4475 data points from several investigators in an attempt to predict the applicable flow pattern. Instead of using a single and generic transition correlation, an attempt was made to enclose all of the data from several investigators belonging to a certain flow regime pattern into a common flow regime area, and to use a series of transition correlations to determine the correct flow pattern. This approach did not provide direct transition correlations, but was used to reduce the number of possible flow regimes for any given flow conditions to two or three. They compared the area of each flow regime from various maps and used a variety of transition criteria that were combinations of basic variables such as liquid and gas flow rates, and non-dimensional parameters such as the Reynolds, Froude, and Weber number of each phase, and the Mach number of the gas to define the flow pattern transitions. A series of ten such correlations were developed for determining the flow patterns, which was able to distinguish between different flow regimes reasonably well. In some cases, there was no overlap between the possible flow patterns, while in others, a maximum overlap of 60.3% was observed.

Mandhane et al. (1974) tested the available flow regime maps with data representing a wide range of flow conditions. Nearly six thousand data points contained in a two-phase flow database covering different fluids and pipe diameters were considered, although their flow regime map was developed using only the air-water data (1178 points). The vast majority of data consisted of the slug, wave, annular-mist, and stratified flow patterns. The authors reported

that no distinction could be made between plug and slug flow, or between annular and annular mist flow. Furthermore, it was found that certain property corrections proposed by other researchers actually reduced the reliability of the data, and that the available flow regime maps were unable to predict dispersed bubble flow. From the flow regime maps of Baker (1954), Hoogendoorn (1959), and Govier and Omer (1962), a “best fit” map was developed along with physical property corrections for gas and liquid density, gas and liquid viscosity, and surface tension. It should be noted that unlike other investigators, these corrections should be applied to the transition lines, rather than the coordinate axes. They concluded that for the range of tube diameters considered, the effect of diameter was adequately taken into account by using superficial velocities as the coordinate axes on the flow regime map. In addition, no significant improvement in flow pattern prediction was achieved through the incorporation of the effect of fluid properties.

Several investigators have attempted mechanistic approaches to predict flow regime transitions (Govier and Aziz 1972, Dukler and Hubbard 1975, Nicholson et al. 1978). Govier and Aziz (1972) provide a good summary of flow regime transitions as well as continuity and momentum balances for each flow regime. The authors also provide a theoretical model of the two-phase pressure drop for horizontal, stratified flows. This model is based upon the in-situ volume fraction of the liquid and gas, and uses a momentum balance on each of the two phases. Two different models using different velocity profiles are proposed based upon whether the liquid and gas are in laminar or turbulent flow. The first solution assumes the liquid is laminar and the gas is turbulent, and uses the Hagen-Poiseuille velocity profile. The second solution assumes both phases are turbulent and uses a one-seventh power law velocity profile. Agrawal et al. (1973) extended the model of Govier and Aziz (1972) and modified the definition of the equivalent diameter used for phase Reynolds numbers, while including interfacial shear between the two phases. The authors tested the two-phase pressure drop model by Govier and Aziz for horizontal, stratified, two-phase flows with air-oil data in a 26.0 mm tube with good agreement.

Dukler and Hubbard (1975) developed a theoretical model of the pressure drop in slug flows for horizontal and near horizontal tubes with validation experiments conducted using air-water flow in a 38.1 mm pipe. The authors described two main contributions to the pressure drop consisting of the acceleration of the liquid to the slug velocity, and the pressure drop due to the wall shear at the back of the slug. The theoretical model calculates the two-phase pressure drop in slug flow based upon four input variables. These variables include the mass flow rates of the liquid and gas, the slug frequency, and the fraction of liquid holdup in the slug. The authors state that no independent relationship for the liquid holdup in the slug exists, but the solution is not very sensitive to the value of the liquid holdup. Flow visualization results

provided insights into the slug flow stages, and pressure-time traces and individual phase velocity measurements demonstrated good agreement with the model. Nicholson et al. (1978) extended the Dukler and Hubbard (1975) model to include the elongated bubble flows. They state that both the bubble flow pattern (also known as plug flow) and the slug flow pattern can be adequately modeled by a single mechanism. The extended model allowed for the evaluation of the pressure gradient without prior knowledge of the slug frequency. While the measured values of the film length varied over a range of two orders of magnitude, the values of the slug length varied over the range of only one order of magnitude. The extended model uses an average and constant value of the slug length, which allows the film length and slug frequency to be determined by a mass balance. This model showed good agreement with experimentally measured pressure drops for air-oil mixtures in both a 25.8 cm and 51.2 cm diameter tubes for most of the intermittent regime. The largest discrepancies occurred in the lowest pressure gradient range, which corresponded to the elongated bubble flow (plug flow). Their procedure also provides for prediction of transitions between intermittent, dispersed, and proto-slug (waves that do not bridge the tube cross section) flows.

Taitel and Dukler (1976) devised a theoretical approach to flow regime mapping for air-water mixtures using a momentum balance on a purely stratified flow pattern. A set of four non-dimensional parameters was created to identify these transition criteria. The transition from stratified flow to intermittent or annular flow was defined using a modified Froude number with the Kelvin-Helmholtz theory as the basis. They reasoned that intermittent flow would result if the instability driven wave growth could be supported by high liquid levels. For liquid levels lower than one-half the tube diameter, stratified flow would transition to annular flow. The boundary between intermittent and annular flow was therefore assumed to occur at a constant value of the Martinelli parameter, X . The transition between stratified-smooth and stratified-wavy flow was based on the requirement for high enough gas velocities to initiate wave formation, but without transition to intermittent or annular flow. They relied on the work of Jeffreys (1925, 1926) and Benjamin (1968) to establish the criterion for wave generation. The intermittent to dispersed flow transition was modeled using a criterion for the turbulent fluctuations to overcome buoyancy forces and thus cause dispersion of the gas phase. Good agreement was demonstrated between their model and the flow regime map of Mandhane et al. (1974) which was developed from experimental data. They also predicted the effect of fluid properties, pipe inclination, and pipe diameters on flow regime transitions.

The effects of fluid properties and pipe diameter on two-phase horizontal flow patterns were investigated extensively by Weisman et al. (1979) for pipe diameters ranging from 12.0 mm to 51.0 mm. The visually observed flow patterns were classified as plug flow, stratified

flow, wavy flow, slug flow, and annular flow. They also presented transition correlations that corrected for the effects of the liquid and gas properties. The effects of liquid viscosity on the flow regime transition lines were measured by varying the liquid viscosity and maintaining a constant surface tension. The surface tension was varied by using a surfactant to decrease the surface tension while maintaining a constant liquid and gas density. The gas density was varied by using various gases in the two-phase flow test setup. Using data from other investigators as well as new experimental data, modifications to existing correlations were developed for the flow-regime transitions. For the range of pipe diameters and fluids tested, it was concluded that the superficial velocities of the gas and liquid have the most influence on the transition lines. The liquid viscosity had a small effect on the transitions to dispersed flow and annular flow. Surface tension appeared to affect only the wavy-to-stratified flow transition. The authors reported that the liquid density affected the transition to dispersed flow as well as the transition from a separated to intermittent flow. The vapor density affected only the transition to an annular and a wavy flow pattern. From this study, Weisman et al. (1979) concluded that the pipe diameters and fluid properties have only moderate influences on the lines of transition.

Traviss and Rohsenow (1973) conducted two-phase flow pattern experiments during condensation of R-12 in an 8.0 mm diameter tube. They developed a transition criterion based upon the liquid film Froude number and compared the theoretical correlation to the current data. The theoretical transition was based upon the von Karman velocity profile in a liquid film and a momentum balance on the liquid. The authors concluded that the transition from annular flow to semi-annular flow (wavy annular) could be predicted at a constant value of the Froude number. Soliman (1982) extended the work of Traviss and Rohsenow (1973) by modeling the transition from wavy to annular flow using a constant Froude number with a liquid film thickness based upon the data of Kosky (1971). The results were compared with data for R-12, R-113, and steam. He concluded that the transition from annular flow to wavy annular flow occurs at a constant value of the Froude number for all three refrigerants and tube diameters ranging from 4.8 mm to 15.9 mm. Soliman (1986) used a similar approach to model the transition from annular flow to annular mist flow using a balance of the stabilizing and destructive forces in annular flow, and applied this approach to predict the heat transfer mechanism. He also stated that this transition could be adequately described by a constant value of the Weber number and reported that the flow was always annular for a Weber number less than 20, and always in the mist flow regime for a Weber number greater than 30. A correlation for the heat transfer coefficient based upon the flow mechanism was presented for the mist flow pattern. For a Froude number greater than 35, the difference between the theoretical and experimentally measured heat transfer coefficient was $\pm 20\%$.

More recently, statistical approaches have been taken to better define the transitions between flow regimes that are difficult to distinguish visually (Moore and Turley 1983, Annunziato and Girardi 1987). These transitions include plug or bubble to slug flow and annular to annular mist flow. This approach utilizes fluctuations in the pressure/time signals, void fraction, root mean square of pressure/time signals, frictional pressure gradients and chaos theory to provide an objective means to interpret flow pattern transitions. Moore and Turley (1983) used the pressure and void fraction fluctuations to identify flow patterns in two-phase flow. They conducted experiments using air and water in a 54 mm diameter horizontal tube. They found that pressure fluctuations alone were not an effective means for detecting the stratified or annular flow regimes. Time traces of the pressure fluctuations showed that the intermittent flows showed a square wave character, whereas homogeneous flows showed time traces that were more random. The void fraction measurements showed that the plug and slug flows appeared as a square wave, but it was difficult to distinguish between the two flow patterns. In annular flow, the void fraction was substantially higher near the wall, indicating a very thin liquid film. They state that, while neither of these two methods can provide a definite means for indicating the flow pattern, the two methods used in conjunction can provide valuable information about the flow. Similar to the work of Moore and Turley (1983), Annunziato and Girardi (1987) used a differential pressure measurement and local void fraction probes to measure the temporal fluctuations in a 90 mm diameter tube. They determined that, while differential pressure fluctuations could recognize flow patterns with an accuracy of 53% to 93%, depending upon the flow regime, local void fraction measurement could consistently recognize the flow patterns with an accuracy of 82%. The most accurate method, however, was using the differential pressure fluctuations in conjunction with a local void fraction measurement, which yielded an accuracy of 96%.

The previous work discussed thus far addressed tubes of relatively large diameters ranging from 11.5 mm to 258.0 mm, for which pipe diameter and fluid properties have only minor effects on the flow-regime transitions. For diameters larger than 200 mm, the Lockhart-Martinelli (1949) correlation for pressure drop predicts a value that is 40 to 60 percent higher than the experimentally measured values. The flow map predictions of Mandhane et al. (1974) and the correlations of Weisman et al. (1979) are based upon pipe diameters that ranged from 12 mm to 165 mm. In the present study, tube diameters significantly smaller than 11.5 mm were used and it is shown that the differences in the relative effects of gravitational, shear, and surface tension forces cause the transitions between flow regimes to be different from those found in the larger tubes. The theoretical flow regime map of Mandhane et al (1974) and the transition lines proposed by Weisman et al. (1979) may not be applicable to these smaller diameters. Thus, the

behavior of the two-phase flow pattern transitions must be identified before the pressure drop and heat transfer characteristics in small diameter round and rectangular tubes can be investigated.

Previous Research on Small Diameter Circular Tubes

There has been relatively little work done on the development of two-phase flow regime maps for small diameter tubes. Suo and Griffith (1964) investigated the elongated bubble flow pattern in capillary tubes with diameters ranging from 1.0 mm to 1.6 mm using air-water, N₂-water, He-Heptane and N₂-heptane as the working fluids. They developed criteria for the transitions from the elongated bubble to the annular flow pattern and the bubbly flow pattern using dimensional analysis to identify the most significant parameters. Two boundaries of the slug flow pattern were identified. The first transition was from slug flow pattern to annular flow, and the second transition involved the breakup of the tails of the bubbles which resulted in a bubbly slug flow. Barnea et al. (1983) made visual observations of air-water two-phase flow patterns in both horizontal and vertical upward flow. The tube diameters ranged from 4.0 mm to 12.0 mm. They classified these flow patterns according to four major regimes (dispersed, annular, intermittent and stratified). They found that all transitions, except the stratified to non-stratified transition were, in general, satisfactorily described by the Taitel and Dukler (1976) theoretical model. They suggested that the discrepancy in the transition from stratified flow to non-stratified flow was due to the effects of surface tension – an effect that is not covered by the Taitel and Dukler (1976) model, and proposed a criterion for this transition. They also suggested that in these smaller diameter tubes, the transition from intermittent to annular flow is better described by a constant liquid level height ratio of 0.35, rather than 0.5 suggested by Taitel and Dukler (1976).

Tandon et al. (1985) conducted flow visualization experiments on mixtures of R-22 and R-12 in a 10 mm diameter tube during condensation. The visual observations were classified into five different patterns including annular, semiannular, wavy, slug, and plug flows. They compared the visual observations to the flow regime maps of several other authors. While there was good agreement with the Baker (1954) map in annular flow and intermittent flow, the wavy flow data did not correlate well and occupied parts of the annular and slug flow regions. The authors developed flow regime maps using the dimensionless gas velocity and the void fraction and found that this format provided a significant improvement in the prediction of the annular, wavy, and slug flow patterns. Wang et al. (1997) measured pressure drops and conducted visual observations of flow patterns of R-22, R-134a, and R-407C in a 6.5 mm circular tube. They classified the flow patterns as stratified, intermittent, annular, and bubble flow. The mass flux ranged from 50 kg/m²-s to 700 kg/m²-s. The visual observations were compared to the flow

regime maps of Baker (1954), Mandhane et al. (1974), and Weisman et al. (1979). They reported that 85% of the data were predicted by the flow regime map of Weisman et al. (1979), whereas the flow regime map of Baker (1954) predicted only 59% of the data. The flow regime map of Mandhane et al. (1974) was the least accurate, with only 12% of the data being correlated correctly. The authors compared the pressure drop data to the Chisholm (1973) correlation. They found a strong relationship between the flow pattern and the constant used in the Chisholm (1973) correlation. When the mass flux was greater than $200 \text{ kg/m}^2\text{-s}$, they were able to correlate the two-phase pressure drop with a two-phase multiplier and 91% of the data were fit within $\pm 20\%$. For a mass flux less than $200 \text{ kg/m}^2\text{-s}$, the mass flux showed a much stronger effect on the two-phase multiplier. The authors concluded that the constant in the Chisholm (1973) correlation was better represented as a function of the Martinelli parameter, X , fluid properties, and the liquid-only Reynolds number. By using this approach, 85% of the data for the lower mass flux cases were correlated within $\pm 20\%$.

Damianides and Westwater (1988) developed individual flow regime maps for air-water mixtures for diameters in the range 1.0 mm to 5.0 mm using visual observation, high speed photography and fast acting pressure transducers. They noted that separated flow is impossible to generate in a 1 mm tube with air and water. Most of the flow regime map for this tube consisted of slug flow, and the transition to annular flow was through the incidence of roll waves. In the 2 mm tube, intermittent regimes continued to occupy a major portion of the map, although wavy stratified flow was also observed. They commented that the transition to annular flow at higher gas velocities was due to surface tension forces that oppose gravity. For the larger tubes, this transition occurred due to deposition of liquid drops on the tube wall. The slug flow-to-annular flow transition was due to thinning of the slugs or wave rings to form a uniform annular liquid film. For a 5 mm tube, they mentioned that the transition from plug to slug flow was due to agglomeration of gas plugs, Kelvin-Helmholtz theory, which assumes the growth of a wave, cannot be used for predicting this transition. They found that the Taitel-Dukler (1976) map predicted the experimentally observed transitions between dispersed bubble flow and intermittent flow well, whereas the intermittent-to-annular transition prediction was not as good. Also, even after using corrections for small tubes proposed by Barnea et al. (1983), the limits for stratified flow were not predicted well. They also found that flow regime transitions in round tubes (2 mm) were not the same as those found in a similar (1.74 mm) compact heat exchanger tube.

Fukano et al. (1989) investigated flow patterns and pressure drop in capillary tubes for air-water flow with diameters ranging from 1.0 mm to 4.9 mm. They found good agreement between their flow regime transitions and those proposed by Barnea et al. (1983); however, the

agreement with Mandhane et al. (1974) was not very good. This led them to conclude that tube diameter plays a significant role in determining flow regimes. They developed expressions for relative velocities between the two phases, liquid slug length (for intermittent flow) and flow regime-based pressure drop equations from first principles. Pressure drop in intermittent flow, in particular, was composed of liquid friction and expansion losses as the liquid flows around large bubbles. Similar considerations were also used to develop criteria for transitions between these regimes.

It appears that flow regime maps presented by Mandhane et al. (1974) cannot sufficiently predict the flow regime transitions in small hydraulic diameter tubes – primarily because this map was developed using tube diameters significantly larger than those studied by Damianides and Westwater (1988), Suo and Griffith (1964) and Fukano et al. (1989). Similarly, the theoretical predictions of Taitel and Dukler (1976) and the correlations presented by Weisman et al. (1979) are not applicable for small hydraulic diameter tubes.

Previous Research on Rectangular Tubes

Most of the research on two-phase flow in small hydraulic diameter rectangular channels uses tubes of either small ($\alpha < 0.50$) or large ($\alpha > 2.0$) aspect ratios (Hosler 1968, Jones and Zuber 1975, Wilmarth and Ishii 1994). Hosler (1968) developed flow regime maps for boiling of steam in a vertical, rectangular, $D_h = 5.64$ mm channel ($H = 3.175$ mm, $W = 25.4$ mm) at pressures ranging from 1034 kPa to 13790 kPa. He found that both the system pressure and mass flow rate had an effect on the flow transitions. As the pressure increased, the overall size of the bubbles decreased, and the transition from bubble flow to slug flow, and slug flow to annular flow, occurred at a higher quality. He pointed out that this change in system pressure has a direct impact on the two-phase fluid properties, and that the effect of pressure on the transition lines may be attributed to the change in specific volume of the gas. As the mass flow rate was increased, Hosler (1968) reported that the flow pattern transitions occurred at a lower bulk enthalpy, and that the slug flow regime becomes smaller. At very high mass flow rates, there appeared to be a direct transition from bubble flow to annular flow. He also noted that flow regime maps developed by Baker (1954), Kozlov (1954), and Quandt (1965) do not adequately predict flow patterns for boiling flow in thin rectangular channels.

Richardson (1959) studied air-water flow patterns, void fraction, slip ratio, and pressure drop in rectangular channels with aspect ratios ranging from 0.125 to 0.50 and hydraulic diameters ranging from 11.30 mm to 33.90 mm. For each of the three channels tested, the width was held constant at 50.80 mm and the height was varied from 6.35 mm to 25.4 mm. The void fraction of the two-phase mixture was determined by measuring changes in the attenuation of gamma radiation. The experimentally measured void fractions were plotted as a function of the

Martinelli parameter, X , and it was determined that the actual void fractions were higher than those predicted by Lockhart and Martinelli. He found that the smaller aspect ratio suppressed the stratified and wavy flow regimes and promoted the onset of elongated bubble and slug flows, which was attributed to the ability of the liquid to more readily rise to the top of the tube. The experimentally measured two-phase pressure drop fit the correlation of Lockhart and Martinelli, but, in general, the two-phase pressure drops were higher than those predicted by Lockhart and Martinelli. He proposed a new two-phase pressure drop correlation based upon the void fraction, which predicted the major portion of the data within $\pm 20\%$. Troniewski and Ulbrich (1984) studied flow patterns in both horizontal and vertical flow. A total of ten different channels with $0.10 \leq \alpha \leq 11.20$ and $7.45 \text{ mm} \leq D_h \leq 13.10 \text{ mm}$ were investigated. The liquid properties were varied using different concentrations of a sugar-water solution. The authors proposed flow regime maps for both horizontal and vertical flows in rectangular channels and concluded that stratified flow did not exist in air-water flows for $\alpha \leq 0.1$. In an aqueous solution of sugar-air, stratified flow did not occur for $\alpha \leq 0.5$. Furthermore, the authors stated that the liquid viscosity has an insignificant effect on the annular flow transition for the range of tube diameters and aspect ratios studied.

Kordyban and Ranov (1970) investigated the transition from a wavy flow pattern to a slug flow pattern in horizontal, rectangular channels using air and water as the working fluids. The channel was 152.4 mm wide by 25.4 mm high with an aspect ratio of 0.167. They extended the Kelvin-Helmholtz instability theory to determine if this instability causes the onset of the slug flow pattern. They derived a simplified instability condition based upon the liquid and gas velocities, properties, wave number, and the liquid level. Reasonably good agreement between the theoretical instability condition and the experimental data were reported. They concluded that there were four primary variables responsible for the transition to slug flow. These variables include the gas velocity, liquid level, wave length, and the wave height.

Wallis and Dobson (1973) investigated the onset of slugging in horizontal, rectangular channels using air and water as the working fluids. Two rectangular channels were investigated: 25.4 mm wide by 25.4 mm high, and an 89 mm wide channel whose height was adjusted from 76 mm to 305 mm. Tests were conducted with stagnant, cocurrent and countercurrent flows of water. At void fractions ranging from 0.2 to 0.5, they reported that waves would form slugs in the channel. A transition correlation for slug flow was presented. This correlation was a function of the relative velocities of the liquid and gas, densities of the liquid and gas, and liquid level height. The proposed correlation was compared to the data obtained in the experiments and reasonable agreement was reported.

Wambsganss et al. (1991) developed a flow pattern map for a 19.05 mm by 3.18 mm

rectangular tube (with the large side being placed in the horizontal and vertical orientations) as well as a quantitative method for detecting the transition to slug flow. Air-water mixtures were tested in the mass flux range of 50-2000 kg/m²-s. The transition was detected by plotting the root mean square pressure fluctuations versus the mass quality of the mixture. Based on the observation that large amplitude waves occur in the regime typically considered to be annular flow, they suggested that the annular flow pattern should be divided into both wavy flow and annular flow. They reported that the stratified regime (stratified pattern and wave pattern) was not seen in the tube with an aspect ratio of 0.167 and suggested that the height of the tube was too small to allow a finite-thickness film. Pressure drop measurements were plotted in terms of a two-phase frictional multiplier and quality, and a discontinuity in the data existed at a quality of approximately 0.002 and a Martinelli parameter of 10. This discontinuity corresponded to a change in the flow pattern from plug or bubble flow to slug flow. No discontinuity was found in any other flow transitions. The authors compared the flow regime map of the rectangular channel with the findings of Mandhane et al. (1974), Govier and Omer (1962), Damianides and Westwater (1988), and Fukano et al. (1989). While there was qualitative agreement, the authors concluded that the data on large diameter tubes is not applicable to small, rectangular channels.

Wambsganss et al. (1994) extended this work to further investigate the RMS pressure fluctuations in a rectangular channel with a hydraulic diameter of 5.45 mm and an aspect ratio of 6.0. They reported that these fluctuations are small in the bubble and annular flow patterns, and large fluctuations occur in the slug and froth flow regions. They identified a local peak in the RMS pressure that corresponded to the transition to slug flow and reaffirmed that there was no change in slope in the two-phase frictional multiplier plotted against quality when the flow pattern changes from slug flow to annular flow. They concluded that the plug flow pattern is characterized by low-frequency, low-amplitude fluctuations in the RMS pressure, while annular flow is characterized by higher amplitude, low frequency fluctuations.

Cai et al. (1996) applied chaos theory to the work of Wambsganss et al. (1991, 1994) to determine the transition to slug flow in horizontal, rectangular channels. Air-water data at a fixed mass flux (500 kg/m²-s) were used in conjunction with various chaos variables to determine whether chaos theory can accurately predict the transition. These variables included the power spectral density (frequency dependent variable), autocorrelation function (time dependent variable), pseudo-phase planes (time dependent variable), Lyapunov exponents (indicator of a chaotic versus non-chaotic system), and correlation dimensions (fractal and dimensional variable). The authors concluded that the pseudo-phase planes and autocorrelation functions predicted that the fluctuations in the RMS pressure measurements were chaotic in nature. Furthermore, the Lyapunov exponents were positive in value, which is a further

indication of chaotic motion. They found that the correlating fractal dimensions were higher in slug flow and suggested that this method may be a good indicator of the flow transition. The authors cautioned, however, that fractal dimension algorithms needed to be improved and at that time, could not be used as an online analysis tool for flow regime identification.

Need for Further Research in Flow Regime Mapping

The above discussions show that there are significant gaps in the understanding of two-phase flow regimes in small diameter round and rectangular tubes. Specifically, the effect of tube diameter and aspect ratio on flow pattern transitions is not well understood, with conflicting trends reported by different investigators. The vast majority of literature available on flow-regime mapping utilizes larger diameter tubes and this information may not be applicable to microchannel geometries. It is postulated that the relative effects of shear (inertia), gravity, and surface tension will be different in microchannel geometries. Little research has been done on the effect of tube geometry, hydraulic diameter and aspect ratio on flow regime transitions in small hydraulic diameter tubes. While these effects may be minimal in larger diameter tubes, it is suspected that geometry, hydraulic diameter and aspect ratio effects will have a large impact on the flow regime transitions.

The variation of flow patterns with tube diameter and shape could reflect the varying influences of surface tension, shear, and gravity. Furthermore, it is expected that a rectangular tube with sharp corners could allow the liquid to be drawn up and held more readily along the tube walls. This will allow plug, slug and annular flows to be sustained at higher gas and liquid superficial velocities while delaying or eliminating stratified, wavy and dispersed flow patterns. The variation of flow patterns with tube diameter and shape could reflect the varying influences of surface tension, shear, and gravity forces. Prior to determining the pressure drop and heat transfer characteristics of small diameter rectangular tube geometries, flow regime maps and the flow mechanisms must be documented.

Finally, the majority of flow regime mapping research uses two-component air-water systems to simulate condensing two-phase flow. Extrapolation of the flow regimes observed in isothermal air-water mixtures to flow regimes during phase change in refrigerants may not be justifiable. The present study therefore first investigates and documents the effect of hydraulic diameter on the flow pattern transitions in air-water systems. This also includes documenting the differences in round and rectangular tubes of similar hydraulic diameters in air-water systems. Next, the effect of tube geometry, hydraulic diameter and aspect ratio for R-134a systems during condensation is investigated. With this accomplished, the pressure drop characteristics for each flow regime in small diameter rectangular tubes are investigated.

Two-Phase Pressure Drop

This section discusses the literature on pressure drop in two-phase flow. Some of the earlier work done on pressure drop in two-phase flow (Boelter and Kepner 1939, Baker 1954, Alves 1954, White and Huntington 1955, Govier et al. 1957, Govier and Omer 1962) has been discussed in the previous section, since those papers also discussed flow regime mapping. There is a substantial amount of literature available on the prediction of pressure drop in two-phase flows. Several of the pressure drop correlations found in the literature are either theoretical, or are based upon experiments carried out using air-water in large diameter round tubes. Very few experiments have been conducted on the two-phase pressure drop in microchannels geometries. Furthermore, it has been shown that current two-phase pressure drop correlations are applicable to a limited range of quality, and large errors occur when these correlations are applied outside the intended range (Ferguson and Spedding, 1995). Therefore, taking the approach of flow regime-based correlations is necessary to more accurately predict the pressure drop in two-phase flows.

Boelter and Kepner (1939) investigated the pressure drop of air-oil and air-water mixtures in 12.7 mm and 19.05 mm diameter tubes. They reported that the two-phase pressure gradient varied as a power of the air mass flow rate. They also compared the pressure drop in a dry pipe to that of a pipe which was previously wetted with oil and then thoroughly blown down and found that there was an increase in the pressure drop due to surface wetting. For an air-oil ratio of 0.315, they reported a two-phase pressure drop that was 5.3 times that of air alone. The effect of liquid viscosity was investigated by using three different oils. The authors reported that the effect of the liquid viscosity on the two-phase pressure drop diminishes at lower viscosities. They suggested that a two-phase mixture tends to flow as slugs at lower viscosities and tends to flow as a spray at higher viscosities. They proposed that two-phase pressure drop should be a function of the liquid and gas Reynolds numbers, the liquid Froude number, and the liquid Weber number.

Lockhart and Martinelli (1949) conducted a series of experiments on tubes with sizes ranging from capillary to 25.4 mm diameter, and found an empirical relationship between the two-phase pressure drop and the superficial gas velocity. Jenkins (1949) measured the liquid-phase pressure drop of air-water mixtures in a 25.4 mm tube and reported that the Lockhart-Martinelli correlation predicted the pressure drop within $\pm 40\%$ of the mean. This degree of accuracy is similar to that reported by Lockhart and Martinelli (1949). He classified the flow into several patterns based upon visual observations. These patterns included bubble, stratified, wave, semi-annular, and annular or turbannular flow. Jenkins (1949) reported that the pressure drops were more than 100% higher in the stratified flows than those reported by Gazley and

Bergelin (1947). Jenkins (1949) stated that this discrepancy may be due to a hydraulic gradient in the liquid phase, and that the two-phase pressure drop may be a function of the liquid level height. The author plotted the two-phase pressure drop as a function of a two-phase friction factor and the gas Reynolds number. The data showed well defined changes in slope that corresponded to a change in flow patterns.

Bergelin and Gazley (1949) investigated the two-phase pressure drop and flow patterns of air-water flows in a 25.4 mm and a 52.45 mm tube. They reported that the correlation by Lockhart and Martinelli (1949) over-predicted the experimentally measured pressure drop and suggested that the correlation may not be valid for stratified flows. Alves (1954) measured the two-phase pressure drop of air-water and air-oil in a 25.4 mm tube and recognized several different flow mechanisms corresponding to different gas and liquid superficial velocities. He used the Lockhart-Martinelli correlation and found that, in general, the experimentally measured pressure drop in annular flow was higher than that predicted by the Lockhart-Martinelli correlation. He also reported that the pressure drop in wavy flow was about 60% less than that predicted by the Lockhart-Martinelli correlation. He suggested that it was necessary to take the flow pattern and regime into account while computing two-phase pressure drops.

The concept of flow-regime based pressure drop correlations is not new. Baker (1954) discussed the importance of the flow patterns in the development of a two-phase pressure drop correlation and plotted an experimentally determined two-phase multiplier versus the Martinelli parameter, X . He suggested that a change in slope in this plot was due to a change in the flow mechanism. Johnson and Abou-Sabe (1952) conducted heat transfer and pressure drop experiments in a horizontal, 22.1 mm inner diameter tube. They reported that the pressure drop data could be correlated to the Lockhart-Martinelli correlation within $\pm 30\%$. They plotted the gas-to-liquid velocity ratio versus the air flow rate and found a good correspondence between the change in slope and a change in flow pattern. From these experiments, it was concluded that the effect of the flow pattern is important and influences both the pressure drop and heat transfer. From this discussion, it is apparent that the concept of flow-regime based pressure drop and heat transfer correlations have existed for over fifty years. However, reliable pressure drop correlations for each of the flow regimes are not available.

Previous Research on Large Hydraulic Diameter Tubes

Hoogendoorn (1957) investigated flow pattern and two-phase flow pressure drop characteristics of air-water and air-oil mixtures in tube diameters ranging from 24 mm to 140 mm. He classified the flow as stratified, plug, froth, slug, wave, mist, and mist-annular flow. Two-phase pressure drop data were compared to the Lockhart-Martinelli correlation and good agreement was found in the plug, slug, and froth flow patterns at atmospheric conditions.

Typically, the data could be predicted within $\pm 30\%$. If the gas density differed from that of air at atmospheric conditions, the authors stated that the Lockhart-Martinelli correlation over-predicted the measured pressure drop. Pressure drops in the stratified, wavy, and mist-annular patterns were not well predicted by the Lockhart-Martinelli (1949) correlation. The authors proposed a two-phase pressure drop correlation which included the influences of gas density and pipe roughness.

Anderson and Russell (1965) investigated several predictive models and found that the flow regime had an effect on the ability of these models to predict the two-phase pressure drop. They recommended the two-phase pressure drop models to be used for different flow regime conditions. For mist, bubble, or slug flow, they determined that the model by Dukler et al. (1964) provided the most accurate results. Akagawa et al. (1971) analyzed the fluctuations in the two-phase pressure drop in vertical tubes in the slug flow pattern using air and water in a 27.6 mm diameter tube. The pressure in the bubble was found to be fairly constant, and the pressure drop in the slug consisted of the sum of the static head, shear stress on the wall, and the pressure recovery due to the liquid moving around the bubble. The authors showed that the fluctuation in the pressure drop in vertical flows was due to the changes in the void fraction. The mean pressure drop was calculated theoretically using the values of the mean lengths of the slug and gas bubble with good agreement between the theoretical and experimental values.

Mandhane et al. (1977) evaluated several correlations and models used to calculate the two-phase pressure drop in horizontal flow. Roughly 10,500 data points were used to evaluate the correlations. A total of sixteen correlations and models were investigated and the authors made recommendations based upon the ability of these models to predict the two-phase pressure drop. Five separate parameters were used to test the correlations including the root mean square error, arithmetic mean absolute error, arithmetic mean error, arithmetic mean percentage absolute error, and the arithmetic mean percentage error. For bubble, annular, and annular-mist flows, the correlation of Chenoweth and Martin (1956) showed the least amount of overall error in the five parameters. The authors recommended the method proposed by Agrawal et al. (1973) for stratified flows. Wave flows were best represented by the Dukler et al. (1964) model. The pressure drop in slug and dispersed bubble flows were best predicted by a modified version of the Lockhart-Martinelli correlation.

Beattie and Whalley (1982) compared several pressure drop correlations to their proposed theoretical model. The authors included the effects of flow pattern by using a pseudo-viscosity based upon the flow pattern and the homogeneous void fraction. They compared this model to the data from the HTFS (Heat Transfer and Fluid Flow Service, England) data bank on horizontal and vertical two-phase pressure drop. The model proposed by Beattie and Whalley

(1982) showed that the pressure drop could be predicted within 2.6 times the actual value. Olujic (1985) proposed a method of predicting the two-phase pressure drop based upon two flow regimes, which were differentiated by the relative magnitude of the gas and liquid velocities. In the first regime (the beta model), the two-phase velocities are relatively equal and this includes such flow patterns as plug and slug flow. The second regime (the alpha model) includes the regions where the gas velocity is significantly higher than the liquid phase (wavy and annular-dispersed flows). The pressure drop in the beta region uses a distributed flow model to predict the pressure drop, whereas the alpha region follows the model proposed by Lockhart and Martinelli (1949). Olujic (1985) extended the Lockhart-Martinelli (1949) correlation to include a two-phase flow parameter, epsilon, that represents the slip between the two phases. He compared the two models with 30 separate experiments with tube diameters ranging from 2.6 mm to 150 mm. The proposed method was able to predict the experimental data better than the Lockhart-Martinelli correlation in 26 of the 30 comparisons. In the smallest tube (2.6 mm), however, Olujic's (1985) model was able to predict only 38% of the data within $\pm 30\%$.

Kadambi (1985) modeled the two-phase flow pressure drop by assuming a polynomial velocity profile in the annular film. This model allows the pressure drop, void-fraction and annular film thickness to be predicted, but a ratio of the gas and liquid friction factor ratio is required. He reported that this ratio of the friction factor of the gas to the friction factor of a smooth interface is typically given as a function of the void fraction. Good agreement between the model and experimental data was found in vertical flows, where droplet entrainment plays a large role. In horizontal flows, the prediction of pressure drop led to inaccurate results.

Hashizume and Ogawa (1987) analyzed existing two-phase pressure drop data from the HTFS data bank and presented a pressure drop correlation for the low quality region. The pressure drop data included results from air-water, steam-water, R-11, and R-12 experiments. The tube diameters ranged from 25.4 mm to 154.1 mm for the air-water data, from 12.3 mm to 304.8 mm for the steam-water data, and 6.0 mm to 25.0 mm for the R-11 and R-12 data. The data were compared to existing methods for calculating the two-phase frictional pressure drop. The authors concluded that the correlation proposed by Bandel (1973) and Storek & Brauer (1980) worked slightly better than the proposed pressure drop model for air-water and steam-water systems. Approximately 80% of the steam-water and 90% of the air-water pressure drop data could be predicted within $\pm 30\%$. The proposed model, however, more accurately predicted the refrigerant pressure drop data: approximately 85% of the data could be predicted within $\pm 30\%$.

Ide and Matsumura (1990) investigated the effects of aspect ratio, hydraulic diameter and angle of inclination on the two-phase pressure drop for air-water flows in rectangular channels

and developed pressure drop correlations based upon the separated flow model. The hydraulic diameters ranged from 7.3 mm to 21.4 mm and the aspect ratios ranged from 1.0 to 40.0. The experiments showed the Chisholm and Liard (1958) correlation (a correction to the Lockhart-Martinelli correlation for pipe roughness) to be in good agreement with the experimental data. They proposed two pressure drop correlations based upon the experimental data. The first correlation is for hydraulic diameters larger than 10 mm and the second correlation is for channels with hydraulic diameters less than 10 mm with large aspect ratios. Their correlations fit the experimental data with an accuracy of $\pm 30\%$.

Behnia (1991) attempted to determine the most accurate pressure-drop correlation and classified pressure drop models into three categories: homogeneous models where the gas and liquid phases move at the same velocities, separated models that assume there is a slip between the two phases, and flow regime models where each flow regime is represented by a different pressure drop correlation. The authors tested seven different correlations – two from the first two types of models, and five that were based upon flow regimes. Two-phase pressure drop data from the American Gas Association was used to test the seven correlations. Three parameters were used to evaluate the correlations including the average error, standard deviation, and the RMS error. Overall, Behnia (1991) determined that the correlation proposed by Brill and Beggs (1973) worked the best at predicting the two-phase flow pressure drop. There have been numerous studies comparing existing correlations to actual pressure drop data. Friedel (1979) tested 14 relationships and found large relative errors in all the predictive models except the Baroczy-Chisholm (Chisholm, 1973) relationship for predicting the pressure drop in air-water systems. Ferguson and Spedding (1995) provided a summary of the findings from these reports as well as several others. They used experimental two-phase pressure drop data from an air-water system and tested the data against available theoretical models and experimental correlations. The two-phase air-water pressure drops in a 9.35 cm tube (12.813 m long) were measured for various flow rates of air and water representing qualities in the range of 0 to 1. The authors reported that a single correlation could not accurately predict the pressure drop in all flow regimes. They stated that some of the tested models were designed for a specific flow regime or for vertical flows, and resulted in large errors when applied to other flow regimes or horizontal flows. The authors emphasized the point that a single pressure drop model could not accurately predict the pressure drop in all flow regimes.

De Souza and de Mattos Pimenta (1995) conducted pressure drop experiments on a wide variety of refrigerants including R-12, R-22, R-134a, MP-39 and R-32/125. The tube diameters ranged from 7.75 mm to 10.92 mm and the mass flux ranged from 100 kg/m²-s to 300 kg/m²-s. The authors introduced a pressure drop correlation based upon the separated flow model and the

Martinelli parameter, X , in conjunction with a non-dimensional fluid property correction factor. Although this correlation was not based upon specific flow regimes, the experimental data were predicted within $\pm 20\%$.

Previous Research on Small Hydraulic Diameter Tubes

Obot et al. (1993) introduced a method for calculating the frictional component of the pressure drop, which was validated for air-water systems with mass fluxes ranging from 50 $\text{kg/m}^2\text{-s}$ to 2000 $\text{kg/m}^2\text{-s}$ using three rectangular tubes and one round tube. The hydraulic diameters and aspect ratios ranged from 6.4 mm to 2.7 mm and 6.0 to 0.2, respectively. They argued that, in principle, a two-phase pressure drop need not be correlated to a friction factor or a Reynolds number. The authors state that there are basically three regions for pressure drop – and this is analogous to the single-phase regions of laminar, transitional and turbulent flows, but caution that there is no criterion for establishing a laminar, transitional and turbulent two-phase flow. The air-water pressure drop data provided by the authors show that the first two regions for pressure drop occur at a quality less than 0.05 and the authors speculate that two-phase laminar flow may exist at very low qualities and mass fluxes of air-water. They proposed that the friction factor of the gas varies with the superficial gas velocity raised to the 0.65 power over most of the range of quality, and that the largest errors occurred in the region where $x \leq 0.2$. They stated that this method showed good agreement with the data, with 85% of the data predicted within $\pm 20\%$, and 92% of the data predicted within $\pm 30\%$.

Wang et al. (1996) investigated the frictional pressure gradient of both R-22 and R-407C in a 7.92 mm tube. The mass flux ranged from 100 $\text{kg/m}^2\text{-s}$ to 300 $\text{kg/m}^2\text{-s}$. Among the two fluids, R-407C had a 45% smaller frictional pressure gradient at the highest mass flux while both fluids exhibited a similar frictional pressure gradient at the lower mass flux. Wang et al. (1996) stated that while both frictional pressure gradients were proportional to the mass flux raised to the power of 2.45, the large differences in the frictional pressure gradients at the high mass flux might be attributed to a difference in flow patterns. This work exemplifies the importance of predicting the flow regime and basing pressure drop correlations on the individual flow mechanisms.

Chang and Ro (1996) investigated the pressure drop in capillary tubes (1.2 mm to 1.6 mm inner diameters) with R-22, R-134a and R-125 as well as mixtures of these substances. A model for predicting the frictional pressure drop of both single and two-phase flow was presented. The tests were conducted at a pressure of 1025 kPa to 2800 kPa and the investigators pointed out that the wall roughness, although small, had a significant impact on the friction factor. The investigators stated that the single-phase friction factor can be increased by as much as 4.6% in the 1.2 mm tube and up to 12% in the 1.6 mm tube simply due to the wall roughness.

The wall roughness of the tubes was calculated to be 0.1963 μm for the 1.2 mm tube and 0.6894 μm for the 1.6 mm tube. They utilized a two-phase flow multiplier to the single phase pressure gradient and a two-phase viscosity suggested by Ciccitti et al. (1960). This method predicted the experimental pressure drops with a relative error of 17.1%.

Yang and Webb (1996) investigated the two-phase pressure drop in a microchannel tube with and without internal fins using R-12 as the working fluid. The mass flux ranged from 400 $\text{kg}/\text{m}^2\text{-s}$ to 1400 $\text{kg}/\text{m}^2\text{-s}$ and the hydraulic diameters of the two tubes were 1.56 mm and 2.64 mm, respectively. The experimentally measured two-phase pressure drop was compared with a theoretical value that uses a two-phase friction factor and includes entrance and exit effects. The ratio of these two values was reported to be in the range of 0.82 to 0.97. Yang and Webb (1996) concluded that the minor losses to the entrance and exit effects are well accounted for by the theoretical calculations. Single phase tests on the two tubes resulted in values that were 14% and 36% higher than those predicted by the Blassius equation for the plain and finned tubes, respectively. They correlated the two-phase pressure drop data with a two-phase friction factor and an equivalent Reynolds number, and separate correlations for each of the two tubes were presented. The agreement between the data and the correlations were within $\pm 20\%$. The authors concluded from these experiments that the two-phase pressure drop was dominated by vapor shear in both the plain and micro-fin tubes and that surface tension forces had no significant effect on the frictional pressure drop.

Yan and Lin (1998) investigated evaporative heat transfer and pressure drop in a round 2.0 mm diameter tube using R-134a as the working fluid. To determine the frictional component of the two-phase pressure drop, the theoretical expansion, contraction and deceleration pressure drops were removed from the total measured pressure drop. The expansion and contraction losses were estimated using the separated flow model. The deceleration pressure drops were estimated from the homogeneous flow model for two-phase gas-liquid flows. They indicated that losses due to expansion/contraction and deceleration were small and that the frictional pressure drop ranged from 95 to 98% of the total measured pressure drop. They proposed an empirical correlation for the frictional pressure drop as a function of the equivalent two-phase Reynolds number. The average deviation between the experimental data and the proposed correlation was 17%.

Need for Further Research on Pressure Drop

From the above discussion, it is apparent that no single correlation adequately predicts the two-phase pressure drop for all flow patterns. Furthermore, microchannel geometries typically have hydraulic diameters less than 1.0 mm, and the vast majority of the correlations currently found in the literature are based upon substantially larger hydraulic diameters. There is

a strong need for pressure drop correlations that are based upon the two-phase flow mechanisms found in microchannel geometries. While there are some flow-regime based pressure drop correlations in the literature, these correlations are based upon substantially larger diameter tubes and may not accurately represent the pressure drop in microchannel geometries. Thus, the focus of the present study is to develop flow regime-based pressure drop correlations for two-phase flow in microchannel geometries.

CHAPTER THREE. EXPERIMENTAL SETUP AND PROCEDURES

Detailed descriptions of the experimental test facilities, equipment, and test procedures used in this study are provided in this chapter. As previously stated, this study was divided into three phases including adiabatic air-water mixture flow visualization (Phase I), flow visualization of R-134a during condensation (Phase II), and two-phase pressure drop in microchannel geometries (Phase III). Therefore, this chapter is organized into three sections that describe the experimental facilities for each of these phases.

Adiabatic Air-Water Flow Visualization

The purpose of this phase of the study was to investigate flow mechanisms established for air-water flow in tubes with hydraulic diameters less than 6 mm. Specifically, this phase of the study addresses the effect of hydraulic diameter and tube geometry on the flow regimes and transitions found in air-water systems. This was accomplished by testing circular tubes of decreasing hydraulic diameters, and a rectangular tube with a hydraulic diameter similar to that of one of the circular tubes. The four circular tubes had diameters of 5.5 mm, 2.6 mm, 1.75 mm, and 1.30 mm. The rectangular channel had a hydraulic diameter of 5.36 mm (4.6 mm H x 6.4 mm W) and an aspect ratio of 0.725. Figure 2 depicts the shapes and sizes of the tubes tested in this phase.

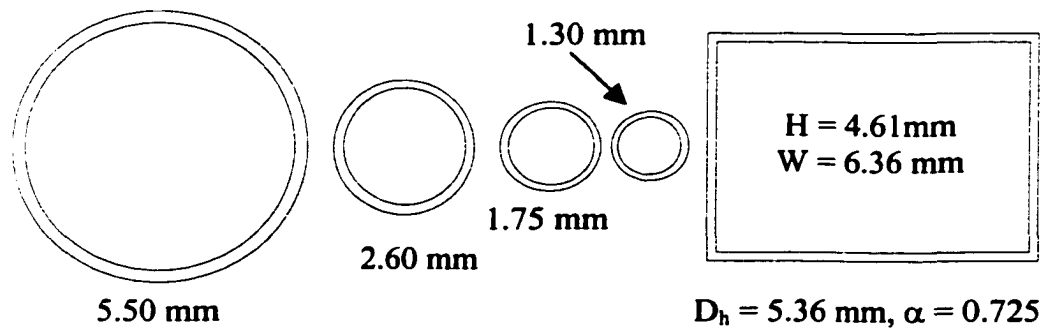


Figure 2. Test Matrix for the Air-Water Flow Visualization Study

The experimental setup used for this phase of the study was designed for adiabatic co-current flow of air-water mixtures in either round or rectangular horizontal tubes. A schematic diagram of the test facility used in Phase I is shown in Figure 3. City water and shop air were used to represent the liquid and gas phases, respectively. In a few cases, a trace amount of a blue dye (Formulabs STD Blue) was injected into the water stream to

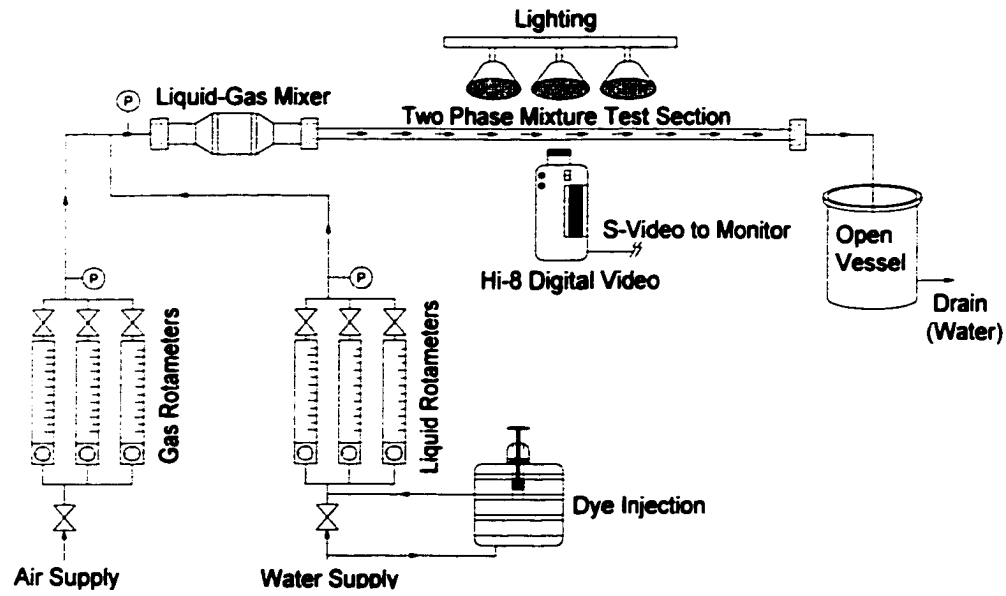


Figure 3. Air-Water Flow Visualization Test Facility

better delineate the two phases. Both the liquid and gas phases flowed separately through a bank of rotameters of the appropriate flow rate ranges before the two phases combined in a straight run of pipe. Table 1 provides the range of volumetric flow for each of the water and air rotameters. The uncertainties in the flow rate measurements are estimated to be ± 4 percent. The mixture then flowed into a liquid-gas mixer before entering the test section. Filtered shop air entered a galvanized tee at a nominal pressure of 517 kPa. City water flowed through the galvanized tee at a nominal pressure of 345 kPa. The precise pressure at which each phase entered the liquid-gas mixer, however, depends upon the flow rate set at the rotameter, the amount of constriction in the rotameter, and the upstream plumbing. The liquid and gas combined at this tee-junction and flow through a straight length of pipe before entering the liquid-gas mixer. The liquid-gas mixer consisted of an expansion, straight length, and contraction and was constructed from PVC fittings. The straight length of the mixer was 254 mm long and contained a tightly packed matrix of copper meshing. The copper meshing was used to force the liquid and gas to combine evenly before exiting the liquid-gas mixer. At the exit of the liquid-gas mixer, a 304.8 mm section of straight length galvanized tubing allowed the two-phase flow to become steady before entering the test section.

The test sections for the round tubes were made of Pyrex glass, while the test section for the rectangular tube was made of transparent plastic. The dimensions of these test sections are provided in Table 2 and the video was recorded at the midpoint of the test

section to document the flow patterns. After flowing through the test section, the two-phase mixture exited to a drain. The flow patterns were recorded at regular intervals of liquid and gas flow rates ranging from 0.0126 liters per minute to 8.33 liters per minute, and from 0.002 m³/s to 1.18 m³/s, respectively. In both Phase I and II of this study, the flow regimes were recorded using a Canon ES5000 digital video camera with a 20X optical zoom and a 40X digital zoom, both with an image stabilizer. The camera utilizes a 10-bit Digital IC to provide high quality digital images and records in a Hi-8 format. The video camera is also equipped with special lenses that allow for high resolution of very small areas. The camera shutter speed can be adjusted from 1/20 second to 1/10,000 second. This camera is connected through an S-Video Jack to a Sony EV-C200 high-resolution Hi-8 VCR, capable of crystal clear still and slow-motion playback, and advanced editing features.

Table 1. Flow Meter Ranges Used in Phase I

Water Flow Meters		Air Flow Meters	
Model Number	Range	Model Number	Range
Dwyer RMC-142	0.2 — 2.2 GPM	Dwyer RMC-103	20 — 200 SCFH
Dwyer RMC-134	2 — 20 GPH	Dwyer RMB-51	2 — 20 SCFH
Key Instruments	0.2 — 2.5 GPH	Dwyer RMA-3	0.2 — 2 SCFH

Table 2. L/D Values for the Tubes Tested in Phase I

Tube Shape	D _h (mm)	L (m)	L/D _h
Circular	5.50	1.07	194.0
Circular	2.60	0.61	234.5
Circular	1.75	0.46	261.3
Circular	1.30	0.30	234.5
Rectangular	5.36	1.07	199.0

The flow regime maps were developed using superficial velocities of the liquid and gas phases, and the corresponding flow regime determined in the video analysis. The *superficial* velocities of the liquid and gas phases are defined as the volumetric flow rate of the gas or liquid divided by the total cross-sectional area of the tube. These velocities are given by:

$$u_l^s = \frac{\dot{V}_l}{A_{tot}} \quad (1)$$

$$u_g^s = \frac{\dot{V}_g}{A_{tot}} \quad (2)$$

It should be noted that this definition of the superficial velocity assumes that each individual phase occupies the entire cross section of the tube, which is obviously not true. However, in the absence of accurate measurements of void fraction, this is an approach widely used in the literature (Barnea et al. 1983, Damianides and Westwater 1989, and Fukano 1990 et al.).

Refrigerant Two-Phase R-134a Flow Visualization

The results from Phase I of this study yielded insights into the effects of the tube geometry and hydraulic diameter on the flow regimes and transitions in air-water mixtures. Thus, air-water mixtures were used to simulate phase-change flow of refrigerants during condensation. However, an adiabatic flow of air-water mixtures may not necessarily represent refrigerant condensation. Therefore, Phase II of this study investigated the effects of tube shape, hydraulic diameter, and aspect ratio on two-phase flow regimes using R-134a *during condensation* in small hydraulic diameter tubes. The effects of tube shape were investigated by testing a square and round tube of similar hydraulic diameter. A series of four square tubes were tested to determine the effects of hydraulic diameter. The effects of aspect ratio were determined by testing two rectangular tubes with the dimensions of 2 mm by 4 mm and 4 mm by 6 mm, and then repeating the experiments with the tubes rotated by 90 degrees. Figure 4 shows the test matrix used in this phase of the study. Multiple tubes in parallel were used for the smaller hydraulic diameters. This is because multiple channels were necessary to increase the refrigerant mass flow rate to a measurable value at the mass flux range of interest. For example, to achieve a mass flux of 150 kg/m²-s in a single 1 mm by 1 mm square tube, the mass flow rate must be equal to 0.00015 kg/s. This value was too low for the mass flow meter to accurately measure and resulted in inaccurate heat balances in the system. When six tubes are used in parallel, the required mass flow rate is equal to 0.0009 kg/s, a measurable value. Also, at the extremely low flow rates necessitated by a single tube, the heat duty in the test section would be a very small fraction of the heat losses to the ambient, which would result in significant inaccuracies. Furthermore, condenser tubes used in heat exchange equipment are constructed of several tubes in parallel, thus this design more accurately represents an actual condenser tube.

The experimental setup in this study is designed for condensing flow of refrigerants in microchannel geometries. A schematic diagram of the test setup is shown in Figure 5 and a photograph of the test facility is shown in Figure 6. The experimental set-up consists of an evaporator, pre-condenser, test section, post condenser, and refrigerant pump. The mass flow

rate of the refrigerant is controlled by either a set of two valves (fine and coarse control) or by a power control on the refrigerant pump. In this section, the test facility (evaporator, pre-condenser, test section, post condenser), the instrumentation, and experimental procedures are described in detail and sample calculations of all heat duties are provided. The methodology used to determine the average test section quality is also discussed.

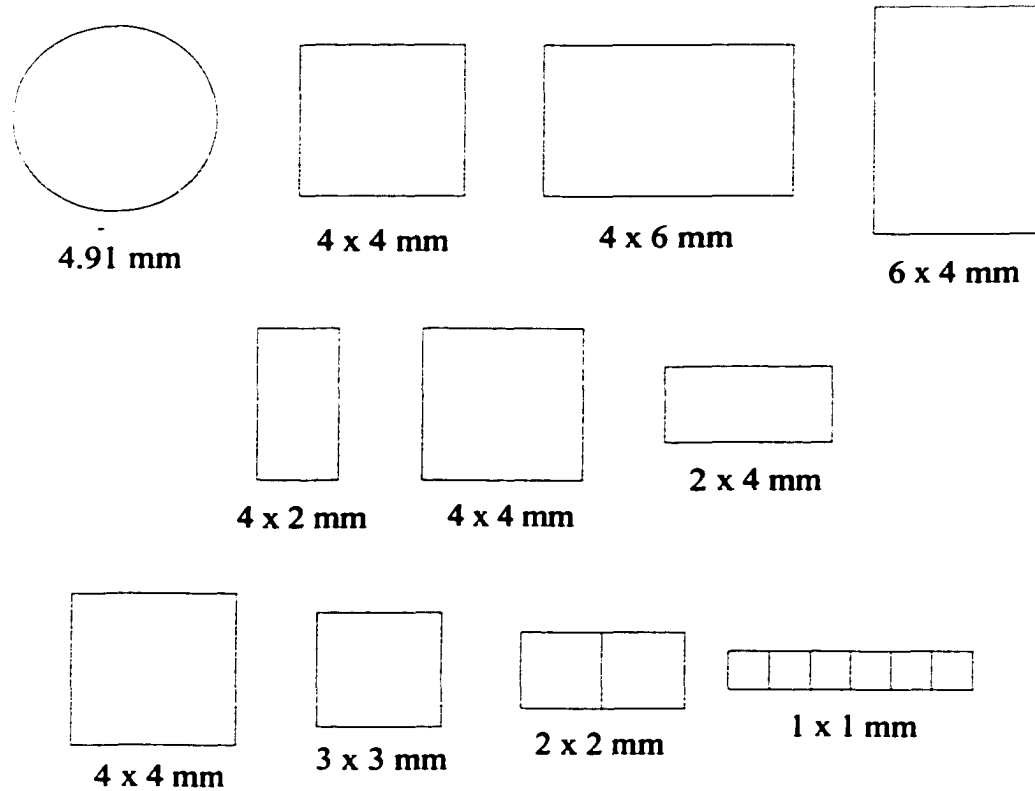


Figure 4. Test Matrix for Condensation Flow Visualization

Test Facility

Post-Condensers, Pump, Evaporator and the Pre-Condensers

A schematic of the test loop fabricated for Phase II of this study is shown in Figure 5. Sub-cooled liquid refrigerant exiting the set of post-condensers flows through the Coriolis mass flowmeter. A sight glass is installed upstream of the flowmeter to ensure single-phase liquid flow. In addition, a temperature and pressure measurement at this state ensures that the refrigerant is a sub-cooled liquid. The sub-cooled refrigerant flows to a pump that circulates it through the test loop. An accumulator with a view port is placed in this line to facilitate charging of the loop with an appropriate amount of refrigerant for each test. The pumped refrigerant flows through a tube-in-tube evaporator, in which hot water or steam

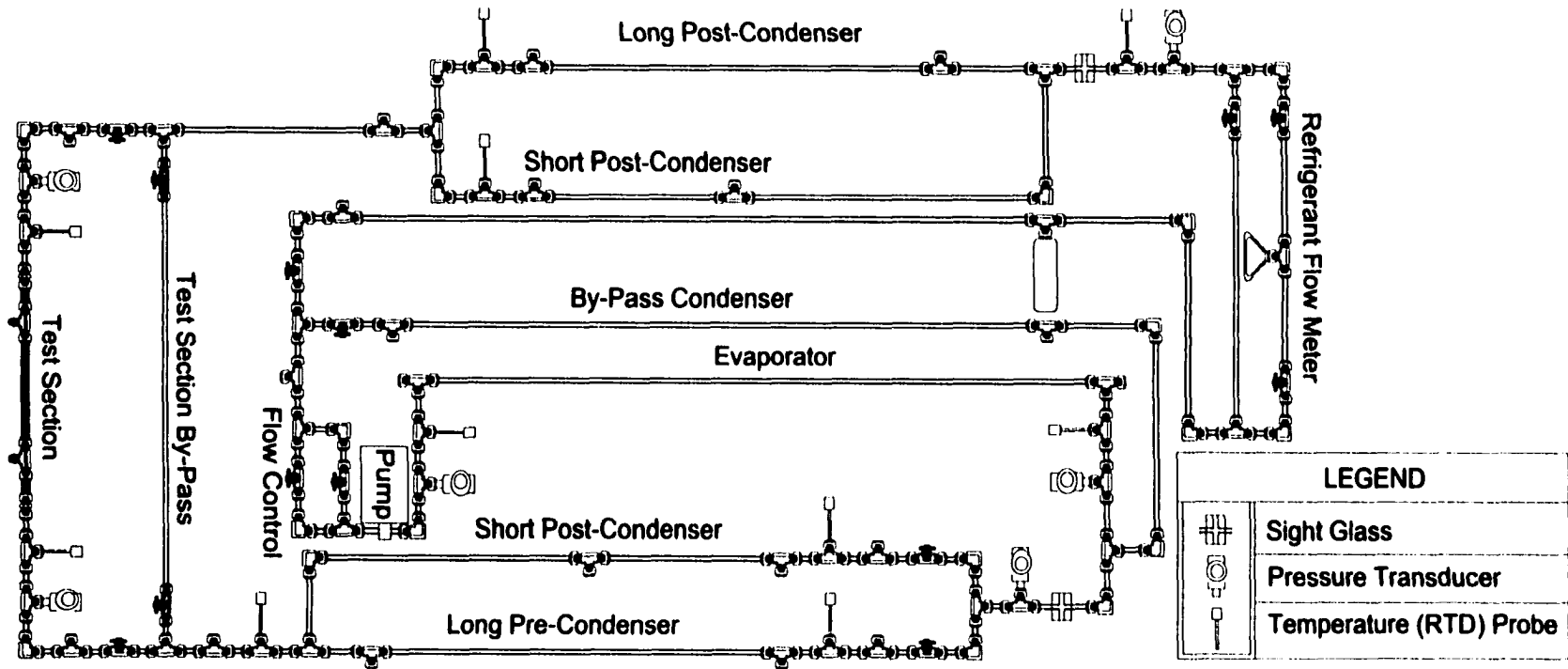


Figure 5. Schematic of the Condensation Test Facility

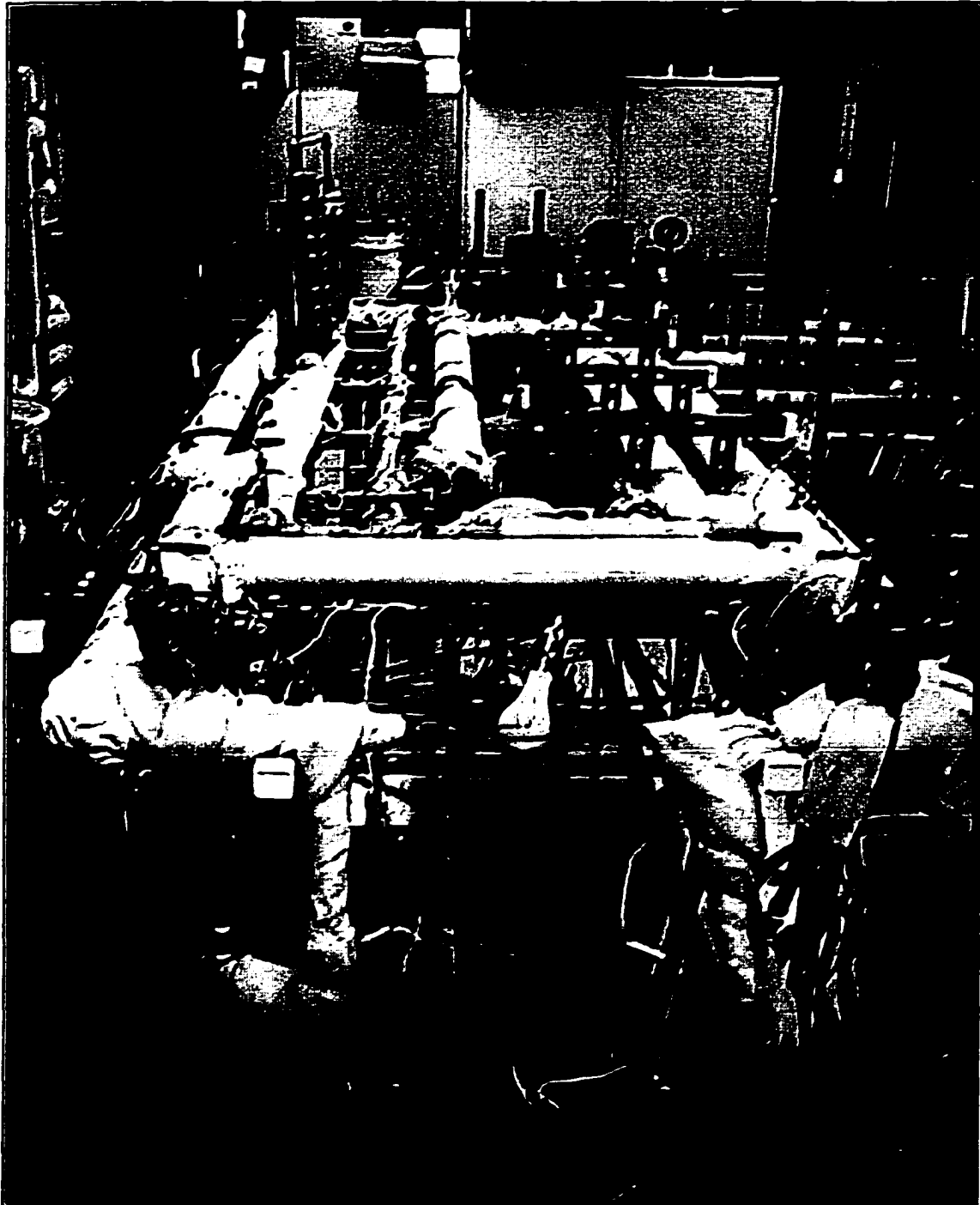


Figure 6. Photograph of the Condensation Test Facility

flows counter-current to the refrigerant to boil and superheat it. The superheated state is ensured by a combination of a sight glass, temperature and pressure measurements. Temperature and pressure measurements at the superheated state enable measurement of the refrigerant enthalpy.

The superheated vapor enters one of two pre-condensers, where city water of the desired (variable) flow rate is used to partially condense the vapor. The two pre-condensers are similar in design. Each pre-condenser is a tube-in-tube heat exchanger (6.35 mm diameter, 0.89 mm wall, and 12.7 mm diameter, 0.89 mm wall tubes), with the difference being that one of the heat exchangers is approximately 3 times longer than the other (0.419 m and 1.35 m long). These two pre-condensers and varying cooling water flow rates through them help establish a wide range of refrigerant conditions at the test section inlet.

The refrigerant exiting the pre-condensers enters the transparent test section. Air flow in a counterflow mode is maintained around the test section for condensation of the refrigerant in the test section. Flow regimes are recorded at the test section for each data point, nominally 10 points per mass flux per tube. The air flow rate and inlet and outlet temperatures are measured to enable calculation of the condensation duty in the test section, which typically represents a Δx of about 0.05. The outlet state of the test section is also validated by a different independent measurement of this state. Thus, the set of post-condensers downstream of the test section are used to completely condense and sub-cool the refrigerant. The sub-cooled refrigerant enthalpy at the exit of the post-condenser and an energy balance on this condenser are used to deduce the refrigerant enthalpy and quality at the outlet of the test section. These two different measurements of test section outlet quality help ensure a high degree of accuracy in the data points. The observed flow mechanisms are assumed to be characteristic of the average quality in the test section.

Numerous bypass lines are installed around the test section to help isolate components and facilitate quick changes in individual components. Similarly, valves are provided around the loop to divide the test loop into different segments, which helps the identification of potential leaks. A variable speed refrigerant pump and control valves are used to circulate the desired flow rate of fluid around the test loop and achieve the required mass flux values. A bypass condenser is installed in parallel with the three condensers described above. Thus, the overall refrigerant flow through the loop as well as the fraction flowing through the test section can be controlled by varying the bypass flow fraction. This approach helps maintain steady conditions through the pump, evaporator and associated plumbing, even as the mass flux through the test section is being changed, thus speeding up the establishment of steady-state conditions. (During the testing phase, it was found out that

the by-pass condenser line was not essential for achieving a faster approach to steady-state conditions.)

The Test Section

The design of the test section for the flow visualization experiments must satisfy the following requirements:

- transparent
- enable refrigerant flow through a range of round and rectangular tubes of different diameters and aspect ratios, while being capable of installation in the same test loop
- withstand the refrigerant pressure at the desired saturation temperature
- enable testing during condensation (not adiabatic)
- permit measurement of the condensation duty

A schematic of the test section designed to satisfy these requirements is shown in Figure 7. The test section may be described as a counterflow tube-in-tube heat exchanger, with refrigerant flowing through an inner glass tube of the cross-section of interest, and air flowing through the space between this inner tube and another transparent outer tube. Heat transfer between the cold air and refrigerant causes condensation. The inner glass tube is epoxied into a stainless steel compression fitting that connects it to the rest of the test loop. Pressure and temperature measurement ports are also provided at the inlet and outlet. Two sections of stainless steel tubing with a diameter larger than the inner tube are attached to these two ends of the inner tube. The total length of these two pieces of tubing is shorter than the length of the inner glass tube to provide a viewing area at the mid-section of the inner tube. Plexiglas tubing is force fit with O-rings around the steel tubing. Air flow in a counter-current direction is maintained in the space between the inner tube and this assembly of Plexiglas and stainless tubing. The choice of air as the cooling medium flowing through this outer transparent section enables the viewing and recording of flow regimes. Hydrostatic

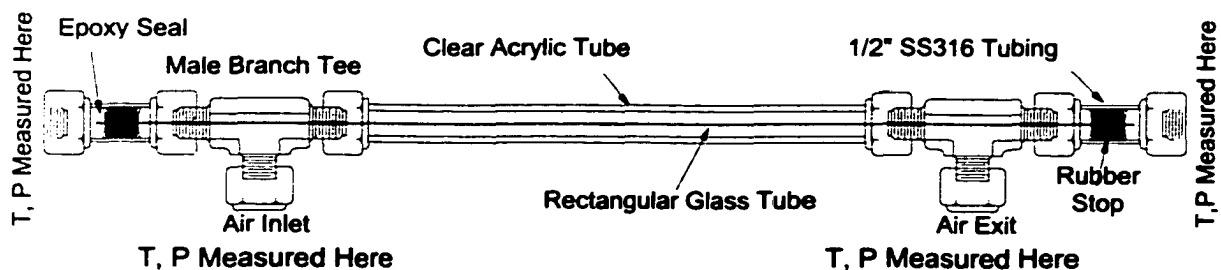


Figure 7. Test Section Schematic for Phase II

tests on the Plexiglas tube showed that it could withstand pressures as high as 4800 kPa. Therefore, compressed air at 480 kPa-825 kPa (depending on the test case) is supplied to the test section. This high air pressure minimized problems associated with low strengths of rectangular glass tubes. The resulting low differential pressure between the two ducts made testing feasible at saturation pressures as high as 1380-1724 kPa. The air flow rate is varied to accommodate different condensation loads at different test conditions.

Instrumentation and Data Acquisition

A summary of the instrumentation, measurement ranges, and accuracies is provided in Table 3. Omega type PR-13 platinum resistance temperature devices (RTDs) with an accuracy of $\pm 0.5^{\circ}\text{C}$ were used to measure all of the temperatures in the two-phase test facility. The RTDs were calibrated using an ice bath at 0°C and boiling water at 100°C . These calibrations helped establish a temperature measurement uncertainty of $\pm 0.25^{\circ}\text{C}$. The system pressure at various locations in the test facility was measured using Rosemount model 2088 absolute pressure transducers with an accuracy of 0.25 percent of the span. The refrigerant transducers have a maximum span ranging from 0.0 kPa to 5515.8 kPa, while the air pressure transducers have a maximum span ranging from 0.0 kPa to 1034.2 kPa. The spans on these pressure transducers are scalable, and to maximize accuracy during testing, the spans on the refrigerant transducers were reduced to 0.0 kPa to 2757.9 kPa. All of the pressure transducers provide an output voltage that varies linearly with the system pressure. Calibration information for these transducers is provided in Appendix A.

Refrigerant flow rates were measured using a Micromotion Elite flow sensor (model number CFM025), which directly measure the mass flow rates in the range from 0.0 to 0.30 kg/s with an accuracy of 0.15% of the reading. The air flow rates were measured using a Micromotion type D6 mass flow meter, which measures flow rates in the range from 0.0 to 0.015 kg/s with an accuracy of 0.15% of the reading. The flow meters were calibrated by measuring the time required to fill a known volume of water using a stopwatch. The mass flow rate was calculated by multiplying the average volumetric flow rate and the density of water. Results of the calibration tests for these flowmeters are provided in Appendix A.

Water flow rates were measured using Gilmont Accucal flow meters. A series of three volumetric flow meters were used on the pre- and post-condensers. The flow meters have an accuracy of ± 2 percent of the reading. The accuracies of the flow meters were tested in a manner similar to that of the refrigerant flow meter – comparing the sensor reading to a value calculated by filling a known volume with water over a period of time. Three separate tests were run at different flow rates for each of the six flow meters. Results of the calibration tests for these flowmeters are provided in Appendix A.

The video equipment used to document the flow patterns was described in conjunction with Phase I of this study. All data were recorded using the fully computerized TEMPSCAN data acquisition system that can be configured to suit the needs of a variety of experiments. Up to 992 inputs for temperature, pressure, flow rate, and other signal measurements, at speeds of up to 960 channels per second, can be recorded with this system for real-time data analysis. Specifications for the TEMPSCAN are provided in Appendix A.

Table 3. Instrumentation Specifications

Fluid	Manufacturer	Model	Range	Accuracy
Temperature				
R-134a and Air	Omega	PR-13	600°C (Max.)	±0.5°C
Mass Flow Rate				
R-134a	Micromotion	CFM025	0.0-0.3 kg/s	±0.15% Reading
Air	Micromotion	D6	0.0-0.015 kg/s	±0.15% Reading
Water	Gilmont	Accucal	0.0-0.78 lpm	±2% Reading
	Gilmont	Accucal	0.0-2.2 lpm	±2% Reading
	Gilmont	Accucal	0.0-4.8 lpm	±2% Reading
Pressure				
R-134a	Rosemount	2088	0.0-5515.8 kPa	0.25% of Span
Air	Rosmount	2088	0.0-1034.2 kPa	0.25% of Span

Experimental Procedures

System Charging

The test facility (shown in Figure 5) was first pressurized to the nominal operating pressure of 1379 kPa (200 psi) with N₂ gas that was doped with a trace amount of R-134a. An electronic refrigerant leak detector (CPS model L-790a) was used around all fittings and connections to confirm that these fittings were leak-tight. The system pressure was also monitored for a period of 24 hours to ensure the absence of leaks. Once system integrity was established, the test facility was evacuated using a vacuum pump (DV Industries model DV-85N) until a vacuum of 200 microns (26.7 Pa) or less was reached. Periodically during the evacuation, the ball valves in the system were toggled to remove any trapped air. A vacuum gage (Thermal Engineering, Model 14571) with the capability of measuring vacuum pressures as low as 10 microns (1.33 Pa) was used to measure the system pressure. Another test of the integrity of the system involved evacuating the system and then monitoring the

pressure over a period of 25 hours. The results of this test are provided in Appendix A.

The charging of the test facility was started immediately after the vacuum pump was turned off, and the system pressure typically rose to a value less than 200 microns (26.7 Pa) before the refrigerant began flowing into the test facility. The system was charged with approximately 3.4 kg of R-134a. After the charging of the system was complete, the system pressure was again monitored over a period of 24 hours to check any potential refrigerant leakage. Minor fluctuations in the system pressure were expected during the 24 hour period due to fluctuations in the ambient temperature.

System Start-up

With the system checked against leakage and charged with R-134a, it was ready to operate. Cold water was supplied to both the pre- and post-condensers from the reservoir. Steam was also supplied through the evaporator to produce a superheated refrigerant vapor. The system was allowed to reach steady state before the first data point was taken. Steady state was determined using three different parameters that were plotted against time: the test section pressure, and cooling water exit temperatures of the pre- and post-condensers. Coolant exit temperatures of the two condensers were the most sensitive to any changes in the system over time, and were therefore used to indicate steady state.

Individual data point test conditions were established through a choice of cooling water flow rates and pre- and post- condenser selection. For example, for a test condition that required a high refrigerant inlet quality at the test section, the short pre-condenser was used with a low cooling water flow rate. This combination of small surface area and low coolant flow rate resulted in a small pre-condenser heat duty. Thus, the refrigerant exited the pre-condenser at qualities in the $x > 0.95$ range. For the subsequent test condition with the lower required vapor quality, the cooling water flow rate was increased to result in a higher condensation duty in the pre-condenser. This process was continued until the point where the increasing cooling water flow rate resulted in a very small ΔT in the water, with the associated low accuracies. At this stage, the long pre-condenser was used at a lower cooling water flow rate. The larger surface area of this condenser allowed a higher heat duty even at the low cooling water flow rates. In addition, the low cooling water flow rate yielded accurately measurable cooling water ΔT s. For subsequent data points with lower required qualities at the test section, the cooling water flow rate in the long pre-condenser was progressively increased until a nominal quality of about $x \cong 0.07$ was achieved at the test section inlet.

For each refrigerant mass flux, selection of the appropriate pre-condenser and the cooling water flow rate helped establish data points in nominal quality increments of $\Delta x =$

0.10. For each data point, this procedure and the measurement of the city water flow rate and inlet and outlet temperatures yielded the heat duty in the pre-condenser. This heat duty, in conjunction with the inlet enthalpy of the refrigerant, was used to calculate the pre-condenser outlet enthalpy. This fluid state also constituted the inlet state to the test section. The post-condenser selection and cooling water flow rate for each data point were also varied to meet the requirements of the particular data point. For example, when the short pre-condenser with a low cooling water flow rate is used, the required post-condenser duty is high, which necessitates the use of the long-post condenser with a relatively high cooling water flow rate. As the condensation rate in the pre-condenser was increased for subsequent data points, lower post-condenser water flow rates were used and the refrigerant flow was switched to the short post-condenser.

Measured temperatures, flow rates, and pressures were continuously displayed and plotted as a function of time to ensure that steady state conditions were reached. Due to the thermal capacity of the system, the establishment of steady state took between 30 minutes (high flow rate cases) to 3 hours (low flow rate cases). To set each data point, the data were analyzed online soon after changing the cooling water flow rates and/or pre- and post-condensers. This provided an estimate of the test section quality, and if it was significantly different from the quality desired for that point, the conditions were changed, and the process repeated. Once steady state was achieved, the sight glasses, and pressure and temperature readings were inspected to ensure an adequate degree of superheat and sub-cooling. The data were then recorded, with each data point representing an average of 121 scans taken every second for a two-minute period. Furthermore, two such data points were taken for each test condition. The averages of these two data points were used for subsequent data analysis. It should be noted that a complete analysis of each data point was conducted during the tests to ensure that data at the required qualities were being taken, and also to confirm energy balances around the test section and the test loop. Once these validations were conducted, the flow patterns were recorded and assigned the appropriate quality and refrigerant flow rate labels. These procedures were used to record flow regimes as a function of quality for five different refrigerant flow rates corresponding to mass fluxes of 150, 300, 450, 600 and 750 $\text{kg/m}^2\text{-s}$ for each of the nine test sections.

Test Condition Establishment and Energy Balances

Engineering Equation Solver Software (Klein and Alvarado, 1998) was used to analyze the data from the tests. The calculation of test section quality is demonstrated here using the data taken at a mass flux of 436.5 $\text{kg/m}^2\text{-s}$ and a quality of $x = 0.501$ for the 4.91 mm inner diameter circular tube. A summary of the measured variables is shown in Table 4.

Table 4. Output from the Data Reduction Program

Variable	Measured Value	Description
$P_{pre,in}$	1255 kPa	Absolute Pressure, Pre-Condenser Inlet
$P_{test,in}$	1241 kPa	Absolute Pressure, Test Section Inlet
$P_{test,out}$	1238 kPa	Absolute Pressure, Test Section Outlet
$P_{post,out}$	1227 kPa	Absolute Pressure, Post Condenser Outlet
\dot{m}_{refg}	8.26×10^{-3} kg/s	Mass Flow Rate, Refrigerant
\dot{V}_{pre}	1.0 liter/min	Volumetric Flow Rate, Pre-Condenser Water
\dot{V}_{post}	2.95 liter/min	Volumetric Flow Rate, Post-Condenser Water
$T_{pre,in}$	63.34°C	Temperature, Pre-Condenser Inlet
$T_{pre,out}$	47.93°C	Temperature, Pre-Condenser Exit
$T_{pre,w,in}$	17.40°C	Temperature, Pre-Condenser Water, Inlet
$T_{pre,w,out}$	28.29°C	Temperature, Pre-Condenser Water, Exit
$T_{test,in}$	47.89°C	Temperature, Test Section, Inlet
$T_{test,out}$	47.85°C	Temperature, Test Section, Exit
$T_{post,in}$	47.80°C	Temperature, Post-Condenser, Inlet
$T_{post,out}$	36.91°C	Temperature, Post-Condenser, Exit
$T_{post,w,in}$	16.60°C	Temperature, Pre-Condenser Water, Inlet
$T_{post,w,o}$	20.30°C	Temperature, Pre-Condenser Water, Exit
$T_{air,in}$	26.90°C	Temperature, Test Section Air, Inlet
$T_{air,out}$	37.06°C	Temperature, Test Section Air, Exit
\dot{m}_{air}	1.26×10^{-3} kg/s	Mass Flow Rate, Air

These values represent the average of 121 instantaneous readings taken over a period of two minutes. The calculations presented here are shown in the order in which the fluid moves through the two-phase test facility, beginning with the pre-condenser.

At the inlet of the pre-condenser, the enthalpy of the superheated refrigerant is determined from the temperature ($T_{pre,in}$) and pressure ($P_{pre,in}$) of the refrigerant. In this example, $T_{pre,in}$ and $P_{pre,in}$ are experimentally measured quantities equal to 63.34°C and 1255 kPa, respectively. The saturation temperature corresponding to this measured pressure ($P_{pre,in}$) is 48.62°C. Therefore, the degree of superheat is given by:

$$\Delta T_{sup} = T_{pre,in} - T_{sat,in} \quad (3)$$

and is equal to 14.72°C.

The two-phase condition is attained by using cold water to partially condense the superheated refrigerant. The mass flow rate of the water is determined from the volumetric flow rate and density as follows:

$$\dot{m}_{H_2O,pre} = \dot{V}_{pre} \cdot \rho_{H_2O} \quad (4)$$

With a volumetric flow rate of 1.0 liters per minute and a density of 999.22 kg/m³, the mass flow rate of water in the pre-condenser is 0.0167 kg/s.

The heat duty of the pre-condenser is determined by the change in enthalpy of the water, which is calculated from the measured inlet and exit water temperatures. Thus:

$$Q_{pre-cond} = \dot{m}_{pre,H_2O} \Delta h_{H_2O} \quad (5)$$

Given water inlet and exit temperatures of 17.40°C and 28.29°C, respectively, the enthalpies of the water at the inlet and exit of the pre-condenser are 73.34 kJ/kg and 118.84 kJ/kg, respectively. Equation (5) yields a heat duty of 760 Watts.

The system was well insulated using three layers of fiberglass pipe-wrap insulation in conjunction with an outer layer of stiff fiberglass insulation. These measures and the small temperature difference between the water and the ambient minimize heat losses/gains to the ambient. The pre-condenser heat duty represents the total amount of energy removed from the refrigerant, which enables the calculation of the quality of the liquid-gas mixture at the exit of the pre-condenser as follows:

$$Q_{pre-cond} = \dot{m}_{refg} (h_{pre,in} - h_{pre,out}) \quad (6)$$

In this equation, the enthalpy of the superheated refrigerant at the inlet of the pre-condenser is calculated from the temperature and pressure of the superheated vapor. At a pressure of 1255 kPa and a temperature of 63.34°C, $h_{pre,in} = 440.5$ kJ/kg. With a heat duty of 760 W, a refrigerant flow rate of 8.26×10^{-3} kg/s, and an inlet refrigerant enthalpy of 440.50 kJ/kg, the enthalpy of the refrigerant at the exit of the pre-condenser given by equation (6) is 349 kJ/kg. The enthalpy of the two-phase mixture is a function of the refrigerant pressure and the quality:

$$h_{pre,out} = f(P_{pre,out}, x_{pre,out}) \quad (7)$$

The resulting quality at the pre-condenser outlet is 0.522. This quality is also used as the quality at the inlet of the test section, $x_{test,i}$.

The liquid-vapor mixture exits the pre-condenser and flows into the test section. The temperature of the air was measured at both the inlet and exit of the test section. A heat

balance on the air determined the amount of energy removed from the refrigerant by the air as follows:

$$Q_{test} = \dot{m}_{air} (h_{air,out} - h_{air,in}) \quad (8)$$

This heat duty corresponds to the condensation occurring in the test section. The enthalpies at the inlet and exit of the air were determined from the measured air temperatures. From Table 4, the inlet and exit air temperatures are 26.9°C and 37.06°C, respectively. The enthalpies of the inlet and exit air are 300.5 kJ/kg and 310.8 kJ/kg, respectively. With an air mass flow rate of 1.26×10^{-3} kg/s, Equation (8) yields a heat duty of 12.9 W.

After exiting the test section, the refrigerant entered one of two post-condensers. Similar to the pre-condenser, the volumetric flow rate and temperatures at the inlet and exit of the cold water were measured to determine the amount of energy removed from the refrigerant by the water. The mass flow rate of the water was determined using the volumetric flow rate and the density of the water:

$$\dot{m}_{H_2O,post} = \dot{V}_{post} \cdot \rho_{H_2O} \quad (9)$$

From Table 4, the volumetric flow rate of the water was 2.95 liters per minute and the density was 999.51 kg/m³. Equation (9) yields a mass flow rate of 0.049 kg/s. The heat duty of the post-condenser was determined by the change in enthalpy of the water as follows:

$$Q_{post-cond} = \dot{m}_{post,H_2O} \Delta h_{H_2O} \quad (10)$$

Given water inlet and exit temperatures of 16.60°C and 20.30°C, respectively, the enthalpy of the water at the inlet and exit of the pre-condenser is 70.1 kJ/kg and 85.5 kJ/kg, respectively. The corresponding post-condenser heat duty is 760 W.

This heat duty represents the total amount of energy removed from the refrigerant by the water. The refrigerant enthalpy at the inlet of the post-condenser is determined from the heat duty, mass flow rate of the refrigerant, and the enthalpy of the sub-cooled liquid as follows:

$$Q_{post-cond} = \dot{m}_{refg} (h_{post,in} - h_{post,out}) \quad (11)$$

The enthalpy of the sub-cooled refrigerant at the exit of the post-condenser is determined from the temperature and pressure. At a pressure of 1227 kPa and a temperature of 36.91°C, the enthalpy of the refrigerant at the exit of the post-condenser is 251.7 kJ/kg. From Equation (11), with a heat duty of 760 W, a mass flow rate of 0.049 kg/s, and an exit enthalpy of 251.7 kJ/kg, the refrigerant enthalpy at the inlet of the post-condenser is 343.8

kJ/kg. This refrigerant enthalpy at the post-condenser inlet is used to calculate the corresponding quality as follows:

$$h_{post,in} = f(P_{post,out}, x_{post,i}) \quad (12)$$

With an inlet enthalpy of 343.8 kJ/kg and a pressure of 1227 kPa, Equation (12) yields a quality at the post-condenser inlet, $x_{post,i}$ of 0.491, which is also used as the test section outlet quality, $x_{test,o}$.

The refrigerant quality at the inlet of the test section was computed using the change in enthalpy of the refrigerant across the pre-condenser and the energy removed by the cooling water. This refrigerant quality was equal to 0.522. Similarly, the refrigerant quality at the exit of the test section was found using the change in enthalpy of the refrigerant across the post-condenser and the energy removed the cooling water. This refrigerant quality was shown to be 0.491. A redundant calculation for the quality at the inlet of the test section was also conducted using the test section heat duty. The sum of the post-condenser and test section heat duties should yield the energy removed from the refrigerant from the inlet of the test section to the exit of the post condenser. This alternative heat balance yields an alternate value of the quality at the inlet of the test section:

$$Q_{post-cond} + Q_{test-sect} = \dot{m}_{refg} (h_{test,i,alt} - h_{post,out}) \quad (13)$$

The sum of the heat duties on the pre-condenser and the test section is 773 W. The resulting alternate value of the enthalpy in Equation (13) is 345.4 kJ/kg, which corresponds to a quality of 0.501. This alternate quality compares very well with the pre-condenser outlet quality of 0.522.

Using the three independent values of the refrigerant quality, the average quality in the test section is taken as

$$x_{test,ave} = \left(\frac{\frac{x_{test,in} + x_{test,in,alt} + x_{test,out}}{2}}{2} \right) \quad (14)$$

With an inlet test section quality of 0.522, an exit test section quality of 0.491, and an alternate test inlet section quality of 0.501, the average test section quality is 0.501. This computed average quality was used for both the flow visualization experiments (Phase II) and the pressure drop experiments (Phase III).

Refrigerant R-134a Two-Phase Pressure Drop Experiments

In Phase III of this study, both single phase (gas and liquid) and two-phase pressure drops were measured for a variety of tube shapes and hydraulic diameters. Single phase pressure drops were measured, and the resulting laminar and turbulent single-phase friction factors were compared to the laminar and turbulent friction factor correlations. The shapes included circular, triangular, square, rectangular, barrel and “N”-shaped, as shown in Figure 8. The differential pressure drops in a total of 13 different tubes were tested at five mass fluxes (corresponding to nominal values of $150 \text{ kg/m}^2\text{-s}$, $300 \text{ kg/m}^2\text{-s}$, $450 \text{ kg/m}^2\text{-s}$, $600 \text{ kg/m}^2\text{-s}$, and $750 \text{ kg/m}^2\text{-s}$) for various vapor qualities in the range of 0.05 to 0.95 in increments of approximately 0.10. Note that the tube cross sections for the C30, ZLI, and ZLII are the same, and that the W29 tube geometry was tested twice with different test sections. A major portion of the test facility used in the pressure drop experiments was identical to the test facility used in Phase II (evaporator, pre-condenser, post-condenser, pump, flow controls), but modifications to the test section were made to more accurately measure the two-phase pressure drop. A schematic of the test section for pressure drop

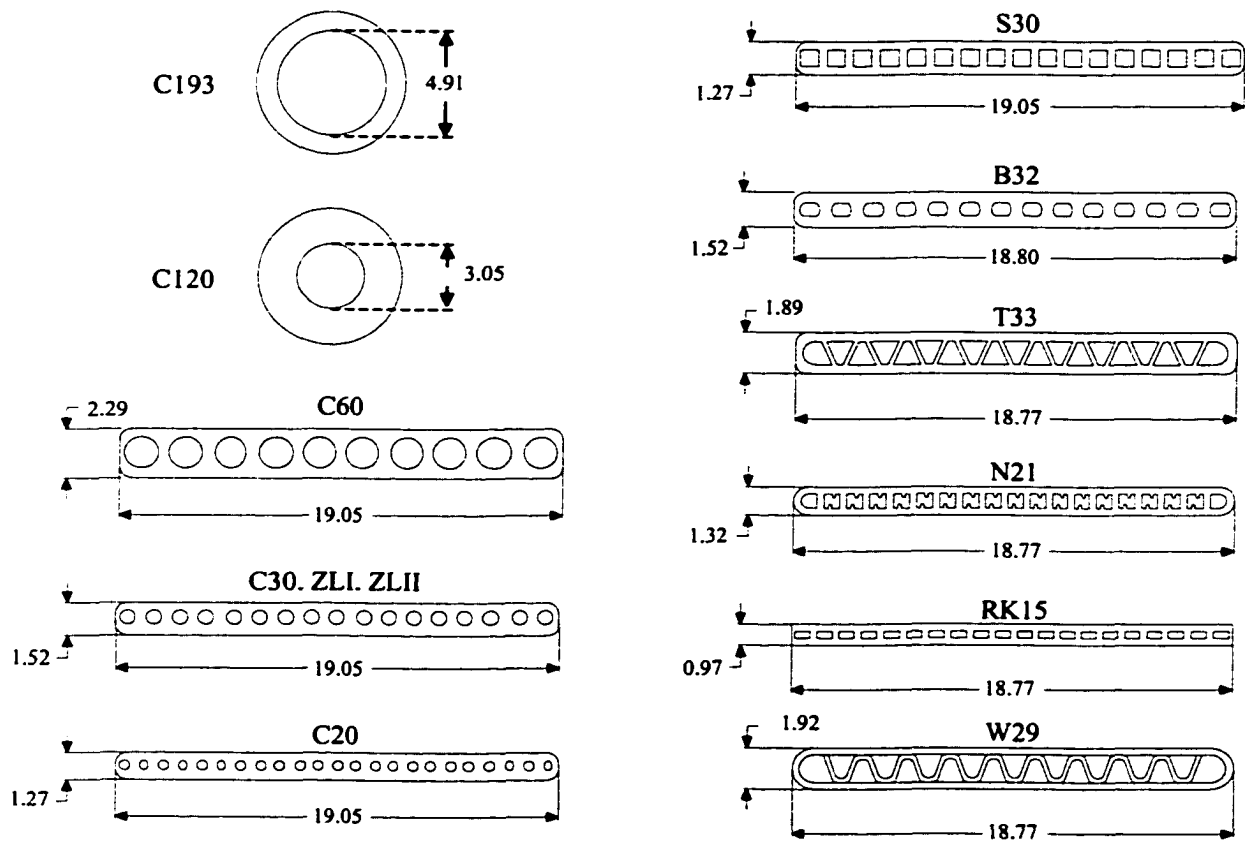


Figure 8. Schematic of the Pressure Drop Test Sections

measurement is shown in Figure 9. This test section consisted of three microchannel tubes that were brazed together. The nominal refrigerant tube length was 0.508 m, while the nominal coolant (air) tube lengths were 0.3048 m. The coolant (air) flowed through the top and bottom tubes and refrigerant flowed in counter-flow through the center tube. The cold air ensured condensation in the test section. To maximize accuracy, the pressure drop across the test section was measured using a bank of three selectable Rosemount model 3051 differential pressure transducers. The individual spans and accuracies of the transducers are shown in Table 5. Whenever possible, all three differential pressure transducers were used to record redundant readings of the pressure drop in the microchannel geometries, and the reading from the most accurate transducer for that pressure drop range was used for the analyses.

Table 5. Differential Pressure Transducer Specifications

Model	Span	Accuracy
Rosemount 3051 (#3)	0 – 248.2 kPa	±0.25% of span
Rosemount 3051 (#2)	0 – 62.2 kPa	±0.25% of span
Rosemount 3051 (#1)	0 – 6.22 kPa	±0.25% of span

Geometry of the Pressure Drop Test Sections

The dimensions of the pressure drop test sections are shown in Table 6. For each tube tested, the relevant dimensions included: the total number of ports (N_p), total wetted perimeter (P_t) and total free flow area (A_t). For tubes C193 and C120 (single circular tubes), these dimensions were measured directly, and the remaining tube dimensions were provided by Modine Manufacturing Company of Racine, Wisconsin. Table 6 provides these tube dimensions as well as the tube hydraulic diameter, and port width, height, and aspect ratio. The values that were calculated from other known parameters are shown in bold and italics in Table 6.

The free flow area of a single port is found from the total flow area and the number of ports:

$$A = \frac{A_t}{N_p} \quad (15)$$

From Table 6, the total number of ports in the S30 tube is 17, and the total free flow area is

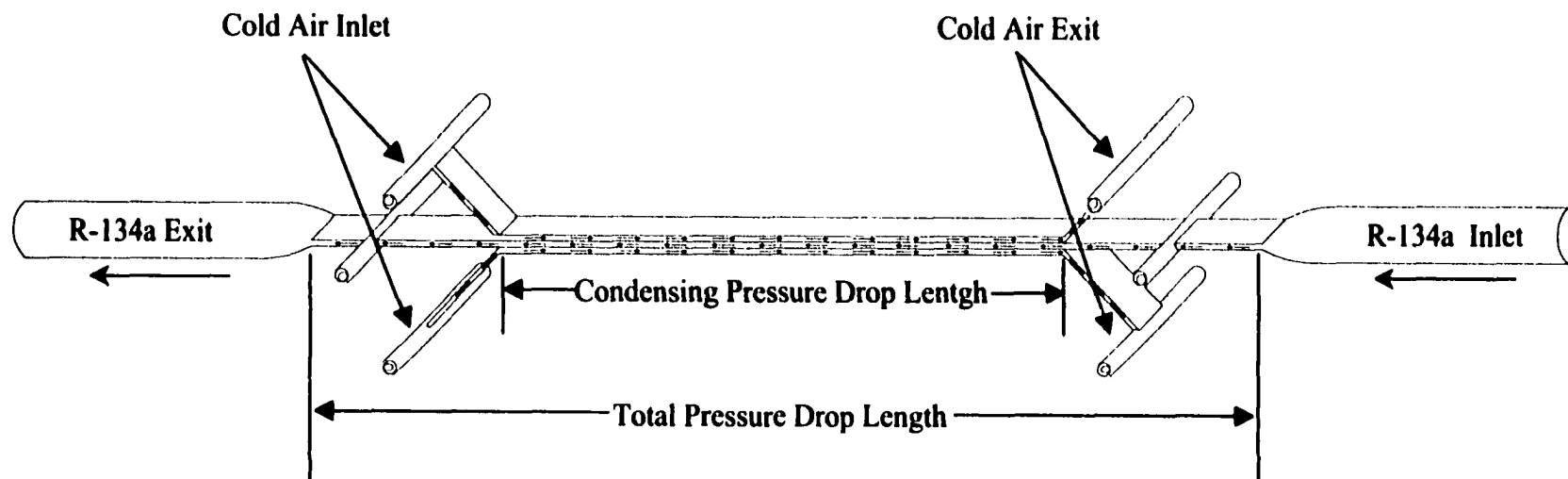


Figure 9. Schematic of the R-134a Pressure Drop Test Section

9.87 mm². The free flow area of a single tube is therefore 0.581 mm². The hydraulic diameter of a single port is given by

$$D_h = \frac{4A_t}{P_t} \quad (16)$$

For tube S30, with a total wetted perimeter of 51.82 mm and a total free flow area of 9.87 mm², equation (16) yields a hydraulic diameter of 0.762 mm.

Table 6. Test Matrix for the Pressure Drop Experiments

Tube	Geometry Type	N _p	P _t , mm	A _t , mm ²	D _h , mm	w, mm	h, mm	α
C193	Circle, Drawn	1	15.425	18.934	4.910	---	---	---
C120	Circle, Drawn	1	9.576	7.297	3.048	---	---	---
C60	Circle, Extruded	10	47.878	18.241	1.524	---	---	---
C30	Circle, Extruded	17	40.696	7.742	0.761	---	---	---
C20	Circle, Extruded	23	36.703	4.645	0.506	---	---	---
S30	Square, Extruded	17	51.816	9.871	0.762	0.762	0.762	1.00
B32	Barrel, Extruded	14	50.056	10.000	0.799	---	---	---
T33	Triangle, Extruded	19	64.008	13.419	0.839	---	---	---
N21	N Shape, Extruded	19	58.763	7.871	0.536	---	---	---
RK15	Rectangle, Extruded	20	38.379	4.065	0.424	0.643	0.317	0.493
W29I	Triangle, Insert	19	67.135	12.277	0.732	---	---	---
W29II	Triangle, Insert	19	67.135	12.277	0.732	---	---	---
ZLI	Circle, Extruded	17	40.696	7.724	0.761	---	---	---
ZLII	Circle, Extruded	17	40.696	7.742	0.761	---	---	---

Note: All tube lengths were 0.5080 m except C193 (0.6096 m), ZLI (0.2032) and ZLII (0.0225 m). Also, the ZLII tube had 10 blocked passages, and seven clear passages.

The aspect ratio, α, is defined as the port height divided by the port width as follows:

$$\alpha = \frac{h}{w} \quad (17)$$

The method used to determine the height and width of a single port depended upon the port geometry. The height (and width) of the square port was found from the total free flow area, and the total number of ports as follows:

$$A_t = N_p A = N_p h^2 \quad (18)$$

As shown in Table 6, this yields the height for the S30 tube to be 0.762 mm (with an aspect ratio of 1).

For the rectangular RK15 tube, the aspect ratio was determined as follows:

$$A_t = N_t h w \quad (19)$$

The total wetted perimeter is calculated as follows:

$$P_t = N_t (2w + 2h) \quad (20)$$

For the RK15 tube, the total number of ports is 20, the total wetted perimeter is equal to 38.38 mm, and the total free flow area is equal to 4.07 mm². This information and equations (19) and (20) yield a port height of 0.317 mm and a port width of 0.643 mm. From equation (17), the aspect ratio of this tube is 0.493.

Pressure Drop Test Section Data

The pressure drop across the test section was measured using a bank of three selectable differential pressure transducers. For example, at a quality of 0.531 and a mass flux of 437.5 kg/m²-s, pressure transducer 3 recorded a differential pressure of 3339 Pa, while pressure transducer 2 recorded a differential pressure of 3447 Pa. The smallest differential pressure transducer was not used since the differential pressure being measured was close to the maximum value of the span. The two readings from transducer 2 and transducer 3, however, are within 3.2 percent of each other. The reading from transducer 2 is used in the subsequent data analysis since the reading more closely matches the span of that transducer.

Table 7 illustrates whether adiabatic, condensing or both pressure drop experiments were performed for each of the test sections shown in Table 6. This table also outlines the attainable mass fluxes for each of the test sections. For the test sections with the smaller free flow areas, the lower mass flux cases were not attainable due to the extremely small mass flow rate of the refrigerant.

Uncertainty Analysis

A detailed uncertainty analysis on the test data was conducted using the uncertainties in the measurements provided in Table 3. The methodology, sample calculations, and results of this analysis are provided in Appendix B for the C193, C30, and RK15 tubes for all qualities and mass fluxes tested. A summary of the uncertainty analysis is shown in Table 8 for the low, medium, and high mass flux and quality cases for the C193, C30, and RK15 tubes. These three tubes represent the range of total free flow areas and provide typical uncertainties for the measurements of quality. Table 8 shows that the uncertainties are

similar for all three tubes and typically range from three to seven percent. Furthermore, the average uncertainties for each tube were similar. Tube RK15 had an average uncertainty of 0.051, the C30 tube had an average uncertainty of 0.053, and the C193 had an average uncertainty of 0.045.

Table 7. Mass Flux Cases Tested in Phase III of This Study

Tube	Total Free Flow Area (mm ²)	Test Type A = Adiabatic C = Condensing	Attainable Mass Fluxes (kg/m ² -s)				
			150	300	450	600	750
C193	18.934	A	✓	✓	✓	✓	✓
C120	7.297	A		✓	✓	✓	✓
C60	18.241	C	✓	✓	✓	✓	✓
C30	7.742	A, C		✓	✓	✓	✓
C20	4.645	C			✓	✓	✓
S30	9.871	A, C	✓	✓	✓	✓	✓
B32	10.000	C	✓	✓	✓	✓	✓
T33	13.419	C	✓	✓	✓	✓	✓
N21	7.871	C		✓	✓	✓	✓
RK15	4.065	C			✓	✓	✓
W29I	12.277	A, C	✓	✓	✓	✓	✓
W29II	12.277	C	✓	✓	✓	✓	✓
ZLI	7.724	A		✓	✓	✓	✓
ZLII	7.742	A		✓	✓	✓	✓

Table 8. Uncertainty in the Quality for the C193, C30 and RK15 Tubes

Tube	A _{free flow} (mm ²)	Quality	G ≅ 150 (kg/m ² -s)	G ≅ 450 (kg/m ² -s)	G ≅ 750 (kg/m ² -s)
C193	18.934	Low	0.09±0.05	0.10±0.07	0.10±0.05
		Medium	0.48±0.04	0.45±0.03	0.50±0.04
		High	0.93±0.04	0.86±0.05	0.85±0.06
C30	7.742	Low	NA	0.09±0.03	0.11±0.04
		Medium	NA	0.51±0.03	0.54±0.05
		High	NA	0.86±0.06	0.87±0.08
RK15	4.065	Low	NA	0.10±0.04	0.10±0.03
		Medium	NA	0.53±0.05	0.47±0.04
		High	NA	0.80±0.05	0.88±0.05

CHAPTER FOUR. DATA ANALYSIS AND RESULTS

The experimental data obtained from the test facilities described in chapter three are presented in this chapter. The chapter is divided into three main sections in accordance with the three main phases in this study. The first section presents the results of the adiabatic, air-water flow visualization experiments. In the second section, the results from the R-134a flow visualization experiments are presented. The last section presents the pressure drop data from the 14 tubes investigated in Phase III of this study. (A discussion of the results and comparisons with other results found in the literature follow in the subsequent chapter entitled "Discussion of Results.")

Adiabatic Air-Water Flow Visualization

Numerous designations have been used by various investigators of two-phase flow mechanisms. The names of various flow regimes and patterns have been changed through the years by various authors. Furthermore, some investigators have subdivided the flow regimes into as many as sixteen distinguishable patterns (Wong and Yau, 1997). Therefore, the specific definitions for these regimes that were used in this study are first described below, followed by the results of Phase I.

Adiabatic Flow Regime Descriptions

For this work, four *major flow regimes* are identified, including stratified, intermittent, annular and dispersed flow (see Table 9). These flow regimes are further subdivided into *flow patterns* (Barnea et al. 1980). The stratified flow regime consists of the stratified flow pattern and the wavy flow pattern. The intermittent flow regime is divided into the plug and slug flow patterns. The dispersed flow regime is divided into the bubble and dispersed flow patterns. Examples of these flow patterns are shown in Figure 10 and consecutive frames of the video corresponding to $t = 0.0$, $t = 0.033$, and $t = 0.066$ seconds are shown in Figure 11. These frames were obtained from the video for the 5.5 mm diameter circular tube; similar flow patterns are observed and recorded for the other tubes also. A brief description of each flow regime and flow pattern is provided below.

Stratified Flow Regime

The stratified flow regime is characterized by a complete separation of the liquid and gas phases. When both the liquid and gas flows are laminar and no fluctuations at the phase interface can be detected, the flow pattern is called stratified (stratified smooth). As the gas mass flow rate is increased, instabilities form at the liquid-gas interface due to the interfacial velocity differential (Kelvin-Helmholtz instability). This flow pattern is called wavy flow (stratified wavy) and is characterized by the formation of small interfacial waves. In larger

diameter tubes, these waves can amplify and crest. The waves are easier to detect in large diameter tubes and the wave height can be large enough to allow the waves to break. In small diameter tubes, such as the ones used for this study, large breaking waves were typically not observed.

Table 9. Air-Water Flow Regime Classifications

Major Flow Regimes	Flow Patterns
Stratified	Stratified Smooth
	Stratified Wavy
Intermittent	Elongated Bubble (Plug)
	Slug Flow
Annular	Wavy Annular
	Annular
Dispersed	Bubble
	Dispersed

Intermittent Flow Regime

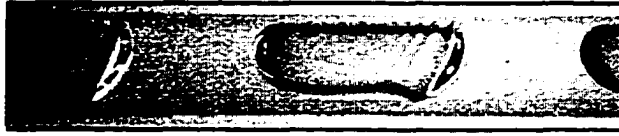
The intermittent flow regime is characterized by discontinuities in the liquid and gas flow. Elongated bubble flow (plug flow) is characterized by a continuous stream of vapor plugs flowing in the liquid. A thin film of liquid coats the tube wall and surrounds the vapor plug. Small disturbances may exist fore and aft of the bubbles, but as a whole the plugs remain intact and uniform. As the gas mass flow rate is increased, these disturbances amplify until the aft portion of the plug breaks apart into smaller bubbles. At this point, the flow pattern becomes slug flow. These smaller bubbles become trapped in the liquid flow and impact the front of the following slug causing disturbances in the front flow profile.

Annular Flow Regime

The annular flow regime consists of a nearly complete separation of the liquid and gas along the circumference of the tube wall. The first form of annular flow occurs when the surfaces of waves in wavy flow amplify to the extent that they touch the top of the tube wall. This flow pattern is known as wavy annular flow (pseudo-slug flow). As the mass flow rate is increased, the liquid is pushed up around the circumference of the tube wall by the increase in the gas momentum and falls downward under gravity in the form of annular waves. When the liquid coats the tube wall completely (forming an annular ring of the liquid phase) and the gas flows through the core of the tube, the flow pattern is known as annular flow. In annular flow



Stratified Flow Regime (Wavy Flow Pattern)



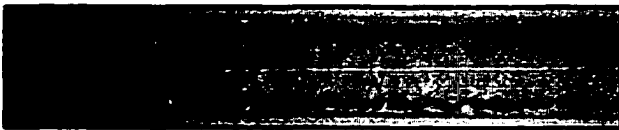
Intermittent Flow Regime (Plug Flow Pattern)



Intermittent Flow Regime (Slug Flow Pattern)



Annular Flow Regime (Wavy-Annular Flow Pattern)



Annular Flow Regime (Annular Flow Pattern)



Dispersed Flow Regime (Dispersed Flow Pattern)



Dispersed Flow Regime (Dispersed Bubble Flow)

Figure 10. Air-Water Flow Regime Descriptions

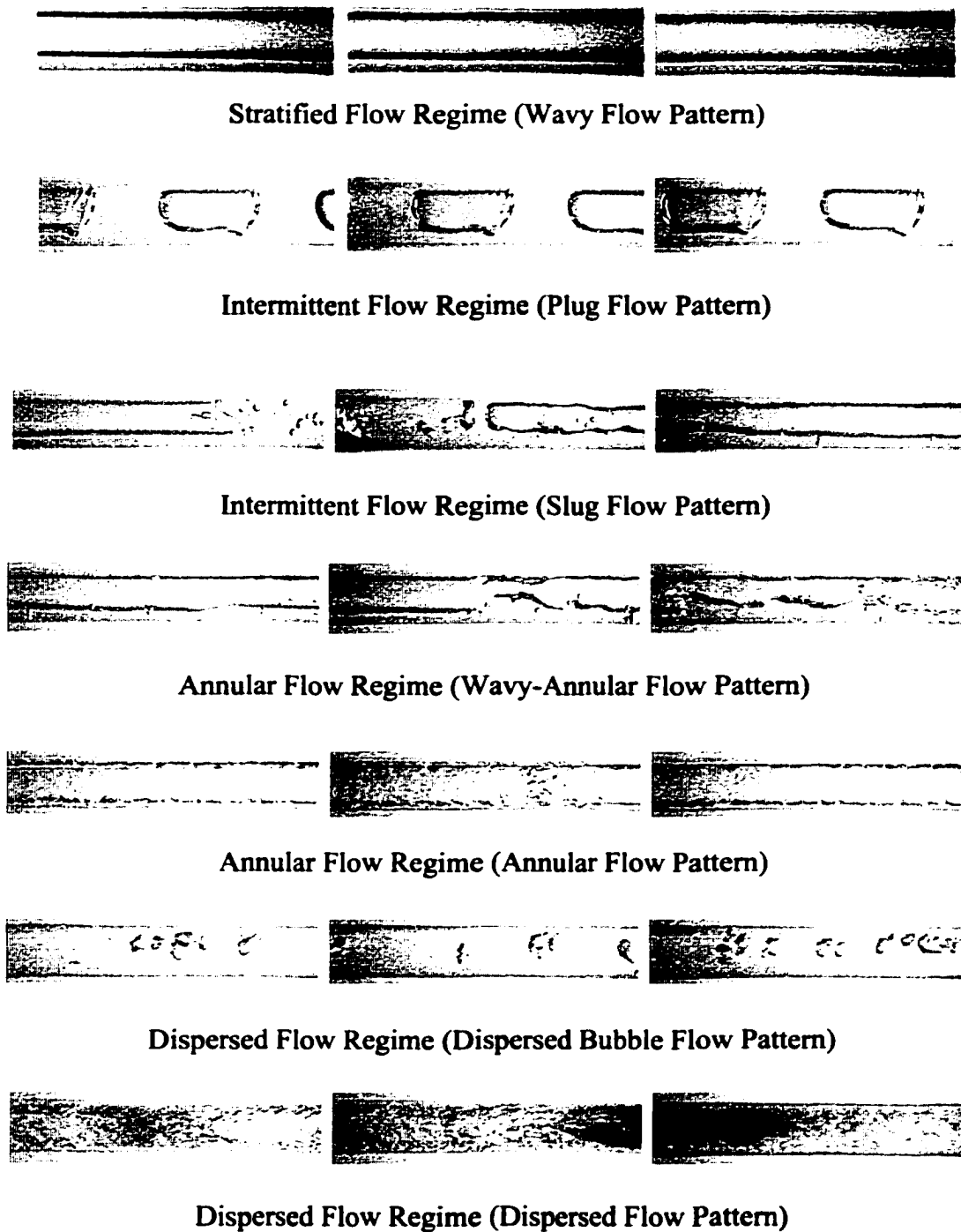


Figure 11. Time Lapse Photographs for $t = 0.000, 0.033$ and 0.066 Seconds

there could also be small droplets entrained in the gas core. This flow is also known as annular mist flow.

Dispersed Flow Regime

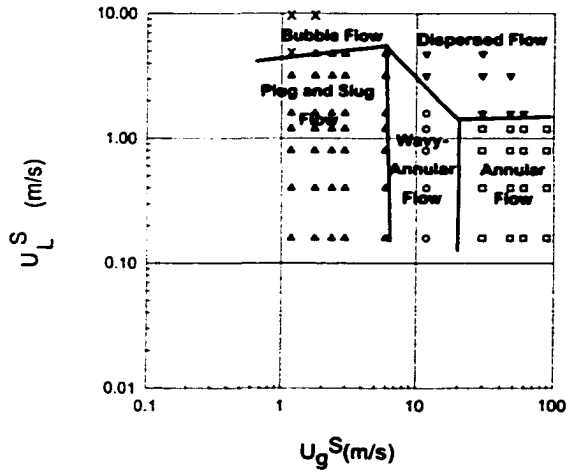
Dispersed flow occurs when the liquid flow is turbulent and the gas phase is in laminar or turbulent flow. When the gas flow is laminar, small bubbles are driven by buoyancy forces and flow primarily in the top half of the tube. This pattern is known as bubble flow. As the Reynolds number of the gas increases, keeping other variables constant, the bubble size decreases and the bubbles begin to disperse across the entire tube cross section. This flow pattern is known as dispersed bubble or dispersed flow.

Circular Tube Results

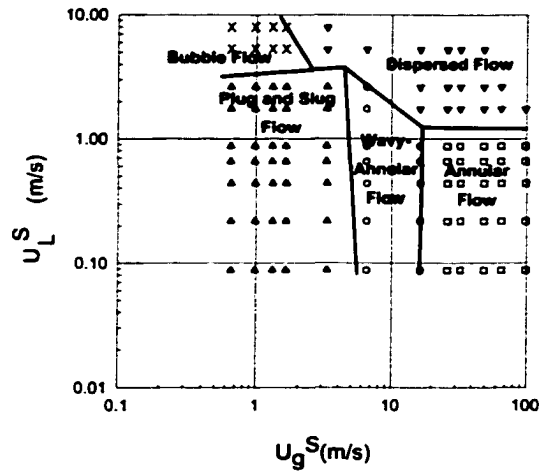
The four circular tubes analyzed in this study included 5.50 mm, 2.60 mm, 1.75 mm and 1.30 mm inner diameter tubes. Individual flow regime maps for each tube are shown in Figure 12. Here, the *superficial* velocities of the liquid and gas phases were calculated from the volumetric flow rates and total cross sectional area of the tube (refer to Equations 1 and 2), and used as the abscissa and ordinate axes, respectively. The flow regime maps were developed using these superficial velocities and the corresponding flow regime determined in the video analysis. The four flow regime maps are superimposed to identify trends in the transition lines as the tube diameter is decreased, as shown in Figure 13. Over 690 data points were used to define the flow maps. The stratified smooth flow pattern was not observed for any of the tubes tested, and for tubes with an inner diameter less than 5.50 mm, the stratified-wavy flow pattern was not observed for the flow velocities tested.

Figure 13 clearly shows that the tube diameter has a significant effect on flow regime transitions. As the tube diameter is decreased, the transition from an intermittent (plug and slug) regime to a dispersed or bubbly regime occurs at progressively higher superficial liquid velocities, u_L^s . It is possible that as the diameter decreases, surface tension effects are more dominant and the liquid may readily coat the circumference of the tube. The result is that the elongated bubble and slug flow patterns are sustained at higher values of u_L^s .

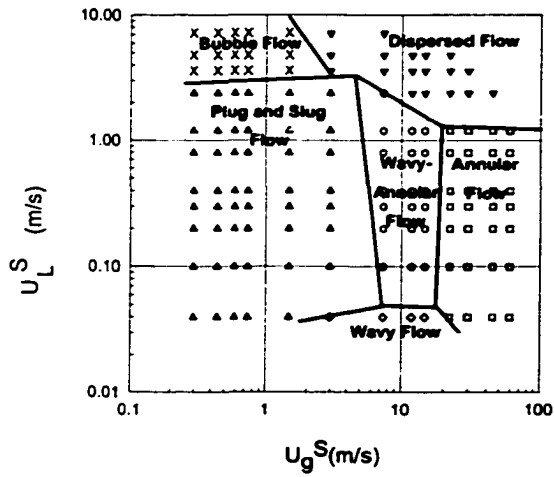
The transition from the intermittent flows to the annular category of flow regimes (wavy-annular and annular flow) occurs at a higher value of u_G^s when the diameter is decreased below 5.50 mm, but remains nearly unchanged as the diameter is further reduced to 1.75 mm and 1.30 mm. With a smaller diameter, the intermittent regime is sustained to a higher value of u_G^s and u_L^s while the transition to the annular flow regime is delayed. Due to the increased ability of the liquid to coat the tube wall, the relative size of the wavy-annular regime is decreased with decreasing diameter. The transition from a wavy-annular flow pattern to a pure annular flow pattern occurs at a slightly higher and nearly constant value of u_G^s .



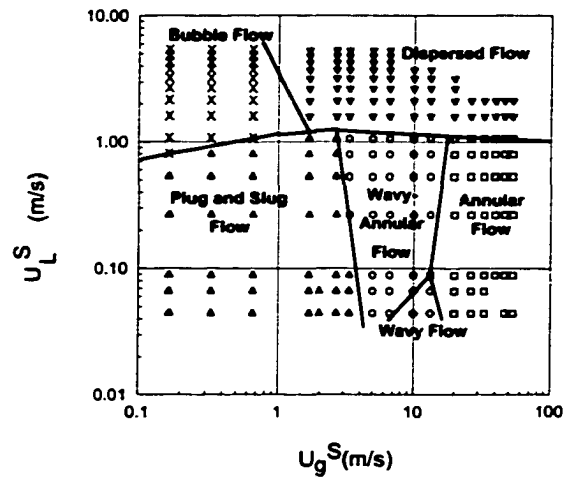
a) 1.30 mm I.D. Round



b) 1.75 mm I.D. Round



c) 2.60 mm I.D. Round



d) 5.50 mm I.D. Round

Figure 12. Flow Regime Maps for the Four Circular Tubes Tested in Phase I of this Study

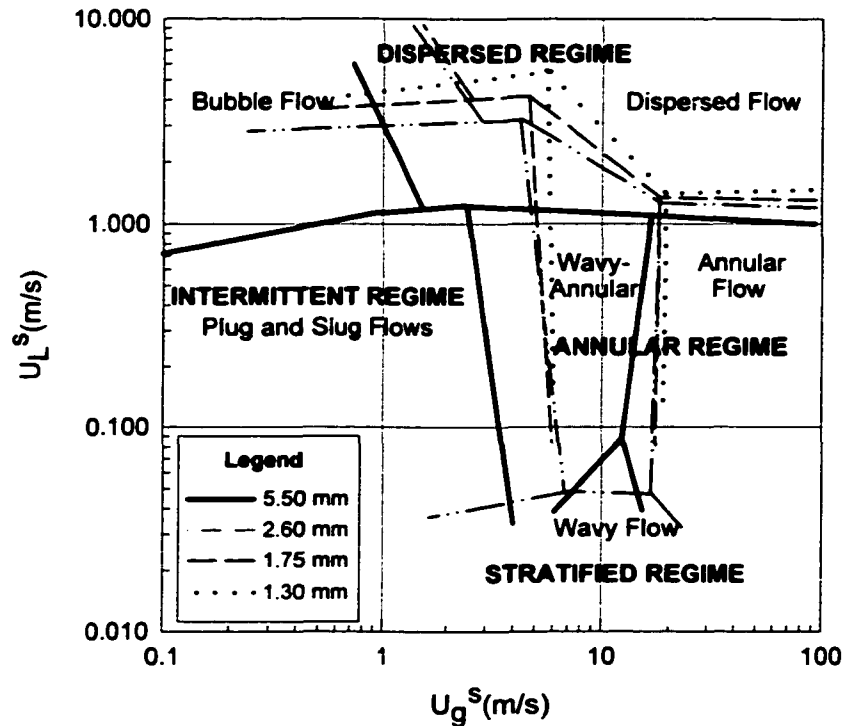


Figure 13. Effect of Diameter on the Air-Water Transition Lines

Rectangular Tube Results

As stated in the introduction, automotive condenser tubes have rectangular cross-sections with internal strengthening webs (refer to Figure 1). Thus, refrigerant flow passages in these condensers can be viewed as several small hydraulic diameter rectangular tubes with aspect ratios close to 1.0 in parallel, as shown in Figure 14. In such rectangular tubes, the effects of surface tension are expected to be more important as the liquid is more readily pulled up into the corners of the tube and held against gravity. Flow regimes in a rectangular tube of hydraulic diameter 5.36 mm with an aspect ratio of 0.725 were also investigated in this phase of the study. This flow regime map is shown in Figure 15, and a comparison between the round and rectangular tube flow patterns is shown in Figure 16. The principal difference between these maps appears to be the transition to the dispersed flow regime at a higher value of u_L^s . It can also be seen that in this rectangular tube, the transition to the annular regime (wavy-annular and annular flow) occurs at a nearly constant value of u_G^s . Both the round and rectangular geometries show stratified flows; however, the stratified flow regime occurs at a lower gas velocity in the rectangular tube, indicating the relatively higher influence of surface tension.

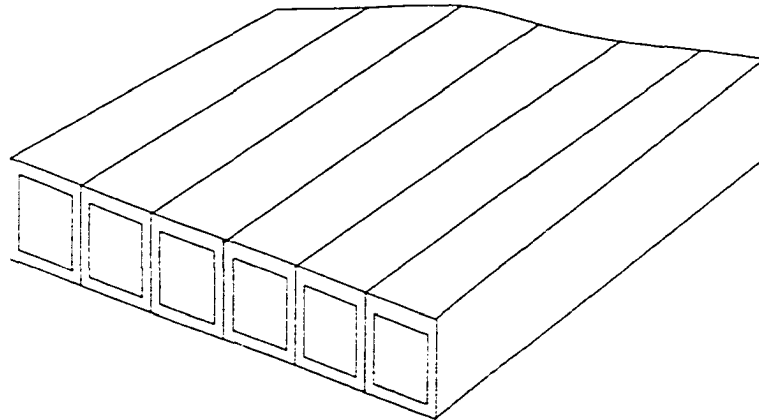


Figure 14. Example of a Condenser Tube

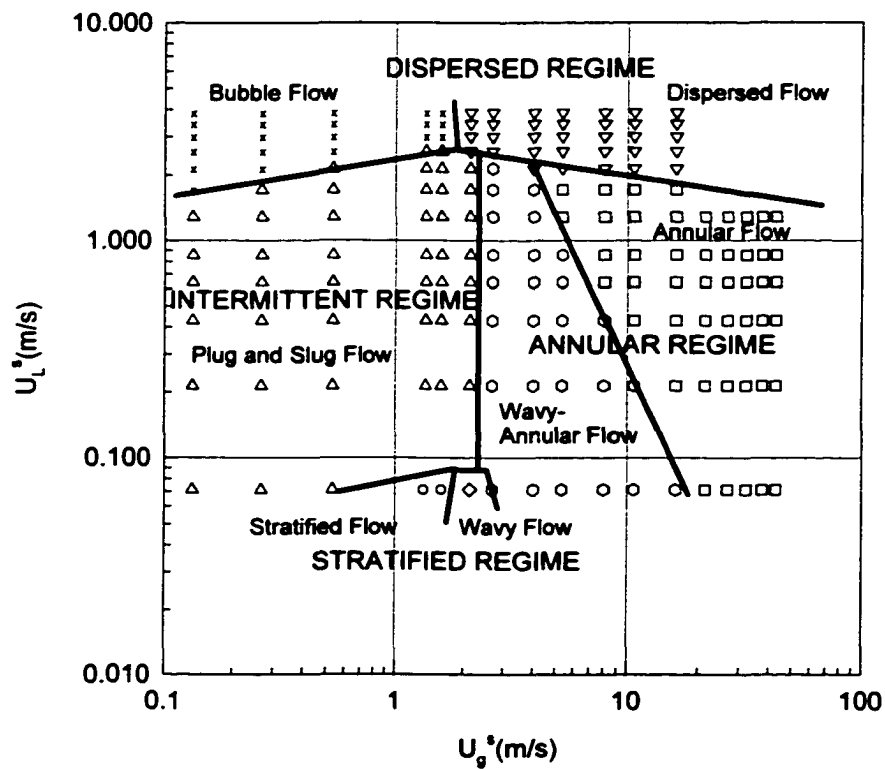


Figure 15. Air-Water Flow Regime Map for the Rectangular Tube ($D_h = 5.36$ mm, $\alpha = 0.725$)

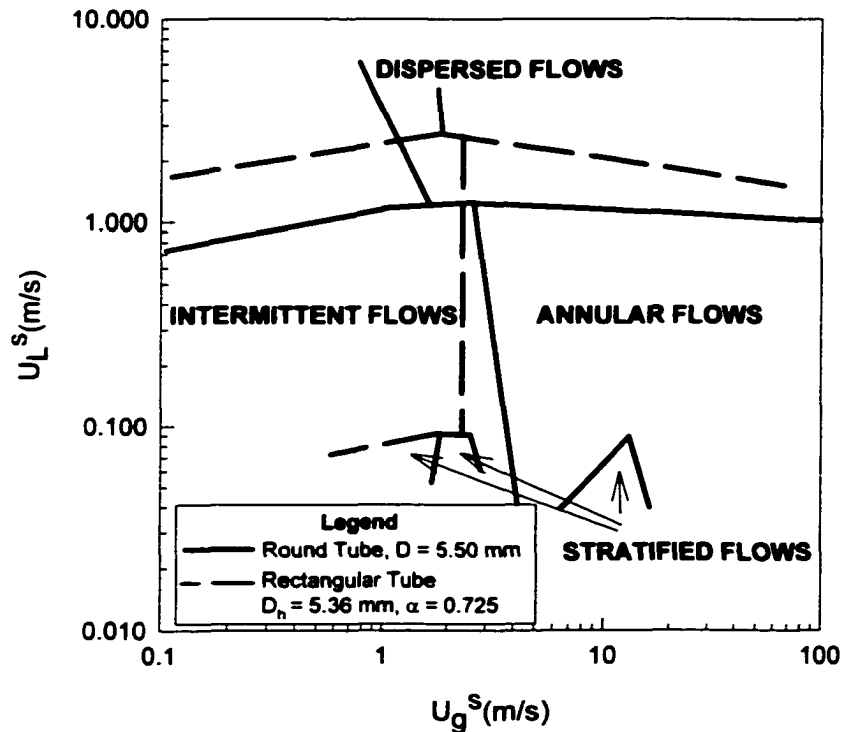


Figure 16. Comparison of the Air-Water Round and Rectangular Flow Regime Maps

R-134A Flow Visualization

The results from the flow visualization experiments using R-134a are described in this section. An album of the flow patterns observed for each quality and mass flux for all the tubes is provided in Appendix C. This album facilitates viewing of the progression of flow patterns with changes in quality, mass flux and tube size and shape. The discussion here describes the important features of each flow pattern and distinctions between them. Subsequently, graphs representing the progression of flow patterns are plotted to develop flow regime maps. In addition, the effect of tube geometry on flow regime maps is discussed.

Condensing Flow Regime Definitions

It is important that specific definitions for these regimes be established and described before the flow regime maps are presented. It should be noted that due to the diabatic nature of the tests in Phase II of this study, i.e., phase-change flow rather than air-water mixture flow, these definitions are different from the ones used in phase I. For the condensation study, four *major flow regimes* were identified, including annular, intermittent, wavy, and dispersed flow regimes. These flow regimes are further subdivided into *flow patterns*. The annular flow regime

is divided into the mist flow, annular ring, wave ring, wave packet and annular film flow patterns. The wavy flow regime is divided into the discrete wave and disperse wave patterns. The intermittent flow regime contains both the plug flow and slug flow patterns, while the dispersed flow regime primarily consisted of a bubble flow pattern. These flow regime and pattern definitions are summarized in Table 10. A similar classification of flow regimes was developed by Barnea *et al.* (1983). However, in their work, the *wavy regime* used here was considered a *flow pattern* (entitled the wavy-annular flow pattern) and was a subdivision of the annular regime. In this work, the wavy-annular flow pattern is categorized as a separate regime and is called the wavy regime. Numerous investigators have included any flow pattern that included a coating of liquid around the circumference of the tube in the annular flow regime. This is appropriate for adiabatic flows (such as air-water mixtures), which have constituted the focus of the majority of flow visualization studies in the past. Adiabatic flows could very well have completely dry portions of the tube surface, particularly at the top of the tube. However, in *condensing* flows, it is to be expected that there will by definition be a coating of liquid around the whole circumference for most of the combinations of mass flux and quality. To consolidate this entire combination of conditions into the annular flow regime definition would, in the opinion of the present author, not provide adequate insights into the actual flow mechanisms. In other words, vastly different flow mechanisms, for example, with substantial differences in the liquid film thickness at the top and bottom would be lumped into the annular flow regime, without accounting for the varying influence of gravity across this spectrum. Therefore, in the present study, flow patterns with an obviously significant influence of gravity (observed through a noticeable difference in film thickness at the top and bottom of the tube) and with a wavy structure of the liquid film are considered to belong to the wavy flow regime. And, as noted above, the characteristics of the waves are used to further subdivide these mechanisms into flow patterns within the wavy flow regime. This method of classification provides a better understanding of the particular flow mechanisms established at a given combination of mass flux and quality. The large number of data points over the entire range of conditions covered in this study enables such a detailed classification of the flow regimes and patterns.

Barnea *et al.* (1983) also included a stratified regime consisting of the stratified flow pattern and the wavy flow pattern. However, in the present work on flow patterns during condensation, a purely stratified smooth or wavy pattern (without a circumferential annular film) was not observed and is therefore not used in the classification of the flow patterns. A brief description of each flow regime and flow pattern is provided below.

Annular Flow Regime

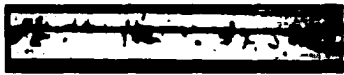
The annular flow regime consists of a nearly complete separation of the liquid and vapor along the circumference of the tube wall. The vapor flows in the core of the tube with a few liquid droplets entrained in the vapor. The flow patterns within the annular flow regime include mist, annular ring, wave ring, wave packet and annular film patterns, as shown in Table 10. The ***Mist Flow Pattern*** consists of a uniform vapor mist with small droplets entrained in the vapor, and without any discrete wavy or ring-like formations in the liquid-vapor mist. The annular liquid layer on the tube wall is barely discernible. This flow pattern was typically found to occur at high mass fluxes and high qualities, as can be seen in the Tables in Appendix C.

The ***Annular Ring Pattern*** (Table 10) is similar to mist flow, but regularly occurring annular “rings” of liquid appear in the flow. These circumferential rings are probably formed from a collection of annular droplets on the surface of the tube wall, and occur periodically between large intervals of mist flow. The ***Wave Ring Pattern*** is observed when the annular rings become noticeably thicker at the bottom than on the top. A large fraction of these wave rings reach the top of the tube and are circumferential, thus creating a thin annular liquid layer on the tube walls. The ***Wave Packet Pattern*** is characterized by packets of individual waves that appear periodically in the flow. The effect of gravity is more noticeable in these wave packets, which typically do not reach the top of the tube, unlike annular rings or wave rings. An annular flow or a thin, wavy annular layer of liquid may coat the tube walls. The ***Annular Film Pattern*** consists of a wavy liquid annular film. There is a significant and easily identifiable liquid layer on the top and bottom of the tube. In some instances, especially at the higher qualities, these waves have a fine structure that is reflected as an undulating “pebble” pattern along the side walls of the tube. The thickness of the liquid layer can vary greatly and as the quality decreases, the wall coating becomes more agitated. The thickness of the liquid layer is larger (with respect to the tube cross-section) in smaller diameter tubes. For example, in the 1 x 1 mm and 2 x 2 mm channels, the large thickness of the annular liquid layer gives the impression of a distinct vapor core that flows in the center of the tube in a “snake-like” pattern. The vapor core is continuous, but occupies a varying portion of the tube cross-section. The core is, however, not blocked or interrupted by any liquid slugs that span the entire cross-section.

Wavy Flow Regime

This flow regime, shown in Table 10, consists of separate liquid and vapor layers with the liquid flowing on the bottom of the tube and the vapor flowing above the liquid. However, even in this regime, an annular film of liquid is present on the tube wall. The waves at the interface between the liquid and the vapor are caused by the interfacial shear between the two phases moving at different velocities. These waveforms can vary from a few, well-defined,

Table 8. Description of Two-Phase Flow Regimes.

FLOW REGIMES				
FLOW PATTERNS	Annular	Wavy	Intermittent	Dispersed
				
	Mist Flow	Discrete Wave (0)	Slug Flow	Bubble Flow
				
	Annular Rings	Discrete Wave (1)	Slug Flow	Bubble Flow
				
Wave Ring	Discrete Wave (2)	Plug Flow	Bubble Flow	
				
Wave Packet	Discrete Wave (3)	Plug Flow (4 Parallel Channels)		
	Note: Numbers above denote intensity of secondary waves			
Annular Film				

discrete waves of larger structure moving along the phase interface to many disperse waveforms with a large range of amplitudes and wavelengths superimposed upon one another. In this study, the waves were subdivided into different categories based on the intensity of the secondary waves, ranging from discrete wave flow to disperse wave flow.

In *Discrete Wave Flow*, the dominant wave pattern is of large wavelengths and amplitudes. A few small wavelength waves could also be superimposed on these larger waves, but the stratified vapor-liquid interface formed by the waves is clearly distinguishable. The wave amplitudes cover a large range from approximately $1/8$ of the tube height to $3/4$ of the tube height or larger. Typically, the waves do not strike the top of the tube. The waves may show signs of shearing or undercutting or both (depending upon the relative velocities of the liquid and vapor phases). Here, shearing is defined as the process when a wave crest projecting into the vapor phase is sheared off and disperses into the typically faster moving vapor. Thus, the crest first bends forward (downstream) and then is sheared off. Undercutting occurs when vapor pushes the base of the wave crest forward while the peak of the wave flows slower, resulting in a wave crest that bends backward. In some instances, this backward bending of the crest causes it to either disperse into the vapor phase or fall under the influence of gravity into the bulk liquid. A range of thicknesses of the annular liquid coating is observed in this wavy flow pattern. In cases where the annular coating is thicker, this coating on the side walls also becomes wavy.

Disperse Waves occur at the higher mass fluxes and the approximate quality range of 0.25 – 0.75, depending on the tube geometry. This pattern is characterized by the simultaneous occurrence of a large number of secondary waves of a variety of structures. There may or may not be a dominant wavelength and amplitude. Due to the preponderance of the different types of waves, the vapor-liquid interface often becomes indistinguishable. The waveforms typically touch the top of the tube, which truncates the wave crests and further disperses them. The waves may have bubble entrainment.

Intermittent Flow Regime

The intermittent flow regime is characterized by discontinuities in the liquid and gas flow. A continuous stream of vapor plugs or slugs flows through the liquid, while a thin film of liquid coats the tube wall and surrounds the vapor plug. This flow regime is further subdivided into slug flow and plug flow patterns.

Slug Flow is characterized by vapor “slugs” moving through the liquid, often accompanied by large discrete waves. The slugs are followed by a trail of bubbles entrained in the liquid. The front of the slugs is typically rounded while the rear of the slugs can be vertical or inclined, or have elongated trails. Typically, slug flow is mixed with intermittent plug flow. This flow pattern is shown in Table 10. In *Plug Flow*, solitary vapor plugs are observed,

typically without trailing bubbles. These plugs can be stratified or non-stratified, depending on the mass flux and tube geometry. The rear portion of the plugs take on various shapes including angled, rippled and square. Plug flow is also shown in Table 10.

R-134a Flow Regime Maps

The observed flow mechanisms for each data point (different qualities and mass fluxes) for all the tubes investigated in this study were assigned to a particular flow pattern from among those described above. In some cases, the flow mechanisms corresponded to more than one flow regime, typically indicating a transition between the respective regimes. These experimentally obtained video frames of the flow patterns and the flow regime assignments were then used to develop flow regime maps for the nine tubes shown in the test matrix (refer to Figure 4). Although four major flow regimes were identified, not all of these four major regimes were observed for each tube. The existence and extent of the respective flow regimes are dependent upon the tube geometry, as will be shown in the following discussion of the individual flow regime maps for the nine tubes.

Choice of Flow Regime Map Coordinates

Previous investigators have used a variety of coordinates to represent two-phase flow regime maps. One of the more common methods is to choose superficial gas and liquid phase velocities as the two coordinate axes. The computation of superficial phase velocities assumes that each phase is occupying the entire flow cross-section, which is obviously not true for either phase. This assumption would at best be approximately true for the vapor phase at high qualities and for the liquid phase at the very low qualities approaching zero. Almost all the other coordinates used by previous investigators are functions of the void fraction or the slip ratio between the respective phases. This implies that some assumptions or empirical models of the void fraction need to be used to compute one or more of the coordinates axes. However, one of the major reasons for conducting the present study is to identify the differences between the well-accepted flow regimes in round tubes and those in square and rectangular tubes with small hydraulic diameters. Thus, assuming void fractions and slip *a priori* would be somewhat contradictory to the premise for the present study. In view of this discussion, a combination of variables (Mass Flux G , and Quality x) that does not require any assumptions about the flow of the respective phases and simply depends on measured quantities was used to report the results of the present work. The following discussion of the flow regimes in each of the nine tubes uses these variables for the coordinate axes.

Circular 4.91 mm I.D. Tube

Figure 17 shows the flow regime map for the 4.91 mm round tube. In this tube, three of the four major flow regimes are present including the annular regime, wavy regime and the intermittent regime. The intermittent regime shows both the plug and slug flow patterns. A major portion of this flow regime map is occupied by the wavy flow regime with a small region where the plug, slug and discrete wave flow patterns coexist. Both discrete and disperse wave patterns are present, and the waves become increasingly disperse as the quality and mass flux is increased (shown by the arrow in Figure 17). A visual distinction between discrete and disperse waves was made using a scale from zero to three where a zero represents a highly discrete and clearly identifiable single wave form (with no secondary waves) and three represents a disperse waveform with numerous secondary waves of different amplitudes and wavelengths. The approximate demarcation between discrete and disperse waves is shown by the dashed line in this figure. It should be noted that this transition occurs gradually and the demarcation line is simply intended to show the approximate region below which the waves may be considered to be discrete, while the waves above this region could be considered to be disperse in nature. Thus, this line was drawn by approximately defining the discrete waveform to be any waveform on this scale from zero to two, while a three indicates a disperse waveform. The annular flow regime includes both the mist flow pattern and the annular film pattern. Some

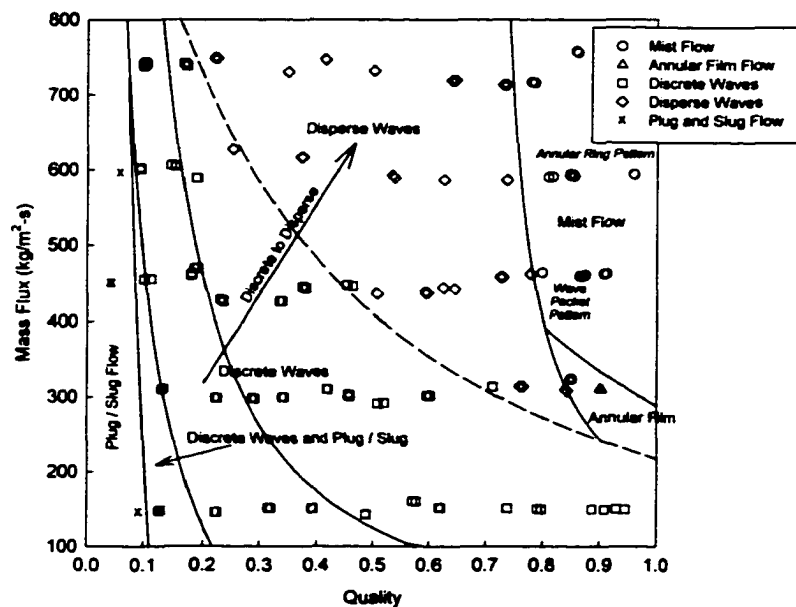


Figure 17. Flow Regime Map for the 4.91 mm I.D. Tube

other observations regarding the flow patterns within this regime can be made, even though definite transition lines between these flow patterns are not shown. At the lower mass fluxes, the wave packet flow pattern is found near the border between the mist flow pattern and dispersed wave pattern. The annular ring flow pattern exists in the mist flow region near the border of the mist flow and disperse wave flow patterns.

Square 4 x 4 mm Tube

The flow regime map for the 4 x 4 mm square tube is shown in Figure 18. This flow regime map shows three of the four major regimes including the annular, wavy, and intermittent regimes. The intermittent regime includes both plug and slug flow patterns and extends to a quality of approximately 0.08. The wavy flow regime occupies a major portion of this map with both discrete and disperse wave patterns present. The waves become increasingly disperse as the quality and mass flux are increased (shown by the arrow in Figure 18). At higher qualities and mass fluxes the disperse wave pattern transitions into the mist flow regime. For this tube, the mist flow pattern is the dominant pattern within the annular flow regime, with the wave packet flow pattern occurring near the border of the annular flow regime and wavy flow regime. At the higher mass fluxes, the wave ring pattern is seen near the border of the annular flow regime and the wavy regime. The dispersed flow regime does not appear on the 4 x 4 mm tube flow regime map.

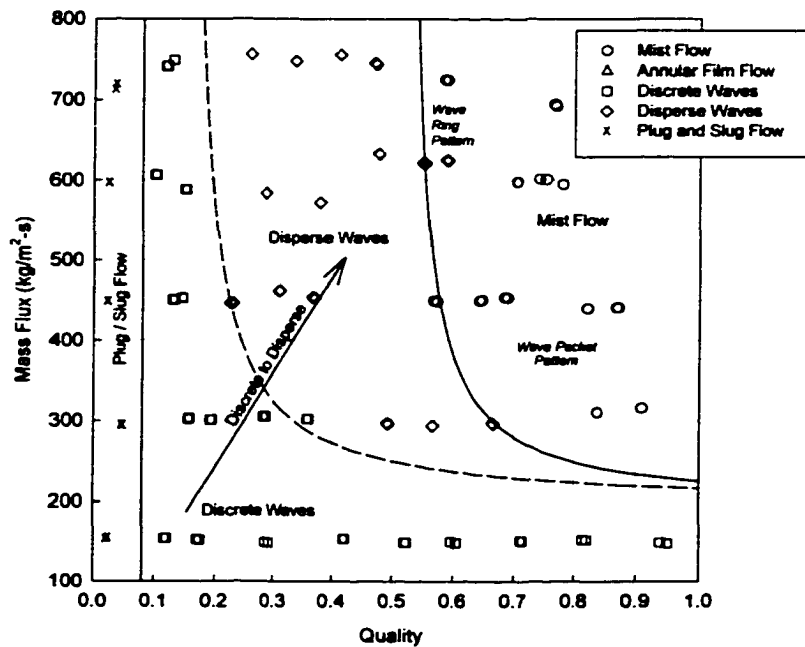


Figure 18. Flow Regime Map for the 4 x 4 mm Tube

Square 3 x 3 mm Tube

The flow regime map for the 3 x 3 mm square tube (Figure 19) shows all four major regimes. The intermittent regime extends from a quality of zero to about 0.09 at the highest mass flux, and up to a quality of 0.18 at the lowest mass flux case. There is a noticeable reduction in the size of the wavy flow regime from that found in the 4 x 4 mm tube flow regime map. In the wavy regime both discrete and disperse wave patterns are present, with the larger fraction being discrete waves. The waves tend to be more disperse at the higher mass fluxes and qualities, as shown by the arrow in Figure 19 with an approximate transition region between these two flow patterns being indicated by the dashed line. There is a small region of overlap in the intermittent and wavy regimes where the slug flow pattern and discrete wave flow pattern coexist, with periodic switching of the flow between these two regimes. The dispersed flow regime appears in this tube at low qualities and high mass fluxes in the form of the bubble flow pattern, which coexists with the plug and slug flow patterns.

Figure 19 also shows that the annular flow regime has increased in size compared to the annular flow regime found in the 4 x 4 mm tube. This regime includes the mist flow pattern and

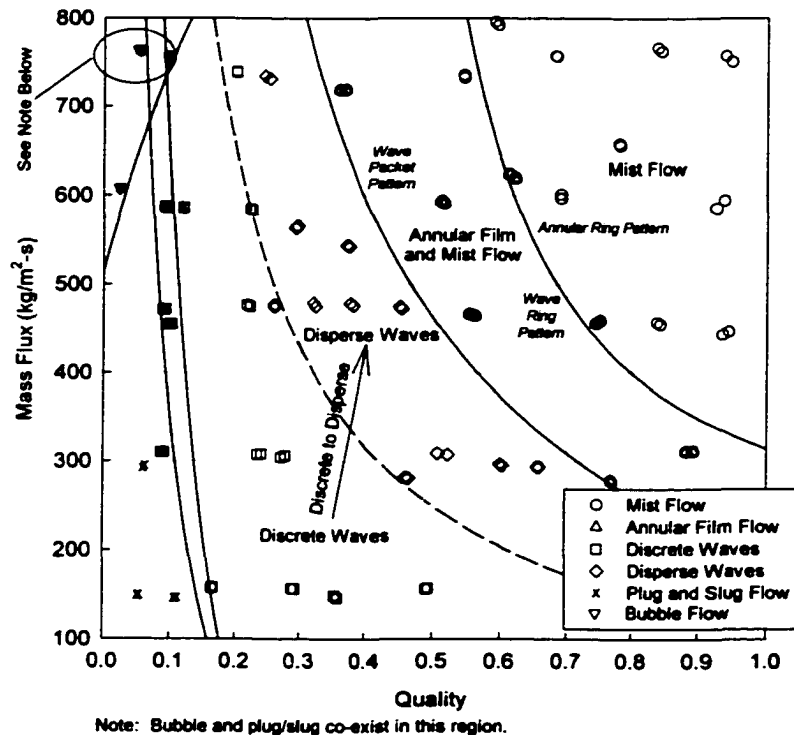


Figure 19. Flow Regime Map for the 3 x 3 mm Tube

the annular film pattern. However, in most cases, the annular film flow pattern is mixed with the mist flow pattern. In addition, in this region where the annular film and mist flow patterns are seen simultaneously, the wave ring pattern is seen at the lower mass fluxes, and the wave packet pattern is seen at the higher mass fluxes. Thus, it appears that both the wave packet pattern and the wave ring pattern may be considered to be indicators of the transition to the wavy regime. The annular ring pattern is seen near the transition between the mist flow pattern and the annular film flow pattern. The annular ring pattern could probably be viewed as an indicator of the transition from the mist flow pattern to the annular film flow pattern.

Square 2 x 2 mm Tube

The flow regime map for the 2 x 2 mm square channel (Figure 20) also shows all four major regimes. The intermittent regime includes both the plug and slug flow patterns and extends into the wavy regime. Thus, this map shows a band of G and x where both the slug flow pattern and the discrete wave flow pattern coexist. In this tube, the wavy flow regime contains only the discrete wave flow pattern (no disperse wave flow pattern). The dispersed regime contains the bubble flow pattern and is mixed with the plug, slug and discrete wave flow patterns at low qualities and high mass fluxes. The annular regime occupies a major portion of this flow map and is divided into three regions. The first region is the annular film flow pattern, which is found adjacent to the discrete wave flow pattern. As the quality and mass flux are increased, the second region shows the annular film flow pattern coexisting with the mist flow pattern. At even higher qualities and mass fluxes, the annular film flow pattern disappears and only the mist flow pattern remains. The wave ring pattern is seen throughout the region where the annular film and mist flow patterns coexist.

Square 1 x 1 mm Tube

Figure 21 shows the flow regime map for the 1 x 1 mm square tube. For this tube, only three of the four major flow regimes are present: the annular, intermittent, and dispersed regimes. The wavy flow regime is not present in this tube, implying a diminishing influence of gravity. The intermittent regime includes both the plug and slug flow patterns and also includes a region where the plug, slug and annular film flow patterns coexist. The dispersed flow regime shows the bubble flow pattern coexisting with the plug, slug and annular film flow patterns. The annular regime occupies a substantial portion of the flow regime map and is divided into five regions. The first region occurs at low qualities (less than 0.16) and high mass fluxes (greater than 340 kg/m²-s) and shows the annular film pattern coexisting with the plug, slug and bubble flow patterns. As the quality is increased, the second region shows the annular film flow pattern coexisting with the plug and slug flow patterns. At higher qualities, the annular film pattern exists by itself. There is also a large region where the annular film flow pattern and mist flow

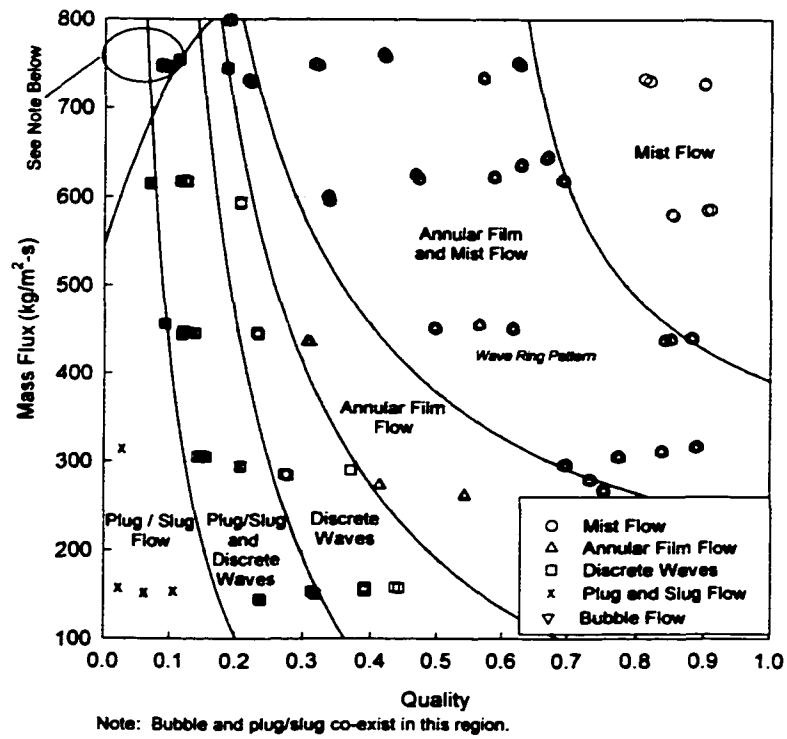


Figure 20. Flow Regime Map for the 2 x 2 mm Tube

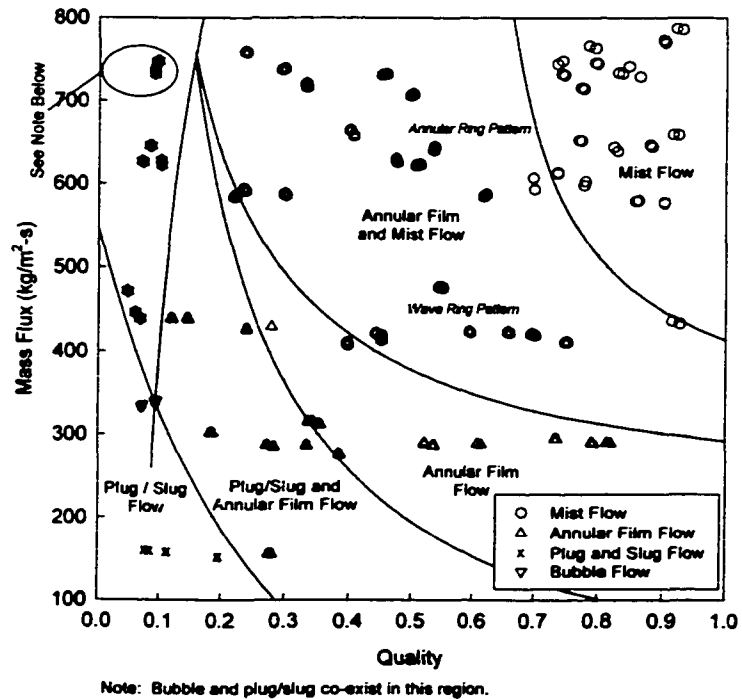


Figure 21. Flow Regime Map for the 1 x 1 mm Tube

pattern coexist. At the highest qualities and mass fluxes, the mist flow pattern is observed. The annular ring pattern is seen near the border of the mist flow pattern and the region where the annular film flow and mist flow patterns coexist. The wave ring pattern is found near the border of the annular film flow pattern and the region where the annular film flow and mist flow patterns coexist.

Rectangular 4 mm (Height) x 2 mm (Width) Tube

The 4 x 2 mm tube flow regime map is shown in Figure 22. For this tube, the annular, wavy and intermittent regimes are present, with the annular and wavy regimes occupying a major portion of the flow regime map. The intermittent regime includes a region containing the plug and slug flow patterns as well as a region where the plug, slug and discrete waves coexist. The wavy flow regime includes both discrete and disperse waves, with the arrow on Figure 22 indicating increasingly disperse waves, and the transition between discrete and disperse wave regions is shown by the dashed line. The annular regime includes a region of the mist flow pattern as well as a region where the mist flow and annular film patterns coexist. The wave ring pattern is found near the border of the mist flow pattern and the region where the mist flow and annular film flow patterns coexist.

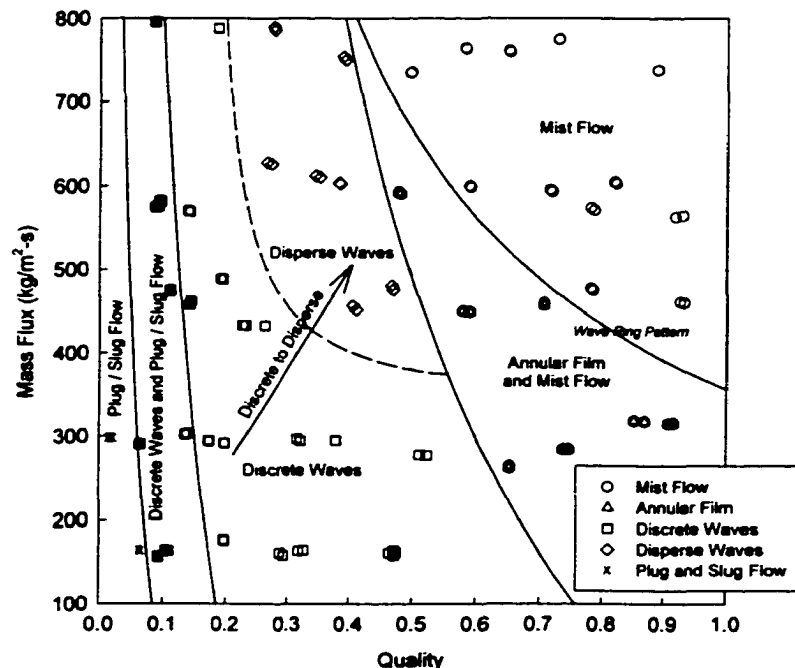


Figure 22. Flow Regime Map for the 4 (Height) x 2 (Width) mm Tube

Rectangular 2 mm (Height) x 4 mm (Width) Tube

Figure 23 shows the flow regime map for the 2 x 4 mm. This flow regime map contains all four of the major flow regimes. The intermittent regime includes a region where both plug and slug flow patterns are present as well as a region where plug, slug and discrete wave flow patterns coexist. The wavy flow regime includes both discrete and disperse waves, with the arrow on Figure 23 indicating increasingly disperse waves, and the transition between discrete and dispersed wave regions is shown by the dashed line. The annular flow regime is divided into three regions. The first region contains only the annular film flow pattern, while annular film flow and mist flow patterns were observed in the second region. The third region (at the highest qualities and mass fluxes) shows the mist flow pattern. Wave rings are found near the border of the mist flow pattern and the region where the mist flow and annular film flow coexist. The annular ring flow pattern exists at the higher qualities within the region where the mist flow and annular film flow patterns coexist. Wave packet flow can be found near the border between annular film flow and the region with annular film flow and mist flow.

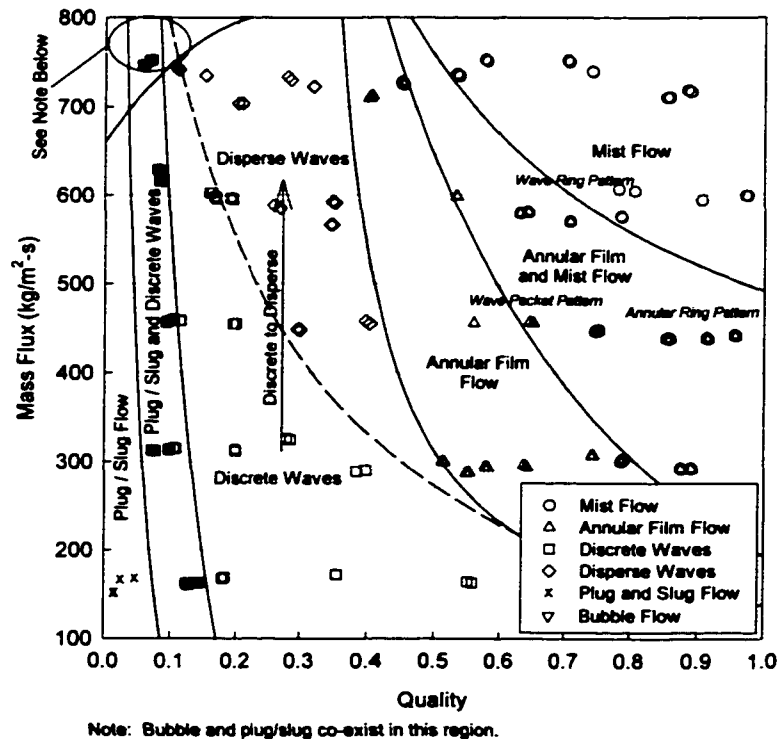


Figure 23. Flow Regime Map for the 2 (Height) x 4 (Width) mm Tube

Rectangular 6 mm (Height) x 4 mm (Width) Tube

The flow regime map for this tube is shown in Figure 24. This map contains three of the four major flow regimes including the intermittent, wavy and annular regimes. The intermittent regime includes both the plug and slug flow patterns and extends into the wavy regime where the plug, slug and discrete wave flow patterns coexist. A major portion of this flow map is occupied by the wavy flow regime, with the arrow in Figure 24 and the dashed line showing the transition from discrete to disperse waves. The annular region shows the simultaneous occurrence of both the annular film and mist flow patterns. Within this region, the wave packet flow pattern is seen at the lower mass fluxes.

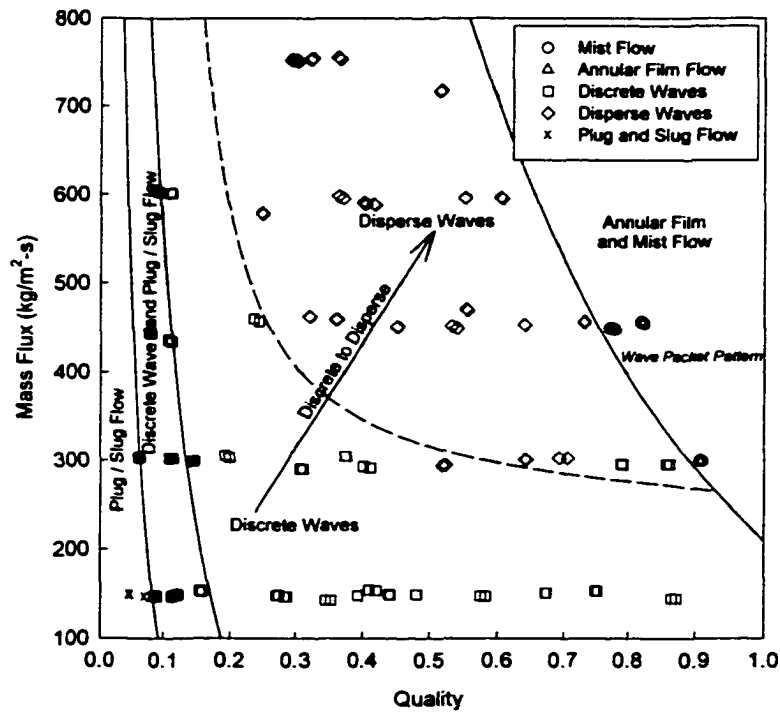


Figure 24. Flow Regime Map for the 6 (Height) x 4 (Width) mm Tube

Rectangular 4 mm (Height) x 6 mm (Width) Tube

The flow regime map for this tube is shown in Figure 25. This flow regime map contains the annular, wavy and intermittent regimes. The intermittent regime contains a region where both plug and slug flow patterns exist as well as a region where the plug, slug and discrete wave patterns coexist. A major portion of this flow map is occupied by the wavy flow regime, with the arrow in Figure 25 and the dashed line showing the transition from discrete to disperse waves. The annular region shows the simultaneous occurrence of both the annular film and mist flow

patterns. Wave packet flow is seen in this region at the lower mass fluxes.

Flow regime maps for individual tubes were discussed above. It was shown that these maps are different for the different tubes investigated in this study. In addition to the above figures, graphs were also plotted in which transition lines for different tubes were superimposed to facilitate a comparison of these maps, and study the effect of various geometric features on the flow regime maps. A discussion of these effects follows in the next chapter entitled "Discussion of Results."

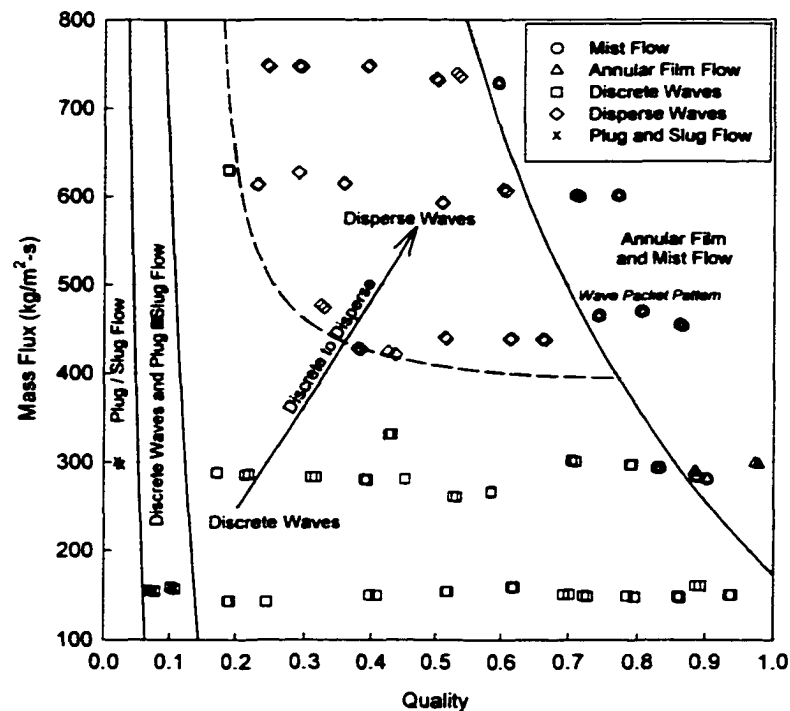


Figure 25. Flow Regime Map for the 4 (Width) x 6 (Height) mm tube

R-134a Pressure Drop Results

Two-phase pressure drop experiments (during condensation) were conducted on a wide variety of tube shapes and sizes. A summary of the tubes tested in this phase of the study was given in Table 6. For each of these test sections, single phase validation tests were first conducted to calculate the single phase friction factors for comparison with correlations found in the literature.

Single Phase Pressure Drop Validation Results

Data for the C120 tube with a hydraulic diameter of 3.05 mm are described in detail here, followed by the results for all tubes. Both single phase liquid and vapor data were taken to span

a wide range of Re values in the laminar, transition and turbulent regimes. The experimentally measured quantities included: pressure and temperature of the fluid at the inlet and exit of the test section, refrigerant mass flow rate, and differential pressure drop across the test section. These tests were conducted under adiabatic conditions.

To accurately measure the single phase pressure drop, the refrigerant must enter and exit the test section either as a fully superheated vapor or fully sub-cooled liquid. Small amounts of liquid droplets in the vapor phase and small vapor bubbles in the liquid phase result in deviations from the correlations. To determine the amount of superheat or sub-cooling of the refrigerant for the vapor and liquid tests, respectively, the saturation temperature was calculated from the average pressure at the inlet and exit of the test section as follows:

$$T_{test,ave} = \frac{T_{test,in} + T_{test,out}}{2} \quad (21)$$

The difference between the saturated condition and the measured temperature measurement determined the amount of superheat or sub-cooling. For the case of a sub-cooled liquid, the amount of sub-cooling is given by:

$$P_{ave} = \frac{P_{in} + P_{out}}{2} \Rightarrow T_{sat}(P_{ave}, x = 0) \Rightarrow \Delta T_{sub} = T_{sat} - T_{test,ave} \quad (22)$$

and similarly, for the case of a superheated vapor, the amount of superheat is given by:

$$P_{ave} = \frac{P_{in} + P_{out}}{2} \Rightarrow T_{sat}(P_{ave}, x = 1) \Rightarrow \Delta T_{sup} = T_{test,ave} - T_{sat} \quad (23)$$

For a representative data point for liquid phase tests on the C120 tube, the test section inlet and exit temperatures were 28.11°C and 28.29°C, respectively, which results in an average test section temperature of 28.20°C. The measured inlet and exit pressures of the test section are 1230.11 kPa and 1226.90 kPa, respectively, which yields an average test section pressure of 1228.51 kPa. At this average pressure, the saturation temperature of R-134a is 47.21°C and, from equation (22), the amount of sub-cooling is 19.01°C, which ensures single-phase flow. The density and viscosity of the refrigerant are determined from the average pressure and temperature of the refrigerant. For this example, the density and viscosity of the liquid refrigerant are 1195.1 kg/m³ and 2.38x10⁻⁴ kg/m-s, respectively.

The mass flux in the test section is equal to the total mass flow rate divided by the total free flow area. This is given by:

$$G = \frac{\dot{m}}{A_{tot}} \quad (24)$$

With a measured mass flow rate of 3.621×10^{-3} kg/s and a total free flow area of 7.30 mm^2 (Table 4), equation (24) yields a mass flux of $496.0 \text{ kg/m}^2\text{-s}$. The Reynolds number of the refrigerant flow is given by:

$$\text{Re} = \frac{GD_h}{\mu_{test,ave}} \quad (25)$$

With a mass flux of $496.0 \text{ kg/m}^2\text{-s}$, a hydraulic diameter of 3.05 mm , and a viscosity of $2.38 \times 10^{-4} \text{ kg/m-s}$, the Reynolds number is 6356. The single-phase liquid and gas experiments run on the C120 test section yielded Reynolds numbers ranging from 5794 to 61,252.

To determine the single-phase friction factor, the minor losses due to expansion and contraction of the fluid in the headers are subtracted from the total measured pressure drop across the test section. For the contraction of a fluid, the head loss is as follows:

$$h_{loss,con} = K_{con} \frac{V_{tube}^2}{2} \quad (26)$$

where K_{con} is the contraction loss coefficient for flow through a sudden change in area (Fox and McDonald, 1992) and V_{tube} is the velocity of the fluid in the microchannel. The velocity of the fluid in the tube is given by:

$$\dot{m} = \rho V_{tube} A_{tube} \quad (27)$$

Similarly, the head loss due to a sudden expansion of a fluid is given by (Fox and McDonald, 1992):

$$h_{loss,exp} = K_{exp} \frac{V_{tube}^2}{2} \quad (28)$$

where K_{exp} is the expansion loss coefficient. The loss coefficients for expansion and contraction are a function of the ratio of the free flow area of the header and the free flow area of the microchannel (A_t/A_{header}). The pressure drop due to the contraction of the fluid is given by

$$\Delta P_{con} = \frac{\rho(V_{tube}^2 - V_{header}^2)}{2} + \rho h_{loss,con} \quad (29)$$

The contraction of the fluid will result in an overall pressure loss since the velocity of the fluid in the microchannel is substantially larger than the velocity of the fluid in the header. The change in system pressure due to the expansion of the fluid is given by:

$$\Delta P_{\text{exp}} = \frac{\rho(V_{\text{header}}^2 - V_{\text{tube}}^2)}{2} + \rho h_{\text{loss,exp}} \quad (30)$$

This expansion of the fluid will result in a pressure recovery due to the decrease in the fluid velocity. The total pressure drop due to expansion and contraction is equal to the sum of the two components. This is shown in Figure 26 for the C120 tube with varying header sizes. With an area ratio of 1.0, the total loss due to expansion and contraction is zero (since there is no change in area). As the area ratio decreases, both the pressure loss due to contraction and the pressure recovery due to expansion increase – and the total pressure loss increases. At very small values of area ratio, the pressure recovery decreases and tends to zero. For these small area ratios, the loss due to contraction is high and little recovery is expected.

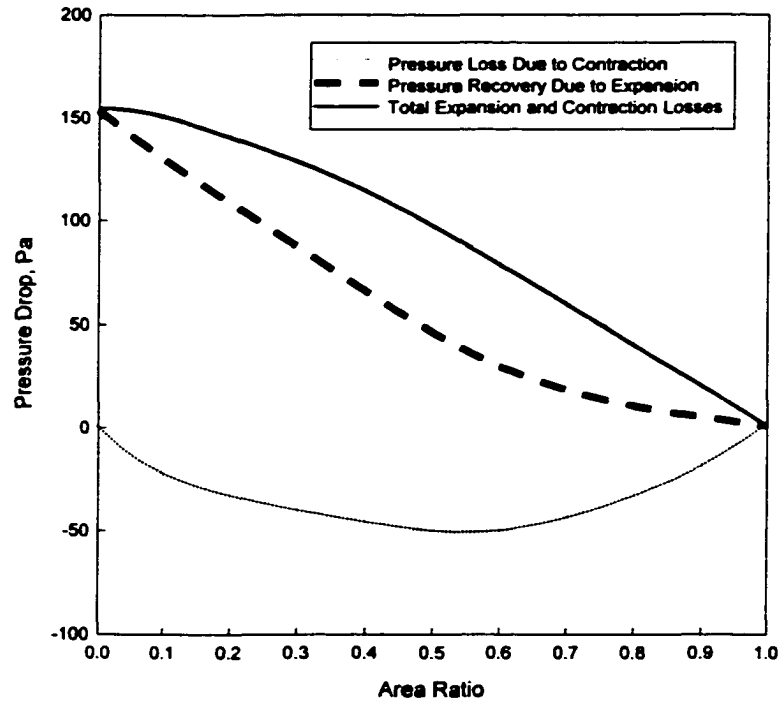


Figure 26. Expansion and Contraction Losses as a Function of the Area Ratio

For the C120 tube, the contraction loss coefficient is 0.28 and the expansion loss coefficient is 0.39. With a mass flow rate of 0.003611 kg/s, a tube area of $7.30 \times 10^{-6} \text{ m}^2$, and a header area of $1.91 \times 10^{-5} \text{ m}^2$, equation (27) yields velocities in the header and tube of 0.158 m/s and 0.414 m/s, respectively. Equations (26) and (28) yield a head loss of 28.66 Pa and 39.91 Pa for contraction and expansion, respectively. The pressure loss due to contraction determined

from equation 29 is 116.03 Pa. The pressure recovery determined from equation 30 is 47.46 Pa. Therefore, the net pressure loss due to expansion and contraction is the sum of these two values, 68.57 Pa. The area ratios and values of K_{con} and K_{exp} for all tubes tested in this study are provided in Table 11.

The frictional pressure drop is found by subtracting the minor losses due to expansion and contraction of the fluid from the measured pressure drop:

$$\Delta P_{frictional} = \Delta P_{measured} - \Delta P_{exp,con} \quad (31)$$

The measured differential pressure drop for the sub-cooled liquid is 652.7 Pa – hence the frictional pressure drop is equal to 584.17 Pa. The experimentally measured friction factor is given by

$$f_{exp} = 2 \frac{\Delta P_{frictional} D_{hyd} \rho_{test}}{G^2 L} \quad (32)$$

With a frictional pressure drop of 584.17 Pa, a hydraulic diameter of 3.05 mm, a density of 1195.1 kg/m³, a mass flux of 496.0 kg/m²-s, and a total length of 0.508 m, the experimentally measured friction factor is 0.034.

Table 11. Loss Coefficients for the Fluid Expansion and Contraction

Tube	Geometry	A_{header} mm²	A_{cs} mm²	K_{exp}	K_{con}
C193	Circle, Extruded	18.93	18.93	0	0
C120	Circle, Extruded	18.93	7.30	0.39	0.29
C60	Circle, Extruded	139.35	18.24	0.74	0.46
C30	Circle, Extruded	139.35	7.75	0.90	0.48
C20	Circle, Extruded	139.35	4.66	0.95	0.50
S30	Square, Extruded	139.35	9.87	0.88	0.48
B32	Barrel, Extruded	139.35	10.03	0.88	0.48
T33	Triangle, Extruded	139.35	13.42	0.80	0.48
N21	N Shape, Extruded	139.35	7.87	0.90	0.49
RK15	Rectangle, Extruded	139.35	4.07	0.95	0.50
W29 (I)	Triangle, Insert	139.35	12.28	0.82	0.48
W29 (II)	Triangle, Insert	139.35	12.28	0.82	0.48
ZL (I)	Circle, Extruded	139.35	7.75	0.90	0.49
ZL (2)	Circle, Extruded	139.35	7.75	0.90	0.49

The experimentally measured friction factor is compared with the Churchill (1977) correlation which is valid for laminar, turbulent, and transitional flow in round tubes:

$$\frac{f_{Churchill}}{8} = \left[\left(\frac{8}{Re_{test}} \right)^{12} + \left(\left[2.457 \ln \left(\frac{1}{\left[\frac{7}{Re_{test}} \right]^{0.9} + 0.27 \frac{\varepsilon}{D_{hyd}}} \right)} + \left[\frac{37530}{Re_{test}} \right]^{16} \right)^{-1.5} \right]^{\frac{1}{12}} \quad (33)$$

This correlation requires a value of the relative roughness of the tube. For laminar flow, the friction factor is independent of the relative roughness. For turbulent flow, it was necessary to estimate the value of the relative roughness. An estimate of the relative roughness was obtained by choosing a value that minimized the absolute error between the Churchill (1977) correlation and the measured friction factors in turbulent flow. The estimated value of the ε/D_{hyd} was then compared with the ε/D_{hyd} of commercially drawn tubing and commercial steel or wrought iron piping to check whether this estimate was reasonable. For the C120 tube, the ε/D_{hyd} value that minimized these errors was 0.0024, and yielded a theoretical friction factor of 0.038. The absolute error in this theoretical friction factor and the experimentally measured friction (0.034) factor is given by

$$\% Error = 100 \cdot \left(\frac{f_{measured} - f_{Churchill}}{f_{Churchill}} \right) = 10.5\% \quad (34)$$

For all single phase data taken on the C120 tube, the average absolute error in the experimentally measured friction factor is 8.78 %. A comparison of these friction factors as a function of Reynolds number is shown in Figure 27. Note that for the C120 tube, only the turbulent flow regime could be tested. The laminar flow case required flow rates that were too small to accurately obtain a system heat balance. A comparison of the measured ε/D_{hyd} versus that of commercially drawn tubing is shown in Figure 28 for all single-phase experiments (Fox and McDonald, 1992). It should be noted that ε/D_{hyd} data are typically available for $D > 25$ mm, and therefore the data from Fox and McDonald (1992) were extrapolated to the smaller tube diameters.

Another example of the single-phase pressure drops is shown in Figure 29 for the C30 tube. This figure compares the experimentally measured friction factor with both the Churchill (1977) friction factor in equation (33), and the friction factor for fully developed laminar flow (Incropera and Dewitt, 1996). The friction factor for fully developed laminar flow in a circular

tube which is given by:

$$f_{lam} = \frac{64}{Re_{test}} \quad (35)$$

For all laminar single-phase data taken on the C30 tube, the average absolute error in the experimentally measured friction factor was 8.34% (shown in Figure 29). The theoretically derived constants in equation (35) vary with port geometry, as shown in Table 12 (Incropera and Dewitt, 1996).

In total, 301 data points were taken for 12 different test sections to validate the tests and analysis procedures using single-phase pressure drops. Table 13 summarizes the average errors in the friction factor for both the laminar and turbulent flow cases and the relative roughness estimates determined from the experiments for the 12 test sections. These values of relative roughnesses are plotted against the relative roughnesses of commercially drawn tubing and commercial steel or wrought iron piping in Figure 28. These results show good agreement between theory and experiment, and validate the procedures. The complete set of graphs for the single-phase experiments is provided in Appendix D.

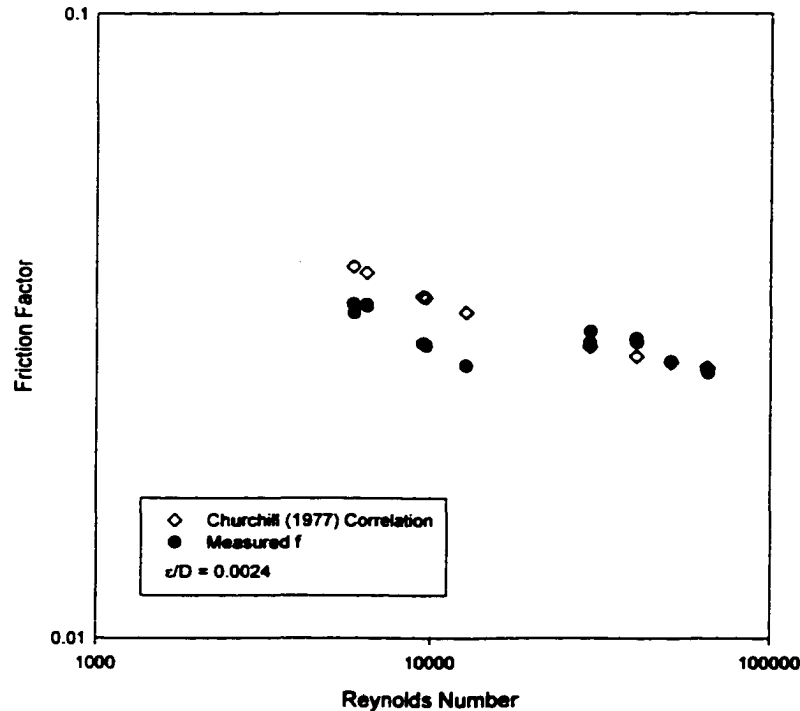


Figure 27. Experimental and Theoretical Single-Phase Friction Factors for Tube C120

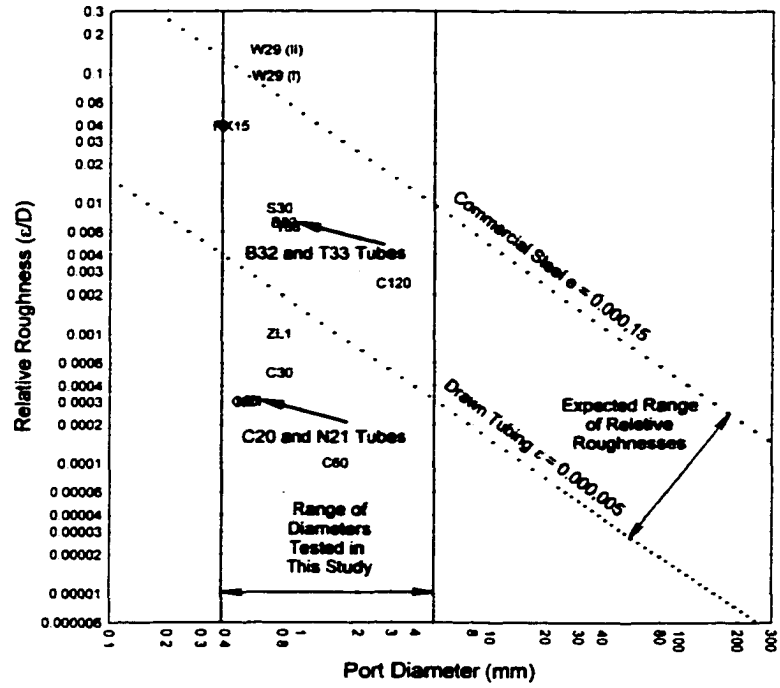


Figure 28. Relative Roughness Estimates for the Tubes Tested in Phase II of This Study

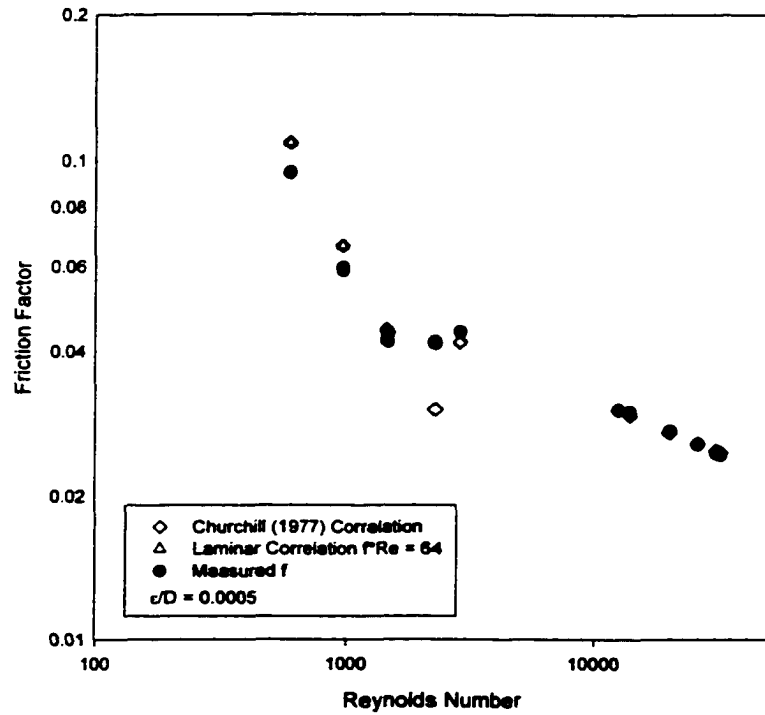


Figure 29. Experimental and Theoretical Single-Phase Friction Factors for Tube C30

Table 12. Laminar Flow Friction Factor Constants, $f \cdot Re = C$

Tube	Geometry	Constant
C120	Circle, Extruded	64
C60	Circle, Extruded	64
C30	Circle, Extruded	64
C20	Circle, Extruded	64
S30	Square, Extruded	57
B32	Barrel, Extruded	64 ^a
T33	Triangle, Extruded	53
N21	N Shape, Extruded	57 ^b
RK15	Rectangle, Extruded	69.4
W29 (I)	Triangle, Insert	53
W29 (II)	Triangle, Insert	53
ZL (I)	Circle, Extruded	64

^a approximated as a circle^b approximated as a square**Table 13.** Experimentally Derived Relative Roughness Estimates and Percent Errors in Single Phase Friction Factors

Tube	D_i (mm)	Geometry	$\epsilon/D_{h,rel}$ Estimate	$\epsilon/D_{h,rel}$ Expected Range	 Error % Lam./Turb.
C120	3.048	Circle, Extruded	0.0024	0.00048-0.016	---/8.78
C60	1.524	Circle, Extruded	0.0001	0.001-0.036	---/4.38
C30	0.761	Circle, Extruded	0.0005	0.002-0.062	9.47/3.85
C20	0.506	Circle, Extruded	0.0003	0.0028-0.09	8.43/3.85
S30	0.762	Square, Extruded	0.0009	0.002-0.062	9.50/3.00
B32	0.799	Barrel, Extruded	0.0070	0.002-0.06	7.46/6.81
T33	0.839	Triangle, Extruded	0.0065	0.002-0.06	14.60/5.63
N21	0.536	N Shape, Extruded	0.0030	0.0028-0.08	7.30/3.00
RK15	0.424	Rectangle, Extruded	0.0390	0.0039-0.12	8.10/6.60
W29(I)	0.732	Triangle, Insert	0.0950	0.0022-0.08	---/0.36
W29(II)	0.732	Triangle, Insert	0.1500	0.0022-0.08	---/1.93
ZL (I)	0.761	Circle, Extruded	0.0010	0.002-0.062	3.40/5.22

Two-Phase Pressure Drop

The experimentally measured two-phase pressure drops for all the tubes investigated in this phase of the study are presented in this section. The two-phase pressure drops of R-134a were measured at five mass fluxes corresponding to 150, 300, 450, 600 and 750 kg/m²-s and for qualities ranging from $x = 0.05$ to $x = 0.95$. The fluctuations in the pressure drop curves are due to variations in the mass flux from these nominal values. In total, 800 data points were taken for two-phase pressure drop in microchannel geometries. For tubes C30, S30, and W29(I), both adiabatic and condensing two-phase pressure drops were measured. Since the difference between them was so small (as will be shown later), all subsequent tests on the microchannel geometries were taken during condensation.

Circular Tube C193

Adiabatic pressure drop data for the C193 ($D_h = 4.91$ mm, $L = 0.6604$ m) round tube for all five mass flux cases are shown in Figure 30. The C193 tube contained a single port and was manufactured from stainless steel. Three independent differential pressure transducers were used to measure the two-phase refrigerant pressure drop with the following ranges:

- Transducer 1 $0.0 \text{ Pa} \leq \Delta P \leq 6,219 \text{ Pa}$
- Transducer 2 $0.0 \text{ Pa} \leq \Delta P \leq 62,190 \text{ Pa}$
- Transducer 3 $0.0 \text{ Pa} \leq \Delta P \leq 248,211 \text{ Pa}$

Figure 31 shows the differences in the three pressure transducer readings for the C193 tube at a mass flux of $G = 300$ kg/m²-s. The differences in the readings are due to the inaccuracies of transducer 2 and 3 at the extreme low end of the scale. A differential pressure measurement of 150 Pa represents only 0.06% of scale for pressure transducer 3 and 0.24% of scale of pressure transducer 2. At the $G = 600$ kg/m²-s mass flux case, the differences in the pressure transducer readings were very small due to the larger pressure drops at this mass flux as shown in Figure 32. Pressure transducer 1 was not used at these higher differential pressures because the differential pressure was close to the maximum value of transducer 1. For each data point, the pressure drop recorded by the transducer with a range that corresponded most closely to the actual ΔP was chosen for the analysis. As expected, Figure 30 shows that the two-phase pressure drop increases with mass flux, and, for a given mass flux, it reaches a maximum value at a quality of 0.80. Beyond a quality of 0.80, the two-phase pressure drop decreases and approaches the single (gas) phase pressure drop value.

Circular Tube C120

The adiabatic pressure drop data taken on the C120 stainless steel, single port ($D_h = 3.048$ mm, $L = 0.508$ m) round tube for four mass flux cases are shown in Figure 33. The mass flux case of $G = 150$ kg/m²-s represented an extremely low refrigerant flow rate that resulted in

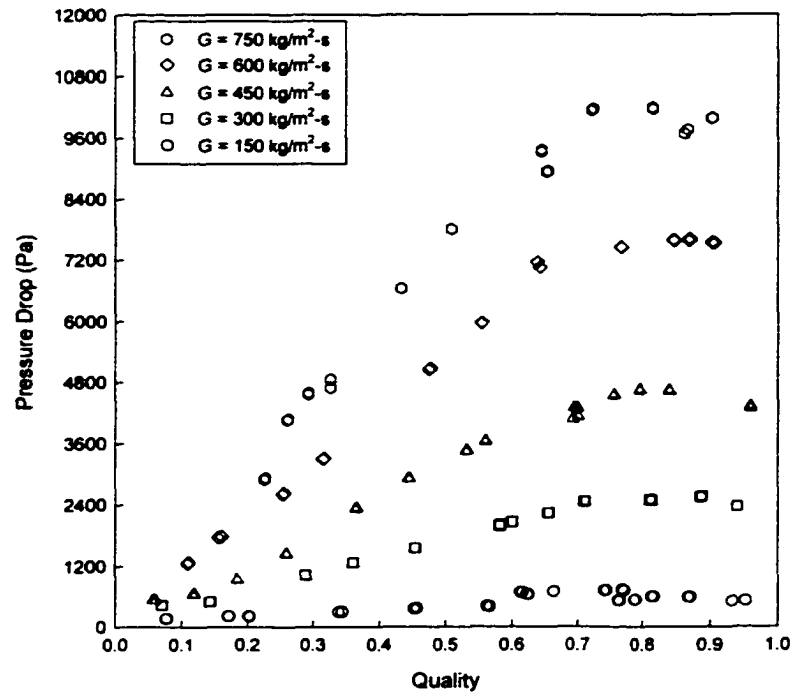


Figure 30. Total Measured Pressure Drop for Tube C193 ($D_b = 4.91$ mm)

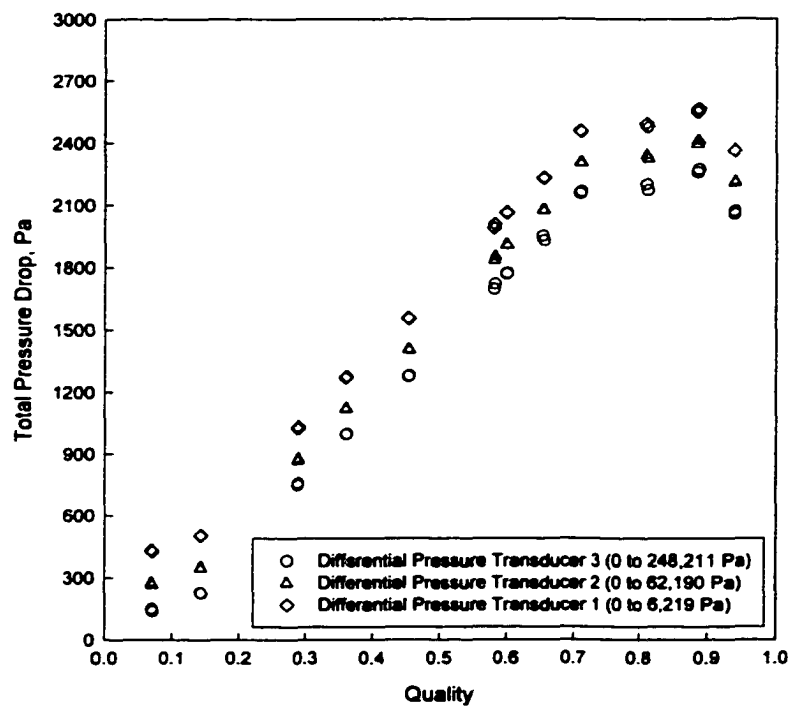


Figure 31. Differential Pressure Transducer Measurements (Tube C193, $G = 300$ kg/m²-s)

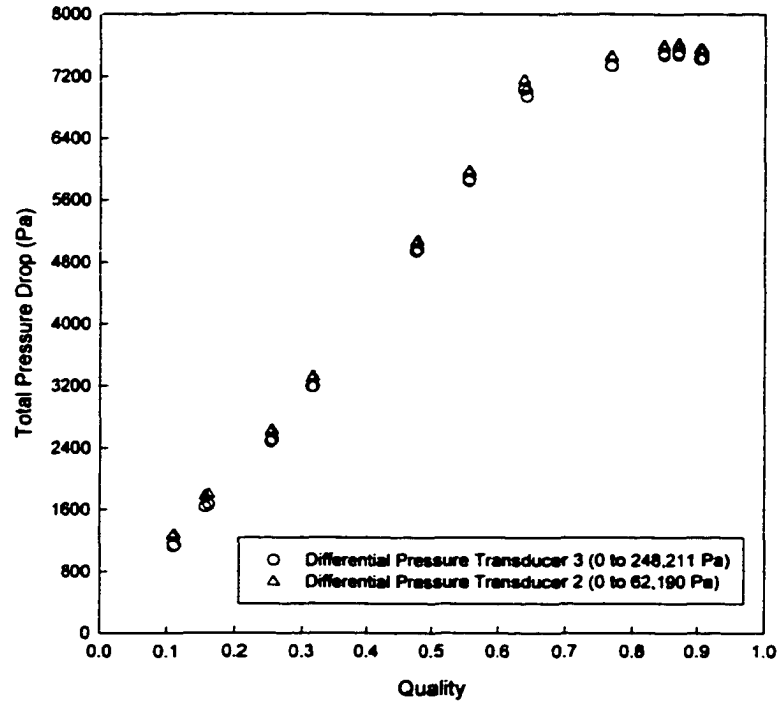


Figure 32. Differential Pressure Transducer Measurements (Tube C193, $G = 600 \text{ kg/m}^2\text{-s}$)

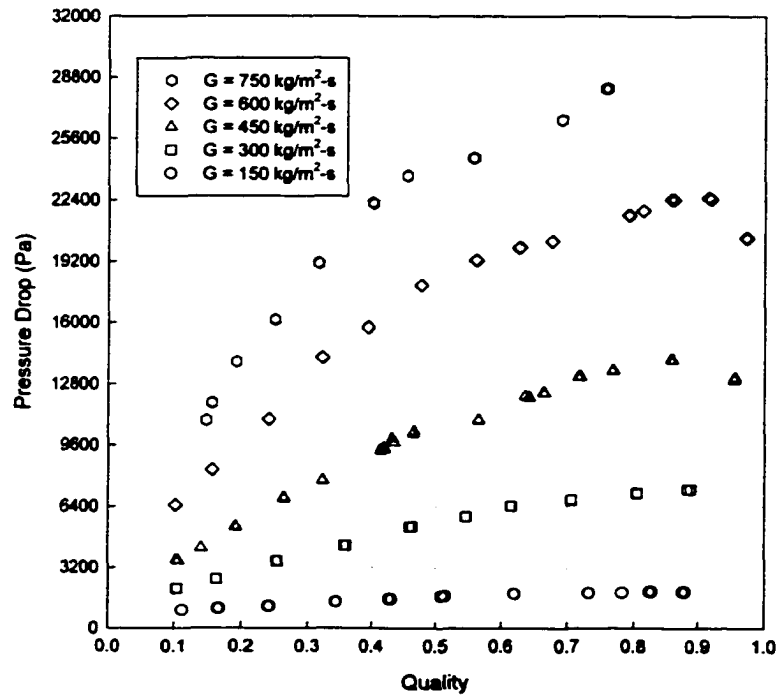


Figure 33. Total Measured Pressure Drop for Tube C120 ($D_h = 3.048 \text{ mm}$)

flux case of $G = 150 \text{ kg/m}^2\text{-s}$ represented an extremely low refrigerant flow rate that resulted in unacceptable inaccuracies on the pre- and post-condenser heat balances. Figure 34 shows the differences in the pressure transducer readings for the $G = 450 \text{ kg/m}^2\text{-s}$ mass flux case. In this figure, the differences in the readings are small due to the larger differential pressure measurements. Pressure transducer 1 was not used above qualities of 0.50 because the differential pressure was close to the maximum value for this transducer. Figure 33 shows that the two-phase pressure drop, at a given mass flux, increases with quality until it reaches a maximum value near a quality of 0.85. Beyond $x = 0.85$, the two-phase pressure drop decreases and approaches the single-phase value.

Circular Tube C60

Pressure drop data for the C60 ($D_h = 1.524 \text{ mm}$, $L = 0.508 \text{ m}$) tube taken during condensation are shown in Figure 35 for all five mass flux cases. The C60 tube was manufactured from extruded aluminum and consisted of 10 ports in parallel. Figure 36 shows minimal differences in the pressure transducer readings for the $G = 450 \text{ kg/m}^2\text{-s}$ mass flux case. Pressure transducer 1 was not used above qualities of 0.20. Figure 35 illustrates that the two-phase pressure drop reaches a maximum value near a quality of 0.90, which is approximately the same quality at which tube C193 shows a maxima.

Circular Tube C30

Tube C30 ($D_h = 0.761 \text{ mm}$, $L = 0.508 \text{ m}$) was manufactured from extruded aluminum and consisted of 17 ports in parallel. Both adiabatic and condensing pressure drops were taken for this tube. The adiabatic pressure drop data are shown in Figure 37 and condensing pressure drop data are shown in Figure 38. In both cases, the mass flux corresponding to $G = 150 \text{ kg/m}^2\text{-s}$ resulted in heat duties on the pre- and post-condensers that were too small to measure accurately. Figure 37 illustrates that the maximum value of the two-phase pressure drop at a given mass flux increases with the quality and reaches a maximum value at a quality of 0.95, and this local maximum is shifted slightly to the right from that found in the C60 tube.

Circular Tube C20

The C20 tube ($D_h = 0.506 \text{ mm}$, $L = 0.508 \text{ m}$) was manufactured from extruded aluminum and consisted of 23 ports in parallel. Condensing pressure drops for this tube are shown in Figure 39. The mass fluxes corresponding to $G = 150 \text{ kg/m}^2\text{-s}$ and $G = 300 \text{ kg/m}^2\text{-s}$ resulted in heat duties on the pre- and post-condensers that were too small to measure accurately. Figure 39 illustrates that the two-phase pressure drop increases with increasing quality. The fluctuations in the total measured two-phase pressure drop are due to the variations in the total mass flux – especially for the high mass flux case. The two-phase differential pressures were quite high in this test section (due to the small hydraulic diameter), and with such large two-

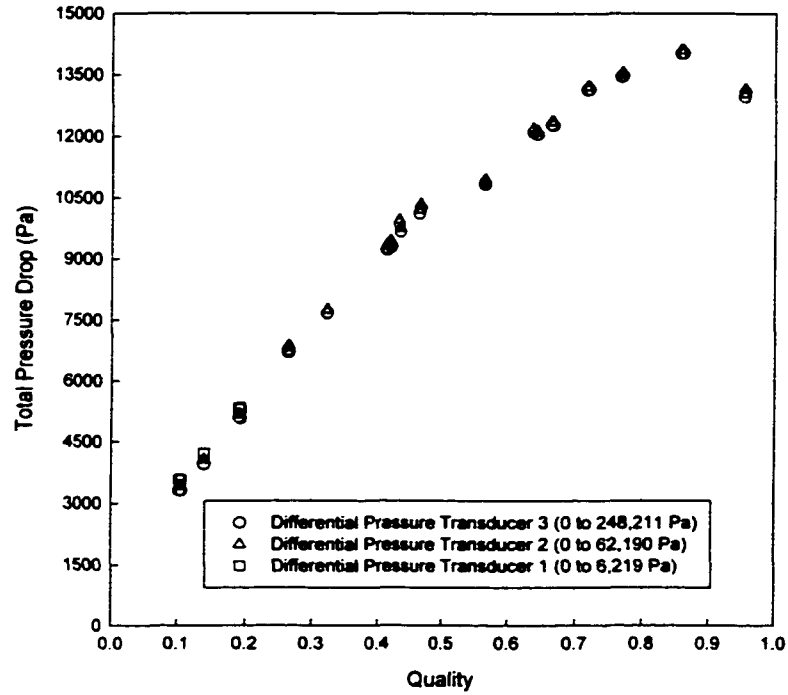


Figure 34. Differential Pressure Transducer Measurements (Tube C120, $G = 450 \text{ kg/m}^2\text{-s}$)

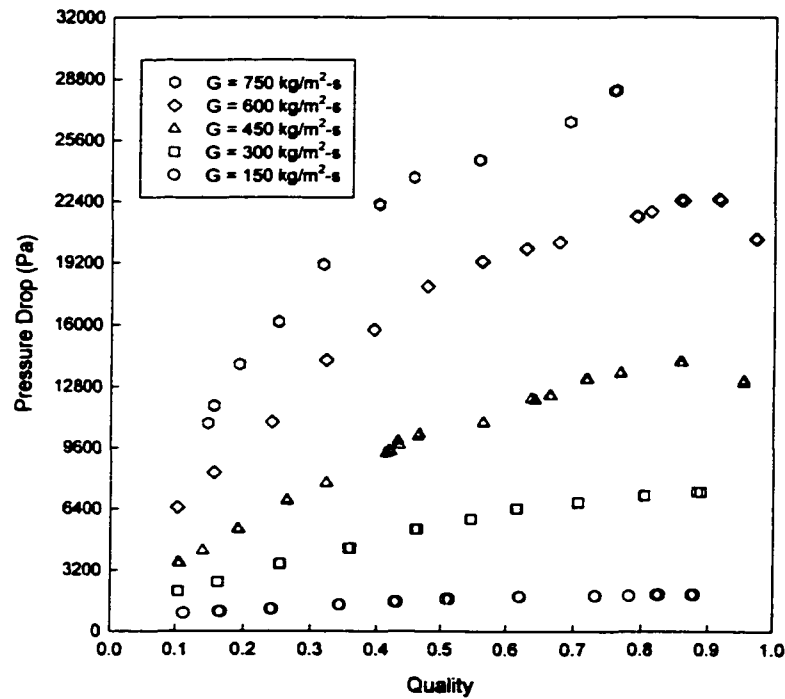


Figure 35. Total Measured Pressure Drop for Tube C60 ($D_h = 1.524 \text{ mm}$)

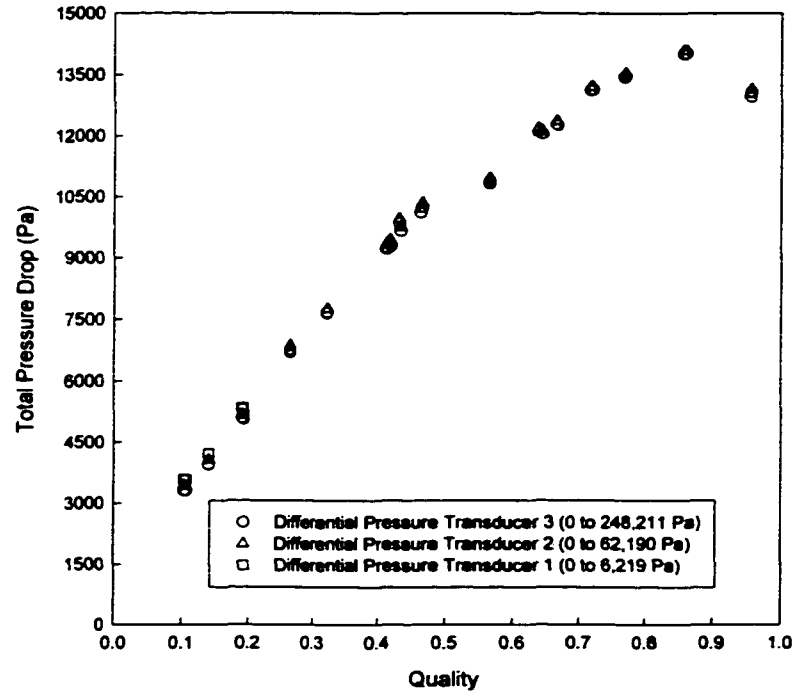


Figure 36. Differential Pressure Transducer Measurements (Tube C60, $G = 450 \text{ kg/m}^2\text{-s}$)

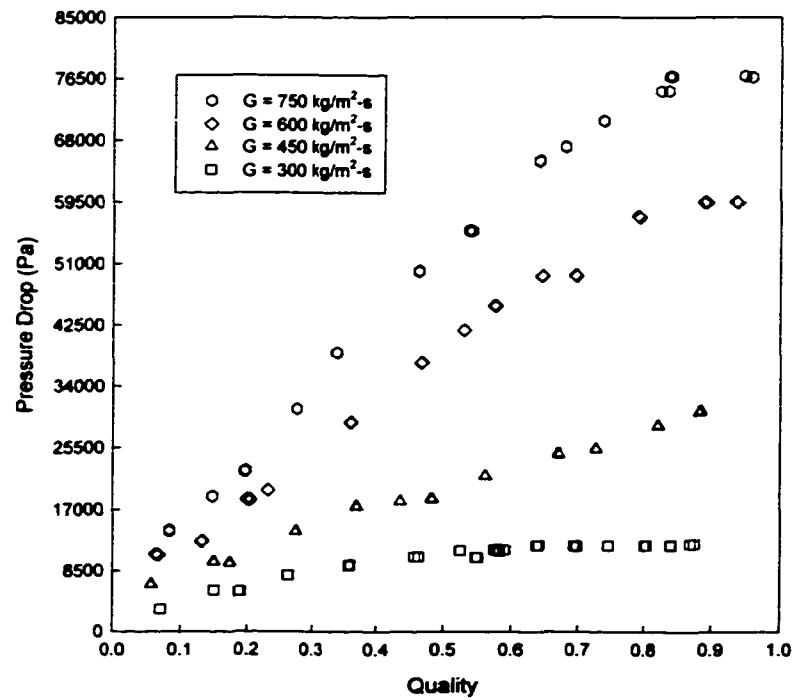


Figure 37. Total Adiabatic Measured Pressure Drop for Tube C30 ($D_h = 0.761 \text{ mm}$)

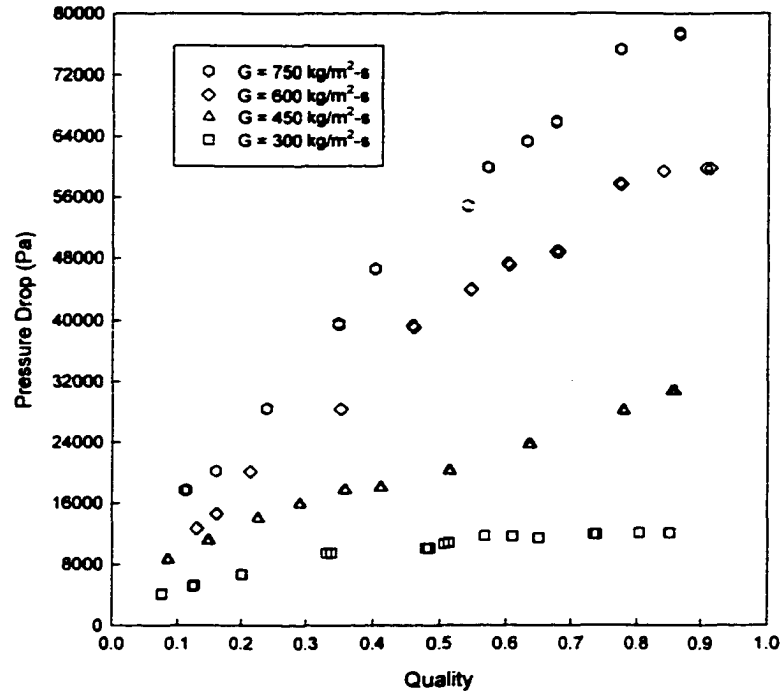


Figure 38. Total Condensing Measured Pressure Drop for Tube C30 ($D_h = 0.761$ mm)

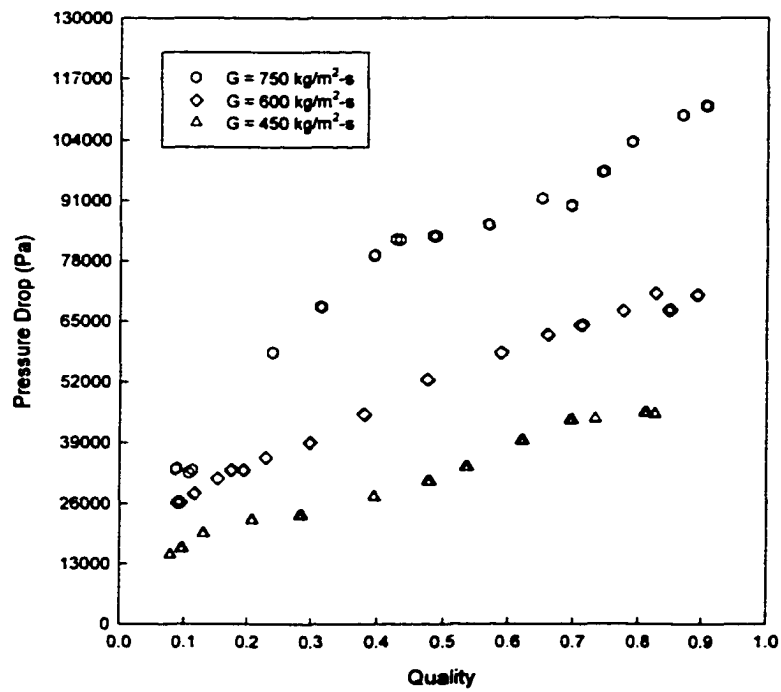


Figure 39. Total Condensing Measured Pressure Drop for Tube C20 ($D_h = 0.506$ mm)

phase pressure drops across the test section, it was not possible to maintain a constant value of the mass flux for all data points. Figure 39 shows that the two-phase pressure drop does not show the local maximum that was seen in the larger hydraulic diameter test sections. This local maximum moved to a higher quality as the test section hydraulic diameter decreases, until in the C20, the local maximum was not seen for the qualities tested.

Square Tube S30

The square S30 tube ($D_h = 0.762$ mm, $L = 0.508$ m) was manufactured from extruded aluminum and consisted of 17 square ports in parallel. Adiabatic and condensing pressure drops for this tube are shown in Figures 40 and 41, respectively. For this tube, all five mass fluxes were attainable. Similar to tube C30, the two-phase pressure drop data show a local maximum near a quality of $x = 0.9$. At the highest mass flux, the highest attainable quality was 0.83 due to cooling water flow limitations on the two-phase test facility. Furthermore, at the lowest mass flux, qualities greater than 0.85 required pre-condenser water flow rates that were too small to accurately measure.

Barrel Shaped Tube B32

The “barrel” shaped B32 tube ($D_h = 0.799$ mm, $L = 0.508$ m) was manufactured from extruded aluminum and consisted of 14 “barrel”-shaped ports in parallel. Condensing pressure

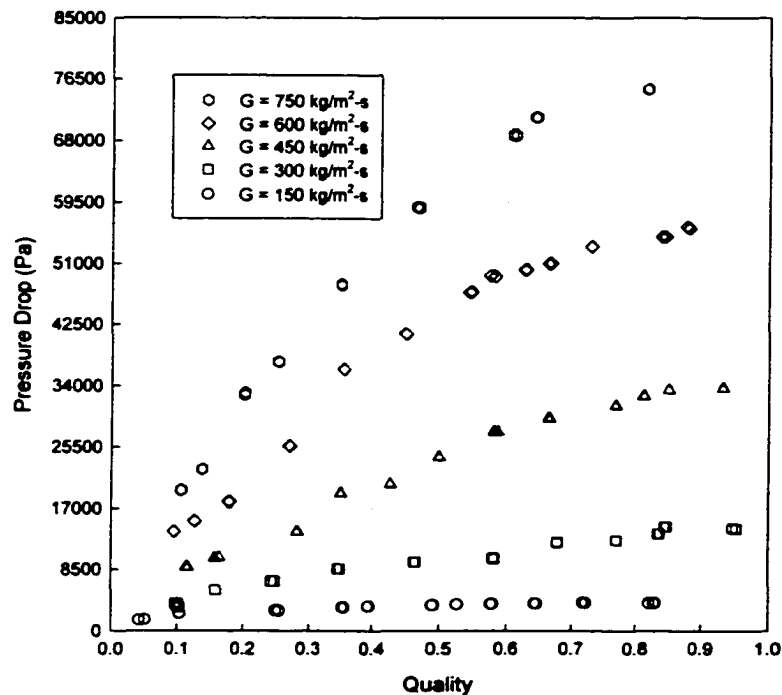


Figure 40. Total Adiabatic Measured Pressure Drop for Tube S30 ($D_h = 0.762$ mm)

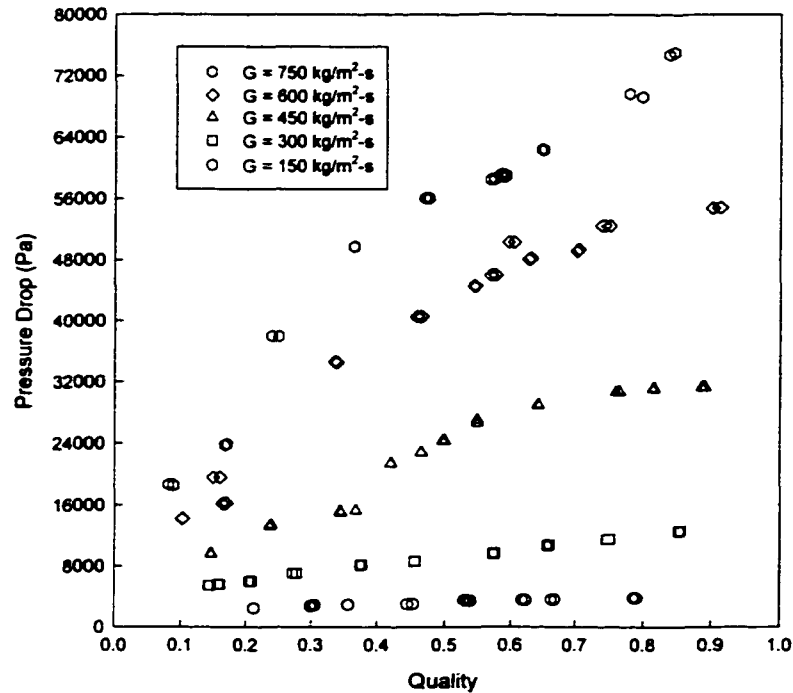


Figure 41. Total Condensing Measured Pressure Drop for Tube S30 ($D_h = 0.762$ mm)

drops for this tube for all five mass flux cases and for qualities ranging from 0.05 to 0.95 are shown in Figure 42. The two-phase pressure drop attains a maximum value around a quality of 0.90, and only a slight decrease is seen beyond this quality.

Triangular Tube T33

The triangular T33 tube ($D_h = 0.839$ mm, $L = 0.508$ m) was manufactured from extruded aluminum and consisted of 19 triangular shaped ports in parallel. Condensing pressure drops for this tube are shown in Figure 43. All five mass fluxes were attainable. At the highest mass flux, two-phase pressure drops beyond a quality of 0.83 could not be accomplished due to limitations on the amount of available cooling water on the post-condenser. Furthermore, at the lowest mass flux case, qualities greater than 0.75 required pre-condenser water flow rates that were too small to accurately measure.

"N" Shaped Tube N21

The "N"-shaped N21 tube ($D_h = 0.536$ mm, $L = 0.508$ m) was manufactured from extruded aluminum and consisted of 19 "N"-shaped ports in parallel. Condensing pressure drops for this tube are shown in Figure 44. For this tube, four of the five mass fluxes were attainable due to the relatively small available free flow area and hydraulic diameter. The two-phase pressure drops show a maximum value occurring near a quality of 0.90. In this tube, the two-

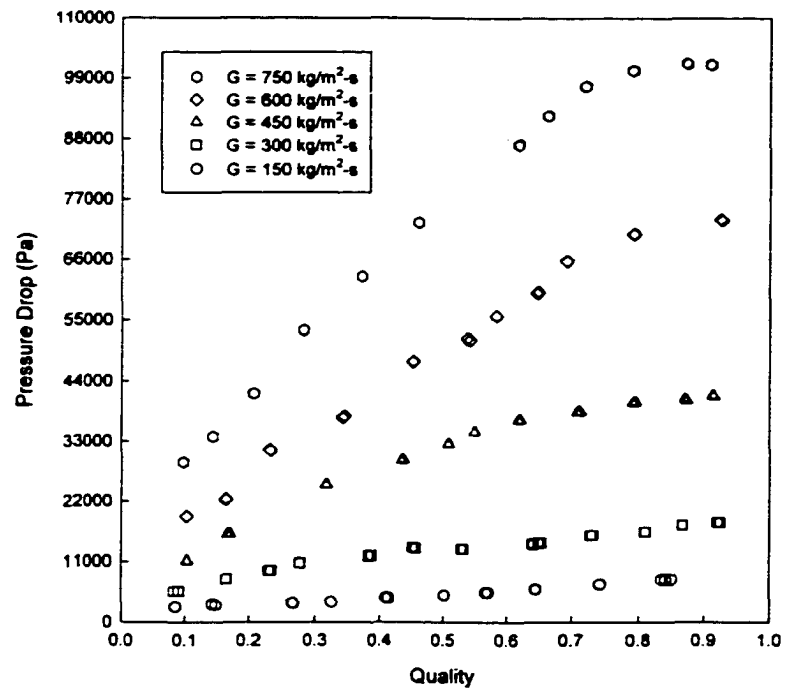


Figure 42. Total Condensing Measured Pressure Drop for Tube B32 ($D_h = 0.799$ mm)

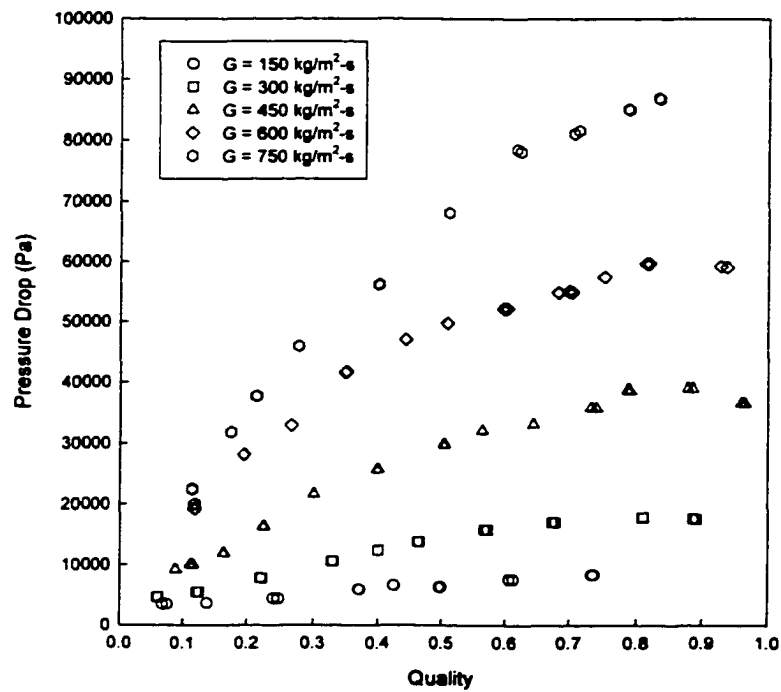


Figure 43. Total Condensing Measured Pressure Drop for Tube T33 ($D_h = 0.839$ mm)

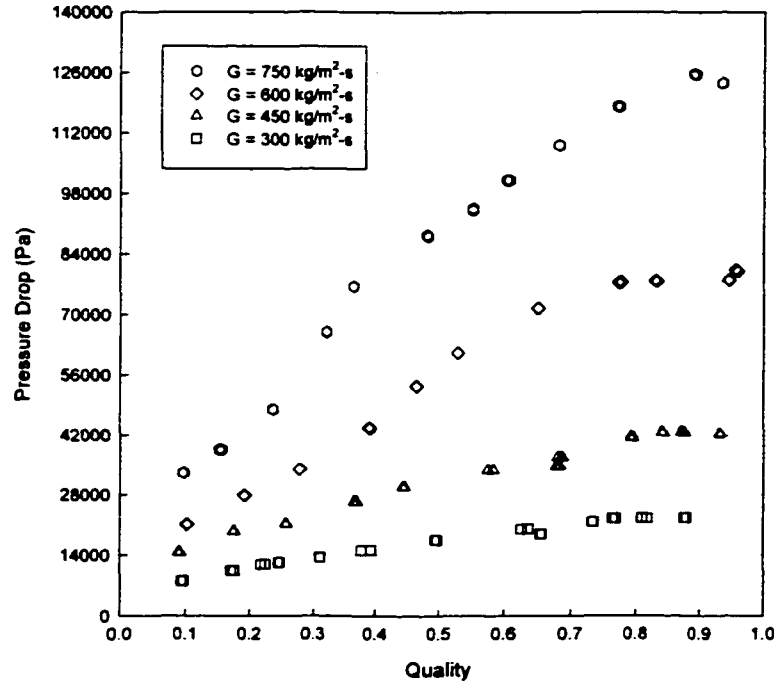


Figure 44. Total Condensing Measured Pressure Drop for Tube N21 ($D_h = 0.536$ mm)

phase pressure drops were much higher than those in other tubes and a constant mass flux was difficult to maintain.

Rectangular Tube RK15

The rectangular shaped RK15 tube ($D_h = 0.424$ mm, $L = 0.508$ m) was manufactured from extruded aluminum and consisted of 20 rectangular ports in parallel. Condensing pressure drops for this tube are shown in Figure 45. Due to the small hydraulic diameter and available free flow area, heat balances were attainable on only three mass fluxes. Furthermore, this test section had the smallest available free flow area of all the test sections, and, as expected, the two-phase pressure drops were the highest of all the extruded tubes. Due to the higher pressure drops, it was more difficult to maintain a constant mass flux and this manifests itself as variations in the two-phase pressure drop curves.

Triangular Insert Tube W29 (I and II)

The triangular W29 tubes ($D_h = 0.732$ mm, $L = 0.508$ m) were manufactured from a rectangular aluminum shell with a corrugated brazed insert that was used to form the triangular ports. Two separate test sections were constructed to ensure repeatability of the data for this tube, which was the only one in the matrix with an insert. These condenser tubes consisted of 19 triangular ports in parallel. Condensing pressure drop data for these tubes are shown in Figures 46 and 47. The two-phase pressure drops for the insert tubes were much higher than

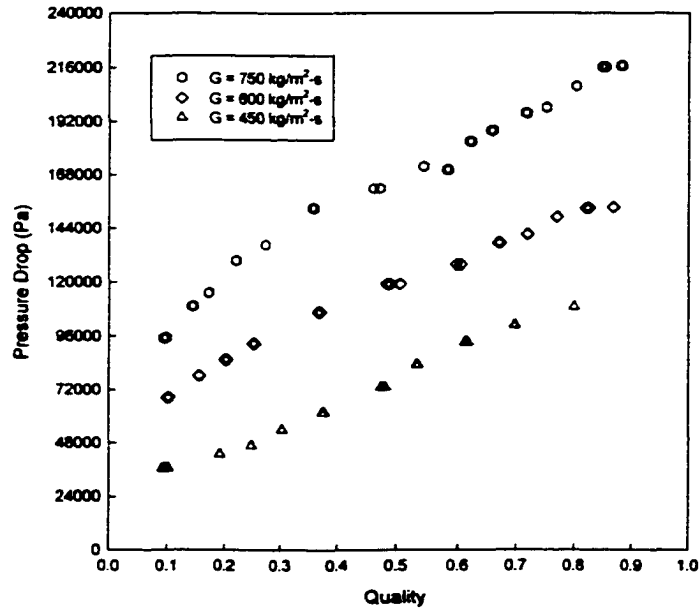


Figure 45. Total Condensing Measured Pressure Drop for Tube RK15 ($D_h = 0.424$ mm)

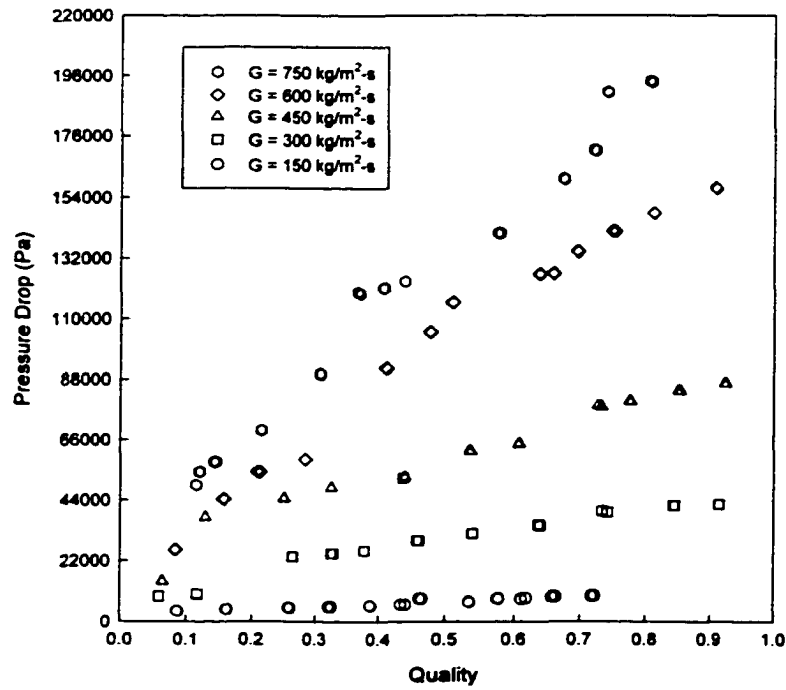


Figure 46. Total Condensing Measured Pressure Drop for Tube W29I ($D_h = 0.732$ mm)

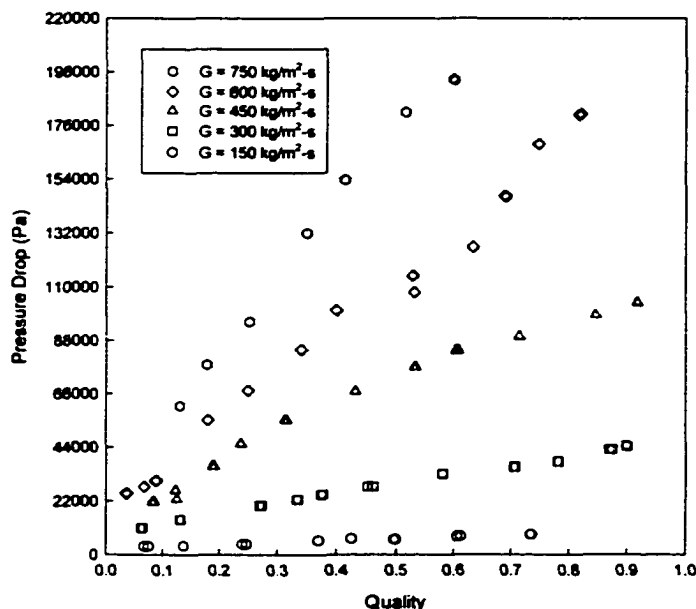


Figure 47. Total Condensing Measured Pressure Drop for Tube W29II ($D_h = 0.732$ m)

those for an extruded tube. Due to the high pressure drops, it was increasingly more difficult to set and maintain a constant total mass flux. As a result, large variations in the total mass flux occurred, especially in the higher mass flux case. Furthermore, it should be noted that the experimentally determined relative roughnesses of the two insert tubes were different, and the insert tube with the higher relative roughness exhibited higher two-phase pressure drops.

“Zero Length” Circular Tubes ZLI and ZLII

The ZL circular tubes ($D_h = 0.761$ mm, $L = 0.2032$ m [ZLI], 0.022 m [ZLII]) were manufactured from an extruded aluminum tube. Two separate test sections were constructed to test the two-phase pressure drops with a near “zero” length of test section. Both of these test sections used the C30 tubes. The ZLI tube consisted of 17 channels in parallel, while the ZLII test section consisted of 6 tubes in parallel (the others being inadvertently blocked during fabrication). The total lengths of the ZLI and ZLII test sections were 0.2032 m and 0.022 m, respectively. Adiabatic pressure drop measurements were taken on both of the test sections with the objective of estimating the contraction and expansion losses better. Two-phase contraction and expansion losses are described in the following section. These data are shown in Figures 48 and 49, respectively. For the ZLI test section consisting of 17 channels, the mass flux case of $G = 150$ kg/m²-s corresponded to a flow rate that was too low to obtain accurate heat balances.

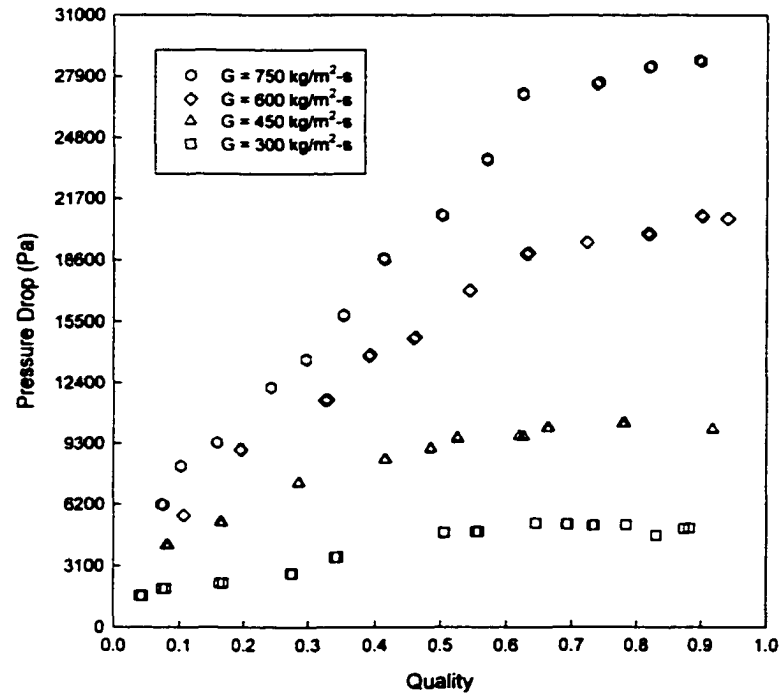


Figure 48. Total Adiabatic Measured Pressure Drop for Tube ZLI ($D_h = 0.761$ mm)

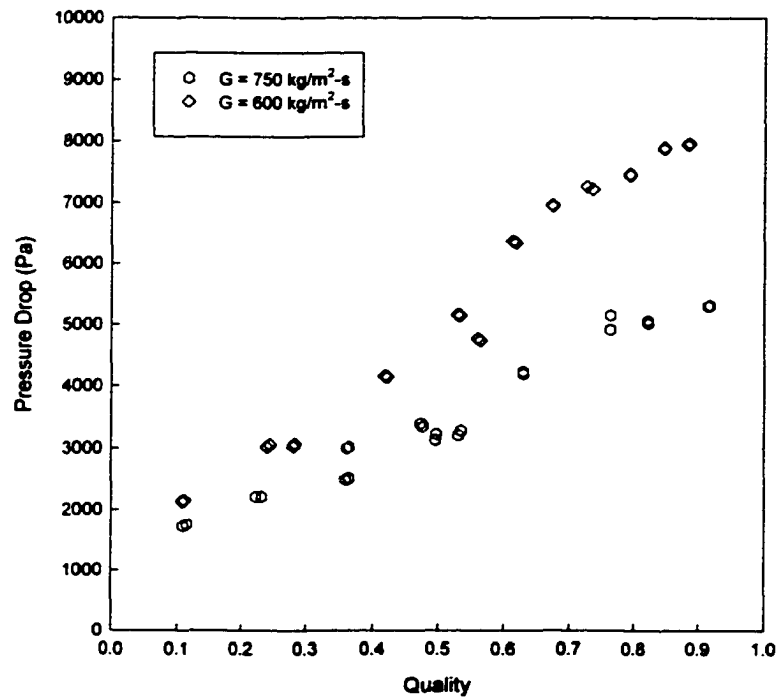


Figure 49. Total Adiabatic Measured Pressure Drop for Tube ZLII ($D_h = 0.761$ mm)

Furthermore, for the ZLII test section, only the 750 kg/m²-s and 600 kg/m²-s mass flux cases could be tested. Also, for the ZLII tube, it was difficult to precisely control the mass flow rate and, therefore, the mass flux.

Expansion, Contraction, and Deceleration Losses

The two-phase pressure drop in a microchannel geometry is the sum of several components. This includes the pressure drop due to friction, deceleration, and expansion and contraction in the headers. This can be expressed as

$$\Delta P_{total} = P_1 - P_2 = \Delta P_{frictional} + \Delta P_{deceleration} + \Delta P_{exp\&con} \quad (36)$$

A comparison of the adiabatic and condensing pressure drop measurements provides an estimate of the contribution of the decelerational component to the total pressure drop. Similarly, a comparison of the pressure drop measurements using test sections of different lengths provides an estimate of the contribution of expansion and contraction to the total pressure drop. These experimental estimates of the various pressure drop components can also be compared with corresponding models from the literature. Once the individual contributions to the total pressure drop are delineated, frictional pressure drops can be interpreted and correlated.

The Decelerational Component

It should be noted that there is a deceleration component in the total pressure drop in both the adiabatic and condensing flow cases. This is because, even at the *same enthalpy* (adiabatic case), the quality at the outlet pressure is different from the quality at the inlet pressure, particularly for the high pressure drop cases. From the separated flow model, the pressure drop due to acceleration/deceleration is given by (Carey, 1992):

$$-\left(\frac{dP}{dz}\right)_{acceleration} = \frac{d}{dz} \left[\frac{G^2 x^2}{\rho_v \alpha} + \frac{G^2 (1-x)^2}{\rho_l (1-\alpha)} \right] \quad (37)$$

Using the measured values of quality (x) at the inlet and exit of the test section, equation (37) can be integrated along the direction of the tube length ($z = 0$ to $z = L_{tube}$). This yields:

$$\Delta P_{acceleration} = \left[\frac{G^2 x^2}{\rho_v \alpha} + \frac{G^2 (1-x)^2}{\rho_l (1-\alpha)} \right]_{x=x_{out}} - \left[\frac{G^2 x^2}{\rho_v \alpha} + \frac{G^2 (1-x)^2}{\rho_l (1-\alpha)} \right]_{x=x_{in}} \quad (38)$$

Equation (38) requires a knowledge of the void fraction (α), and several models and correlations that estimate the void fraction are available in the literature. These include the homogeneous model (Carey, 1992), and models by Lockhart and Martinelli (1949), Zivi (1964), Wallis (1965), Thom (1964), and Baroczy (1965). These correlations are of the form:

$$\alpha = \left[1 + B_B \left(\frac{1-x}{x} \right)^{a_1} \left(\frac{\rho_g}{\rho_l} \right)^{a_2} \left(\frac{\mu_l}{\mu_g} \right)^{a_3} \right]^{-1} \quad (39)$$

where B_B , a_1 , a_2 , and a_3 are constants corresponding to different models and correlations. These constants are provided in Table 14. Of these models, the Baroczy (1965) correlation has been shown to yield good agreement with experimental data for a wide range of conditions (Carey, 1992) and was therefore used here. With this void fraction model, equation (38) was used to calculate the decelerational component of the pressure drop for the adiabatic and condensing tests. The net difference between these two values yields the pressure drop that can be attributed to heat removal in the condensation process. In this example, the adiabatic case, for $G = 446.8 \text{ kg/m}^2\text{-s}$, $x_{\text{test, in}} = 0.439$, and $x_{\text{test, out}} = 0.435$, the void fraction was calculated to be 0.775. Similarly, for the condensing case, with $G = 446.3 \text{ kg/m}^2\text{-s}$, $x_{\text{test, in}} = 0.441$, and $x_{\text{test, out}} = 0.390$, the void fraction was 0.760. Using these values, the deceleration pressure drop components were 98.9 Pa and 2.04 Pa for the adiabatic and condensing cases, respectively. The difference between these values is 96.76 Pa, which is a very small fraction of the total measured pressure drop in either case, 18175 Pa (0.53%) and 20133 Pa (0.48%).

Adiabatic and condensing pressure drop measurements were taken for three different geometries including a circular (C30), square (S30), and triangular insert (W29) geometry. Each one of these tests corroborates the extremely small contribution of the deceleration component that was predicted above using correlations from the literature. This is illustrated graphically in Figure 50 for tube C30 at a nominal mass flux of $G = 450 \text{ kg/m}^2\text{-s}$. A line break in the graph is used to amplify the deceleration contributions. Without this line break, the difference is negligible compared to the total pressure drop, as shown in Figure 50. Figures 51-53 show the decelerational pressure drop in relation to the total pressure drop for the remaining three mass flux cases for tube C30. These figures illustrate the fact that the contributions due to deceleration/acceleration are small when compared to the total pressure drop. Similar results were found for the square and triangular geometries. Comparisons of the adiabatic and condensing pressure drops for the square and triangular tubes are provided in Appendix E.

Expansion and Contraction Pressure Drop

In this section, the theoretical expansion and contraction pressure drops are estimated and also compared with data obtained from test sections of different lengths. The pressure loss due to the expansion and contraction of a two-phase fluid may be estimated using the separated and homogeneous flow models, respectively (Hewitt et al. 1993). For a sudden enlargement (exit effects), the pressure drop is given by (Hewitt et al., 1993):

$$\Delta P_{\text{exp}} = \frac{G^2 \beta (1 - \beta) \Psi_S}{\rho_L} \quad (40)$$

where β is the area ratio (A_t/A_{header}) and Ψ_S , the separated flow multiplier, is given by

$$\Psi_S = \left[1 + \left(\frac{\rho_L}{\rho_G} - 1 \right) \left(\frac{x}{4} (1 - x) + x^2 \right) \right] \quad (41)$$

Using the data provided in Table 4, with a mass flux of $446.25 \text{ kg/m}^2\text{-s}$, an area ratio of 0.059, an average quality of 0.41, and liquid and vapor densities of 1081.71 kg/m^3 and 73.71 kg/m^3 , respectively, the separated flow multiplier given in equation (41) is 4.04, which yields a pressure recovery due to expansion of 42.53 Pa.

Table 14. Constants for the Void Fraction Models

Model or Correlation	B_B	a_1	a_2	a_3
Homogeneous (Carey, 1992)	1	1	1	0
Lockhart-Martinelli (1949)	0.28	0.64	0.36	0.07
Zivi (1964)	1	1	0.67	0
Wallis (1965)	1	0.72	0.4	0.08
Thom (1964)	1	1	0.89	0.18
Baroczy (1965)	1	0.74	0.65	0.13

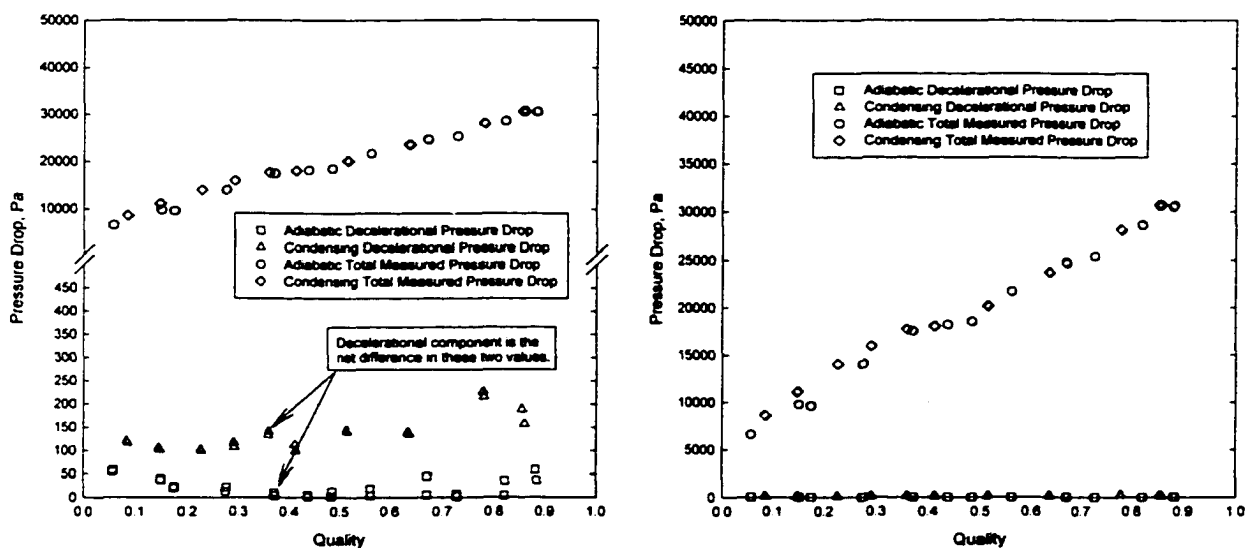


Figure 50. Decelerational Pressure Drop (Tube C30, $G = 450 \text{ kg/m}^2\text{-s}$)

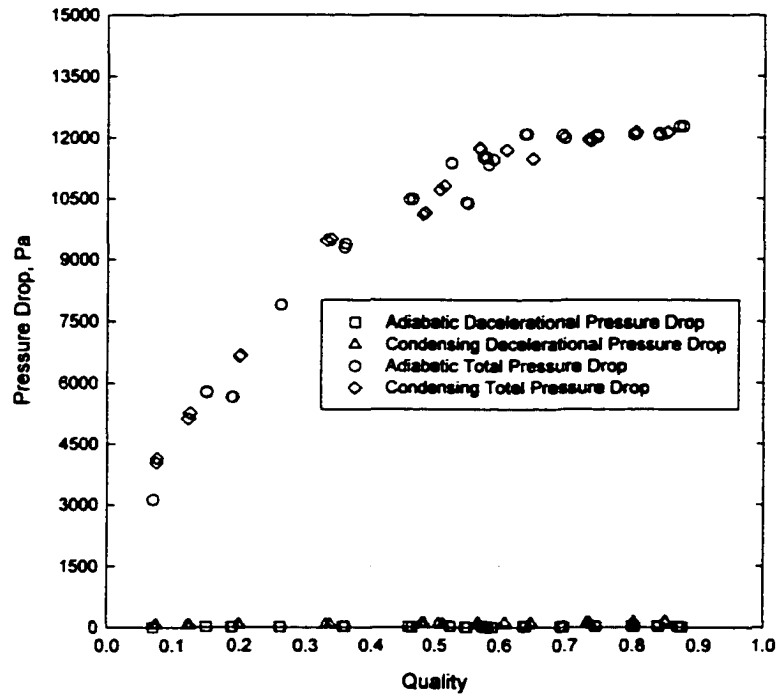


Figure 51. Decelerational Pressure Drop (Tube C30, $G = 300 \text{ kg/m}^2\text{-s}$)

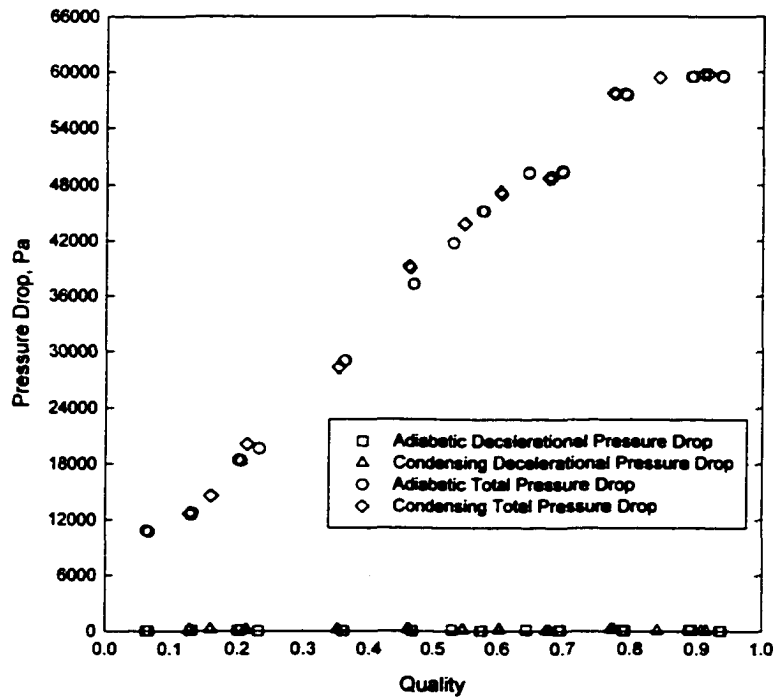


Figure 52. Decelerational Pressure Drop (Tube C30, $G = 600 \text{ kg/m}^2\text{-s}$)

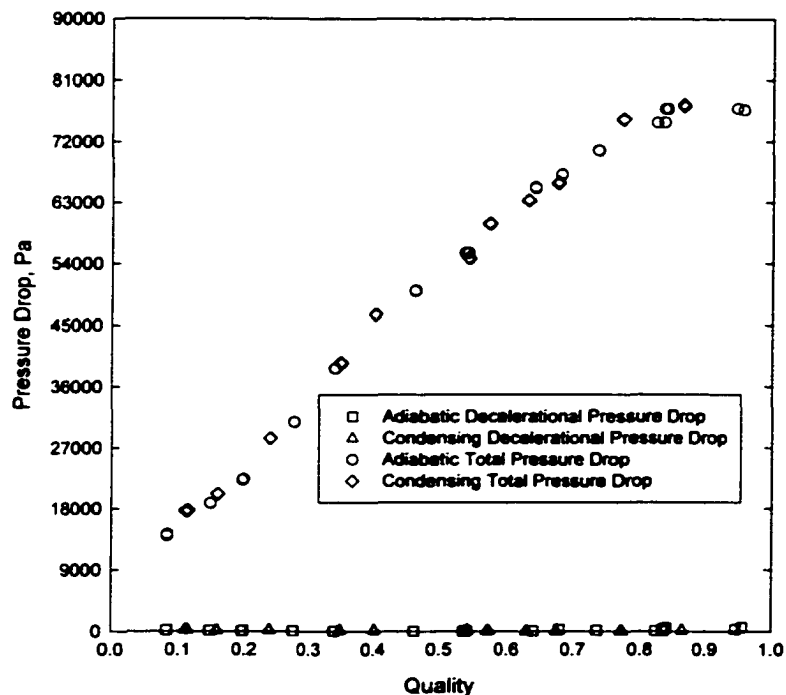


Figure 53. Decelerational Pressure Drop (Tube C30, $G = 750 \text{ kg/m}^2\text{-s}$)

The estimated pressure drop due to a sudden contraction (entrance effect) is given by

$$\Delta P_{con} = \frac{G^2}{2\rho_L} \left[\left(\frac{1}{C_C} - 1 \right)^2 + 1 - \frac{1}{\gamma^2} \right] \Psi_H \quad (42)$$

where γ is the area ratio (A_{headcr}/A_v), and C_C is a constant given by

$$C_C = \frac{1}{0.639 \left(1 - \frac{1}{\gamma} \right)^{0.5} + 1} \quad (43)$$

The homogeneous flow multiplier, Ψ_H , is given by

$$\Psi_H = 1 + x \left(\frac{\rho_L}{\rho_G} - 1 \right) \quad (44)$$

For this example, $\gamma = 16.96$ and $C_C = 0.62$. The homogeneous multiplier given in equation (44) is 6.65. The pressure drop due to contraction is 845.09 Pa. The net loss due to expansion and contraction is the difference between these two values and is equal to 802.56 Pa. In this example,

the total measured pressure drop is 18175 Pa. This implies that the pressure drop contribution due to the expansion and contraction of the fluid is less than 5% of the total measured pressure drop. This result was subtracted from the total measured adiabatic and condensing pressure losses. The remaining pressure drop was due to the deceleration of the fluid, and due to friction.

The minor losses due to expansion and contraction were also estimated using the pressure drop data from the ZLII tube and the C30 tube. Both the C30 and ZLII tubes have identical port geometries with the major difference being the total length of each section. The C30 tube has a total length of 0.508 m, whereas the ZLII tube has a total length of 0.0225 m. The frictional component of the C30 tube was fit to an equation, and this equation was used to estimate the frictional component of the ZLII tube. Figure 54 compares the sum of the estimated frictional component and the theoretical expansion/contraction component to the actual pressure

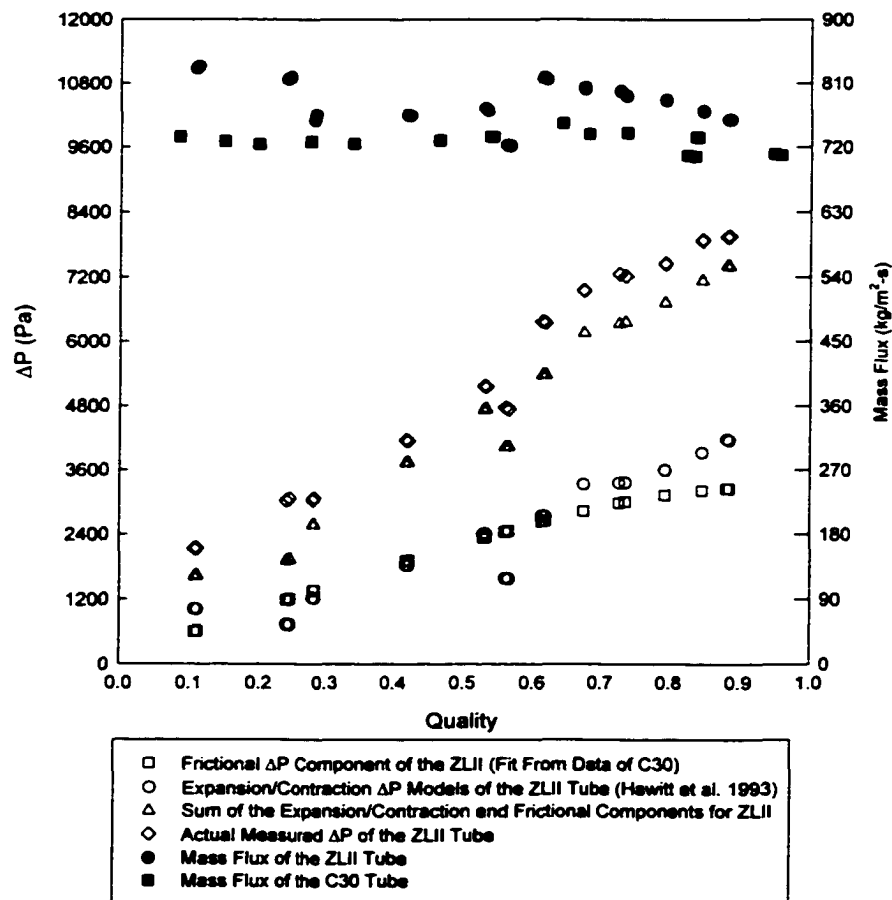


Figure 54. Comparison of the ZLII and C30 Data Using the Expansion/Contraction Models

drop in the ZLII tube for the $G = 750 \text{ kg/m}^2\text{-s}$ case. The mass fluxes for the individual data points for the C30 and ZLII tubes are also shown for reference. Good agreement between these two approaches was found. Therefore, the models previously presented were used as a good estimate of the minor losses due to expansion and contraction of the fluid. With the minor losses due to expansion, contraction, and deceleration identified, the frictional component of the two-phase pressure drop can be calculated using equation (36). For all the tubes tested in this phase of the study, the frictional component of the two-phase pressure drop is shown in Figures 55-69. These results, in conjunction with the results of Phase II of this study, were used to develop flow regime based two-phase pressure drop correlations.

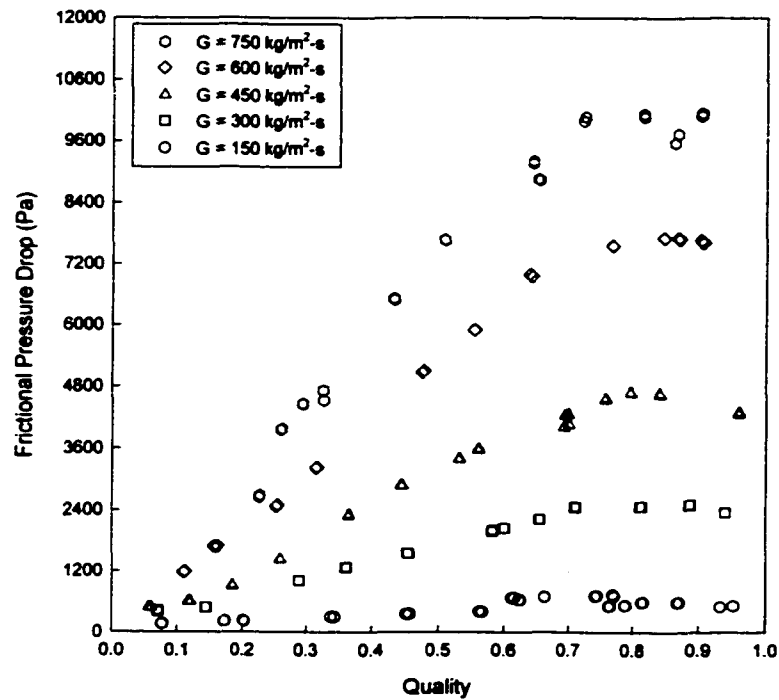


Figure 55. Adiabatic Frictional Pressure Drop for Tube C193 ($D_h = 4.91 \text{ mm}$)

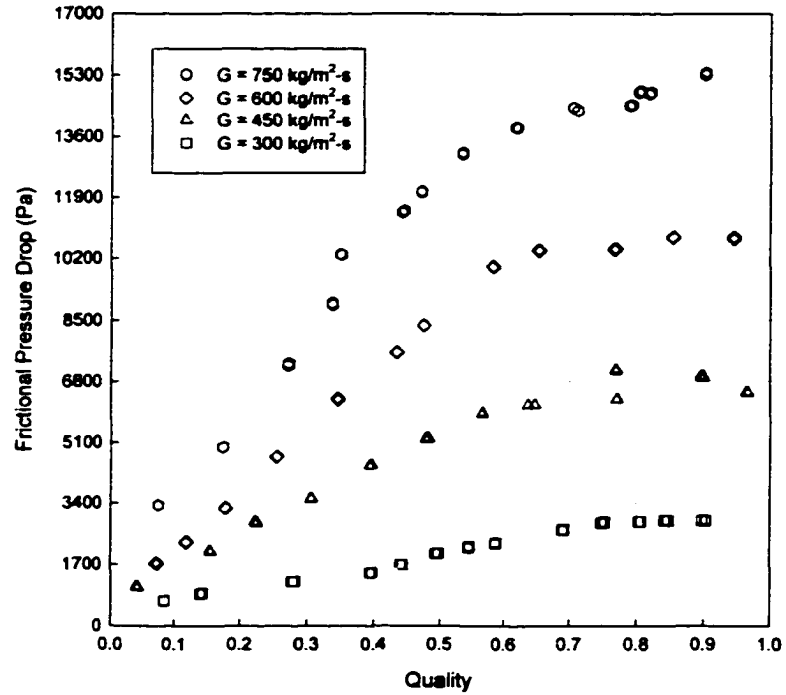


Figure 56. Adiabatic Frictional Pressure Drop for Tube C120 ($D_h = 3.048$ mm)

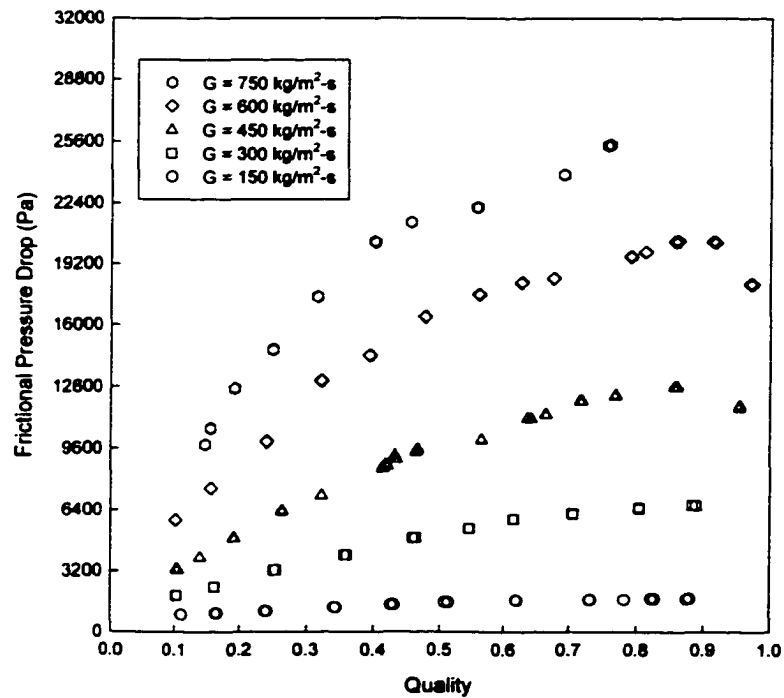


Figure 57. Condensing Frictional Pressure Drop for Tube C60 ($D_h = 1.524$ mm)

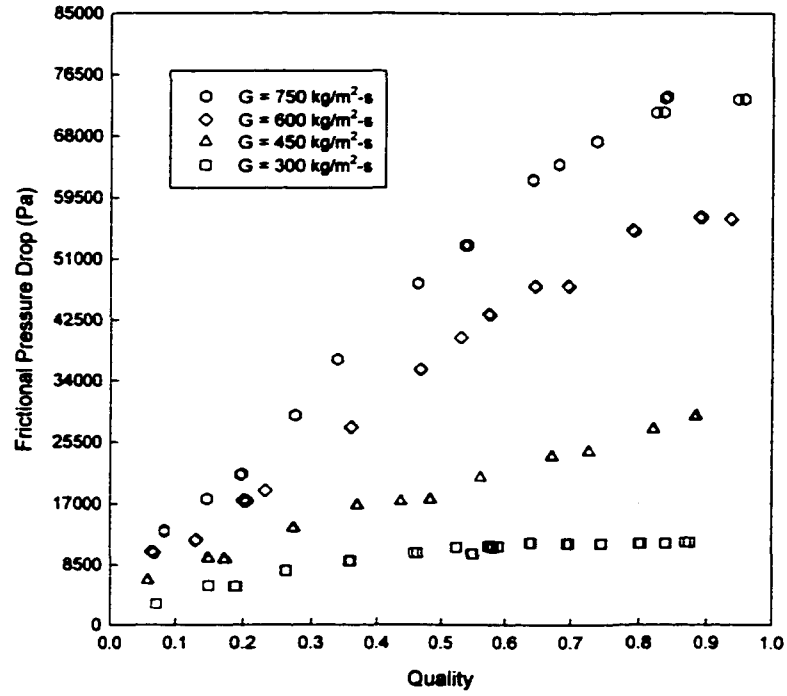


Figure 58. Adiabatic Frictional Pressure Drop for Tube C30 (D_h = 0.761 mm)

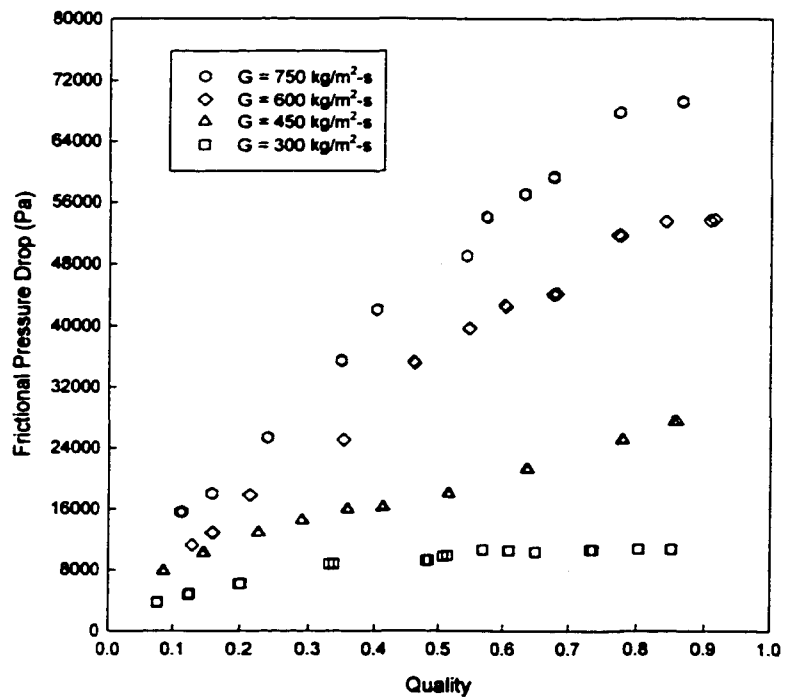


Figure 59. Condensing Frictional Pressure Drop for Tube C30 (D_h = 0.761 mm)

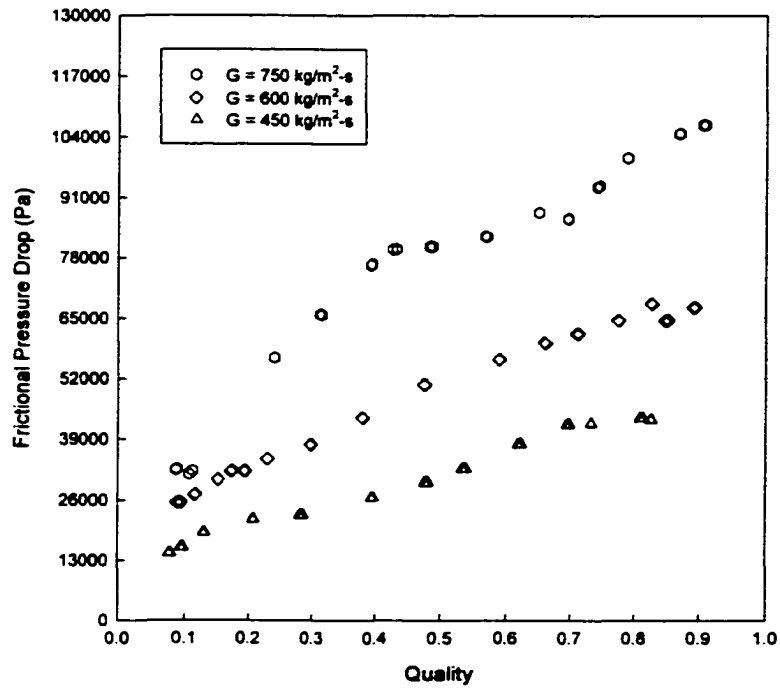


Figure 60. Condensing Frictional Pressure Drop for Tube C20 ($D_h = 0.506$ mm)

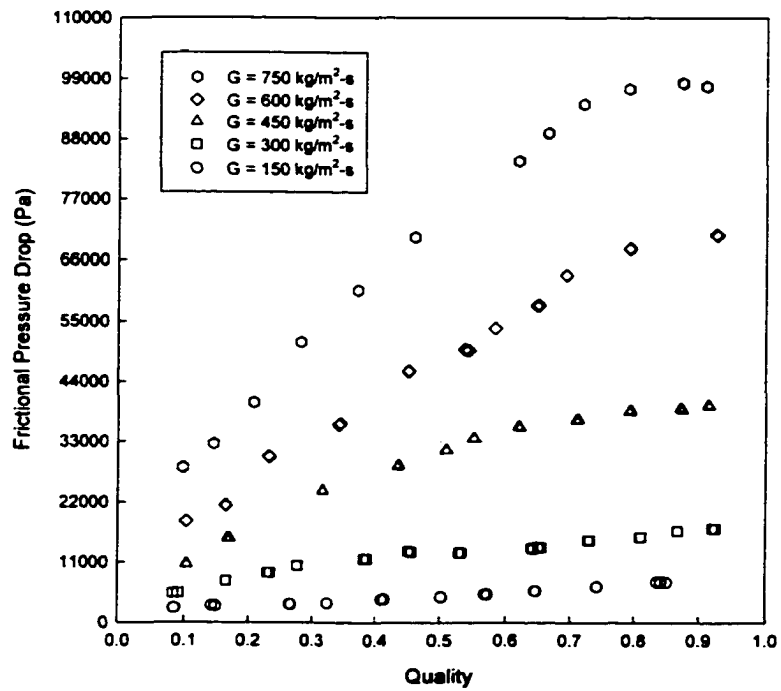


Figure 61. Condensing Frictional Pressure Drop for Tube B32 ($D_h = 0.799$ mm)

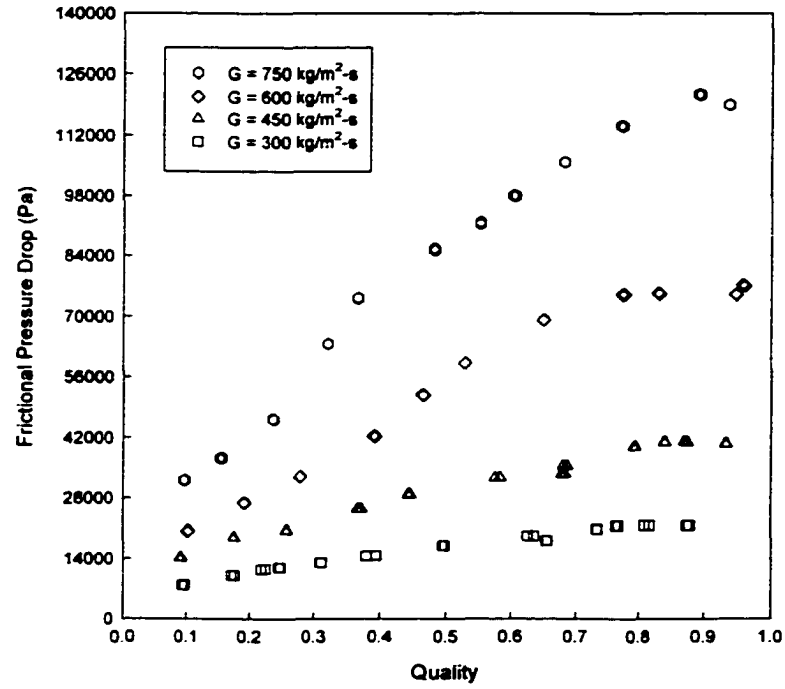


Figure 62. Condensing Frictional Pressure Drop for Tube N21 ($D_h = 0.536$ mm)

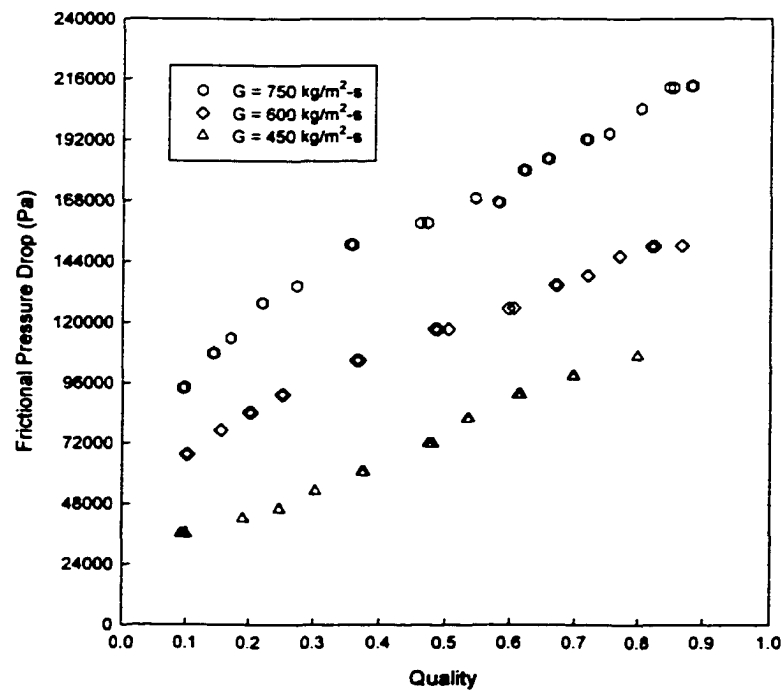


Figure 63. Condensing Frictional Pressure Drop for Tube RK15 ($D_h = 0.424$ mm)

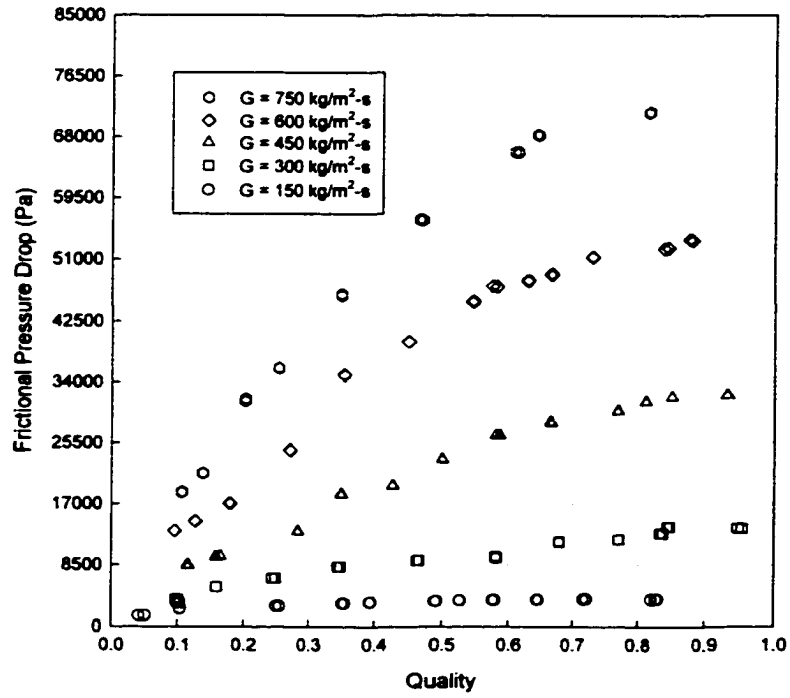


Figure 64. Adiabatic Frictional Pressure Drop for Tube S30 ($D_h = 0.762$ mm)

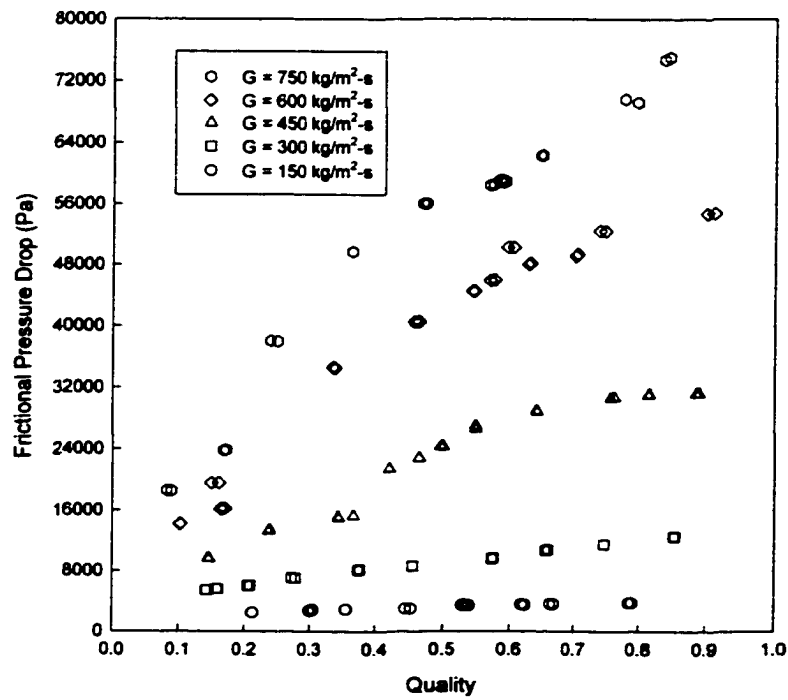


Figure 65. Condensing Frictional Pressure Drop for Tube S30 ($D_h = 0.762$ mm)

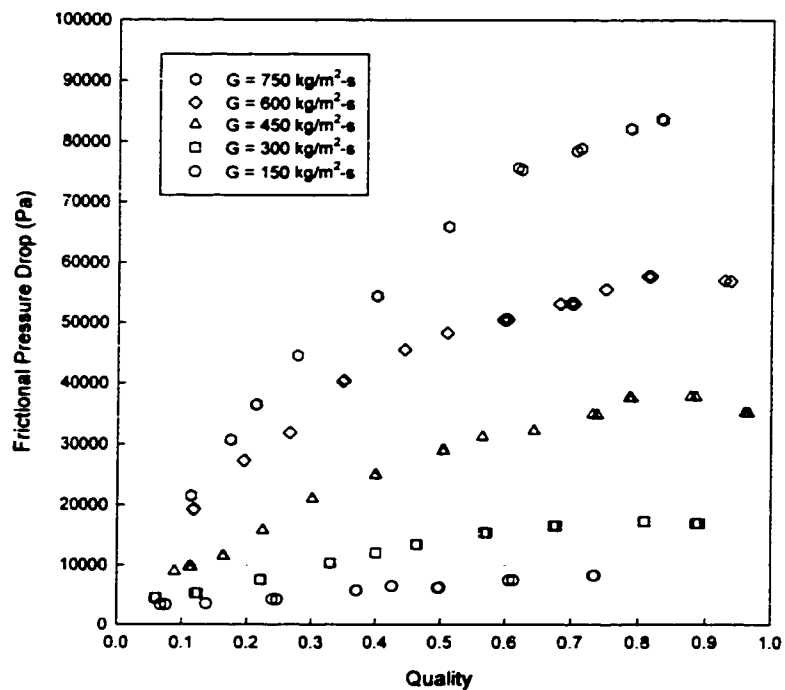


Figure 66. Condensing Frictional Pressure Drop for Tube T33 ($D_h = 0.839$ mm)

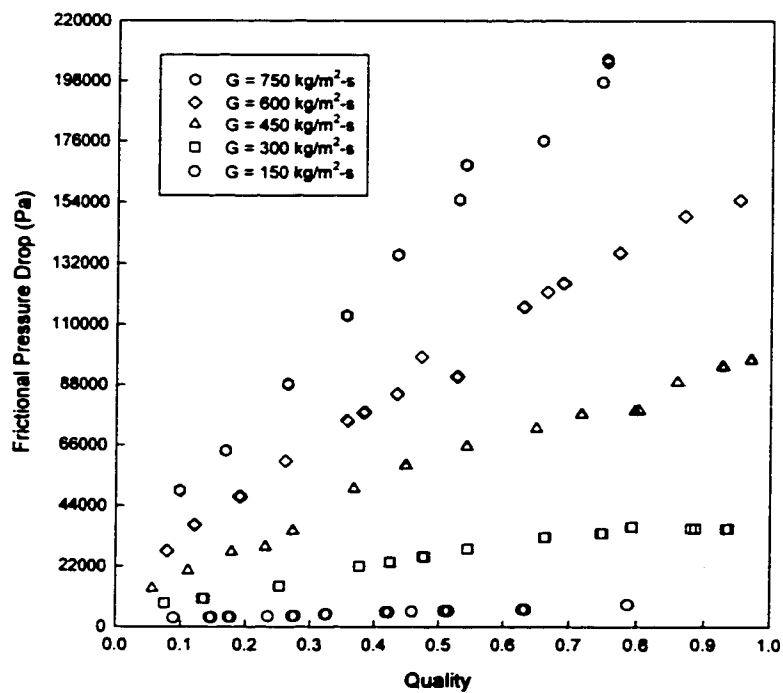


Figure 67. Condensing Frictional Pressure Drop for Tube W29I ($D_h = 0.732$ mm)

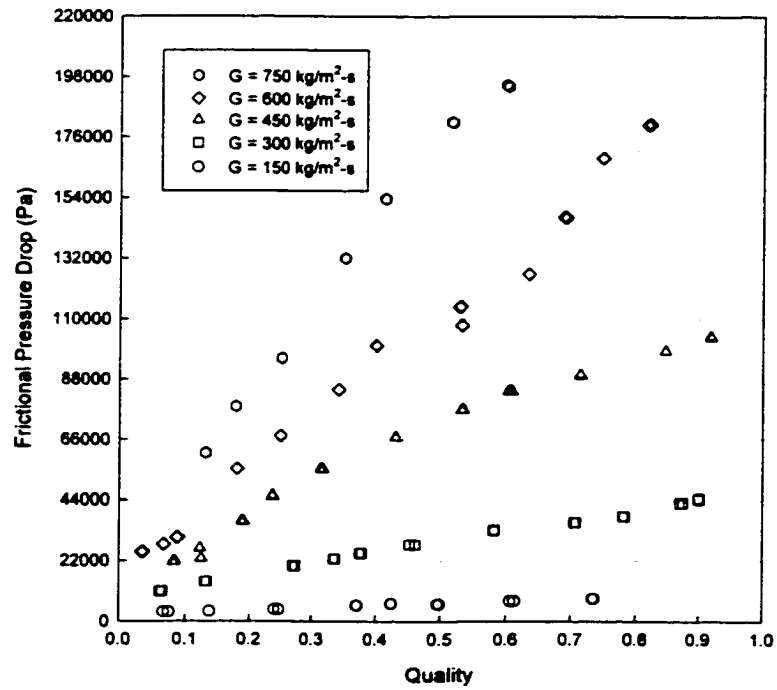


Figure 68. Condensing Frictional Pressure Drop for Tube W29II ($D_h = 0.732 \text{ mm}$)

CHAPTER FIVE. DISCUSSION OF RESULTS

A discussion of the experimental results for all three phases of this study is provided in this chapter. The isothermal air-water flow regime maps and flow regime transition lines are compared with both theoretical and experimental results found in the literature. The effects of tube shape and hydraulic diameter on air-water flow transitions are also discussed. Furthermore, the R-134a flow regime maps are analyzed and compared with experimental results found in the literature. The effects of hydraulic diameter, tube shape, and aspect ratio on the refrigerant flow regime transitions are discussed. The experimentally determined R-134a flow-regime transition lines are compared with both experimental and theoretical results found in the literature. The measured frictional pressure drops are compared with existing correlations found in the literature. Finally, flow regime based pressure drop correlations are presented.

Adiabatic Air-Water Flow Regimes

In this section, the isothermal air-water flow regime maps (shown in Figures 12 and 15) are compared with the theoretical results of Taitel and Dukler (1976), and the experimental results of Damianides and Westwater (1988), and Weisman et al. (1979).

Comparison with Taitel and Dukler (1976) Results

Taitel and Dukler (1976) attempted to predict the flow regimes for co-current gas-liquid flow in pipes using a momentum balance on the liquid and gas phases. The momentum balance is non-dimensionalized with respect to D for length, D^2 for area, and u_L^s and u_G^s for velocities. Each flow regime transition is defined by a separate transition criterion using the following non-dimensional parameters:

$$X = \left[\frac{(dP/dx)_l^s}{(dP/dx)_g^s} \right]^{1/2} \quad (45)$$

$$F = \sqrt{\frac{\rho_g}{(\rho_l - \rho_g)}} \frac{u_g^s}{\sqrt{D_{hyd} g \cos \theta}} = \sqrt{\frac{\rho_g}{(\rho_l - \rho_g)}} Fr^{0.5} \quad (46)$$

$$T = \left[\frac{(dP/dx)_l^s}{(\rho_l - \rho_g) g \cos \theta} \right]^{1/2} \quad (47)$$

$$K^2 = \left[\frac{\rho_g \rho_l u_g^{s2} u_l^s}{(\rho_l - \rho_g) g \mu_l \cos \theta} \right] \quad (48)$$

For the transition from stratified flow to wavy flow, Taitel and Dukler (1976) use a condition for wave propagation of air on still water. In dimensionless form, this condition can be expressed as:

$$K \geq \frac{2}{\sqrt{\tilde{u}_l \tilde{u}_g} \sqrt{s}} \quad (49)$$

where s is the sheltering coefficient for the waves proposed by Jeffreys (1925). For the transition between the stratified regime and the intermittent regime, the Kelvin-Helmholtz theory is extended to a wave height equal to half of the tube inside diameter. This led to the following transition criterion:

$$F^2 \left[\frac{\tilde{u}_g^2 (d\tilde{A}_l / d\tilde{h}_l)}{\tilde{A}_g (1 - h_l / D_{hyd})^2} \right] \geq 1 \quad (50)$$

For the transition between intermittent flow and annular flow, a constant value of liquid height is used ($h_l / D_{hyd} = 0.5$). For a horizontal tube, this leads to a constant value of $X = 1.6$. The transition between intermittent and dispersed is assumed to occur when the turbulent forces overcome the buoyancy forces. This leads to the transition condition:

$$T^2 \geq \left(\frac{8\tilde{A}_g}{\tilde{S}_l \tilde{u}_l^2 (\tilde{u}_l \tilde{D}_l)^{-n}} \right) \quad (51)$$

Taitel and Dukler found good agreement between their transition predictions and data from Mandhane et al. (1974) for a 25.0 mm diameter tube. For smaller tubes, large deviations from this theory have been reported by Damianides and Westwater (1988). A comparison between the Taitel-Dukler predictions, the data of Damianides and Westwater, and experimental results from the present work for the 5.50 mm circular tube is presented in Figure 69.

The reasons for the deviations seen in Figure 69 can be explained on the basis of the transition criteria chosen by Taitel and Dukler (1976). Their criterion for transition from the stratified smooth regime to the stratified wavy regime makes use of a wave sheltering coefficient as proposed by Jeffreys (1925). This coefficient is difficult to determine experimentally and the authors suggest the coefficient be adjusted to fit the data (Taitel and Dukler, 1976). In small diameter tubes, however, only a limited stratified region may exist. It appears that surface tension forces will pull the liquid up around the tube wall and force the onset of intermittent or annular flow even though the Taitel-Dukler theory will predict a stratified flow pattern. These deviations have also been reported by Barnea et al. (1983) for tube diameters ranging from 4.0

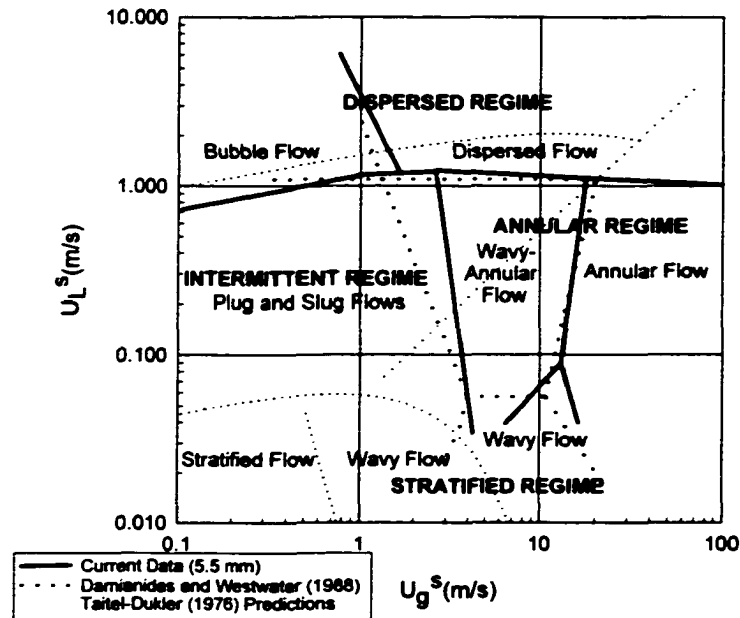


Figure 69. Comparison of Baseline Circular Tube ($D_h = 5.5$ mm) Air-Water Mixture Results with the Literature

mm to 12.30 mm, who suggested a modification to the criterion for transition between stratified and non-stratified regimes to better account for the effects of surface tension. They suggested that the transition to intermittent flows occurs when the equilibrium gas height is less than $\pi D_{hyd}/4$. It was found that this modification resulted in a better fit to the data for tubes larger than 4.00 mm.

The Taitel-Dukler (1976) correlation for the transition from intermittent to annular flow is based upon a non-dimensional liquid equilibrium height of 0.50 which leads to a constant value of $X = 1.60$. However, for most published data, the transition to annular flow more closely approximates a constant value of the modified Froude number, F , rather than a constant value of X (Weisman et al. 1979, Coleman and Garimella 1999). This implies that the transition is a strong function of the superficial gas velocity, with a weak dependence upon the superficial liquid velocity. Barnea et al. (1983) suggested that this transition should be assumed to occur at $h_L/D_{hyd} = 0.35$ rather than $h_L/D_{hyd} = 0.50$ to better fit the data for tube diameters larger than 5.0 mm. This modification will shift the transition to include more data points but will not change the slope to that of a nearly vertical line. Hence, this modification also does not completely explain the differences in the transition prediction and the experimental data.

Comparison with Damianides and Westwater (1988) and Fukano et al. (1989)

Several of the results from the present study are in very good agreement with the experimental work of Damianides and Westwater (1988) on tubes ranging in diameter from 1.00 mm to 5.00 mm. As a baseline case, a comparison between their 5.00 mm tube data and the results of the present work for the 5.50 mm tube is shown in Figure 69. This figure demonstrates the agreement between the present study and the work of Damianides and Westwater (1988); however, both these experimental studies show large deviations from the theoretical results of Taitel and Dukler (1976). The transition to annular flow at a nearly constant value of the superficial gas velocity was observed by the present investigators, Damianides and Westwater (1988), and Weisman et al. (1979). Stratified flow was not observed for the range of diameters investigated in the present study as well as in the work of Damianides and Westwater. Furthermore, the wavy flow pattern was observed at a higher gas velocity than that predicted by Taitel and Dukler (1976). The present study is also in agreement with the findings of Damianides and Westwater (1988) that show a decrease in the size of the wavy-annular flow regime and an increase in size of the intermittent flow regime as the tube diameter decreases. The most striking difference between these two experimental studies, however, is the transition from the intermittent regime to the dispersed regime. Damianides and Westwater (1988) show this transition occurring at a lower value of u_L^s , whereas the present study shows this transition to occur at a higher value of u_L^s as diameter decreases. This finding of the present study is substantiated by Fukano et al. (1989), who presented results for tubes with diameters of 1.00 mm, 2.40 mm, and 4.90 mm. Although no flow pattern maps were provided by Fukano et al., the data provided clearly show the transition to dispersed flow occurring at a higher value of u_L^s as the diameter decreases.

Comparison with Weisman et al. (1979)

Weisman et al. (1979) proposed property and diameter corrections to an overall flow map and presented several new transition correlations. These correlations are based upon a compilation of data from other investigators and also extensive amounts of new data. While general conclusions can be drawn about the effect of diameter on flow patterns, it should be noted that all tube diameters used in developing these correlations were substantially larger than those analyzed in the present work.

The transition from stratified flow to intermittent flow is given by:

$$\frac{u_g^s}{(gD_{hyd})^{1/2}} = 0.25 \left(\frac{u_g^s}{u_i^s} \right)^{1.1} \quad (52)$$

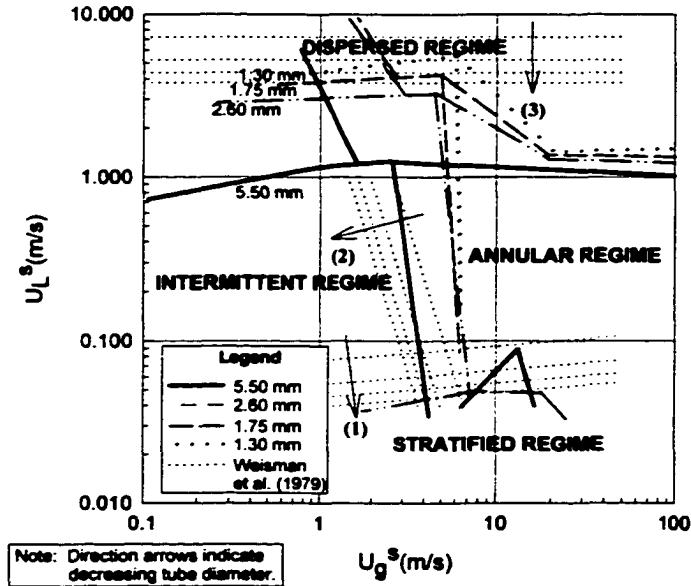


Figure 70. Comparison of Air-Water Mixture Results with Weisman et al. (1979): Hydraulic Diameter Effects

This correlation appears to imply that liquid density, liquid viscosity, and surface tension have no effect on this transition line. The transition to annular flow is given by:

$$1.9 \left(\frac{u_g^s}{u_l^s} \right)^{\frac{1}{8}} = \left(\frac{u_g^s \rho_g^{0.5}}{[g(\rho_l - \rho_g)\sigma]^{0.25}} \right) \left(\frac{u_g^{s2}}{gD_{hyd}} \right)^{0.18} \quad (53)$$

This correlation appears to imply that liquid viscosity has no effect and liquid density and surface tension have only minor effects on this transition line. The transition to dispersed flow is given by:

$$\left[\frac{(dP/dx)_l^s}{(\rho_l - \rho_g)g} \right]^{0.5} \left[\frac{\sigma}{(\rho_l - \rho_g)D_{hyd}g^2} \right]^{-0.25} = 9.7 \quad (54)$$

where

$$(dp/dx)_l^s = \frac{f}{2} \frac{G_l^2}{g\rho_l D_{hyd}} \quad (55)$$

Transitions observed in the present study are compared with the transitions predicted by the

above equations developed by Weisman et al. (1979) in Figure 70. Weisman et al. predict a transition between stratified flows and other regimes at decreasing liquid velocities as the tube diameter decreases as shown by trend (1) in Figure 70. While this trend was observed in the present study, Weisman et al. predict the transition occurring at a nearly constant value of u_L^* , whereas the present work shows peaks in these transition lines. This departure from transition at a constant value of u_L^* is in fact consistent with the data of Damianides and Westwater (1988), as shown in Figure 69. This implies that the correlation by Weisman et al. (1979) for this transition does not adequately account for the effects of decreasing tube diameter and surface tension.

For a given tube diameter, Weisman et al. (1979) predict the transition between intermittent and annular flows to occur at a nearly constant value of u_G^* , as shown by trend (2) on Figure 70. This is in agreement with the current data. However, as the tube diameter decreases, they predict a shift in the transition line to a lower value of u_G^* , whereas the present data show the transition line to shift to an increasing value of u_G^* . Similarly, their correlation for transition to dispersed flows (shown by (3) on Figure 70) predicts this transition to occur at a high and constant value of u_L^* for a given diameter. However, the present data show that there is a definite change in slope for this transition line, and the effect of decreasing tube diameter is to move the transition line to a higher value of u_L^* , which contradicts the results of Weisman et al (1979). Thus, it appears that while there is some agreement in transition predictions between the present work and the correlations by Weisman et al., especially at the larger diameter, their correlations may not be suitable for the prediction of the effect of tube diameter on the shifts in transition. This is understandable because their work was based on larger diameter tubes than those investigated in the present study and may not adequately account for the effects of tube diameter, surface tension and liquid viscosity.

It is evident from the above discussion that there are many difficulties in determining a set of consistent, and reliable transition correlations due to the number of parameters that need to be considered. These parameters include the density and viscosity of the two phases, surface tension, and tube shape and hydraulic diameter. If the transition criteria are based solely upon air and water experiments, it is likely that these correlations may not adequately account for the variations in fluid properties. Furthermore, if transition correlations are based upon large hydraulic diameter tubes, the interactive effects of gravity, shear (inertia) and surface tension may not be properly represented by these transition correlations for smaller diameter circular and non-circular tubes. Phase II of this study utilizes R-134a as the working fluid, whose properties are quite different from those of air and water. Therefore, the experimentally determined flow regime transitions for R-134a during condensation from this study are discussed below before comprehensive transition correlations are presented.

R-134a Flow Regimes

In this section, the nine flow regime maps presented in the previous chapter will be compared with existing flow regime maps found in the literature. The baseline case (4.91 mm I.D.) is compared with the data of Wang et al. (1997) and the transition lines presented by Weisman et al. (1979). The effects of tube shape, tube diameter, and aspect ratio on the transition lines are also discussed. The flow regime transition lines for both the air-water experiments and the R-134a experiments are analyzed and a set of general transition correlations is presented.

Baseline Case Comparisons

Comparison with the Baker (1954) and Taitel and Dukler (1976) Maps

A widely used flow regime map found in the literature is attributed to Baker (1954) and uses the mass flux and quality as the axes. The Baker map is based upon air-water and oil-air experiments using tube diameters much larger than those used in the present study. Property corrections are made to the axes using air and water at standard temperature and pressure as reference values. The abscissa uses the function $G(1-x)\psi$ where ψ is a property correction factor given by:

$$\psi = \left(\frac{\sigma_{H_2O}}{\sigma} \right) \left[\left(\frac{\mu_l}{\mu_{H_2O}} \right) \left(\frac{\rho_{H_2O}}{\rho_l} \right)^2 \right]^{\frac{1}{3}} \quad (56)$$

and the ordinate uses the mass flux, quality, and a property correction factor, λ , given by:

$$\lambda = \left(\frac{\rho_g \rho_l}{\rho_{air} \rho_{H_2O}} \right)^{\frac{1}{2}} \quad (57)$$

From Table 15, it is evident that the properties of R-134a and air/water mixtures are substantially different. The results of Phase I (air-water experiments – $D_h = 5.50$ mm) and Phase II (R-134a, $D_h = 4.91$ mm) are superimposed on the Baker map in Figures 71 and 72, respectively. In these two figures, the original flow regime terminology of Baker (1954) is shown in *italics*, and the terminology used in this study is shown in **bold**. The flow regime transitions proposed by Baker (1954) are shown using dashed lines in these figures. It should be emphasized that the Baker map is based upon data from much larger tubes ($D_h > 22$ mm) than those tested in Phase I and Phase II of this study, and does not provide a correction for small hydraulic diameters. Despite the vast differences in hydraulic diameter, however, good agreement between the data of Phase

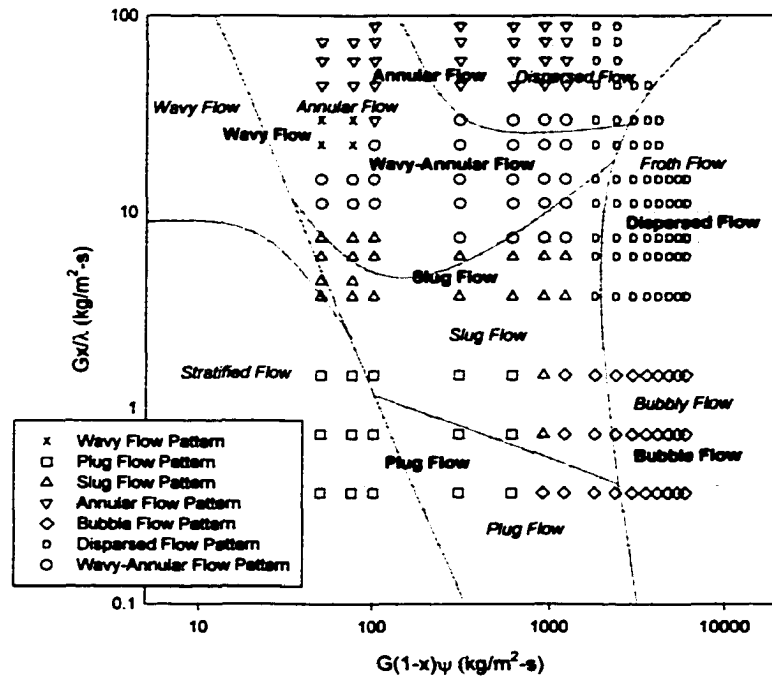


Figure 71. Comparison of the Air-Water Data ($D_h = 5.50$ mm) With the Baker (1954) Map

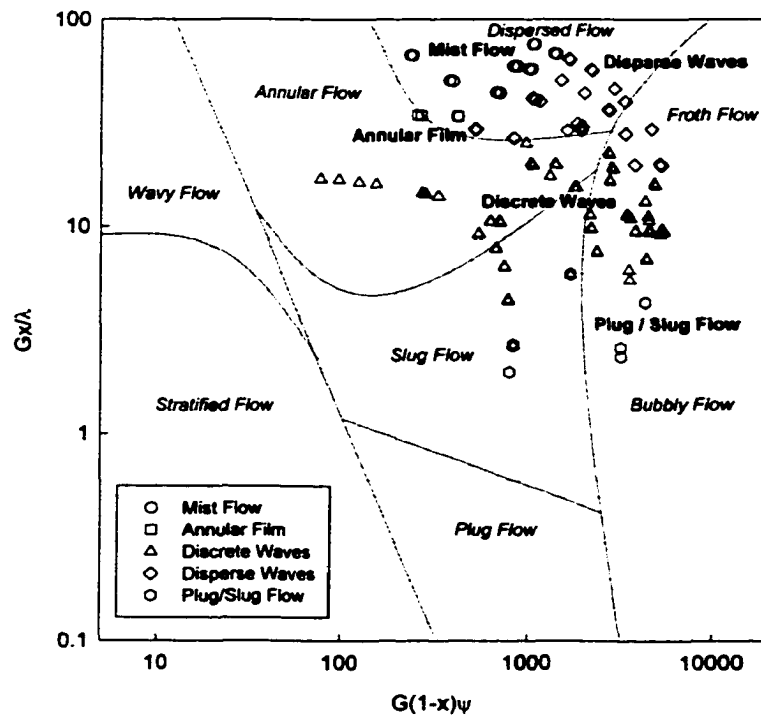


Figure 72. Comparison of the R-134a Data ($D_h = 4.91$ mm) With the Baker (1954) Map

I and the Baker map was found. Both the bubble flow pattern (*bubbly flow*) and dispersed flow pattern (*froth flow*) are well predicted by the Baker map. Furthermore, the plug and slug flow patterns show very good agreement with the Baker map. The plug flow pattern data from the present study extends into the stratified flow pattern region of the Baker map, which is consistent with the previously discussed effects of a smaller hydraulic diameter. The Baker map does not make any distinction between an annular flow pattern and a wavy-annular flow pattern and, as expected, both the annular flow data and the wavy-annular data fall into the same region (*annular flow*). The annular flow pattern data extends to higher values of Gx/λ into a mist flow pattern (Baker's *dispersed flow*), although no distinction between annular flow and mist flow was made in Phase I of this study.

Table 15: Liquid/Gas Properties and Non-Dimensional Numbers

	ρ kg/m ³	$\mu \times 10^4$ kg/m-s	σ mN/m	Bo	Ga $\times 10^{-6}$	Re
R-134a Gas	69.7	0.160	---	51.81	22.4	69565
R-134a Liquid	1094.0	1.420	4.68	---	---	7795
Air	2.3	0.182	---	3.24	0.018	60698
Water	999.5	10.01	72.73	---	---	1104
Gas Ratio	30.4	0.873	---	16.0	1212	1.15
Liquid Ratio	1.09	0.142	0.064	---	---	7.06
<i>Note:</i> $P_{air} = P_{wat} = 193.1$ kPa, $T_{air} = T_{wat} = 20^\circ\text{C}$, $P_{refg} = 1379$ kPa						

Figure 72 compares the data from Phase II of this study with the Baker (1954) flow regime map. The mist flow pattern data corresponds to Baker's definition of a *dispersed flow*, and the disperse wave pattern data reside in two main regions (*dispersed flow* and *froth flow*). The distinction between the mist pattern and the disperse wave pattern is the existence of a thin stratified layer of liquid at the bottom of the tube, and this is the same distinction made by Baker (1954) for the *dispersed flow* and *froth flow* regions. The discrete wave pattern data from this study occupy most of the annular flow region on the Baker map. The discrete wave pattern can be viewed as a form of wavy-annular flow, but Baker (1954) made no distinction between this pattern and a purely annular flow. Furthermore, the discrete wave data extends into the froth flow and bubbly flow regions, which suggests that the transition line from *slug flow* to *bubbly flow* should be shifted to the right. The plug and slug pattern data occupy both the *slug flow* region as well as part of the *bubbly flow* region, and this also suggests that the transition line proposed by Baker (1954) should be shifted to the right. Thus, while some of these differences

may be attributed to the smaller hydraulic diameter used in this study, many of these differences are perhaps because the fluid property corrections offered by Baker (1954) do not adequately account for the large differences in air-water and R-134a properties.

The air-water flow regime map for the circular tube with hydraulic diameter $D_h = 5.50$ mm was compared with the theoretical results of Taitel and Dukler (1976) in Figure 69. It was shown that these transition correlations did not adequately account for the effects of hydraulic diameter, and may not be applicable to microchannel geometries. Figure 73 compares the Taitel and Dukler (1976) theoretical transition lines with the R-134a results from Phase II of this study. This figure shows results similar to those found in Phase I. The plug and slug flow region (shown in *italics* in Figure 73) predicts the plug and slug flow data, but also covers part of the discrete wave flow pattern. For the mass fluxes and qualities tested in Phase II of the study, no stratified flow or dispersed flow was observed, which is consistent with the Taitel-Dukler criteria. Taitel and Dukler (1976) also predict that the transition from intermittent to annular flow occurs at a liquid level height equal to half of the tube inner diameter, which corresponds to a constant Martinelli parameter of $X = 1.6$. Barnea et al. (1983) proposed a modification for small hydraulic diameter tubes with the transition occurring at a liquid level height of 0.35, rather than 0.50. The dashed line in Figure 73 represents this modification, which results in a shift in the line, rather than a change in slope. However, neither of these criteria adequately depict the transition from intermittent flows to discrete wave flow and annular flow at high gas velocities. Therefore, similar to the results of the air-water experiments (Phase I), the transition from an intermittent flow to an annular flow may best be described by a constant value of Froude number, rather than a constant value of the Martinelli parameter. Also, the theoretical map of Taitel and Dukler (1976) does not make any further distinctions in the flow patterns found within the annular flow regime. Specifically, no distinction between wavy-annular (discrete and disperse waves) and annular film or mist flow is made, which partly explains the difference between the results of this study and their transition criteria.

Comparison with Weisman et al. (1979)

The R-134a 4.91 mm baseline case was also compared with the transitions predicted by Weisman et al. (1979), as shown in Figure 74. This figure shows that 83% of the data are in accordance with the transitions proposed by Weisman et al. (1979). The annular regime identified by Weisman et al. consists of both the wavy-annular and the annular flow patterns (which correspond to the discrete and disperse wave patterns documented in the present study). The stratified flow pattern transition reported by them occurs at a value of U_G^* lower than 0.1 m/s and is not seen on the flow regime map shown in Figure 74. This is consistent with the findings of the present study because stratified flow was not observed in the 4.91 mm round tube.

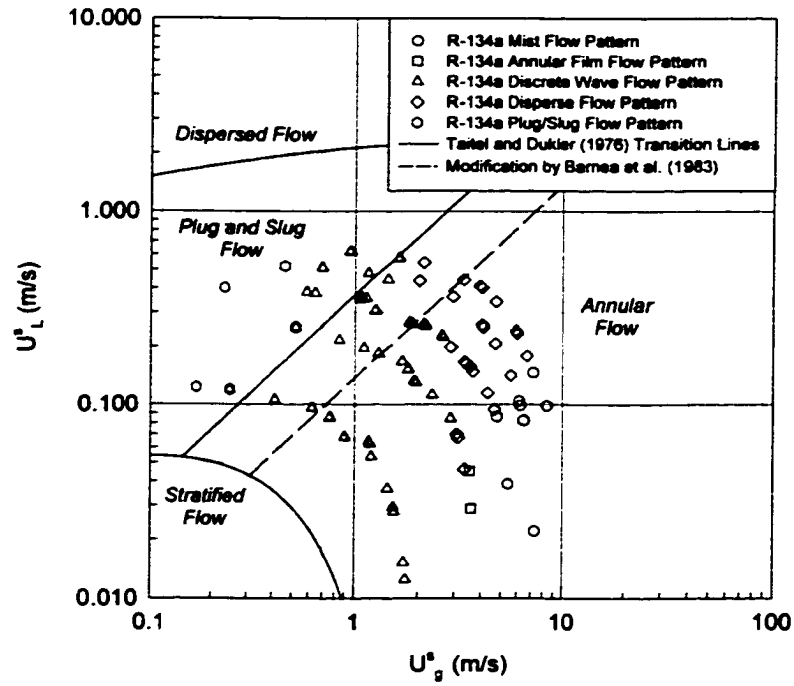


Figure 73. Comparison of R-134a Data ($D_h = 4.91$ mm) and Taitel and Dukler (1976) Map

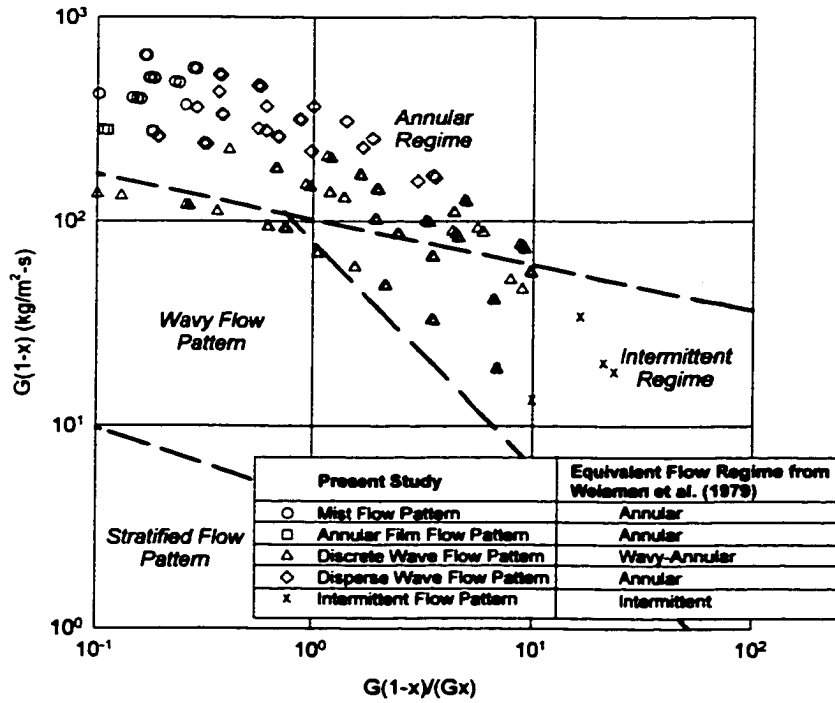


Figure 74. Comparison of R-134a Data ($D_h = 4.91$ mm) With Transition Correlations of Weisman et al. (1979)

Figure 74 also shows that Weisman et al. (1979) predict a larger intermittent regime than was observed in the present study. Thus, according to their transition line, several of the data points characterized as discrete waves in the present study would be considered to be in the intermittent regime. This finding is consistent with the data of Wang et al. (1997) discussed below at the higher values of the superficial liquid velocity. The wavy flow pattern predicted by Weisman et al. (1979) includes data points from the present study that exhibit the discrete wave flow pattern, and thus represent good agreement between the two studies.

Comparison with the data of Wang et al. (1997)

The R-134a data for the 4.91 mm round tube were also compared with the results from a study by Wang et al. (1997), who developed a two-phase flow pattern map for a 6.5 mm round tube. This comparison is shown in Figure 75, which shows very good agreement between the two maps. The terminology used by Wang et al. (1997) for the flow patterns is shown in the legend. Their data points are plotted in this figure with the transition lines from Figure 17 developed in the present study. Figure 75 shows that the intermittent regime (plug and slug flows) in the 4.91 mm round tube is slightly larger than the data of Wang et al. (for the 6.5 mm tube) would suggest. Thus, there are a few points in this regime that are labeled W and WA indicating that Wang et al. (1997) observed wavy and wavy annular flow here. This smaller intermittent regime for the larger diameter tube is to be expected, and is discussed further in a subsequent section in connection with the square tube data from the present study.

Wang et al. (1997) defined annular and wavy-annular patterns within the annular flow regime, which they considered to be adjacent to the intermittent flow regime. In the present study, however, wavy flow of different types was found to exist over a wide range of conditions. Therefore, wavy flow was treated as a separate flow regime consisting of discrete and disperse wave patterns. It should be noted that the distinction made by Wang et al. (1997) between the wavy, wavy-annular and annular flow patterns follows closely the distinction made in the present study between discrete and disperse waves. It can be argued that the difference between the wavy, annular-wavy and annular flow patterns as defined by the authors is related to the progression between discrete and disperse waves identified in this study. Similarly, the mist flow, annular ring, wave packet, and annular film patterns identified in the present study correspond to annular flow regime data of Wang et al. (1997). The large database from the present study, however, enables the identification of more detailed subdivisions within this flow regime.

The data of Wang et al. (1997) and the present data show both waves and plugs coexisting in the same region. At the lowest mass fluxes, Wang et al. (1997) show a stratified

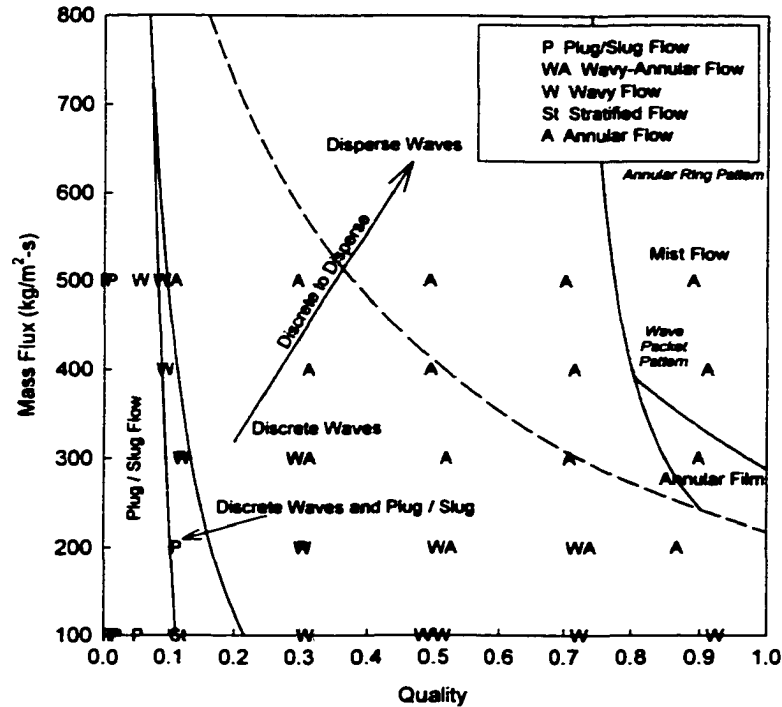


Figure 75. Comparison of R-134a Data ($D_h = 4.91$ mm) With the Results of Wang et al. (1997)

data point whereas no stratification was found in the present study. The reason for this may be due to a combination of the mass flux tested and the tube diameter. The present study utilized a smaller diameter that tends to suppress the stratified flow pattern, and also the lowest mass flux tested in the present study was $150 \text{ kg/m}^2\text{-s}$, which is higher than the lowest mass flux tested by Wang et al. (1997).

Comparison with Troniewski and Ulbrich (1984) and Wambsganss et al. (1991)

The few studies in the literature that address two-phase flow in somewhat similar rectangular channels, even if they are not for phase change flow of refrigerants, are used here as a basis for comparison with the results of the present study. Data from the 4 mm and 3 mm tubes are compared with the flow regime map of Troniewski and Ulbrich (1984) in Figure 76 and 77, respectively, which is a modified form of the Baker (1954) map, with a correction factor, $\omega = (\alpha/2)^{0.16}$ to account for the tube aspect ratio. (This map was based on data for channels with $D_h > 7.45$ mm, with $\alpha \ll 1$ or $\alpha \gg 1$ for air-water mixtures; representing conditions much different from those of the present study). Their map shows that the stratified regime (stratified flow and wavy flow) will not occur for the range of qualities and mass fluxes tested here, which

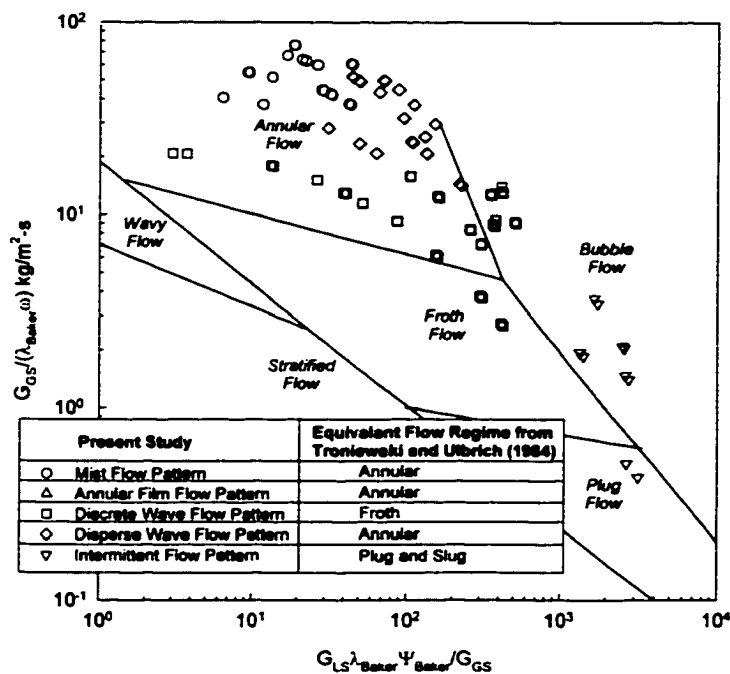


Figure 76. Comparison of 4 x 4 mm R-134a Data With the Flow Regime Map of Troniewski and Ulbrich (1984)

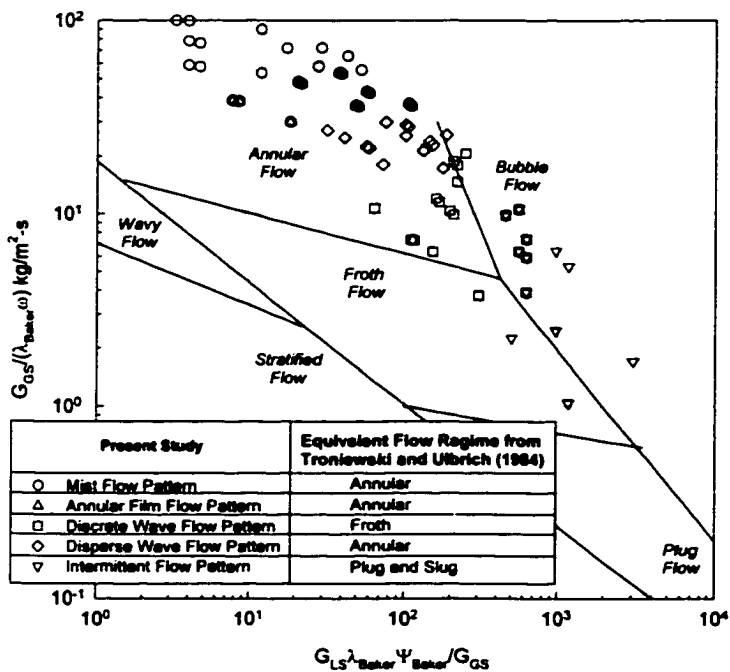


Figure 77. Comparison of 3 x 3 mm R-134a Data With the Flow Regime Map of Troniewski and Ulbrich (1984)

concur with the flow mechanisms observed in the present study. While some of the intermittent flow data from the present study are in agreement with their map, several of these points would belong in the bubble (dispersed flow) regime according to their map, probably due to the significantly lower density of air compared to the density of R-134a vapor. Most of the annular flow regime (mist, annular film, and disperse waves – which were categorized by them in the annular flow regime) data from the present study lie within the corresponding annular flow regime predicted by Troniewski and Ulbrich (1984). The flow regime entitled froth flow by them is equivalent to the discrete wave pattern from the present study; however, this comparison shows that froth flow extends to higher vapor fluxes in the present study than for their air-water map. Once again, this could be due to the higher gas velocities in air-water mixtures at the same gas flux than for refrigerant flow, which would promote annular flow. Thus, there is some qualitative agreement in the trends predicted by these two studies, with the differences being due to the difference in fluid properties and geometries.

The 2(H) x 4(W) mm, 4(H) x 2(W) mm, 4(H) x 6(W) mm and 6(H) x 4(W) mm tubes were also compared with the flow regime map of Troniewski and Ulbrich (1984) as shown in Figures 78 and 79. The solid data points represent data from the tube with the larger aspect ratio, i.e. (H/W). Inspection of Figure 78 and Figure 76 shows that the degree of agreement between the present data and the work of Troniewski and Ulbrich (1984) is approximately the same for similar hydraulic diameter tubes. Thus, for these similar hydraulic diameters, changing the tube shape from a square to a rectangular cross-section does not significantly affect the flow patterns. Furthermore, the tube orientation, i.e., a change in aspect ratio from $4/6 = 0.667$ to $6/4 = 1.5$ also does not appreciably modify the flow mechanisms. It could very well be that much more drastic changes in aspect ratio (similar to those studied by Troniewski and Ulbrich, 1984) are required for the flow mechanisms to be altered. Essentially similar observations can be made by comparing figures 77 and 79, i.e. the 3 x 3 mm square, and the 2(H) x 4(W) mm and the 4(H) x 2(W) mm rectangular tubes.

Figures 80 and 81 show the 4 mm and 3 mm tube data from the present study plotted on the flow regime maps of Wambsganss et al. (1991) for air-water flow, $D_h = 5.44$ mm, and aspect ratios of 6 (solid transition lines) and 0.167 (dashed transition lines). Both flow regime maps predict that stratified flow will not occur for the range of qualities and mass fluxes tested, which agrees with the results of the present study. The intermittent flow data are also in agreement with their map. Discrete wave data from the present study lie in the region predicted as slug flow by them; although it should be noted that their definition of slug flow has sometimes been referred to as wavy-annular flow by other investigators. Furthermore, discrete wave flow was

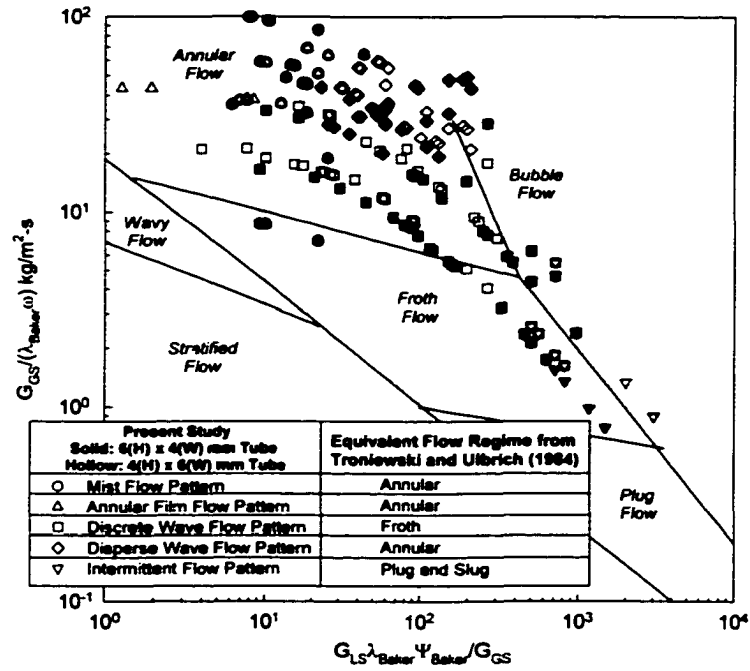


Figure 78. Comparison of the 4(H) x 6(W) mm and 6(H) x 4(W) mm R-134a Data With the Flow Regime Map of Troniewski and Ulbrich (1984)

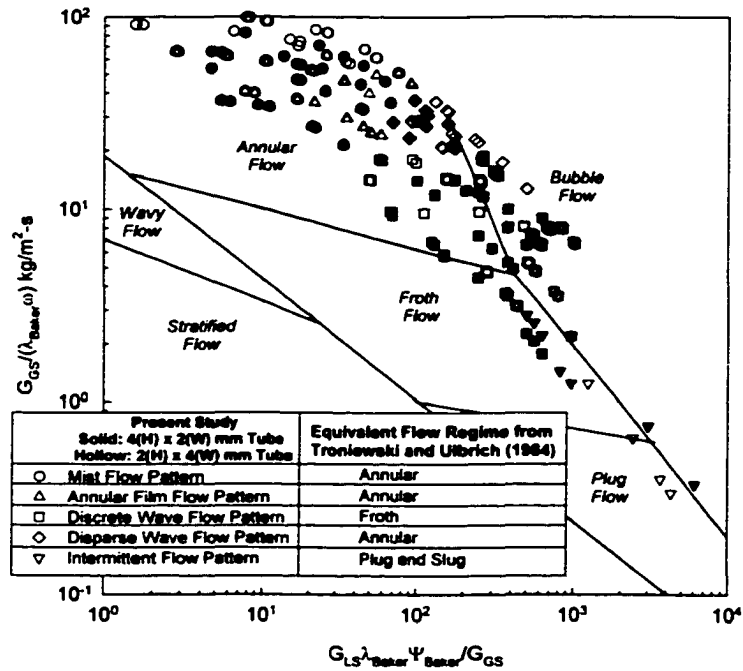


Figure 79. Comparison of the 2(H) x 4(W) mm and 4(H) x 2(W) mm R-134a Data With the Flow Regime Map of Troniewski and Ulbrich (1984)

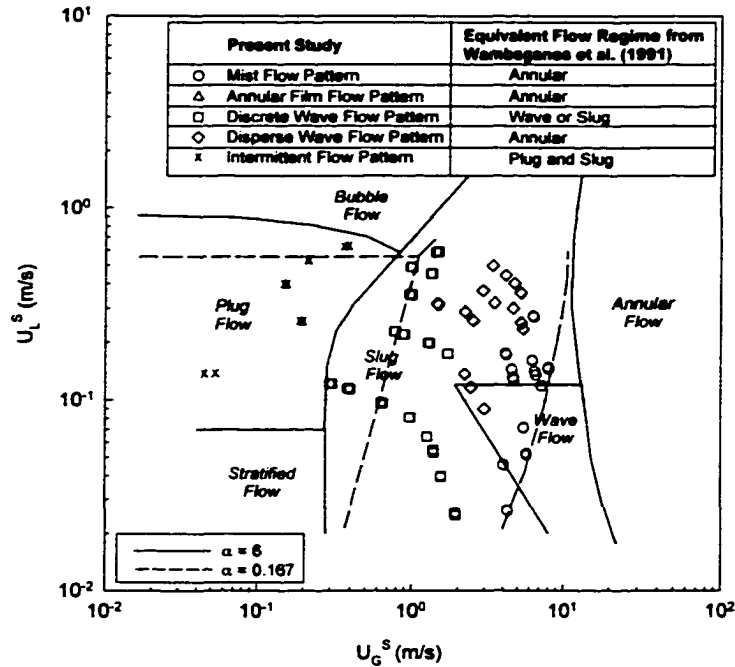


Figure 80. Comparison of the 4 x 4 mm R-134a Data With the Flow Regime Map of Wambsganss et al. (1991)

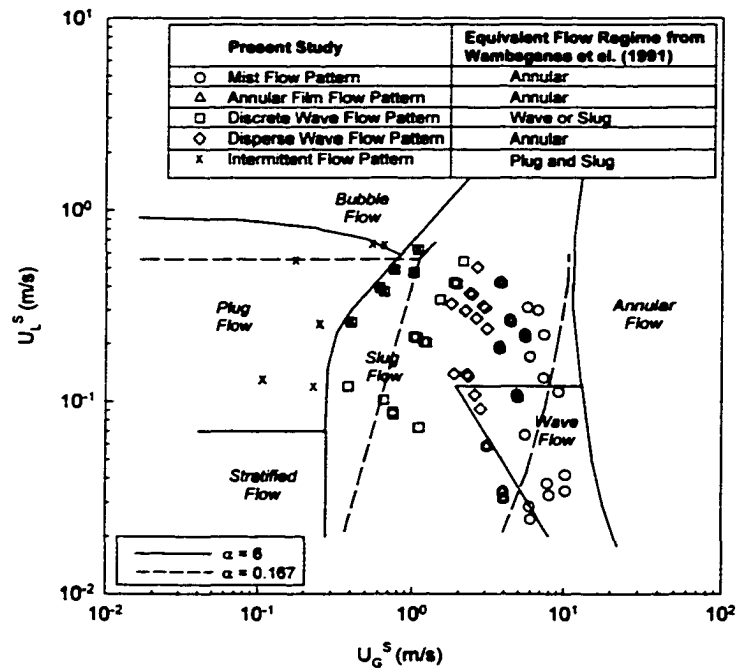


Figure 81. Comparison of the 3 x 3 mm R-134a Data With the Flow Regime Map of Wambsganss et al. (1991)

usually the precursor to slug flow in the present study. For both the 3 mm and 4 mm tubes, much of the annular flow data from the present study is predicted by their map to belong to the slug flow or wavy flow regimes. In their map, the transition to annular flow occurs at $5 < U_g^s < 20$ m/s, while in the present study, various forms of the annular flow regime are seen for $U_g^s > 2$ m/s for the 4 mm tube, and $U_g^s > 1$ m/s for the 3 mm tube. At the same velocity, inertia forces in the refrigerant vapor phase are higher than those in air, due to the significantly lower density of air. These higher inertia forces at the same velocity promote annular flow at lower velocities, which is a corollary to the explanation given above in terms of the vapor phase mass flux when comparing the present work to the study by Troniewski and Ulbrich (1984).

Data from the rectangular tubes investigated in this study are compared with the flow regime maps of Wambsganss et al. (1991) in Figures 82 and 83 for the 4(H) x 6(W) and 6(H) x 4(W) mm tubes, and 2(H) x 4(W) and 4(H) x 2(W), respectively. In both figures, the tubes with the larger aspect ratio (i.e. H/W) are represented using solid data points. Once again, it appears that within the aspect ratio range considered, agreement with the work of Wambsganss et al. (1991) is about the same, regardless of the orientation of the tube. Additional discussion about the specific effects of aspect ratio observed in the present study is provided in a subsequent subsection.

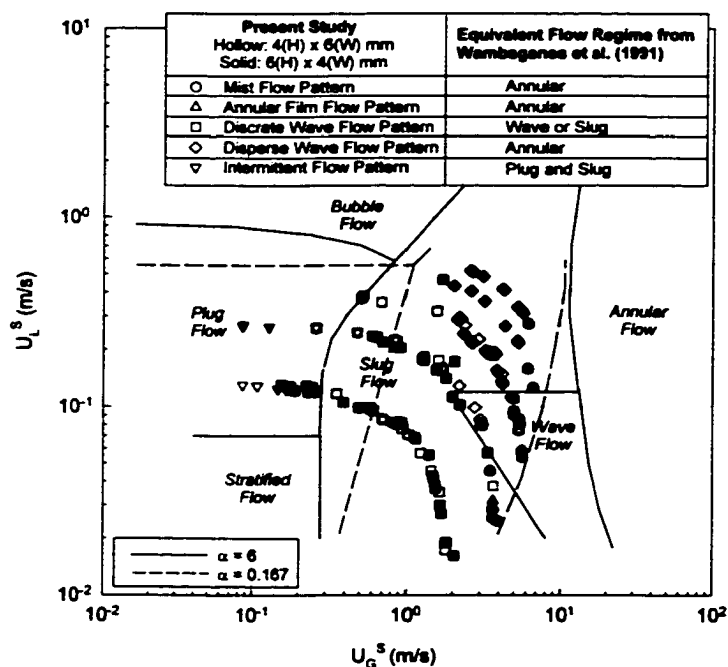


Figure 82. Comparison of the 4(H) x 6(W) mm and 6(H) x 4(W) mm R-134a Data With the Flow Regime Map of Wambsganss et al. (1991)

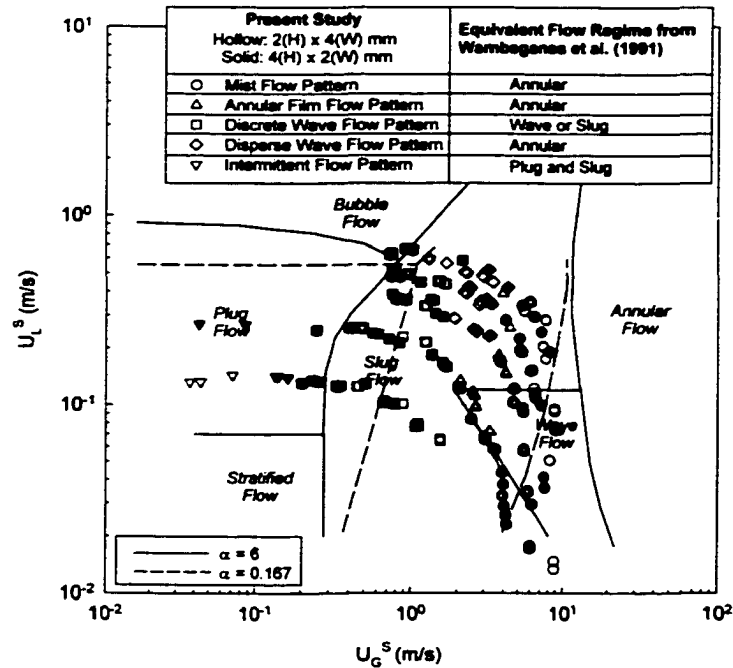


Figure 83. Comparison of the 2(H) x 4(W) mm and 4(H) x 2(W) mm R-134a Data With the Flow Regime Map of Wambsganns et al. (1991)

Effects of Tube Shape, Hydraulic Diameter, and Aspect Ratio on Transition Lines

In this section, the effects of tube shape, hydraulic diameter, and aspect ratio on the flow regime transitions are discussed. A systematic discussion and a rationale of the movement of the transition lines are presented. In a subsequent section, the criteria for transition and transition correlations are presented for both the air-water flow regime transitions (Phase I) and the R-134a flow regime transitions (Phase II).

Effect of Tube Shape on Transition Lines

A comparison of the R-123a flow regime maps for the 4.91 mm round tube and the 4 x 4 mm square tube is presented in this section. These two tubes are of similar hydraulic diameter (4.91 mm and 4.0 mm), with the primary difference being tube shape. The intermittent regime transition lines for both the circular and square tubes are shown in Figure 84. These lines were plotted by curve-fitting the lines of transition between the respective regimes on G-x plots. The curve fit equations are provided in Appendix F. This figure shows that the intermittent regime is larger in the round tube at lower mass fluxes and approximately the same at higher mass fluxes. Figure 85 compares the wavy flow regime areas for the round 4.91 mm and the square 4 x 4 mm tubes. This figure shows that the size of the wavy flow regime is larger in the round

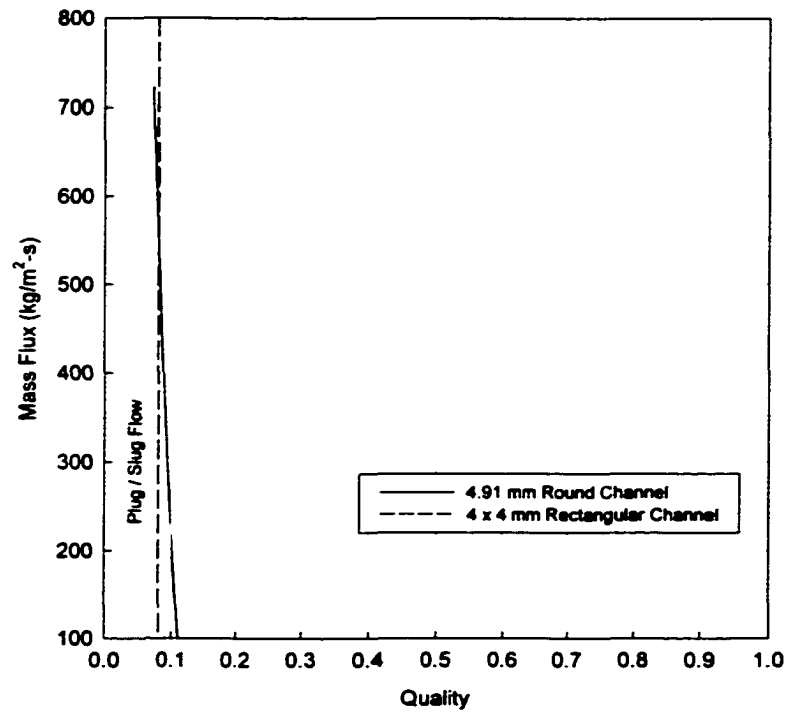


Figure 84. Intermittent Flow Regime Transitions (4.91 mm Circular and 4 x 4 mm Square Tubes)

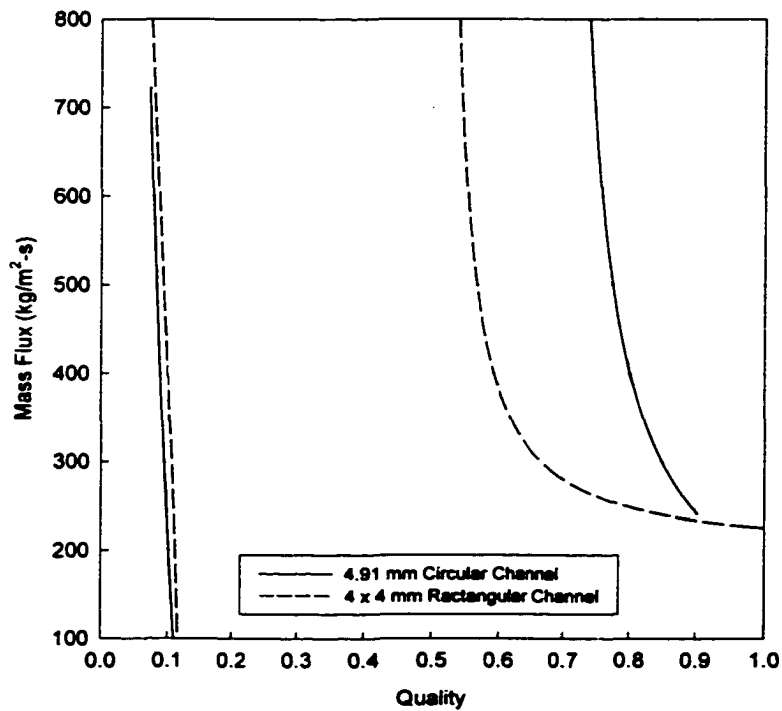


Figure 85. Wavy Flow Regime Transitions (4.91 mm Circular and 4 x 4 mm Square Tubes)

tube. The progression from discrete to disperse waves within this wavy flow regime for both tubes is shown in Figures 86 and 87. As previously mentioned, a scale from zero to three was used here to distinguish between discrete and disperse waves, where a zero represents a highly discrete and clearly identifiable single waveform (with no secondary waves) and three represents a disperse waveform. These two figures show that both the discrete wave and disperse wave regions are larger in the round tube than in the square tube. It is possible that this larger wavy flow regime in the round tube is partly due to the slightly larger hydraulic diameter compared to the square tube. A similar influence of the hydraulic diameter in square tubes is discussed in a subsequent section; however, the tube shape is probably more responsible for this difference in the size of the wavy flow regime between the round and square tubes. The annular regime transition for the round and square geometries is shown in Figure 88. In both cases, the entire annular regime primarily consists of the mist flow pattern with the exception of a small region of an annular film flow pattern appearing in the round tube. The round tube has a smaller mist flow region as compared to that of the 4 x 4 mm square tube and this could be partially explained on the basis of the slightly different hydraulic diameters, as discussed in a subsequent section.

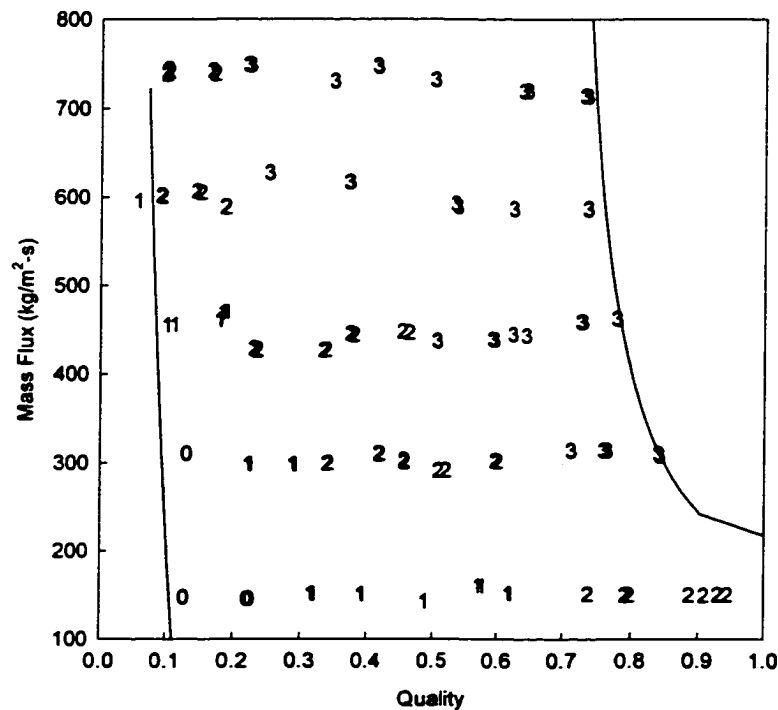


Figure 86. Progression from Discrete (0) Waves to Disperse (3) Waves: 4.91 mm Circular Tube

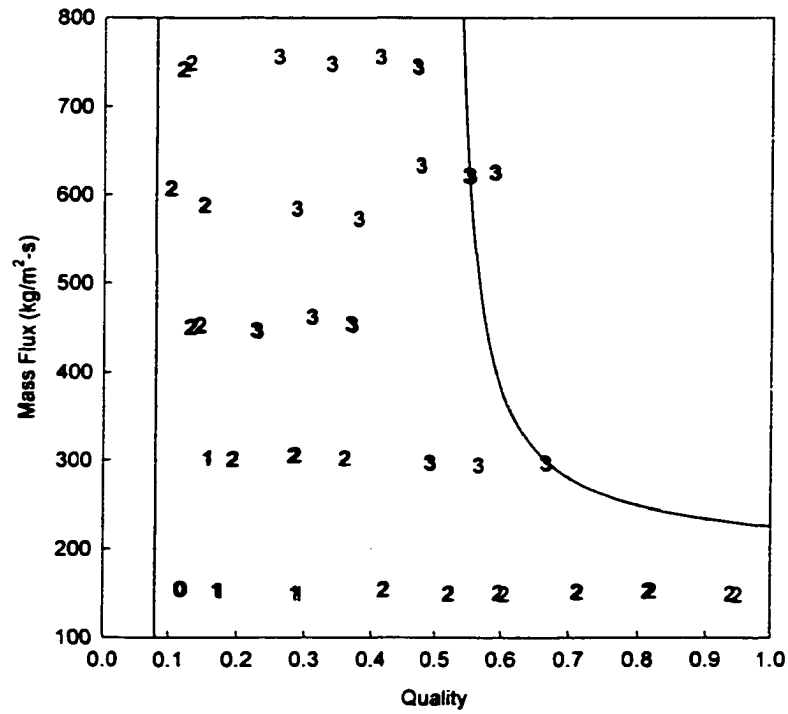


Figure 87. Progression from Discrete (0) Waves to Disperse (3) Waves: 4 x 4 mm Square Tube

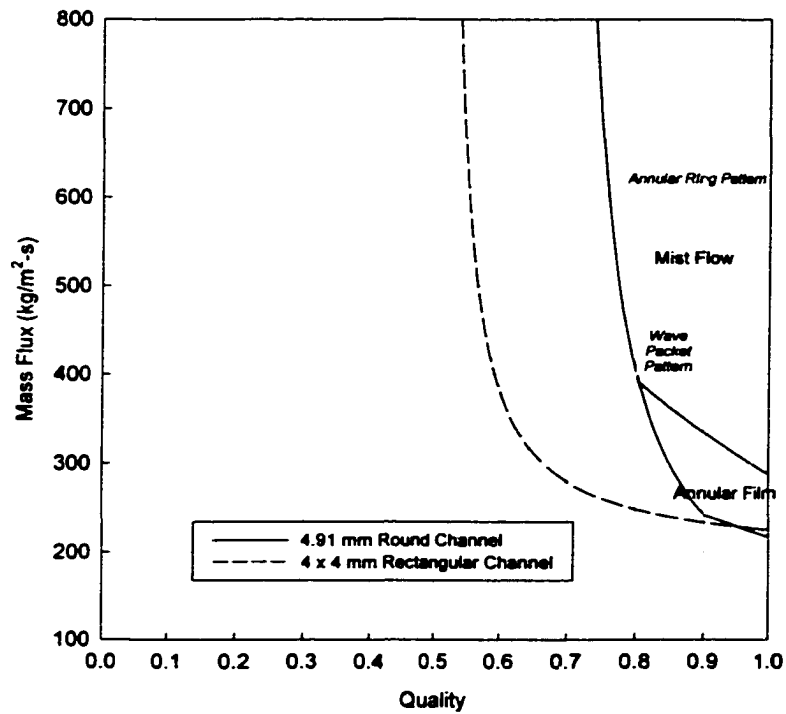


Figure 88. Annular Flow Regime Transitions (4.91 mm Circular and 4 x 4 mm Square Tubes)

Effect of Hydraulic Diameter on Transition Lines

One of the major contributions of the present study is the characterization of the effect of decreasing tube sizes on flow regimes. Therefore, to investigate the effect of hydraulic diameter on the flow regimes and transitions, the four flow regime maps for the 4 x 4 mm, 3 x 3 mm, 2 x 2 mm and 1 x 1 mm square tubes were compared. Specifically, the movement of each transition line and the relative size of each flow regime and flow pattern were documented. The transition from the intermittent regime (plug and slug flow patterns) for the four square tubes is shown in Figure 89. From this figure, it is clear that the effect of the decreasing hydraulic diameter is to increase the size of the intermittent regime. At a low mass flux of 150 kg/m²-s, the intermittent regime extends from a quality of 0.00 to 0.08 in the 4.0 mm hydraulic diameter tube, and to a quality of 0.60 in the 1.0 mm hydraulic diameter tube. The effect of hydraulic diameter is less dramatic at the higher mass fluxes. The intermittent regime ends at a maximum quality of 0.08 (mass flux of 750 kg/m²-s) in the 4.0 mm hydraulic diameter tube and extends to a quality of 0.16 in the 1.0 mm hydraulic diameter tube. The dramatic increase in the size of the intermittent regime can be explained by the effect of surface tension. In the smaller hydraulic diameter tubes, surface tension allows the liquid to readily coat the tube walls. This effect might also be due to the fact that in square channels, it is easier for the liquid to be held in the sharp corners, counteracting to some extent, the effects of gravity. This facilitates plug and slug flow at higher qualities as the hydraulic diameter is decreased. Figure 90 shows the effect of hydraulic diameter on the annular film pattern in the annular regime. It should be noted that the annular film flow pattern was not observed for the largest hydraulic diameter (4.0 mm) tube. For the 3.0 mm hydraulic diameter tube, there is a small region enclosed by the dotted lines in which the annular film pattern exists. This region grows rapidly as the hydraulic diameter is decreased and covers the major portion of the 1 x 1 mm square tube flow regime map. These observations seem to imply that in the case of the 4 x 4 mm square tube, the effects of gravity dominate, resulting in most of the flow regime map being covered by the wavy flow regime. As the hydraulic diameter decreases, the effects of surface tension increasingly counteract the effects of gravity, thus promoting and extending the size of the annular film flow pattern region. In the case where the hydraulic diameter is decreased to 1.0 mm, the wavy flow regime is completely replaced by the annular film flow pattern.

The effect of hydraulic diameter on the wavy flow regime is shown in Figure 91. This figure clearly shows that as the hydraulic diameter decreases, the size of the wavy flow regime decreases. This regime occupies the major portion of the 4 x 4 mm tube map. As the hydraulic diameter is decreased from 4.0 mm to 2.0 mm, the size of the wavy flow regime region decreases dramatically. And in the case of the 1.0 mm hydraulic diameter tube, the wavy flow

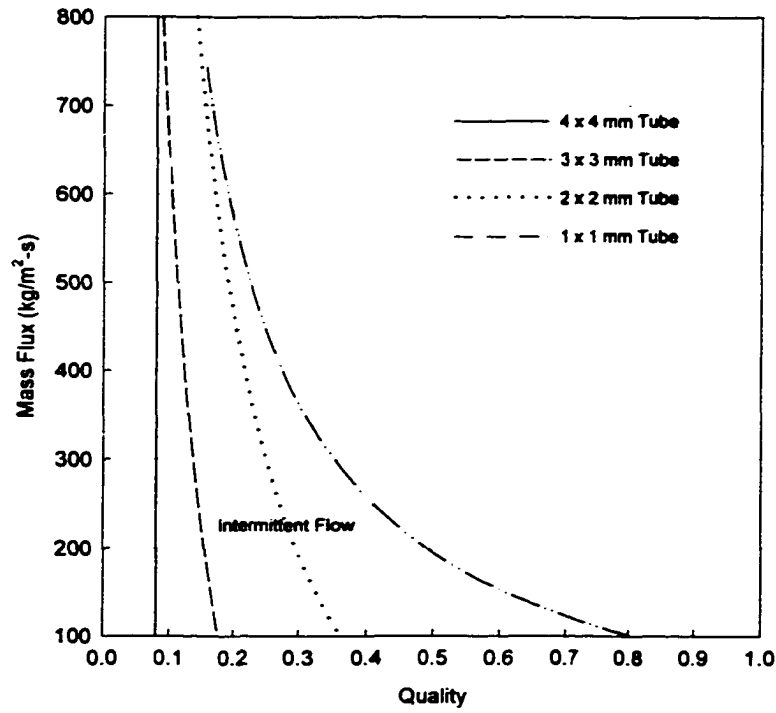


Figure 89. Intermittent Flow Regime Transition for the 4 x 4, 3 x 3, 2 x 2 and 1 x 1 mm Tubes

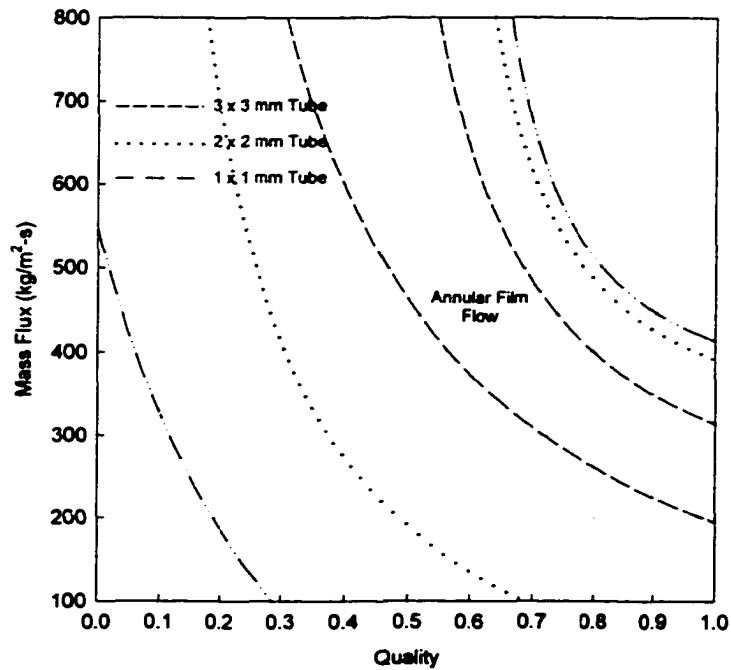


Figure 90. Effect of Hydraulic Diameter on the Annular Film Flow Pattern

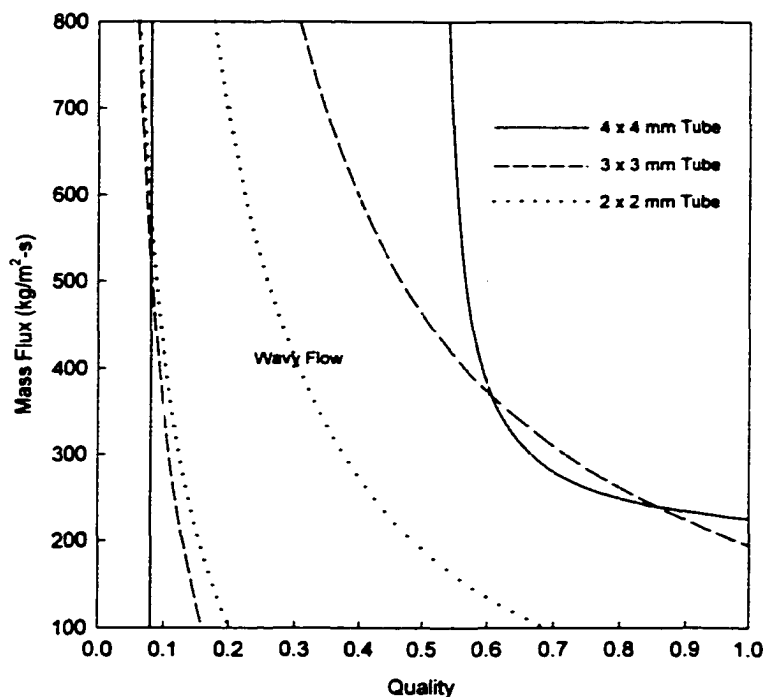


Figure 91. Effect of Hydraulic Diameter on the Wavy Flow Regime

regime is not observed at all. In addition to the effect on the size of the wavy flow regime, the hydraulic diameter also has a strong effect on the flow patterns within the wavy flow regime. Figures 87, 92 and 93 show the progression of the waves within the wavy flow regime from discrete to disperse in the 4 x 4, 3 x 3, and 2 x 2 mm square tubes, respectively. As mentioned above, a scale from zero to three was used here to distinguish between discrete and disperse waves, where a zero represents a highly discrete and clearly identifiable single waveform (with no secondary waves) and three represents a disperse waveform. These figures with each data point identified by a 0, 1, 2 or 3, show that as the hydraulic diameter is decreased from 4.0 mm (Figure 87) to 3.0 mm (Figure 92), not only does the size of the wavy flow regime decrease, but also the overall effect is to move from more disperse waves to more discrete waves. Furthermore, in the case of a hydraulic diameter of 2.0 mm (Figure 93), the wavy flow regime is again reduced in size and the waves are all discrete in nature, with an absence of the disperse wave flow pattern. From these graphs, it is apparent that the effect of decreasing diameter is twofold. First, the overall size of the wavy flow regime region is smaller, and second, the wave patterns tend toward discrete waves. It could be postulated that surface tension plays a role in both these trends. Surface tension might have the effect of stabilizing the waves. Thus, as the

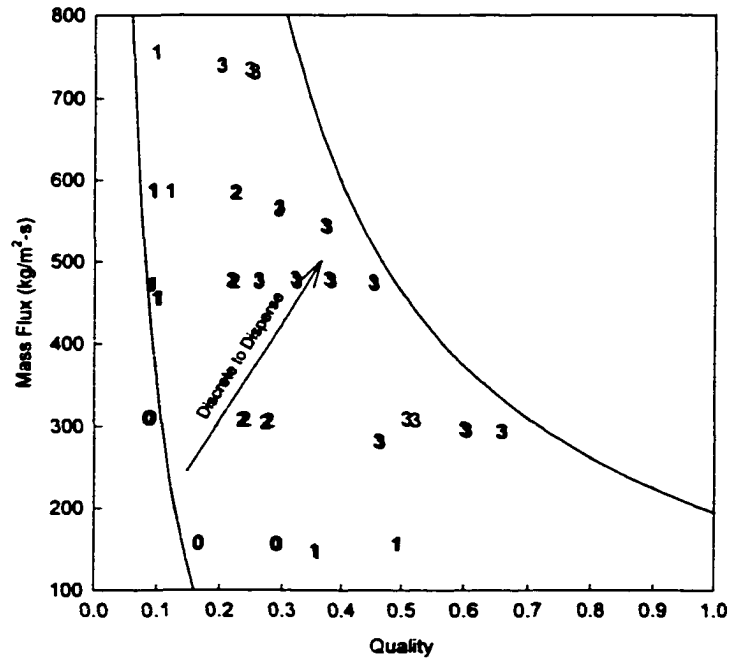


Figure 92. Progression From Discrete (0) to Disperse (3) Waves: 3 x 3 mm Square Tube

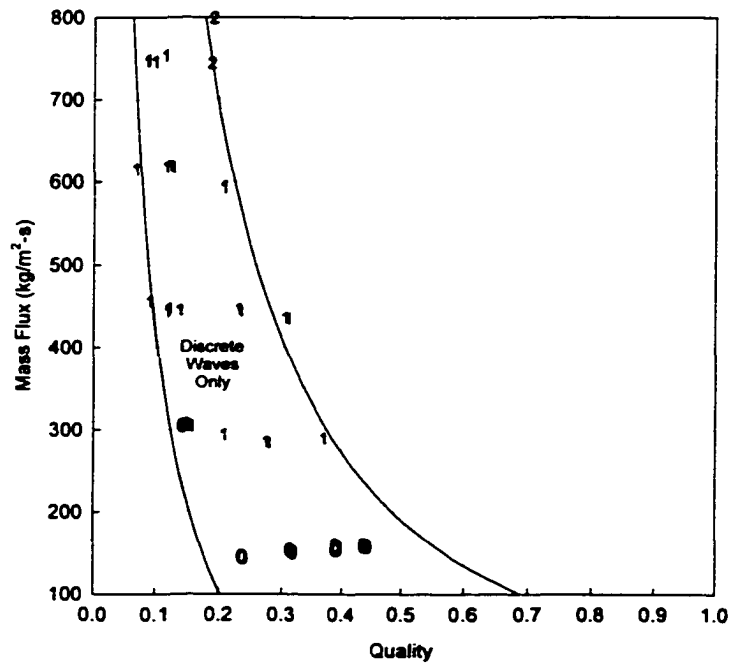


Figure 93. Progression From Discrete (0) to Disperse (3) Waves: 2 x 2 mm Square Tube

hydraulic diameter decreases, the greater prominence of surface tension causes the waves to become more discrete. Furthermore, as the hydraulic diameter decreases, the wavy flow regime is replaced by the annular film pattern as more liquid is held in the sharp corners of the smaller tubes and along the entire circumference of the tube, rather than preferentially at the bottom of the tube, as would be the case in the wavy flow regime.

Figure 94 depicts the effect of the hydraulic diameter on the mist flow pattern (the mist flow pattern exists above the transition lines shown in this figure). In larger diameter tubes the mist flow pattern occurs at relatively high qualities. As the hydraulic diameter is decreased, this pattern is extended to lower qualities. In the case of the 1 x 1 mm square tube, this pattern covers nearly 40% of the flow regime map. It should however be noted that in the smaller hydraulic diameter tubes, the mist flow pattern and the annular film flow pattern are both observed simultaneously for a large number of data points. In fact, when viewing the individual flow regime maps for the four square tubes (Figures 18 - 21), it can be seen that the region in which the mist flow pattern occurs by itself (the region in which there is no overlapping with the annular film flow pattern) actually decreases in size as the hydraulic diameter is decreased. This implies that as the hydraulic diameter is decreased, the liquid droplets entrained in the mist

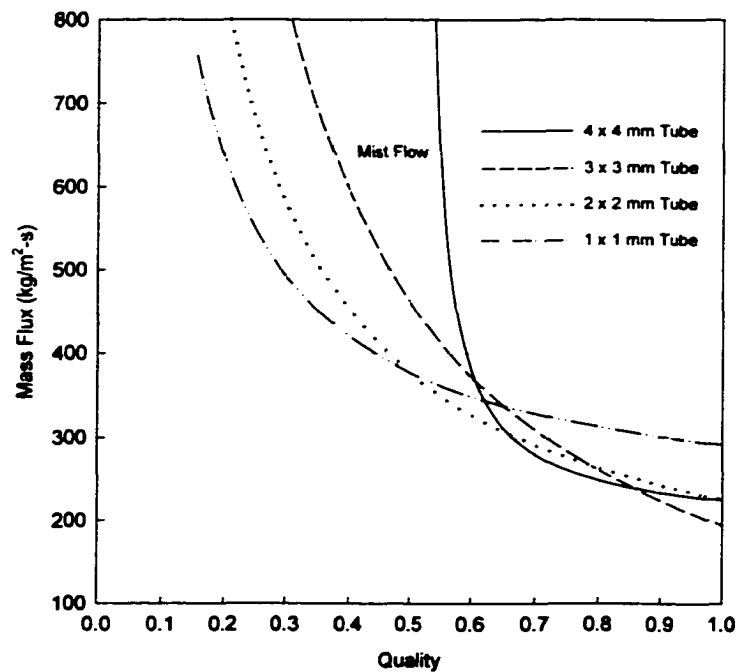


Figure 94. Effect of Hydraulic Diameter on the Mist Flow Pattern

deposit themselves more readily in the corners and walls of the tube surface. This could be because of the increase in the ratio of the exposed wall perimeter to the cross sectional area of the tube as the hydraulic diameter decreases ($\text{Ratio} = 4L/L^2$). Thus, the likelihood of the droplets coalescing on the tube wall increases as the hydraulic diameter decreases. For example, in the 4 x 4 mm square tube, the ratio of the wall perimeter to the total cross sectional area is equal to 1.0 whereas in the 1 x 1 mm square tube, this ratio is increased by a factor of 4. The combination of the decrease in the hydraulic diameter (increase in the ratio of the wetted perimeter to the cross sectional area) and the counteracting surface tension and gravity forces together explain the increase in the total area of the mist flow pattern and the reduction in the area in which the mist flow pattern occurs alone.

Effect of Aspect Ratio on Transition Lines

To determine the effect of aspect ratio on flow regimes, two rectangular tubes with different hydraulic diameters were tested in one orientation, and then rotated by 90 degrees and tested again. This resulted in four flow regime maps including the 2 x 4 mm tube ($\alpha = 0.5$), 4 x 2 mm tube ($\alpha = 2.0$), 4 x 6 mm tube ($\alpha = 0.67$) and the 6 x 4 mm tube ($\alpha = 1.5$). Here, the aspect ratio (α) is defined as the tube height divided by the tube width. Figure 95 shows the effect of the aspect ratio on the intermittent regime for the two hydraulic diameters. In the 2 x 4 mm and 4 x 2 mm tubes, the larger aspect ratio results in a slight increase in the size of the intermittent regime for all mass fluxes tested. In the 4 x 6 mm and 6 x 4 mm tubes, the larger aspect ratio results in a slight increase in the size of the intermittent regime at the lower mass fluxes, and a small reduction in the size of this regime at the higher mass fluxes. These effects are however very small, and it can be concluded that this transition line is only weakly dependent on the aspect ratio.

Figure 96 shows the effect of the aspect ratio on the annular film flow pattern. In both cases, the smaller aspect ratio results in a larger annular film flow pattern region, which is to be expected because of the reduced influence of gravity for the tubes with the smaller height. Also, this increase is more pronounced in the smaller hydraulic diameter tube (2 x 4 mm or 4 x 2 mm). This is perhaps due to the greater influence of surface tension in the smaller hydraulic diameter tube. Also, as discussed above in the description of the individual flow regime maps, the annular film flow pattern was observed by itself only in the 2 x 4 mm tube. In the other three cases, the annular film flow pattern is found only in coexistence with the mist flow pattern.

The effect of the aspect ratio on the wavy flow regime is shown in Figure 97. For both of the hydraulic diameters tested, the smaller aspect ratio results in a smaller wavy flow regime, which may be viewed as a corollary to the above-mentioned effect on the size of the annular film flow region. This effect is more pronounced in the smaller hydraulic diameter tube than in the

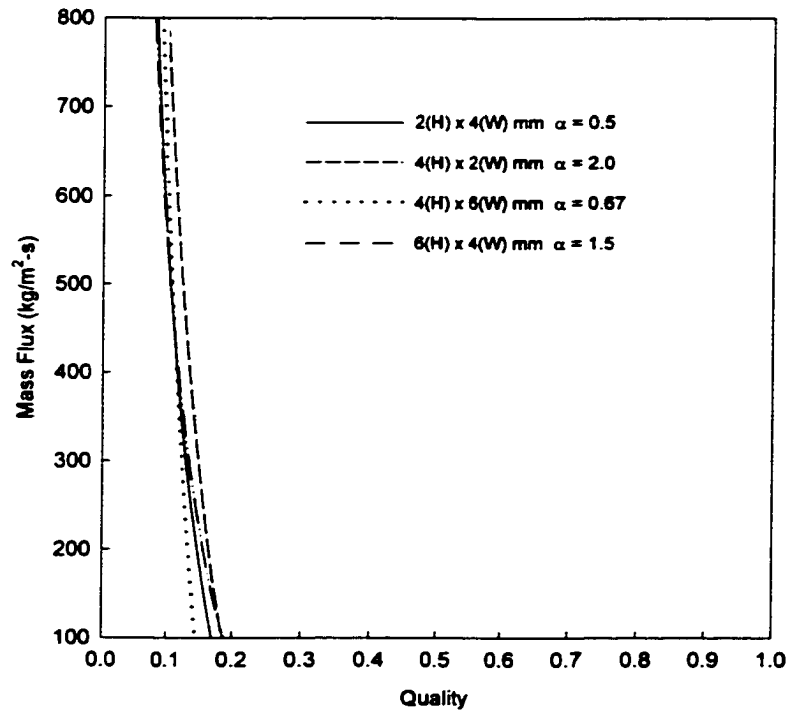


Figure 95. Effect of Aspect Ratio on the Intermittent Regime

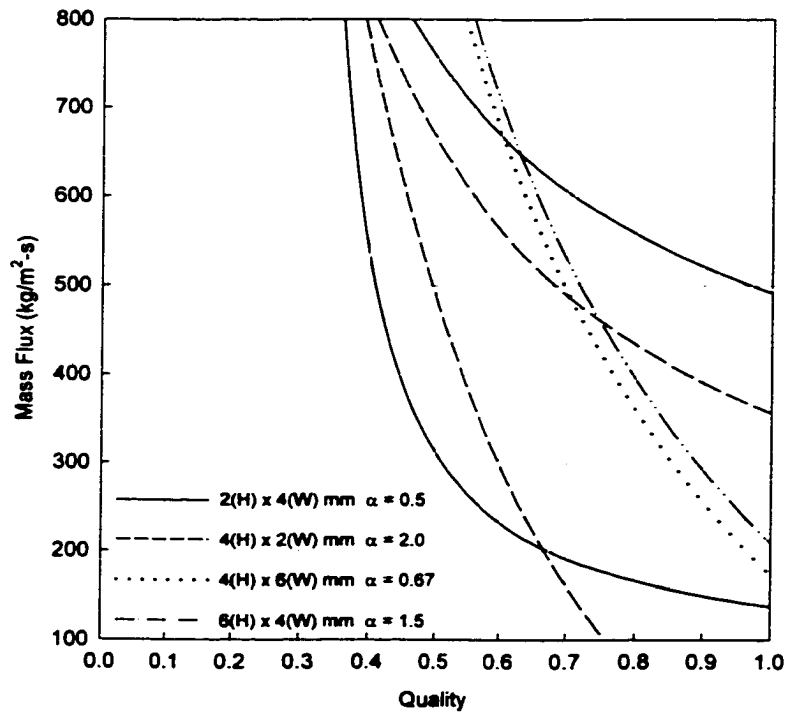


Figure 96. Effect of Aspect Ratio on the Annular Film Flow Pattern

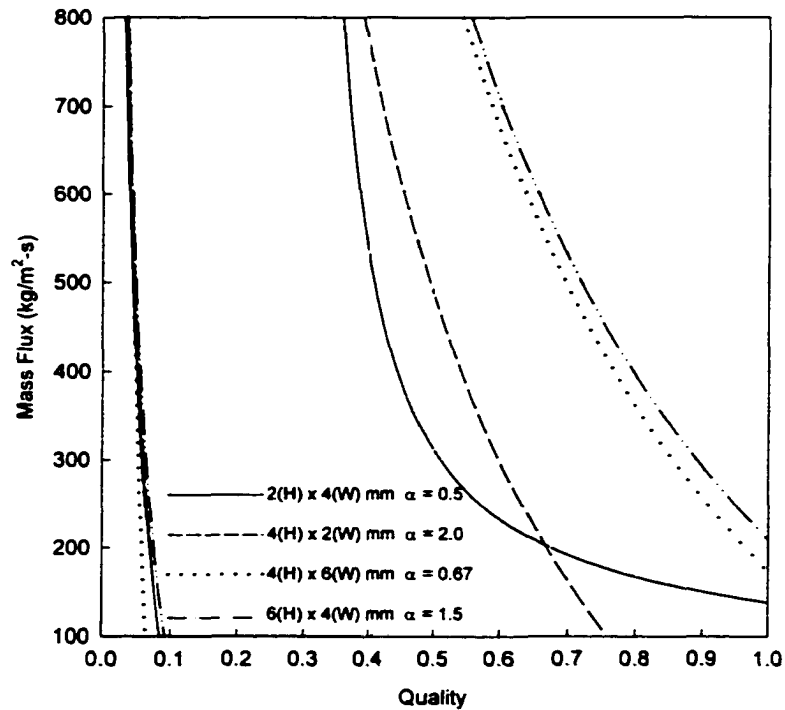


Figure 97. Effect of Aspect Ratio on the Wavy Flow Regime

larger hydraulic diameter tube. Within the wavy flow regime, the types of waves (progressing from discrete to disperse) observed at each data point are shown in Figures 98 to 101 for the two tubes. These figures show that while the smaller aspect ratio results in a smaller wavy flow regime, the larger aspect ratio results in a higher concentration of discrete waves.

The effect of aspect ratio on the mist flow pattern is shown in Figure 102, where mist flow exists above the lines in the graph. In both cases, the smaller aspect ratio causes the mist flow pattern to extend to the lower mass fluxes, and this effect is more pronounced in the smaller hydraulic diameter tubes. At the higher mass fluxes, the effect of the aspect ratio is negligible.

Flow Regime Transition Correlations in Microchannel Geometries

In this section, the flow regime transitions observed in this study are compared with transition correlations found in the literature, and specific criteria for flow regime transitions in microchannel geometries are presented. The hydraulic diameters of extruded microchannel condenser tubes are typically much less than 1.0 mm and it was shown above that there are two primary flow regimes found in these small hydraulic diameter microchannel geometries: the intermittent regime (the plug and slug flow patterns) and the annular regime (the annular film and mist flow patterns). For hydraulic diameters less than 2.0 mm, the wavy flow regime was not observed. Thus, specific attention will be given to these two flow regimes.

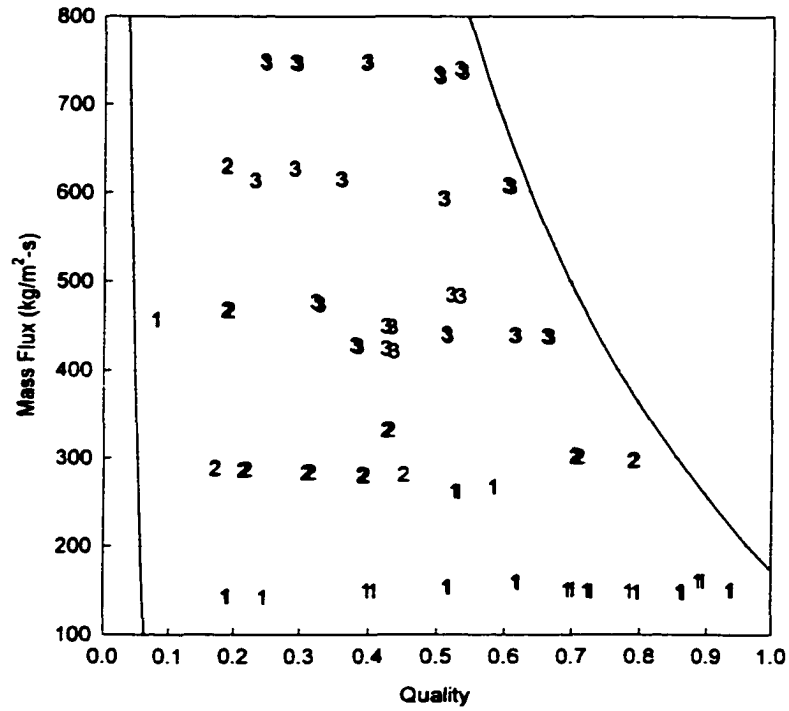


Figure 100. Progression From Discrete (0) to Disperse (3) Waves: 4(H) x 6(W) mm Rectangular Tube

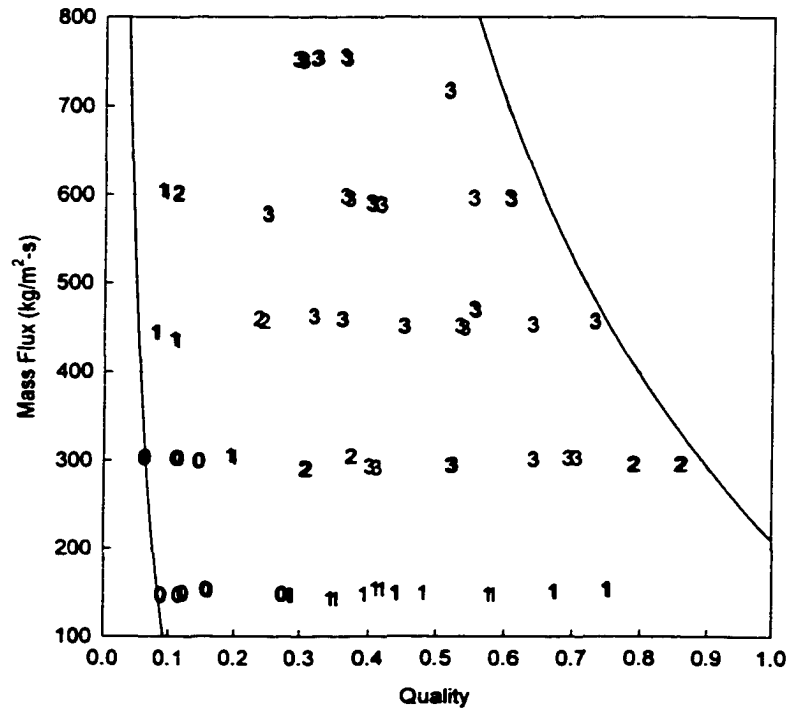


Figure 101. Progression From Discrete (0) to Disperse (3) Waves: 6(H) x 4(W) mm Rectangular Tube

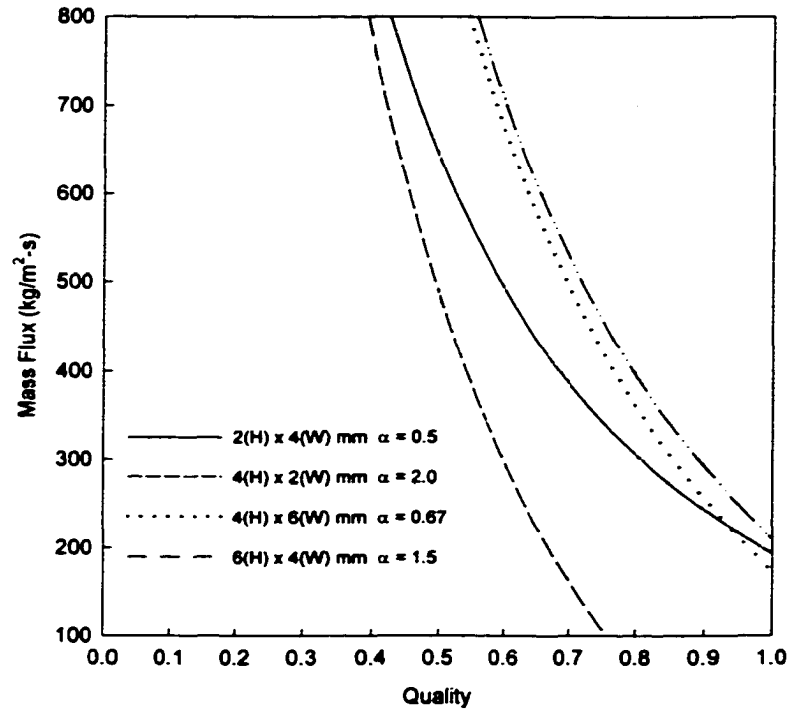
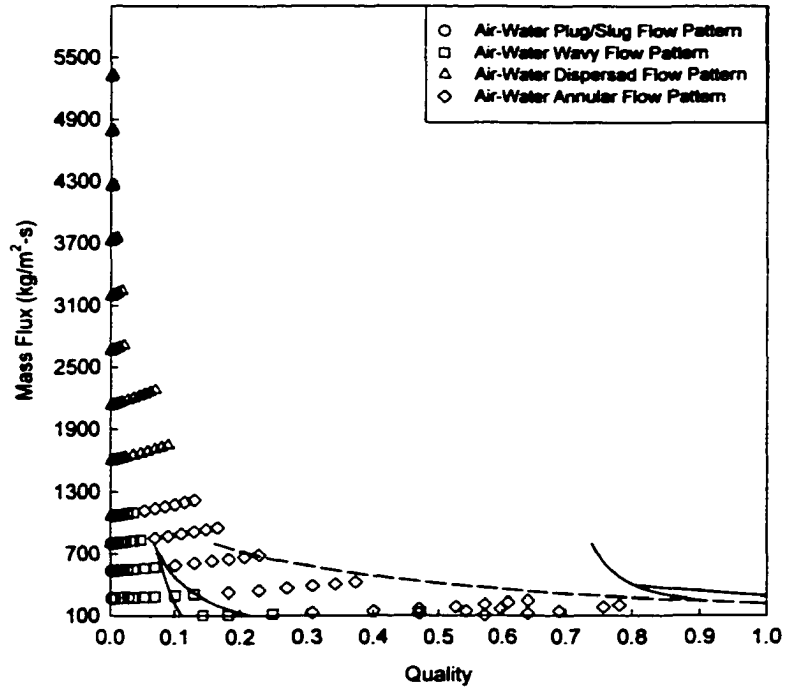
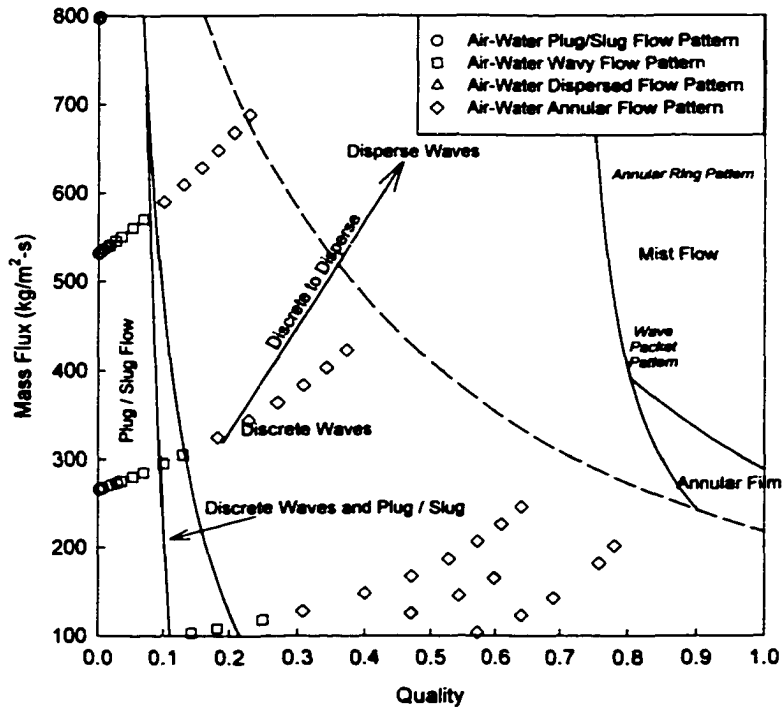


Figure 102. Effect of Aspect Ratio on the Mist Flow Pattern

Figure 103(a) shows the air-water data and refrigerant flow pattern transition lines from the present work using the G - x scales. The air-water data extend to much higher mass fluxes ($5,500 \text{ kg/m}^2\text{-s}$) compared to the maximum flux for the refrigerant data of $800 \text{ kg/m}^2\text{-s}$. However, these high mass air-water data are available only at qualities less than about 15 percent. At higher qualities, the mass flux for the air-water data is less than $700 \text{ kg/m}^2\text{-s}$. The area of interest for the refrigerant flow patterns, therefore, occupies only a small portion of this graph. This is because, at the nominal test conditions, the ratio of the density of the liquid phase (water) to the density of the gas phase (air) is about 600, while the liquid/vapor density ratio for the refrigerant at the nominal saturation pressure of 1379 kPa (200 psi) is about 16. The low density of air implies that even at high volumetric flow rates of air, the quality remains low. Conversely, the data points at the high end of the mass flux scale in this graph are achieved due to the high density of the liquid phase. However, these high flux-low quality data are largely irrelevant to most space-conditioning condensation applications. Therefore, these data are re-plotted in Figure 103(b), showing the scale that is relevant to the present study. This figure shows that none of the air-water data lie above the discrete-to-disperse wave transition line. Once again, this is because high qualities and high mass fluxes are difficult to sustain



(a). Full Scale View



(b). Relevant Subset

Figure 103. Superposition of the Air-Water Data on the R-134a Flow Map

simultaneously in the air-water case. Below this line, there are some predictable trends. Intermittent (slug/plug) flow occupies the same low quality region for both fluid combinations, but this regime extends to higher qualities in the refrigerant flow case. The wavy-annular flow data for air-water approximately correspond to the transition region in the present study where discrete waves and plug/slug flow coexist. The data corresponding to the air-water annular flow case fall into the region where the refrigerant exhibits the discrete wave flow pattern. However, as was stated above, in the present study, most of the wavy flow cases exhibited an annular ring of liquid around the tube circumference, and other investigators have chosen to characterize such flows as annular flows.

The data from the present study are plotted using superficial velocity scales and the air-water transition lines in Figure 104. This figure also shows that the superficial velocities of the refrigerant data are much lower than those investigated in the air-water study; thus, there are no data points in the dispersed and bubble flow regimes. The data occupying the region corresponding to air-water wavy-annular flow are primarily the refrigerant data exhibiting mist flow and disperse wave flow. As was stated above, most of these refrigerant flows do exhibit an annular liquid ring. Thus, some of these differences can be attributed to the different categorizations adopted in the present study for the non-adiabatic refrigerant flows, such as the classification of different types of wavy flow patterns (even with annular rings) as a wavy flow regime. Figure 104 also shows that the discrete wave refrigerant data occupy the air-water intermittent flow regime. It was noticed during the refrigerant flow visualization experiments in the present study that as the mass flux and quality was reduced, discrete wave flow was a precursor to intermittent flow. Large discrete waves eventually crest at the upper wall of the tube to form intermittent slugs. The overall conclusion that can be drawn from this graph is that the transitions between the respective flow regimes and patterns occur at lower gas and liquid superficial velocities than the air-water flow regime map would indicate. Stated otherwise, it appears that due to the above-mentioned significant difference in properties such as phase densities in the air-water and refrigerant cases, superficial velocities alone may not be adequate in plotting the flow regime map for the refrigerant. This issue was investigated further by comparing the data versus several relevant non-dimensional parameters and transition criteria.

Taitel and Dukler (1976) assume the transition from an intermittent regime to a wavy regime (or annular regime in air-water systems) occurs at a liquid level height of 0.5. This corresponds to a constant value of the Martinelli parameter, X . The data show that the transition from an intermittent flow, however, more closely follows a near vertical line on the u_g^* and u_l^* axes, which represents a constant value of the Froude number, rather than a constant value of the Martinelli parameter, X . Many researchers have concluded that the transition from an

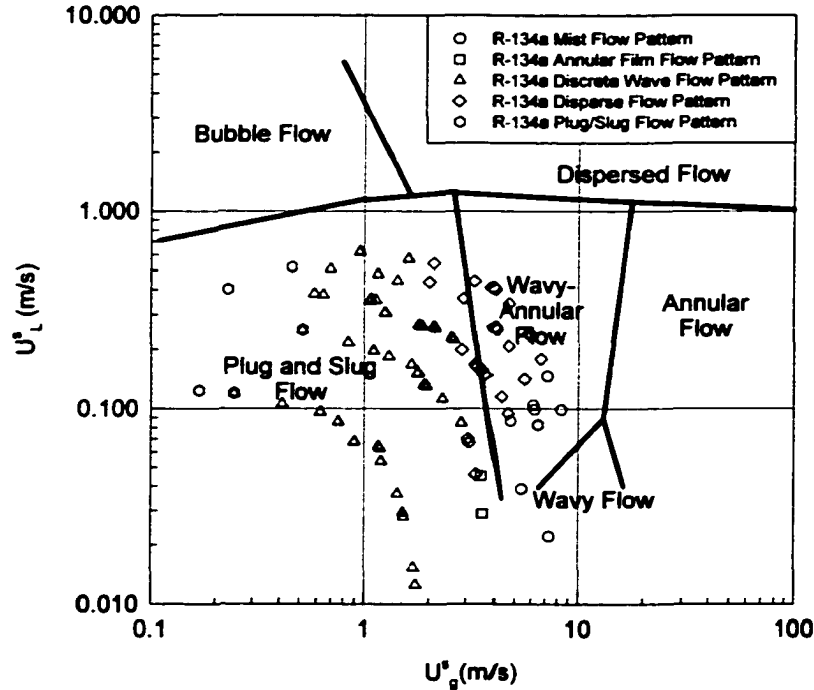


Figure 104. Comparison of Superficial Velocities for R-134a Data With Air-Water Transition Lines

intermittent regime to a wavy regime or annular regime (wavy-annular regime in air-water systems) occurs at a nearly constant value of Froude number (Traviss and Rohsenow, 1973, Weisman et al, 1979, Soliman, 1982, Dobson et al, 1994). The Froude number represents the ratio of inertia forces to gravity forces and has been defined in various ways with researchers using the Martinelli parameter (Dobson et al, 1994), the superficial gas velocity (Weisman et al 1979 – refer to Figure 70), or the two-phase density (Friedel, 1979).

At a representative mass flux of $450 \text{ kg/m}^2\text{-s}$ and a quality of 50 percent, the Froude number of the air-water system is 9 times larger than that of the R-134a system. Thus, gravitational forces are relatively stronger in the R-134a system, extending the wavy regime to higher qualities and delaying the transition to the annular regime. Furthermore, for the transition from the wavy regime to the annular regime to occur at a near constant value of Froude number, this transition will occur at a substantially lower quality on the G-x plot for the air-water system compared to the refrigerant case. This is borne out by the plot shown in Figure 103(b). A comparison of the Bond numbers ($Bo = g(\rho_1 - \rho_2)D_h^2/\sigma$) for the two cases also confirms this conclusion. The Bond number is the ratio of gravity forces to surface tension forces, and is approximately 16 times higher for the refrigerant than for the air-water mixture. Thus, relatively

higher gravitational forces for R-134a lead to a larger wavy flow region. Also, the shift in the wavy flow regime toward the lower qualities in the air-water case can be reasoned based on the discussion of superficial velocities given above. The superficial velocity of the air at the same quality is substantially higher than that of the refrigerant vapor. This implies that the more dominant shear forces will trigger the transition from the intermittent flow regime to the wavy flow regime at a much lower quality in the air-water system. This is also true for the transition from the wavy flow regime to the annular flow regime.

The Transition From Intermittent Flow

Traviss and Rohsenow (1973) developed a correlation for the transition from intermittent flow to annular flow based upon a momentum balance on the liquid film. The Froude number for the liquid film is defined as:

$$Fr_l^2 = \frac{\bar{V}_l^2}{g\delta} \quad (58)$$

where \bar{V}_l is the average velocity of the liquid film and δ is the film thickness. They used the von Karman universal velocity profile for the liquid film velocity, which is given by:

$$v^+ = y^+ \quad 0 < y^+ < 5 \quad (59a)$$

$$v^+ = -3.05 + 5 \ln y^+ \quad 5 < y^+ < 30 \quad (59b)$$

$$v^+ = 5.5 = 2.5 \ln y^+ \quad y^+ > 30 \quad (59c)$$

and the variables v^+ and y^+ are defined as:

$$v^+ = \frac{v_l}{u_\tau} \quad y^+ = \frac{y u_\tau}{\nu_l} \quad (60)$$

The Reynolds number of the liquid film is given by:

$$Re_l = \frac{G(1-x)D_{hyd}}{\mu_l} \quad (61)$$

Using the Reynolds number of the liquid film and continuity, Traviss and Rohsenow (1973) redefined the Froude number as follows:

$$Fr_l^2 = \frac{Re_l^2}{16g\nu_l} \left(\frac{u_\tau}{\delta^+} \right)^3 \quad (62)$$

The non-dimensional thickness of the liquid film, δ^+ , and the Reynolds number of the liquid film are related using continuity as follows:

$$\text{Re}_l = 4 \int_0^{\delta^+} v^+ dy^+ \quad (63)$$

By substituting equations (59 a-c) into equation (62), Traviss and Rohsenow relate the non-dimensional film thickness to the liquid Reynolds number as follows:

$$\text{Re}_l = 2(\delta^+)^2 \quad 0 < \delta < 5 \quad (64a)$$

$$\text{Re}_l = 50 - 32.2\delta^+ + 20\delta^+ \ln \delta^+ \quad 5 < \delta < 30 \quad (64b)$$

$$\text{Re}_l = -256 + 12\delta^+ + 10\delta^+ \ln \delta^+ \quad \delta > 30 \quad (64c)$$

The relationships given above are approximated by Traviss and Rohsenow (1973) with an error less than 4% by:

$$\delta^+ = \sqrt{2} \text{Re}_l^{0.5} \quad 0 < \text{Re}_l < 50 \quad (65a)$$

$$\delta^+ = 0.482 \text{Re}_l^{0.585} \quad 50 < \text{Re}_l < 1125 \quad (65b)$$

$$\delta^+ = 0.095 \text{Re}_l^{0.812} \quad \text{Re}_l > 1125 \quad (65c)$$

The wall shear stress is related to the two-phase frictional pressure drop by:

$$\tau_o = -\frac{D_{hyd}}{4} \left(\frac{dP}{dz} \right)_f \quad (66)$$

and the two-phase pressure gradient is equal to the pressure gradient of the gas times a two-phase multiplier as follows:

$$\left(\frac{dP}{dz} \right)_f = \phi_g^2 \left(\frac{dp}{dz} \right)_g \quad (67)$$

Traviss and Rohsenow (1973) suggest using the following correlation from Soliman et al. (1968) for the two-phase multiplier:

$$\phi_g^2 = 1 + 2.85 X_{tt}^{0.523} \quad (68)$$

where X_{tt} is the Martinelli parameter defined as:

$$X_{tt} = \left(\frac{(dp/dz)_l}{(dp/dz)_g} \right)^{0.5} = \left(\frac{\mu_l}{\mu_g} \right)^{0.1} \left(\frac{1-x}{x} \right)^{0.9} \left(\frac{\rho_g}{\rho_l} \right)^{0.5} \quad (69)$$

By using this relationship in conjunction with the Lockhart and Martinelli two-phase pressure drop correlation, given by:

$$\left(\frac{dP}{dz}\right)_g = -\frac{4}{D_{hyd}} \left(\frac{0.045}{\text{Re}_g^{0.2}}\right) \frac{G^2 x^2}{2g_o \rho_g} \quad (70)$$

equations (61), (62), (66), (67), (68), and (69) may be combined to yield:

$$Fr_l^2 = \frac{[F(X_u)]^3 \text{Re}_l^{4.7}}{Ga(\delta^+)^3} \quad (71)$$

where $F(X_u)$ is equal to:

$$F(X_u) = 0.15 \left(\frac{\phi_g}{X_u}\right) = 0.15 \left(\frac{1 + 2.85 X_u^{0.524}}{X_u}\right) \quad (72)$$

where Ga is the Galileo number (ratio of gravity to viscous forces) defined by:

$$Ga = \frac{g \rho_l^2 D_{hyd}^3}{\mu_l^2} \quad (73)$$

By combining equation (71) and equations (65 a-c), Traviss and Rohsenow (1973) developed a set of transition criteria:

$$\text{Re}_l = 1.38 Ga^{0.31} Fr_l^{0.68} [F(X_u)]^{-0.94} \quad \text{Re} \leq 50 \quad (74a)$$

$$\text{Re}_l = 0.474 Ga^{0.34} Fr_l^{0.68} [F(X_u)]^{-1.02} \quad 50 < \text{Re} \leq 1125 \quad (74b)$$

$$\text{Re}_l = 0.0442 Ga^{0.44} Fr_l^{0.88} [F(X_u)]^{-1.33} \quad \text{Re} > 1125 \quad (74c)$$

They tested this correlation for the transition from intermittent flow to annular flow against R-12 data in an 8 mm I.D. tube as well as data from Soliman (1968). They found that this transition occurs at a constant value of Froude number equal to 45. This transition correlation is plotted against the current air-water data ($D_h = 5.50$ mm) and the R-134a data ($D_h = 4.91$ mm) in Figure 105. It appears that the transition correlation developed by Traviss and Rohsenow (1973) shows promise for both fluids.

Soliman (1982) modified the approach outlined by Traviss and Rohsenow (1973) and used a correlation for the liquid film thickness developed by Kosky (1971). The non-dimensional liquid film thickness is related to the Reynolds number by:

$$\delta^+ = 0.707 \text{Re}_l^{0.5} \quad \text{Re}_l \leq 1250 \quad (75a)$$

and

$$\delta^+ = 0.0504 \text{Re}_l^{0.875} \quad \text{Re}_l > 1250 \quad (75b)$$

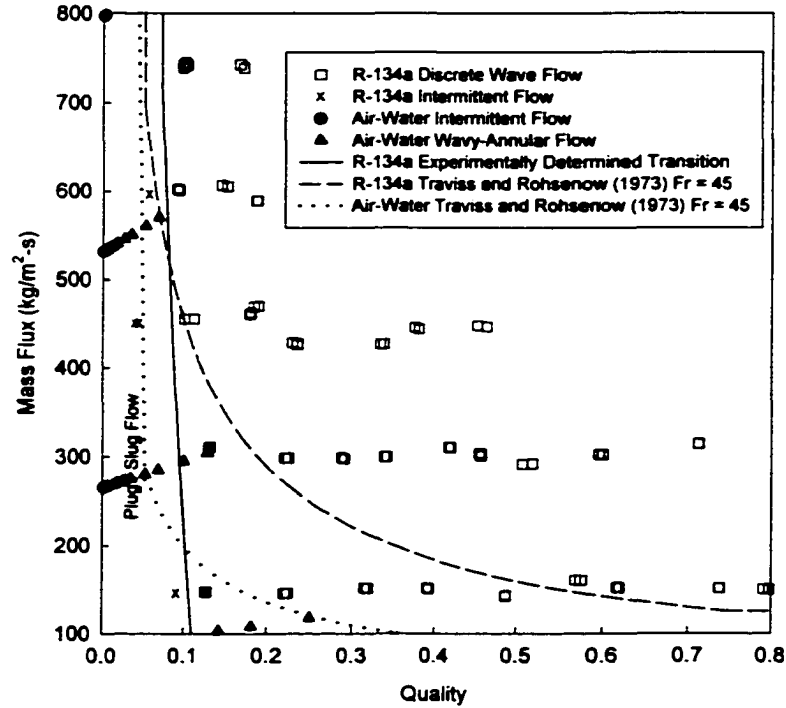


Figure 105. Transition From Intermittent Flow, Comparison with Travis and Rohsenow (1973)

The results of the analysis by Soliman (1982) yield a Froude number as follows:

$$Fr = 0.0244 Re_i^{1.60} \left[\frac{\phi_v}{X_{tt}} \right]^{1.5} \frac{1}{Ga^{0.5}} \quad Re_i \leq 1250 \quad (76a)$$

$$Fr = 1.28 Re_i^{1.04} \left[\frac{\phi_v}{X_{tt}} \right]^{1.5} \frac{1}{Ga^{0.5}} \quad Re_i > 1250 \quad (76b)$$

where:

$$\phi_v = 1 + 1.09 X_{tt}^{0.039} \quad (77)$$

It should be noted that the square of this term, ϕ_v^2 , is the two-phase multiplier. Soliman (1982) suggests that the transition from the intermittent flow regime to the wavy flow regime is best described by using equation (76) at a constant Froude number equal to 7. He tested this correlation against existing flow regime maps for R-12 ($D_h = 4.8$ mm, 12.7 mm, 13.4 mm and 15.9 mm), R-113 ($D_h = 4.8$ mm, 12.7 mm, and 15.9 mm), steam ($D_h = 13.4$ mm), and air-water ($D_h = 25.4$ mm) two-phase mixtures. He reported good agreement between the correlation and

the data, especially for the larger diameter tubes. This transition correlation is plotted against the current data for both the air-water and R-134a systems in Figure 106. It appears that for the small diameter ($D_h = 5.50$ mm, air/water; $D_h = 4.91$ mm, R134a), the Soliman (1982) correlation for transition over predicts the size of the intermittent regime.

While transition criteria based on a specific single value of Fr, as proposed by Travis and Rohsenow (1973) and Soliman (1982), did not predict the present data adequately, this approach has inherent merit, and was explored further in this study. Figures 107 – 110 show the R-134a data and air-water data for several diameters of tubes tested in this study. The experimentally determined transition lines for the R-134a experimental data are shown using solid lines in these figures. Constant Froude number lines with $Fr = 1.75$, are also shown for both fluids and it appears that the $Fr = 1.75$ criterion is successful in predicting the transition from the intermittent regime to the wavy-annular flow pattern in air-water mixtures ($D_h = 5.5$ mm), and a transition from the intermittent regime to the wavy regime in R-134a ($D_h = 4.91$ mm). Figure 108 shows the air-water and R-134a data for the 2.6 mm and 3.0 mm tubes, respectively. The two solid lines in Figure 108 represent the experimentally determined transition lines for the R-134a data. The intermittent regime exists to the left of these lines, while both the intermittent regime and the wavy-regime co-exist in the band formed by these two lines. This band extends from a Froude number of 2.7 to a Froude number of 4.5 and can be viewed as a transition region, rather than a transition line. The air-water transition is represented by a single line with $Fr = 2.7$. The 2.0 mm tube (R-134a) and the 1.75 mm tube (air-water data) are shown in Figure 109. The transition from intermittent flow to wavy-annular or wavy flow is well represented by a constant Froude number of 3.2 and the R-134a transition is represented by two lines which form a region where both the intermittent and wavy flow patterns co-exist. This band ranges from a Froude number of 3.2 to a Froude number of 9.0. Figure 110 shows the data for the 1.3 mm tube (air-water) and the 1.0 mm tube (R-134a). This figure shows that the transitions are well represented by a constant Froude number of 3.5. It should be noted that transition is from the intermittent regime to the annular film flow pattern. Similar to the other tubes shown in Figures 108-109, the transition from intermittent flow is represented by a region, rather than a line. In the larger tubes, this region consisted of both intermittent and wavy flows. In the smaller tube, however, because the wavy flow regime was replaced by the annular film flow pattern, this region now consists of intermittent and annular film flow. This region covers the range from a Froude number of 3.5 to a Froude number of 20. These findings are summarized in Table 16.

Wavy Flow Regime Boundaries

The wavy flow regime transition lines for several tubes tested in this study are shown in Figures 111 - 114. The solid lines in these figures indicate the experimentally determined

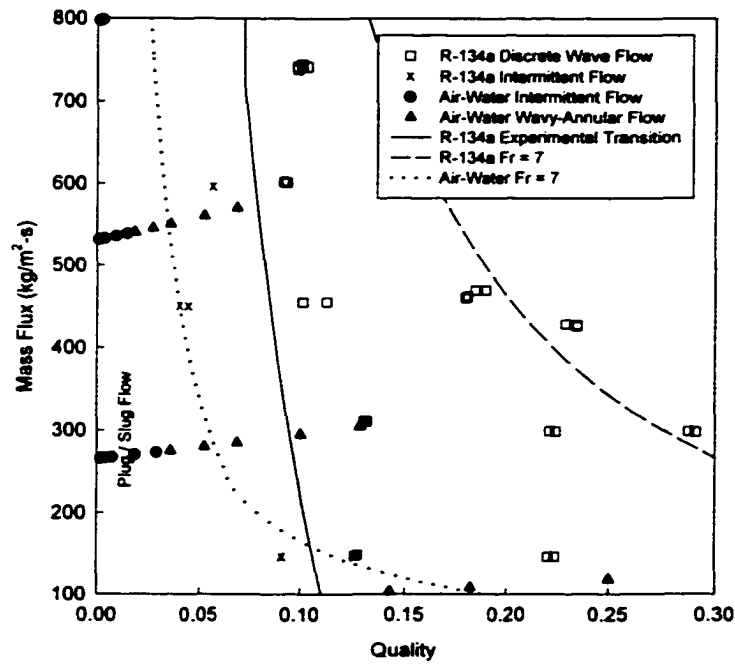


Figure 106. Transition From Intermittent Flow for Air-Water ($D_h = 5.5$ mm) and R-134a ($D_h = 4.91$ mm) Data Using $Fr=7$ (Soliman 1982 Criterion)

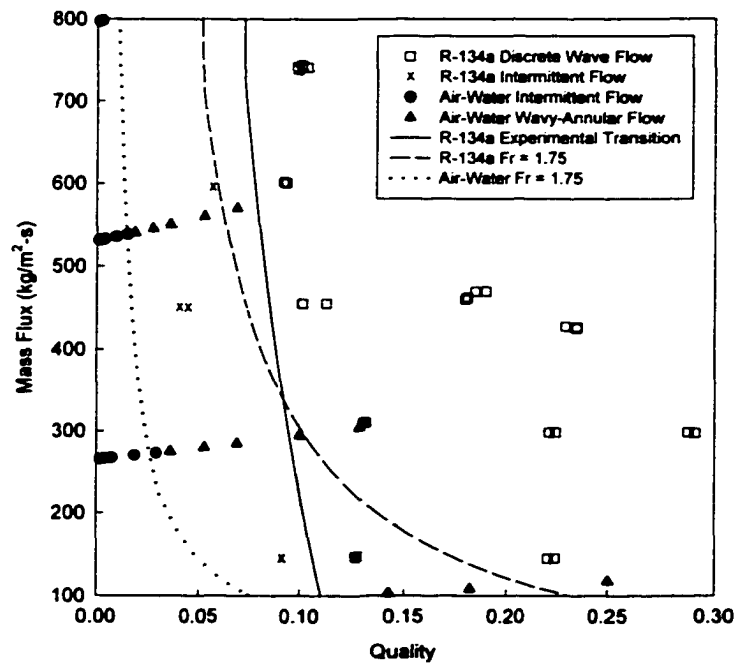


Figure 107. Transition from Intermittent Flow for Air-Water ($D_h = 5.50$ mm) and R-134a ($D_h = 4.91$ mm)

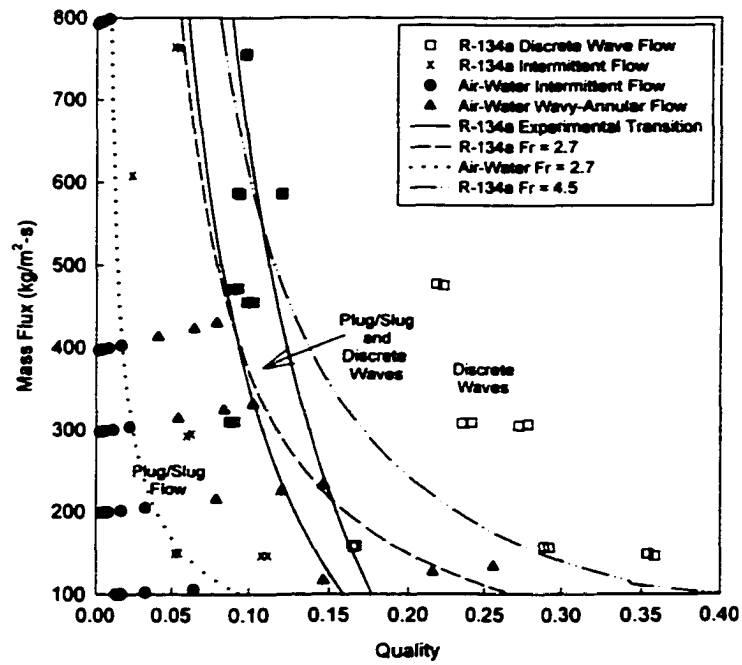


Figure 108. Transition from Intermittent Flow for Air-Water ($D_h = 2.60$ mm) and R-134a ($D_h = 3.0$ mm)

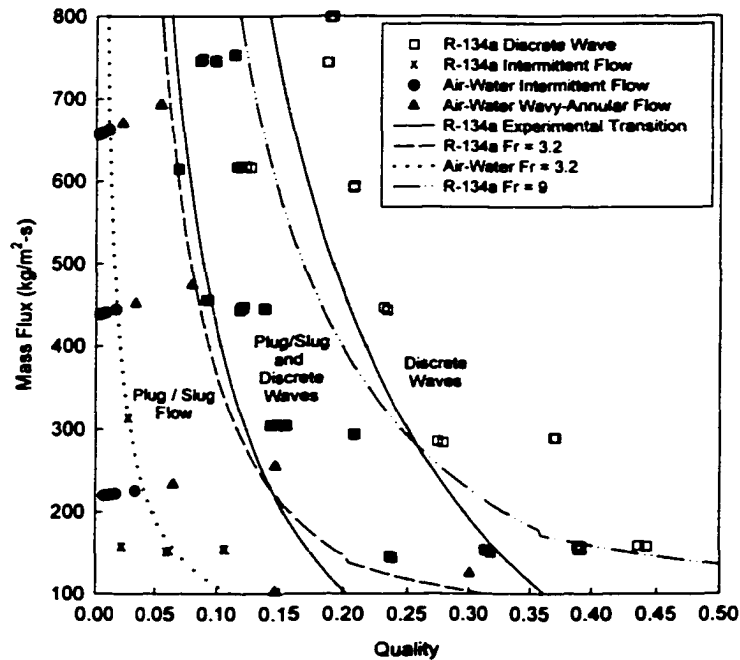


Figure 109. Transition from Intermittent Flow for Air-Water ($D_h = 1.75$ mm) and R-134a ($D_h = 2.0$ mm)

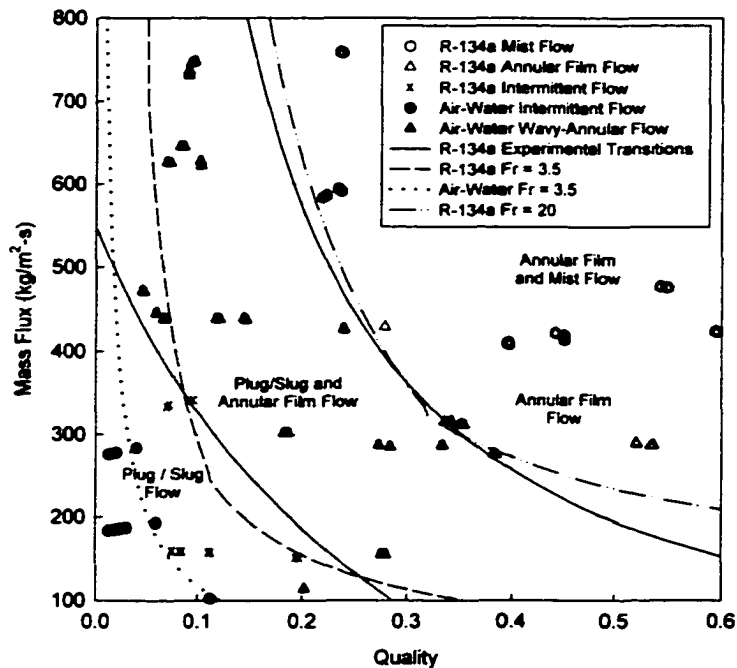


Figure 110. Transition from Intermittent Flow for Air-Water ($D_h = 1.30$ mm) and R-134a ($D_h = 1.0$ mm)

transition lines. Data from the 4.91 mm tube (R-134a) and the 5.5 mm tube (air-water) are shown in Figure 111. In this figure, it appears that for air-water mixtures, the transition from a wavy-annular flow to an annular flow pattern occurs at a constant Froude number equal to 18. In addition, the transition from discrete to disperse waves in R-134a also occurs at this same Froude number. Figure 112 compares the theoretical and experimental transition lines for air-water (2.6 mm tube) and R-134a (3.0 mm tube). The transition from intermittent flow to wavy flow can be represented very well by a constant Froude number of 2.6. The transition from wavy-annular flow to annular flow in air-water occurs at $Fr = 20$, and this also coincides with a transition from discrete waves to disperse waves in R-134a. Thus, in the R-134a system, the discrete waves are found in a region bounded by constant Froude numbers of 2.6 and 20.

Figure 113 compares the theoretical and experimental transition lines for the 1.75 mm tube (air-water mixtures) and the 2.0 mm tube (R-134a). The transition from the intermittent regime to the wavy regime occurs at a Froude number of 3.5. Both the transition from wavy-annular to annular flow in air-water, and the transition from discrete waves to annular film flow in R-134a occur at a Froude number of 18, and there is good agreement between the theoretical

and the experimental transitions. The R-134a flow visualization experiments for the smallest tube (1.0 mm) showed that the wavy regime was replaced by the annular film flow pattern. The air-water and R-134a data for the 1.30 mm and 1.0 mm tubes, respectively, are shown in Figure 114. Both the transition from wavy-annular flow to annular flow (air-water mixtures) and the transition from intermittent flow to annular film flow (R-134a) are well represented by a constant Froude number of 20. These findings are summarized in Table 17.

Table 16. Summary of the Non-Dimensional Transition Criteria for Intermittent Flow Developed in This Study

D_h (mm)		Fr		Transition	
Air/Water	R-134a	Air/Water	R-134a	Air/Water	R-134a
5.50	4.91	1.75	1.75	Intermittent to Wavy-Annular	Intermittent to Wavy Flow
2.60	3.0	2.70	2.70	Intermittent to Wavy-Annular	Intermittent to Wavy Flow
---	3.0	---	2.7 - 4.5	---	Intermittent and Wavy Co-exist
1.75	2.0	3.2	3.2	Intermittent to Wavy-Annular	Intermittent to Wavy Flow
---	2.0	---	3.2 - 9	---	Intermittent and Wavy Co-exist
1.30	1.0	3.5	3.5	Intermittent to Wavy-Annular	Intermittent to Annular Film
---	1.0	---	3.5 - 20	---	Intermittent and Annular Film Co-exist

Table 17. Summary of the Non-Dimensional Transition Criteria for Wavy Flow Developed in This Study

D_h (mm)		Fr		Transition	
Air/Water	R134a	Air/Water	R134a	Air/Water	R-134a
5.50	4.91	18	18	Wavy Annular To Annular	Discrete To Disperse Waves
2.6	3	20	20	Wavy Annular To Annular	Discrete To Disperse Waves
1.75	2	18	18	Wavy Annular To Annular	Disc. Wave to Annular Film
1.3	1	20	20	Wavy Annular To Annular	Intermittent to Annular Film

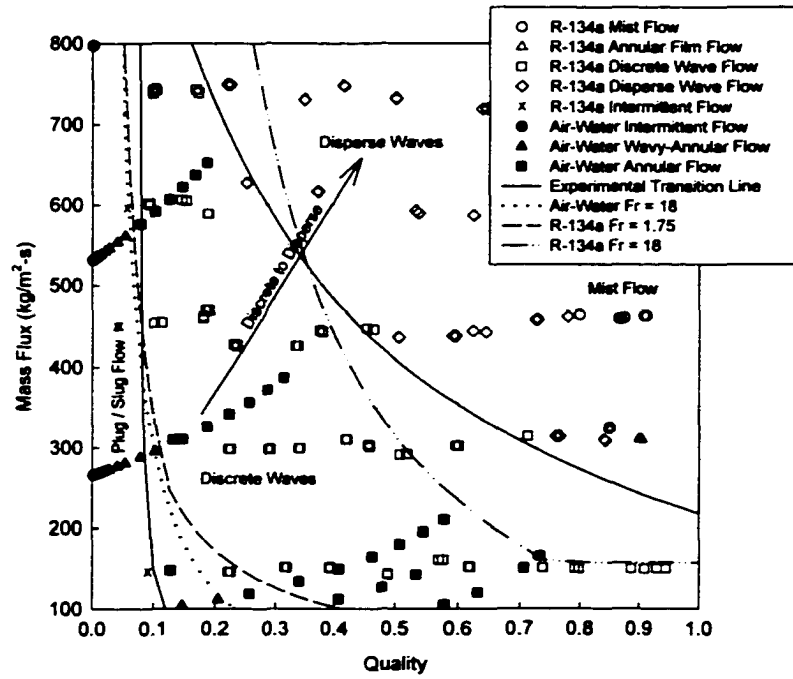


Figure 111. Wavy Flow Regime Boundaries for Air-Water ($D_h = 5.50$ mm) and R-134a ($D_h = 4.91$ mm)

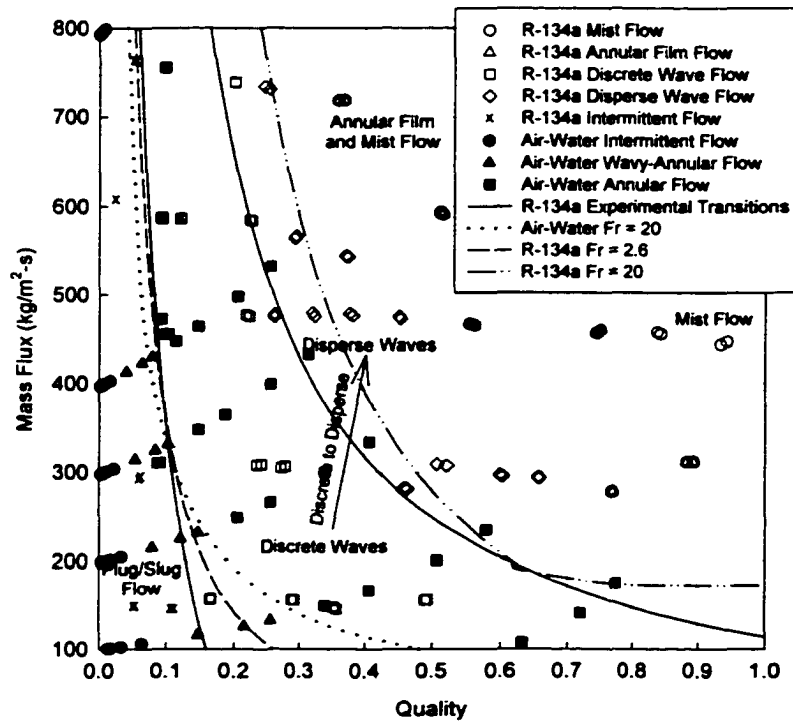


Figure 112. Wavy Flow Regime Boundaries for Air-Water ($D_h = 2.6$ mm) and R-134a ($D_h = 3.0$ mm)

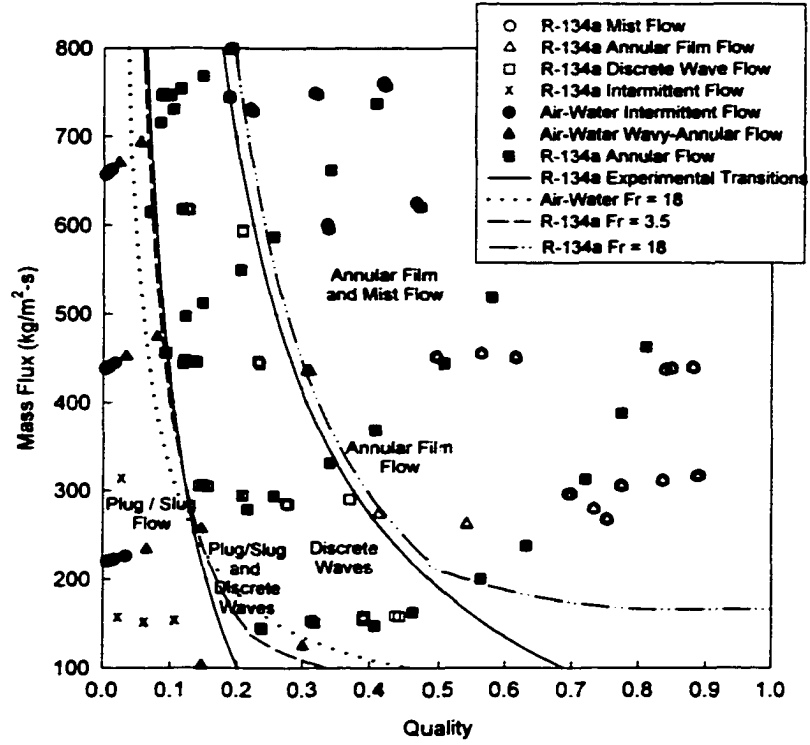


Figure 113. Wavy Flow Regime Boundaries for Air-Water ($D_h = 1.75$ mm) and R-134a ($D_h = 2.0$ mm)

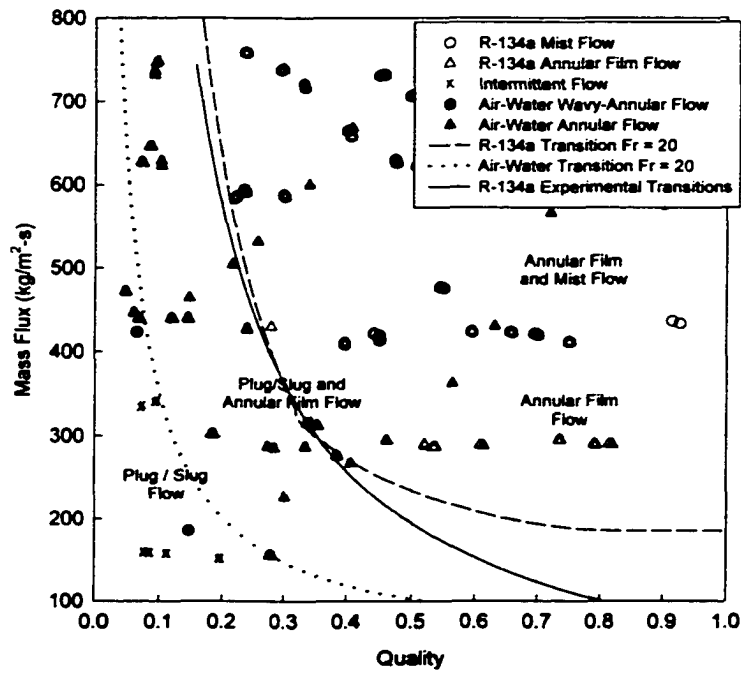


Figure 114. Transition to Annular Flow in Air-Water ($D_h = 1.3$ mm) and R-134a ($D_h = 1.0$ mm)

Transition to Annular Film and Mist Flow

Constant Froude number lines were used to model the experimentally determined transition lines. The Froude number represents the ratio of surface tension to gravity forces. While the Froude number basis is primarily valid for transition to and from gravity dominated flow regimes, this method showed good agreement with shear dominated flow regimes, even though the fundamental basis for this method is not very clear. Other approaches to modeling the flow regime transitions were attempted including liquid and gas Reynolds numbers and the Weber number with less than satisfactory results.

It should be noted that in the air-water study, no further distinctions were made within the annular flow regime. Therefore, the transition lines presented here are for the R-134a data. The refrigerant R-134a transitions to annular film flow and mist flow are shown in Figures 115 – 118. Solid lines indicate the experimentally determined transition lines. In Figure 115, the transition to the mist flow pattern is shown for the 4.91 mm tube. The transition to mist flow is best represented by a constant Froude number of 65. As seen in this figure, the theoretical line predicts a transition at a slightly higher quality than found in the experiments. The general shape of the two regions is similar, however, and the theoretical line appears to do an adequate job in predicting the transition from the wavy regime to the annular regime (mist flow pattern). The transition to the annular film and mist flow pattern for the 3.0 mm tube is shown in Figure 116. Good agreement between the theoretical and experimental transition lines was found. The transition to the annular film flow pattern occurs at a constant Froude number of 35 and extends to a Froude number of 65. Beyond a Froude number of 65, only the mist flow pattern was observed. The transition to annular flow in the 2 mm tube is shown in Figure 117, and good agreement between the theory and the experiments was found. The annular film flow pattern occurs at a constant Froude number of 17 and extends to a Froude number of 100. For Froude numbers larger than 100, only the mist flow pattern is found. The transition to annular flow and mist flow for the 1 mm tube is shown in Figure 118. The annular film flow pattern extends from a Froude number of 3 to a Froude number of 100. Beyond a Froude number of 100, only the Mist flow pattern is found. These findings are summarized in Table 18.

R-134a Pressure Drop

In this section, the two-phase pressure drop data are analyzed and compared with experimental and theoretical correlations found in the literature. These correlations include those of Lockhart and Martinelli (1949), Chisholm (1973), Friedel (1979), De Souza and de Mattos-Pimenta (1995), Yang and Webb (1996), Wang et al. (1997), and Yan and Lin (1998). Flow regime-based pressure drop correlations are developed and discussed. Also, the effects of tube diameter and tube shape are discussed.

Table 18. Summary of the Non-Dimensional Transition Criteria for Annular Flow Developed in This Study

D_h (mm)	Fr	Transition
R134a	R134a	R-134a
4.91	18 - 65	Annular Film Flow
4.91	65	Annular Film to Mist Flow
3	20-65	Annular Film Flow
3	65	Annular Film to Mist Flow
2	18 - 100	Annular Film Flow
2	100	Annular Film to Mist Flow
1	20 - 100	Annular Film Flow
1	100	Annular Film to Mist Flow

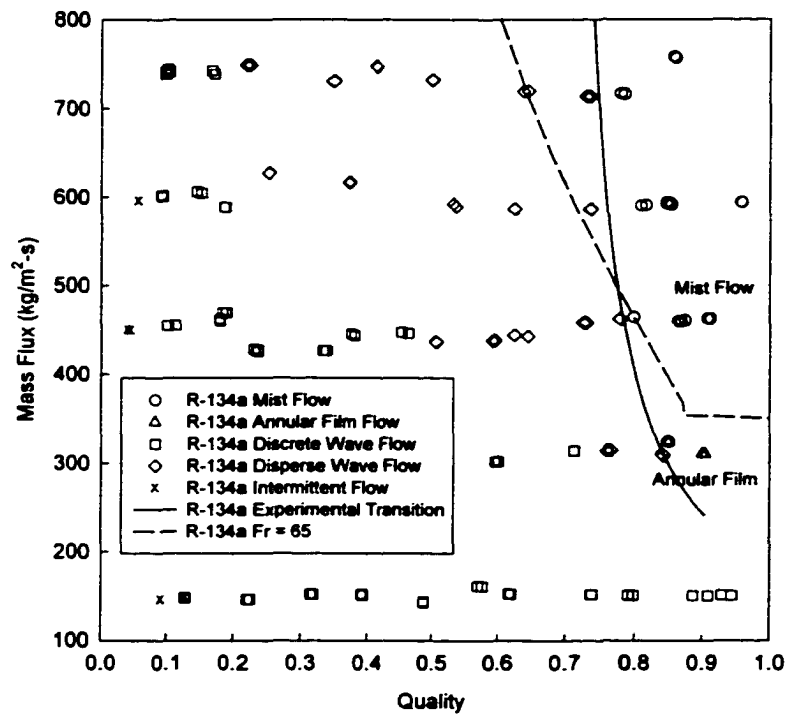


Figure 115. Transition to Annular Flow (R-134a, $D_h = 4.91$ mm)

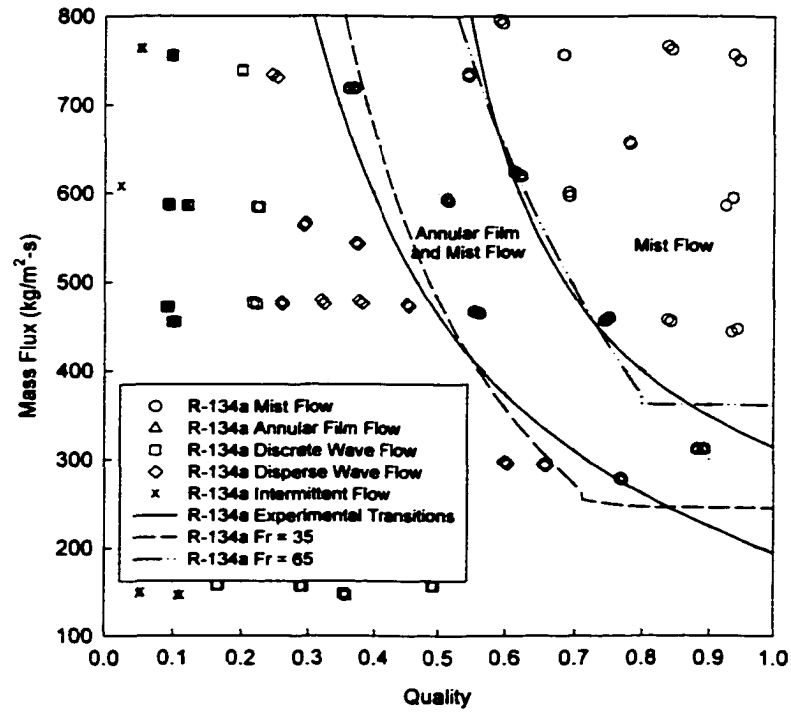


Figure 116. Annular Film and Mist Flow Pattern Transitions (R-134a, $D_h = 3.0$ mm)

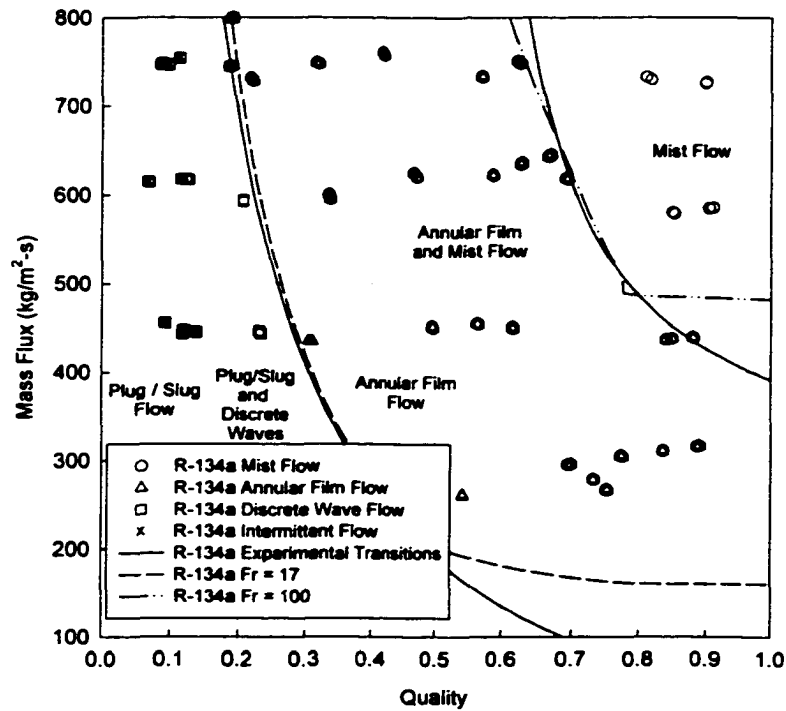


Figure 117. Annular Film and Mist Flow Pattern Transitions (R-134a, $D_h = 2.0$ mm)

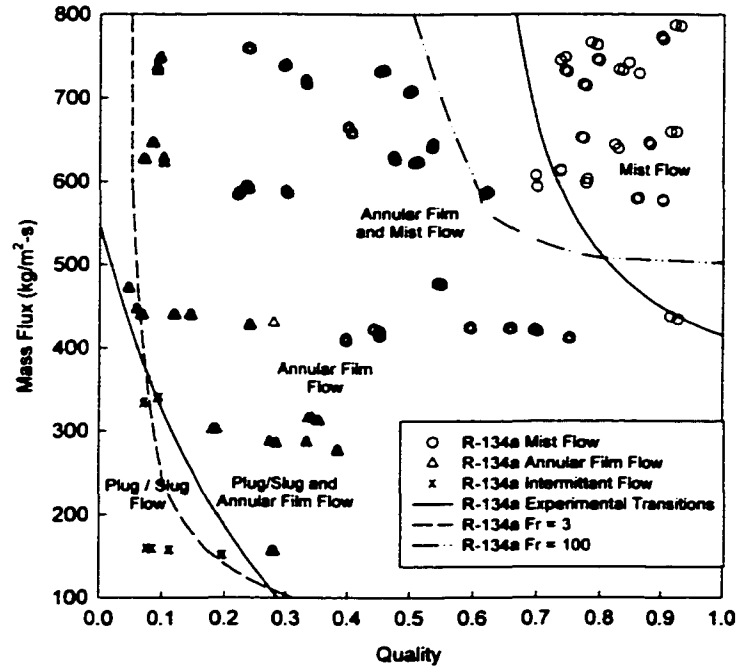


Figure 118. Annular Film and Mist Flow Pattern Transitions (R-134a, $D_h = 1.0$ mm)

Baseline Case Comparisons

In this section, several two-phase pressure drop correlations are presented, and the results of the two-phase pressure drop measurements for the baseline case (4.91 mm) are compared with these correlations. The equations used in the two-phase pressure drop correlations found in the literature are also discussed and sample calculations for each two-phase pressure drop correlation are also provided. Representative results for each of these correlations are reported based on the test data point summarized in Table 19.

Table 19. C193 Tube Data Used in the Baseline Case Comparison Calculations

Geometry and Test Conditions					
D_h (mm)	L (m)	G (kg/m ² -s)	x	P (kPa)	T (C)
4.91	0.6096	437.47	0.531	1367	52.0
Fluid Properties					
ρ_l (kg/m ³)	ρ_v (kg/m ³)	μ_l (kg/m-s)	μ_v (kg/m-s)	σ (kg/m-s)	
1092.6	69.28	1.81×10^{-4}	1.37×10^{-5}	4.76×10^{-3}	

The Lockhart-Martinelli (1949) Correlation

The Lockhart-Martinelli (1949) correlation for pressure drop in two-phase flow uses a two-phase multiplier to the single-phase liquid pressure gradient as follows:

$$\left(\frac{dP}{dx}\right) = \Phi_L^2 \left(\frac{dP}{dx}\right)_l \quad (78)$$

This two-phase multiplier is given by:

$$\Phi_L^2 = 1 + \frac{C}{X} + \frac{1}{X^2} \quad (79)$$

where C is a constant based upon whether the liquid and vapor are in turbulent or laminar flow:

$$C = 20 \text{ if } Re_l > 2300 \text{ and } Re_g > 2300 \quad (80a)$$

$$C = 12 \text{ if } Re_l \leq 2300 \text{ and } Re_g > 2300 \quad (80b)$$

$$C = 10 \text{ if } Re_l > 2300 \text{ and } Re_g \leq 2300 \quad (80c)$$

$$C = 5 \text{ if } Re_l \leq 2300 \text{ and } Re_g \leq 2300 \quad (80d)$$

The liquid and vapor Reynolds numbers are given by:

$$Re_l = \frac{G(1-x)D_h}{\mu_l} \quad Re_g = \frac{GxD_h}{\mu_g} \quad (81)$$

Using data from the C193 tube given in Table 19, equation (81) yields liquid and vapor Reynolds numbers of 5,566 and 83,254 respectively. In this example, the both the liquid and the gas are turbulent. The constant C is given in equation (80a) and is equal to 20.

The variable X in equation (79) is the liquid-vapor Martinelli parameter given by:

$$X = \sqrt{\left(\frac{dP}{dx}\right)_l / \left(\frac{dP}{dx}\right)_g} \quad (82)$$

where $(dP/dx)_L$ is the frictional pressure gradient of the liquid phase and $(dP/dx)_G$ is the frictional pressure gradient of the gas phase. These pressure gradients are given by:

$$\left(\frac{dP}{dz}\right)_l = \frac{f_{Churchill} G^2 (1-x)^2}{2D_{hyd} \rho_l} \quad (83)$$

and

$$\left(\frac{dP}{dz}\right)_g = \frac{f_{Churchill} G^2 (x)^2}{2D_{hyd} \rho_g} \quad (84)$$

The Churchill (1977) correlation (refer to equation 33) yields a liquid and gas friction factor of 0.037 and 0.019, respectively. Equations (83) and (84) yield liquid and vapor pressure gradients equal to 0.144 kPa/m and 1.47 kPa/m, respectively. The resulting Martinelli parameter given in equation (82) is 0.31. With the Martinelli parameter and constant C known, the two-phase multiplier, Φ_L^2 , is 75.9. Thus, the Lockhart-Martinelli correlation predicts the two-phase pressure gradient to be 75.9 times higher than the pressure gradient of the single-phase liquid. For a tube length of 0.6096 m, the pressure drop for this case is 6.66 kPa. The Lockhart-Martinelli (1949) correlation is compared with the results of the current study for the C193 tube for the $G = 750, 600, 450, 300,$ and $150 \text{ kg/m}^2\text{-s}$ in Figures 119-123, respectively. These figures show that the correlation proposed by Lockhart and Martinelli (1949) substantially over-predicts the measured two-phase pressure drop. This is not an unexpected result. Although this correlation is still widely used in both the literature and industry, it is not a good representation of two-phase pressure drop data and should not be used at higher pressures (Hewitt et al., 1994). Furthermore, two-phase multipliers are strong functions of the mass flux and may not adequately account for the effects of fluid properties (Hewitt et al., 1993).

The Chisholm (1973) Correlation

The Chisholm (1973) correlation is an adaptation of the Lockhart-Martinelli (1949) correlation. It uses a two-phase multiplier which is a function of the parameter Y, which is in turn a function of the pressure gradient in the gas-only and liquid-only phases. Thus,

$$Y = \sqrt{\left(\frac{dP}{dx}\right)_{go} / \left(\frac{dP}{dx}\right)_{lo}} \quad (85)$$

The liquid-only and vapor-only pressure gradients are given by:

$$\left(\frac{dP}{dz}\right)_{lo} = \frac{f_{Churchill} G^2}{2D_{hyd} \rho_l} \quad (86)$$

and

$$\left(\frac{dP}{dz}\right)_{go} = \frac{f_{Churchill} G^2}{2D_{hyd} \rho_g} \quad (87)$$

The liquid-only and gas-only Reynolds numbers used in the Churchill (1977) correlation are given by:

$$Re_{lo} = \frac{GD_h}{\mu_l} \quad Re_{go} = \frac{GD_h}{\mu_g} \quad (88)$$

Using data from the C193 tube at a quality of 0.531 and a mass flux of 437.47 kg/m²-s, equation (88) yields liquid-only and gas-only Reynolds numbers of 11,866 and 157,216, respectively. The Churchill (1977) correlation (refer to equation 33) yields a liquid-only and vapor-only friction factor of 0.030 and 0.016, respectively. Equations (86) and (87) yield liquid-only and vapor-only pressure gradients are 0.53 kPa/m and 4.5 kPa/m, respectively. The resulting Chisholm parameter given in equation (85) is 2.92. The corresponding two-phase pressure drop is given by:

$$\left(\frac{dP}{dx}\right) = \Phi_{LO}^2 \left(\frac{dP}{dx}\right)_{lo} \quad (89)$$

and the two-phase multiplier, Φ_{LO}^2 , is given by:

$$\Phi_{LO}^2 = 1 + (Y^2 - 1) \left[Bx^{(2-n)/2} (1-x)^{(2-n)/2} + x^{2-n} \right] \quad (90)$$

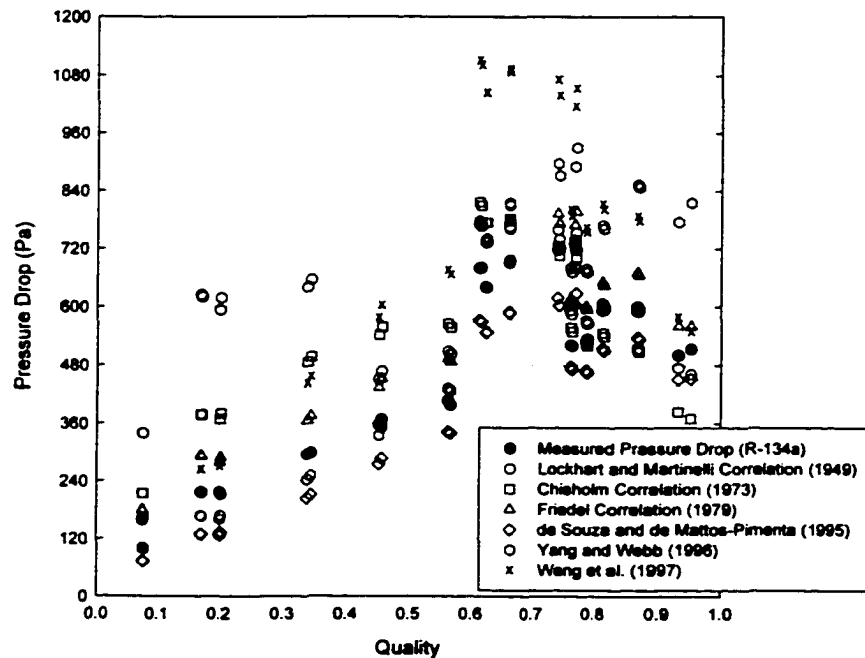


Figure 119. Comparison of the C193 Tube Data with the Literature ($G \approx 150 \text{ kg/m}^2\text{-s}$)

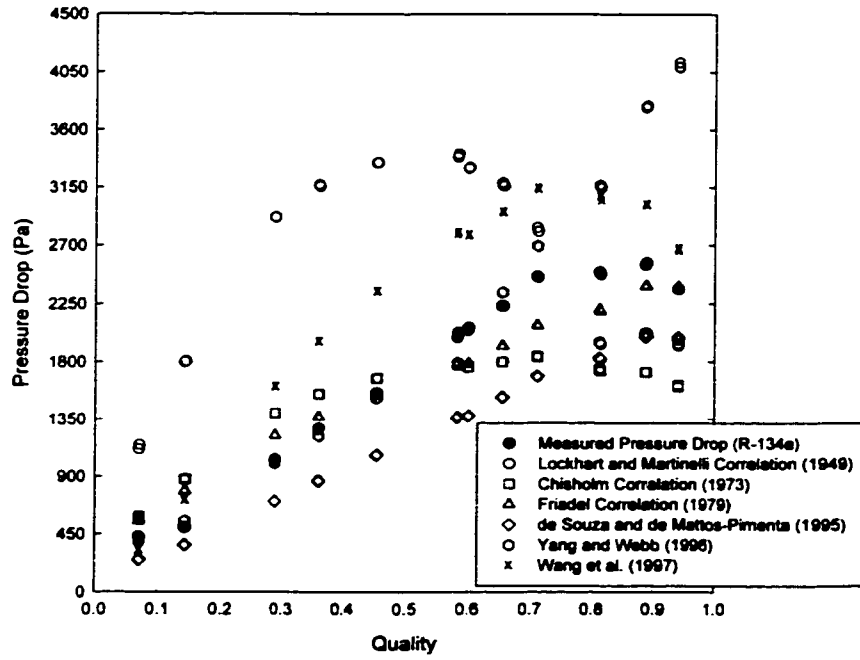


Figure 120. Comparison of the C193 Tube Data with the Literature ($G \approx 300 \text{ kg/m}^2\text{-s}$)

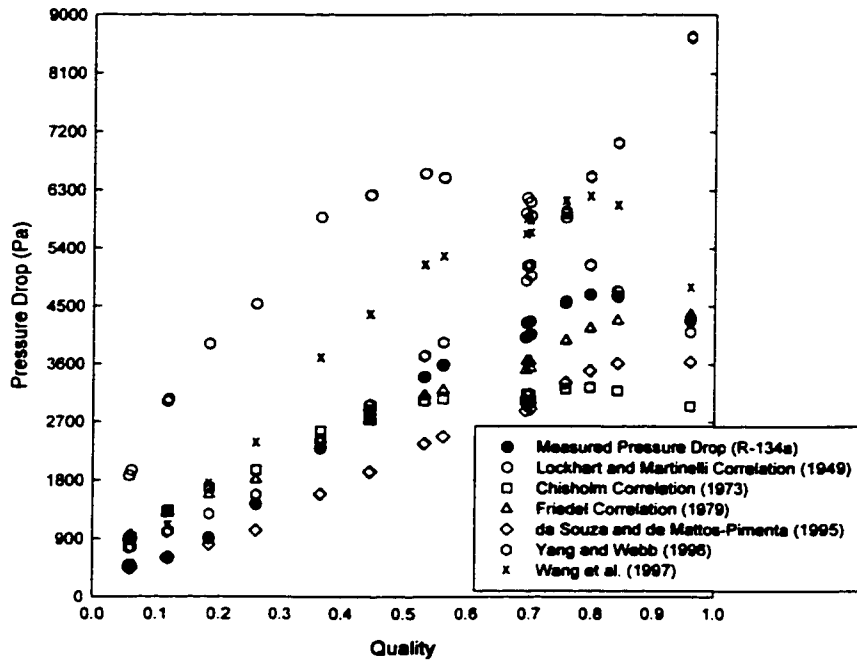


Figure 121. Comparison of the C193 Tube Data with the Literature ($G \approx 450 \text{ kg/m}^2\text{-s}$)

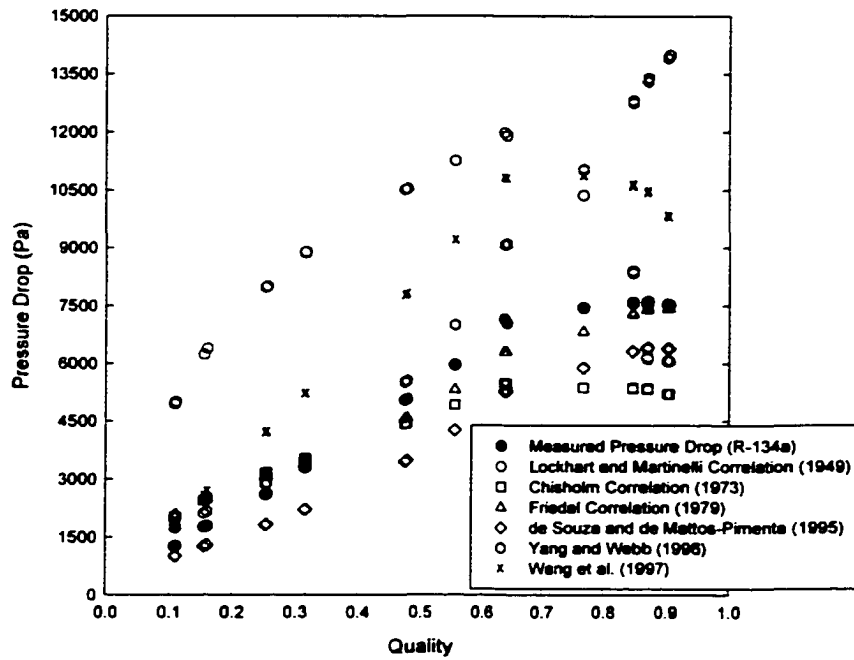


Figure 122. Comparison of the C193 Tube Data with the Literature ($G \cong 600 \text{ kg/m}^2\text{-s}$)

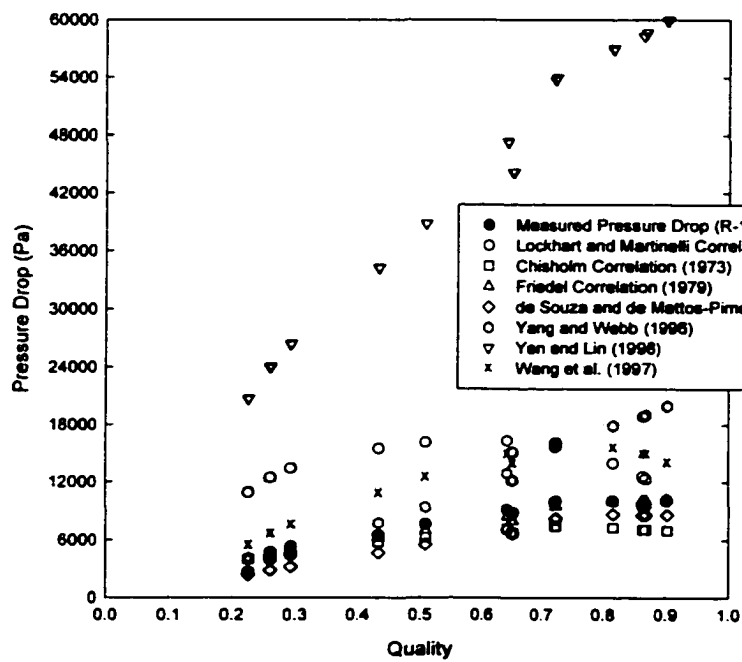


Figure 123. Comparison of the C193 Tube Data with the Literature ($G \cong 750 \text{ kg/m}^2\text{-s}$)

The values of B and n in equation (90) are dependent upon the liquid only-vapor only Martinelli parameter, Y, and liquid-only Reynolds number, respectively, as follows:

$$B = \frac{55}{G^{0.5}} \text{ if } Y \leq 9.5 \quad (91a)$$

$$B = \frac{520}{Y \cdot G^{0.5}} \text{ if } 9.5 < Y \leq 28 \quad (91b)$$

$$B = \frac{15000}{Y^2 G^{0.5}} \text{ if } Y > 28 \quad (91c)$$

and

$$n = 1 \text{ if } Re_{lo} \leq 2300 \quad (92a)$$

$$n = 0.25 \text{ if } 2300 < Re_{lo} \leq 20000 \quad (92b)$$

$$n = 0.2 \text{ if } Re_{lo} > 20000 \quad (92c)$$

With a Chisholm parameter of 2.92 and a liquid-only Reynolds number of 11,867, B is equal to 2.63 and n is equal to 0.25. Equation (90) yields a two-phase multiplier of 9.55. This correlation predicts the two-phase pressure drop to be 9.55 times higher than that of the single-phase liquid *flowing alone*. For a tube length of 0.6096 m, the pressure drop for this case is 3.08 kPa. The two-phase pressure drop correlation proposed by Chisholm (1973) is compared with the data from the C193 tube ($G = 150, 300, 450, 600, \text{ and } 750 \text{ kg/m}^2\text{-s}$) in Figures 119-123. For all five mass fluxes tested, the Chisholm (1979) correlation tends to over-predict the pressure drop at lower qualities. At higher qualities and lower mass fluxes, this correlation tends to under-predict the two-phase pressure drop.

The Friedel (1979) Correlation

The Friedel (1979) pressure drop correlation is given by:

$$\left(\frac{dP}{dx} \right) = \Phi_{LO}^2 \left(\frac{dP}{dz} \right)_{LO} \quad (93)$$

Here, Φ_{LO}^2 is a two-phase multiplier similar to that used by Lockhart-Martinelli (1949) and by Chisholm (1973). In this case, Φ_{LO}^2 is based on the entire fluid flowing as a liquid. This multiplier Φ_{LO}^2 is correlated as follows:

$$\Phi_{LO}^2 = E + \frac{3.24FH}{Fr^{0.045} We^{0.035}} \quad (94)$$

and the values of E, F, H are given by:

$$E = (1-x)^2 + x^2 \left(\frac{\rho_L f_{GO}}{\rho_G f_{LO}} \right) \quad (95)$$

$$F = x^{0.78} (1-x)^{0.24} \quad (96)$$

$$H = \left(\frac{\rho_L}{\rho_G} \right)^{0.91} \left(\frac{\mu_G}{\mu_L} \right)^{0.19} \left(1 - \frac{\mu_G}{\mu_L} \right)^{0.7} \quad (97)$$

This correlation is based upon a two-phase pressure drop database of over 25,000 points and is valid for both horizontal and vertical upward flows. Using data from Table 19 for the C193 tube, the values of E, F, and H in equations (95) to (97) are 2.67, 0.51 and 7.13, respectively. The Froude (Fr) and Weber (We) numbers in equation (94) are defined as follows:

$$Fr = \frac{G^2}{gD\rho_{TP}^2} \quad (98)$$

$$We = \frac{G^2 D}{\rho_{TP} \sigma} \quad (99)$$

and the two-phase density is defined as follows:

$$\rho_{TP} = \left[\frac{x}{\rho_G} + \frac{1-x}{\rho_L} \right]^{-1} \quad (100)$$

The two-phase density is 123.6 kg/m³. Data on the surface tension of R-134a are provided by Chae et al. (1990). While surface tension is known to vary linearly with temperature, the data of Chae et al. (1990) are best fit to a polynomial of order 4. This polynomial yields a near-linear relationship between the surface tension and the temperature, but also minimizes the error between the function and the experimental data. The surface tension as a function of temperature is given by:

$$\sigma = 1.170x10^{-2} - 1.418x10^{-4} T_{test} + 1.885x10^{-7} T_{test}^2 - 1.692x10^{-9} T_{test}^3 + 2.307x10^{-11} T_{test}^4 \quad (101)$$

At an average test section temperature of 52.0°C, the surface tension of the liquid-vapor mixture is 4.76x10⁻³ kg/s². Using equations (98) and (99), the Froude number is equal to 260 and the Weber number is equal to 1598. With these parameters determined, the two-phase multiplier given in equation (94) is equal to 9.74. Thus, the Friedel (1979) correlation predicts the two-phase pressure drop to be 9.74 times higher than that of the single-phase liquid flowing alone. For a tube length of 0.6096 m, the pressure drop for this case is 3.13 kPa. The two-phase

pressure drop correlation proposed by Friedel (1979) is plotted against the two-phase differential pressure data from the C193 tube ($G = 150, 300, 450, 600, \text{ and } 750 \text{ kg/m}^2\text{-s}$) in Figures 119-123. For all mass fluxes and qualities tested, the Friedel (1979) correlation tends to systematically over-predict the two-phase pressure drop.

De Souza and de Mattos-Pimenta (1995)

The de Souza and de Mattos-Pimenta correlation for two-phase pressure drop is given by:

$$\left(\frac{dP}{dx}\right) = \Phi_{LO}^2 \left(\frac{dP}{dz}\right)_{LO} \quad (102)$$

The two-phase multiplier, Φ_{LO}^2 , is given by:

$$\Phi_{LO}^2 = 1 + (\Gamma^2 - 1) \cdot x^{1.75} \cdot (1 + 0.9524 \cdot \Gamma \cdot X_u^{0.4126}) \quad (103)$$

where Γ is a property correction factor given as follows:

$$\Gamma = \left(\frac{\rho_l}{\rho_g}\right)^{0.5} \left(\frac{\mu_g}{\mu_l}\right)^{0.125} \quad (104)$$

and

$$X_u = \left(\frac{1-x}{x}\right)^{0.875} \left(\frac{\rho_g}{\rho_l}\right)^{0.5} \left(\frac{\mu_l}{\mu_g}\right)^{0.125} \quad (105)$$

This correlation is based upon two-phase pressure drop data of R-134a, MP-39 and R-32/125 with tube diameters ranging from 7.75 mm to 10.92 mm. The proposed correlation is similar to the others presented thus far in that it makes use of a two-phase multiplier applied to the liquid-only pressure gradient. Using data from Table 19 for the C193 tube, the property correction factor, Γ , is equal to 2.88. With X_u equal to 0.31, the two-phase multiplier for the de Souza and de Mattos-Pimenta (1995) correlation is 7.47. This correlation predicts the two-phase pressure drop to be 7.47 times higher than that of the single-phase liquid flowing alone. For a tube length of 0.6096 m, the pressure drop for this case is 2.40 kPa. The two-phase pressure drop data for the C193 tube is plotted against the correlation proposed by de Souza and de Mattos-Pimenta (1995) in Figures 119-123 for all five mass flux cases tested in this study. Relatively good agreement between the correlation and the baseline case two-phase pressure drop is found.

Yang and Webb (1996)

Yang and Webb correlated two-phase pressure drop of R-12 in a rectangular tube with $D_h = 2.64$ mm using a two-phase friction factor. This two-phase friction factor is a function of the liquid and gas Reynolds numbers. The two-phase pressure drop is given by:

$$\left(\frac{dP}{dx}\right) = 2f_{tp} \text{Re}_{eq}^2 \frac{\mu_l^2}{\rho_l D_{hyd}^3} \quad (106)$$

The equivalent Reynolds number is defined as follows:

$$\text{Re}_{eq} = \frac{G_{eq} D_{hyd}}{\mu_l} \quad (107)$$

with an equivalent mass flux taken as follows:

$$G_{eq} = G \left[1 - x + x \cdot \left(\frac{\rho_l}{\rho_g}\right)^{0.5} \right] \quad (108)$$

Using the data from Table 19 for the C193 tube, the equivalent mass flux is 1128 kg/m²-s. The equivalent Reynolds number given in equation (107) is equal to 30,597. The two-phase friction factor, f_{tp} , proposed by Yang and Webb (1996) is given by:

$$f_{tp} = 0.435 f_p \text{Re}_{eq}^{0.12} \quad (109)$$

and

$$f_p = 0.0676 \text{Re}_{lo}^{-0.22} \quad (110)$$

Equations (109) and (110) yield values of f_p equal to 0.0086 and a two-phase friction factor, f_{tp} , of 0.013. The resulting two-phase pressure gradient given in equation (106) is 6.11 kPa/m. For a tube length of 0.6096 m, the pressure drop for this case is 3.73 kPa. The correlation proposed by Yang and Webb (1996) is plotted against the two-phase pressure drop data for the C193 tube ($G = 150, 300, 450, 600,$ and 750 kg/m²-s) in Figure 119-123. For all mass fluxes and qualities tested, this correlation tends to over-predict the two-phase pressure drop. Furthermore, the difference between the correlation proposed by Yang and Webb (1996) and the experimental data is higher at the higher qualities.

Wang et al. (1997)

Wang et al. (1997) proposed a simpler two-phase multiplier for $G > 200$ kg/m²-s that is a function of only the Martinelli parameter. The two-phase flow pressure drop is given by:

$$\left(\frac{dP}{dx}\right) = \Phi_v^2 \left(\frac{dP}{dz}\right)_v \quad (111)$$

where the two-phase multiplier is given by:

$$\Phi_v^2 = 1 + 10 \cdot X^{0.636} \quad (112)$$

This correlation is based upon data using R-134a in a 6.5 mm inner diameter tube. With a Martinelli parameter of 0.31 (refer to equation 82), the two-phase multiplier in the Wang et al. (1997) correlation is 5.75. The resulting two-phase pressure gradient given in equation (111) is 8.47 kPa/m. For a tube length of 0.6096 m, the pressure drop for this case is 5.16 kPa. The two-phase pressure drop data for the C193 tube ($G = 150, 300, 450, 600,$ and $750 \text{ kg/m}^2\text{-s}$) are plotted against the correlation proposed by Wang et al. (1997) in Figure 119-123. While the hydraulic diameter of the baseline case in this study and that of Wang et al. (1997) are similar, this correlation tends to over-predict the experimentally measured two-phase pressure drop. These differences in the two-phase pressure drop may be attributed to differences in the fluid properties. The two-phase multiplier proposed by Wang et al. (1997) is a function of the Martinelli parameter, and thus, a function only of the fluid properties and quality. Their two-phase pressure drop data were taken at saturation temperatures of 6°C and 20°C, while the data from the present study were taken at a saturation temperature of 52°C. The differences in saturation temperatures and fluid properties may account for the over-predictive nature of the correlation proposed by Wang et al. (1997).

Yan and Lin (1998)

The correlation proposed by Yan and Lin (1998) is similar to the correlation proposed by Yang and Webb (1996) in that it makes use of a two-phase friction factor. They proposed the following correlation for two-phase pressure drop in a 2.0 mm circular tube using R-134a as the working fluid:

$$\left(\frac{dP}{dx}\right) = 2f_{ip} G^2 \frac{v_m}{D_{hyd}} \quad (113)$$

where v_m is the average specific volume given by:

$$v_m = \frac{x}{\rho_g} + \frac{(1-x)}{\rho_l} \quad (114)$$

and the two phase friction factor is a function of the equivalent Reynolds number (refer to equation 107) given by:

$$f_{tp} = 0.11 \text{Re}_{eq}^{-0.1} \quad (115)$$

where

$$\text{Re}_{eq} = \frac{GD}{\mu_l} \left[(1-x) + x \left(\frac{\rho_l}{\rho_g} \right)^{0.5} \right] \quad (116)$$

Using data from Table 19 for the C193 tube, the average specific volume is equal to 0.0081 m³/kg. With an equivalent Reynolds number of 30,597, the two-phase friction factor is equal to 0.039. The resulting two-phase pressure gradient given in equation (113) is equal to 24.71 kPa/m. For a tube length of 0.6096 m, the pressure drop for this case is 15.07 kPa. The two-phase pressure drop data for the C193 tube ($G = 150, 300, 450, 600, \text{ and } 750 \text{ kg/m}^2\text{-s}$) are plotted against the correlation proposed by Yan and Lin (1998) in Figures 119-123. As seen in these figures, the correlation proposed by Yan and Lin (1998) results in a substantial over-prediction of the two-phase pressure drop. Part of this discrepancy may be due to the simplicity and range of applicability of the proposed correlation.

Each of the correlations investigated yield different results. Figure 124 illustrates the relative errors in the different correlations for the $G = 450 \text{ kg/m}^2\text{-s}$ mass flux case. This figure shows that the correlation proposed by de Souza and de Mattos-Pimenta (1995) yielded the best result with the largest errors occurring in the middle quality range ($0.25 < x < 0.75$). This correlation was based upon two-phase pressure drop data using R-134a (and other fluids) and similar hydraulic diameters. The correlations proposed by Lockhart and Martinelli (1949), Chisholm (1973), and Friedel (1979) showed good agreement with the experimental data at the higher qualities ($x > 0.75$). These correlations produced large errors in the estimated pressure drop in the low quality region ($x < 0.25$). The correlation proposed by Yang and Webb (1996) showed good agreement with the experimental data in the middle quality region ($0.25 < x < 0.75$), but large errors were found at both the high and low qualities. The correlation proposed by Yang and Webb (1996) produced fair agreement, but over-predicted the two-phase pressure drop throughout the entire range of quality. The correlation proposed by Yan and Lin (1998) produced the largest errors across the entire range of quality. This correlation was based upon data using R-134a in a 2.0 mm tube and may not adequately take hydraulic diameter into account. Data for the remaining round tubes ($D_h = 3.05, 1.52, 0.762, 0.508 \text{ mm}$) are compared with the correlations found in the literature in Appendix G.

Hewitt et al. (1993) suggest that the only way of making significant progress in correlating two-phase pressure drops is to base the correlations on the flow regimes. For the baseline case, three major regimes were identified including intermittent flow (low quality

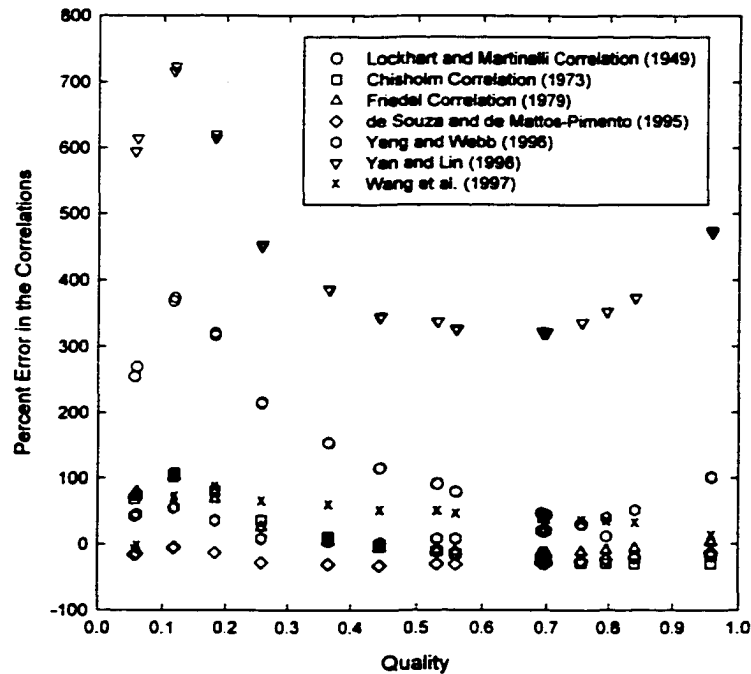


Figure 124. Percent Errors in the Correlations for Tube C193 ($G \cong 450 \text{ kg/m}^2\text{-s}$)

region), wavy flow (middle quality region), and annular flow (high quality region). These changes in the flow pattern may help explain why the pressure drop correlations proposed by de Souza and de Mattos-Pimenta (1995), Chisholm (1973), and Friedel (1979) produce large errors in the low quality region (intermittent flow), and good agreement in the high quality region (wavy and annular flow).

Flow Regime Models

Flow regime based pressure drop correlations for circular and non-circular tubes are presented in this section. Thus, specific correlations are developed for each of the following flow regimes: intermittent and discrete wave flow, disperse wave and annular film flow, annular film and mist flow, and mist flow.

Intermittent and Discrete Wave Flow Model

Circular Tubes

Both intermittent and discrete wave flow are characterized by a separation of the liquid and gas by either wave structures that may touch the top of the tube or by slugs of liquid. In this study, it is assumed that both the discrete waves and the intermittent flow can be represented by a single model. In this model, the unit cell is divided into two segments: a gas bubble segment followed by a slug of liquid segment, as shown in Figures 125 and 126. The following

assumptions are made:

- Overall steady flow
- Equal and uniform cell sizes
- Gas and liquid pressure gradients across the cross-section are equal

Representative results for the Intermittent and Discrete Wave Flow Model are reported based on the test data points summarized in Table 20.

The total pressure drop in the unit cell length, l_u , is equal to the pressure losses due to friction in the slug over the liquid slug length l_s , the expansion and contraction of the liquid film around the gas bubble, and the pressure losses due to friction in the liquid film over the film length l_f . This is given by:

$$\Delta P_{cell} = \Delta P_{slug} + \Delta P_{exp/con} + \Delta P_{film} \quad (117)$$

The pressure drop across the liquid slug is given by

$$\Delta P_{slug} = 0.5 \rho_l V_s^2 \frac{l_s}{D} f_s \quad (118)$$

The friction factor in equation (117) is determined from the Churchill (1977) correlation provided by equation (33). The velocity of the slug is determined from the mass flow rate of the

Table 20. C120 Tube Data Used in the Intermittent Flow Model

Geometry and Test Conditions					
D_h (mm)	L (m)	G (kg/m ² -s)	x	P (kPa)	T (C)
3.05	0.5080	294.66	0.085	1393	52.2
Fluid Properties					
ρ_l (kg/m ³)	ρ_g (kg/m ³)	μ_l (kg/m-s)	μ_g (kg/m-s)	σ (kg/m-s)	
1091.8	70.38	1.81×10^{-4}	1.37×10^{-5}	4.74×10^{-3}	

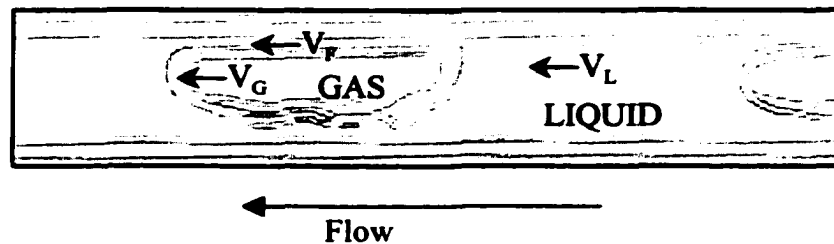


Figure 125. Model Schematic for Slug and Discrete Wave Flow

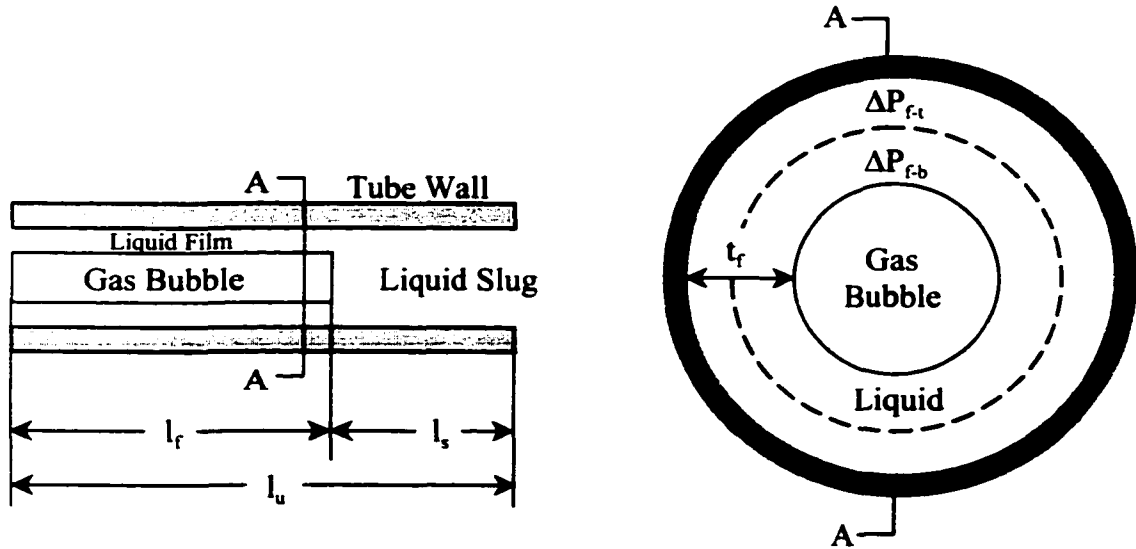


Figure 126. Details of the Slug Flow and Discrete Wave Flow Model

liquid as follows:

$$\dot{m}_l = (1-x)\dot{m}_{Total} = (1-x)GA = \rho_l V_s A \quad (119)$$

Using the data in Table 20 for the C120 tube, the slug velocity is 0.247 m/s. The friction factor, f_s , is determined from the Churchill (1977) equation using the Reynolds number of the slug, Re_s , given by:

$$Re_s = \frac{\rho_l V_s D}{\mu_l} \quad (120)$$

With a slug Reynolds number of 4544, the Churchill (1977) equation yields a slug friction factor of 0.039.

The pressure drop due to the contraction of the liquid around the gas bubble is given by:

$$\Delta P_{con} = \left(\frac{V_f^2 - V_s^2}{2} \right) \rho_L + \rho_L K_c \frac{V_f^2}{2} \quad (121)$$

The pressure recovery due to the expansion of the liquid film is as follows:

$$\Delta P_{exp} = \left(\frac{V_s^2 - V_f^2}{2} \right) \rho_L + \rho_L K_e \frac{V_f^2}{2} \quad (122)$$

The film velocity is obtained from the mass flow rate of the liquid as follows:

$$\dot{m}_l = \rho_l V_f A_f \quad (123)$$

The area of the film, A_f , is determined from the thickness of the liquid film, t_f :

$$A_f = \frac{\pi}{4} D^2 - \frac{\pi}{4} (D - 2t_f)^2 \quad (124)$$

and this value is, in turn, determined from the void fraction model as follows:

$$A_g = \alpha A = \frac{\pi}{4} (D - 2t_f)^2 \quad (125)$$

Using the data in Table 20, the void fraction (Baroczy (1965), refer to equation 39) is 0.42 and the film thickness, t_f , is 0.53 mm. Thus, the area of the film is $4.2 \times 10^{-6} \text{ m}^2$ and equation (123) yield a film velocity of 0.43 m/s. The net loss of pressure due to the expansion and contraction of the liquid over the gas bubble is the sum of equations (121) and (122). Furthermore, K_e and K_c in equations (121) and (122) are functions of the expansion or contraction area ratios, as described in the previous chapter. In this example, with an area ratio (A_f/A) of 0.58, K_e and K_c are equal to 0.18 and 0.16, respectively. The net pressure loss due to the expansion and contraction of the liquid around the gas bubble is equal to 33.4 Pa.

The remaining pressure drop is due to the frictional losses in the liquid film. This frictional pressure loss occurs over two separate boundaries, namely the film-to-tube interface (ΔP_{f-t}), and the film-to-gas bubble interface (ΔP_{f-b}). The total pressure drop in the liquid film is assumed to be the sum of these two frictional components:

$$\Delta P_{film} = \Delta P_{f-t} + \Delta P_{f-b} \quad (126)$$

as shown schematically in Figure 126. The pressure drop due to the friction at the film-tube wall interface is given by:

$$\Delta P_{f-t} = 0.5 \rho_l V_{f-t}^2 \frac{l_f}{D_{f-t}} f_{f-t} \quad (127)$$

Assuming a no-slip condition at the tube wall exists, a simple linear velocity profile is chosen and the average velocity of the film V_{f-t} , is taken as:

$$V_{f-t} = \left(\frac{V_f + V_{wall}}{2} \right) = \frac{V_f}{2} \quad (128)$$

Thus, the velocity of the film in the film-to-tube region, V_{f-t} , is 0.214 m/s. The hydraulic

diameter, $D_{f,t}$, is given by:

$$D_{f-t} = \left(\frac{D^2 - (D - t_f)^2}{D} \right) \quad (129)$$

The friction factor, $f_{f,t}$, is determined from the Churchill (1977) equation using the Reynolds number of the liquid film, $Re_{f,t}$, given by:

$$Re_{f-t} = \frac{\rho_l V_{f-t} D_{f-t}}{\mu_l} \quad (130)$$

Using the data from Table 20, the hydraulic diameter $D_{f,t}$ and the Reynolds number, $Re_{f,t}$ are 0.974 mm and 1260.1, respectively. At this Reynolds number, the friction factor, $f_{f,t}$, is 0.051.

The pressure drop due to the friction at the film-gas bubble interface is given by:

$$\Delta P_{f-b} = 0.5 \rho_l V_{f-b}^2 \frac{l_f}{D_{f-b}} f_{f-b} \quad (131)$$

The average velocity of the film $V_{f,b}$, is taken as:

$$V_{f-b} = \left(\frac{V_g + V_f}{2} \right) \quad (132)$$

The gas velocity is obtained from the mass flow rate of the gas as follows:

$$\dot{m}_g = x \dot{m}_{total} = \rho_g V_g A_g \quad (133)$$

Using the data in Table 20, equation (133) yields a gas velocity of 0.84 m/s. This results in a film-to-bubble velocity of 0.634 m/s. The friction factor, $f_{f,b}$, is determined from the Churchill (1977) equation using the Reynolds number of the liquid film, $Re_{f,b}$, given by:

$$Re_{f-b} = \frac{\rho_l V_{f-b} D_{f-b}}{\mu_l} \quad (134)$$

The hydraulic diameter, $D_{f,b}$, is given by:

$$D_{f-b} = \left(\frac{(D - t_f)^2 - (D - 2t_f)^2}{D - 2t_f} \right) \quad (135)$$

In this example, the hydraulic diameter, $D_{f,b}$, and film-to-bubble Reynolds number are 1.21 mm and 4,646, respectively. At this Reynolds number, the friction factor, $f_{f,b}$, is 0.039.

This model requires an equation that relates the film length to the unit cell length. In the

absence of accurate experimentally measured unit cell dimensions, the following relationship between the film length and the unit cell length was assumed as a first-order approximation. Thus, the film length increases linearly with quality and inversely with Re_s .

$$l_f = \left(\frac{l_u x}{Re_s} \right) \quad (136)$$

The above set of equations can be closed if the unit cell length (the only undetermined quantity in these equations) can be estimated. Thus, the experimentally determined pressure drops were used to determine the unit cell length as follows:

$$\Delta P_{measured} = \Delta P_{cell} \left(\frac{L_{tube}}{l_u} \right) \quad (137)$$

Using this model, the data were fit to determine a relationship for the unit cell length as follows:

$$\left(\frac{l_u}{D} \right) = a \left(\frac{\Psi}{\lambda} \right)^b = 0.991 \left(\frac{\Psi}{\lambda} \right)^{0.312} \quad (138)$$

The variables Ψ and λ are suggested by Suo and Griffith (1964) for correlating the intermittent flow transition in capillary air-water two-phase flow. These parameters are given by

$$\Psi = \frac{\mu_l V_g}{\sigma} \quad (139)$$

and

$$\lambda = \frac{2\mu_l^2}{\rho_l \sigma D} \quad (140)$$

The parameters suggested by Suo and Griffith (1964), Ψ and λ in equations (139) and (140) are equal to 0.0319 and 4.135×10^{-6} , respectively. Thus, equation (138) yields a non-dimensional unit cell length, l_u/D , of 16.3. The non-dimensional slug length is plotted as a function of the variables Ψ and λ is shown in Figure 127. Pressure drops predicted using this approach are plotted against the measured values in Figure 128 for all five circular tubes. This figure shows that 91% of the data were predicted within an error band of $\pm 25\%$.

Non-Circular Geometries

The intermittent and discrete wave flow model was modified for non-circular geometries. Modifications included basing the Reynolds number calculations on the hydraulic diameter of the tube and using the appropriate laminar friction factor correlations (given in Table 12). Data

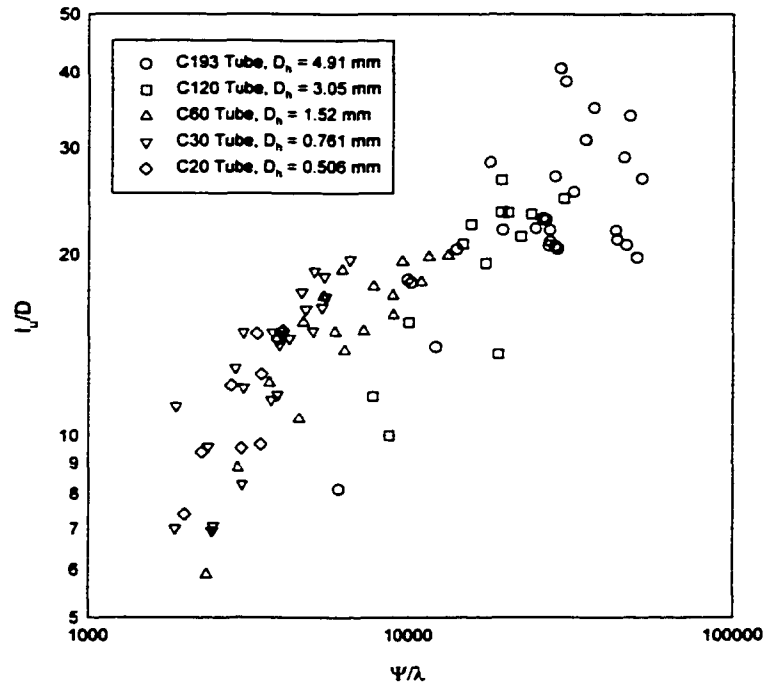


Figure 127. Non-Dimensional Unit Cell Length versus Ψ and λ , Circular Tubes

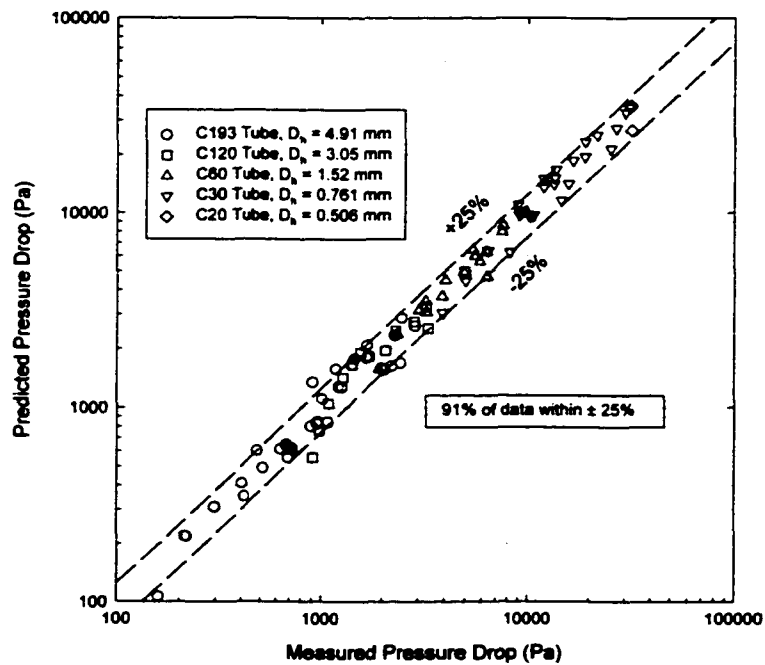


Figure 128. Predicted Versus Measured Pressure Drops, Intermittent Model, Circular Tubes

for the T33, S30, B32, N21, RK15, W29I and W29II tubes were fit to equation (136), as shown in Figure 129. The constants a and b in equation (136) are given in Table 21 for each of the non-circular geometries tested in this study. Pressure drops predicted using this approach are plotted against the measured values in Figure 130 for all non-circular geometries. This figure shows that 91% of the data were predicted within an error band of $\pm 25\%$.

Annular Film and Disperse Wave Flow Model

Circular Tubes

Annular film and disperse wave flows are characterized by a relatively thick annular coating of liquid on the tube wall. In annular film flow, the liquid is distributed equally around the circumference of the tube, while in disperse wave flow, the liquid may be more prevalent on the bottom of the tube. Schematics of these flows are shown in Figure 131. Representative results for the Intermittent and Discrete Wave Flow Model are reported based on the test data points summarized in Table 22.

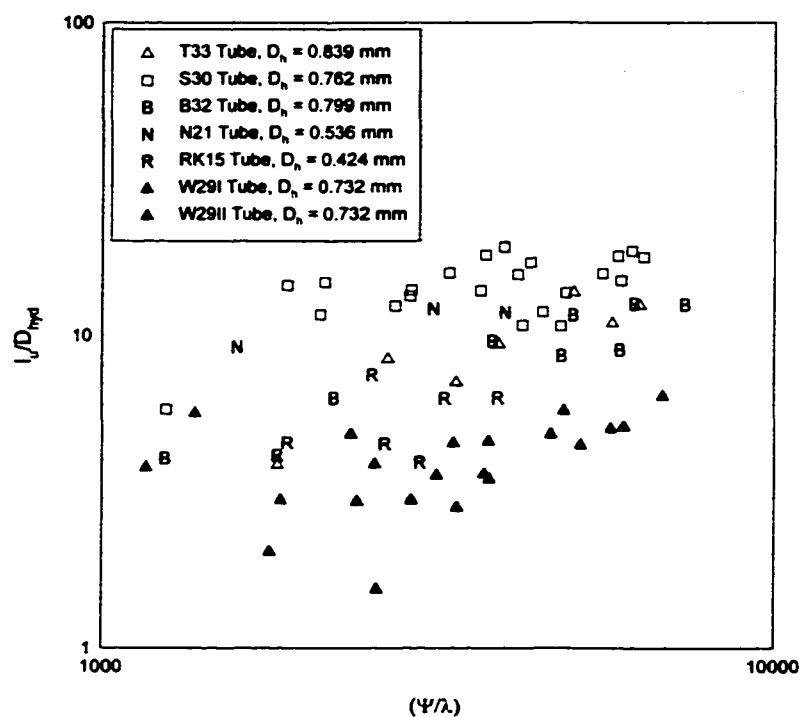


Figure 129. Non-Dimensional Unit Cell Length versus Ψ and λ , Non-Circular Geometries

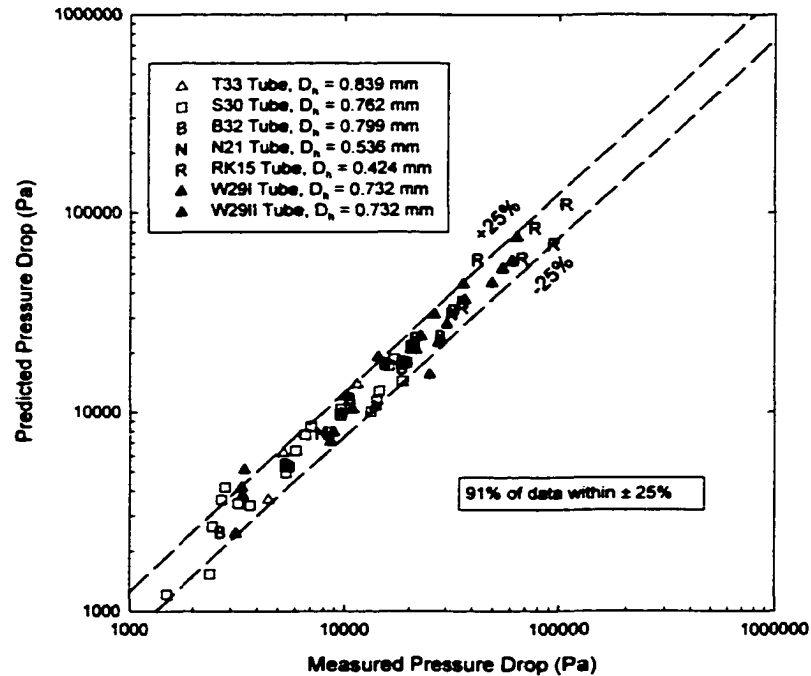


Figure 130. Measured versus Predicted Pressure Drop, Intermittent Model, Non-Circular Geometries

Table 21. Intermittent/Discrete Wave Model Constants

Tube	Shape	D_h (mm)	Constant a	Constant b
T33	Triangle	0.839	0.021	0.736
S30	Square	0.762	2.62	0.213
B32	Barrel	0.799	0.076	0.573
N21	“N”	0.536	1.13	0.288
RK15	Rectangle	0.424	0.181	0.428
W29I	Triangle (Insert)	0.732	0.506	0.267
W29II	Triangle (Insert)	0.732	0.0072	0.761

Table 22. C120 Tube Data Used in the Baseline Case Comparison Calculations

P (kPa)	D_h (mm)	L (m)	G ($\text{kg/m}^2\text{-s}$)	x	ρ_l (kg/m^3)	ρ_v (kg/m^3)	μ_l (kg/m-s)	μ_v (kg/m-s)
1493	3.05	0.5080	279.9	0.546	1078	76.12	1.75×10^{-4}	1.39×10^{-5}

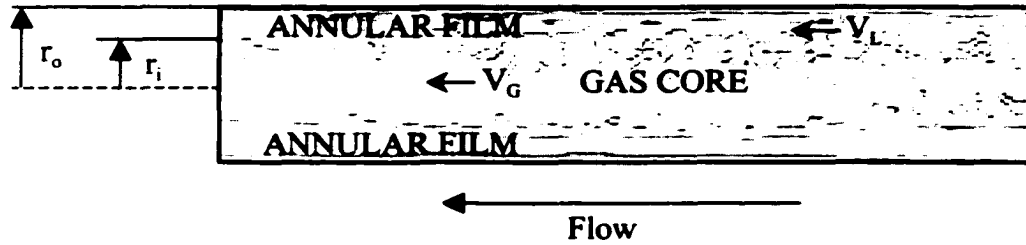


Figure 131. Model Schematic for Annular Film and Disperse Wave Flow

A model for such a flow is provided by Carey (1992). This model makes the following assumptions:

- Steady flow
- Pressure gradients in the liquid and gas core are equal across the cross section
- Uniform thickness of the liquid film and a smooth interface
- No entrainment of the liquid in the gas core

A force-momentum balance on the liquid, assuming negligible gravitational effects, is as follows:

$$\tau_i = -\frac{r_i}{2} \left[\frac{dP}{dz} + \underbrace{\left(\frac{r_o}{r_i} \right)^2 \frac{d}{dz} \left(G^2 \left(\frac{r_o}{r_i} \right)^2 \frac{x^2}{\rho_G} \right)}_{\text{Acceleration Term}} \right] \quad (141)$$

where τ_i is the shear stress at the liquid-gas interface and the void fraction, α (Baroczy (1965), refer to equation 39), is equal to $(r_o/r_i)^2$. The acceleration term in equation (141) can be rewritten as (Carey, 1992):

$$\left[\left(\frac{r_o}{r_i} \right)^2 \frac{d}{dz} \left(G^2 \left(\frac{r_o}{r_i} \right)^2 \frac{x^2}{\rho_G} \right) \right] = \frac{2G^2 x}{\alpha^2 \rho_G} \left(\frac{dx}{dz} \right) \left[1 - \frac{x}{2\alpha} \left(\frac{d\alpha}{dx} \right) \right] \quad (142)$$

Furthermore, the derivative of the void fraction with quality is much less than unity, and therefore, the second term in the brackets is neglected. The pressure gradient can now be rewritten as follows:

$$\frac{dP}{dz} = \frac{-4\tau_i}{D} - \frac{2xG^2}{\alpha^2 \rho_G} \left(\frac{dx}{dz} \right) \quad (143)$$

From a conservation of energy on the test section, the term dx/dz can be written as follows (Carey, 1992):

$$\frac{dx}{dz} = \frac{4(Q/A)}{DGh_{lv}} \quad (144)$$

The term dx/dz is quite small compared to the first term in equation (143), and during adiabatic conditions, $Q = 0$, which implies that $dx/dz = 0$. The shear stress at the interface, τ_i , can be written in terms of an interfacial friction factor (Carey, 1992) as follows:

$$\tau_i = \frac{f_i G^2 x^2}{2\rho_G \alpha^2} \quad (145)$$

Substituting this expression into Equation (143) above, and using the experimentally measured pressure drop over the test section length yields:

$$f_i = \frac{1}{2} \frac{D}{L} \frac{\rho_g \alpha^2}{G^2 x^2} \Delta P_{\text{exptl}} \quad (146)$$

Using the data from Table 22, the void fraction model (Baroczy (1965), refer to equation 39) yields a void fraction of 0.822. With a test section length of 0.508 m, and an experimentally measured pressure drop of 2,186 Pa, equation (144) yields an interfacial friction factor of 0.014.

This interfacial friction factor was normalized by the liquid friction factor using the Churchill (1977) equation and the liquid Reynolds number defined by:

$$\text{Re}_l = \frac{\rho_l V_l D}{\mu_l} \quad (147)$$

where the liquid velocity is given by:

$$\dot{m}_{\text{Total}}(1-x) = \rho_l V_l A_l \quad (148)$$

The area of the liquid is determined from the void fraction model given in equation (39). Using the data in Table 22, with a void fraction of 0.822, the area occupied by the liquid is equal to $1.3 \times 10^{-6} \text{ m}^2$. Equation (148) yields a liquid velocity of 0.662 m/s. Equation (147) yields a liquid Reynolds number of 12,430. The Churchill (1977) equation yields a liquid friction factor of 0.029.

This normalized interfacial friction factor was plotted against the Martinelli parameter (refer to equation 105), and this equation was used for both laminar and turbulent flows. The results are shown in Figure 132. This figure shows that the slope for all five tubes is approximately constant, and the friction factor ratio decreases with decreasing tube diameter.

The data were fit to the following correlation:

$$\left(\frac{f_i}{f_L}\right) = C_1(X)^{C_2} = C_1(X)^{0.30} \quad (149)$$

It was further assumed that the leading constant C_1 would be a function of the Bond number, Bo , given by

$$Bo = \frac{g(\rho_l - \rho_g)D^2}{\sigma} \quad (150)$$

and this in turn represents tube diameter effects. It was found that the following function adequately correlates C_1 :

$$C_1 = 0.45(Bo)^{0.073} \quad (151)$$

Using the data in Table 22, equation (150) yields a Bond number of 20.76, and equation (151) yields a constant C_1 of 0.562. This function for C_1 as a function of the Bond number is shown in Figure 133. With a Martinelli parameter of 0.311 (refer to equation 105), equation (149) yields a predicted interfacial friction factor equal to 0.0115. Pressure drops predicted using this approach are plotted against the measured values in Figure 134 for all five circular tubes. This figure shows that 93% of the data were predicted within an error band of $\pm 20\%$.

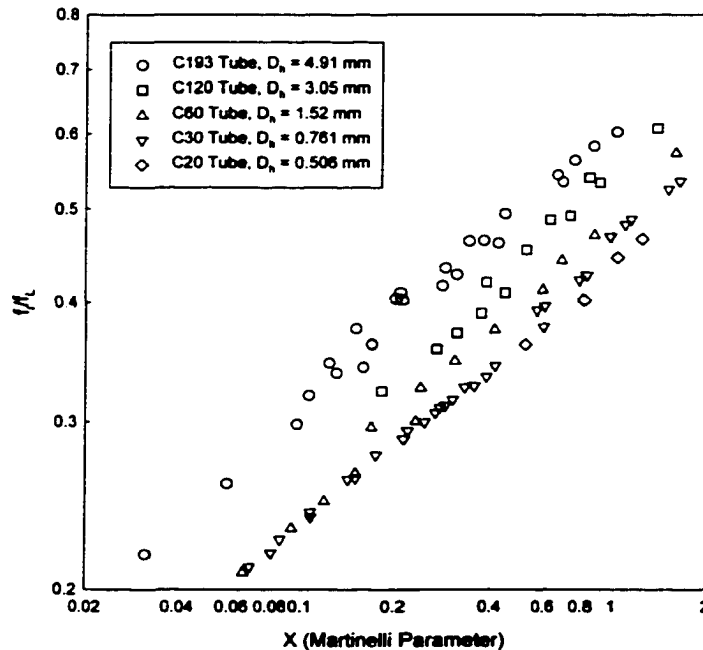


Figure 132. Normalized Interfacial Friction Factor Versus Martinelli Parameter, Circular Tubes

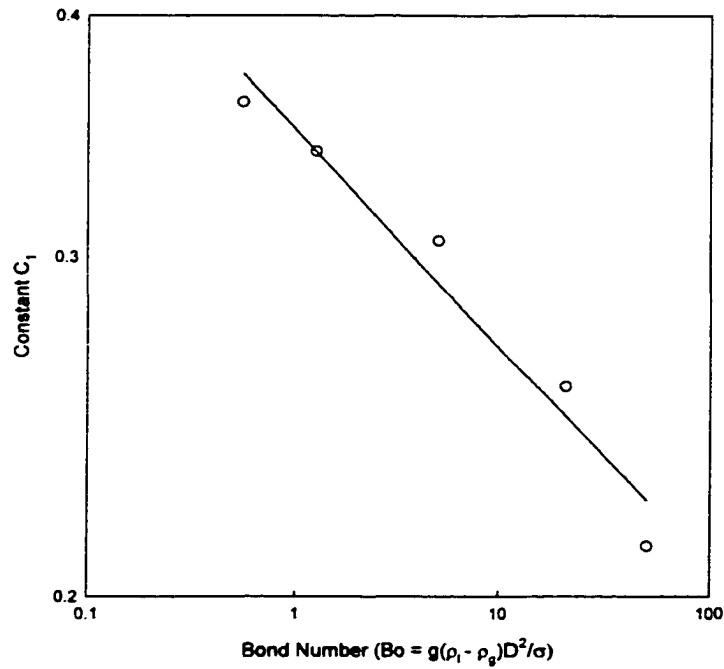


Figure 133. Constant C_1 as a Function of the Bond Number, Circular Tubes

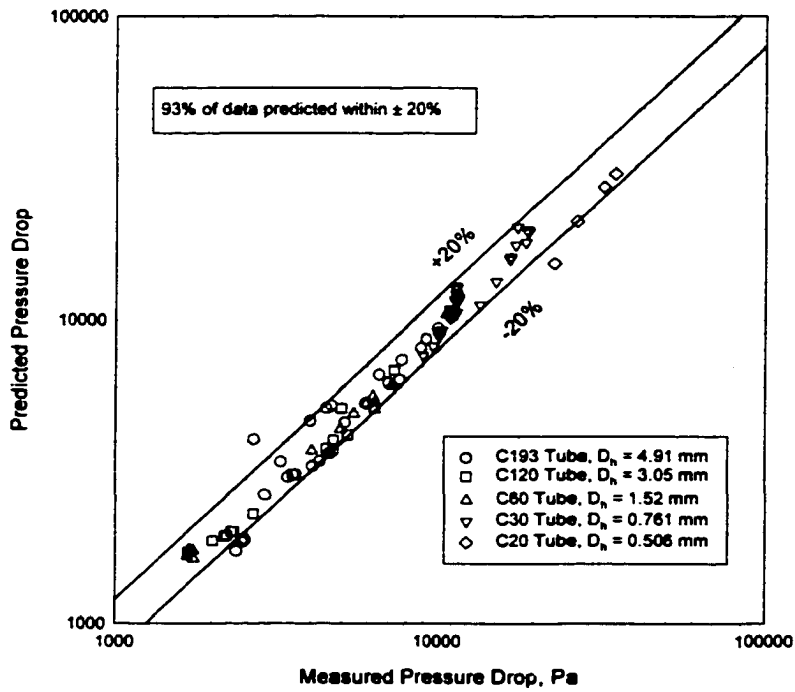


Figure 134. Predicted versus Measured Pressure Drops, Annular Film Model, Circular Tubes

Non-Circular Geometries

The annular film and disperse wave model was modified to accommodate non-circular geometries by basing the Reynolds number of the liquid film, Re_f , on the hydraulic diameter of the tube. Data for the T33, S30, B32, N21, RK15, W29I and W29II tubes were fit to equation (147), as shown in Figure 135 for the laminar flow case, and Figure 136 for the turbulent flow case. The constants in equation (147) are given in Table 23 for each tube tested in this study. At the lower mass fluxes, the liquid film friction factor can be laminar, and therefore, the data were fit based upon the laminar friction factors shown in Table 12. For turbulent flow, the Churchill (1977) equation was used to represent the single-phase friction factor, f_i . Two different correlations for each tube, depending upon whether the liquid film is laminar, or turbulent, were developed. Since only one hydraulic diameter for each tube shape was tested, the value of C_1 is a constant and not a function of the Bond number. Pressure drops predicted using this approach are plotted against the measured values in Figure 137 for the non-circular geometries. This figure shows that 90% of the non-circular geometry data could be fit within an error band of $\pm 20\%$.

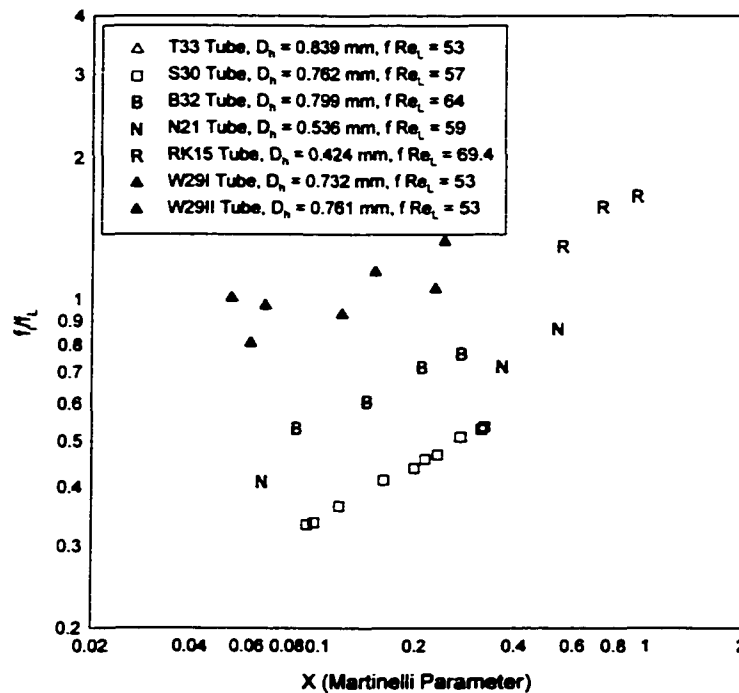


Figure 135. Laminar Normalized Interfacial Friction Factor Versus Martinelli Parameter, Non-Circular Tubes

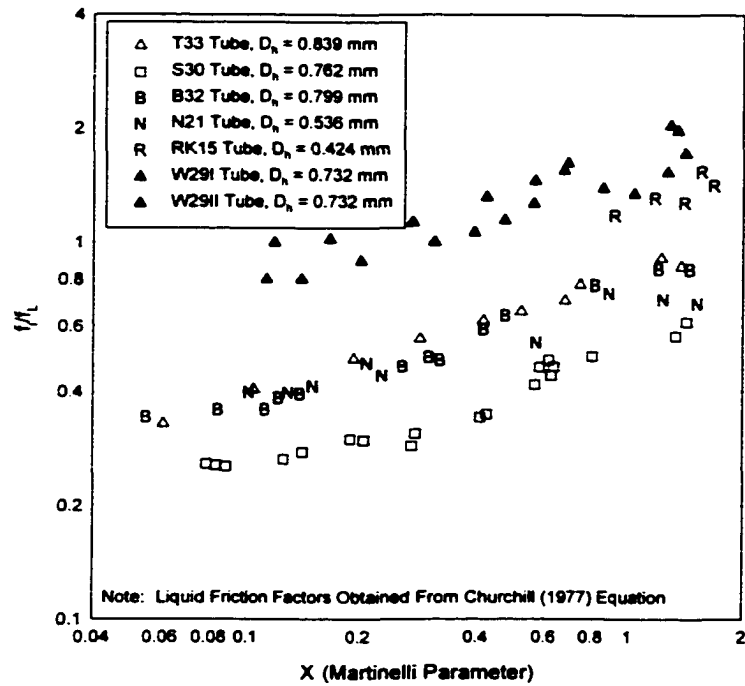


Figure 136. Turbulent Normalized Interfacial Friction Factor Versus Martinelli Parameter, Non-Circular Tubes

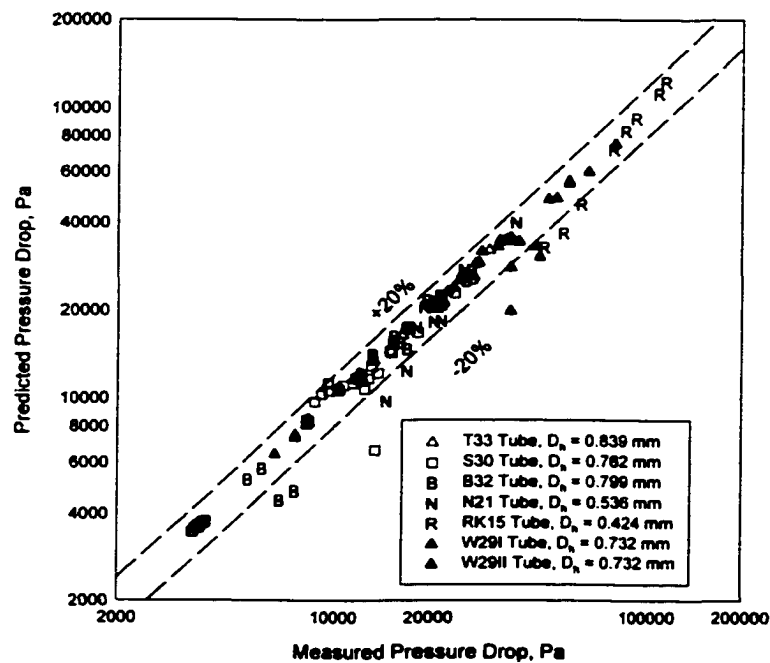


Figure 137. Predicted Versus Measured Pressure Drops, Annular Film Model, Non-Circular Tubes

Table 23. Constants for the Annular Film and Disperse Wave Flow

Tube	Constant C_1 (Laminar)	Constant C_2 (Laminar)	R^2 (Laminar)	Constant C_1 (Turb.)	Constant C_2 (Turb.)	R^2 (Turb.)
T33	2.663	0.300	1.00	0.816	0.314	0.986
S30	0.821	0.378	0.998	0.525	0.340	0.938
B32	1.163	0.322	0.988	0.779	0.334	0.973
N21	1.060	0.356	0.993	0.664	0.239	0.920
RK15	1.749	0.461	0.918	1.210	0.352	0.983
W29I	1.417	0.200	0.999	1.450	0.299	0.961
W29II	1.729	0.200	0.930	1.801	0.326	0.980

Annular Film and Mist Flow Model

Circular Tubes

Annular film flow with mist entrainment is shown schematically in Figure 138. To model this flow, the two-phase pressure drop data in the annular film and mist flow region were used to calculate the interfacial friction factor. Similar to the annular film flow model, the results were normalized with respect to the liquid phase friction factor and plotted against the Martinelli parameter. The results of this analysis are shown in Figure 139. Again, the friction factor ratio was correlated with the Martinelli parameter, X , as follows:

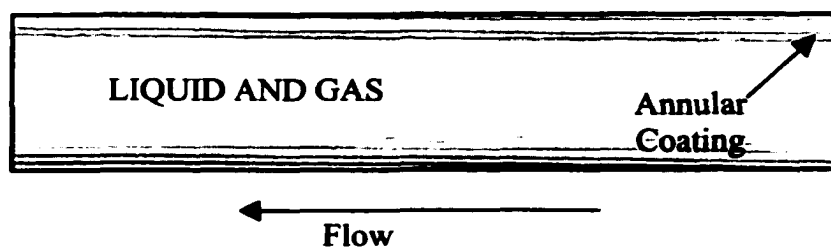
$$\left(\frac{f_i}{f_L}\right) = C_1(X)^{C_2} \quad (152)$$

The variable C_1 is correlated as a function of the Bond number as follows:

$$C_1 = 0.44(Bo)^{0.146} \quad (153)$$

This equation had a correlation coefficient R^2 of 0.971. The constant C_2 is also correlated as a function of the Bond number with an R^2 of 0.964 as follows:

$$C_2 = 0.229(Bo)^{0.126} \quad (154)$$

**Figure 138. Schematic of Combined Mist and Annular Film Flow**

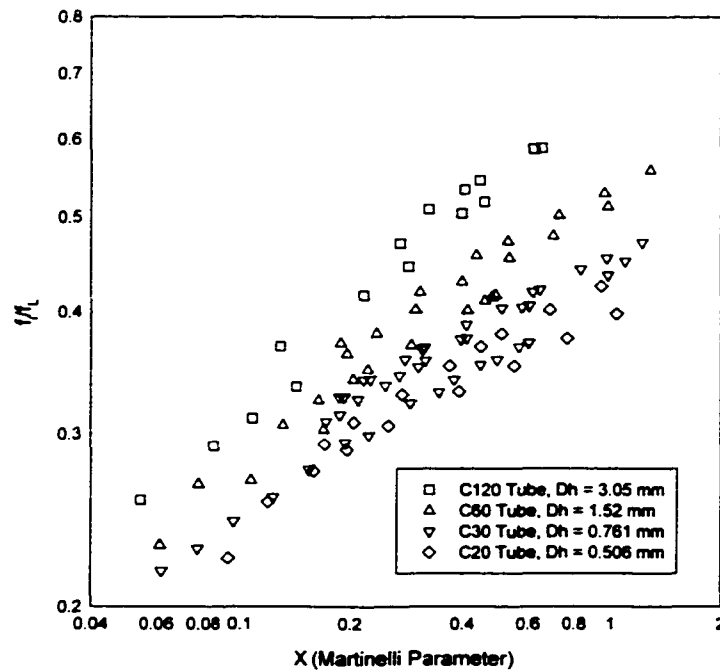


Figure 139. Normalized Interfacial Friction Factor Versus Martinelli Parameter, Annular Film and Mist Flow, Circular Tubes

Figure 140 shows the correlations for both the C_1 and C_2 constants. Pressure drops predicted using this approach are plotted against the measured values in Figure 141. This figure shows that 95% of the non-circular geometry data could be fit within an error band of $\pm 15\%$.

Non-Circular Geometries

The annular film and mist flow model was modified to accommodate non-circular geometries by basing the Reynolds number of the liquid film, Re_f , on the hydraulic diameter of the tube. Unlike the modeling of the annular film and disperse wave pressure drops, data for the T33, S30, B32, N21, RK15, W29I and W29II tubes were fit to a single equation (152), regardless of whether the liquid flow was laminar or turbulent, as shown in Figure 142. (This was justifiable because of the 171 data points in this regime, the liquid film was in the laminar regime for only 1 data point). The constants in equation (152) are given in Table 24 for each tube tested in this study. For the one data point with laminar liquid flow, the laminar liquid friction factor was calculated from constants shown in Table 12. For turbulent flow, the Churchill (1977) equation was used to represent the single-phase friction factor, f_i . Pressure drops predicted using this approach are plotted against the measured values in Figure 143 for the non-circular geometries. This figure shows that 91% of the non-circular geometry data could be fit within an error band of $\pm 10\%$.

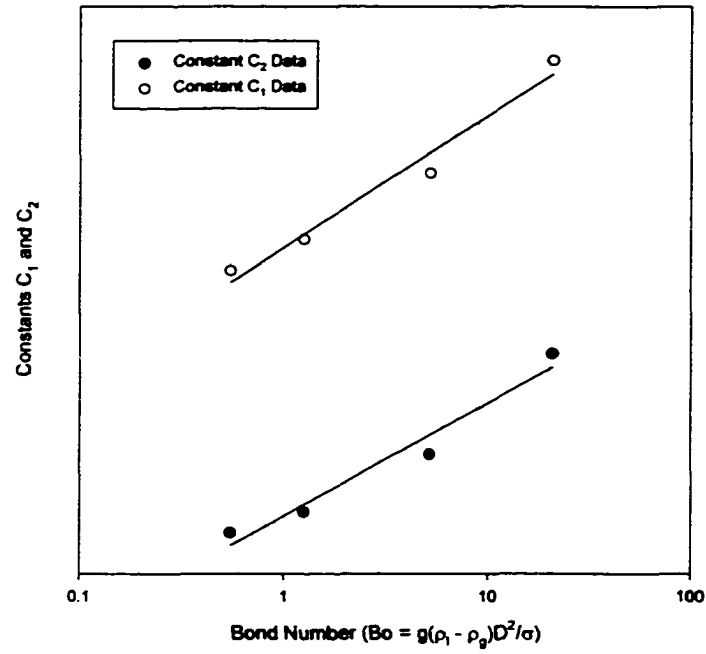


Figure 140. Constants C_1 and C_2 as a Function of the Bond Number, Annular Film and Mist Flow, Circular Tubes

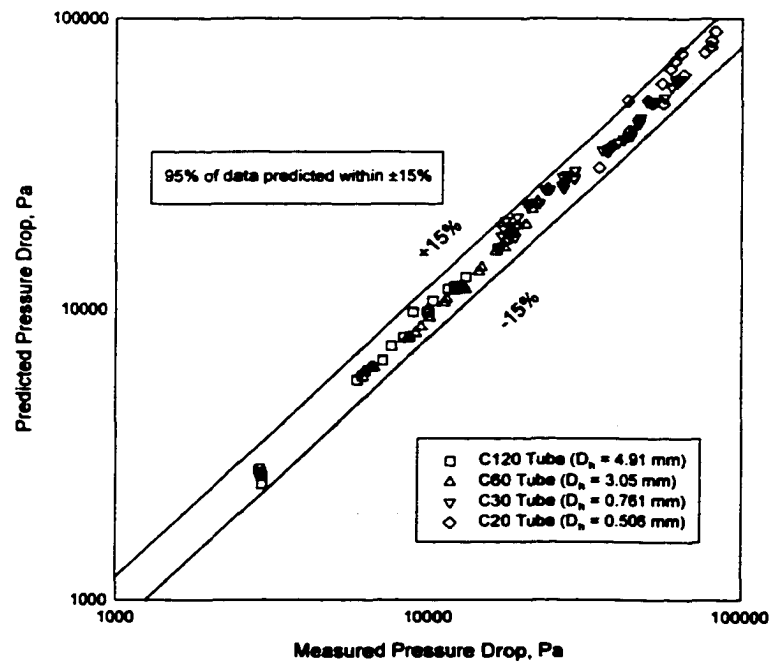


Figure 141. Predicted Versus Measured Pressure Drop, Annular Film and Mist Flow, Circular Tubes

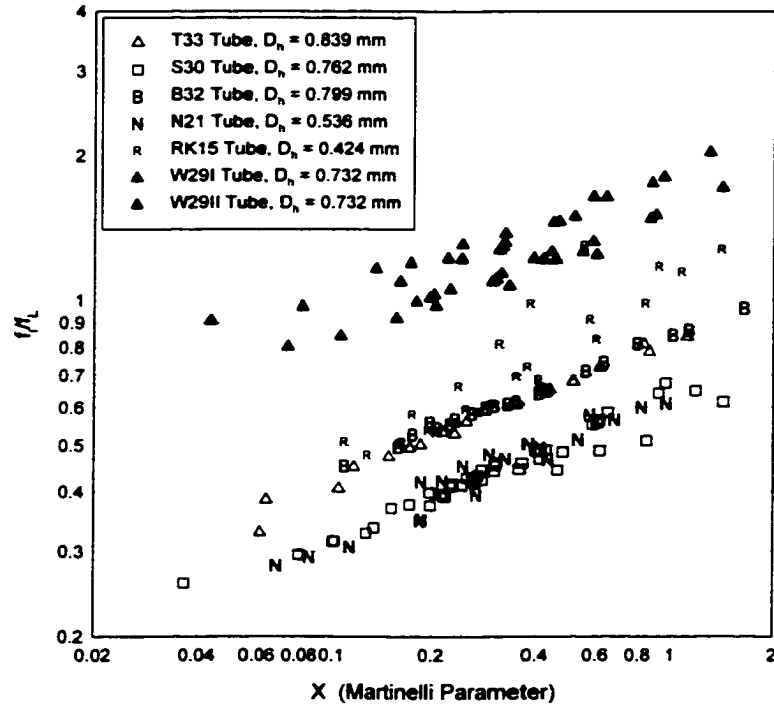


Figure 142. Normalized Interfacial Friction Factor Versus Martinelli Parameter, Annular Film and Mist Flow, Non-circular Geometries

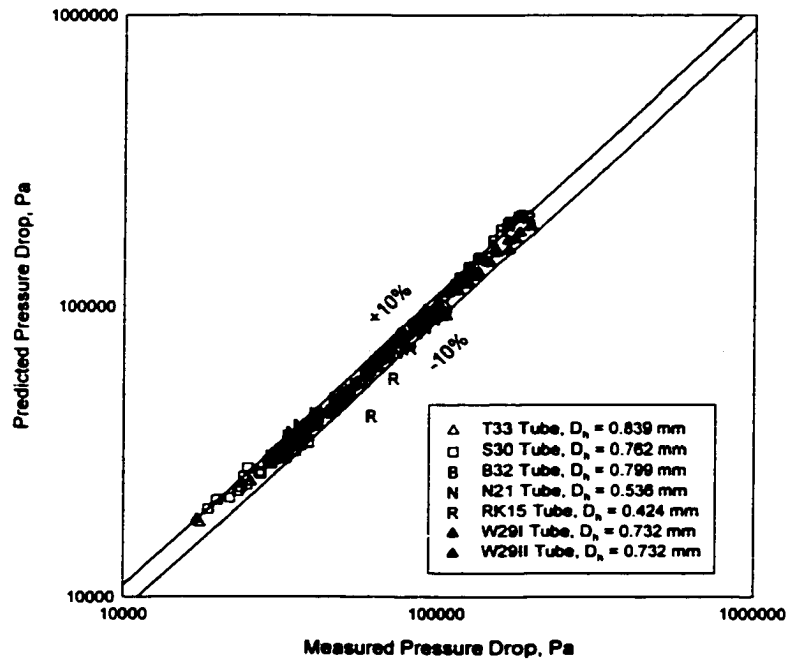


Figure 143. Predicted versus Measured Pressure Drop, Annular Film and Mist Flow Model, Non-Circular Geometries

Table 24. Constants for the Annular Film and Mist Flow Model

Tube	Shape	D_h (mm)	Constant C_1	Constant C_2	R^2
T33	Triangle	0.839	0.832	0.298	0.991
S30	Square	0.762	0.613	0.279	0.927
B32	Barrel	0.799	0.840	0.278	0.995
N21	“N”	0.536	0.640	0.306	0.933
RK15	Rectangle	0.424	1.149	0.421	0.811
W29I	Triangle (Insert)	0.732	1.521	0.264	0.974
W29II	Triangle (Insert)	0.732	1.821	0.259	0.966

Mist Flow Model

Circular Tubes

Mist flow is characterized by a fine mist flowing through the core of the tube. The annular film is very thin or non-existent in this flow pattern. A schematic of this flow was shown in Figure 138. To model this flow pattern, the two-phase pressure drop data in the mist flow pattern were used to calculate the interfacial friction factor. The results were normalized by the liquid friction factor and plotted against the Martinelli parameter as shown in Figure 144. Although the liquid-vapor interface is different in mist flow than in annular flows, it was found that even in this case, the interface-to-liquid film friction factor ratio could be correlated as follows:

$$\left(\frac{f_i}{f_L}\right) = C_1(X)^{0.30} \quad (155)$$

where C_1 is a function of the Bond number as follows:

$$C_1 = 0.492(Bo)^{0.11} \quad (156)$$

The constant C_1 is plotted against the Bond number in Figure 145 and this equation had a correlation coefficient R^2 of 0.94. Pressure drops predicted using this approach are plotted against the measured values in Figure 146 for the mist flow data. This figure shows that 96% of the data could be fit within an error band of $\pm 20\%$.

Non-Circular Geometries

The mist flow model was modified to accommodate non-circular geometries by basing the Reynolds number of the liquid film, Re_f , on the hydraulic diameter of the tube. Unlike the modeling of the annular film and disperse wave pressure drops, data for the T33, S30, B32, N21, RK15, W29I and W29II tubes were fit to a single equation (152), regardless of whether the

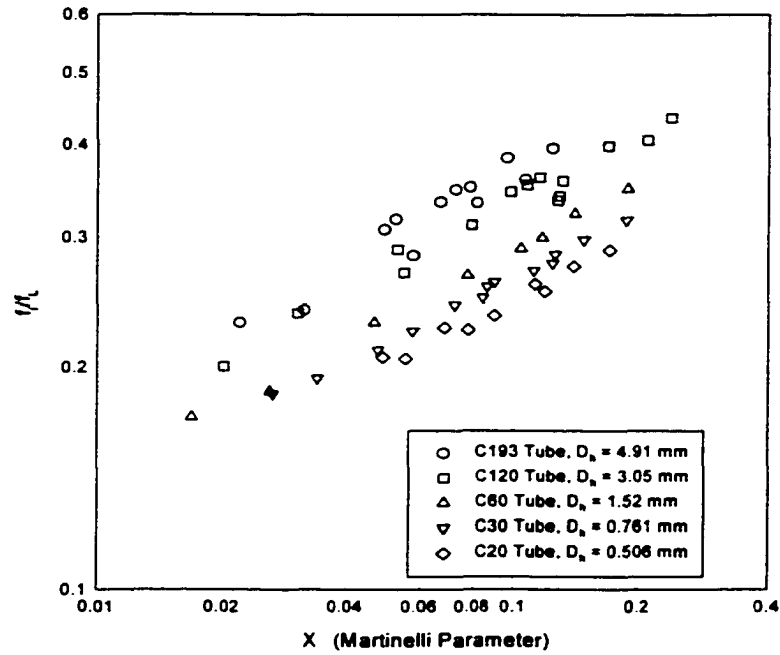


Figure 144. Normalized Interfacial Friction Factor Versus Martinelli Parameter, Mist Flow, Circular Tubes

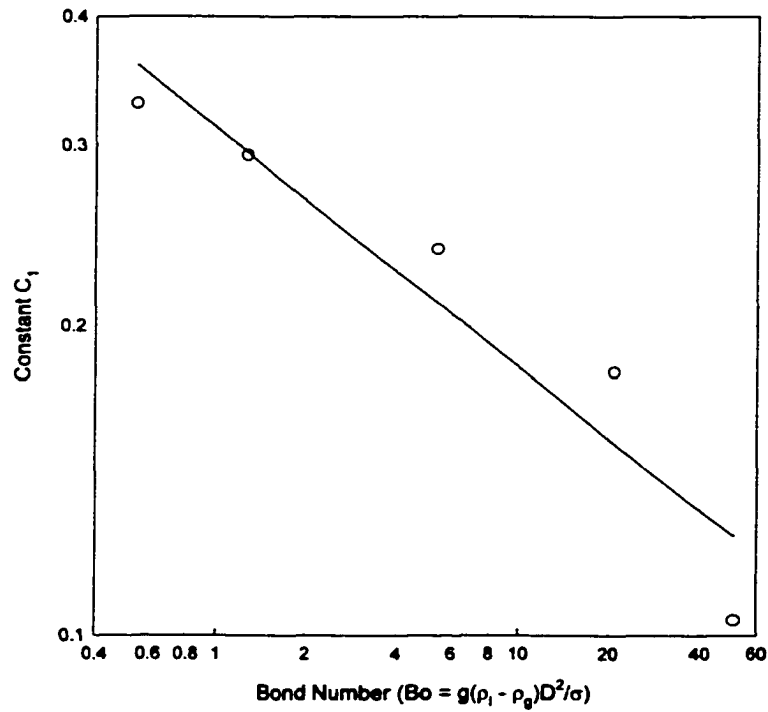


Figure 145. Constant C_1 Versus the Bond Number, Mist Flow Model, Circular Tubes

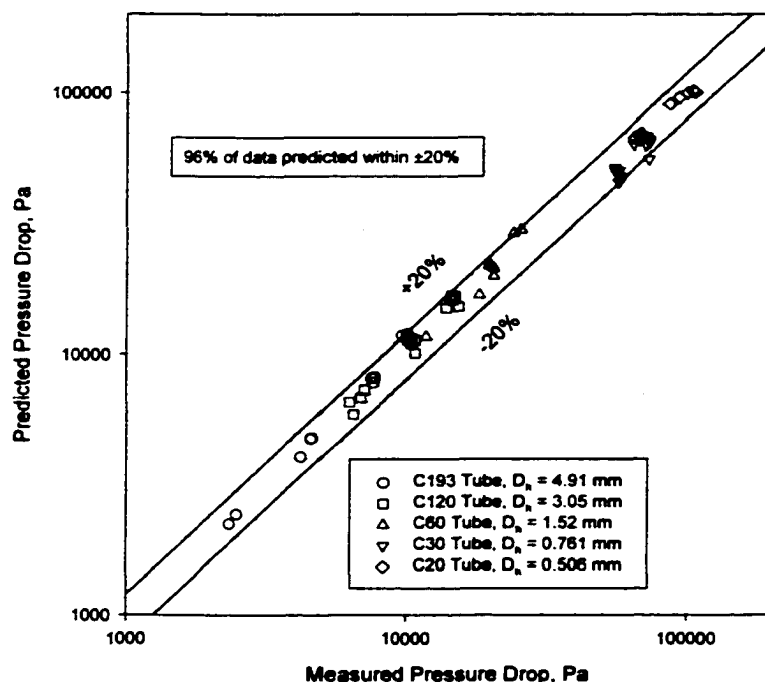


Figure 146. Measured Versus Predicted Pressure Drop, Mist Flow Model, Circular Tubes

liquid flow was laminar or turbulent, as shown in Figure 147. (This was justifiable because of the 50 data points in this regime, all liquid film data were in the turbulent regime). The constants in equation (152) are given in Table 25 for each tube tested in this study. For turbulent flow, the Churchill (1977) equation was used to represent the single-phase friction factor, f_i . Pressure drops predicted using this approach are plotted against the measured values in Figure 148 for the non-circular geometries. This figure shows that 94% of the non-circular geometry data could be fit within an error band of $\pm 20\%$.

Table 25. Constants for the Mist Flow Model

Tube	Shape	D_h (mm)	Constant C_0	Constant C_1	R^2
T33	Triangle	0.839	0.777	0.253	0.993
S30	Square	0.762	0.554	0.226	0.901
B32	Barrel	0.799	0.801	0.226	0.946
N21	"N"	0.536	0.612	0.233	0.989
RK15	Rectangle	0.424	0.696	0.177	0.972
W29I	Triangle (Insert)	0.732	1.336	0.165	0.960
W29II	Triangle (Insert)	0.732	1.828	0.221	0.984

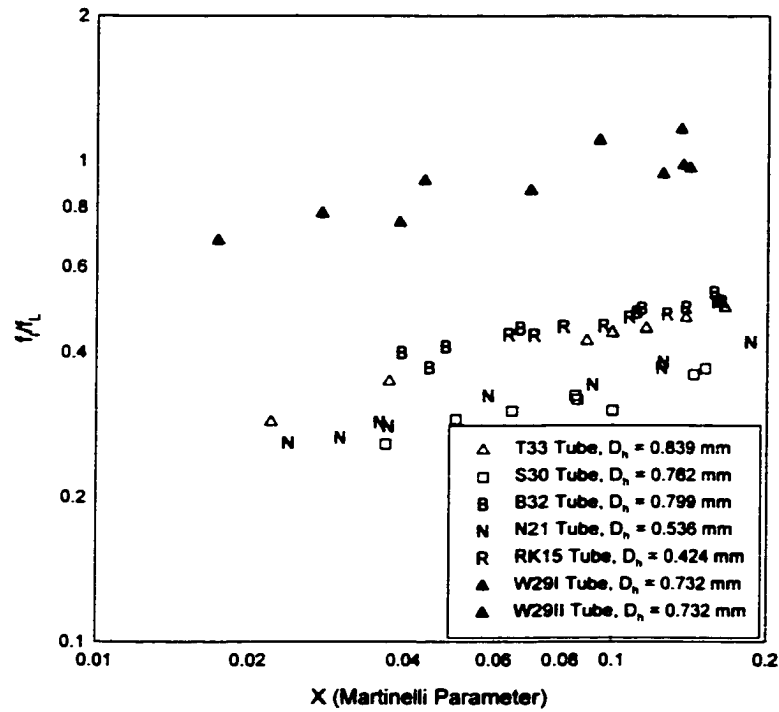


Figure 147. Normalized Interfacial Friction Factor versus Martinelli Parameter, Mist Flow Model, Non-circular Geometries

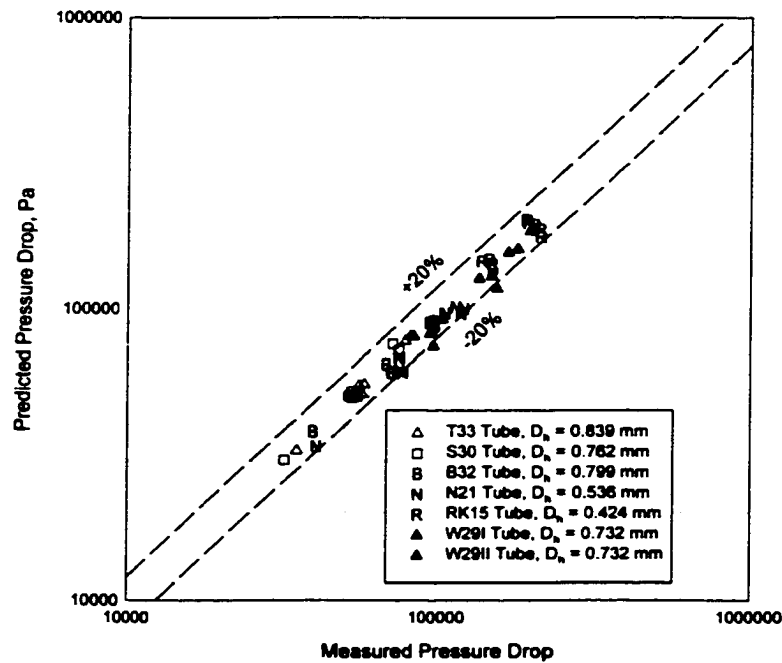


Figure 148. Measured versus Predicted Pressure Drop, Mist Flow Model, Non-circular Geometries

Figure 149 shows the experimentally measured two-phase pressure drops versus those predicted by the models for the five circular tubes tested in this study. As shown in this Figure, 90% of the circular tube data are predicted within $\pm 20\%$. Similarly, Figure 150 shows the experimentally measured two-phase pressure drops versus those predicted by the models for the non-circular geometries. This figure shows that 92% of the non-circular tube data are predicted within 20%.

Overall Model Predictions

Figures 151-155 show the experimentally measured two-phase pressure drops versus those predicted by the models for the five circular tubes tested in this study. The experimentally determined transition lines were used to predict the flow pattern and the resulting two-phase flow pressure drop correlation. As shown in these figures, the measured pressure drop and the predictions by the models show good agreement for all five circular tubes. In Figures 156-163, the experimentally measured pressure drops are shown for the non-circular geometries tested in this study including the T33, S30, B32, N21, RK15, W29I and W29II tubes. Due to the small hydraulic diameter and available free flow area, of the RK15 tube, heat balances and pressure drop data were attainable on only three mass fluxes. This lack of data resulted in correlations with higher errors than the others as seen in Figure 161. Overall, these models show good agreement for all the non-circular geometries tested in this study and closely follow the trends seen in the data.

These models were also used to predict the two-phase pressure drops at constant nominal mass fluxes using both the theoretical and experimental transition lines, as shown in Figures 164-168 for the five circular tubes. The pressure drops shown in these figures are based upon the respective tube lengths. While the majority of the data are in agreement, there are regions where the theoretical and experimental transitions predict different flow regimes. For example, in Figure 164, the $G = 750 \text{ kg/m}^2\text{-s}$ case shows four data points where the theoretical and experimental transition lines predict two different regimes. The experimental lines predict disperse waves, while the theoretical lines predict discrete waves, which leads to discrepancies in the calculated pressure drops.

Figures 169 – 174 show the two-phase pressure drop using both the theoretical and experimental transition lines for the non-circular tube geometries. Again, there are regions where the experimental and theoretical transition lines differ, and this results in differences in the predicted two-phase pressure drop. Figure 170 illustrates a series of data points that are predicted differently for the $G = 300 \text{ kg/m}^2\text{-s}$ case. The experimental transition lines predict this regime to be a mist flow pattern, while the theoretical transition lines predict this region to be an annular film flow pattern, resulting in the difference in predicted pressure drops.

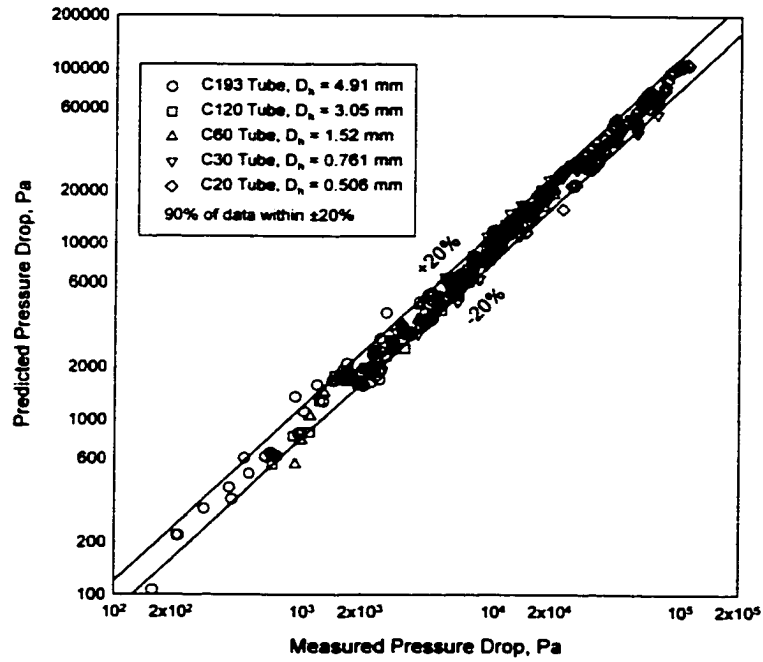


Figure 149. Overall Model Predictions, Circular Tubes

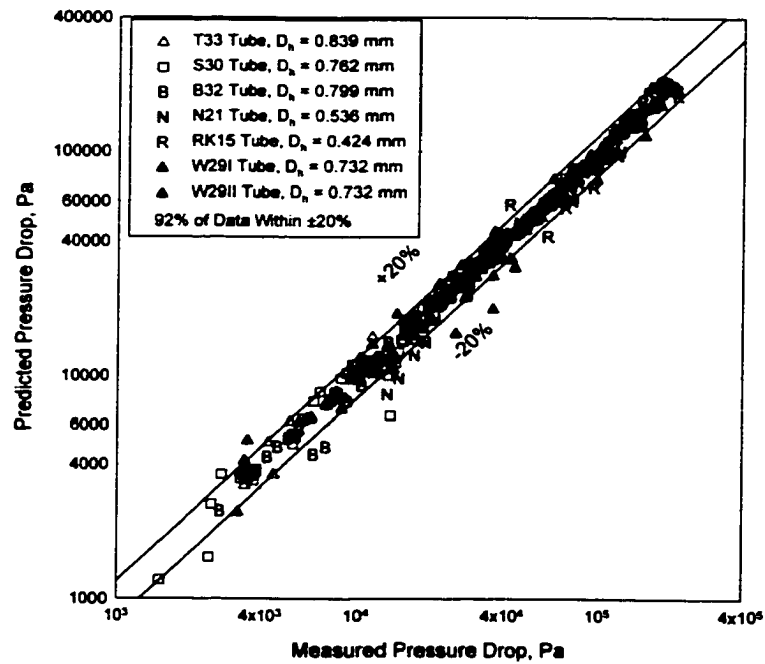


Figure 150. Overall Model Predictions, Non-Circular Geometries

Furthermore, the RK15 tube (refer to Figure 173) shows the most amount of deviation due to the relatively few data for this particular tube. Overall, good agreement between the experimental and theoretical transition lines was found.

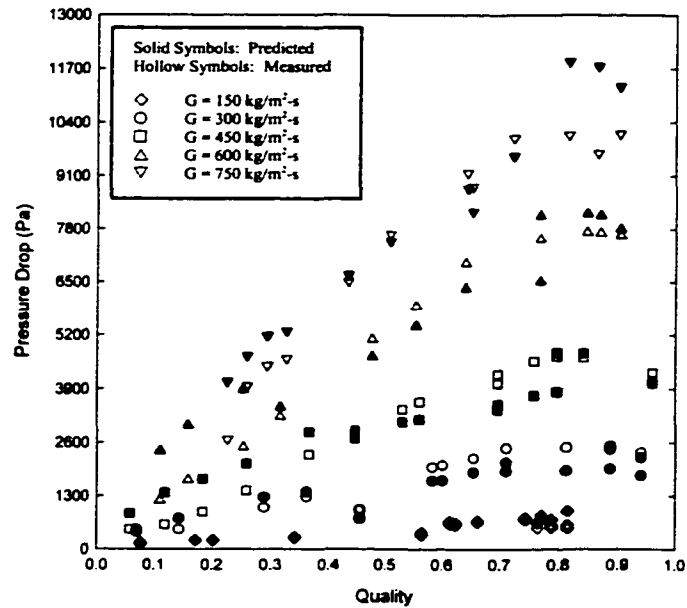


Figure 151. Measured versus Predicted Pressure Drop for All Models (C193 Tube, $D_h = 4.91 \text{ mm}$)

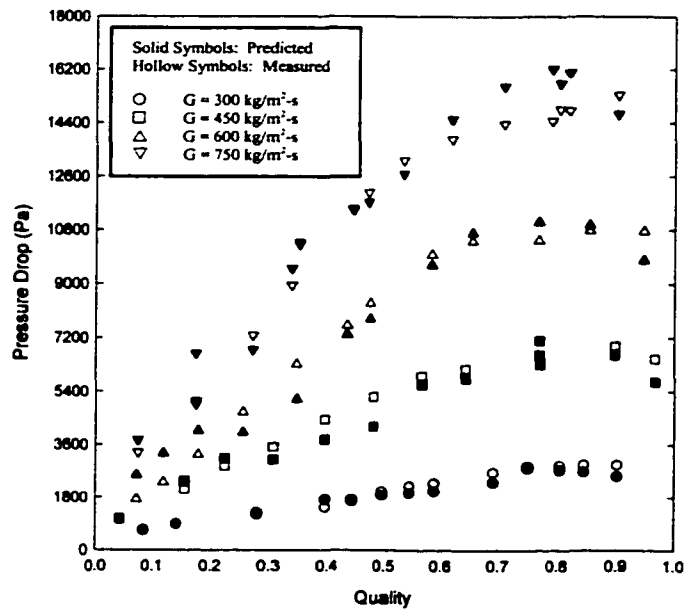


Figure 152. Measured versus Predicted Pressure Drop for All Models (C120 Tube, $D_h = 3.05 \text{ mm}$)

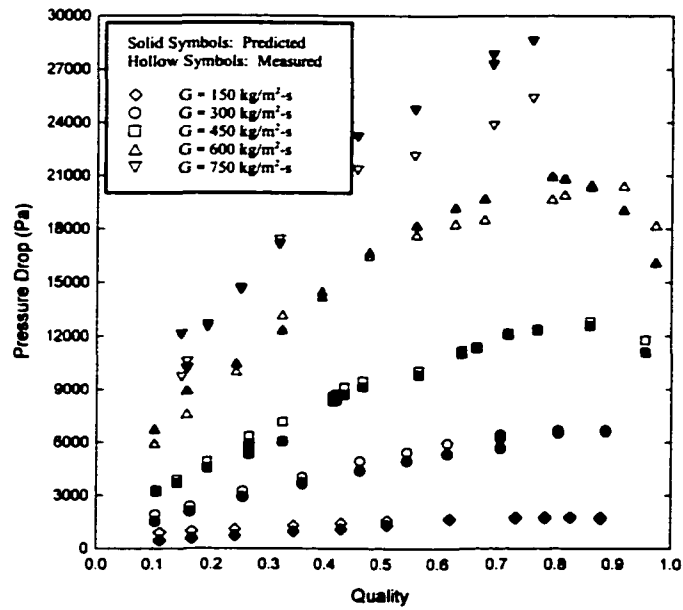


Figure 153. Measured versus Predicted Pressure Drop for All Models (C60 Tube, $D_h = 1.52$ mm)

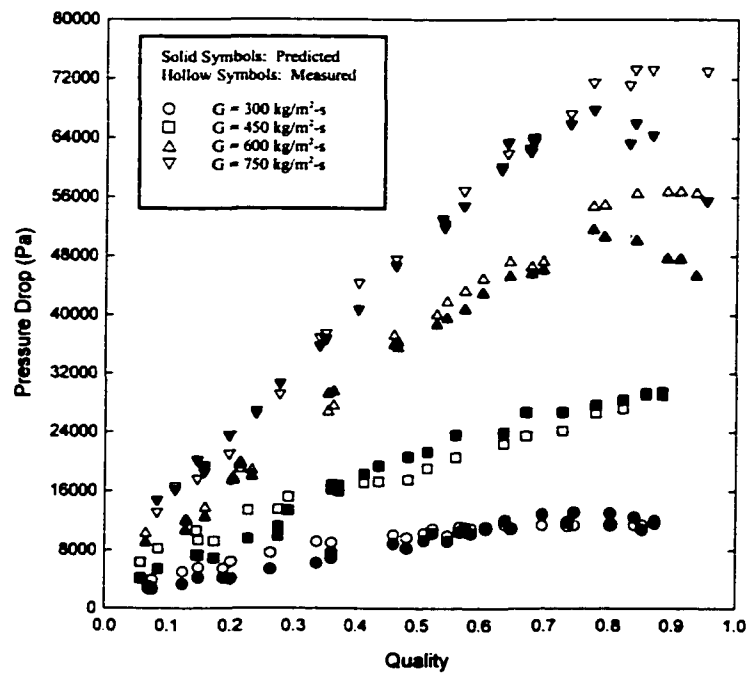


Figure 154. Measured versus Predicted Pressure Drop for All Models (C30 Tube, $D_h = 0.761$ mm)

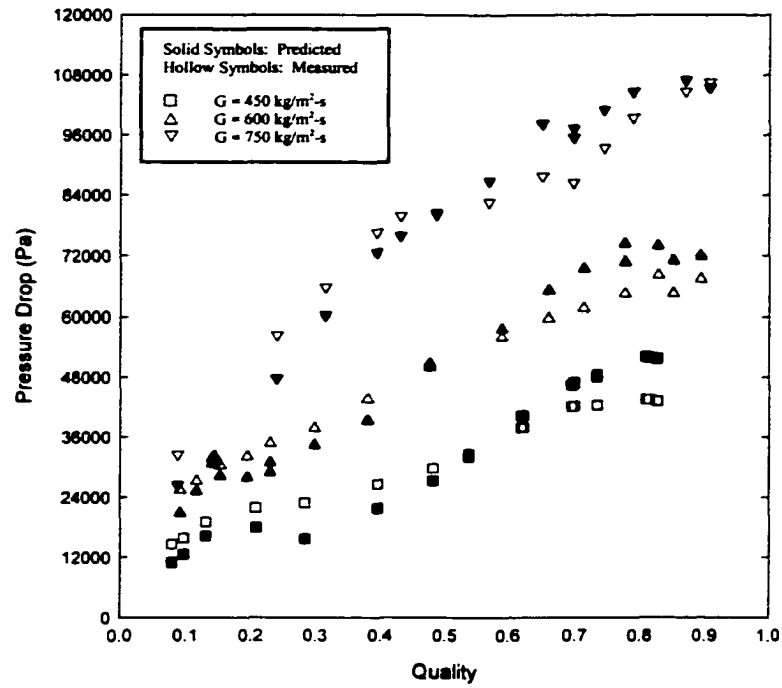


Figure 155. Measured versus Predicted Pressure Drop for All Models (C20 Tube, $D_h = 0.506$ mm)

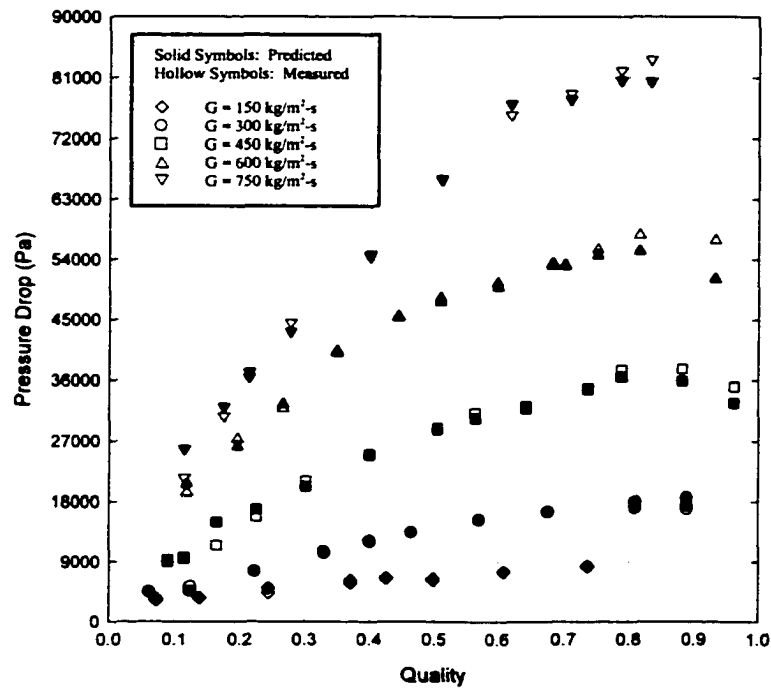


Figure 156. Measured versus Predicted Pressure Drop for All Models (T33 Tube, Triangle, $D_h = 0.839$ mm)

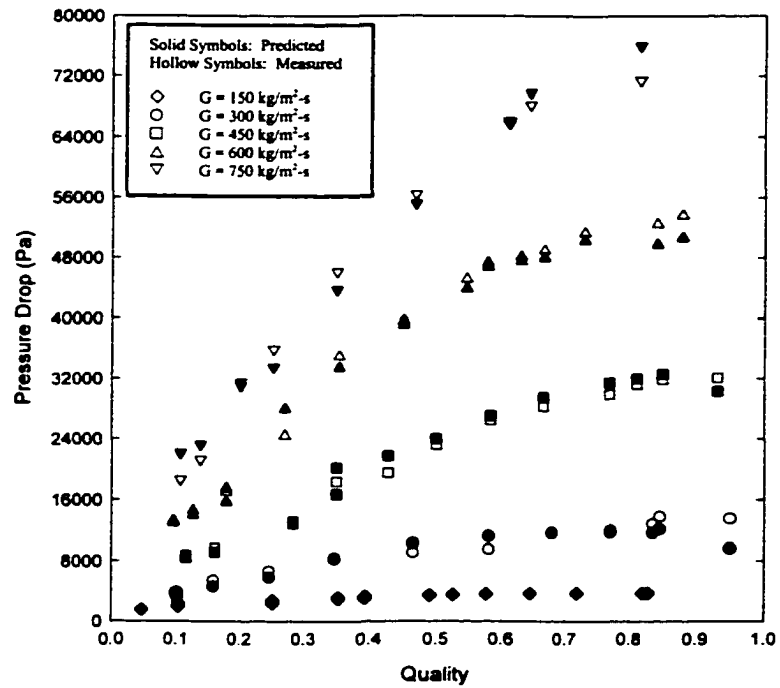


Figure 157. Measured versus Predicted Pressure Drop for All Models (S30 Tube, Square, $D_h = 0.762$ mm - Adiabatic)

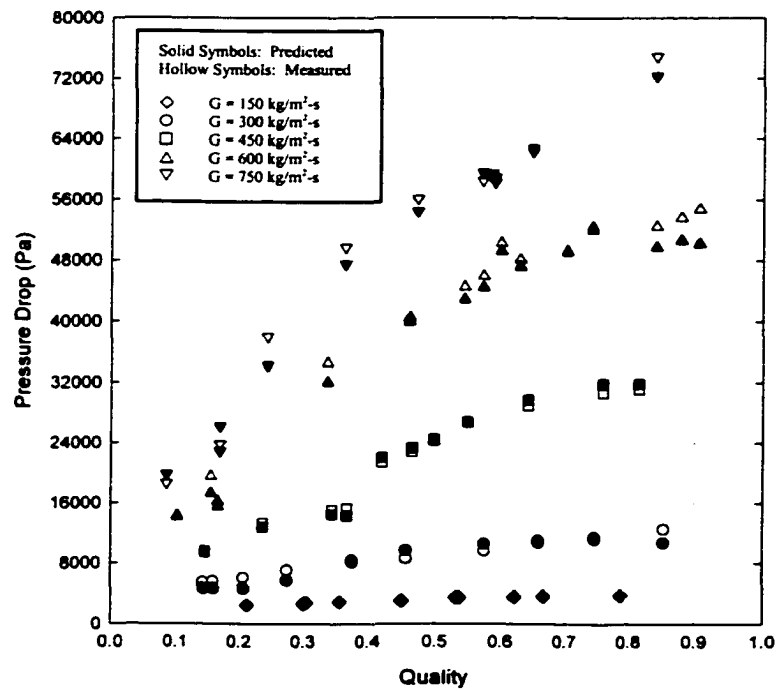


Figure 158. Measured versus Predicted Pressure Drop for All Models (S30 Tube, Square, $D_h = 0.762$ mm - Diabatic)

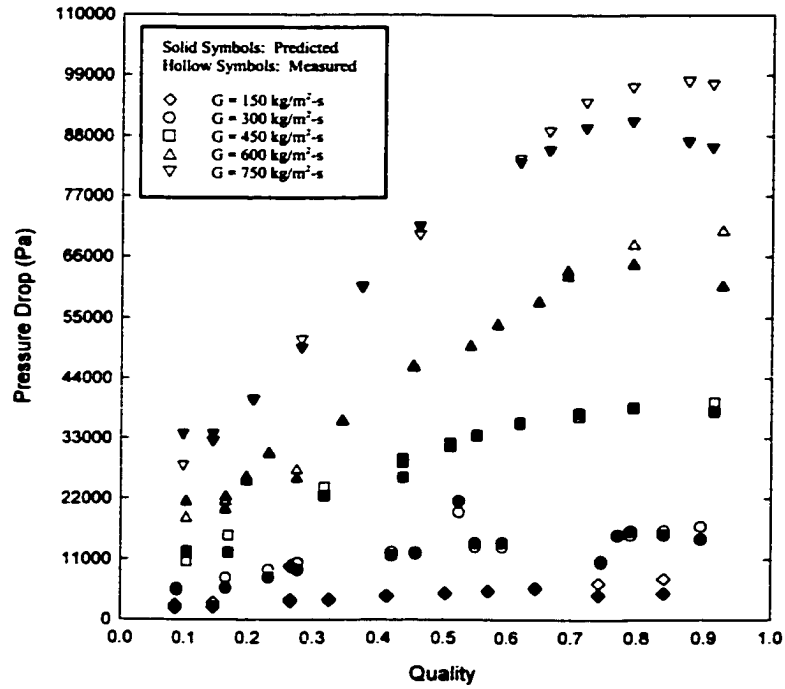


Figure 159. Measured versus Predicted Pressure Drop for All Models (B32 Tube, Barrel, $D_h = 0.799$ mm)

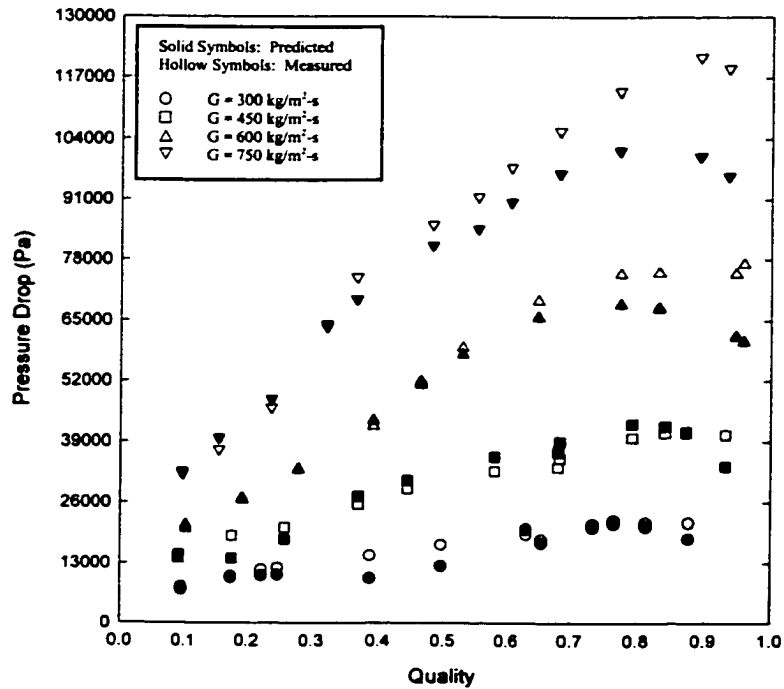


Figure 160. Measured versus Predicted Pressure Drop for All Models (N21 Tube, "N"-Shape, $D_h = 0.536$ mm)

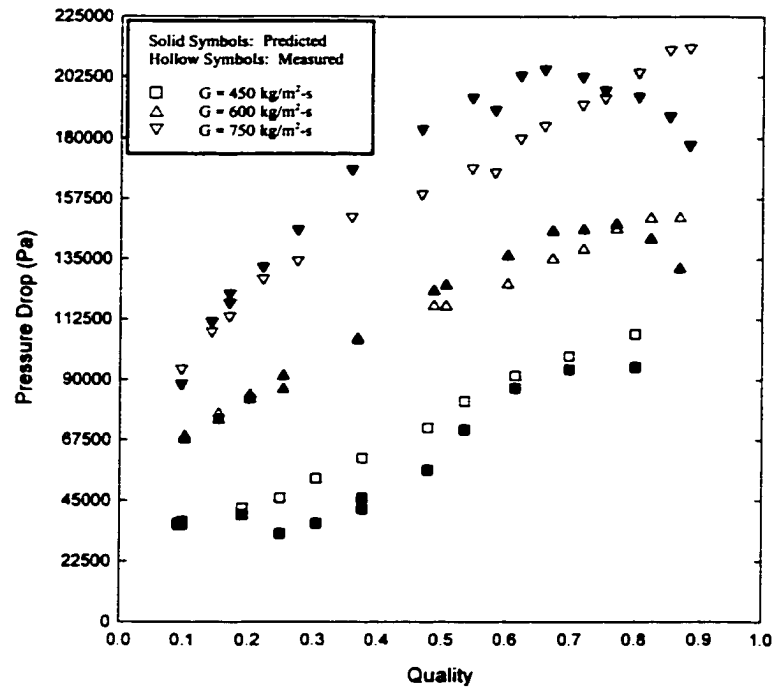


Figure 161. Measured versus Predicted Pressure Drop for All Models (RK15 Tube, Rectangle, $D_h = 0.424$ mm)

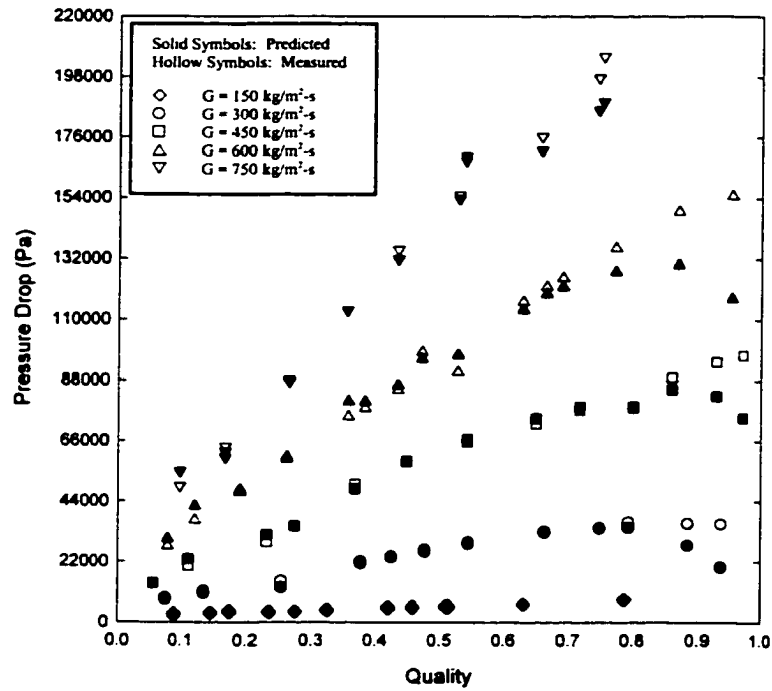


Figure 162. Measured versus Predicted Pressure Drop for All Models (W29I Tube, Triangle Insert, $D_h = 0.732$ mm)

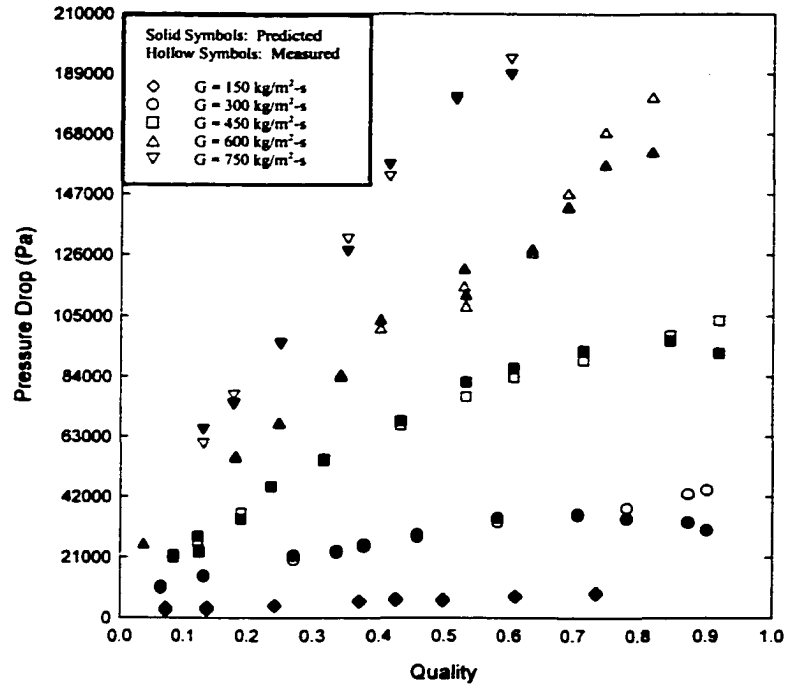


Figure 163. Measured versus Predicted Pressure Drop for All Models (W29II Tube, Triangle Insert, $D_h = 0.732$ mm)

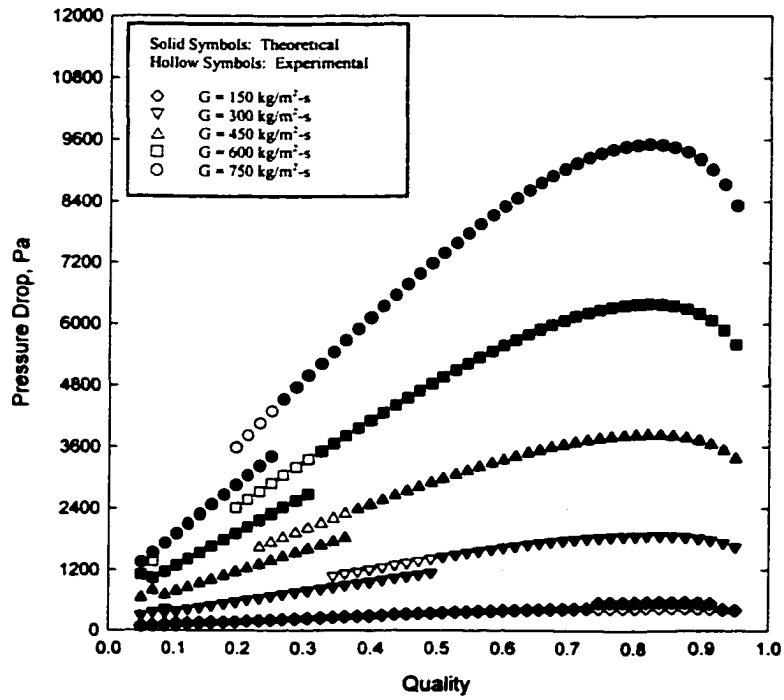


Figure 164. Predicted Pressure Drop for All Models Using Theoretical and Experimental Transition Lines (C193 Tube, $D_h = 4.91$ mm)

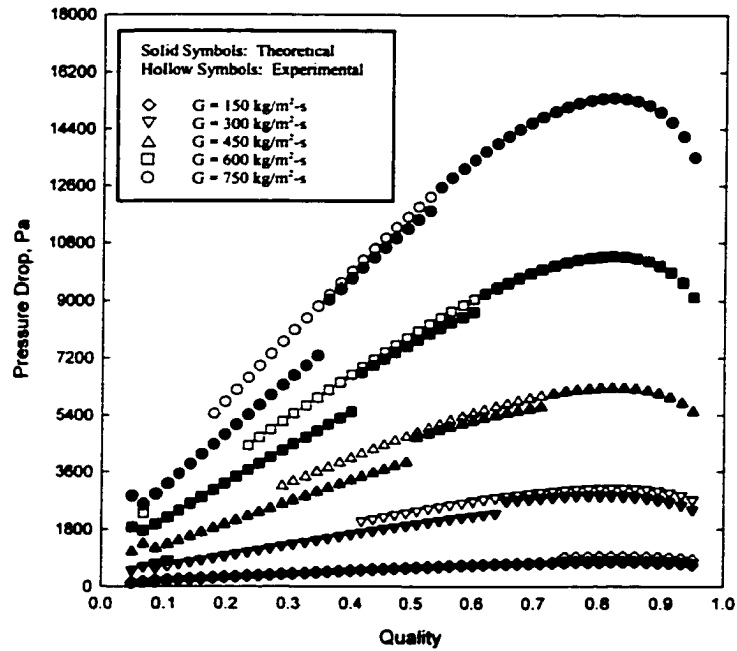


Figure 165. Predicted Pressure Drop for All Models Using Theoretical and Experimental Transition Lines (C120 Tube, $D_h = 3.05$ mm)

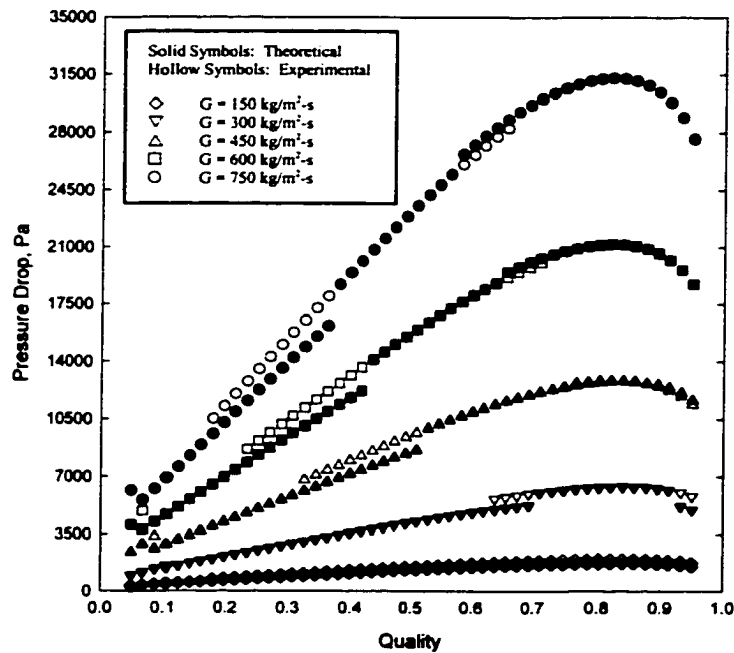


Figure 166. Predicted Pressure Drop for All Models Using Theoretical and Experimental Transition Lines (C60 Tube, $D_h = 1.52$ mm)

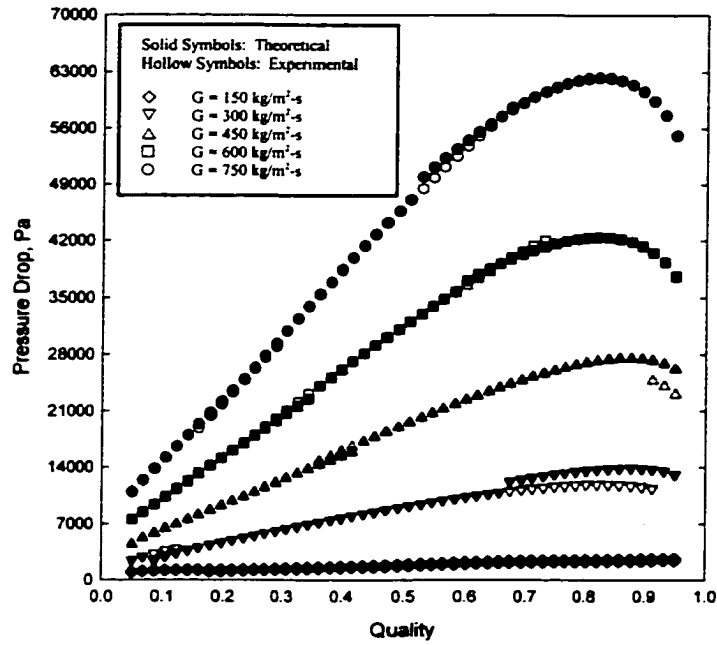


Figure 167. Predicted Pressure Drop for All Models Using Theoretical and Experimental Transition Lines (C30 Tube, $D_h = 0.761$ mm)

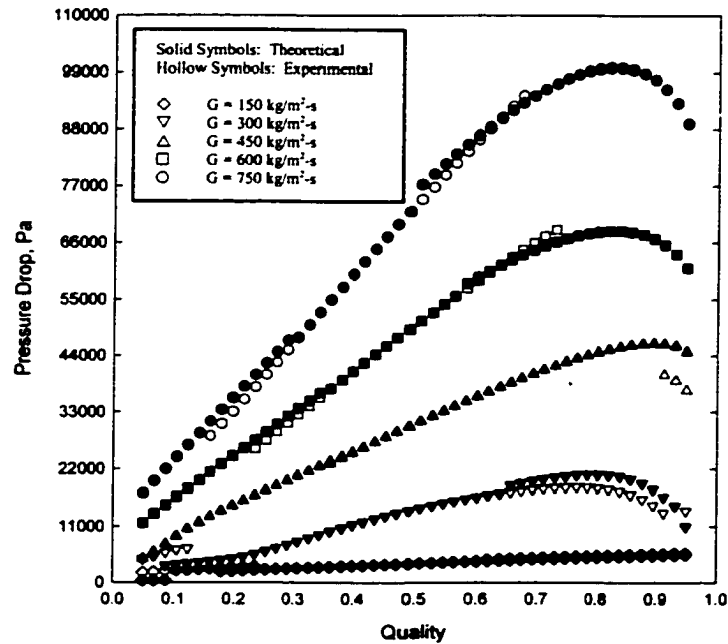


Figure 168. Predicted Pressure Drop for All Models Using Theoretical and Experimental Transition Lines (C20 Tube, $D_h = 0.506$ mm)

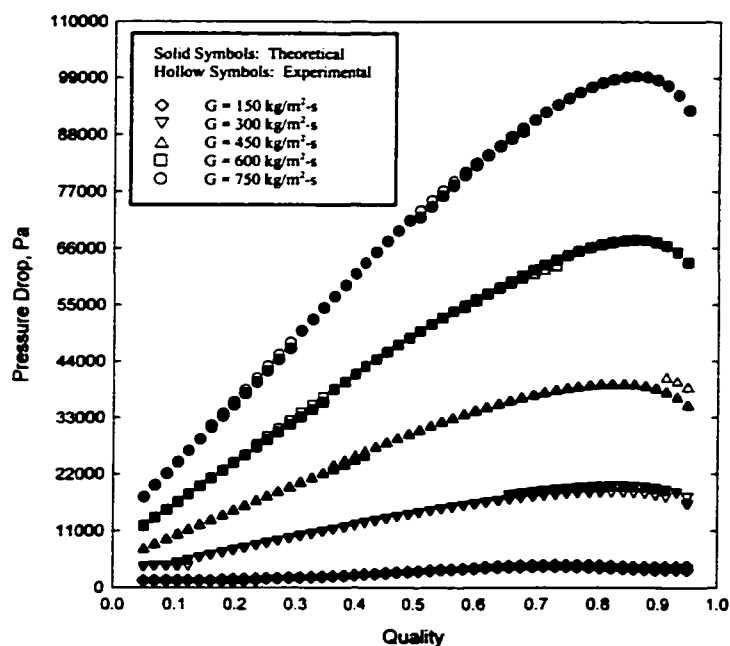


Figure 169. Predicted Pressure Drop for All Models Using Theoretical and Experimental Transition Lines (T33 Tube, Triangle, $D_h = 0.839$ mm)

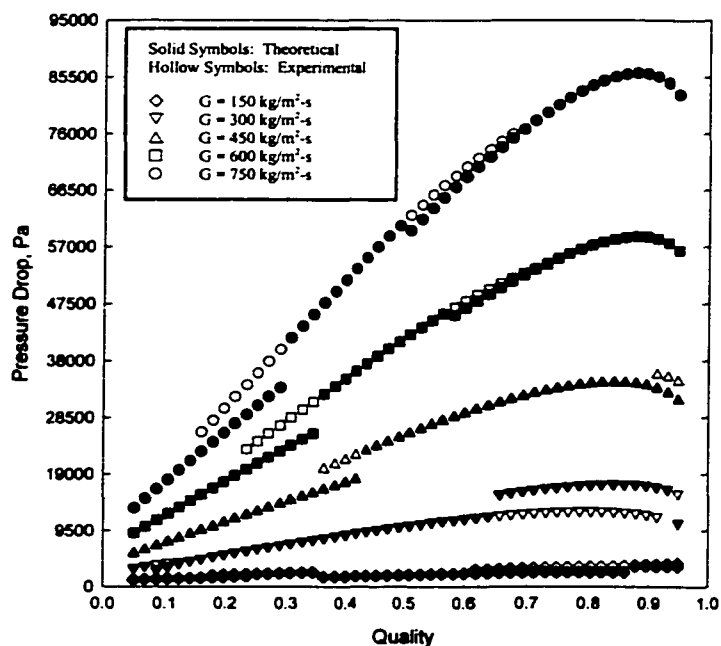


Figure 170. Predicted Pressure Drop for All Models Using Theoretical and Experimental Transition Lines (S30 Tube, Square, $D_h = 0.762$ mm)

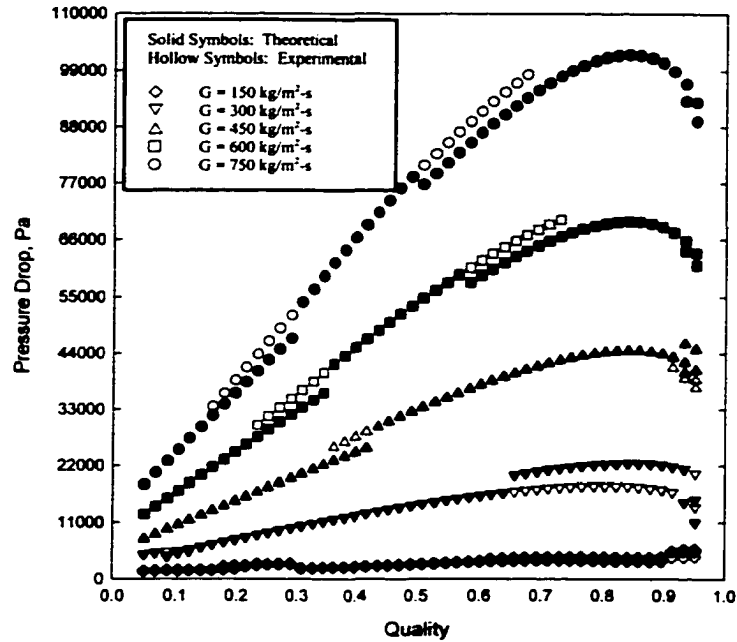


Figure 171. Predicted Pressure Drop for All Models Using Theoretical and Experimental Transition Lines (B32 Tube, Barrel, $D_h = 0.799$ mm)

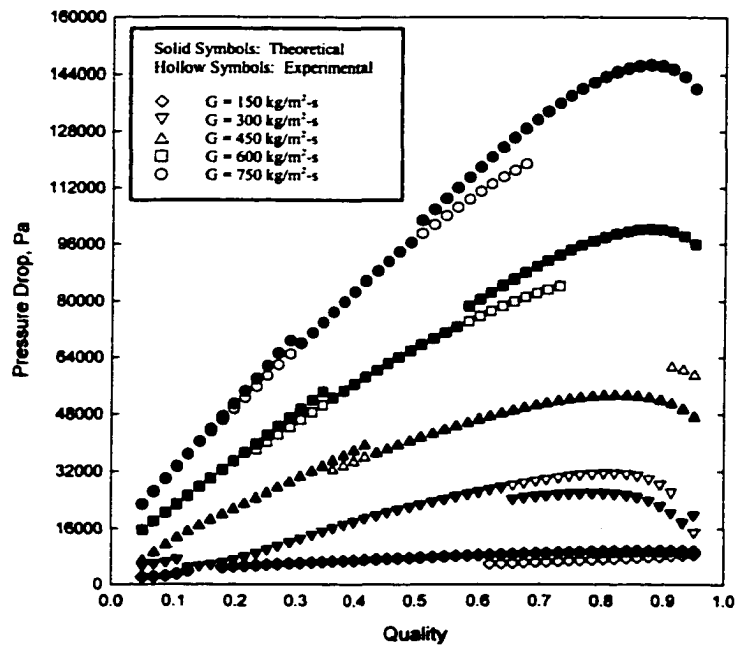


Figure 172. Predicted Pressure Drop for All Models Using Theoretical and Experimental Transition Lines (N21 Tube, "N" Shape, $D_h = 0.536$ mm)

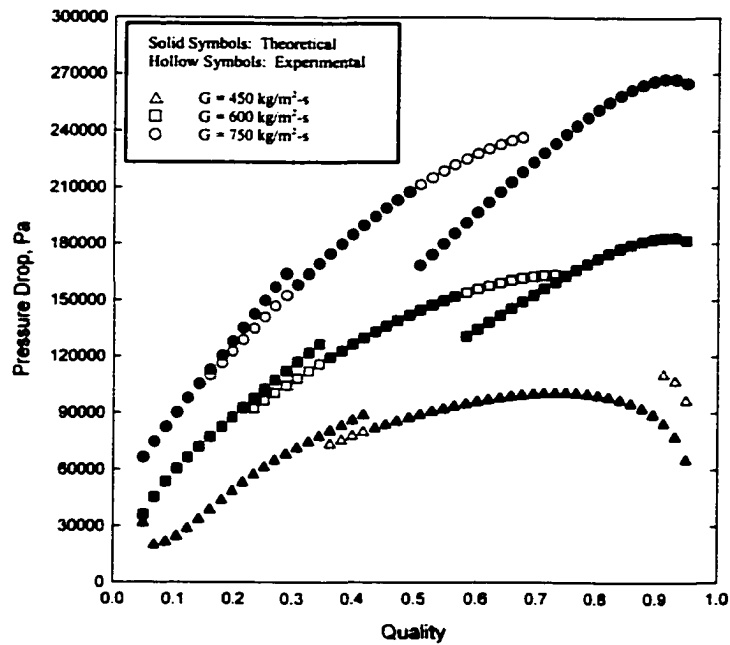


Figure 173. Predicted Pressure Drop for All Models Using Theoretical and Experimental Transition Lines (RK15 Tube, Rectangle, $D_h = 0.424$ mm)

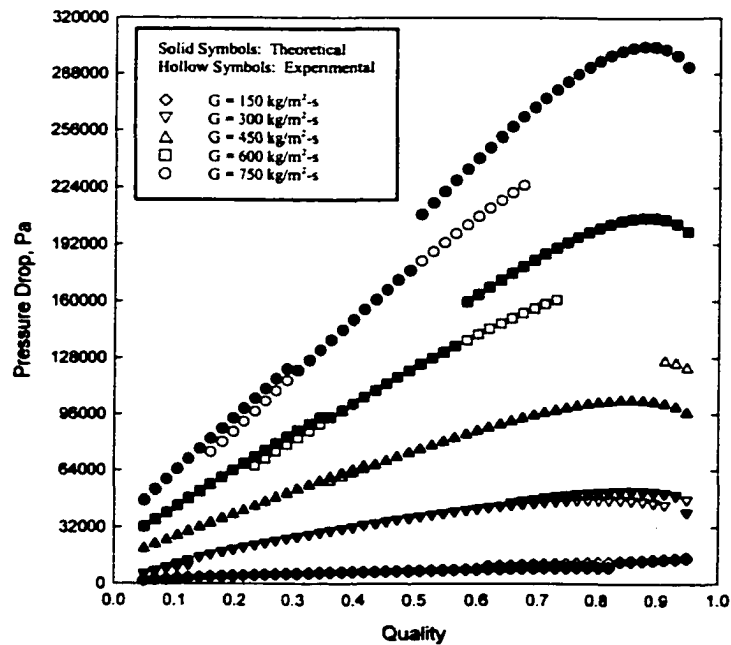


Figure 174. Predicted Pressure Drop for All Models Using Theoretical and Experimental Transition Lines (W29I Tube, Triangle Insert, $D_h = 0.732$ mm)

Effect of Hydraulic Diameter and Tube Shape on Pressure Drop

Table 7 (refer to Chapter 3) lists the tube geometries, hydraulic diameters, total free flow area, and mass flux cases on which the correlations developed in this study are based. For some of these tubes, data were not taken at the lower mass fluxes because heat balances could not be established at such low flow rates. It is recommended that the models presented be used only for the range of diameters and mass fluxes tested. A comparison of the predicted pressure drop using the pressure drop models for the five circular tubes at a representative value of L/D_h ratio of 500 is shown in Figures 175 – 179 for the tested mass flux cases. These figures show the trend that, in general, for a constant L/D_h , a smaller circular tube yields a higher pressure drop. Figure 177 illustrates discontinuities that may occur in the models when there is a change in the flow pattern. For example, in Figure 177, tube C120 illustrates a discontinuity at a quality of about 50 percent. This represents a flow pattern change from disperse wave flow to annular film and mist flow. Similar discontinuities due to changes in flow regimes are also shown in the graphs for the other mass flux cases.

Figures 180 – 184 illustrate the two-phase pressure drops predicted by the models for the microchannel geometries at a constant L/D equal to 500. The pressure drops for the insert tube (W29) were much higher than the extruded tubes and, for purposes of clarity, the pressure drops for this tube are shown only for $G = 450 \text{ kg/m}^2\text{-s}$ in Figure 180. Figure 181 shows a discontinuity in tube RK15 due to a transition from annular film flow to annular film and mist flow. The relatively larger discontinuities seen in this tube are due to the few data points taken for this extremely small tube. Discontinuities in the pressure drop curves are also seen in the other tubes due to such flow regime transitions, but the jumps are not as large because of a better match between the pressure drop correlations for the different regimes. Another aspect of the variation in the pressure drop with quality in these tubes is shown in Figure 184. The pressure drop curves exhibit several discontinuities and changes in slope. This can be better understood with the aid of the corresponding liquid-phase Reynolds number and friction factor. The Reynolds number is a function of the film velocity, which is in turn a function of liquid-phase flow rate and film thickness. As the quality increases, the void fraction increases, while the film thickness and the liquid-phase flow rate decreases. The combination of these effects leads to an increase in Reynolds number. At qualities greater than about 65%, the decrease in the liquid phase flow rate dominates, leading to a decrease in Reynolds number. The corresponding single-phase friction factor graphs show the linear decrease with increasing Re that is typical of laminar flow. For $2200 < Re < 2400$, the friction factor slope changes, representing the transition region. For $x > 0.7$, the

decreasing Re once again results in an increasing friction factor. The two-phase pressure drop correlations developed here were of the form $f_i/f_L = C_1(X)^{C_2}$ (equation 149). Thus, the interface friction factor, and therefore, the two-phase pressure drop, follow these trends in the single-phase liquid-film friction factor. Because of the inherent uncertainties in the prediction of single-phase friction factors in the transition regime, caution is advised in using these correlations in this regime. Finally, the large discontinuities in the pressure drop graphs in Figure 184 are due to the relatively higher measurement and correlation uncertainties at such low mass fluxes.

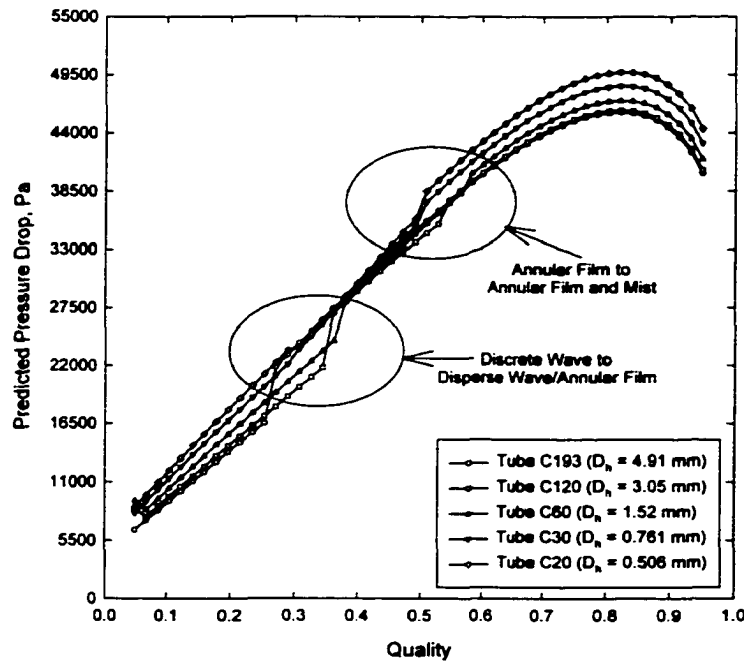


Figure 175. Comparison of Circular Tube Pressure Drops, $L/D = 500$, $G = 750 \text{ kg/m}^2\text{-s}$

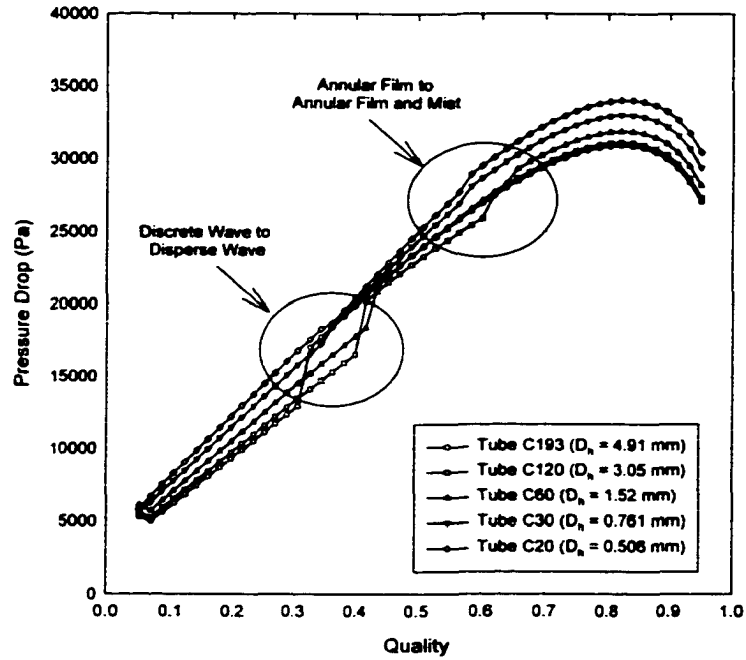


Figure 176. Comparison of Circular Tube Pressure Drops, $L/D = 500$, $G = 600 \text{ kg/m}^2\text{-s}$

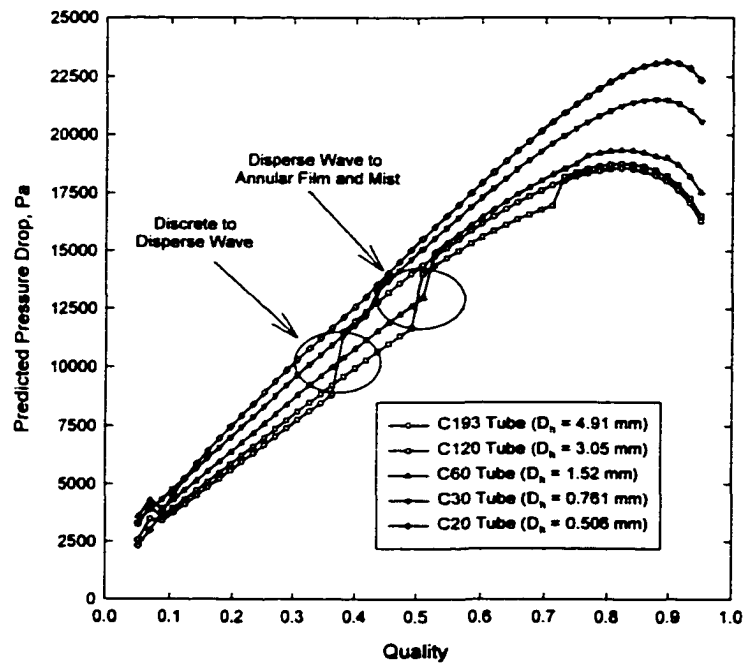


Figure 177. Comparison of Circular Tube Pressure Drops, $L/D = 500$, $G = 450 \text{ kg/m}^2\text{-s}$

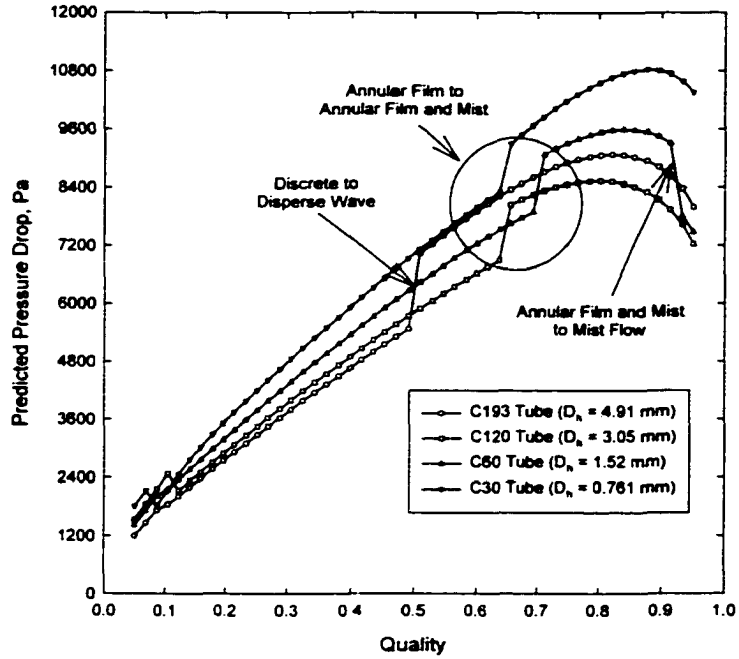


Figure 178. Comparison of Circular Tube Pressure Drops, $L/D = 500$, $G = 300 \text{ kg/m}^2\text{-s}$

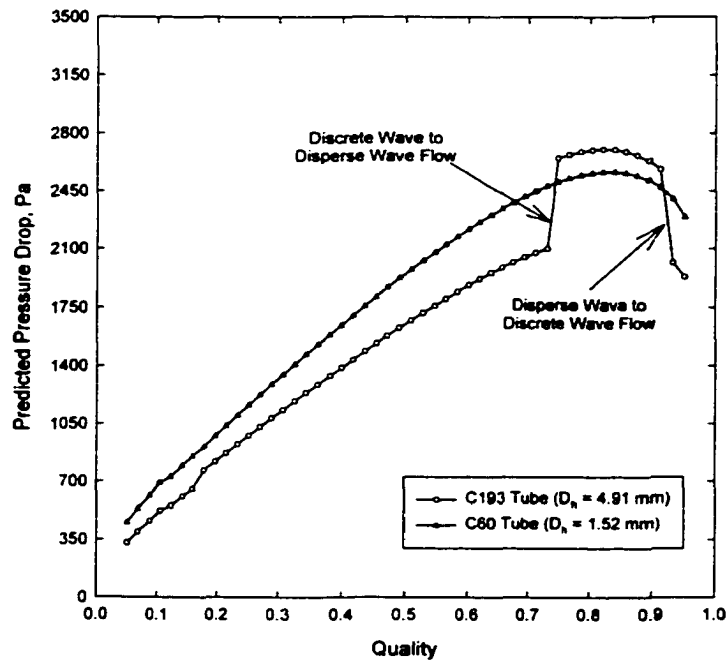


Figure 179. Comparison of Circular Tube Pressure Drops, $L/D = 500$, $G = 150 \text{ kg/m}^2\text{-s}$

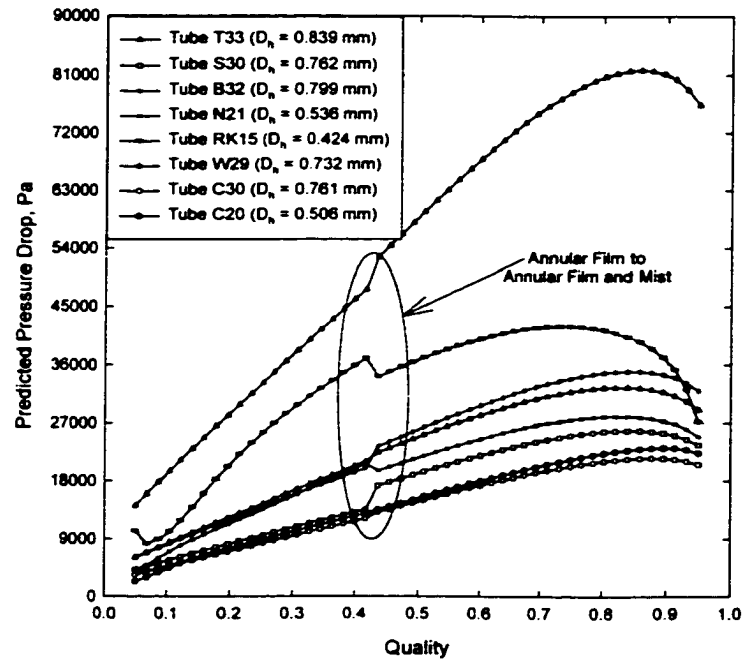


Figure 180. Comparison of Non-Circular Tube Pressure Drops, $L/D = 500$, $G = 450 \text{ kg/m}^2\text{-s}$

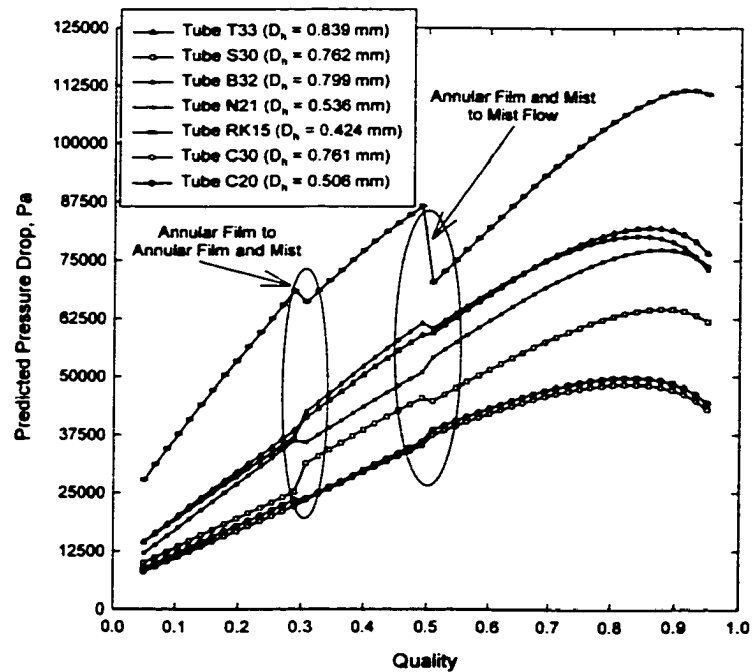


Figure 181. Comparison of Non-Circular Tube Pressure Drops, $L/D = 500$, $G = 750 \text{ kg/m}^2\text{-s}$

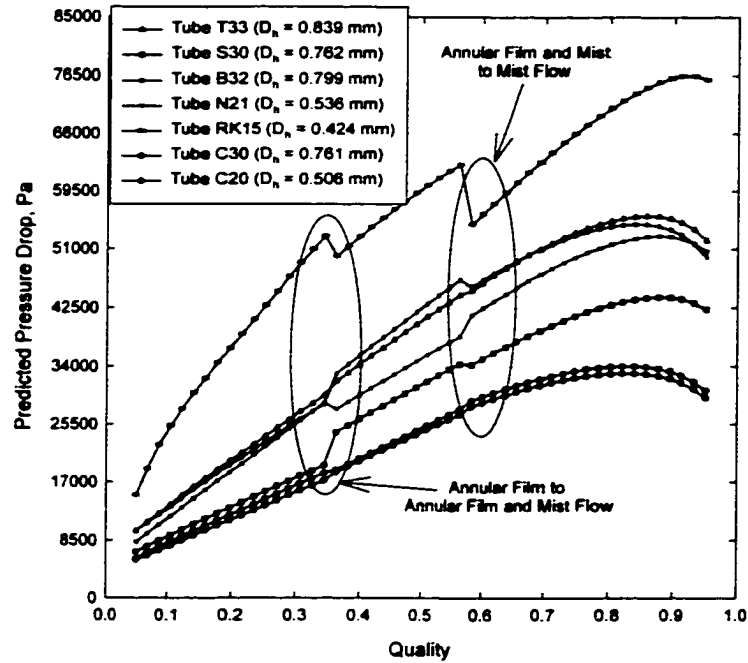


Figure 182. Comparison of Non-Circular Tube Pressure Drops, $L/D = 500$, $G = 600 \text{ kg/m}^2\text{-s}$

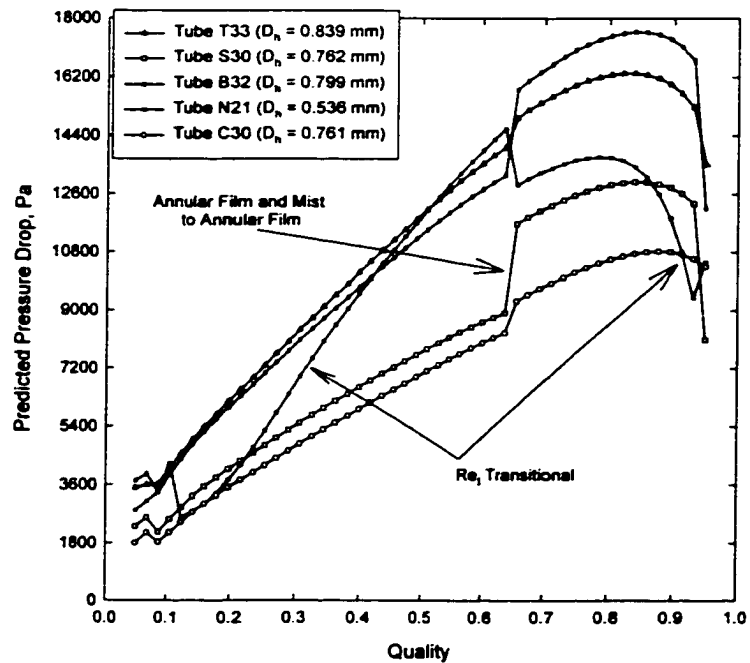


Figure 183. Comparison of Non-Circular Tube Pressure Drops, $L/D = 500$, $G = 300 \text{ kg/m}^2\text{-s}$

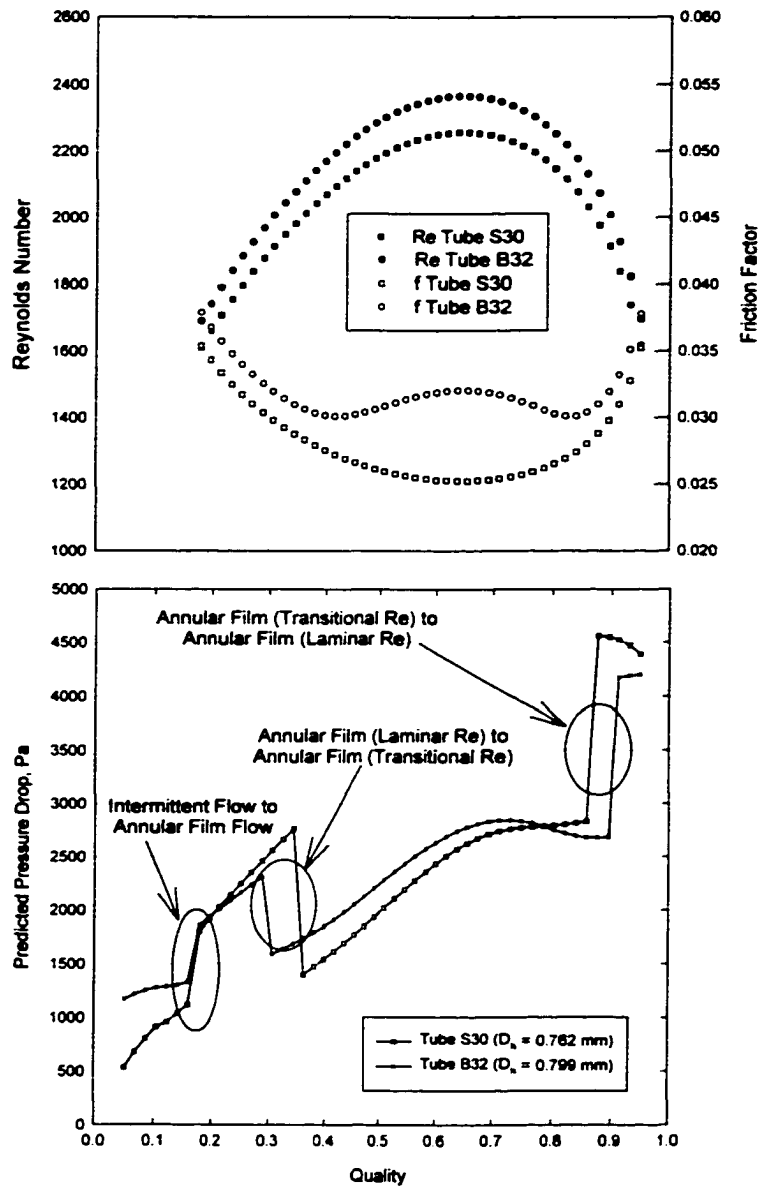


Figure 184. Comparison of Non-Circular Tube Pressure Drops, $L/D = 500$, $G = 150 \text{ kg/m}^2\text{-s}$ (with Corresponding Reynolds Numbers and Friction Factors)

CHAPTER SIX. CONCLUSIONS AND RECOMMENDATIONS FOR FUTURE WORK

A comprehensive study of two-phase flow mechanisms and pressure drop in small hydraulic diameter circular and non-circular tubes was conducted. The first part of the study investigated the flow of air-water mixtures in four round tubes and one rectangular tube with hydraulic diameters ranging from 5.5 mm to 1.3 mm. Bubble, dispersed, elongated bubble, slug, stratified, wavy, annular-wavy, and annular flow patterns were observed for these air-water mixtures, with gas and liquid superficial velocities ranging from 0.1 m/s to 100 m/s, and 0.01 m/s to 10.0 m/s, respectively. Flow regime maps developed from the analysis of video recordings were used to investigate the effect of tube diameter and shape on the flow regime transitions. The effect of tube diameter and shape on the flow patterns is documented and compared with the literature. The results of this work show that for such small hydraulic diameter geometries, diameter and surface tension effects play an important role in determining the flow patterns and transitions between them. Therefore, flow regime maps such as those developed by Mandhane et al. (1974) based upon data from larger tubes may not be applicable for a smaller tube diameter range. It was also shown that the theoretical results of Taitel and Dukler (1976) and the inherent assumptions in these analyses may not be valid for small diameter tubes. Similarly, transition correlations, such as those presented by Weisman et al. (1979), also based upon data from large diameter tubes, were demonstrated to be inapplicable to the small diameter round or rectangular tubes considered in this study.

From the five new air-water flow regime maps presented here for round and rectangular tubes, it can be concluded that as the tube diameter decreases, transitions between these flow regimes occur at different combinations of superficial gas and liquid velocities. Decreasing the tube diameter shifts the transition to a dispersed flow regime to a higher value of u_L^s due to the combined effects of surface tension and tube diameter. The transition to purely annular flow occurs at a nearly constant value of u_G^s and approaches a limiting value as the tube diameter decreases. Another effect of surface tension and tube diameter is to suppress the stratified regime in small diameter tubes and to increase the size of the intermittent regime.

The importance of aspect ratio, hydraulic diameter and surface tension in determining the locations of flow regime transitions in air-water mixtures prompted a similar study on flow mechanisms during condensation of refrigerants in small hydraulic diameter tubes. A total of nine different tube geometries were investigated to determine the effects of tube shape, hydraulic diameter and aspect ratio on the flow regimes and transitions during the

condensation of refrigerant R134a for the entire range of qualities from 100 percent vapor to 100 percent liquid and over the mass flux range $150 < G < 750 \text{ kg/m}^2\text{-s}$. From over 500 data points for these tubes and the corresponding video recordings, the flow regimes were classified into four overall flow regimes including annular, wavy, intermittent and dispersed. The large amount of data also allowed the further subdivision of the data in each flow regime into different flow patterns. For example, the annular regime is divided into the mist flow, annular film flow, annular ring flow, wave ring flow and wave packet flow patterns. The wavy flow regime consists of discrete and disperse wave flow patterns. The disperse flow regime is divided into the bubble flow and disperse flow pattern, although only bubble flow was found to exist in the tubes investigated in this study. The intermittent regime is divided into the plug and slug flow patterns. The flow regime map for the baseline case (4.91 mm round tube) showed good qualitative agreement with the results of Weisman et al. (1979) and Wang et al. (1997).

The effect of the tube shape was investigated by comparing the flow regime maps for the 4.91 mm I.D. round tube and a 4 x 4 mm square tube. Three flow regimes (annular, wavy and intermittent) were observed in both tubes. It was found that the intermittent regime (plug and slug flows) is slightly larger in the round tube. In both cases, the annular regime consists primarily of the mist flow pattern. A small region of annular film flow was found in the round tube, but it was absent in the square tube. The annular regime, however, is substantially larger in the square tube, and conversely, the wavy regime is smaller.

It was found that the hydraulic diameter has a substantial effect on the flow patterns and transitions. As the hydraulic diameter decreases, the overall size of the annular regime increases. Progressing from a hydraulic diameter of 4.0 mm to 3.0 mm, the annular film flow pattern emerges and continues to grow in size as the hydraulic diameter decreases. At a hydraulic diameter of 1.0 mm, the annular film flow pattern occupies nearly the entire range of qualities and mass fluxes tested. The mist flow pattern also increases in size as the hydraulic diameter decreases. Between a hydraulic diameter of 4.0 mm and 3.0 mm, a region is formed where mist flow and annular film flow coexist, and this region continues to grow as the hydraulic diameter decreases. The wavy regime decreases in size as the hydraulic diameter decreases. Progressing from a hydraulic diameter of 3.0 mm to 2.0 mm, the disperse wave pattern disappears and only the discrete wave pattern remains. A further decrease in hydraulic diameter to 1.0 mm causes the wavy regime to disappear completely, and this regime is replaced by the annular film flow pattern.

One of the more significant findings of this study is that the overall size of the intermittent regime increases as the hydraulic diameter decreases, indicating a diminishing

influence of gravity forces. Thus, the 3 x 3 mm tube contains a small region where the intermittent regime and discrete waves coexist. The size of this region increases in the 2 x 2 mm tube. In the 1 x 1 mm tube, the intermittent regime is particularly large. There is also a region where the intermittent flow regime and the annular film flow pattern coexist, but as stated above, the wavy regime is absent. The dispersed regime (bubble flow pattern) is not found in the 4 x 4 mm tube. A small region of the bubble flow pattern coexists with the intermittent regime and the discrete flow pattern in the 3 x 3 mm and 2 x 2 mm tubes. This occurs at low qualities and high mass fluxes. The size of this region increases as the hydraulic diameter decreases. In the case of the 1 x 1 mm tube, the bubble flow pattern coexists with the intermittent regime.

Aspect ratio was found to be less significant in affecting flow regimes than the tube hydraulic diameter, based on the range of aspect ratios investigated in the present study. It was found that a smaller aspect ratio results in a slightly larger annular flow regime at the higher mass fluxes, and an increase in the size of the annular film flow pattern. A smaller aspect ratio also results in a slightly smaller wavy flow regime. In both cases, the smaller aspect ratio has no appreciable effect on the intermittent flow regime. In all cases, the effect of the aspect ratio is more pronounced in the smaller hydraulic diameter tube (which had a larger change in the aspect ratio from 0.5 to 2.0, compared to the change from 0.67 to 1.5 in the larger tube.)

An attempt was also made to develop criteria for transition between the respective flow regimes using the pertinent non-dimensional parameters. Using the work of Traviss and Rohsenow (1973) and Soliman (1982) as a starting point, it was found that many of the significant transition lines can be represented or approximated by constant Froude number lines. Thus, these $Fr = \text{constant}$ lines closely matched the transition lines (on G - x graphs) that were initially developed from experimental data. In addition, similar $Fr = \text{constant}$ criteria were demonstrated to be adequate for representing the transitions in air-water mixtures. This common non-dimensional basis for transitions in fluids of widely different phase properties could be particularly useful for extending the transition criteria from this study to other fluids, geometries and operating conditions.

Two-phase flow pressure drop measurements were taken on a set of 5 circular tubes with diameters ranging from $0.506 \text{ mm} < D_h < 4.91 \text{ mm}$. and also on 7 non-circular tubes (triangular, square, rectangular, barrel, and "N" shaped extruded tubes; and a tube with triangular ports fabricated by placing a corrugated insert in a rectangular tube.) For each of these tubes, single-phase (gas and liquid) validation tests were first conducted to compare the experimentally determined single-phase friction factors with correlations found in the

literature. The laminar friction factor data agreed well with the literature, while the turbulent single-phase data corresponded to the values that would result for typically encountered relative roughnesses of commercially drawn tubing and commercial steel or wrought iron piping. These tests confirmed the validity of the testing and analysis procedures.

The deceleration component of the two-phase pressure drop was determined from adiabatic and condensing pressure drop measurements, and also from an estimation of the change in fluid velocities (and momentum) due to the change in quality from the test section inlet to the outlet. Each one of the tests corroborated the extremely small contribution of the deceleration component that was predicted from these momentum change considerations. The minor losses in the headers due to expansion and contraction were estimated using the separated and homogeneous models, respectively, and were also demonstrated to be a small fraction of the total pressure drop. Furthermore, experimentally measured pressure drops on tubes of various lengths showed that these models provide a good estimate of the minor losses due to expansion and contraction of the fluid.

Frictional pressure drops were determined from the total measured pressure drop for all 14 tubes tested in this study. The frictional two-phase pressure drop for the baseline case (4.91 mm round tube) was compared to several correlations found in the literature including Lockhart-Martinelli (1949), Chisholm (1973), Friedel (1979), De Souza and de Mattos-Pimenta (1995), Yang and Webb (1996), Wang et al. (1997), and Yan and Lin (1998). Relatively good agreement between the correlation by De Souza and de Mattos-Pimenta (1995) was found for the baseline case. This correlation was based upon two-phase pressure drop data using R-134a (and other fluids) and similar hydraulic diameters. Good agreement was also found at the higher quality range ($x > 0.75$) with the correlations by Chisholm (1973) and Friedel (1979). However, several of the other correlations, particularly those by Yan and Lin (1998) and Lockhart-Martinelli (1949) substantially over-predicted the pressure drops. Changes in flow pattern from intermittent flow ($x < 0.25$ - low quality region), to wavy flow ($0.25 < x < 0.5$ - middle quality region), and annular flow ($x > 0.5$ - high quality region) may help explain why the pressure drop correlations proposed by de Souza and de Mattos-Pimenta (1995), Chisholm (1973), and Friedel (1979) produced large errors in the low quality region (intermittent flow), and good agreement in the high quality region (wavy and annular flow).

Flow regime-based pressure drop models and correlations were developed by combining the results of the pressure drop tests and the flow visualization studies. For the Intermittent flow model, 91% of the circular tube two-phase pressure drop data could be predicted within $\pm 25\%$. For the non-circular geometries, 91% of the data could be predicted

within $\pm 25\%$. The Annular Film and Disperse Wave model predicted 93% the circular tube two-phase pressure drop data within $\pm 20\%$, and 90% of the non-circular pressure drop data were predicted within $\pm 20\%$. The Annular Film and Mist Flow Model predicted 95% of the circular two-phase pressure drop data within $\pm 15\%$, and 91% of the non-circular tube data within $\pm 10\%$. Finally, the mist flow model predicted 96% of the circular tube data within $\pm 20\%$, and 94% of the non-circular tube data within $\pm 20\%$.

The above discussion shows that the present work has characterized two-phase flow mechanisms in air-water mixtures and refrigerant R134a with a high degree of accuracy over a large range of geometric and flow parameters. These flow regime maps yield insights into the effects of tube miniaturization, aspect ratio, and tube geometry. These results have facilitated the development of flow regime-based pressure drop correlations and can also be used in the future to develop corresponding heat transfer correlations. These results will enable the design of more optimal tube geometries and pass arrangements for a variety of condenser applications without large design margins that were previously required to account for large uncertainties in design correlations. This will, in turn, result in smaller condensers that use less material and require less refrigerant charge.

The research conducted in this study may be viewed as the beginning of an overall attempt to develop more thermally efficient and cost effective two-phase heat exchangers. A comprehensive experimental research project for the measurement of heat transfer in microchannel tubes over a range of mass fluxes and qualities will complement the results of the present study. Flow visualization studies for tubes with hydraulic diameters < 1 mm are also indicated, based on the findings of the present study. This will help establish any potential fundamental differences in the flow patterns when the diameter is decreased to much smaller values than were investigated in the present study. Similar studies are also recommended for other refrigerants, and for refrigerant-oil mixtures. This is expected to be particularly useful in view of the transition toward CFC and HCFC-free refrigerants. In addition, phase-change flow visualization, pressure drop, and heat transfer studies for evaporation would significantly improve the design of evaporators. System-oriented analytical optimization and experimental demonstration studies would further help in the determination of the appropriate trade-offs between capital and operating costs for such vapor compression-based systems.

APPENDIX A

RESULTS OF INSTRUMENTATION CALIBRATION

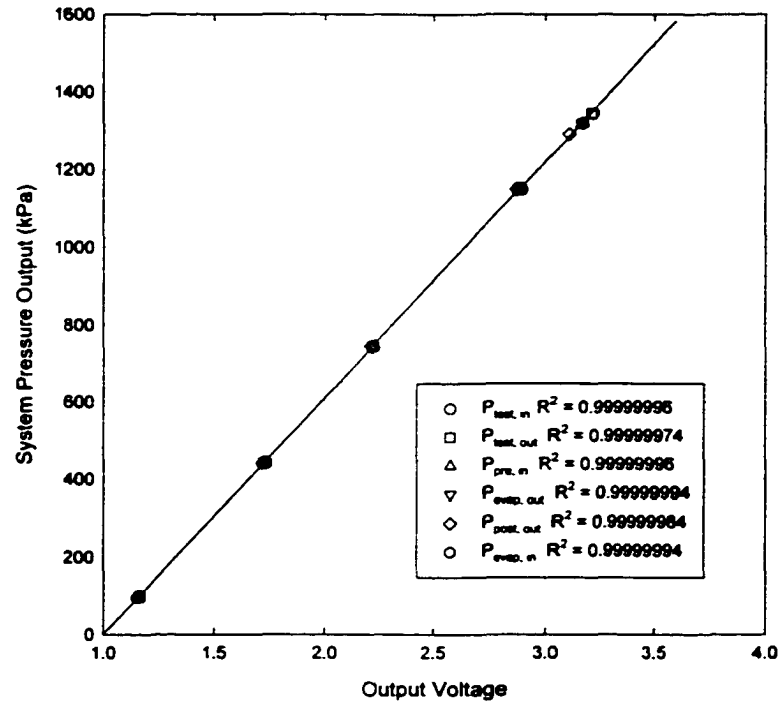


Figure A1. Pressure Transducer Calibration.

Table A1. Mass Flow Meter Calibration.

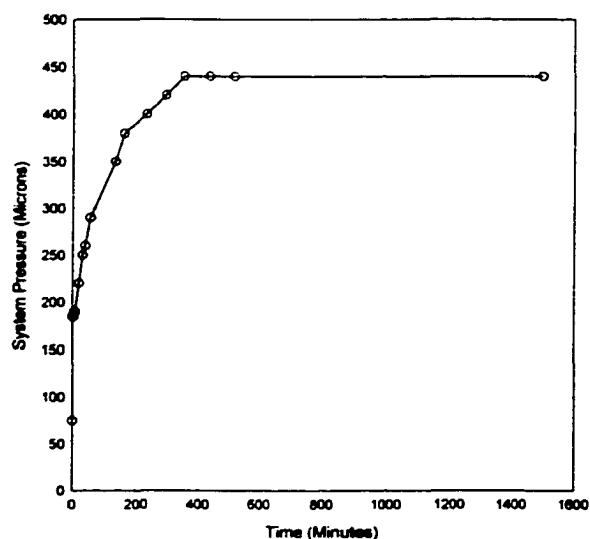
Run Time (seconds)	Volume (liters)	CFM025 (kg/s)	D6 (kg/s)	Actual Rate (kg/s)	Percent Error CFM025	Percent Error D6
164	7.57	0.047	0.047	0.0464	1.95	1.78
256	7.57	0.029	0.029	0.0294	0.01	-0.04
395	7.57	0.019	0.019	0.0191	0.01	-0.04
393	3.79	0.0096	0.0096	0.0096	0.18	0.13
161	1.00	0.0062	0.0062	0.0062	-1.13	-0.65
173	0.80	0.0046	0.0046	0.0046	0.002	-0.04
288	0.80	0.0028	0.0028	0.0028	0.01	0.04

Table A2. Volumetric Flow Meter Calibration.

Flow Meter	Flow Rate (liter/min)	Volume (liters)	Time (seconds)	Actual Flow Rate (liter/min)	Error (percent)
Pre-Cond #1	4.00	11.36	169	4.03	-0.74
	2.50	7.58	183	2.49	0.40
	1.00	3.79	230	0.99	1.01
Pre-Cond #2	2.10	3.79	110	2.07	1.45
	1.00	1.00	61	0.98	2.04
	0.30	1.00	205	0.293	2.40
Pre-Cond #3	0.70	1.00	88	0.68	2.94
	0.40	1.00	153	0.39	2.56
	0.10	0.20	119	.101	-0.99
Post-Cond #1	4.00	15.14	230	3.950	1.27
	2.50	15.14	364	2.496	0.16
	0.50	3.79	452	0.503	-0.60
Post-Cond #2	2.00	7.57	223	2.04	-1.96
	1.20	3.79	192	1.18	1.69
	0.50	1.89	232	0.49	2.04
Post-Cond #3	0.70	1.00	85	0.706	-.85
	0.40	1.00	151	0.397	0.76
	0.10	0.30	175	0.103	-2.91

Table A3. Tempscan Data Acquisition System Specifications

Speed Channels/sec	Analog Range (V)	Resolution Temperature	Resolution Voltage	Bits
966	0.1 - 10	0.1°C	3 μ V	16

**Figure A2. System Pressure After Evacuation as a Function of Time.**

APPENDIX B
UNCERTAINTY ANALYSIS

The uncertainty of any quantity that is not directly measured is a function of the uncertainty of its dependent variables. For a given function F , the uncertainty in the function, ε_F , can be expressed as follows:

$$\varepsilon_F = \sqrt{\sum_i \left(\frac{\partial F}{\partial X_i} \right)^2 \varepsilon_{X_i}^2} \quad (\text{B1})$$

where X_i are the independent variables of the function, F , and ε_{X_i} are the uncertainties of these independent variables. In this study, refrigerant quality was not directly measured: it was calculated based upon energy balances on the pre- and post- condensers and the test section, which determine the uncertainty in the computed values of quality. The calculations presented here illustrate the methodology used in determining the uncertainty in the test section quality. These calculations are based upon the measurement uncertainties provided in Chapter 3 and the data provided in Table 4.

At the inlet of the pre-condenser, the enthalpy of the superheated refrigerant is determined from the temperature ($T_{\text{pre,in}}$) and pressure ($P_{\text{pre,in}}$) of the refrigerant. Temperature and pressure are experimentally measured quantities equal to 63.34°C and 1255 kPa, respectively. Calibration experiments showed that the temperature measurements have an uncertainty of $\pm 0.25^\circ\text{C}$, and the pressure measurements have an uncertainty of 0.25% of the span, or 6.89 kPa. The uncertainty in the enthalpy at the inlet of the pre-condenser is given by:

$$\varepsilon_{h_{\text{pre,inlet}}} = \sqrt{\left(\frac{\partial h}{\partial T} \right)^2 \varepsilon_T^2 + \left(\frac{\partial h}{\partial P} \right)^2 \varepsilon_P^2} \quad (\text{B2})$$

The partial derivatives of the enthalpy with respect to temperature or pressure are given by:

$$\frac{\partial h}{\partial T} = \lim_{\Delta \rightarrow 0} \left(\frac{\Delta h}{\Delta T} \right)_{P=\text{constant}} \quad \frac{\partial h}{\partial P} = \lim_{\Delta \rightarrow 0} \left(\frac{\Delta h}{\Delta P} \right)_{T=\text{constant}} \quad (\text{B3})$$

In this example, the partial derivative of the enthalpy with respect to temperature is 1.12 kJ/kg-K, and the partial derivative of the enthalpy with respect to pressure is -0.02 kJ/kg-kPa. Equation (B2) yields an uncertainty in the enthalpy at the inlet of the pre-condenser of ± 0.31 kJ/kg.

The heat duty of the pre-condenser is determined by the change in enthalpy of the water, which is calculated from the measured inlet and exit water temperatures. From equation (B1), the associated uncertainty in the enthalpy of the water at the inlet or exit of the pre-condenser is given by:

$$\varepsilon_{h_{pre,inlet}} = \sqrt{\left(\frac{\partial h}{\partial T}\right)^2 \varepsilon_T^2} \quad (B4)$$

Given water inlet and exit temperatures of 17.40°C and 28.29°C, respectively, and uncertainties in temperature measurements of $\pm 0.25^\circ\text{C}$, the enthalpies of the water at the inlet and exit of the pre-condenser are 73.34 ± 1.05 kJ/kg and 118.84 ± 1.04 kJ/kg, respectively. The heat duty of the pre-condenser is determined by the change in enthalpy of the water. The mass flow rate of the water was determined using the volumetric flow rate and the density of the water:

$$\dot{m}_{H_2O,post} = \dot{V}_{post} \cdot \rho_{H_2O} \quad (B5)$$

Thus:

$$Q_{pre-cond} = \dot{m}_{pre,H_2O} \Delta h_{H_2O} \quad (B6)$$

The uncertainty in the head duty of the pre-condenser is a function of the water flow rate, and the inlet and exit temperatures of the water. From equation (B1), the associated uncertainty in the heat duty of the pre-condenser given by:

$$\varepsilon_{Q_{pre-cond}} = \sqrt{\left(\frac{\partial Q}{\partial T_{pre,w,in}}\right)^2 \varepsilon_{T_{pre,w,in}}^2 + \left(\frac{\partial Q}{\partial T_{pre,w,out}}\right)^2 \varepsilon_{T_{pre,w,out}}^2 + \left(\frac{\partial Q}{\partial \dot{m}_{pre,w}}\right)^2 \varepsilon_{\dot{m}_{pre,w}}^2} \quad (B7)$$

Equations (B6) and (B7) yield a pre-condenser heat duty and associated uncertainty of 760 ± 28.97 Watts.

The pre-condenser heat duty represents the total amount of energy removed from the refrigerant, which enables the calculation of the quality of the liquid-gas mixture at the exit of the pre-condenser as follows:

$$Q_{pre-cond} = \dot{m}_{refg} (h_{pre,in} - h_{pre,out}) \quad (B8)$$

In this equation, the enthalpy of the superheated refrigerant at the inlet of the pre-condenser is a function of the temperature and pressure of the superheated vapor. At a pressure of 1255 kPa and a temperature of 63.34°C, $h_{pre,in} = 440.5 \pm 0.31$ kJ/kg as calculated above. With a heat duty of 760 ± 28.97 W, a refrigerant flow rate of 8.26×10^{-3} kg/s, and an inlet refrigerant enthalpy of 440.50 ± 0.31 kJ/kg, equations (B1) and (B8) yield an exit pre-condenser refrigerant enthalpy of 349 ± 3.52 kJ/kg. The quality of the two-phase mixture is a function of the refrigerant pressure and the enthalpy:

$$x_{pre,out} = f(P_{pre,out}, h_{pre,out}) \quad (B9)$$

Using a similar propagation of errors approach, the resulting quality at the pre-condenser outlet

is 0.522 ± 0.023 . This quality is also used as the quality at the inlet of the test section, $x_{\text{test},i}$.

The liquid-vapor mixture exits the pre-condenser and flows into the test section. The temperature of the air was measured at both the inlet and exit of the test section. A heat balance on the air determined the amount of energy removed from the refrigerant by the air as follows:

$$Q_{\text{test}} = \dot{m}_{\text{air}} (h_{\text{air},\text{out}} - h_{\text{air},\text{in}}) \quad (\text{B10})$$

This heat duty corresponds to the condensation occurring in the test section. The enthalpies at the inlet and exit of the air were determined from the measured air temperatures and hence, the uncertainty is also a function of the temperature. Using equation (B1), the enthalpies of the inlet and exit air are 300.5 ± 0.25 kJ/kg and 310.8 ± 0.25 kJ/kg, respectively. With an air mass flow rate of 1.26×10^{-3} kg/s, equations (B1) and (B10) yield an air-side heat duty of 12.9 ± 0.45 W.

After exiting the test section, the refrigerant entered one of two post-condensers. Similar to the pre-condenser, the volumetric flow rate and temperatures at the inlet and exit of the cold water were measured to determine the amount of energy removed from the refrigerant by the water. The mass flow rate of the water was determined using the volumetric flow rate and the density of the water:

$$\dot{m}_{\text{H}_2\text{O},\text{post}} = \dot{V}_{\text{post}} \rho_{\text{H}_2\text{O}} \quad (\text{B11})$$

With an uncertainty in the volumetric flow rate of 2%, and assuming a constant density equal to 999.51 kg/m³, equations (B1) and (B11) yield a mass flow rate of 0.049 ± 0.001 kg/s. The heat duty of the post-condenser was determined by the change in enthalpy of the water as follows:

$$Q_{\text{post-cond}} = \dot{m}_{\text{post},\text{H}_2\text{O}} \Delta h_{\text{H}_2\text{O}} \quad (\text{B12})$$

Given water inlet and exit temperatures of 16.60°C and 20.30°C , respectively, the enthalpies and associated uncertainties of the water at the inlet and exit of the post-condenser are 70.1 ± 1.05 kJ/kg and 85.5 ± 1.05 kJ/kg, respectively. Equations (B1) and (B12) yield a post-condenser heat duty and associated uncertainty of 760 ± 74.3 W.

The refrigerant enthalpy at the inlet of the post-condenser is a function of the heat duty, mass flow rate of the refrigerant, and the enthalpy of the sub-cooled liquid as follows:

$$Q_{\text{post-cond}} = \dot{m}_{\text{refg}} (h_{\text{post},\text{in}} - h_{\text{post},\text{out}}) \quad (\text{B13})$$

Similar to the superheated enthalpy, the enthalpy of the sub-cooled refrigerant at the exit of the post-condenser is determined from the temperature and pressure. At a pressure of 1227 kPa and a temperature of 36.91°C , the enthalpy of the refrigerant at the exit of the post-condenser is 251.7 ± 0.37 kJ/kg. From Equation (B13), with a heat duty of 760 ± 74.3 W, a mass flow rate of

0.049±0.001 kg/s, and an exit enthalpy of 251.7±0.37 kJ/kg, the refrigerant enthalpy at the inlet of the post-condenser is 343.8±9.0 kJ/kg. This refrigerant enthalpy at the post-condenser inlet is used to calculate the corresponding quality as follows:

$$x_{post,in} = f(P_{post,out}, h_{post,i}) \quad (B14)$$

With an inlet enthalpy of 343.8±9.0 kJ/kg and a pressure of 1227 kPa, Equation B14 yields a quality at the post-condenser inlet, $x_{post,i}$ of 0.491±0.058, which is also used as the test section outlet quality, $x_{test,o}$.

The above discussion shows that the refrigerant quality at the inlet of the test section was computed using the change in enthalpy of the refrigerant across the pre-condenser and the energy removed by the cooling water. This refrigerant quality was equal to 0.522±0.023. Similarly, the refrigerant quality at the exit of the test section was found using the change in enthalpy of the refrigerant across the post-condenser and the energy removed the cooling water. This refrigerant quality was shown to be 0.491±0.058. A redundant calculation for the quality at the inlet of the test section was also conducted using the test section heat duty. The sum of the post-condenser and test section heat duties should yield the energy removed from the refrigerant from the inlet of the test section to the exit of the post condenser. This alternative heat balance yields an alternate value of the quality at the inlet of the test section:

$$Q_{post-cond} + Q_{test-sec} = \dot{m}_{refg} (h_{test,i,alt} - h_{post,out}) \quad (B15)$$

The sum of the heat duties on the post-condenser and the test section is 773±74.8 W. The resulting alternate value of the enthalpy and corresponding uncertainty is 345.4±9.0 kJ/kg, which corresponds to a quality of 0.501±0.058. This alternate quality compares very well with the pre-condenser outlet quality of 0.522±0.023.

The associated uncertainty in the quality was taken as the mean square average of the three values. This is given by:

$$\epsilon_{test,ave} = \left(\frac{\frac{\epsilon_{test,in}^2 + \epsilon_{test,in,alt}^2 + \epsilon_{test,out}^2}{2}}{2} \right)^{0.5} \quad (B16)$$

Equation (B16) yields an average test section uncertainty in the quality of 0.052. Thus, the average test section quality is taken as 0.501±0.052. The uncertainties in the quality measurements for all data taken on Tube C193, with the largest free flow area tested, are shown in Figure B1. The uncertainties in the quality measurements for the smallest free flow area tube

(RK15) are shown in Figure B2. Finally, the uncertainties in the quality measurements for the tube C30 are shown in Figure B3. The majority of the hydraulic diameters tested in Phase III of this study were on the order of the size of tube C30.

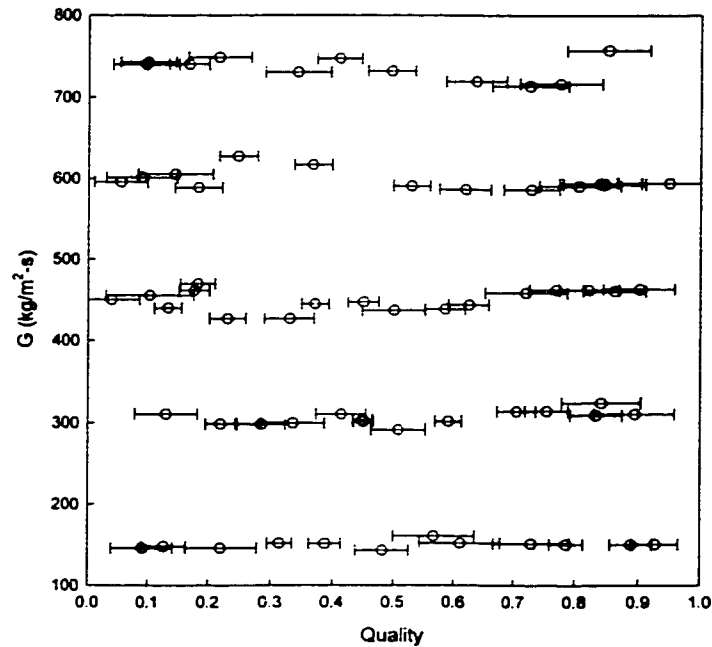


Figure B1. Uncertainties in the Quality for Tube C193

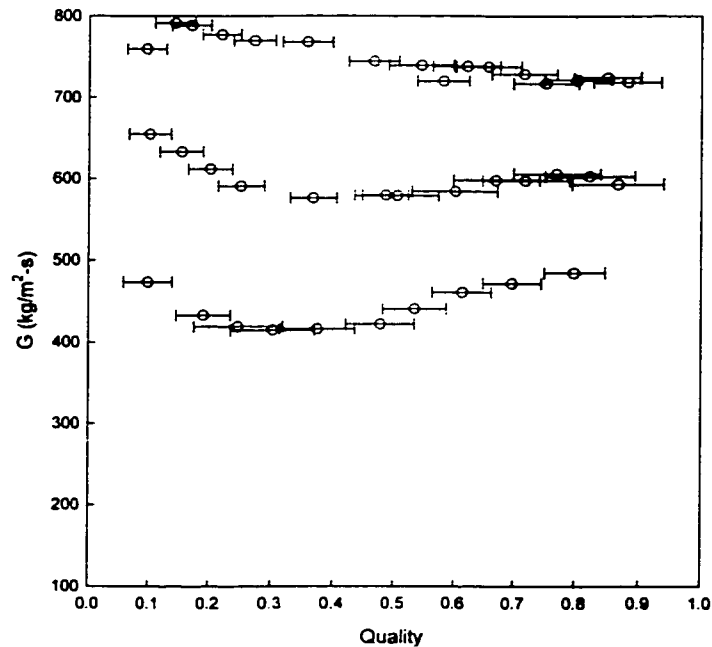


Figure B2. Uncertainties in the Quality for Tube RK15

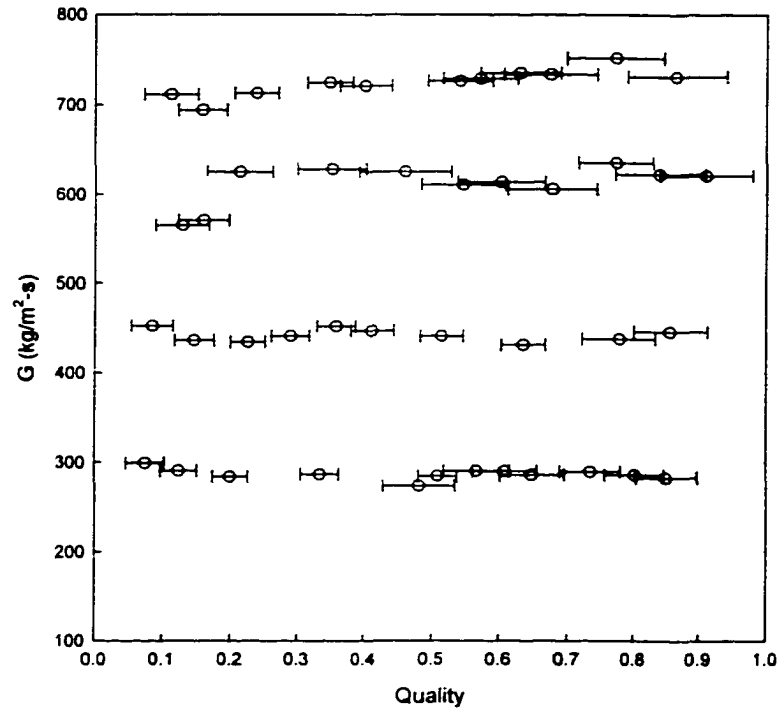


Figure B3. Uncertainties in the Quality for the Tube C30

APPENDIX C
ALBUM OF FLOW VISUALIZATION

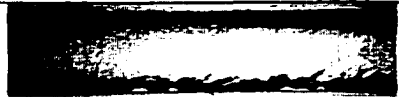
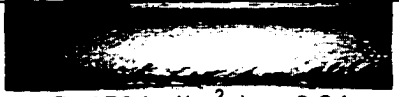
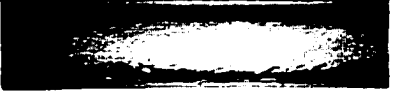
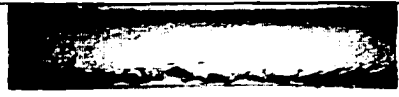
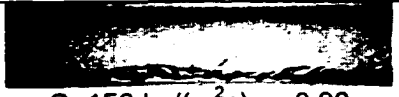
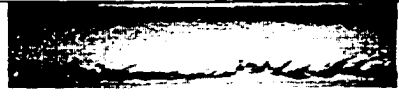
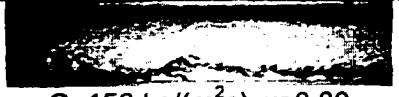
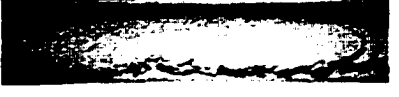
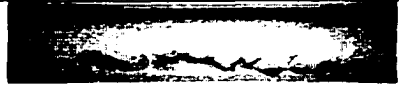
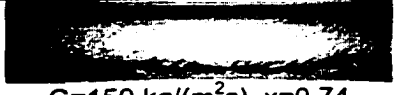
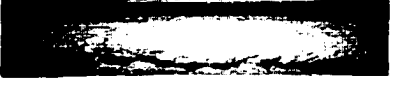
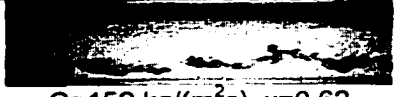
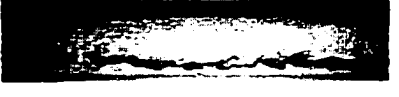
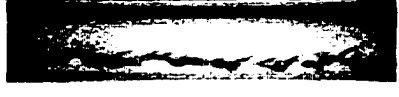
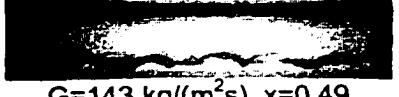
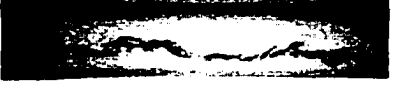
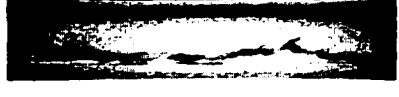
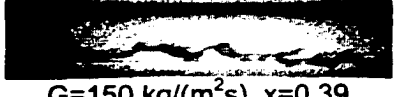
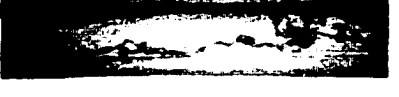
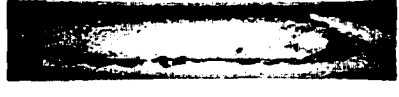
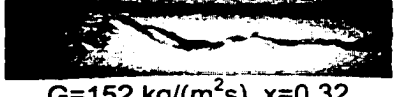
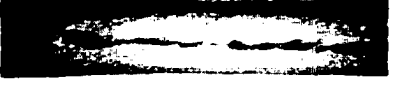
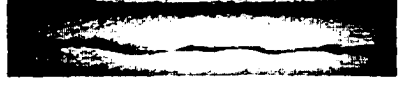
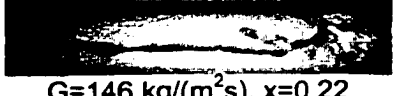
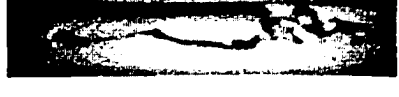
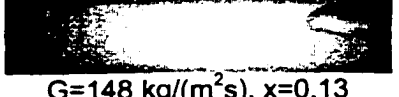
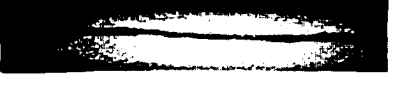
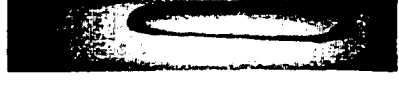
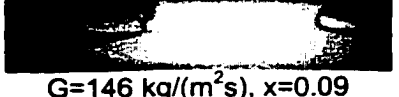
	 G=150 kg/(m ² s), x=0.94	
	 G=150 kg/(m ² s), x=0.90	
	 G=150 kg/(m ² s), x=0.80	
	 G=150 kg/(m ² s), x=0.74	
	 G=152 kg/(m ² s), x=0.62	
	 G=143 kg/(m ² s), x=0.49	
	 G=150 kg/(m ² s), x=0.39	
	 G=152 kg/(m ² s), x=0.32	
	 G=146 kg/(m ² s), x=0.22	
	 G=148 kg/(m ² s), x=0.13	
	 G=146 kg/(m ² s), x=0.09	

Table C1. Flow Visualization Photographs for the 4.91 mm Round Tube [G = 150 kg/(m²s)]

	G=311 kg/(m ² s), x=0.90	
	G=324 kg/(m ² s), x=0.85	
	G=314 kg/(m ² s), x=0.76	
	G=314 kg/(m ² s), x=0.71	
	G=291 kg/(m ² s), x=0.51	
	G=302 kg/(m ² s), x=0.46	
	G=310 kg/(m ² s), x=0.42	
	G=300 kg/(m ² s), x=0.34	
	G=298 kg/(m ² s), x=0.29	
	G=299 kg/(m ² s), x=0.22	
	G=311 kg/(m ² s), x=0.13	

Table C2. Flow Visualization Photographs for the 4.91 mm Round Tube [$G = 300 \text{ kg}/(\text{m}^2\text{s})$]

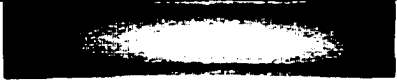
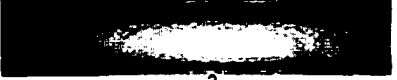
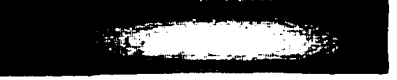
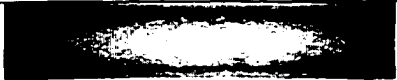
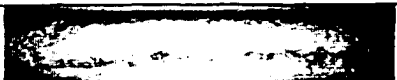
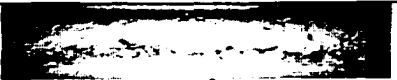
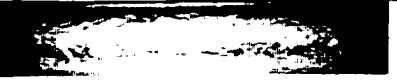
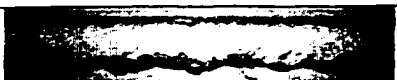
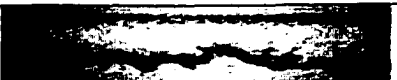
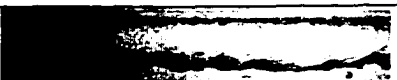
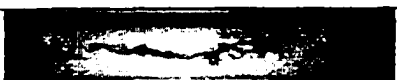
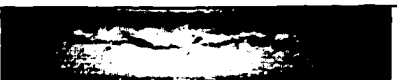
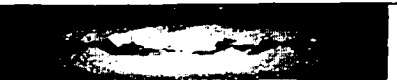
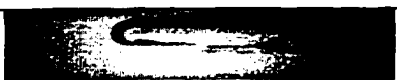
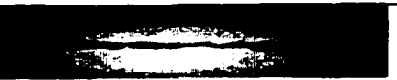
	 G=463 kg/(m ² s), x=0.91	
	 G=462 kg/(m ² s), x=0.80	
	 G=458 kg/(m ² s), x=0.73	
	 G=444 kg/(m ² s), x=0.63	
	 G=437 kg/(m ² s), x=0.51	
	 G=445 kg/(m ² s), x=0.38	
	 G=427 kg/(m ² s), x=0.34	
	 G=427 kg/(m ² s), x=0.23	
	 G=461 kg/(m ² s), x=0.18	
	 G=455 kg/(m ² s), x=0.11	
	 G=450 kg/(m ² s), x=0.04	

Table C3. Flow Visualization Photographs for the 4.91 mm Round Tube [$G = 450 \text{ kg}/(\text{m}^2\text{s})$]

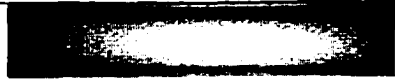
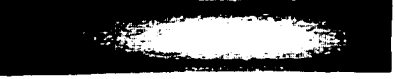
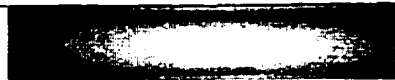
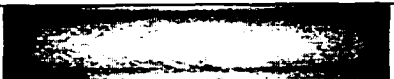
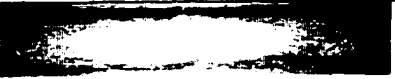
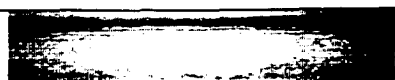
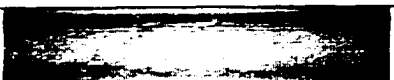
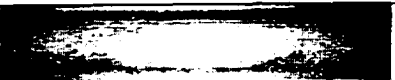
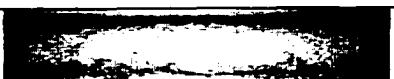
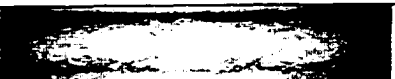
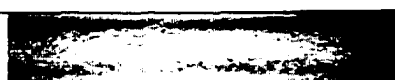
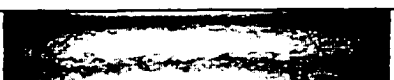
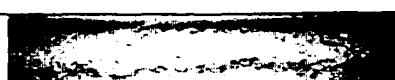
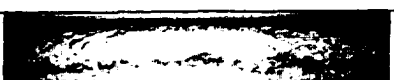
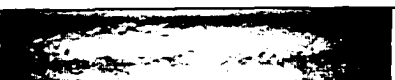
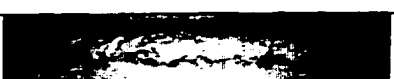
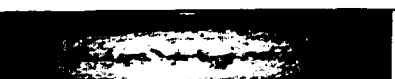
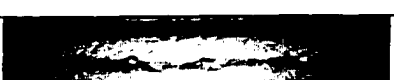
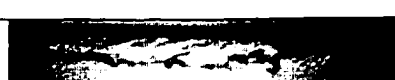
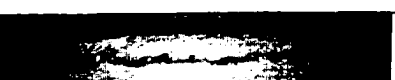
	 G=594 kg/(m ² s), x=0.96	
	 G=592 kg/(m ² s), x=0.85	
	 G=587 kg/(m ² s), x=0.74	
	 G=587 kg/(m ² s), x=0.62	
	 G=591 kg/(m ² s), x=0.54	
	 G=617 kg/(m ² s), x=0.37	
	 G=628 kg/(m ² s), x=0.25	
	 G=589 kg/(m ² s), x=0.19	
	 G=606 kg/(m ² s), x=0.15	
	 G=602 kg/(m ² s), x=0.09	
	 G=596 kg/(m ² s), x=0.06	

Table C4. Flow Visualization Photographs for the 4.91 mm Round Tube [G = 600 kg/(m²s)]

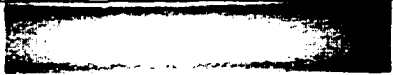
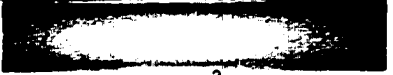
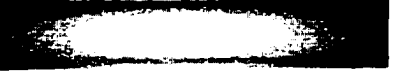
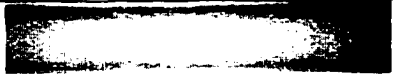
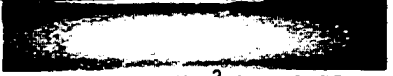
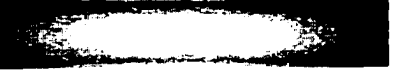
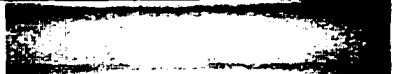
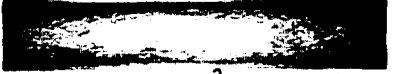
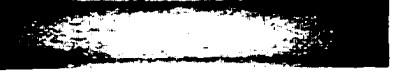
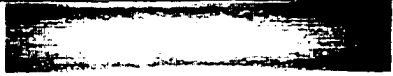
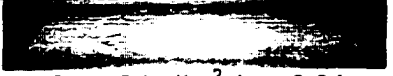
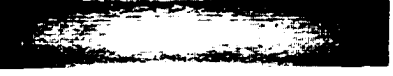
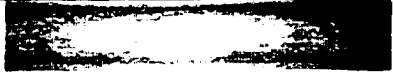
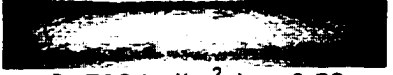
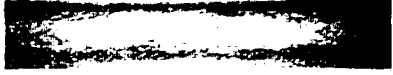
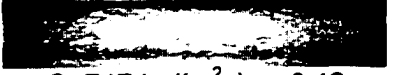
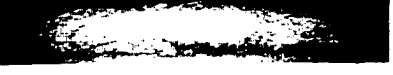
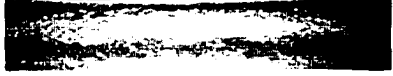
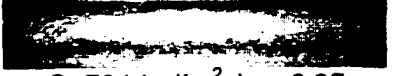
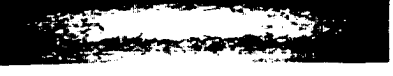
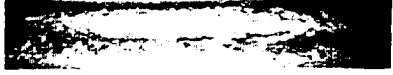
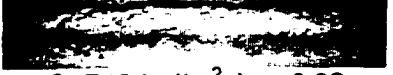
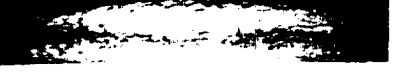
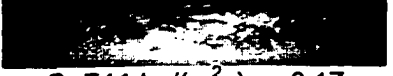
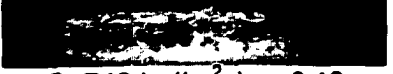
	 G=757 kg/(m ² s), x=0.86	
	 G=716 kg/(m ² s), x=0.78	
	 G=714 kg/(m ² s), x=0.73	
	 G=719 kg/(m ² s), x=0.64	
	 G=732 kg/(m ² s), x=0.50	
	 G=747 kg/(m ² s), x=0.42	
	 G=731 kg/(m ² s), x=0.35	
	 G=749 kg/(m ² s), x=0.22	
	 G=741 kg/(m ² s), x=0.17	
	 G=743 kg/(m ² s), x=0.10	

Table C5. Flow Visualization Photographs for the 4.91 mm Round Tube [G = 750 kg/(m²s)]

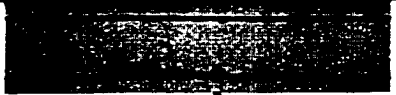
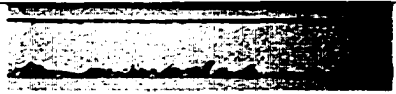
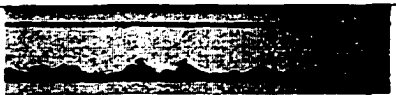
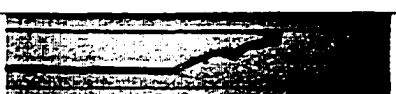
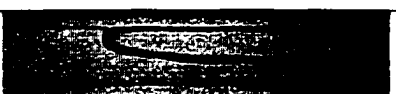
	 G=149 kg/(m ² s), x=0.94	
	 G=152 kg/(m ² s), x=0.82	
	 G=151 kg/(m ² s), x=0.71	
	 G=149 kg/(m ² s), x=0.60	
	 G=149 kg/(m ² s), x=0.52	
	 G=154 kg/(m ² s), x=0.42	
	 G=149 kg/(m ² s), x=0.29	
	 G=153 kg/(m ² s), X=0.17	
	 G=155 kg/(m ² s), x=0.12	
	 G=155 kg/(m ² s), x=0.02	

Table C6. Flow Visualization Photographs for the 4 x 4 mm Square Tube [G = 150 kg/(m²s)]

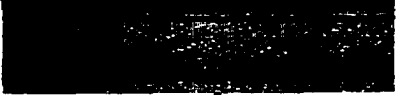
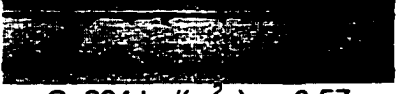
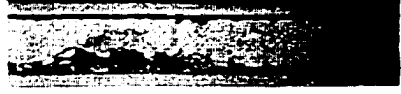
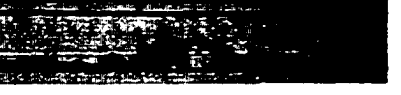
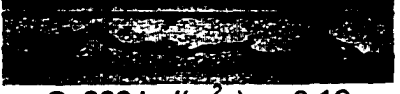
		
	G=315 kg/(m²s), x=0.91	
		
	G=310 kg/(m²s), x=0.84	
		
	G=296 kg/(m²s), x=0.67	
		
	G=294 kg/(m²s), x=0.57	
		
	G=297 kg/(m²s), x=0.49	
		
	G=302 kg/(m²s), x=0.36	
		
	G=305 kg/(m²s), x=0.28	
		
	G=301 kg/(m²s), x=0.19	
		
	G=302 kg/(m²s), x=0.16	
		
	G=294 kg/(m²s), x=0.05	

Table C7. Flow Visualization Photographs for the 4 x 4 mm Square Tube [$G = 300 \text{ kg}/(\text{m}^2\text{s})$]

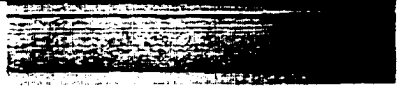
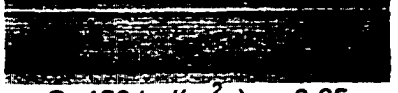
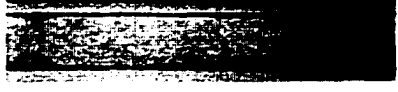
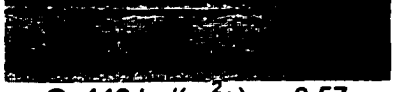
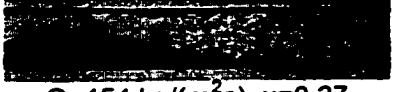
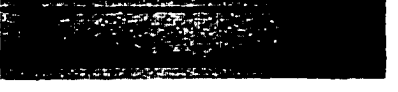
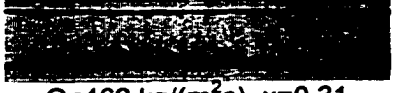
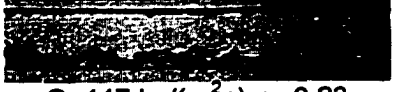
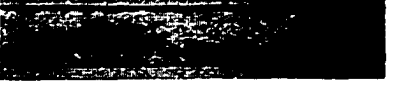
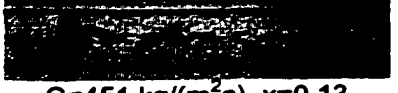
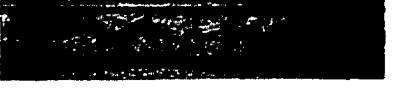
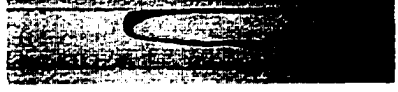
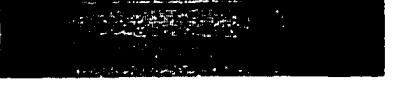
	 G=441 kg/(m ² s), x=0.87	
	 G=440 kg/(m ² s), x=0.82	
	 G=454 kg/(m ² s), x=0.69	
	 G=450 kg/(m ² s), x=0.65	
	 G=449 kg/(m ² s), x=0.57	
	 G=454 kg/(m ² s), x=0.37	
	 G=462 kg/(m ² s), x=0.31	
	 G=447 kg/(m ² s), x=0.23	
	 G=451 kg/(m ² s), x=0.13	
	 G=449 kg/(m ² s), x=0.02	

Table C8. Flow Visualization Photographs for the 4 x 4 mm Square Tube [G = 450 kg/(m²s)]

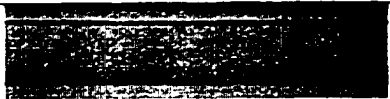
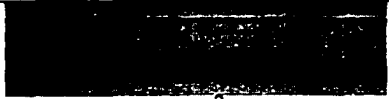
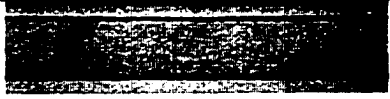
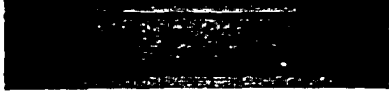
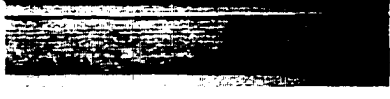
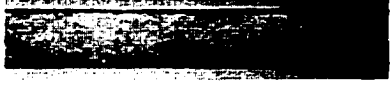
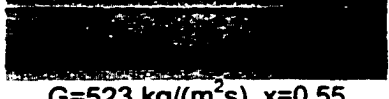
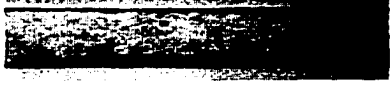
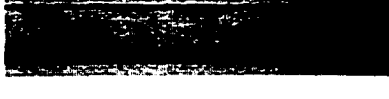
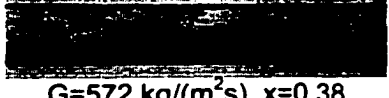
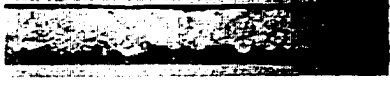
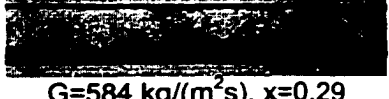
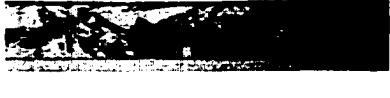
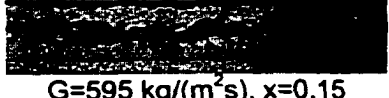
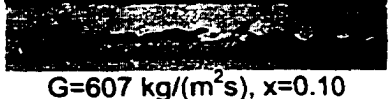
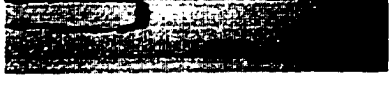
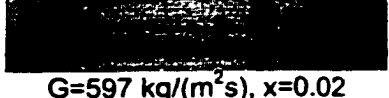
		
	G=595 kg/(m ² s), x=0.78	
		
	G=601 kg/(m ² s), x=0.75	
		
	G=598 kg/(m ² s), x=0.71	
		
	G=625 kg/(m ² s), x=0.59	
		
	G=523 kg/(m ² s), x=0.55	
		
	G=633 kg/(m ² s), x=0.48	
		
	G=572 kg/(m ² s), x=0.38	
		
	G=584 kg/(m ² s), x=0.29	
		
	G=595 kg/(m ² s), x=0.15	
		
	G=607 kg/(m ² s), x=0.10	
		
	G=597 kg/(m ² s), x=0.02	

Table C9. Flow Visualization Photographs for the 4 x 4 mm Square Tube [G = 600 kg/(m²s)]

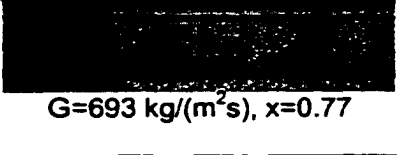
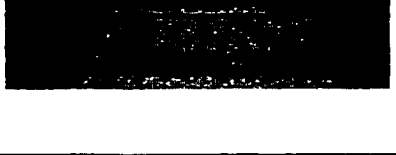
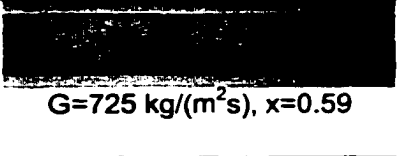
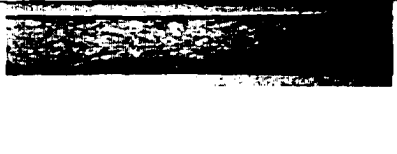
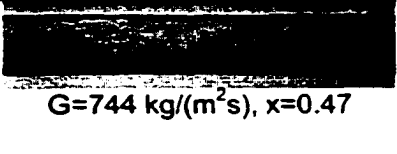
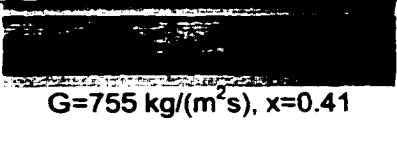
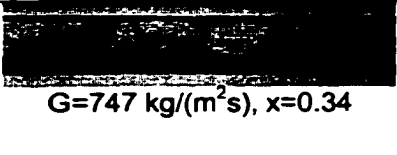
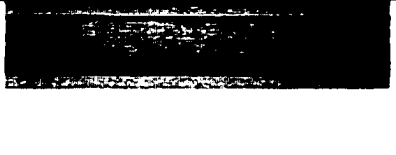
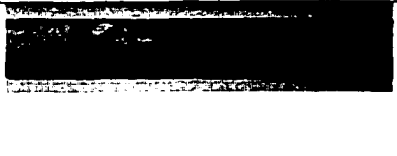
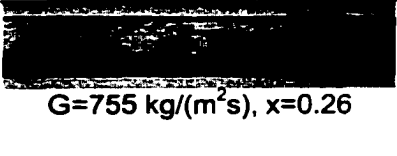
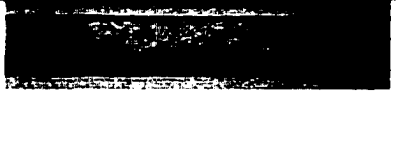
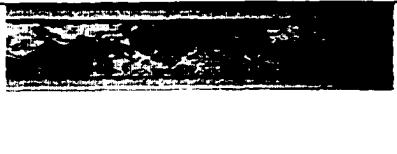
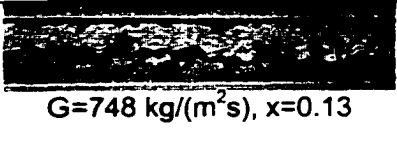
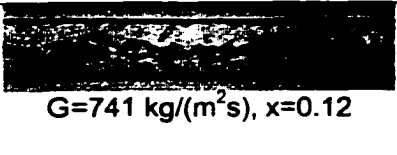
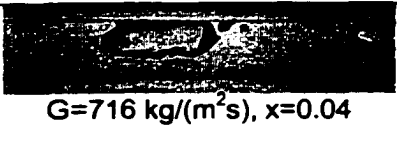
	 G=693 kg/(m ² s), x=0.77	
	 G=725 kg/(m ² s), x=0.59	
	 G=744 kg/(m ² s), x=0.47	
	 G=755 kg/(m ² s), x=0.41	
	 G=747 kg/(m ² s), x=0.34	
	 G=755 kg/(m ² s), x=0.26	
	 G=748 kg/(m ² s), x=0.13	
	 G=741 kg/(m ² s), x=0.12	
	 G=716 kg/(m ² s), x=0.04	

Table C10. Flow Visualization Photographs for the 4 x 4 mm Square Tube [$G = 750 \text{ kg}/(\text{m}^2\text{s})$]

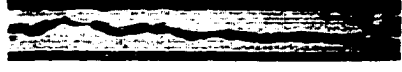
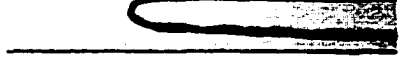
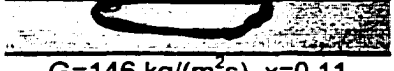
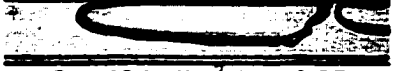
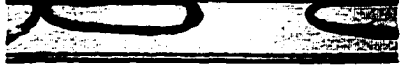
	 G=157 kg/(m ² s), x=0.49	
	 G=147 kg/(m ² s), x=0.36	
	 G=157 kg/(m ² s), x=0.29	
	 G=158 kg/(m ² s), x=0.16	
	 G=146 kg/(m ² s), x=0.11	
	 G=149 kg/(m ² s), x=0.05	

Table C11. Flow Visualization Photographs for the 3 x 3 mm Square Tube [G = 150 kg/(m²s)]

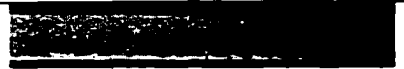
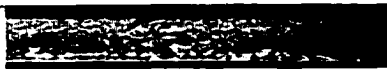
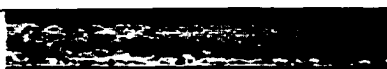
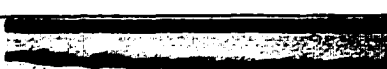
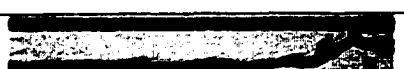
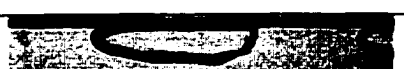
	 G=312 kg/(m ² s), x=0.89	
	 G=278 kg/(m ² s), x=0.77	
	 G=294 kg/(m ² s), x=0.66	
	 G=296 kg/(m ² s), x=0.60	
	 G=308 kg/(m ² s), x=0.51	
	 G=281 kg/(m ² s), x=0.46	
	 G=306 kg/(m ² s), x=0.28	
	 G=308 kg/(m ² s), x=0.24	
	 G=310 kg/(m ² s), x=0.09	
	 G=293 kg/(m ² s), x=0.06	

Table C12. Flow Visualization Photographs for the 3 x 3 mm Square Tube [G = 300 kg/(m²s)]

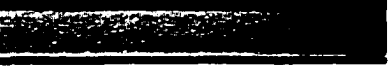
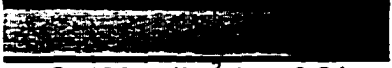
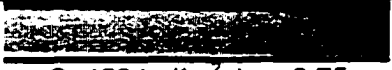
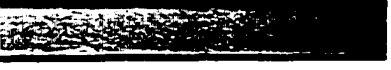
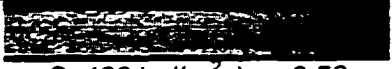
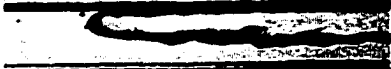
	 G=445 kg/(m ² s), x=0.94	
	 G=456 kg/(m ² s), x=0.84	
	 G=458 kg/(m ² s), x=0.75	
	 G=466 kg/(m ² s), x=0.56	
	 G=474 kg/(m ² s), x=0.45	
	 G=477 kg/(m ² s), x=0.38	
	 G=477 kg/(m ² s), x=0.32	
	 G=476 kg/(m ² s), x=0.26	
	 G=476 kg/(m ² s), x=0.22	
	 G=455 kg/(m ² s), x=0.10	
	 G=472 kg/(m ² s), x=0.09	

Table C13. Flow Visualization Photographs for the 3 x 3 mm Square Tube [G = 450 kg/(m²s)]

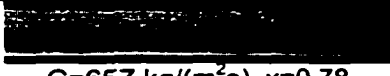
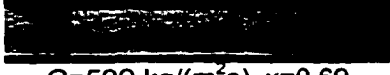
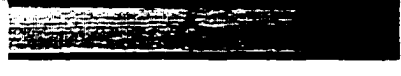
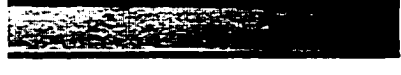
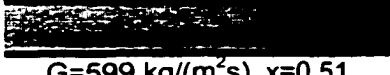
	 G=590 kg/(m ² s), x=0.93	
	 G=657 kg/(m ² s), x=0.78	
	 G=599 kg/(m ² s), x=0.69	
	 G=622 kg/(m ² s), x=0.62	
	 G=599 kg/(m ² s), x=0.51	
	 G=544 kg/(m ² s), x=0.37	
	 G=565 kg/(m ² s), x=0.29	
	 G=584 kg/(m ² s), x=0.22	
	 G=586 kg/(m ² s), x=0.12	
	 G=587 kg/(m ² s), x=0.09	
	 G=608 kg/(m ² s), x=0.02	

Table C14. Flow Visualization Photographs for the 3 x 3 mm Square Tube [G = 600 kg/(m²s)]

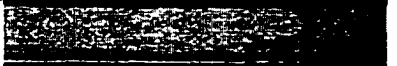
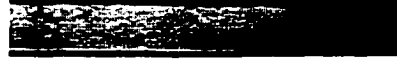
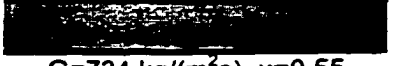
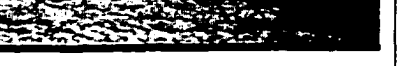
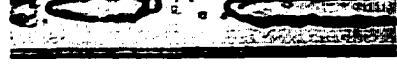
	 G=754 kg/(m ² s), x=0.94	
	 G=764 kg/(m ² s), x=0.84	
	 G=756 kg/(m ² s), x=0.68	
	 G=794 kg/(m ² s), x=0.59	
	 G=734 kg/(m ² s), x=0.55	
	 G=719 kg/(m ² s), x=0.36	
	 G=733 kg/(m ² s), x=0.25	
	 G=739 kg/(m ² s), x=0.20	
	 G=755 kg/(m ² s), x=0.10	
	 G=763 kg/(m ² s), x=0.05	

Table C15. Flow Visualization Photographs for the 3 x 3 mm Square Tube [G = 750 kg/(m²s)]

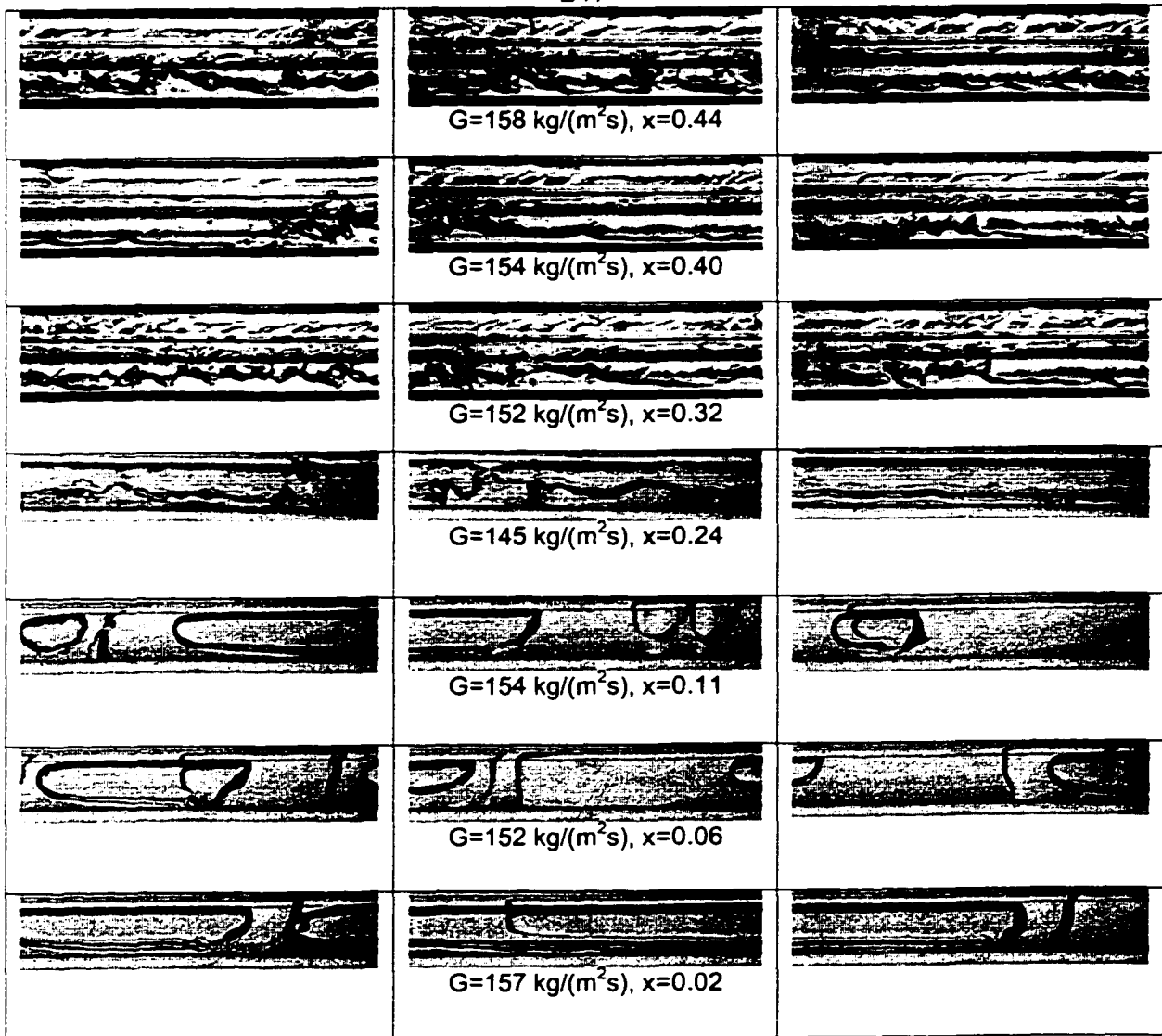


Table C16. Flow Visualization Photographs for the 2 x 2 mm Square Tube [$G = 150 \text{ kg}/(\text{m}^2\text{s})$]

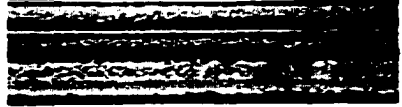
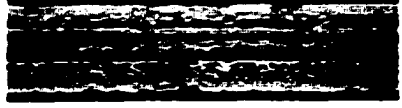
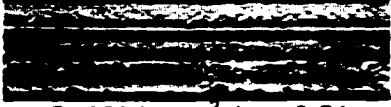
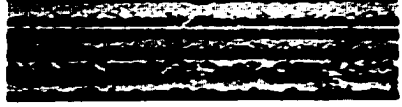
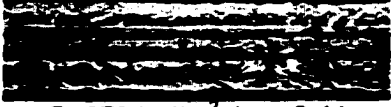
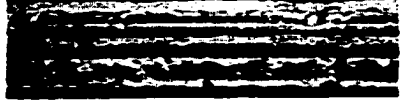
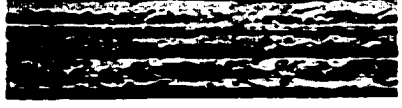
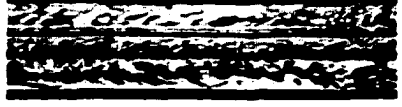
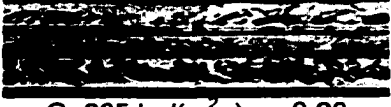
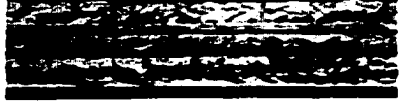
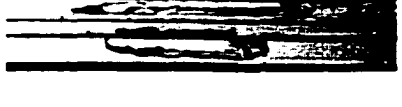
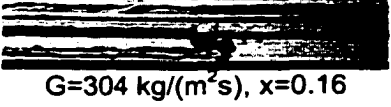
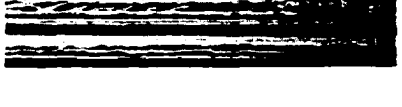
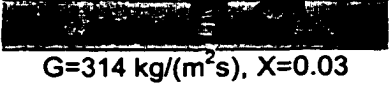
	 G=316 kg/(m ² s), x=0.89	
	 G=311 kg/(m ² s), x=0.84	
	 G=305 kg/(m ² s), x=0.77	
	 G=296 kg/(m ² s), x=0.70	
	 G=262 kg/(m ² s), x=0.54	
	 G=273 kg/(m ² s), x=0.41	
	 G=290 kg/(m ² s), x=0.37	
	 G=285 kg/(m ² s), x=0.28	
	 G=294 kg/(m ² s), x=0.21	
	 G=304 kg/(m ² s), x=0.16	
	 G=314 kg/(m ² s), X=0.03	

Table C17. Flow Visualization Photographs for the 2 x 2 mm Square Tube [G = 300 kg/(m²s)]

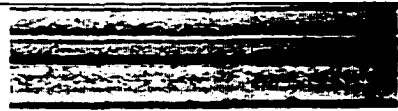
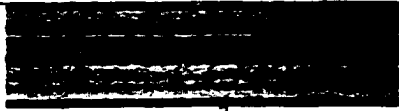
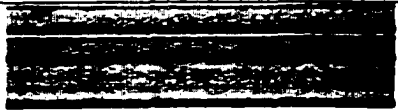
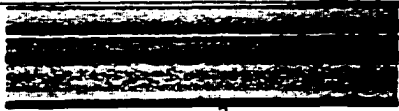
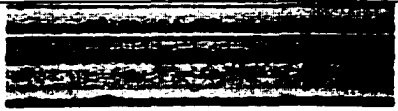
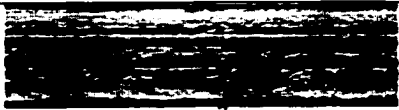
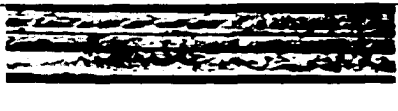
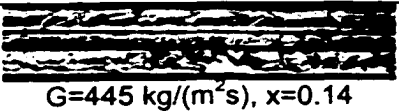
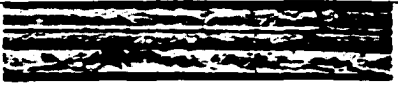
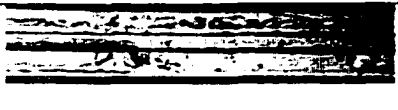
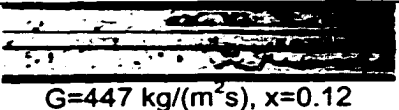
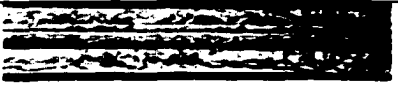
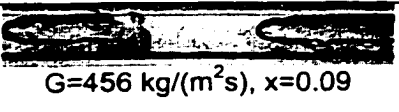
	 G=440 kg/(m ² s), x=0.88	
	 G=438 kg/(m ² s), x=0.85	
	 G=450 kg/(m ² s), x=0.62	
	 G=455 kg/(m ² s), x=0.56	
	 G=451 kg/(m ² s), x=0.50	
	 G=436 kg/(m ² s), x=0.31	
	 G=445 kg/(m ² s), x=0.23	
	 G=445 kg/(m ² s), x=0.14	
	 G=447 kg/(m ² s), x=0.12	
	 G=456 kg/(m ² s), x=0.09	

Table C18. Flow Visualization Photographs for the 2 x 2 mm Square Tube [G = 450 kg/(m²s)]

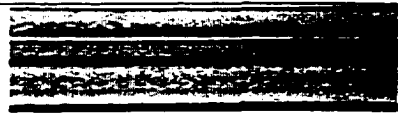
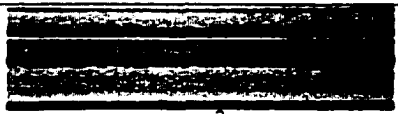
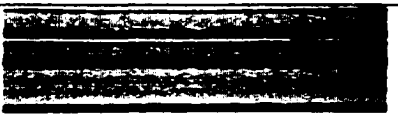
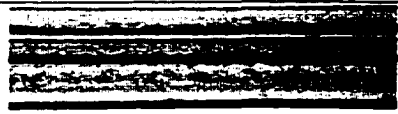
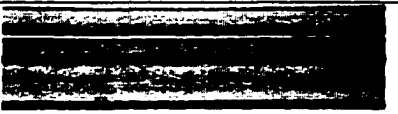
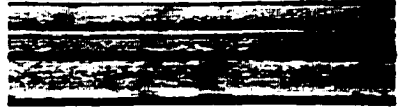
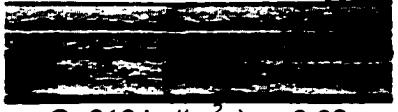
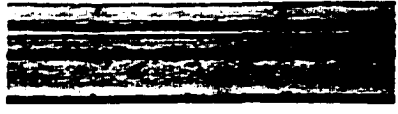
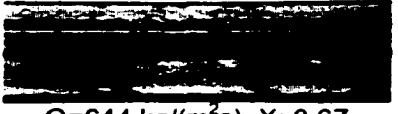
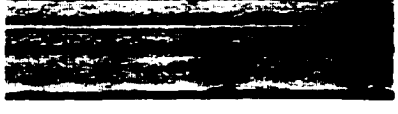
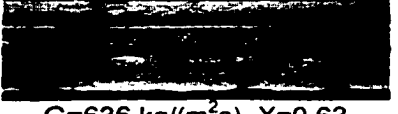
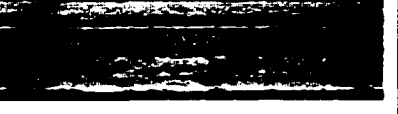
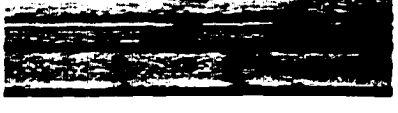
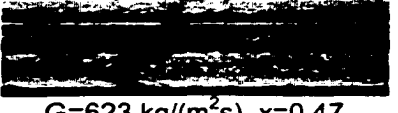
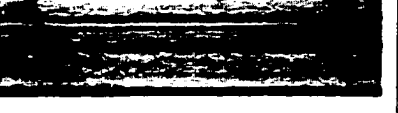
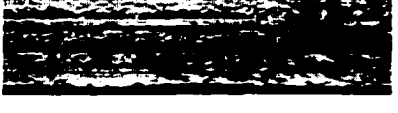
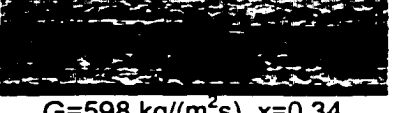
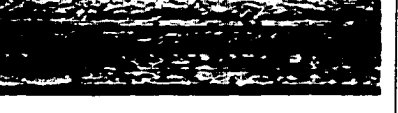
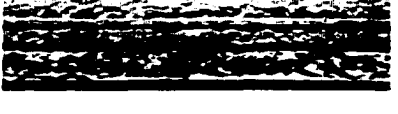
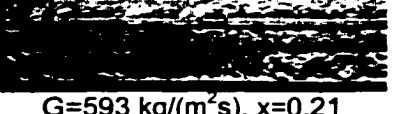
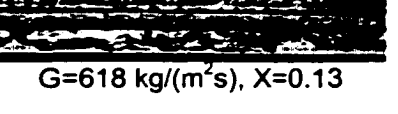
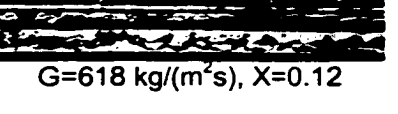
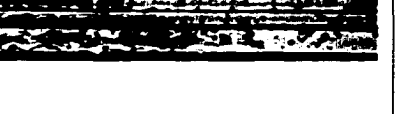
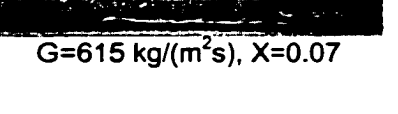
	 G=585 kg/(m ² s), x=0.91	
	 G=580 kg/(m ² s), x=0.85	
	 G=618 kg/(m ² s), x=0.69	
	 G=644 kg/(m ² s), X=0.67	
	 G=636 kg/(m ² s), X=0.63	
	 G=623 kg/(m ² s), x=0.47	
	 G=598 kg/(m ² s), x=0.34	
	 G=593 kg/(m ² s), x=0.21	
	 G=618 kg/(m ² s), X=0.13	
	 G=618 kg/(m ² s), X=0.12	
	 G=615 kg/(m ² s), X=0.07	

Table C19. Flow Visualization Photographs for the 2 x 2 mm Square Tube [G = 600 kg/(m²s)]

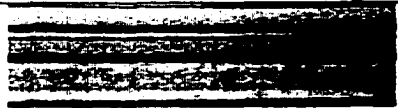
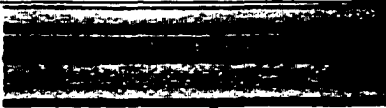
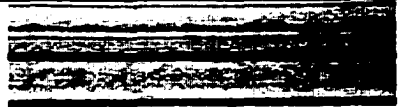
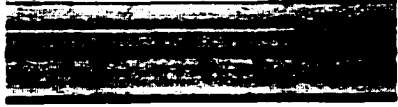
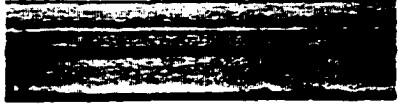
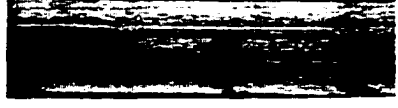
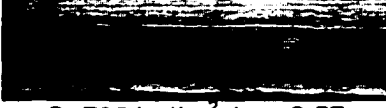
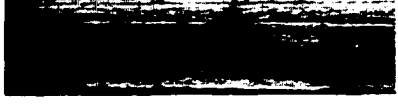
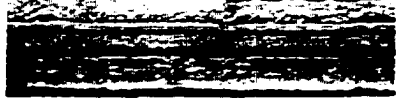
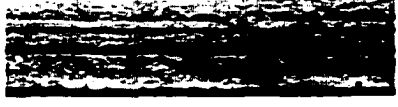
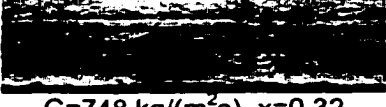
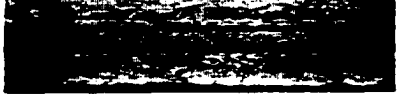
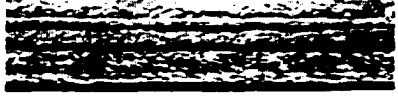
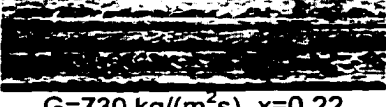
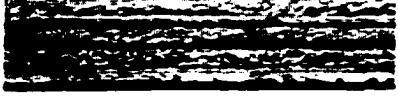
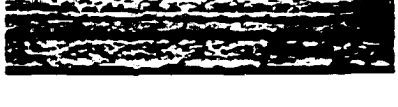
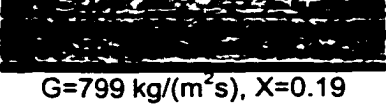
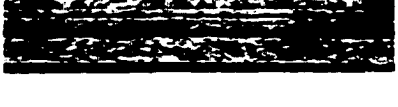
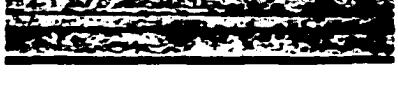
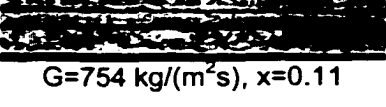
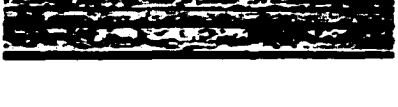
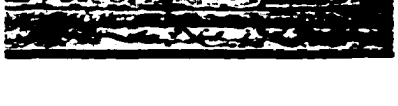
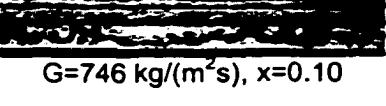
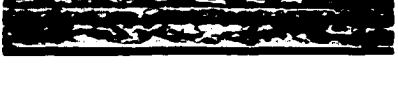
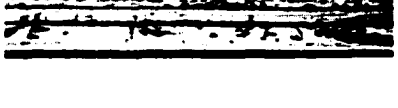
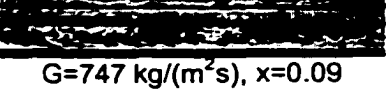
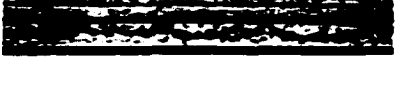
	 G=726 kg/(m ² s), x=0.90	
	 G=731 kg/(m ² s), x=0.81	
	 G=749 kg/(m ² s), x=0.62	
	 G=735 kg/(m ² s), x=0.57	
	 G=759 kg/(m ² s), x=0.42	
	 G=748 kg/(m ² s), x=0.32	
	 G=730 kg/(m ² s), x=0.22	
	 G=799 kg/(m ² s), X=0.19	
	 G=754 kg/(m ² s), x=0.11	
	 G=746 kg/(m ² s), x=0.10	
	 G=747 kg/(m ² s), x=0.09	

Table C20. Flow Visualization Photographs for the 2 x 2 mm Square Tube [G = 750 kg/(m²s)]

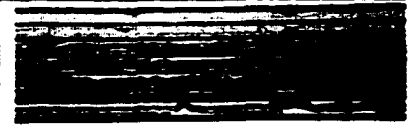
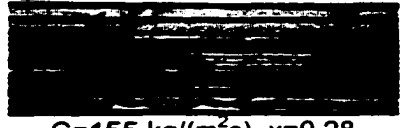
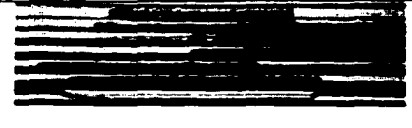
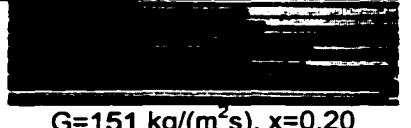
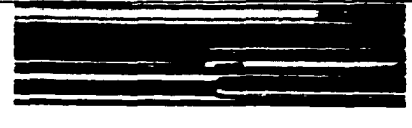
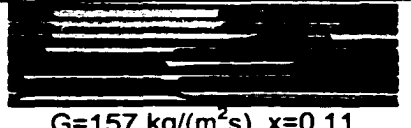
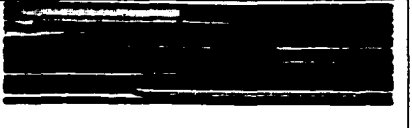
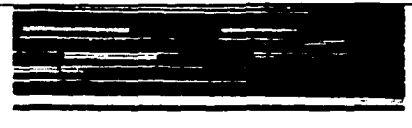
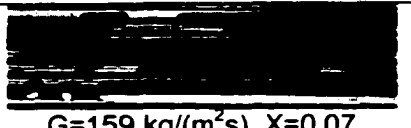
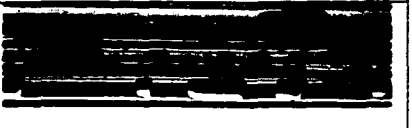
	 G=155 kg/(m ² s), x=0.28	
	 G=151 kg/(m ² s), x=0.20	
	 G=157 kg/(m ² s), x=0.11	
	 G=159 kg/(m ² s), x=0.08	
	 G=159 kg/(m ² s), X=0.07	

Table C21. Flow Visualization Photographs for the 1 x 1 mm Square Tube [G = 150 kg/(m²s)]

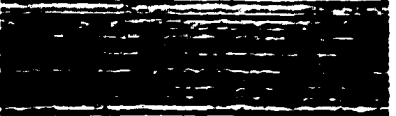
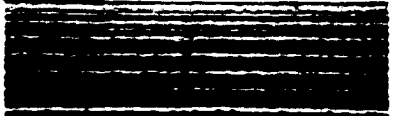
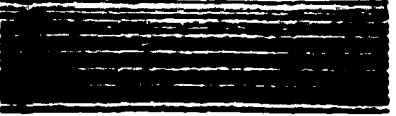
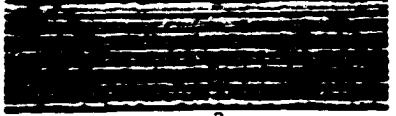
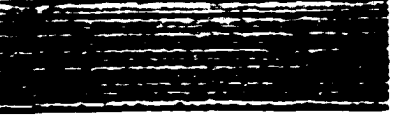
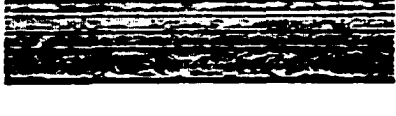
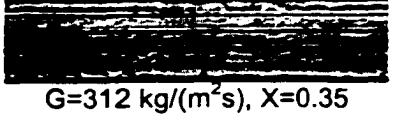
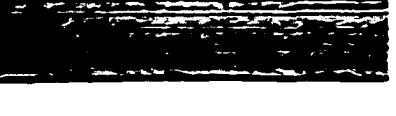
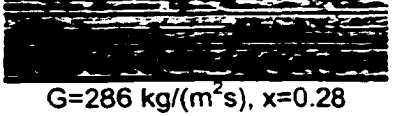
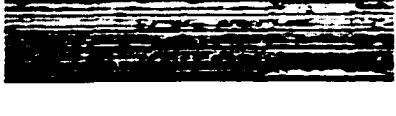
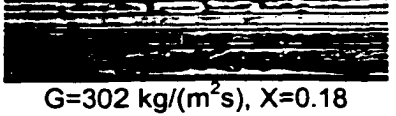
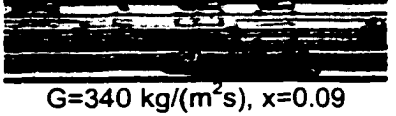
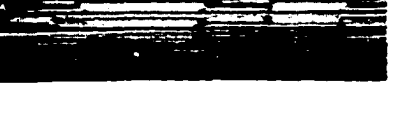
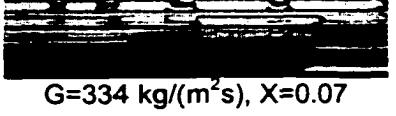
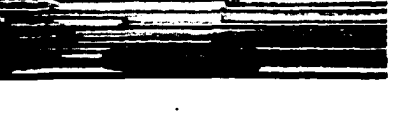
	 G=290 kg/(m ² s), x=0.82	
	 G=290 kg/(m ² s), x=0.79	
	 G=295 kg/(m ² s), x=0.74	
	 G=289 kg/(m ² s), x=0.61	
	 G=287 kg/(m ² s), x=0.54	
	 G=312 kg/(m ² s), X=0.35	
	 G=287 kg/(m ² s), x=0.33	
	 G=286 kg/(m ² s), x=0.28	
	 G=302 kg/(m ² s), X=0.18	
	 G=340 kg/(m ² s), x=0.09	
	 G=334 kg/(m ² s), X=0.07	

Table C22. Flow Visualization Photographs for the 1 x 1 mm Square Tube [$G = 300 \text{ kg}/(\text{m}^2\text{s})$]

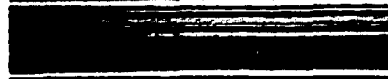
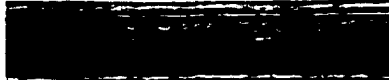
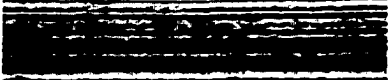
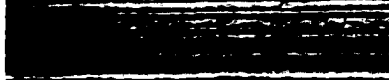
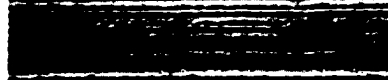
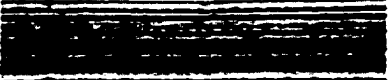
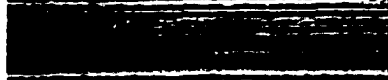
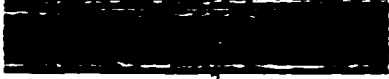
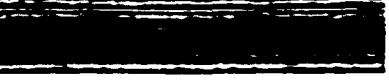
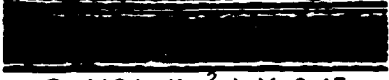
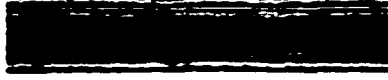
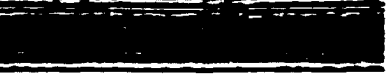
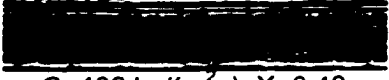
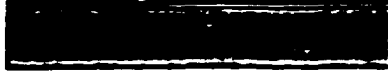
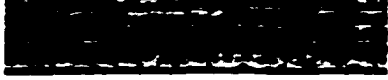
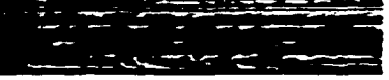
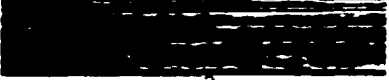
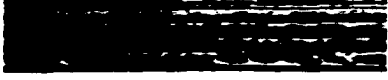
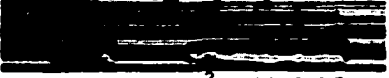
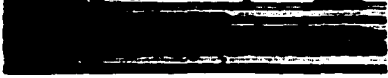
	 G=435 kg/(m ² s), x=0.92	
	 G=411 kg/(m ² s), x=0.75	
	 G=420 kg/(m ² s), x=0.70	
	 G=423 kg/(m ² s), x=0.66	
	 G=424 kg/(m ² s), X=0.60	
	 G=476 kg/(m ² s), x=0.55	
	 G=416 kg/(m ² s), X=0.45	
	 G=409 kg/(m ² s), X=0.40	
	 G=430 kg/(m ² s), X=0.28	
	 G=439 kg/(m ² s), X=0.15	
	 G=439 kg/(m ² s), X=0.07	

Table C23. Flow Visualization Photographs for the 1 x 1 mm Square Tube [G = 450 kg/(m²s)]

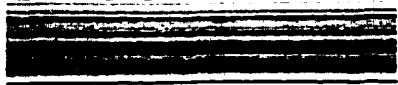
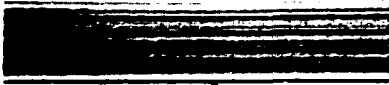
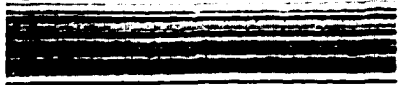
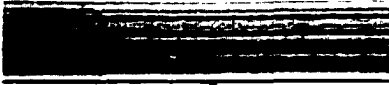
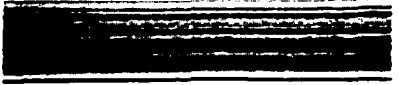
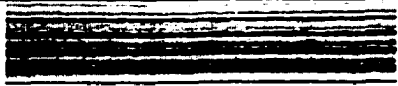
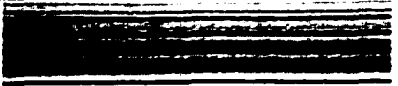
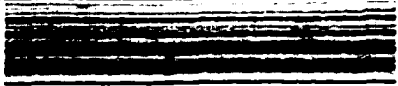
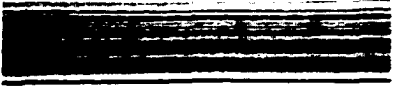
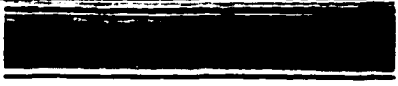
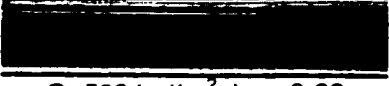
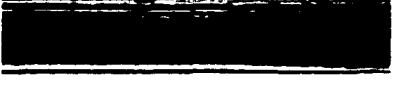
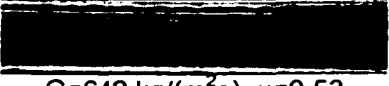
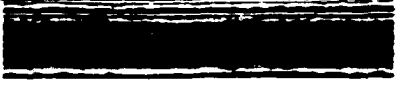
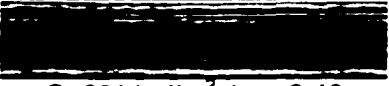
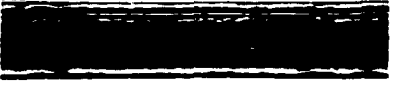
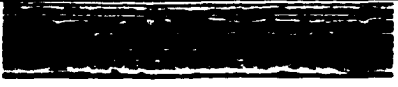
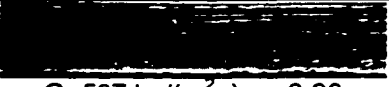
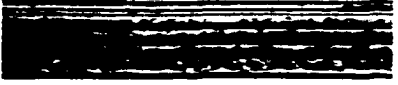
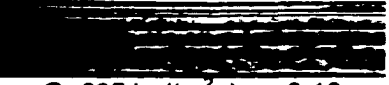
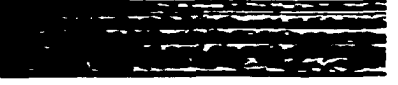
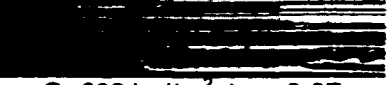
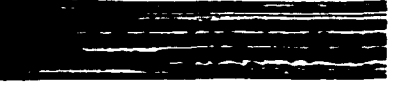
	 G=659 kg/(m ² s), x=0.92	
	 G=646 kg/(m ² s), x=0.88	
	 G=642 kg/(m ² s), x=0.83	
	 G=653 kg/(m ² s), x=0.77	
	 G=586 kg/(m ² s), x=0.62	
	 G=642 kg/(m ² s), x=0.53	
	 G=661 kg/(m ² s), x=0.40	
	 G=587 kg/(m ² s), x=0.30	
	 G=585 kg/(m ² s), x=0.22	
	 G=625 kg/(m ² s), x=0.10	
	 G=626 kg/(m ² s), x=0.07	

Table C24. Flow Visualization Photographs for the 1 x 1 mm Square Tube [G = 600 kg/(m²s)]

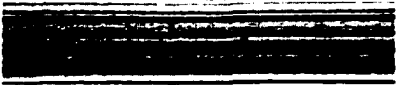
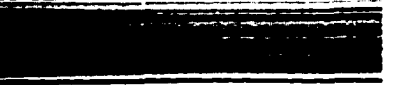
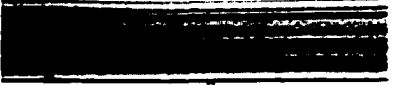
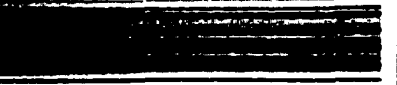
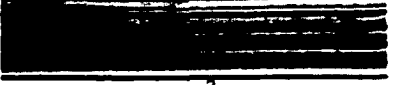
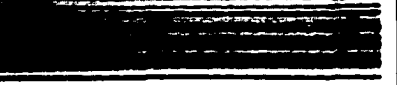
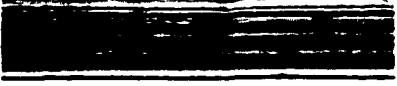
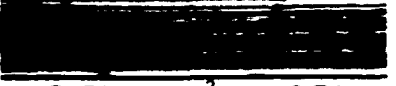
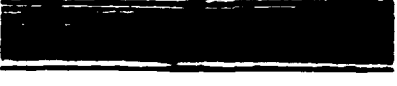
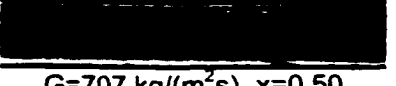
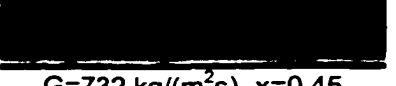
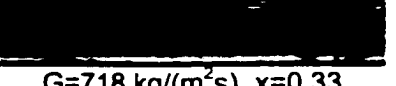
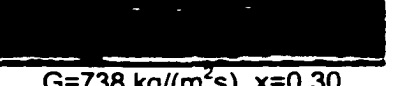
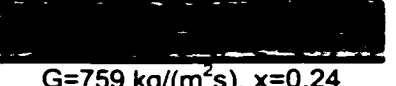
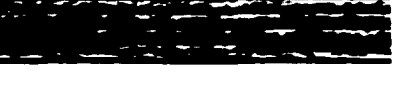
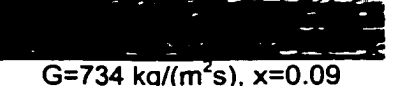
	 G=786 kg/(m ² s), x=0.93	
	 G=772 kg/(m ² s), x=0.90	
	 G=745 kg/(m ² s), x=0.80	
	 G=732 kg/(m ² s), x=0.74	
	 G=707 kg/(m ² s), x=0.50	
	 G=732 kg/(m ² s), x=0.45	
	 G=718 kg/(m ² s), x=0.33	
	 G=738 kg/(m ² s), x=0.30	
	 G=759 kg/(m ² s), x=0.24	
	 G=734 kg/(m ² s), x=0.09	

Table C25. Flow Visualization Photographs for the 1 x 1 mm Square Tube [G = 750 kg/(m²s)]

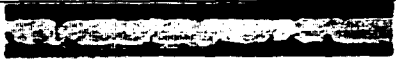
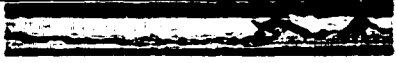
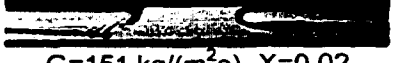
	 G=163 kg/(m ² s), x=0.55	
	 G=172 kg/(m ² s), x=0.36	
	 G=168 kg/(m ² s), x=0.18	
	 G=163 kg/(m ² s), x=0.14	
	 G=161 kg/(m ² s), X=0.13	
	 G=167 kg/(m ² s), X=0.04	
	 G=151 kg/(m ² s), X=0.02	

Table C26. Flow Visualization Photographs for the 2 (Height) x 4 (Width) mm Rectangular Tube [G = 150 kg/(m²s)]

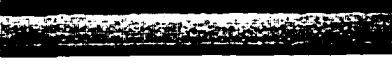
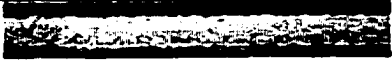
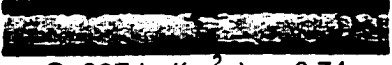
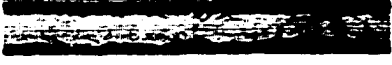
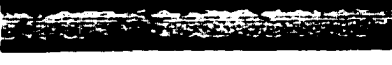
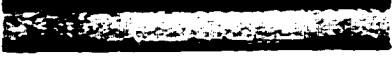
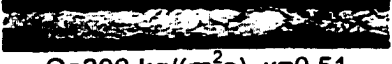
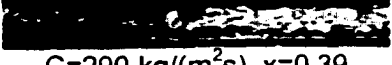
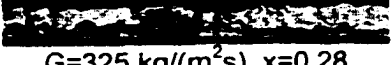
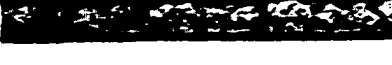
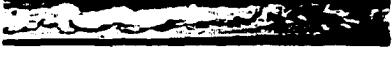
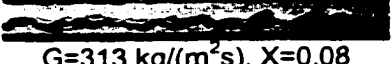
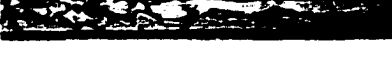
	 G=293 kg/(m ² s), x=0.88	
	 G=302 kg/(m ² s), x=0.79	
	 G=307 kg/(m ² s), x=0.74	
	 G=295 kg/(m ² s), x=0.64	
	 G=294 kg/(m ² s), x=0.58	
	 G=300 kg/(m ² s), x=0.51	
	 G=290 kg/(m ² s), x=0.39	
	 G=325 kg/(m ² s), x=0.28	
	 G=313 kg/(m ² s), X=0.20	
	 G=315 kg/(m ² s), X=0.11	
	 G=313 kg/(m ² s), X=0.08	

Table C27. Flow Visualization Photographs for the 2 (Height) x 4 (Width) mm Rectangular Tube [$G = 300 \text{ kg}/(\text{m}^2\text{s})$]

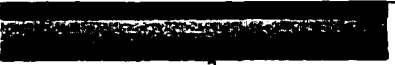
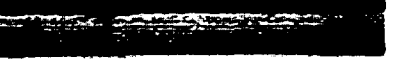
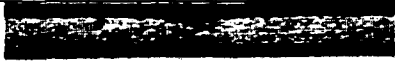
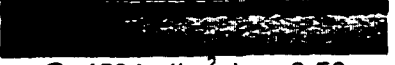
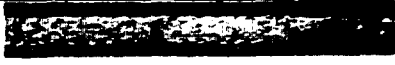
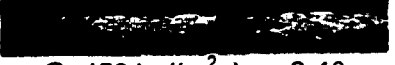
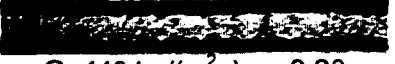
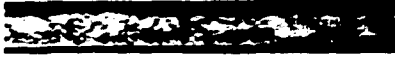
	 G=442 kg/(m ² s), x=0.96	
	 G=439 kg/(m ² s), X=0.91	
	 G=439 kg/(m ² s), x=0.86	
	 G=447 kg/(m ² s), x=0.75	
	 G=456 kg/(m ² s), x=0.65	
	 G=456 kg/(m ² s), x=0.56	
	 G=456 kg/(m ² s), x=0.40	
	 G=448 kg/(m ² s), x=0.30	
	 G=455 kg/(m ² s), x=0.20	
	 G=459 kg/(m ² s), x=0.11	
	 G=457 kg/(m ² s), x=0.09	

Table C28. Flow Visualization Photographs for the 2 (Height) x 4 (Width) mm Rectangular Tube [G = 450 kg/(m²s)]

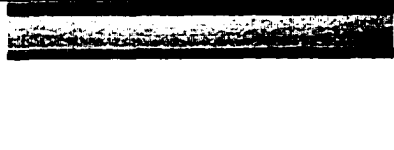
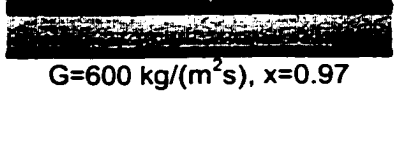
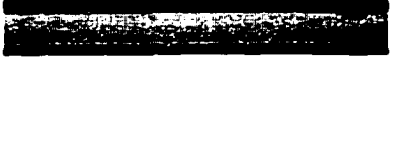
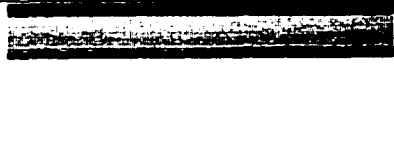
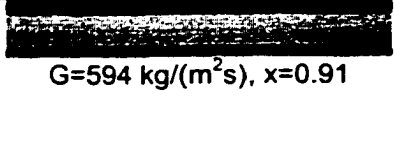
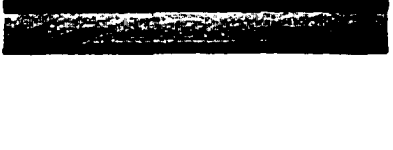
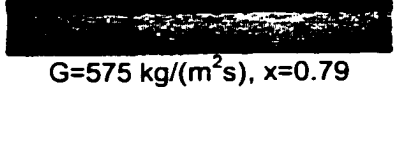
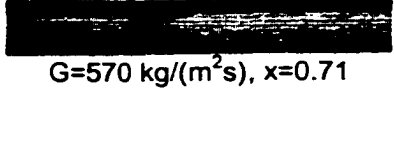
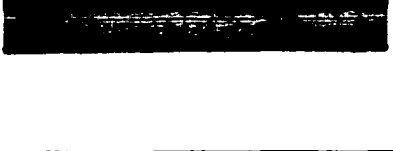
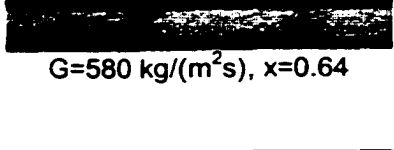
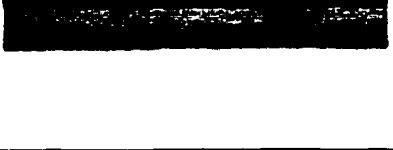
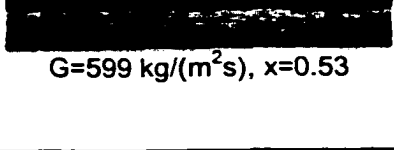
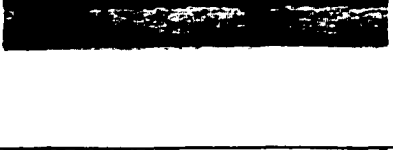
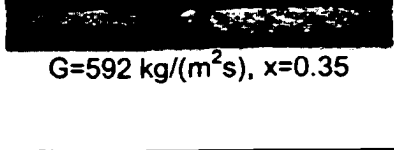
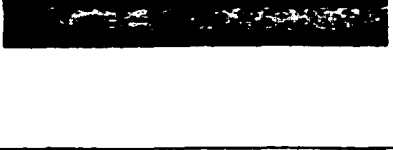
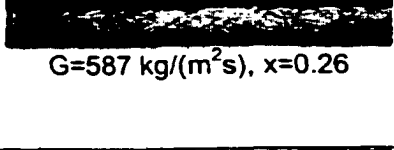
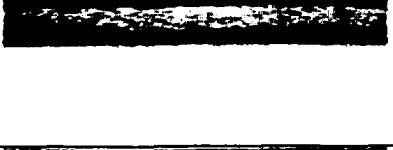
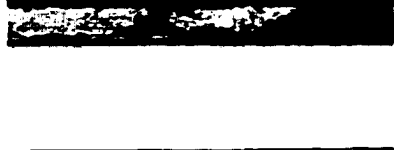
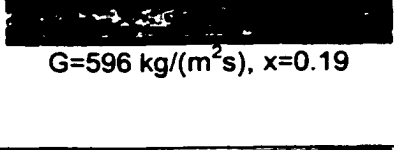
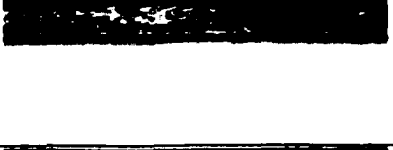
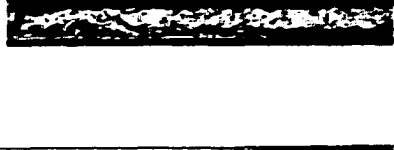
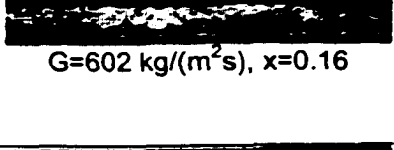
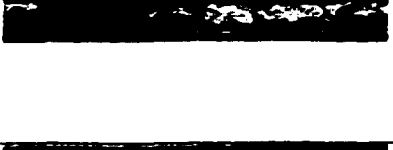
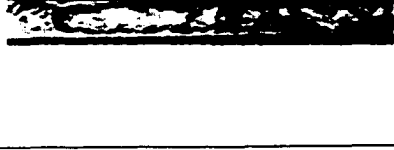
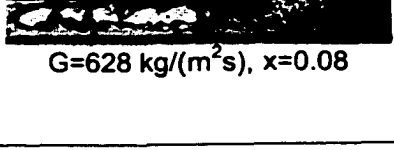
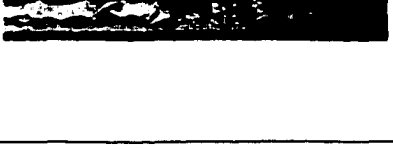
	 G=600 kg/(m ² s), x=0.97	
	 G=594 kg/(m ² s), x=0.91	
	 G=575 kg/(m ² s), x=0.79	
	 G=570 kg/(m ² s), x=0.71	
	 G=580 kg/(m ² s), x=0.64	
	 G=599 kg/(m ² s), x=0.53	
	 G=592 kg/(m ² s), x=0.35	
	 G=587 kg/(m ² s), x=0.26	
	 G=596 kg/(m ² s), x=0.19	
	 G=602 kg/(m ² s), x=0.16	
	 G=628 kg/(m ² s), x=0.08	

Table C29. Flow Visualization Photographs for the 2 (Height) x 4 (Width) mm Rectangular Tube [G = 600 kg/(m²s)]

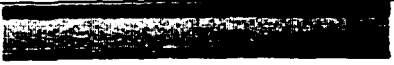
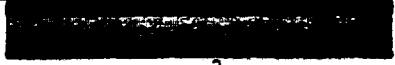
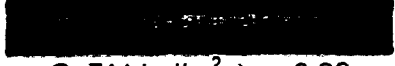
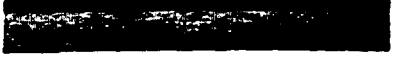
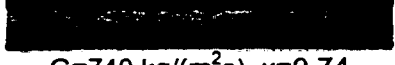
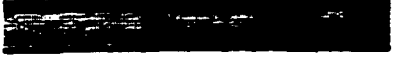
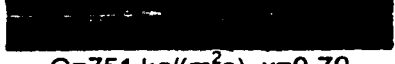
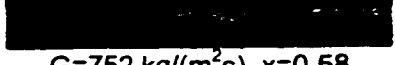
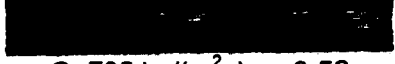
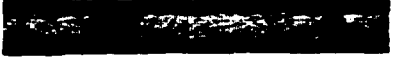
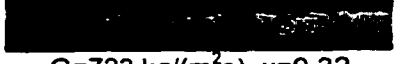
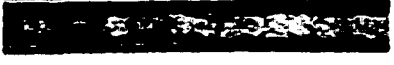
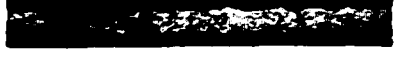
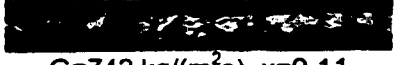
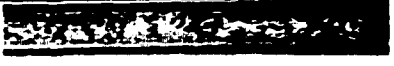
		
	G=718 kg/(m ² s), x=0.89	
		
	G=711 kg/(m ² s), x=0.86	
		
	G=740 kg/(m ² s), x=0.74	
		
	G=751 kg/(m ² s), x=0.70	
		
	G=752 kg/(m ² s), x=0.58	
		
	G=735 kg/(m ² s), x=0.53	
		
	G=711 kg/(m ² s), x=0.40	
		
	G=723 kg/(m ² s), x=0.32	
		
	G=704 kg/(m ² s), x=0.21	
		
	G=742 kg/(m ² s), x=0.11	
		
	G=752 kg/(m ² s), x=0.07	

Table C30. Flow Visualization Photographs for the 2 (Height) x 4 (Width) mm Rectangular Tube [G = 750 kg/(m²s)]

	 G=163 kg/(m ² s), x=0.47	
	 G=164 kg/(m ² s), x=0.32	
	 G=160 kg/(m ² s), x=0.29	
	 G=176 kg/(m ² s), x=0.20	
	 G=164 kg/(m ² s), x=0.11	
	 G=157 kg/(m ² s), x=0.09	
	 G=164 kg/(m ² s), x=0.06	

Table C31. Flow Visualization Photographs for the 4 (Height) x 2 (Width) mm Rectangular Tube [G = 150 kg/(m²s)]

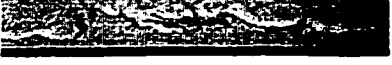
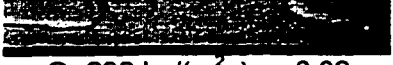
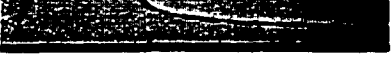
	 G=318 kg/(m ² s), x=0.86	
	 G=284 kg/(m ² s), x=0.74	
	 G=263 kg/(m ² s), x=0.65	
	 G=277 kg/(m ² s), x=0.52	
	 G=295 kg/(m ² s), x=0.38	
	 G=296 kg/(m ² s), x=0.32	
	 G=294 kg/(m ² s), x=0.20	
	 G=294 kg/(m ² s), x=0.17	
	 G=302 kg/(m ² s), x=0.14	
	 G=290 kg/(m ² s), x=0.06	
	 G=298 kg/(m ² s), x=0.02	

Table C32. Flow Visualization Photographs for the 4 (Height) x 2 (Width) mm Rectangular Tube [G = 300 kg/(m²s)]

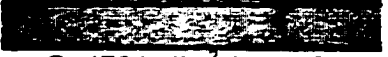
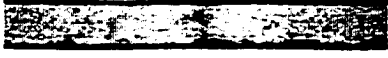
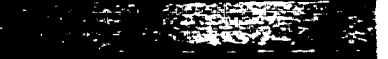
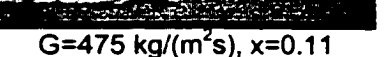
	 G=460 kg/(m ² s), x=0.93	
	 G=476 kg/(m ² s), x=0.78	
	 G=458 kg/(m ² s), x=0.71	
	 G=450 kg/(m ² s), x=0.58	
	 G=478 kg/(m ² s), x=0.47	
	 G=454 kg/(m ² s), x=0.41	
	 G=433 kg/(m ² s), x=0.26	
	 G=433 kg/(m ² s), x=0.23	
	 G=488 kg/(m ² s), x=0.19	
	 G=460 kg/(m ² s), x=0.14	
	 G=475 kg/(m ² s), x=0.11	

Table C33. Flow Visualization Photographs for the 4 (Height) x 2 (Width) mm Rectangular Tube [G = 450 kg/(m²s)]

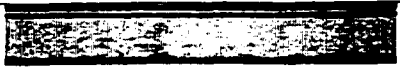
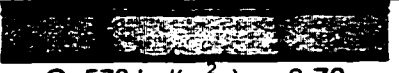
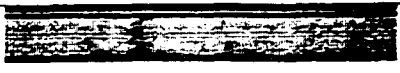
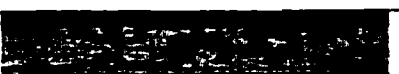
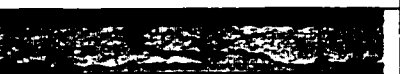
	 G=564 kg/(m ² s), x=0.93	
	 G=604 kg/(m ² s), x=0.82	
	 G=573 kg/(m ² s), x=0.78	
	 G=594 kg/(m ² s), x=0.72	
	 G=600 kg/(m ² s), x=0.59	
	 G=592 kg/(m ² s), x=0.48	
	 G=603 kg/(m ² s), x=0.38	
	 G=611 kg/(m ² s), x=0.35	
	 G=627 kg/(m ² s), x=0.27	
	 G=570 kg/(m ² s), x=0.14	
	 G=581 kg/(m ² s), x=0.10	

Table C34. Flow Visualization Photographs for the 4 (Height) x 2 (Width) mm Rectangular Tube [G = 600 kg/(m²s)]

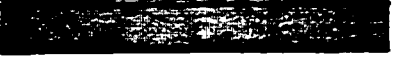
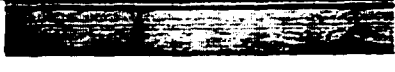
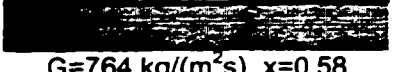
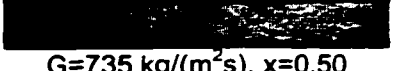
	 G=738 kg/(m ² s), x=0.89	
	 G=775 kg/(m ² s), x=0.73	
	 G=760 kg/(m ² s), x=0.65	
	 G=764 kg/(m ² s), x=0.58	
	 G=735 kg/(m ² s), x=0.50	
	 G=752 kg/(m ² s), x=0.39	
	 G=788 kg/(m ² s), x=0.28	
	 G=788 kg/(m ² s), x=0.19	
	 G=796 kg/(m ² s), x=0.09	

Table C35. Flow Visualization Photographs for the 4 (Height) x 2 (Width) mm Rectangular Tube [G = 750 kg/(m²s)]

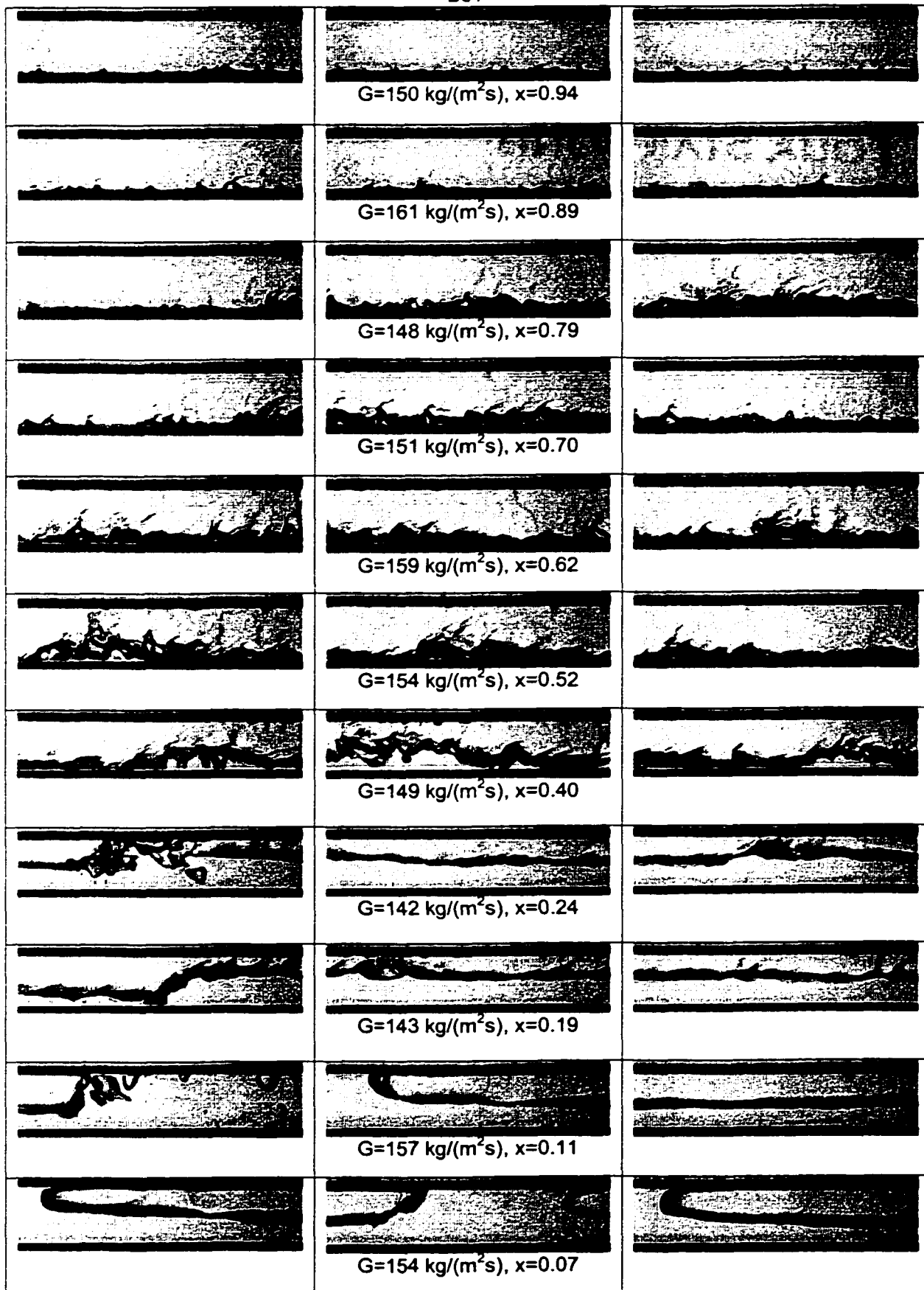


Table C36. Flow Visualization Photographs for the 4 (Height) x 6 (Width) mm Rectangular Tube [G = 150 kg/(m²s)]

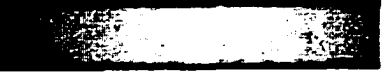
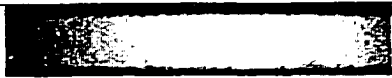
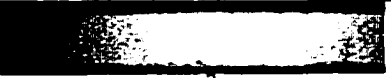
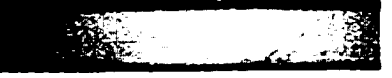
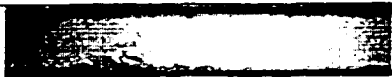
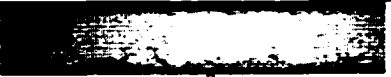
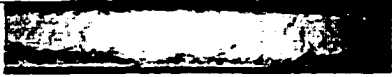
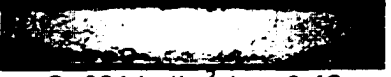
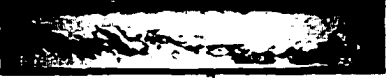
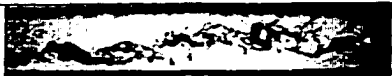
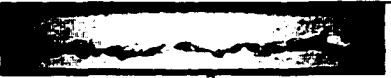
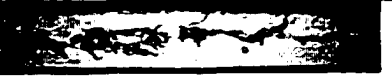
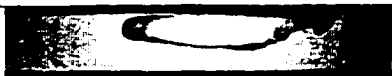
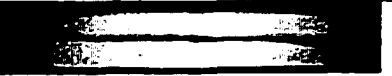
	 G=298 kg/(m ² s), x=0.98	
	 G=282 kg/(m ² s), x=0.90	
	 G=293 kg/(m ² s), x=0.83	
	 G=301 kg/(m ² s), x=0.71	
	 G=266 kg/(m ² s), x=0.58	
	 G=261 kg/(m ² s), x=0.53	
	 G=331 kg/(m ² s), x=0.43	
	 G=283 kg/(m ² s), x=0.31	
	 G=286 kg/(m ² s), x=0.22	
	 G=288 kg/(m ² s), x=0.17	
	 G=297 kg/(m ² s), x=0.03	

Table C37. Flow Visualization Photographs for the 4 (Height) x 6 (Width) mm Rectangular Tube [G = 300 kg/(m²s)]

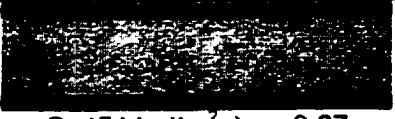
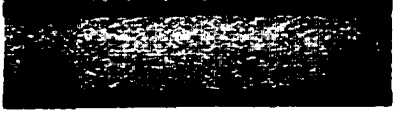
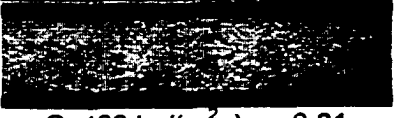
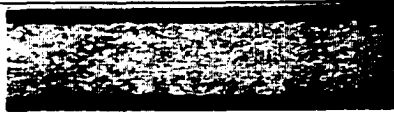
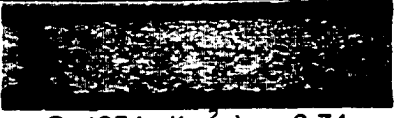
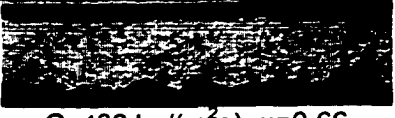
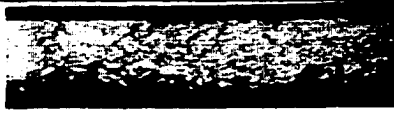
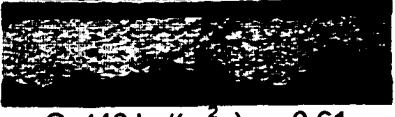
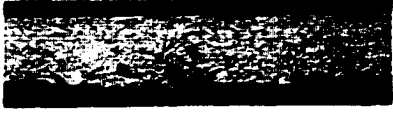
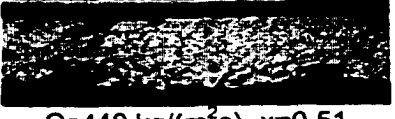
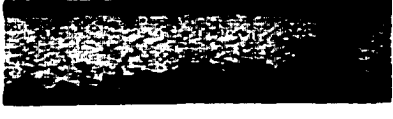
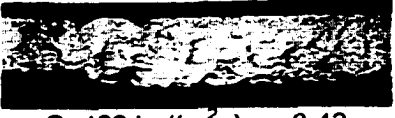
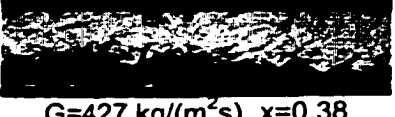
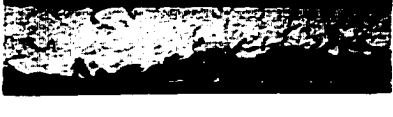
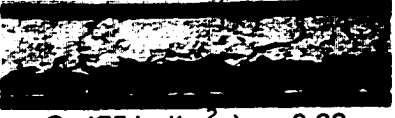
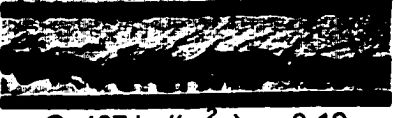
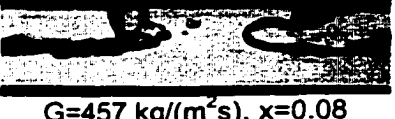
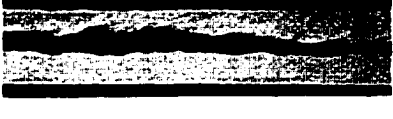
	 G=454 kg/(m ² s), x=0.87	
	 G=469 kg/(m ² s), x=0.81	
	 G=465 kg/(m ² s), x=0.74	
	 G=438 kg/(m ² s), x=0.66	
	 G=440 kg/(m ² s), x=0.61	
	 G=440 kg/(m ² s), x=0.51	
	 G=423 kg/(m ² s), x=0.43	
	 G=427 kg/(m ² s), x=0.38	
	 G=475 kg/(m ² s), x=0.33	
	 G=467 kg/(m ² s), x=0.19	
	 G=457 kg/(m ² s), x=0.08	

Table C38. Flow Visualization Photographs for the 4 (Height) x 6 (Width) mm Rectangular Tube [G = 450 kg/(m²s)]

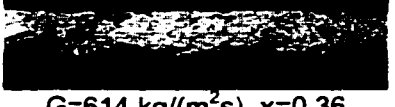
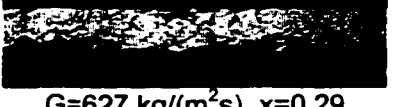
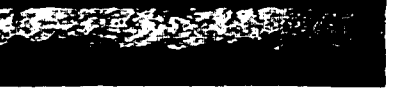
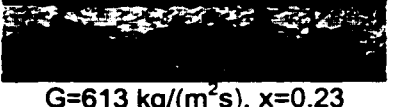
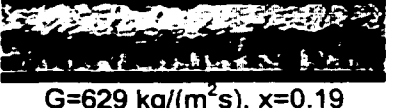
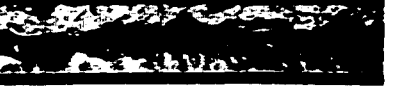
	 G=601 kg/(m ² s), x=0.77	
	 G=600 kg/(m ² s), x=0.71	
	 G=607 kg/(m ² s), x=0.61	
	 G=593 kg/(m ² s), x=0.51	
	 G=614 kg/(m ² s), x=0.36	
	 G=627 kg/(m ² s), x=0.29	
	 G=613 kg/(m ² s), x=0.23	
	 G=629 kg/(m ² s), x=0.19	

Table C39. Flow Visualization Photographs for the 4 (Height) x 6 (Width) mm Rectangular Tube [G = 600 kg/(m²s)]

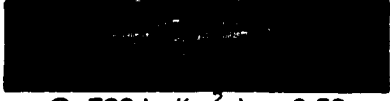
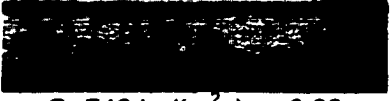
	 G=729 kg/(m ² s), x=0.59	
	 G=738 kg/(m ² s), x=0.53	
	 G=733 kg/(m ² s), x=0.50	
	 G=748 kg/(m ² s), x=0.39	
	 G=745 kg/(m ² s), x=0.29	
	 G=748 kg/(m ² s), x=0.25	

Table C40. Flow Visualization Photographs for the 4 (Height) x 6 (Width) mm Rectangular Tube [G = 750 kg/(m²s)]

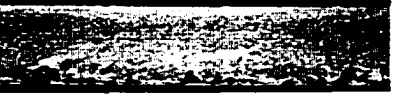
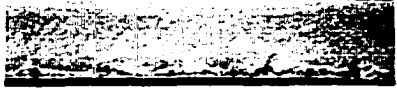
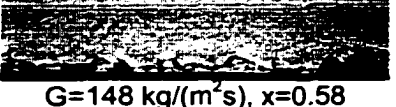
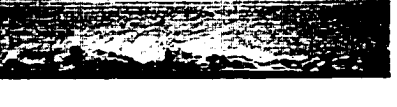
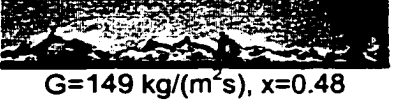
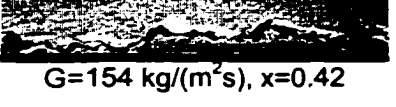
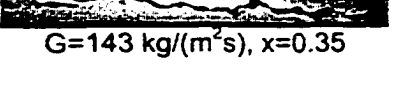
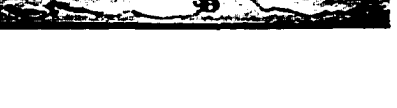
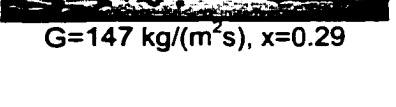
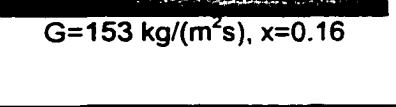
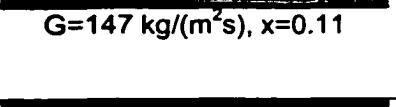
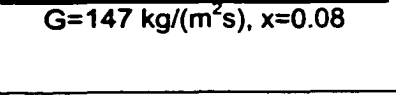
	 G=145 kg/(m ² s), x=0.87	
	 G=153 kg/(m ² s), x=0.75	
	 G=151 kg/(m ² s), x=0.67	
	 G=148 kg/(m ² s), x=0.58	
	 G=149 kg/(m ² s), x=0.48	
	 G=154 kg/(m ² s), x=0.42	
	 G=143 kg/(m ² s), x=0.35	
	 G=147 kg/(m ² s), x=0.29	
	 G=153 kg/(m ² s), x=0.16	
	 G=147 kg/(m ² s), x=0.11	
	 G=147 kg/(m ² s), x=0.08	

Table C41. Flow Visualization Photographs for the 6 (Height) x 4 (Width) mm Rectangular Tube [$G = 150 \text{ kg}/(\text{m}^2\text{s})$]

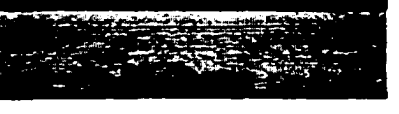
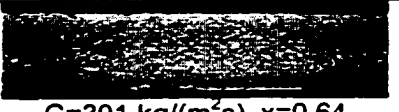
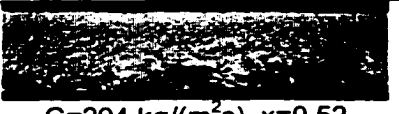
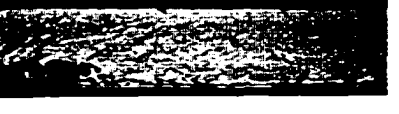
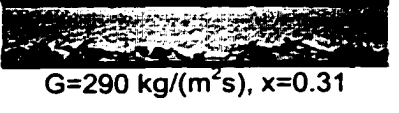
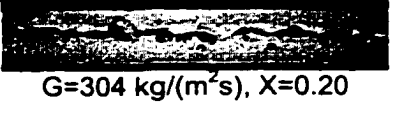
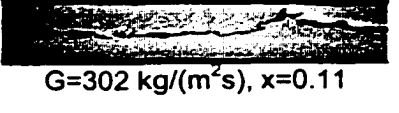
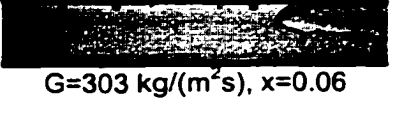
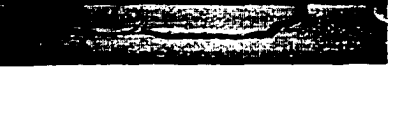
	 G=300 kg/(m ² s), x=0.91	
	 G=296 kg/(m ² s), x=0.86	
	 G=295 kg/(m ² s), x=0.79	
	 G=303 kg/(m ² s), x=0.70	
	 G=301 kg/(m ² s), x=0.64	
	 G=294 kg/(m ² s), x=0.52	
	 G=292 kg/(m ² s), x=0.41	
	 G=290 kg/(m ² s), x=0.31	
	 G=304 kg/(m ² s), X=0.20	
	 G=302 kg/(m ² s), x=0.11	
	 G=303 kg/(m ² s), x=0.06	

Table C42. Flow Visualization Photographs for the 6 (Height) x 4 (Width) mm Rectangular Tube [$G = 300 \text{ kg}/(\text{m}^2\text{s})$]

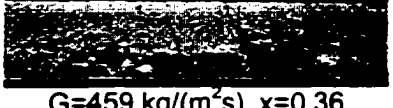
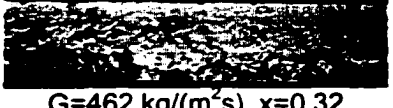
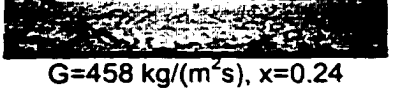
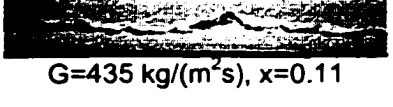
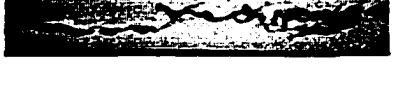
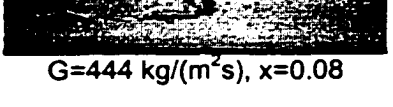
	 G=456 kg/(m ² s), x=0.82	
	 G=449 kg/(m ² s), x=0.78	
	 G=456 kg/(m ² s), x=0.73	
	 G=453 kg/(m ² s), x=0.64	
	 G=470 kg/(m ² s), x=0.56	
	 G=451 kg/(m ² s), x=0.45	
	 G=459 kg/(m ² s), x=0.36	
	 G=462 kg/(m ² s), x=0.32	
	 G=458 kg/(m ² s), x=0.24	
	 G=435 kg/(m ² s), x=0.11	
	 G=444 kg/(m ² s), x=0.08	

Table C43. Flow Visualization Photographs for the 6 (Height) x 4 (Width) mm Rectangular Tube [G = 450 kg/(m²s)]

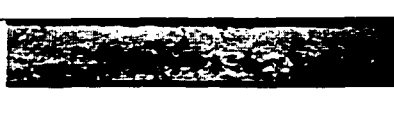
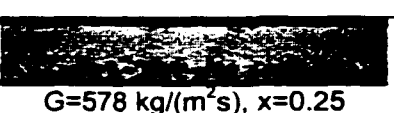
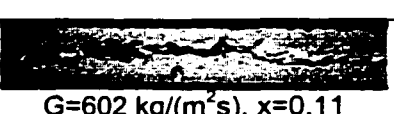
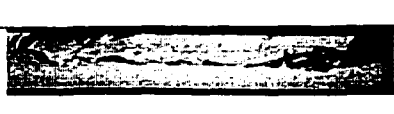
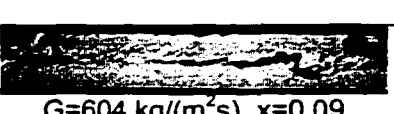
	 G=596 kg/(m ² s), x=0.61	
	 G=596 kg/(m ² s), x=0.55	
	 G=589 kg/(m ² s), x=0.42	
	 G=597 kg/(m ² s), x=0.37	
	 G=578 kg/(m ² s), x=0.25	
	 G=602 kg/(m ² s), x=0.11	
	 G=604 kg/(m ² s), x=0.09	

Table C44. Flow Visualization Photographs for the 6 (Height) x 4 (Width) mm Rectangular Tube [G = 600 kg/(m²s)]

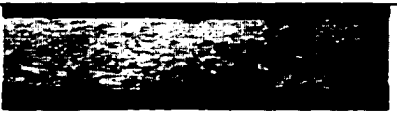
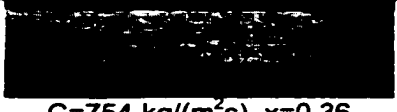
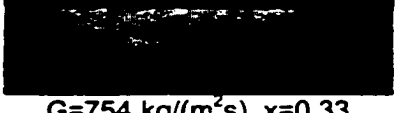
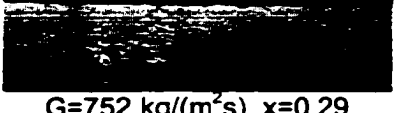
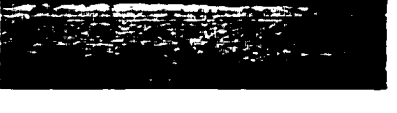
	 $G=717 \text{ kg}/(\text{m}^2\text{s}), x=0.52$	
	 $G=754 \text{ kg}/(\text{m}^2\text{s}), x=0.36$	
	 $G=754 \text{ kg}/(\text{m}^2\text{s}), x=0.33$	
	 $G=752 \text{ kg}/(\text{m}^2\text{s}), x=0.29$	

Table C45. Flow Visualization Photographs for the 6 (Height) x 4 (Width) mm Rectangular Tube [$G = 750 \text{ kg}/(\text{m}^2\text{s})$]

APPENDIX D
SINGLE PHASE TESTS AND TUBE VALIDATION

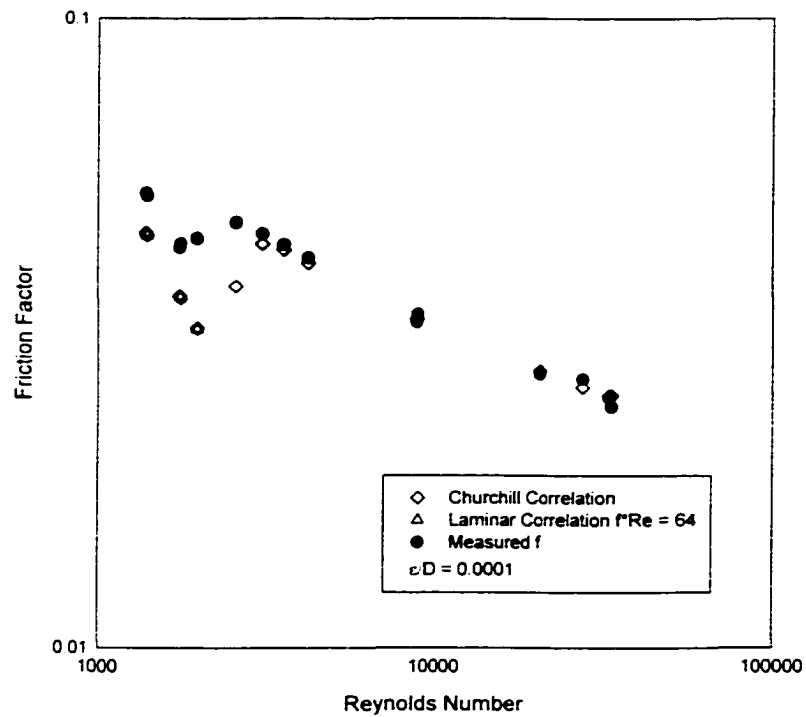


Figure D1. Experimental and Theoretical Single-Phase Friction Factors for Tube C60

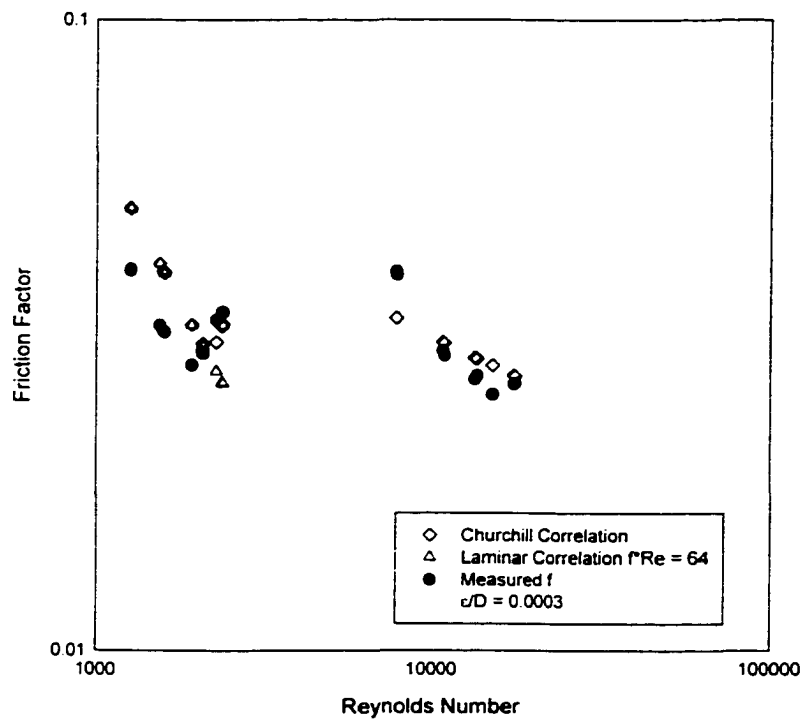


Figure D2. Experimental and Theoretical Single-Phase Friction Factors for Tube C20

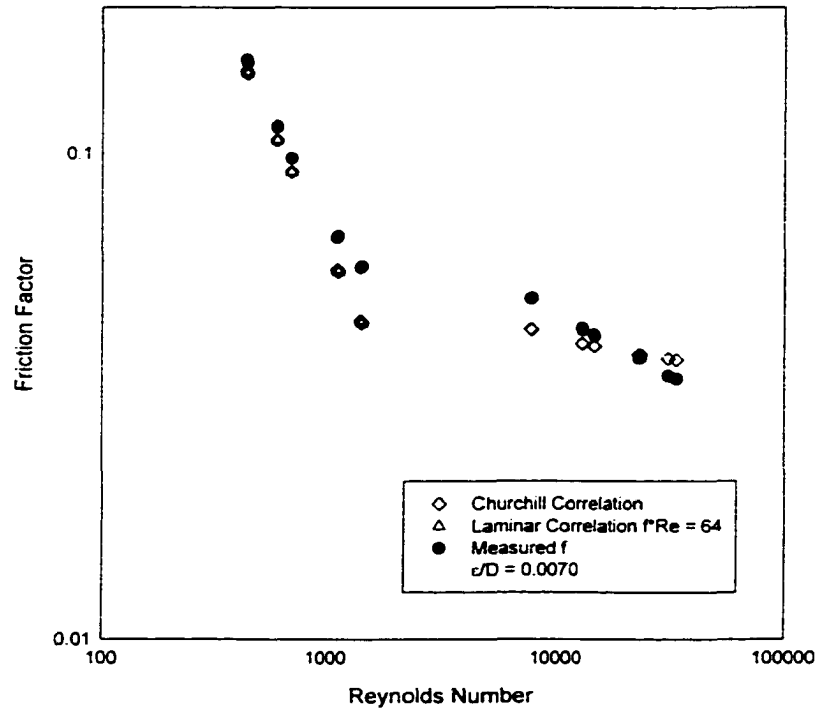


Figure D3. Experimental and Theoretical Single-Phase Friction Factors for Tube B32

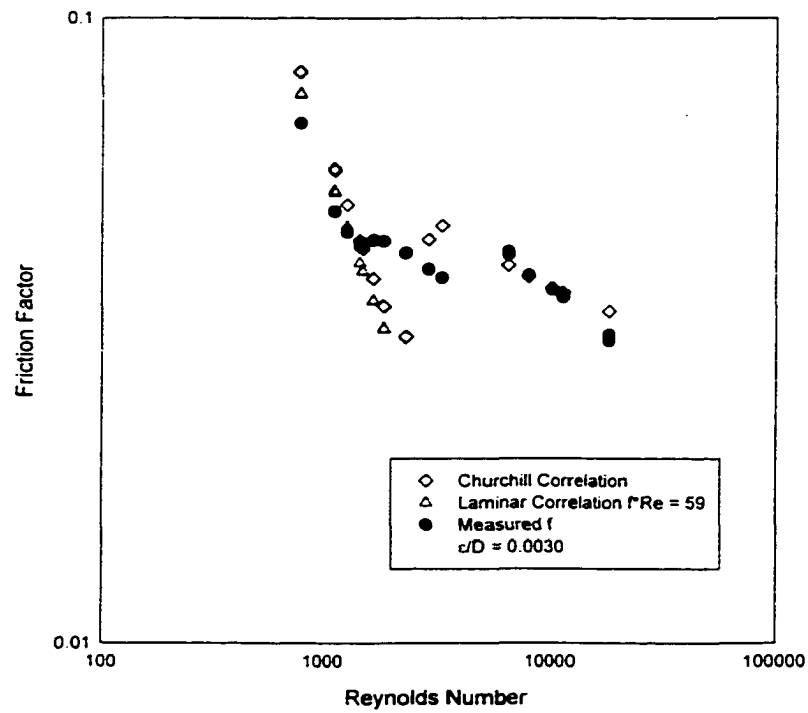


Figure D4. Experimental and Theoretical Single-Phase Friction Factors for Tube N21

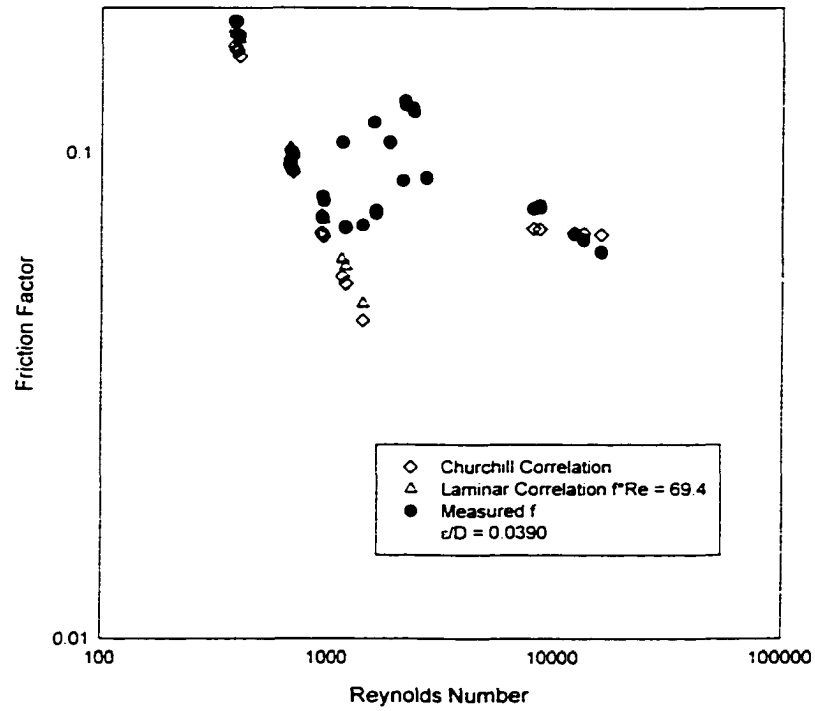


Figure D5. Experimental and Theoretical Single-Phase Friction Factors for Tube RK15

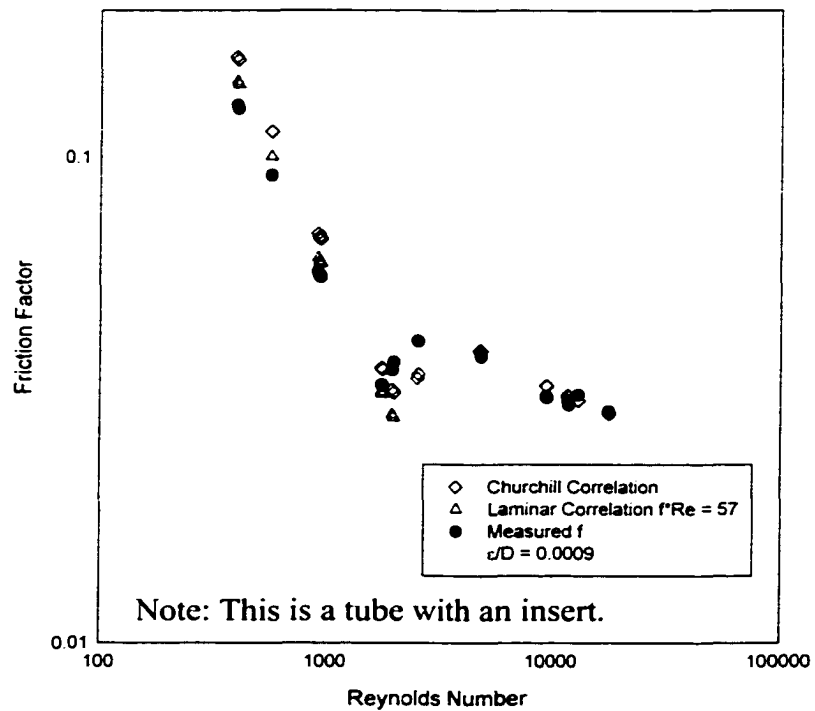


Figure D6. Experimental and Theoretical Single-Phase Friction Factors for Tube S30

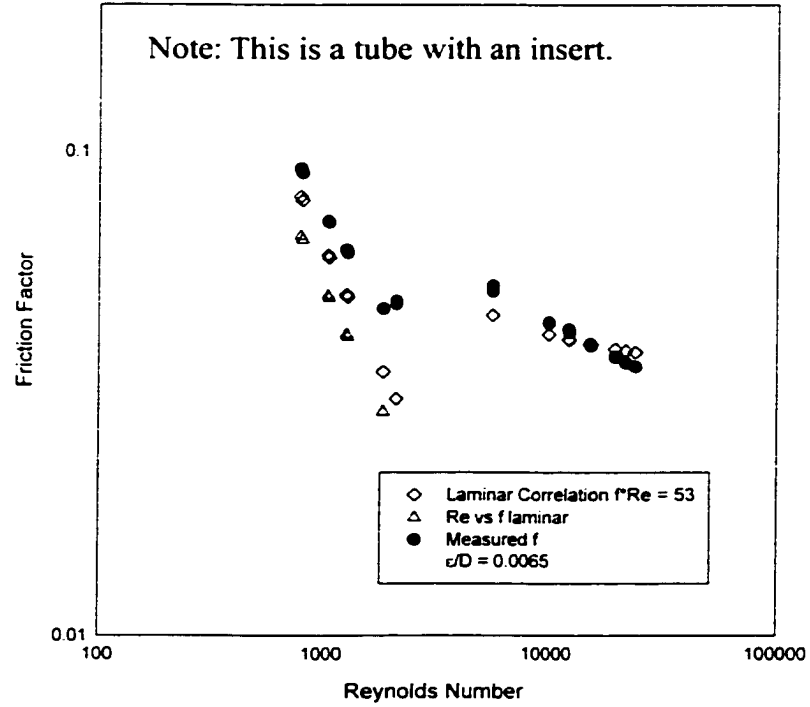


Figure D7. Experimental and Theoretical Single-Phase Friction Factors for Tube T33

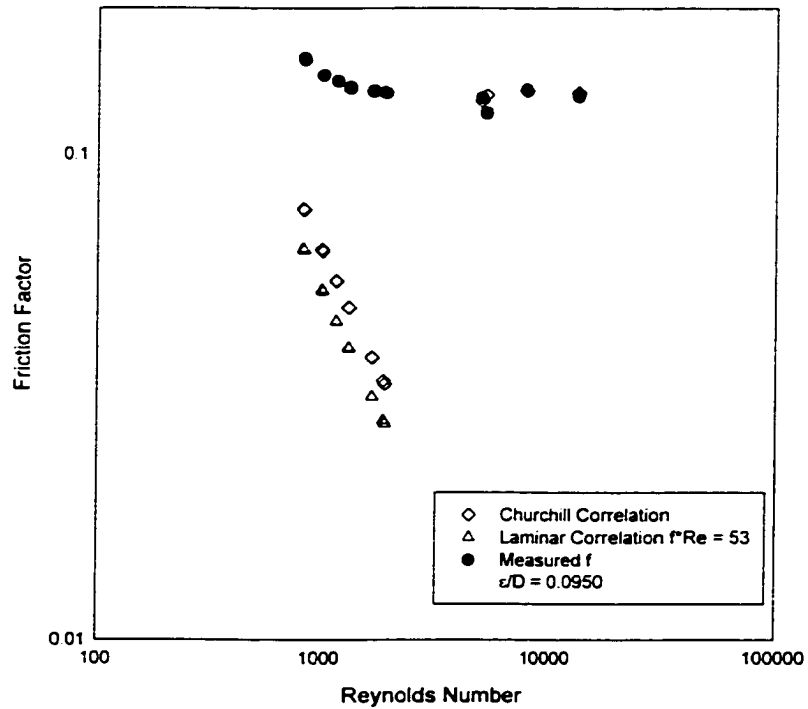


Figure D8. Experimental and Theoretical Single-Phase Friction Factors for Tube W291

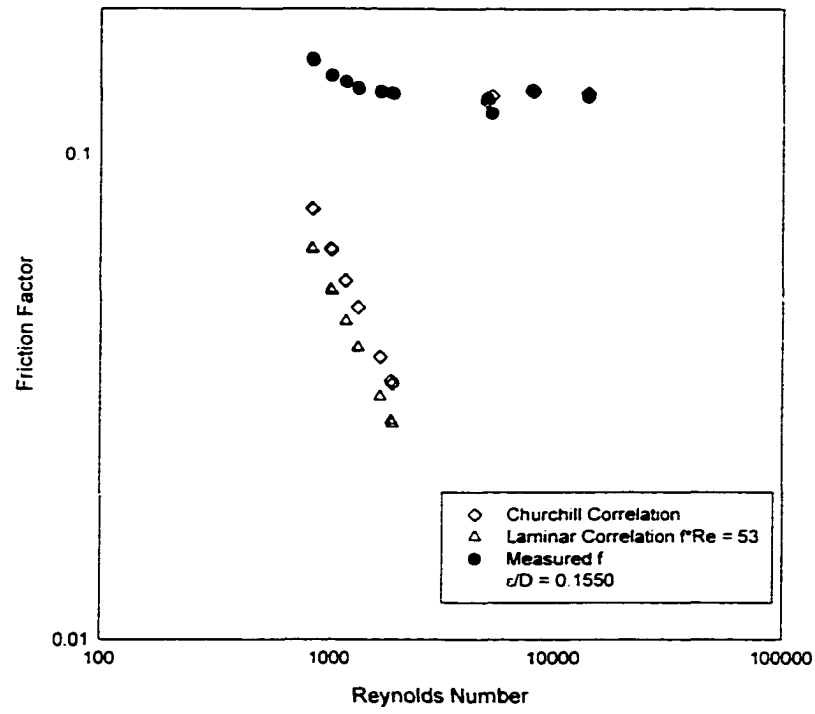


Figure D9. Experimental and Theoretical Single-Phase Friction Factors for Tube W29II

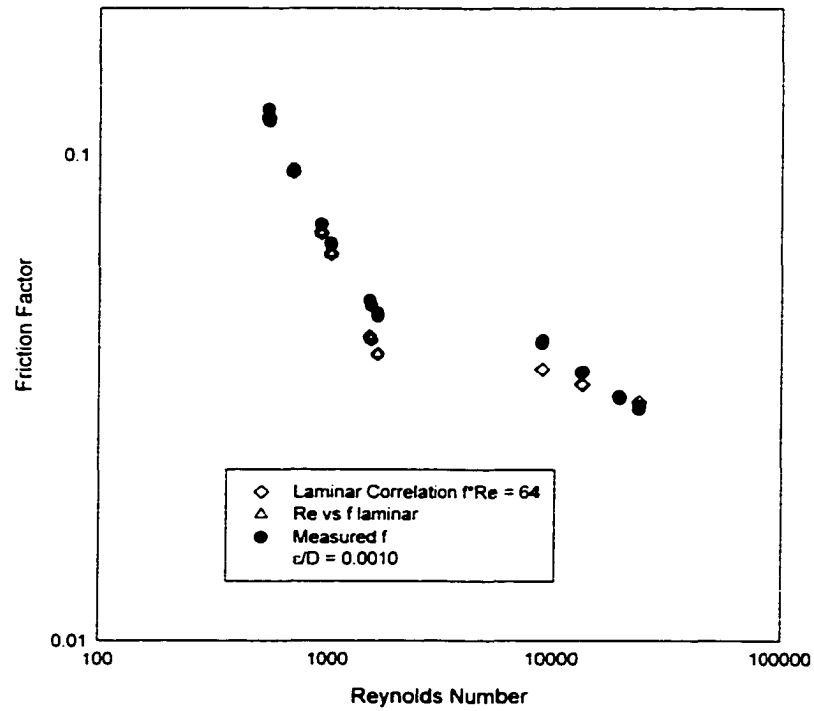


Figure D10. Experimental and Theoretical Single-Phase Friction Factors for Tube ZLI

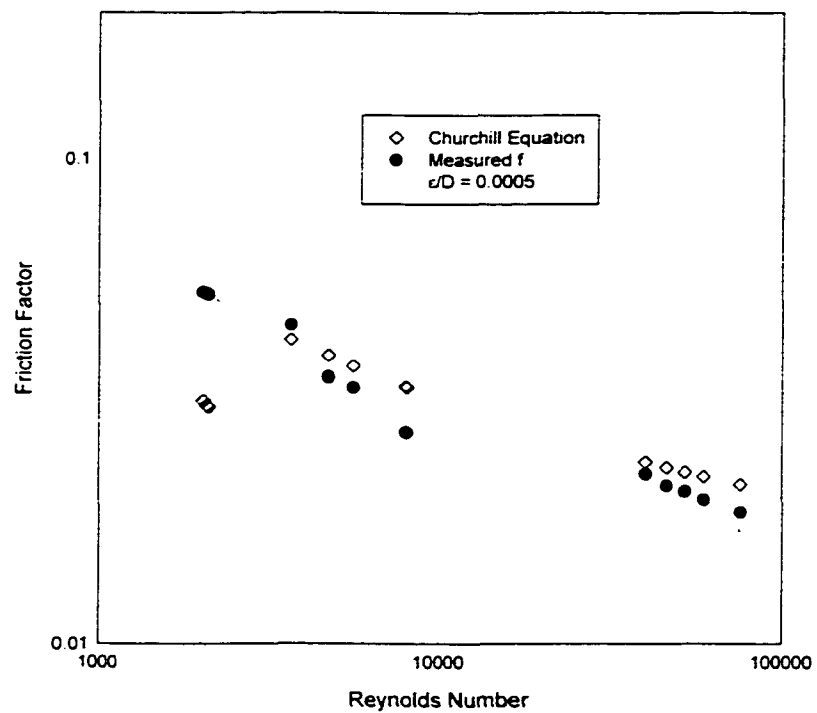


Figure D11. Experimental and Theoretical Single-Phase Friction Factors for Tube ZLII

APPENDIX E

ADIABATIC AND CONDENSING PRESSURE DROPS

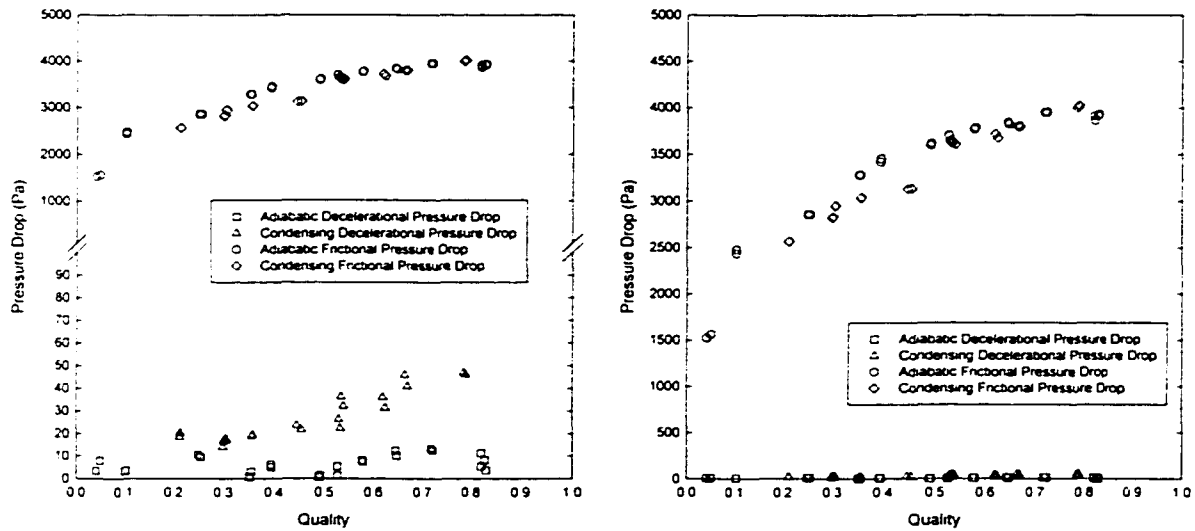


Figure E1. Decelerational Pressure Drop (Tube S30, $G = 150 \text{ kg/m}^2\text{-s}$)

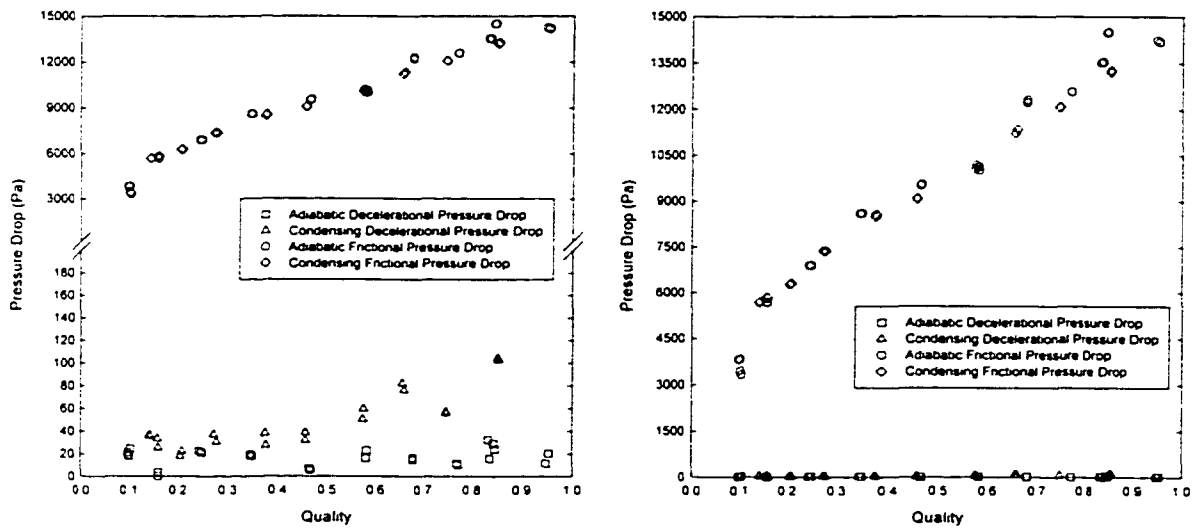


Figure E2. Decelerational Pressure Drop (Tube S30, $G = 300 \text{ kg/m}^2\text{-s}$)

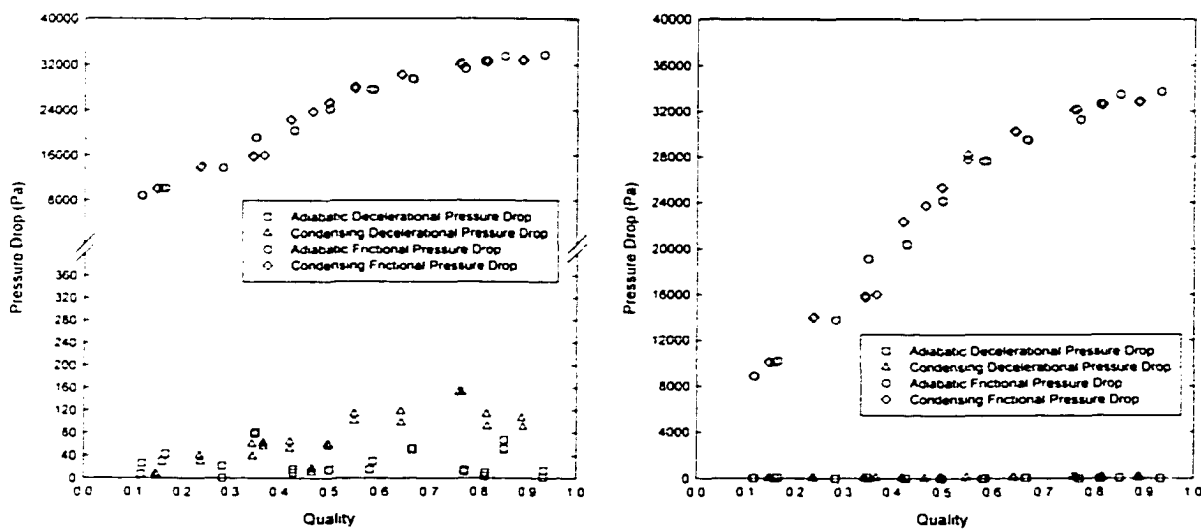


Figure E3. Decelerational Pressure Drop (Tube S30, $G = 450 \text{ kg/m}^2\text{-s}$)

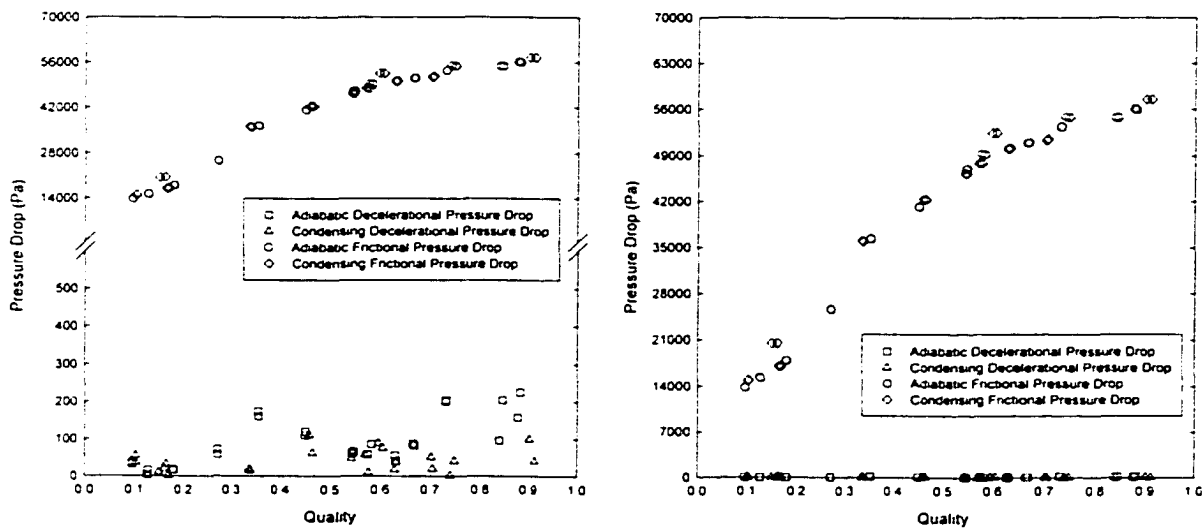


Figure E4. Decelerational Pressure Drop (Tube S30, $G = 600 \text{ kg/m}^2\text{-s}$)

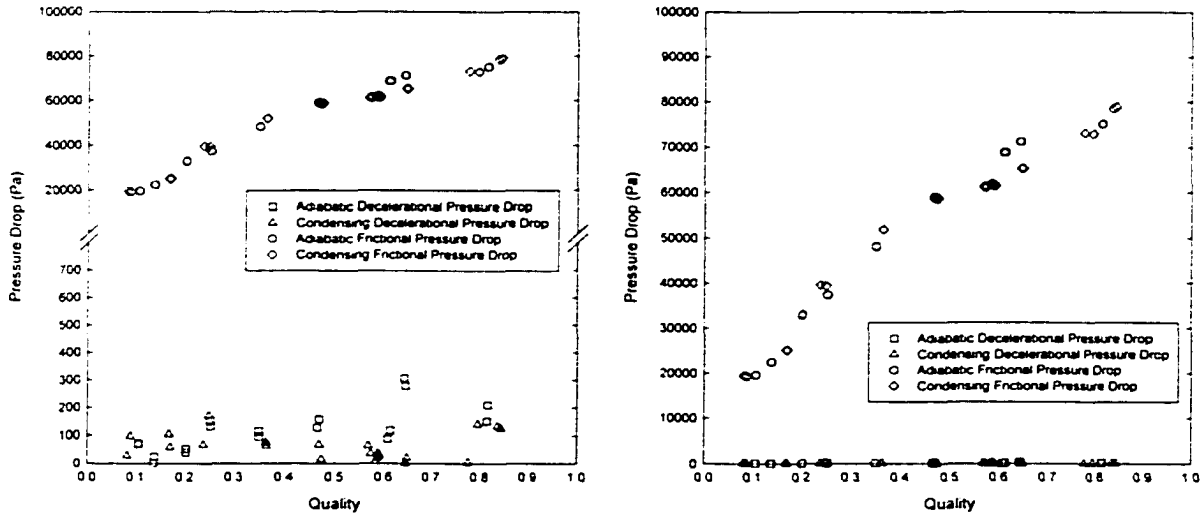


Figure E5. Decelerational Pressure Drop (Tube S30, $G = 750 \text{ kg/m}^2\text{-s}$)

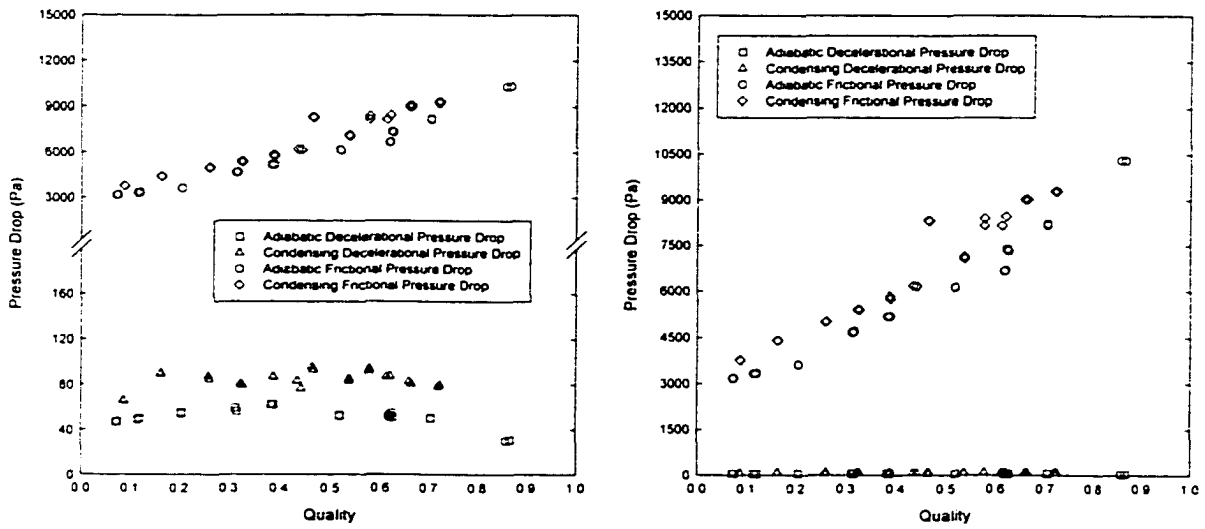


Figure E6. Decelerational Pressure Drop (Tube W29I, $G = 150 \text{ kg/m}^2\text{-s}$)

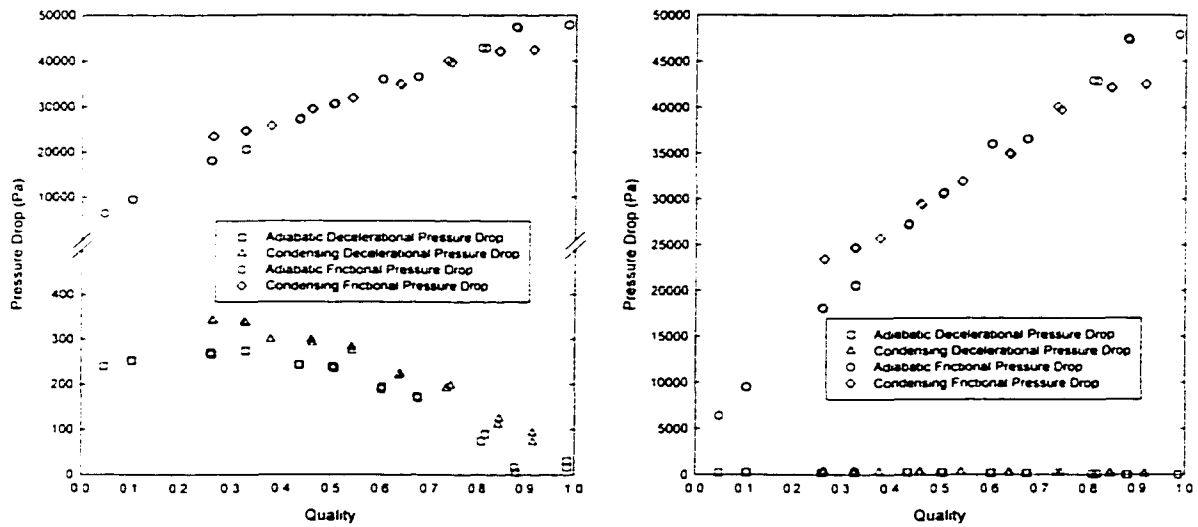


Figure E7. Decelerational Pressure Drop (Tube W29I, $G = 300 \text{ kg/m}^2\text{-s}$)

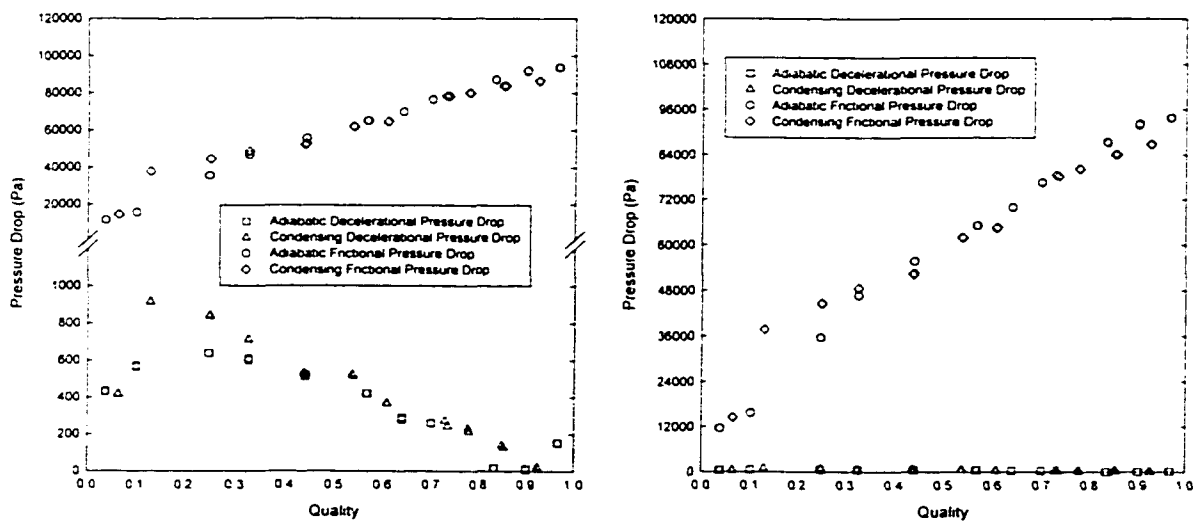


Figure E8. Decelerational Pressure Drop (Tube W29I, $G = 450 \text{ kg/m}^2\text{-s}$)

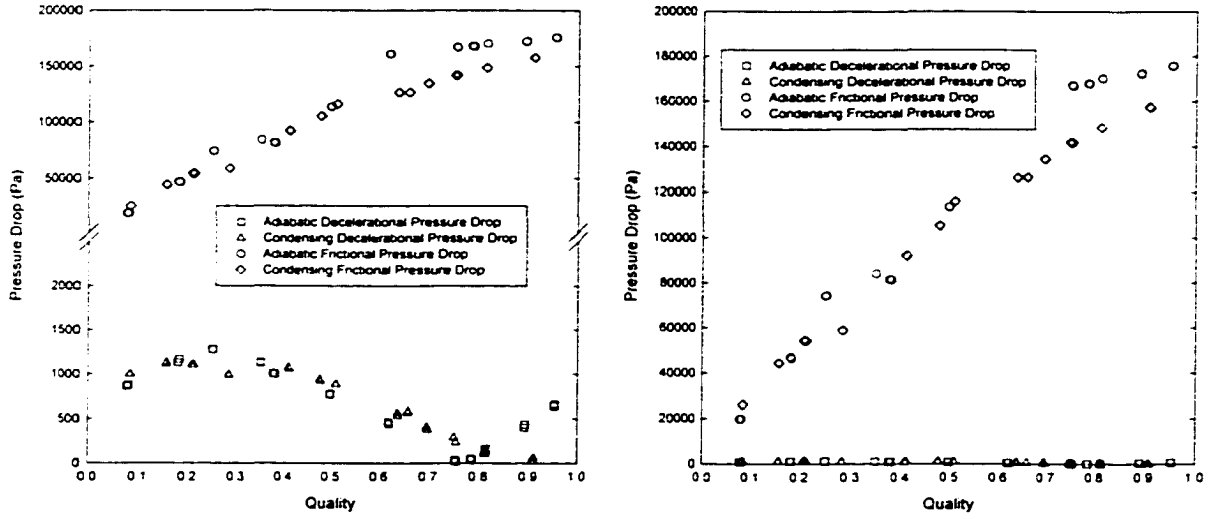


Figure E9. Decelerational Pressure Drop (Tube W29I, $G = 600 \text{ kg/m}^2\text{-s}$)

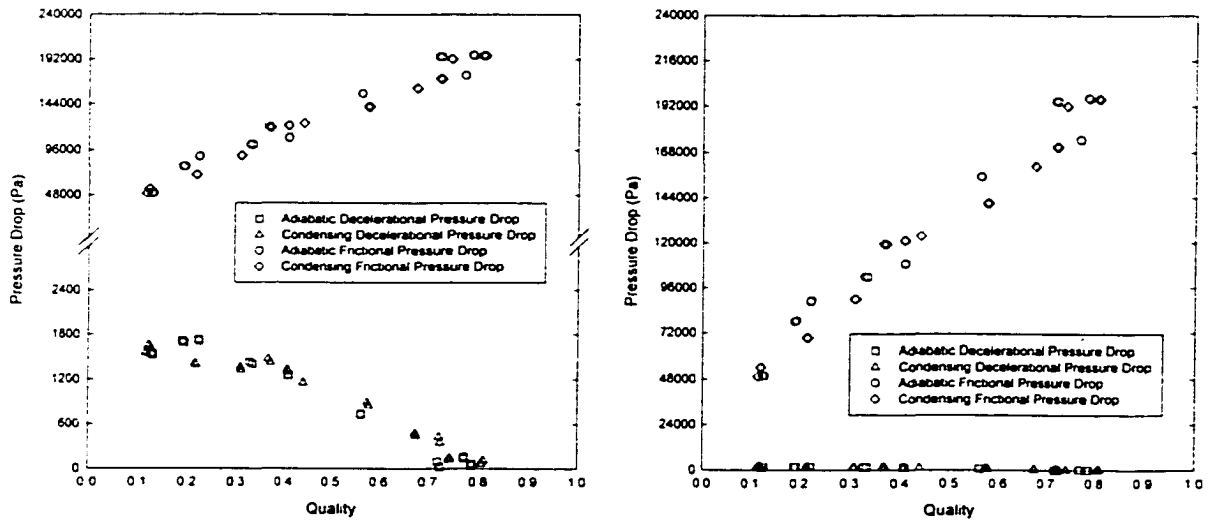


Figure E10. Decelerational Pressure Drop (Tube W29I, $G = 750 \text{ kg/m}^2\text{-s}$)

APPENDIX F
EXPERIMENTAL TRANSITION CORRELATIONS

4.91 mm Circular Tube Transition Lines

Intermittent Flow to Intermittent and Discrete Wave Flow

$$G = -1097 + 132.1/x$$

Intermittent and Discrete Wave Flow to Discrete Wave Flow

$$G = -223.2 + 69.9/x$$

Discrete Wave Flow to Disperse Wave Flow

$$G = \frac{1340 - 283.6x}{1 + 3.86x}$$

Annular Film and Mist Flow to Mist Flow

$$G = -134.8 + 422.6/x$$

4 x 4 mm Square Tube Transition Lines

Intermittent to Discrete Wave Flow

$$x = 0.08$$

Discrete Wave Flow to Disperse Wave Flow

$$G = \frac{51.43 - 1323x}{1 - 6.9x}$$

Disperse Wave Flow to Mist Flow

$$G = \frac{158.4 - 372.4x}{1 - 1.95x}$$

3 x 3 mm Square Tube Transition Lines

Intermittent Flow to Intermittent and Discrete Wave Flow

$$G = -603.2 + 124.2/x$$

Intermittent and Discrete Wave Flow to Discrete Wave Flow

$$G = -328.7 + 68.1/x$$

Discrete Wave Flow to Disperse Wave Flow

$$G = -21 + 135.2/x$$

Disperse Wave Flow to Annular Film and Mist Flow

$$G = -73.3 + 269.7/x$$

Annular Film and Mist Flow to Mist Flow

$$G = \frac{-157.9 - 354.3x}{1 - 263x}$$

To Disperse Bubble Flow

$$G = 515.7 + 2813x - 4922x^2$$

2 x 2 mm Tube Transition Lines

Intermittent Flow to Intermittent and Discrete Wave Flow

$$G = -213.3 + 63.22/x$$

Intermittent and Discrete Wave Flow to Discrete Wave Flow

$$G = -348.0 + 162/x$$

Discrete Wave Flow to Annular Film Flow

$$G = -140.3 + 165.2/x$$

Annular Film Flow to Annular Film and Mist Flow

$$G = 74.7 + 151.4/x$$

Annular Film and Mist Flow to Mist Flow

$$G = \frac{135.7 - 497.7x}{1 - 1.925x}$$

Disperse Bubble Flow

$$G = 546.7 + 2418x - 5278x^2$$

1 x 1 mm Tube Transition Lines

Intermittent Flow to Intermittent and Annular Film Flow

$$G = \frac{547.7 - 1227x}{1 + 2.856x}$$

Intermittent and Annular Film Flow to Annular Film Flow

$$G = -56.13 + 125.4/x$$

Annular Film Flow to Annular Film and Mist Flow

$$G = 206.1 + 85.8/x$$

Annular Film and Mist Flow to Mist Flow

$$G = \frac{207.2 - 527.5x}{1 - 1.774x}$$

Dispersed Bubble Flow

$$G = 1376 - 97.1/x$$

4(H) x 2(W) mm Tube Transition Lines

Intermittent Flow to Intermittent and Discrete Wave Flow

$$G = -388 + 41.2/x$$

Intermittent Flow and Discrete Wave Flow to Discrete Wave Flow

$$G = -710.8 + 150.5/x$$

Discrete Wave Flow to Disperse Wave Flow

$$G = \frac{217.2 - 2015x}{1 - 6.17x}$$

Discrete Wave/Disperse Wave Flow to Annular Film and Mist Flow

$$G = -651.2 + 569.1/x$$

Annular Film Flow to Mist Flow

$$G = 48.53 + 308/x$$

2(H) x 4(W) mm Tube Transition Lines

Intermittent and Discrete Wave Flow to Discrete Wave Flow

$$G = -548.6 + 110.4/x$$

Discrete Wave Flow to Disperse Wave Flow

$$G = \frac{1304 - 373.5x}{1 - 6.2x}$$

Disperse Wave Flow to Annular Film Flow

$$G = \frac{-116.8 - 222.3x}{1 - 3.46x}$$

Annular Film Flow to Annular Film and Mist Flow

$$G = -256.1 + 449.2/x$$

Annular Film and Mist Flow to Mist Flow

$$G = \frac{-1304 - 373.5x}{1 - 6.19x}$$

Disperse Bubble Flow

$$G = 660.6 + 1087x - 2067x^2$$

4(H) x 6(W) mm Tube Transition Lines

Intermittent Flow to Intermittent and Discrete Wave Flow

$$G = -850 + 60/x$$

Intermittent and Discrete Wave Flow to Discrete Wave Flow

$$G = -1075 + 170/x$$

Discrete Wave Flow to Disperse Wave Flow

$$G = \frac{276.3 - 2494x}{1 - 6.75x}$$

Discrete Wave or Disperse Wave Flow to Annular Film and Mist Flow

$$G = -575.4 + 748.3/x$$

6(H) x 4(W) mm Tube Transition Lines

Intermittent Flow to Intermittent and Discrete Wave Flow

$$G = -339 + 40.6/x$$

Intermittent and Discrete Wave Flow to Discrete Wave Flow

$$G = -411.2 + 96/x$$

Discrete Wave Flow to Disperse Wave Flow

$$G = \frac{-169.4 - 2337x}{1 - 10.48x}$$

Discrete Wave or Disperse Wave Flow to Annular Film and Mist Flow

$$G = -533.3 + 742.8/x$$

APPENDIX G

ROUND TUBE ΔP COMPARISON WITH LITERATURE

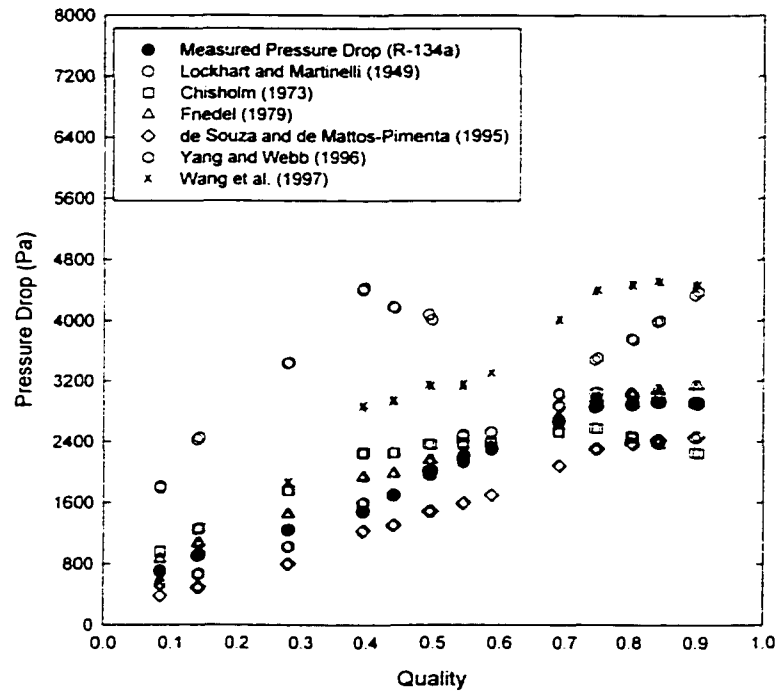


Figure G1. Comparison of the C120 Tube ($D_h = 3.05$ mm) with the Literature ($G \cong 300$ kg/m²-s)

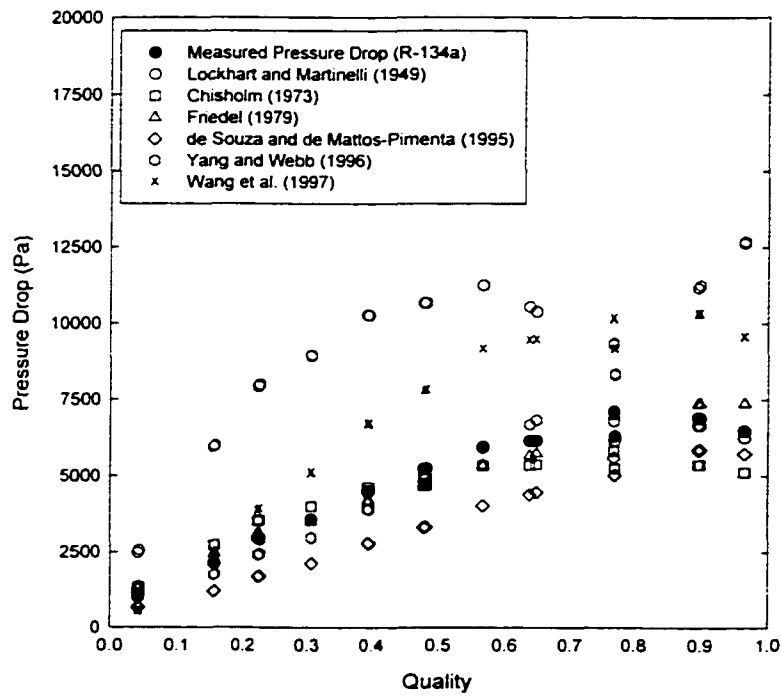


Figure G2. Comparison of the C120 Tube ($D_h = 3.05$ mm) with the Literature ($G \cong 450$ kg/m²-s)

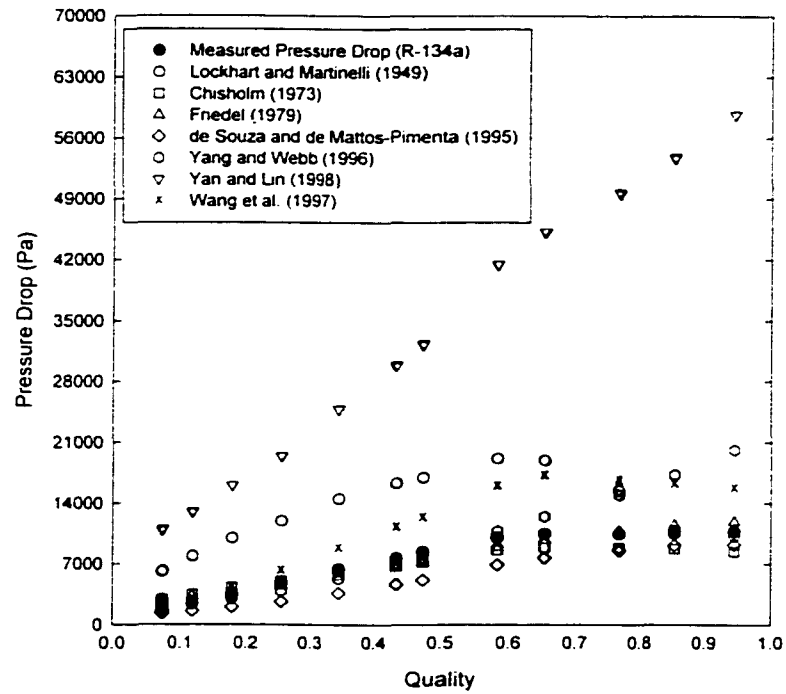


Figure G3. Comparison of the C120 Tube ($D_h = 3.05$ mm) with the Literature ($G \cong 600$ kg/m²-s)

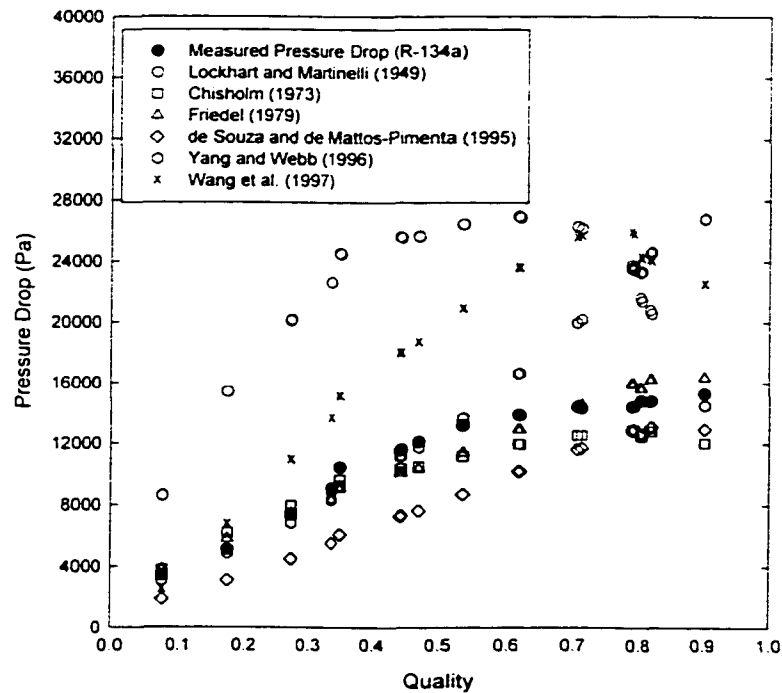


Figure G4. Comparison of the C120 Tube ($D_h = 3.05$ mm) with the Literature ($G \cong 750$ kg/m²-s)

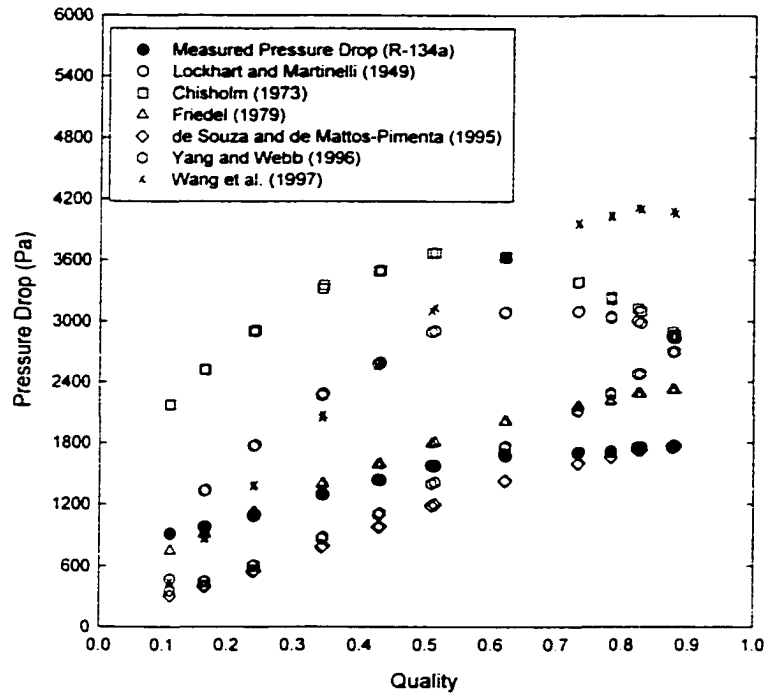


Figure G5. Comparison of the C60 Tube ($D_h = 1.52$ mm) with the Literature ($G \cong 150$ kg/m²-s)

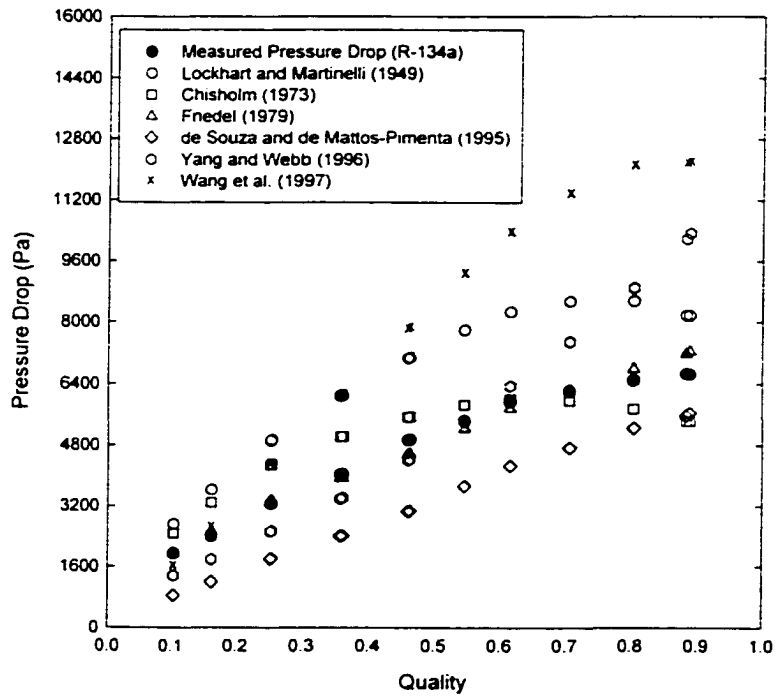


Figure G6. Comparison of the C60 Tube ($D_h = 1.52$ mm) with the Literature ($G \cong 300$ kg/m²-s)

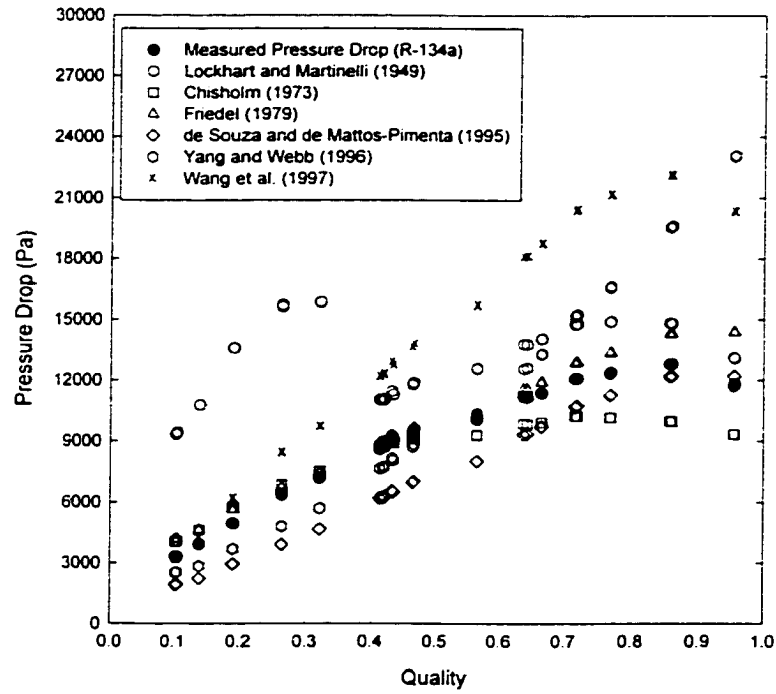


Figure G7. Comparison of the C60 Tube ($D_h = 1.52$ mm) with the Literature ($G \cong 450$ kg/m²-s)

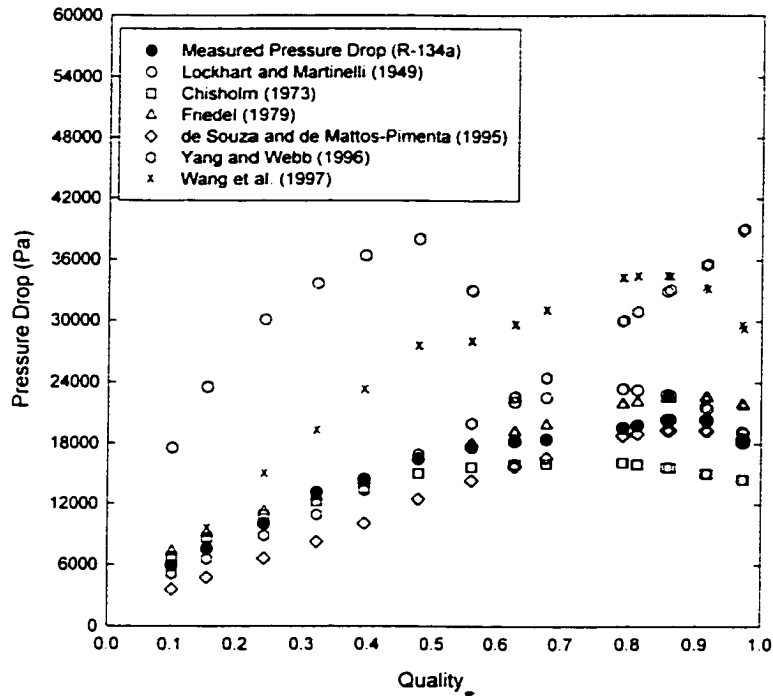


Figure G8. Comparison of the C60 Tube ($D_h = 1.52$ mm) with the Literature ($G \cong 600$ kg/m²-s)

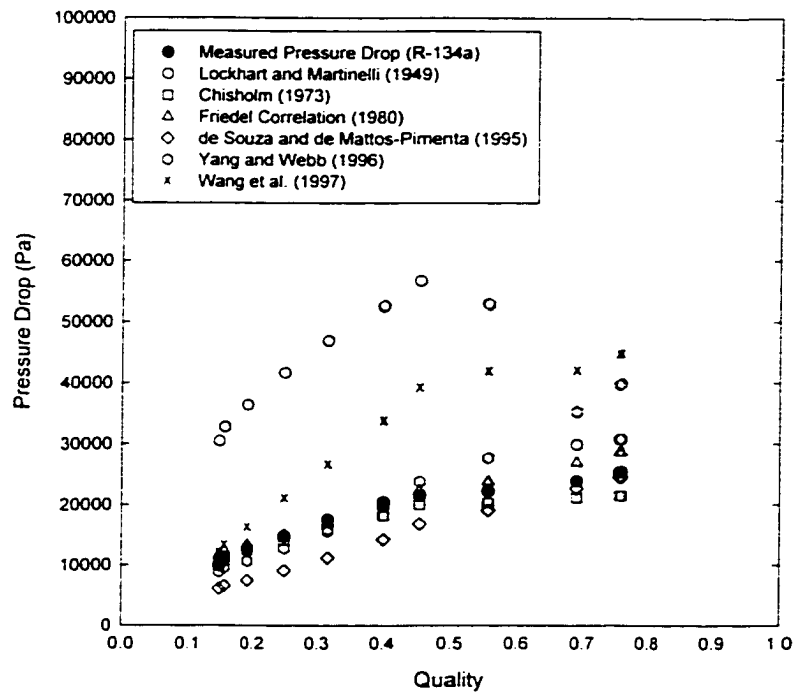


Figure G9. Comparison of the C60 Tube ($D_h = 1.52$ mm) with the Literature ($G \cong 750$ kg/m²-s)

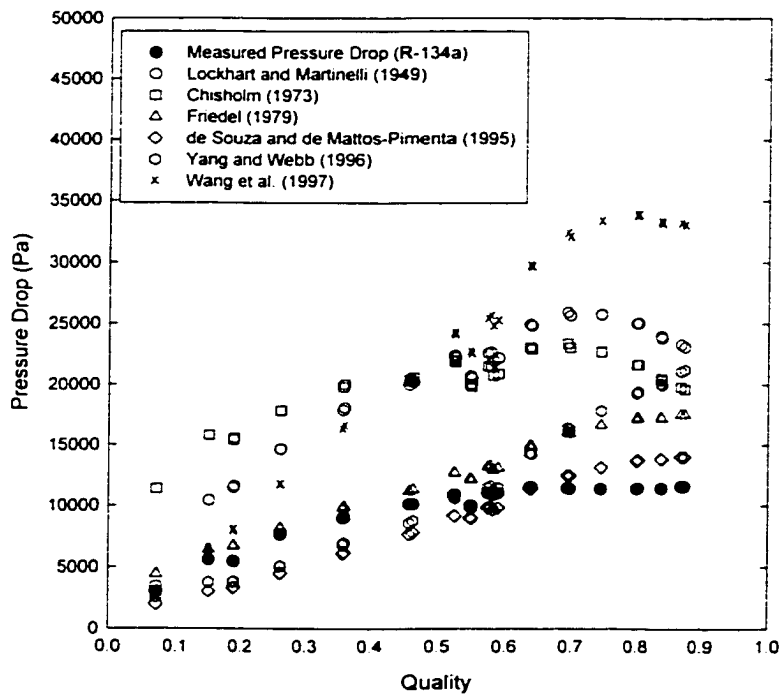


Figure G10. Comparison of the C30 Tube ($D_h = 0.762$ mm) with the Literature ($G \cong 300$ kg/m²-s)

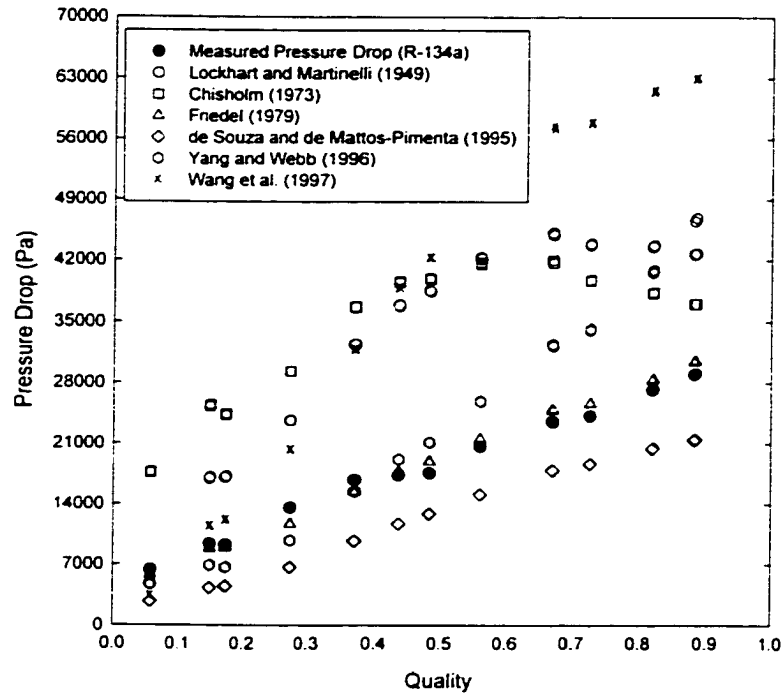


Figure G11. Comparison of the C30 Tube ($D_h = 0.762$ mm) with the Literature ($G \cong 450$ kg/m²-s)

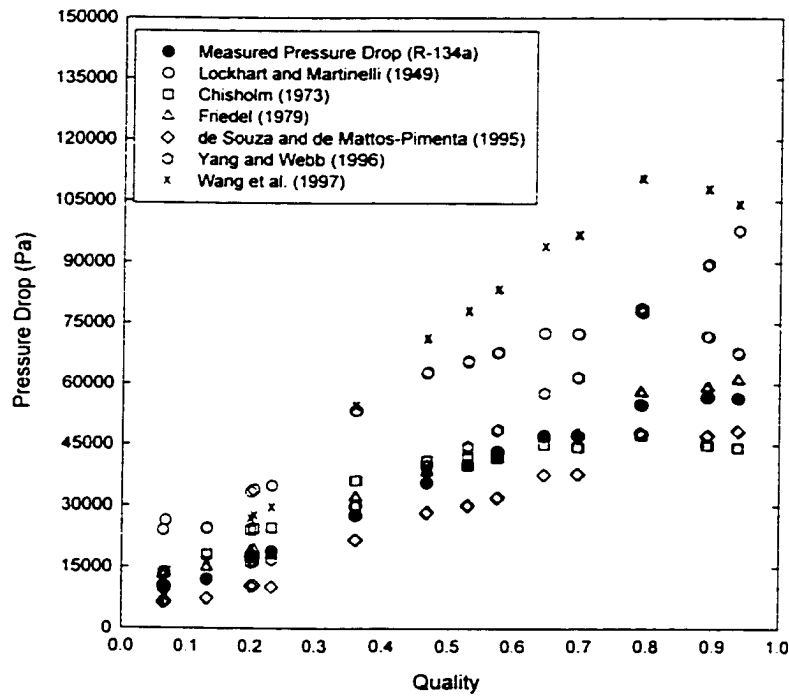


Figure G12. Comparison of the C30 Tube ($D_h = 0.762$ mm) with the Literature ($G \cong 600$ kg/m²-s)

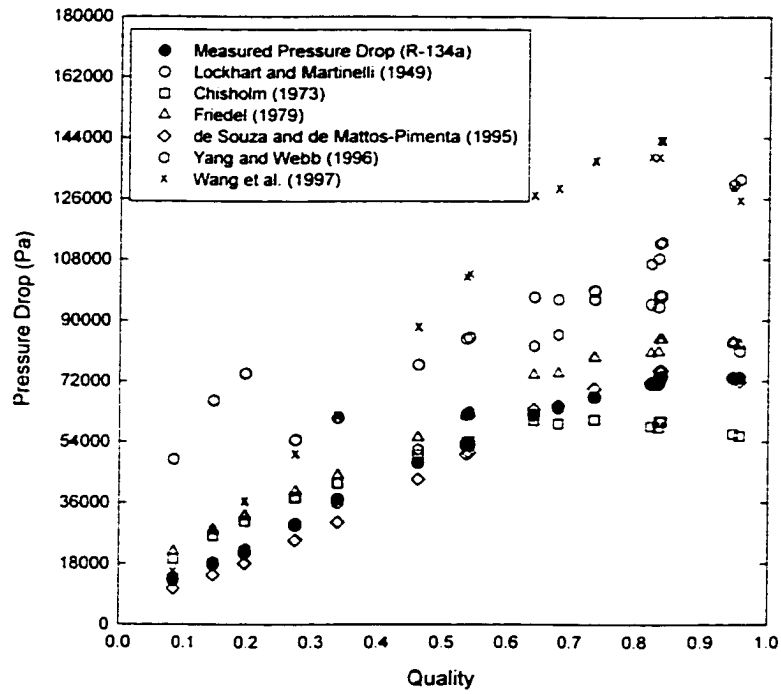


Figure G13. Comparison of the C30 Tube ($D_h = 0.762$ mm) with the Literature ($G \cong 750$ kg/m²-s)

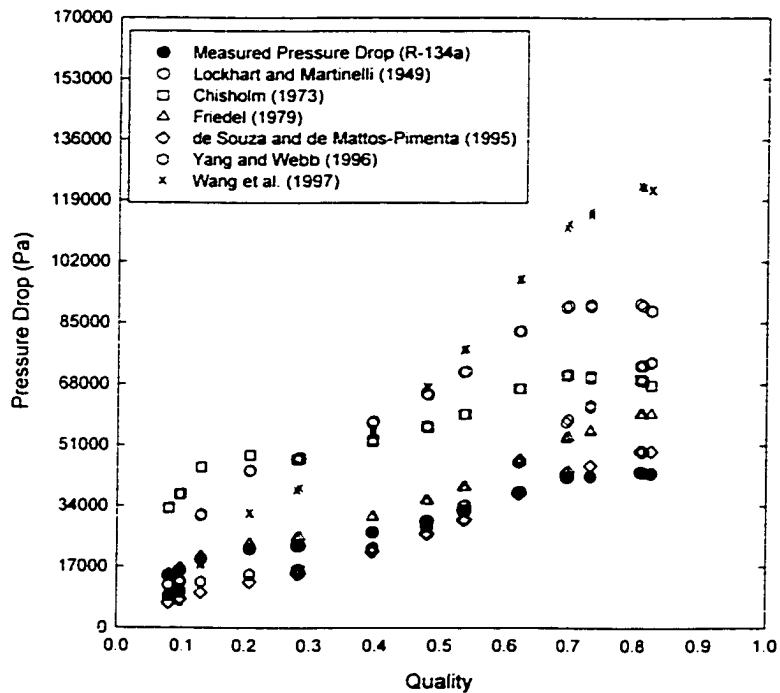


Figure G14. Comparison of the C20 Tube ($D_h = 0.508$ mm) with the Literature ($G \cong 450$ kg/m²-s)

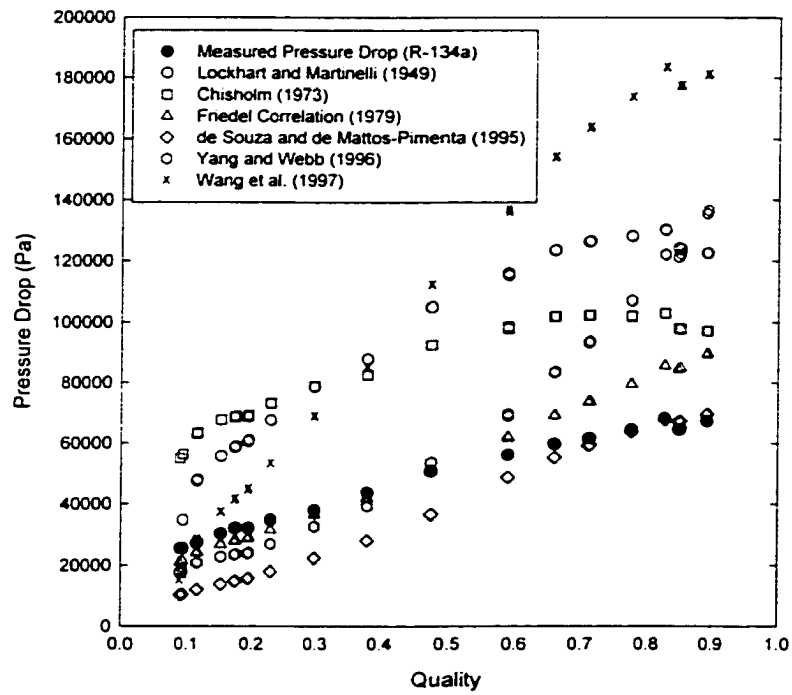


Figure G15. Comparison of the C20 Tube ($D_h = 0.508$ mm) with the Literature ($G \cong 600$ kg/m²-s)

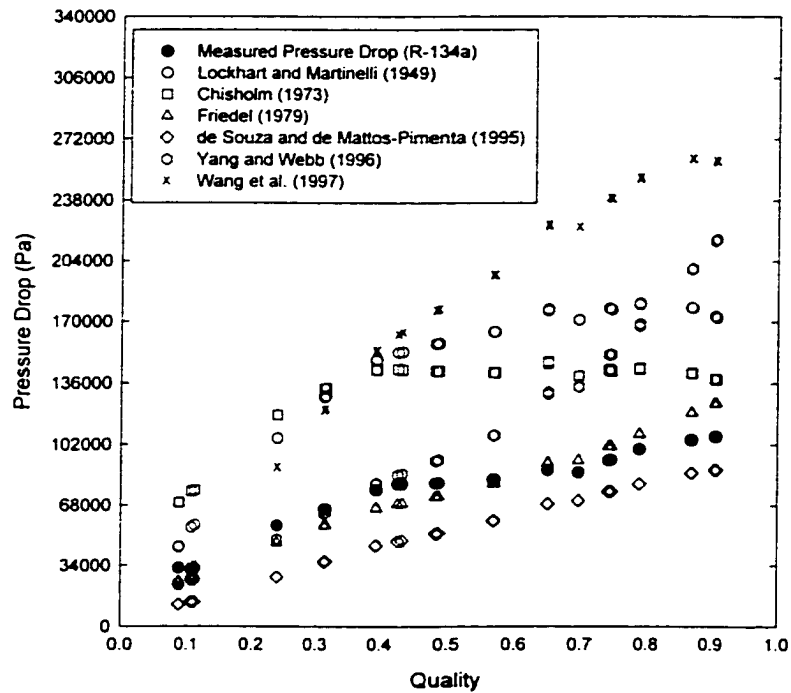


Figure G16. Comparison of the C20 Tube ($D_h = 0.508$ mm) with the Literature ($G \cong 750$ kg/m²-s)

REFERENCES CITED

- Agrawal, S. S., Gregory, G. A., and Govier, G. W., 1973, "An Analysis of Horizontal Stratified Two Phase Flow in Pipes," *Can. J. Chem. Eng.*, **Vol. 51**, pp. 280-286.
- Akagawa, K., Hamaguchi, H., Sagaguchi, T., and Ikari, T., 1971, "Studies on the Fluctuation of Pressure Drop in Two-Phase Slug Flow," *Bulletin of the JSME*, **Vol. 14(71)**, pp. 455-469.
- Al-Sheikh, J. N., Saunders, D. E. and Brodkey, R. S., 1970, "Prediction of Flow Patterns in Horizontal Two-Phase Pipe Flow," *Can. J. Chem. Eng.*, **Vol. 48**, pp. 21-29.
- Alves, G. E., 1954, "Cocurrent Liquid-Gas Flow in a Pipe-Line Contactor," *Chemical Engineering Progress*, **Vol. 50(9)**, pp. 449-456.
- Anderson, R. J. and Russell, T. W. F., 1965, "Designing for Two-Phase Flow Part II," *Chem. Eng.*, pp. 99-104.
- Annunziato M. and Girardi, G., 1987, "Horizontal Two Phase Flow: A Statistical Method For Flow Pattern Recognition," *Proceedings of the 3rd Int. Conf. Multi-Phase Flow*, The Hague, Netherlands, Paper F1, pp. 169-185.
- Baker, O., 1954, "Simultaneous Flow of Oil and Gas," *Oil and Gas J.*, **Vol. 53**, pp.185-195.
- Bandel, J., 1973, "Druckverlust und Wärmeübergang Bei der Verdampfung Seidender Kältemittel im Durchströmten Waagerechten, Dissertation, University of Karlsruhe, Germany.
- Barnea, D., Luninski, Y. and Taitel, Y., 1983, "Flow Pattern in Horizontal and Vertical Two Phase Flow in Small Diameter Pipes," *Can. J. Chem. Eng.*, **Vol. 61**, pp. 617-620.
- Barnea, D., Shoham, O., Taitel, Y., and Dukler, A. E., 1980, "Flow Pattern Transition for Gas-Liquid Flow in Horizontal and Inclined Pipes," *Int. J. Multiphase Flow*, **Vol. 6**, pp. 217-225.
- Baroczy, C. J., 1965, "Correlation of Liquid Fraction in Two-Phase Flow With Applications to Liquid Metals," *Chem. Eng. Prog. Symp. Series*, **Vol. 61(57)**, pp. 179-191.
- Beattie, D. R. H. and Whalley, P. B., 1982, "A Simple Two-Phase Frictional Pressure Drop Calculation Method," *Int. J. Multiphase Flow*, **Vol. 8**, pp. 83-87.
- Beggs, H. D. and Brill, J. P., 1973, "A Study of Two-Phase Flow in Inclined Pipes," *J. Pet. Tech.*, **Vol. 25**, pp. 607-617.
- Behnia, M., 1991, "Most Accurate Two-Phase Pressure-Drop Correlation Identified," *Oil & Gas J.*, pp. 90-95.

Benjamin, T. B., 1968, "Gravity Currents and Related Phenomena," *J. Fluid Mech.*, **Vol. 31**, pp. 209-248.

Bergelin, O. P. and Gazley, C., 1949, "Co-Current Gas-Liquid Flow, I. Flow in Horizontal Tubes," Heat Transfer and Fluid Mechanics Institute, Berkeley, CA.

Boelter, L. M. K. and Kepner, R. H., 1939, "Pressure Drop Accompanying Two-Component Flow Through Pipes," *Ind. and Eng. Chem.*, **Vol. 31(4)**, pg. 426-434.

Cai, Y., Wambsganss, M. W., and Jendrzeczyk, J. A., 1996, "Applications of Chaos Theory in Identification of Two-Phase Flow Patterns and Transitions in a Small, Horizontal, Rectangular Channel," *J. Fluids Engineering*, **Vol. 118**, pp. 383-390.

Carey, Van P., 1992, *Liquid-Vapor Phase Change Phenomena*, Taylor & Francis Series in Mechanical Engineering, Hemisphere Publishing, New York, pp. 432-471.

Chae, H. B., Schmidt, J. W., and Moldover, M. R., 1990, "Surface Tension of Refrigerants R123 and R134a," *J. Chem. Engineering Data*, **Vol. 35(1)**, pp. 6-8.

Chang, S. D. and Ro, T. S., 1996, "Pressure Drop of Pure HFC Refrigerants and Their Mixtures Flowing in Capillary Tubes," *Int. J. Multiphase Flow*, **Vol. 22(3)**, pp. 551-561.

Chenoweth, J. M. and Martin, M. W., 1955, "Turbulent Two-Phase Flow," *Pet. Ref.*, **Vol. 34(10)**, pp. 151-155.

Chisholm, D., 1973, "Pressure Gradients Due to Friction During the Flow of Evaporating Two-Phase Mixtures in Smooth Tubes and Channels," *Int. J. Heat and Mass Transfer*, **Vol. 16**, pp. 347-358.

Chisholm, D. and Laird, A. D. K., 1958, "Two Phase Flow in Rough Tubes," *Trans. ASME*, **Vol. 80(2)**, pp. 276-286.

Churchill, S. W., 1977, "Friction Factor Equation Spans All Fluid Flow Regimes," *Chem. Eng.*, pp. 91-92.

Ciccitti, A., Lombardi, C., Silvestri, M., Soldaini, G. and Zavalluilli, R., 1960, "Two-Phase Cooling Experiments-Pressure Drop, Heat Transfer and Burnout Measurements," *Energia Nucleare*, **Vol. 7**, pp. 407-425.

Coleman, J. W. and Garimella, S., 1999, "Characterization of Two-Phase Flow Patterns in Small Diameter Round and Rectangular Tubes," *Int. J. Heat and Mass Transfer*, **Vol. 42(15)**, pp. 2869-2881.

Damianides, C. and Westwater, J. W., 1988, "Two Phase Flow Patterns in a Compact Heat Exchanger and in Small Tubes," *Proc. 2nd U.K. National Conf. On Heat Transfer*, Glasgow, Scotland, **Vol. II**, pp. 1257-1268.

De Souza, A. L. and De Mattos, P., 1995, "Cavitation and Multiphase Flow", *ASME FED*, **Vol. 210**, pp. 161-171.

Dobson, M. K., Chato, J. C., Hinde, D. K., and Wang, S. P., 1994, "Experimental Evaluation of Internal Condensation of Refrigerants R-12 and R-134a," *ASHRAE Transactions Symposia*, **NO-94-5-3**, pp. 744-754.

Dukler, A. E., Wicks, M. and Cleveland, R. G., 1964, "Frictional Pressure Drop in Two-Phase Flow: B. An Approach Through Similarity," *AIChE J.*, **Vol. 10**, pp. 44-51.

Dukler, A. E. and Hubbard, M. G., 1975, "A Model for Gas-Liquid Slug Flow in Horizontal and Near Horizontal Tubes," *Ind. Eng. Chem. Fundamentals*, **Vol. 14 (4)**, pg. 337-347.

Ferguson, M. E. G. and Spedding, P. L., 1995, "Measurement and Prediction of Pressure Drop in Two-Phase Flow," *J. Chem. Tech. Biotechnol.*, **Vol. 62**, pg. 262-278.

Friedel, L., 1979, "Pressure Drop During Gas/Vapour-Liquid Flow in Pipes," *Int. Chem. Eng.*, **Vol. 20**, pp. 253-267.

Fox, R. W. and McDonald, A. T., *Introduction to Fluid Mechanics*, 4th edition, John Wiley and Sons, New York, 1992, pp. 347-357.

Fukano, T., Kariyasaki, A., and Kagawa, M., 1989, "Flow Patterns and Pressure Drop in Isothermal Gas-Liquid Concurrent Flow in a Horizontal Capillary Tube," *ANS Proc. 1989 Natl. Heat Transfer Conf.*, **Vol. 4**, pp. 153-161.

Garimella, S. and Coleman, J.W., 1998, "Design of Crossflow Condensers for Ammonia-Water Absorption Heat Pumps," *ASHRAE Transactions*, **Vol. 104(1)**, pp. 1553-1564.

Garimella, S., Coleman, J. W., and Wicht, A., 1996, "Novel Geometries for Hydronic-Air Heat Exchangers in Residential Space-conditioning Applications," *Proceedings of the ASME Advanced Energy Systems Division*, AES-Vol. 36, pp. 381-394.

Garimella, S., Coleman, J. W., and Wicht, A., 1997, "Tube and Fin Geometry Alternatives for the Design of Absorption-Heat Pump Heat Exchangers," *J. Enhanced Heat Transfer*, **Vol. 4**, pp. 217-235.

Garimella S., and Wicht, A., 1995, "Air-Cooled Condensation of Ammonia in Flat-Tube, Multi-Louver Fin Heat Exchangers," *Advances in Enhanced Heat/Mass Transfer and Energy Efficiency*, ASME HTD-Vol. 320, PID-Vol. 1, pp. 47-58.

Gazley, C., and Bergelin, O. P., 1947, "A Preliminary Investigation of Two-Phase Flow," Report TPF-1, The University of Delaware (Division of Chemical Engineering).

Govier, G. W. and Aziz, K., 1972, *Flow of Complex Mixtures in Pipes*, Van Nostrand-Reinhold Co., New York, pp. 554-613.

Govier, G. W. and Omer, M. M., 1962, "The Horizontal Pipeline Flow of Air-Water Mixtures," *Can. J. Chem. Eng.*, pp. 93-104.

Govier, G. W., Radford, B. A., and Dunn, J. S. C., 1957, "The Upwards Vertical Flow of Air-Water Mixtures: I. Effect of Air and Water Rates on Flow Pattern, Holdup, and Pressure Drop," *Can. J. Chem. Eng.*, pp. 58-70.

Govier, G. W. and Short, W. L., 1958, "The Upward Vertical Flow of Air-Water Mixtures, II. Effect of Tubing Diameter on Flow Pattern, Holdup, and Pressure Drop," *Can. J. Chem. Eng.*, pp. 195-202.

Hashizume, K., Ogriwara, H. and Taniguchi, H., 1985, "Flow Pattern, Void Fraction and Pressure Drop of Refrigerant Two Phase Flow in a Horizontal Pipe," *Int. J. Multiphase Flow*, Vol. 11, pp. 643-658.

Hewitt, G. F., Shires, G. L. and Bott, T. R., 1993, *Process Heat Transfer*, CRC Press, Inc., Ann Arbor, Michigan, pp. 401-402.

Hewitt, G. F. and Roberts, D.N., 1969, "Studies of Two-Phase Flow Patterns by Simultaneous X-Ray and Flash Photography," *Atomic Energy Research Establishment*, U.K.A.E.A. Research Group, Chemical Engineering Division, Paper **AERE-M2159**.

Hoogendoorn, C. J., 1959, "Gas-Liquid Flow in Horizontal Pipes," *Chem. Eng. Sci.*, Vol. 9, pp. 205-217.

Hosler, E. R., 1968, "Flow Patterns in High Pressure Two-Phase (Steam-Water) Flow with Heat Addition," *AIChE Symp. Series*, Vol. 64, pp. 54-66.

Ide, H. and Matsumura, H., 1990, "Frictional Pressure Drop of Two Phase Gas-Liquid Flow in Rectangular Channels," *Exp. Thermal and Fluid Sci.*, Vol. 3, pp. 362-372.

Incropera, F. P. and Dewitt, D. P., *Fundamentals of Heat and Mass Transfer*, 4th edition, John Wiley and Sons, New York, pp. 449-456.

Jeffreys, H., 1925, "On the Formation of Water Waves by Wind," *Proc. Royal Soc.*, Vol. A107, pp. 189-206.

Jeffreys, H., 1926, "On the Formation of Water Waves by Wind," (Second Paper), *Proc. Royal Soc.*, Vol. A110, pg. 241.

Jenkins, R., 1947, "Two-Phase Two-Component Flow of Water and Air," M.S. Thesis, University of Delaware.

Johnson, H. A. and Abou-Sabe, A. H., 1952, "Heat Transfer and Pressure Drop for Turbulent Flow of Air-Water Mixtures in a Horizontal Pipe," *Trans. ASME*, pp. 977-987.

Jones, O. C., and Zuber, N., 1975, "The Interrelation Between Void Fraction Fluctuations and Flow Patterns in Two-Phase Flow," *Int. J. Multiphase Flow*, Vol. 2, pp. 273-306.

Kadambi, V., 1985, "Prediction of Pressure Drop and Void-Fraction in Annular Two-Phase Flows," *Can. J. Chem. Eng.*, Vol. 63, pp. 728-734.

Klein, S. A. and Alvarado, F. L., *Engineering Equation Solver*, Version 5.155, F-Chart Software, Middleton Wisconsin.

Kordyban, E. S., and Ranov, T., 1970, "Mechanism of Slug Formation in Horizontal Two-Phase Flow," *J. Basic Engineering*, pp. 857-864.

Kosky, P. G., 1971, "Thin Liquid Films Under Simultaneous Shear and Gravity Forces," *Int. J. Heat Mass Transfer*, Vol. 14, pp. 1220-1224.

Kozlov, B. K., 1954, *Zhur. Tekh. Fiz.* (Assoc. Tech Services, P. O. Box 271, East Orange, NJ), Vol. 22, pp. 2285.

Lockhart, R. W. and Martinelli, R. C., 1949, "Proposed Correlation of Data for Isothermal Two-Phase, Two-Component Flow in Pipes," *Chem. Eng. Prog.*, Vol. 45 (1), pp. 39-48.

Mandhane, J. M., Gregory, G. A., and Aziz, K., 1974, "A Flow Pattern Map for Gas-Liquid Flow in Horizontal Pipes," *Int. J. Multiphase Flow*, Vol. 1, pp. 537-553.

Mandhane, J.M., Gregory, G. A., and Aziz, K. A., 1977, "A Critical Evaluation of Friction Pressure Drop Methods for Gas Liquid Flow in Horizontal Pipes," *J. Pet. Tech.*, Vol. 29, pp. 1348-1358.

Moore, A. E. and Turley, D. N., 1983, "Two Phase Flow Information from Simple, Rapid Response Time Instruments," *Proceedings of the 1st Int. Conf. On The Physical Modeling of Multi-Phase Flow*, Coventry, England, pp. 354-376.

Nicholson, M. K., Aziz, K., and Gregory, G. A., 1978, "Intermittent Two Phase Flow in Horizontal Pipes: Predictive Models," *Can. J. Chem. Eng.*, Vol. 56, pp. 653-663.

Obot, N. T., Wambsganss, M. W. and Jendrzeczyk, J. A., 1993, "Correlation of Adiabatic Two-Phase Pressure Drop Using the Frictional Law of Corresponding States," *J. Fluids Eng.*, Vol. 115, pp. 317-323.

- Olujic, Z., 1985, "Predicting Two-Phase Flow Friction Loss in Horizontal Pipes," *Chem. Eng.*, pp. 45-50.
- Quandt, E. R., 1965, *AIChE J.*, **Vol. 11**, pg. 311.
- Richardson, B. L., 1959, "Some Problems in Horizontal Two-Phase Two-Component Flow," Ph.D. Dissertation, Purdue University, West Lafayette, Indiana.
- Soliman, H. M., 1982, "On the Annular-to-Wavy Pattern Transition during Condensation Inside Horizontal Tubes," *Can. J. Chem. Engineering*, **Vol. 60**, pp. 475-481.
- Soliman, H. M., 1986, "The Mist-Annular Transition During Condensation and its Influence on the Heat Transfer Mechanism," *Int. J. Multiphase Flow*, **Vol. 12(2)**, pp. 277-288.
- Soliman, H. M., Schuster, J. R., and Berenson, P. J., 1968, "A General Heat Transfer Correlation for Annular Flow Condensation," *J. Heat Transfer Trans. ASME, Series C*, **Vol. 90(2)**.
- Storek, H. and Brauer, H., 1980, "Reibungsdruckverlust der adiabaten Gas/Flüssigkeit-Strömung in Horizontalen Und Vertikalen Rohren", VDI-Forsch-Heft, pp. 599.
- Suo, M. and Griffith, P., 1964, "Two-Phase Flow in Capillary Tubes," *J. Basic Engineering*, pp. 576-582.
- Taitel, Y. and Dukler, A. E., 1976, "A Model for Predicting Flow Regime Transitions in Horizontal and Near Horizontal Gas-Liquid Flow," *AIChE J.*, **Vol. 22(1)**, pp. 47-55.
- Tandon, T. N., Varma, H. K., and Gupta, C. P., 1985, "Prediction of Flow Patterns During Condensation of Binary Mixtures in a Horizontal Tube," *Trans. ASME*, **Vol. 107**, pp. 424-430.
- Thom, J. R. S., 1964, "Prediction of Pressure Drop During Forced Circulation of Boiling Water," *Int. J. Heat Mass Transfer*, **Vol. 7**, pp. 709-724.
- Traviss, D. P. and Rohsenow, W. M., 1973, "Flow Regimes in Horizontal Two-Phase Flow With Condensation," *ASHRAE Transactions*, **Vol. 79**, pp. 31-39.
- Troniewski, L. and Ulbrich, R., 1984, "Two-Phase Gas-Liquid Flow in Rectangular Channels," *Chem. Eng. Sci.*, **Vol. 39**, pp. 751-765.
- Wallis, G. B., 1965, *One-Dimensional Two-Phase Flow*, John Wiley and Sons, New York.
- Wallis, G. B., and Dobson, J. E., 1973, "The Onset of Slugging in Horizontal Stratified Air-Water Flow," *Int. J. Multiphase Flow*, **Vol. 1**, pp. 173-193.

- Wambsganss, M. W., Jendrzejczyk, J. A., and France, D. M., 1991, "Two-Phase Flow Patterns and Transitions in a Small, Horizontal, Rectangular Channel," *Int. J. Multiphase Flow*, **Vol. 17(3)**, pp. 327-342.
- Wambsganss, M. W., Jendrzejczyk, J. A., and France, D. M., 1994, "Determination and Characteristics of the Transition to Two-Phase Slug Flow in Small Horizontal Channels," *J. Fluids Engineering*, **Vol. 116**, pp. 140-146.
- Wang, C., Chiang, C., Lin, S., and Lu, D., 1997, "Two-Phase Flow Pattern for R-134a Inside a 6.5-mm (0.25-in.) Smooth Tube," *ASHRAE Transactions*, PH-97-10-2, **Vol. 103(1)**.
- Wang, C., Chang, Y., Kuo, C. S. and Lu, D. C., 1996, "Two-Phase Flow Heat Transfer and Friction Characteristics of R-22 and R-407C," *ASHRAE Trans. Symp.*, AT-96-12-3, pp. 830-838.
- Weisman, J., Duncan, D., Gibson, J. and Crawford, T., 1979, "Effects of Fluid Properties and Pipe Diameter on Two-Phase Flow Patterns in Horizontal Lines," *Int. J. Multiphase Flow*, **Vol. 5**, pp. 437-462.
- White, P. D. and Huntington, R. L., 1955, "Horizontal Co-Current Two-Phase Flow of Fluids in Pipe Lines," *Petroleum Engineer*, pp. D40 - D45.
- Wilmarth, T. and Ishii, M., 1994, "Two-Phase Flow Regimes in Narrow Rectangular Vertical and Horizontal Channels," *Int. J. Heat Mass Trans.*, **Vol. 37(12)**, pp. 1749-1758.
- Wong, T. N. and Yau, Y. K., 1997, "Flow Patterns in Two-Phase Air-Water Flow," *Int. Comm. Heat Mass Transfer*, **Vol. 24(1)**, pp. 111-118.
- Yan, Y. and Lin, T., 1998, "Evaporation Heat Transfer and Pressure Drop of Refrigerant R-134a in a Small Pipe," *Int. J. Heat and Mass Transfer*, **Vol. 41**, pp. 4183-4194.
- Yang, C. Y. and Webb, R. L., 1996, "Friction Pressure Drop of R-12 in Small Hydraulic Diameter Extruded Aluminum Tubes With and Without Micro-fins," *Int. J. Heat Mass Transfer*, **Vol. 39(4)**, pp. 801-809.
- Zivi, S. M., 1964, "Estimation of Steady-State Steam Void-Fraction by Means of the Principle of Minimum Entropy Production," *J. Heat Transfer*, **Vol. 86**, pp. 247-252.

BIOGRAPHICAL SKETCH

John Wesley Coleman was born on July 13, 1968 in Dearborn, Michigan. Son of John Wesley and Terry May Coleman, he graduated from the University of Michigan, Ann Arbor, with a Bachelors degree in German Literature and Mechanical Engineering. John received his Masters degree from Western Michigan University in Kalamazoo, and his Doctorate from Iowa State University in Ames Iowa, both in Mechanical engineering. He has been the recipient of several awards including the Outstanding Student Leader of the Year Award (1989) from the University of Michigan, Special Resolutions Honor and Special Recognition Award from the Michigan Society of Professional Engineers (1990), Western Michigan University Departmental Graduate Research and Creative Scholar Award (1996) and All-University Graduate Research and Creative Scholar Award (1997), Phi Kappa Phi (1999), and the ASHRAE Grant-in-Aid Scholarship (1999). John has made several contributions to the literature with publications in the International Journal of Heat and Mass Transfer, ASHRAE Transactions, and the Journal of Enhanced Heat Transfer. John is a member of the Epeians honor society, the Order of Omega, ASHRAE, ASME and he is listed in Marquis' *Who's Who in America*.